# EFFECT OF MICHIGAN MULTI-AXLE TRUCKS ON PAVEMENT DISTRESS

Volume II – Flexible Pavements

Karim Chatti, Ph.D.
Anshu Manik, Ph.D.
Hassan Salama, Ph.D.
Chadi El Mohtar, Ph.D.
Hyung Suk Lee, M.S.

**Michigan State University**
**Department of Civil and Environmental Engineering**
**Pavement Research Center of Excellence**


Final Report
Volume II
Project RC-1504

February 2009

**Technical Report Documentation Page**

| 1. Report No. | 2. Government Accession No. | 3. MDOT Project Manager |
|---|---|---|
| RC-1504 | | Mr. Mike Eacker |

| 4. Title and Subtitle | 5. Report Date |
|---|---|
| EFFECT OF MICHIGAN MULTI-AXLE TRUCKS ON PAVEMENT DISTRESS AND PROFILE<br>Volume II – Flexible Pavements | February 2009 |
| | **6. Performing Organization Code** |

| 7. Author(s) | 8. Performing Org. Report No. |
|---|---|
| Karim Chatti, Anshu Manik, Hassan Salama, Nicholas Brake, Syed W. Haider, Chadi El Mohtar, Hyung Suk Lee | |

| 9. Performing Organization Name and Address | 10. Work Unit No. (TRAIS) |
|---|---|
| Department of Civil and Environmental Engineering<br>Michigan State University<br>East Lansing, MI 48823 | **11. Contract No.** |
| | **11(a). Authorization No.** |

| 12. Sponsoring Agency Name and Address | 13. Type of Report & Period Covered |
|---|---|
| Michigan Department of Transportation<br>Construction & Technology Division<br>8885 Ricks Road<br>Lansing, MI 48909 | Final Report |
| | **14. Sponsoring Agency Code** |

**15. Supplementary Notes**
Volume II of III

**16. Abstract**

With the adoption of the new mechanistic-empirical pavement design method and the employment of axle load spectra, the question of evaluating the pavement damage resulting from different axle and truck configurations has become more relevant. In particular, the state of Michigan is unique in permitting several heavy truck axle configurations that are composed of up to 11 axles, sometimes with as many as 8 axles within one axle group. Thus, there is a need to identify the relative pavement damage resulting from these multiple axle trucks.

The study looked at both flexible and rigid pavement systems, and comprised of three main components: (1) in-service pavement performance data; (2) laboratory testing under multiple axles, and (3) mechanistic-empirical analyses. The results from in-service pavement performance data indicated that multiple axle groups appear to cause less damage in fatigue per load carried for both pavement types, whereas they cause more damage in rutting of flexible pavements and roughness for rigid pavements. Laboratory testing of asphalt concrete confirmed that multiple axles cause less fatigue damage per load carried, and that rutting is nearly proportional to the number of axles within an axle group. Results from flexural concrete beam fatigue testing showed significant variability; multiple linear regression analysis (independent variables: stress ratio, stress impulse and initial modulus of elasticity) indicated, on average, similar findings to asphalt concrete fatigue for a given stress ratio; however, mechanistic analysis showed that multiple axles cause considerable stress reduction leading to significantly lower fatigue damage. The mechanistic analysis also showed that multiple axles cause more faulting in rigid pavements. Mechanistic analyses of flexible pavements confirmed that multiple axles cause less fatigue damage per load carried, and rutting damage that is nearly proportional to the number of axles within an axle group. However, the mechanistic-empirical results suggest that the AASHTO Load Equivalency Factors (LEF) for large axle groups may be unconservative. Finally, Full scale slab testing to study joint/crack deterioration in plain concrete pavements was inconclusive.

| 17. Key Words | 18. Distribution Statement |
|---|---|
| Multi-Axle Trucks, Michigan Trucks, Pavement Distress, Truck Factors | No restrictions. This document is available to the public through the Michigan Department of Transportation. |

| 19. Security Classification - report | 20. Security Classification - page | 21. No. of Pages | 22. Price |
|---|---|---|---|
| Unclassified | Unclassified | 295 | |

**TABLE OF CONTENTS**

## LIST OF FIGURES

## LIST OF TABLES

# CHAPTER 1
# INTRODUCTION

## 1.1 INTRODUCTION

The state of Michigan hosts several trucks that have unusual axle configurations, up to eleven axles and 164 kips in gross weight and 8 axles within an axle group. The relationship between these trucks and pavement distresses has not been determined, since earlier research studies have not addressed the damage caused by multiple axle/truck configurations. Therefore, there is a need to examine the relative effect of these heavy vehicles on pavement distresses using field data from in-service pavements, laboratory experimentation, and mechanistic analyses.

Analysis of in-service data, shown in Volume I of this report, indicated that multiple axles may be less damaging per load carried in cracking, while they may cause more rutting in flexible pavements. In this volume, the analyses are focused on asphalt pavements by simulating the effect of these Michigan multiple axle trucks using laboratory testing in fatigue and rutting modes and mechanistic analysis to further explain their relative effect on pavement damage. The conclusions and recommendations of this research can be accomplished by combining the findings using in-service data with those from mechanistic analysis and the laboratory experiments.

## 1.2 RESEARCH OBJECTIVE

The objective of the research conducted in this part of the study is to determine the effect of heavy multi-axle Michigan trucks on asphalt pavement fatigue cracking and rutting. This was accomplished in the laboratory using cyclic fatigue and rut testing under multiple load pulse configurations, and with mechanistic analysis.

## 1.3 RESEARCH APPROACH

In addition to the investigation of in-service pavement traffic and distress data presented in volume I, the research problem was investigated using: 1) laboratory experimentation, and 2) mechanistic analysis. A brief description of each approach follows.

### 1.3.1 Laboratory experiments

The indirect tensile cyclic test with loading cycles that simulate different axle/truck configurations was used to examine their relative effect on fatigue cracking of an asphalt mixture. The unconfined compression cyclic load test with similar loading cycles was used to examine their relative effect on permanent deformation of an asphalt mixture. Five different axle configurations and five different truck configurations were studied.

### 1.3.2 Mechanistic analysis

The mechanistic based computer programs SAPSI-M and KENPAVE were used to analyze the effect of multiple axles on fatigue and rutting, respectively, of different pavement structures. The SAPSI-M program was needed to calculate the dissipated energy density per cycle, which correlated best with fatigue failure under multiple axles. Also, the mechanistic-empirical rutting model (VESYS), calibrated using field data from the SPS-1 experiment, was used to predict the rutting in the various layers within the pavement structure.

## 1.4 REPORT ORGANIZATION

This report consists of four volumes:

Volume I: Includes background information, literature review and statistical analyses using truck traffic and pavement performance data from in-service pavements.

Volume II: Contains the analyses pertaining to asphalt pavements, including laboratory fatigue and rut data, and mechanistic analysis. Conclusions from the study, implications for design and implementation recommendations as well as recommendations for future research are presented.

Volume III: Contains the analyses pertaining to concrete pavements, including laboratory fatigue and joint deterioration data, and mechanistic analysis. Conclusions from the study, implications for design and implementation recommendations as well as recommendations for future research are presented.

This volume is divided into six chapters:

Chapter 1 presents some background information, the research objective and approaches used.
Chapter 2 presents the laboratory fatigue investigation of asphalt concrete under multiple load pulses.
Chapter 3 contains the mechanistic analyses for asphalt concrete fatigue.
Chapter 4 contains the calibration of the mechanistic-empirical rutting model for the various flexible pavements layers using in-service data from the long-term pavement performance (LTPP) SPS-1 experiment.
Chapter 5 presents the laboratory rutting investigation of asphalt concrete under multiple load pulses.
Chapter 6 contains the mechanistic analyses for rutting of asphalt pavement systems.

# CHAPTER 2
# FATIGUE CRACKING – LABORATORY INVESTIGATION

## 2.1 INTRODUCTION

Determining the strength and fatigue life characteristics of asphalt based mixes has been a major focus of research and testing since the early 1960's. Many different accelerated tests were developed and studied to determine the long term performance of the asphalt mixes. Different test procedures ended up giving various results depending on the testing setup and conditions and approaches used in analyzing the results. Tests such as the Flexural Beam, Trapezoidal, Direct Tension, Tri-axial and Indirect Tensile tests have been used to develop models for a new mechanistic approach in pavement design. Some of these tests were performed under controlled stress mode while others were conducted under controlled strain mode. This resulted in different approaches when analyzing the results. One approach is to monitor the stresses in the tested specimens; another involves monitoring the strains and permanent deformations. A new approach has been proposed in the recent years in which the dissipated energy is used as the criterion for failure. This method incorporates viscoelastic properties of materials and tries to establish relationships between the repetitive load applications to the materials by accounting for both stresses and strains simultaneously. The main purpose of this research is to come up with an energy formulation for the indirect tensile test predicting the performance of asphalt based mixtures under different axle configurations. By using laboratory test results, energy based criteria and laws would be established for fatigue life prediction and determining Load Equivalency Factors (LEFs) for different axles and truck configurations.

## 2.2 SAMPLE PREPARATION

This section details the specimen preparation procedure including compaction and surface preparation prior to testing. Four 30 kg bags of HMA were obtained from the Spartan Asphalt mix plant for two typical MDOT mixes: 4E3 and 4E10. The bags were labeled and stored in the lab at room temperature. To prepare a 4-inch diameter, 2.5- inch thick sample, it will require 1 to 1.3 kg of the mix. Thus each bag can be used to prepare about 25 samples. More detailed calculations are presented later in this section.

### 2.2.1 Determining Mass Required For Each Sample

Knowing the target air void ($V_a$) and the maximum theoretical specific gravity of the asphalt concrete mix ($G_{mm}$), the bulk specific gravity of the compacted sample can be calculated using the following equation:

$$G_{mb} = G_{mm}(1 - V_a) \tag{2.1}$$

Knowing the expected bulk specific gravity and volume of the sample, we can calculate the required mass using the following equation:

$$M = G_{mb} * \rho_w * V \tag{2.2}$$

Where: $\rho_w$ is the density of water,
$V$ is the final volume of the compacted specimen

First, a trial specimen is compacted. The actual specific gravity, volume and air void content of the specimen are determined by running a specific gravity test (details on specimen preparation and specific gravity test calculations are discussed later). Then the actual height of the specimen is measured. The difference between the theoretical and measured height, volume and air void content can be explained by looking at Figures 2.1A and 2.1B. All the calculations, performed before the test, are based on Figure 2.1A. The target air void includes the voids within the specimen only, and not those between the asphalt and the mold, as shown in Figure 2.1B. Thus, the calculated mass is more than the required one since the voids between the asphalt and the compaction mold occupy some volume without using any of the asphalt mix. Therefore, the actual air void of the sample is lower than the expected $V_a$ and the actual height is larger.

The volume of the sample calculated from specific gravity test does not include the external voids. Knowing the actual height of the sample, the theoretical volume (assuming a perfect disc without external voids) can be calculated from the equation:

$$V_{Th} = \pi * R^2 * H \tag{2.3}$$

From the theoretical volume and the actual specimen volume, the volume of the external voids can be determined as follows:

$$V_{External\,Voids} = V_{Th} - V_{Sample} \tag{2.4}$$

A corrected mass can now be calculated by modifying equation (2.2):

$$M = G_{mb} * \rho_w * \left[ V_{Th} - \left( V_{External\,Voids} * \frac{2.5}{H} \right) \right] \tag{2.5}$$

### 2.2.2 Specimen Compaction

The following details the procedure for compacting the specimens:

i) The target air void content of each asphalt mix was set to 4%.

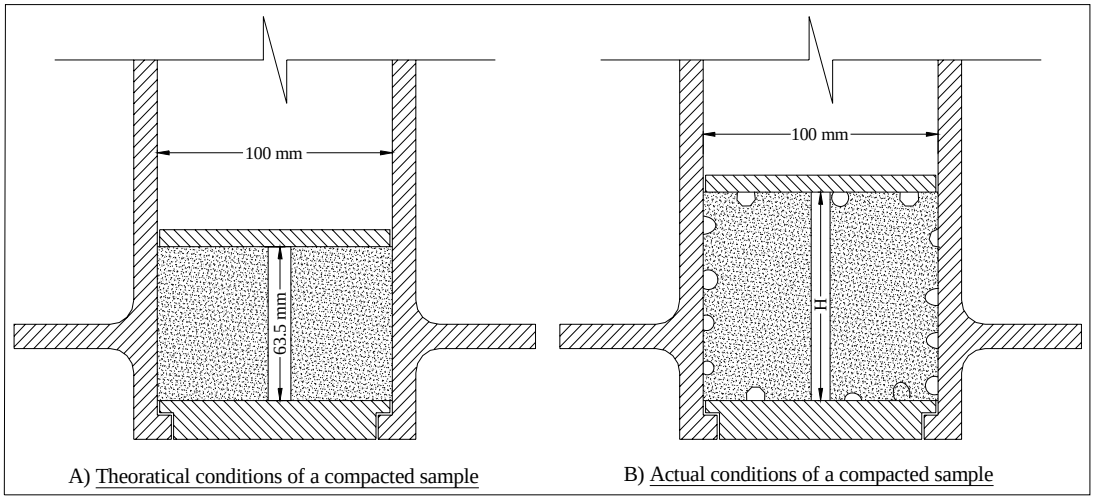


Figure 2.1. Gyratory Compaction Mold

ii) Each bag is placed in a conventional oven preset at 90$^{o}$C (194$^{o}$F) for eight hours. This would increase the workability of the mix, and allow easy extraction from the bags.

iii) The asphalt is then extracted from the bag and inspected for any impurities or asphalt and aggregate lumps. All impurities, such as threads from the bag or any other materials, are taken out, and all the lumps of asphalt are broken down. The loose asphalt is then remixed and distributed into mixing bowls such that there is enough mix in each bowl for three specimens (since three compaction molds were used). The samples are then covered with aluminum foil and stored. (Note that the final weight required for each specimen was determined as mentioned in the previous section after a first trial specimen). The same steps used in this procedure apply to the first specimen preparation with the exception that the amount of asphalt mix placed in the mixing bowl was for one specimen instead of three.

iv) One bowl at a time is placed in a conventional oven preset at 140$^{o}$C (284$^{o}$F) for 3 hours.

v) The three sets of compaction molds (each set includes a compaction mold, bottom plate and upper plate) are placed in a conventional oven preset at 140$^{o}$C (284$^{o}$F) one and a half hour before compaction.

vi) One set of compaction mold and plates are moved from the oven. The bottom plate is first placed in the mold and a paper disk is placed over it.

vii) The mixing bowl is removed from the oven and the predetermined weight of asphalt mix for one specimen is added to the mold. The mixing bowl is re-covered with the aluminum foil and returned to the oven.

viii) Another disk paper is placed on top of the asphalt mix in the mold and the upper plate is placed over it. The mold is then placed in the gyratory compactor, and compaction starts. The gyratory compactor is set as follows:

Table 2.1. Gyratory Compactor Setup

| Setup | Value |
|---|---|
| Angle of tilt | $1.25^{o}$ |
| Loading ram pressure | 600 kPa |
| Rotation speed | 30 rpm |
| Specimen height | 2.5” |

ix) Once the compaction is complete, the mold is removed from the compactor and the specimen is extracted from the mold. The disk papers are removed, and the specimen is left to cool down.

x) Steps (vi) to (ix) are repeated twice for the second and third molds. The remaining asphalt mix is thrown away.

xi) The samples are given 3 digit numbers. The first digit represents the mix type where 1 stands for the 4E3 mix and 2 stands for the 4E10 mix. The second two digits represent the order in which the sample was compacted. For example, the fifth sample that was compacted using the 4E3 mix will have the number 105.

### 2.2.3 Specific Gravity Test

The bulk specific gravity tests were performed according to ASTM D-2726 standard test procedure [12]. The ASTM procedure defines the bulk specific gravity as the ratio of the mass of a given volume of material at $25^{o}$C to the mass of an equal volume of water at the same temperature. The bulk specific gravity of the mix, $G_{mb}$, is calculated as shown in equation (2.6):

$$G_{mb} = \frac{W_{dry\ in\ air}}{(W_{SSD} - W_{Submerged}) * \rho_w} \qquad (2.6)$$

Where: $W_{dryinair}$ is the dry weight of the specimen
$W_{SSD}$ is the weight of the specimen saturated surface dry
$W_{Submerged}$ is the submerged weight of the specimen
$\rho_w$ is the density of water

The volume of the specimen and its air void content are calculated as shown in equations (2.7) and (2.8), respectively:

$$V_{sample} = (W_{SSD} - W_{Submerged}) * \rho_w \qquad (2.7)$$

$$Va\% = \frac{G_{mm} - G_{mb}}{G_{mm}} * 100 \qquad (2.8)$$

Where: $Va\%$ is the air void content
$G_{mm}$ is the maximum theoretical specific gravity of the asphalt mix

### 2.2.4 Specimen Surface Preparation

This procedure is conducted on all samples that are to be tested using the Indirect Tensile Cyclic Load Test (ITCLT). The purpose of this procedure is to provide a smooth surface for the Linear Variable Displacement Transformer (LVDT) to reduce noise in the monitored deformation signals.

i) Check the perimeter of the specimen along its thickness, and mark the two smoothest diagonally opposite sides. These sides will be used as the seating sides, and no patching would be applied to these areas.

ii) Seat the sample in a similar position to the one in the loading frame with the two smooth surfaces lying on the vertical diameter. Draw a line along the specimen vertical diameter and another one perpendicular to it on each of the specimen faces. Draw a line along the thickness of the specimen connecting the ends of the horizontal lines on both faces.

iii) Apply plaster patching on the intersection of the two lines (described in item (ii) above) on both faces of the specimen. Figure 2.2 shows the location of the patching on a specimen.

iv) Let the patching set for at least 4 hours. Using a sand paper number 150, remove all excess plaster over the patched area until there is no more plaster thickness. The asphalt mix should appear inside the patch and the plaster will be only filling the surface cavities.

Figure 2.3a shows an actual specimen before patching with the smooth surfaces located at the top and bottom. Figure 2.3 b shows the specimen after the plaster was applied. Figure 2.3c shows the specimen in its final condition ready to be tested. The black dots inside the plaster show that the thickness of the patch is just enough to fill the surface cavities.

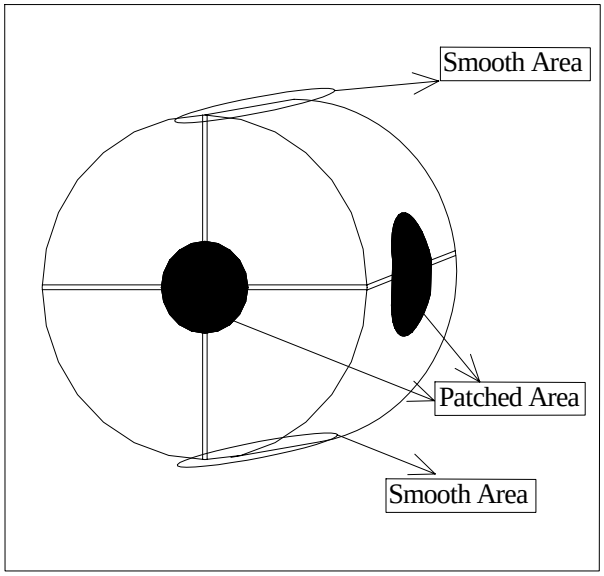


Figure 2.2. Patching Location

a) Mark the smoothest surface

b) Apply the plaster

c) Remove extra plaster with a sand paper

Figure 2.3. Specimen Patching

## 2.3 INDIRECT TENSILE TEST

The Indirect Tensile Test (ITT) is conducted by applying a vertical compressive strip load on a cylindrical specimen. The load is distributed over the thickness of the specimen through two loading strips at the top and bottom as shown in Figure2.4. The strips are curved at the interface with the specimen and have a radius equal to that of the specimen to ensure full contact over the entire seating area.

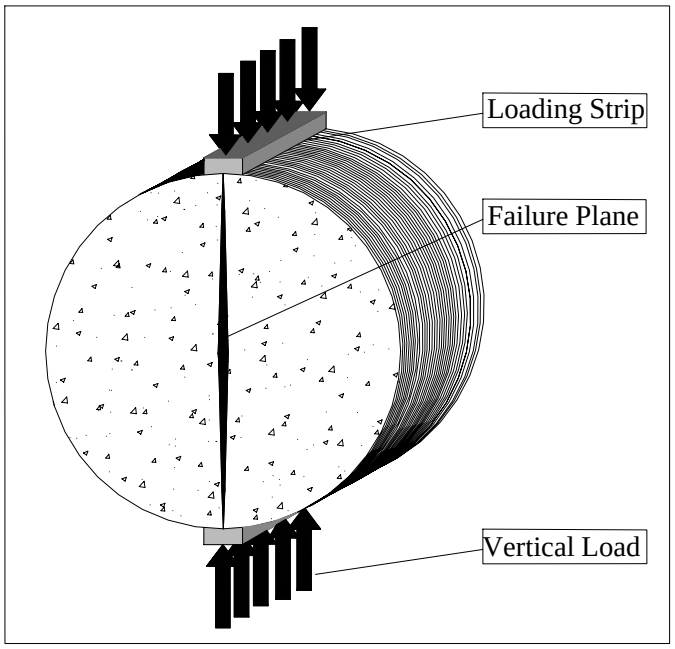


Figure 2.4. ITT Setup

This combination of specimen geometry and boundary conditions induce tensile and compressive stresses along both the vertical and horizontal diameters (Figure2.5). The tensile stresses, developed perpendicular to the direction of the load, have a relatively constant value over a large portion of the vertical diameter. This would result in the failure of the specimen by splitting along the vertical diameter as shown in Figure2.4. Note that under high vertical loads, local shear failure might occur near the loading strips.

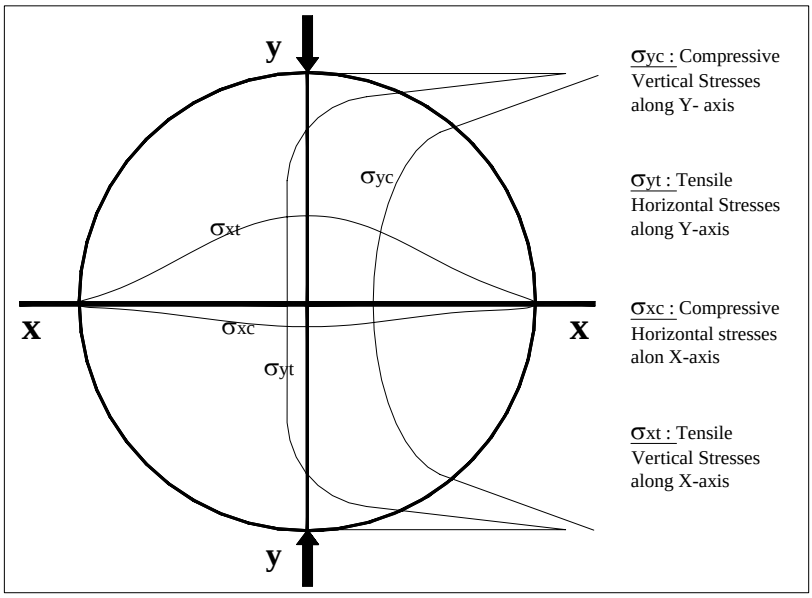


Figure 2.5. Stresses in ITT Specimen

The specimens for the ITT test are normally 4.0 inch or 6.0 inch in diameter with 0.5 or 0.75 inches wide loading strips, respectively. The thickness of the specimen ranges between 2.5 and 3.0 inches. For this report, all the specimens tested have a 4.0 inch diameter and 2.5 inch thickness with a 0.5 inch wide loading strip.

Five LVDTs are used to measure the response of the specimen to the loading. Two LVDTs are aligned horizontally along the thickness of the specimen (parallel to the loading strip) and the summation of these two reading results in the Longitudinal Deformation ($D_L$). Another two LVDTs are set horizontally, but along the diameter of the specimen (that is, perpendicular to the loading strip), and the summation of these two readings gives the Horizontal Deformation ($D_h$). Note that ($D_h$) is along the tensile stresses causing the specimen to fail. The final LVDT is used to monitor the vertical deformation. Figure 2.6 shows the LVDT configuration. Figure 2.7 shows the actual test setup.

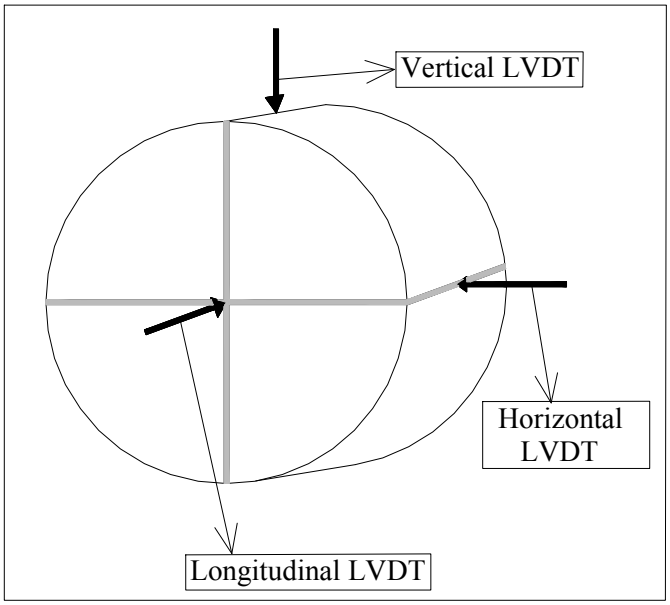


Figure 2.6. LVDT Configuration

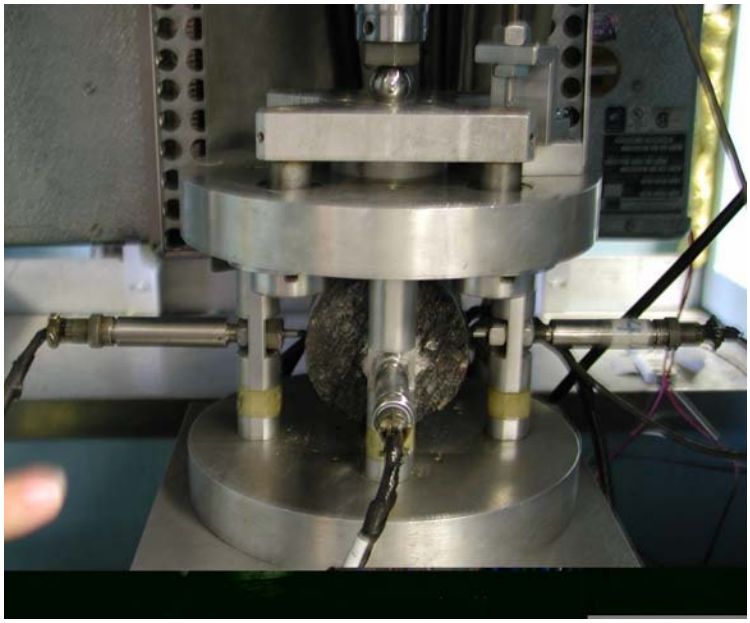

Figure 2.7. Actual ITT Setup

### 2.3.1 Analytical Models

The analytical models used to calculate stresses and strains in a cylindrical asphalt mix are based on plane stress theory and thus, the stresses and strains along the thickness are neglected. Additionally, these models assume that the asphalt concrete mix is homogenous, isotropic, and behave according to the theory of elasticity. Vertical and horizontal stresses and strains have a closed-form solution relating them to the applied

load, measured deformations, and Poison's ratio [1, 13]. For all later calculations, a Poison's ratio of 0.35 is assumed as suggested by ASTM D4123 [14]. The tensile stress ($\sigma_x$) and the compressive stress ($\sigma_y$) can be determined from the following equations (Figure2.8):

$$\sigma_x = \frac{-2qR}{\pi * L} * \{ \int_{-\phi o}^{\phi o} \frac{(\cos\theta_1) * [\sin^2(\phi + \theta_1)]}{r1} d\phi + \int_{-\phi o}^{\phi o} \frac{(\cos\theta_2) * [\sin^2(\phi - \theta_2)]}{r2} d\phi - \frac{\phi o}{R} \} \quad (2.9)$$

$$\sigma_y = \frac{-2qR}{\pi * L} * \{ \int_{-\phi o}^{\phi o} \frac{(\cos\theta_1) * [\cos^2(\phi + \theta_1)]}{r1} d\phi + \int_{-\phi o}^{\phi o} \frac{(\cos\theta_2) * [\cos^2(\phi - \theta_2)]}{r2} d\phi - \frac{\phi o}{R} \} \quad (2.10)$$

where $q = \dfrac{Po}{2R(\sin\phi o)}$

$$Po = \int_{-\phi o}^{\phi o} qR(\cos\phi) d\phi = 2qR\sin\phi o$$

$Po$ = applied total load (lb)

$$r1 = \sqrt{x^2 + (R-y)^2}, \quad r2 = \sqrt{x^2 + (R+y)^2}$$

$$\sin\theta_1 = \frac{x}{\sqrt{(R-y)^2 + x^2}}, \quad \cos\theta_1 = \frac{(R-y)}{\sqrt{(R-y)^2 + x^2}}$$

$$\sin\theta_2 = \frac{x}{r2}, \quad \cos\theta_2 = \frac{R+y}{r2}$$

L = thickness of specimen and R = radius of specimen

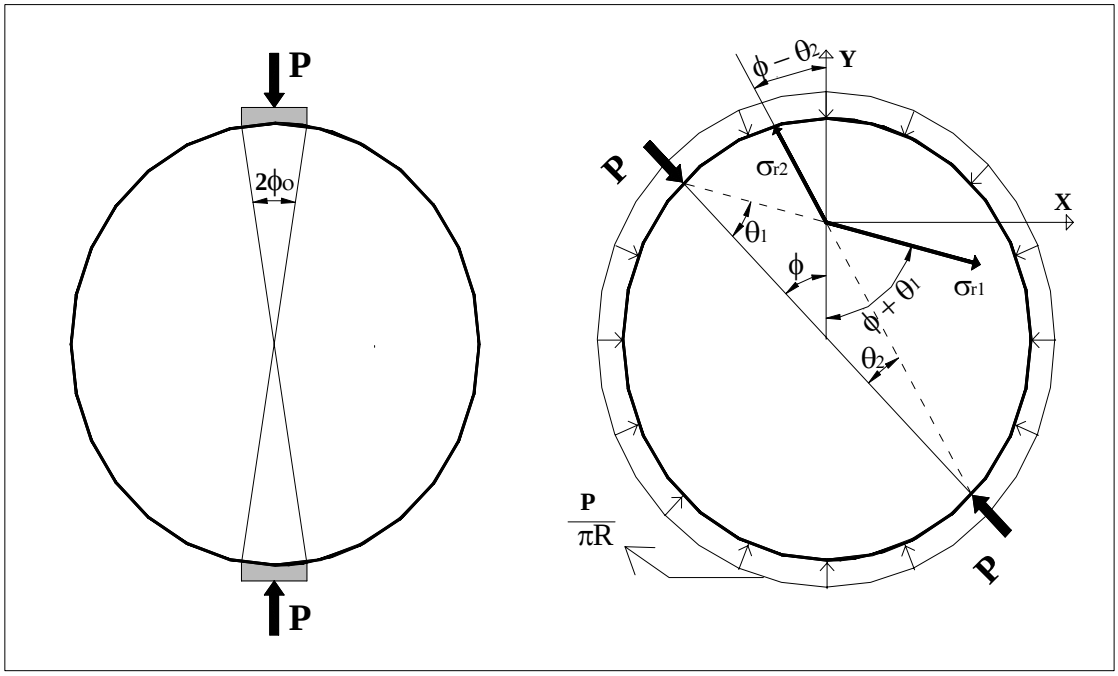


Figure 2.8. Stresses in a Circular Disk Subjected to a Frictionless Strip Loading (Baladi, 1988)

The stresses are maximum at the center where x=0 and y=0. For a 4 inch diameter specimen and a 0.5 inch wide loading strip, the maximum stresses can be calculated from equations (2.9) and (2.10) to be:

$$\sigma_x = 0.156241 * \frac{Po}{L} \tag{2.11}$$

$$\sigma_y = -0.475386 * \frac{Po}{L} \tag{2.12}$$

From plane elasticity theory,

$$\varepsilon_x = \frac{1}{E} * (\sigma_x - \upsilon * \sigma_y) \tag{2.13}$$

$$\varepsilon_y = \frac{1}{E} * (\sigma_y - \upsilon * \sigma_x) \tag{2.14}$$

Where,

E is the elastic modulus of specimen

$\upsilon$ is Poisson's ratio

The horizontal tensile strain ($\varepsilon_x$) along the horizontal diameter of the indirect tensile specimen under the strip loading can be written as:

$$\varepsilon_x = \frac{1}{\pi * L * E} * [-4 * q * (\frac{0.501 - 1.984 * \frac{1}{x^2+4} - 0.496 * \frac{x^2}{x^2+4}}{x^2+4} - 0.063) + 1.4 * q * (\frac{0.501 + 1.984 * \frac{1}{x^2+4} - 0.496 * \frac{x^2}{x^2+4}}{x^2+4} - 0.063)] \tag{2.15}$$

The vertical compressive strain ($\varepsilon_y$) along the horizontal diameter of the indirect tensile specimen under the strip loading can be written as:

$$\varepsilon_y = \frac{1}{\pi * L * E} * [-4 * q * (\frac{0.501 + 1.984 * \frac{1}{x^2+4} - 0.496 * \frac{x^2}{x^2+4}}{x^2+4} - 0.063) + 1.4 * q * (\frac{0.501 - 1.984 * \frac{1}{x^2+4} + 0.496 * \frac{x^2}{x^2+4}}{x^2+4} - 0.063)] \tag{2.16}$$

Integration of equations (2.15) and (2.16) along the horizontal diameter of the specimen produces the equation for the horizontal and the vertical deformations:

$$D_h = 0.6159 * \frac{Po}{L * E} \tag{2.17}$$

$$D_v = -1.0895 * \frac{Po}{L * E} \tag{2.18}$$

The largest horizontal and vertical strains occur at the center of specimen, and are obtained by replacing the variable x by zero.

$$\varepsilon_x = 1.0136 * \frac{Po}{E * \pi * L} \tag{2.19}$$

$$\varepsilon_y = -1.6653 * \frac{Po}{E * \pi * L} \tag{2.20}$$

Combining Equations (2.13) and (2.14) with Equations (2.17) and (2.18) and (2.19) and (2.20) produce the following equations:

$$\varepsilon_x = 0.523 * D_h \tag{2.21}$$

$$\varepsilon_y = 0.487 * D_h \tag{2.22}$$

Therefore, the strains at the center of the specimen can be expressed uniquely as a function of deformations.

### 2.3.2 Indirect Tensile Strength Test

The indirect tensile strength test (ITST) uses the same setup described in Section 2.3. A ramp loading is applied to the sample at a constant rate of 2 inches per minute until failure. The magnitude of the load resisted by the sample as a function of the vertical deformation is directly obtained from the ITST machine. The horizontal and vertical deformations are collected as a function of time by a separate data acquisition system. By matching the vertical deformation from both graphs, the force versus time graph can be obtained. The properties that can be determined from this test are:

- The tensile strength
- The compressive stress at failure
- The equivalent modulus
- The stored energy density until cracking

#### *2.3.2.1 Tensile Strength*

The Tensile Strength (TS) is the maximum tensile stress a sample can accommodate before failure. A higher tensile strength results in higher resistance to

cracking. TS is determined by equation (2.23) where $P_u$ is the ultimate vertical force resisted by the specimen.

$$TS = 0.156241 * \frac{P_u}{L} \tag{2.23}$$

### *2.3.2.2 Compressive Stress at Failure*

The Compressive Stress at Failure (CSF) is the maximum compressive stress the specimen is subjected to during testing. A higher CSF results in better rut resistance. Note that the specimens tested in ITST fail in tension and not in compression, and thus, the compressive strength determined in this test might not be the highest compressive stress the asphalt mix can handle. The CSF is determined by equation (2.24) where $P_u$ is the ultimate vertical force resisted by the specimen.

$$CSF = -0.475386 * \frac{P_u}{L} \tag{2.24}$$

### *2.3.2.3 Equivalent Modulus*

The Equivalent Modulus (EM) is an indication of the material stiffness. A higher modulus results in higher resistance to deformation. Since the load deformation curve remains linear for the first part of the curve (up to half the maximum load), the EM is determined as the slope of that part of the curve (Figure 2.9).

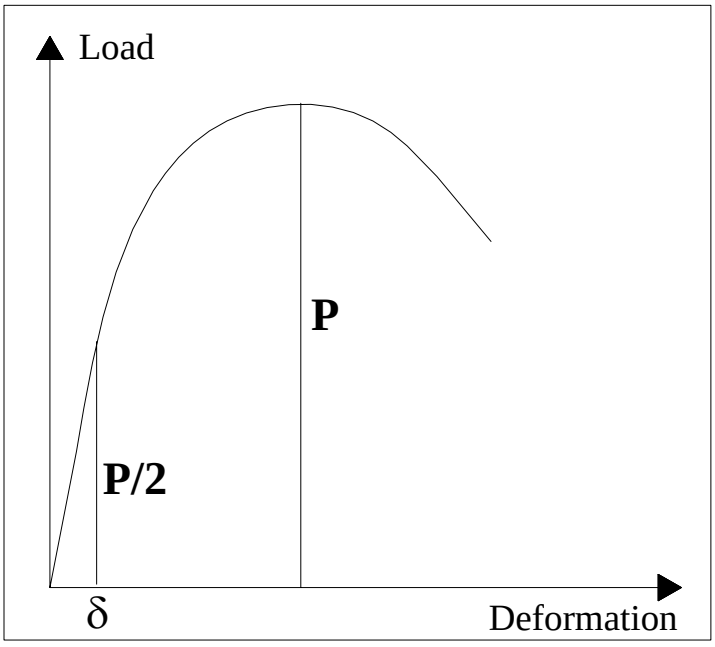


Figure 2.9. ITST Load Deformation Curve

$$EM = \frac{1}{2}\frac{P}{\delta} \tag{2.25}$$

where:

P is the ultimate vertical load at failure in pounds,

δ is the deformation corresponding to P/2 (in inches).

### *2.3.2.4 Stored Energy Density until Cracking*

The Stored Energy Density until Cracking (SEC) is the total energy density (pounds per square inch) required to start the failure of the specimen. It is determined as the area under the stress-strain curve starting from the origin until the peak, as shown in Figure 2.10. This value will be later used as part of the new failure criterion. The stresses and strains used are the tensile ones in the horizontal direction and are calculated from the monitored load, horizontal deformation ($D_h$) and vertical deformation ($D_v$) as shown in equations (2.11) and (2.21) respectively.

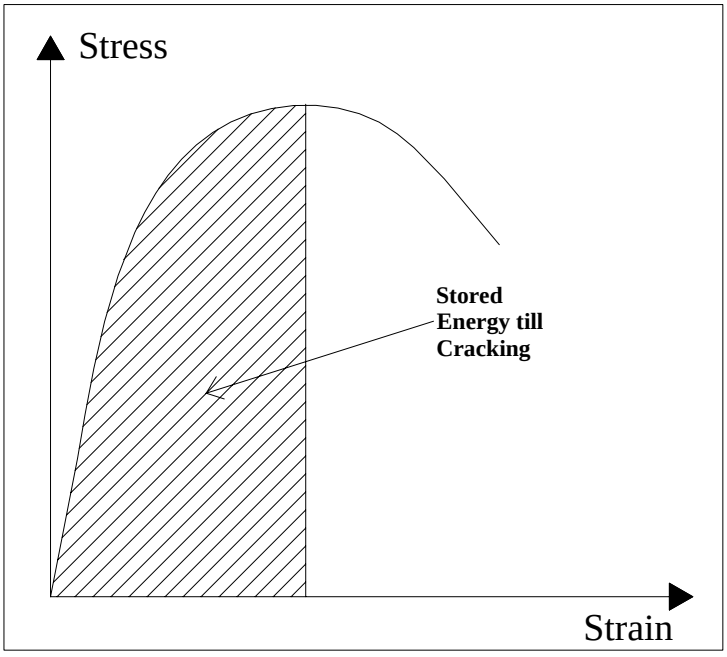


Figure 2.10. Stored Energy Density until Cracking

## 2.3.3 Indirect Tensile Cyclic Load Test

The indirect tensile cyclic load test (ITCLT) uses the same setup described in section 2.3. With the MTS system used for this research, the load can be applied to the specimen as a combination of sine, haversine, ramp, and constant level pulses. In addition to any load pulse, a constant sustained load of 20 pounds is applied to the specimen to insure contact between specimen and the loading strips. The horizontal, longitudinal and

transverse deformations are measured and recorded as a function of time. These deformations can be divided into three components: elastic, viscoelastic and plastic deformations, as shown in Figure 2.11.

The portion of deformation that is immediately recovered upon unloading is called the elastic deformation. Another recoverable portion is the viscoelastic deformation; however, this part is recovered after the unloading is over. Finally, the last portion of the deformation, the plastic deformation, is permanent and will not be recovered. The properties that can be determined from this test are:

- Recoverable deformation
- Permanent deformation
- Resilient modulus
- Dissipated energy density

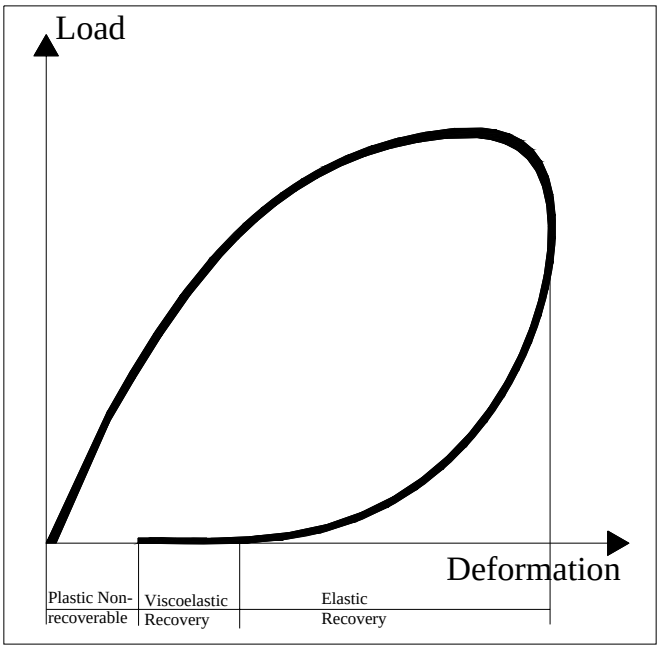


Figure 2.11. Load-Deformation Curve under Cyclic Loading

### *2.3.3.1 Recoverable Deformations*

The recoverable deformation is the summation of the elastic and viscoelastic deformations. For elastic materials, the recoverable deformation is simply the elastic deformation and the loading and unloading portions of the stress strain curve coincide. However, for viscoelastic materials, the loading and unloading portions are different, thus producing the hysteresis loop and the corresponding dissipated energy. The recoverable deformation can be determined in both horizontal and vertical directions, and is calculated per cycle to calculate the dissipated energy density and the resilient modulus.

#### *2.3.3.1.1 Permanent Deformation*

Permanent deformation, known also as plastic deformation, can be determined in both horizontal and vertical directions. Both, the horizontal plastic deformation (HPD) and the vertical plastic deformation (VPD) per cycle can be determined as a function of number of load repetitions by calculating the difference between the deformation at the beginning and end of each cycle. Additionally, VPD and HPD can be determined based on a reference load cycle (second load cycle in this study) for obtaining the cumulative permanent deformation directly. The cumulative PD is used as an indicator of the mix resistance to rutting.

#### *2.3.3.1.2 Resilient Modulus*

The resilient modulus is calculated for each cycle and its reduction as a function of the number of repetitions increases is recorded. The resilient modulus is calculated based on the following equation [15]:

$$M_R = \frac{P(\nu + 0.2734)}{\delta * L} \tag{2.26}$$

where: P is the applied vertical load
$\delta$ is the recoverable deformation
$\nu$ is Poisson's ratio, and
L is the specimen width.

#### *2.3.3.1.3 Dissipated Energy Density*

Dissipated energy density is defined as the area within a stress-strain hysteresis loop and represents the energy lost at a specific point due to a load application. The tensile stresses and strains at the center of the specimen are used to calculate the dissipated energy density. The dissipated energy density is calculated at each cycle where data collected, The cumulative dissipated energy density is then determined by superposition.

### 2.3.4 Determining Load Pulse Magnitude and Shape

A three layer pavement cross-section was analyzed using the SAPSI-M computer program to get the field response under the wheel loads. The SAPSI-M program uses finite layer analysis and a polar coordinates system (Figure 2.12). Knowing the radial distance (R) to any point and the angle of inclination ($\theta$), two stresses are calculated first: the radial stress ($\sigma_r$) and the tangential stress ($\sigma_t$). From these two stresses, all the critical stresses mentioned in the earlier sections can then be calculated. The value of the elastic

modulus for the asphalt layer was calculated from the resilient modulus obtained from the lab. Based on an FHWA study in 1998 [16], it was concluded that the elastic modulus in the field is approximately three times that from the lab.

The pavement response is obtained as a function of time at a specific point at the bottom of the AC layer as the load (truck, axle group) passes over the pavement surface. Once the pavement response is determined, these values can be converted into a load pulse applied by the actuator on the specimen using either of the following equations:

$$P = 6.4 * \sigma_t * L \tag{2.27}$$

$$P = 0.8031 * \varepsilon_t * L \tag{2.28}$$

where: $\sigma_t$ is the tensile stress in psi

$\varepsilon_t$ is the tensile strain in micro-strain.

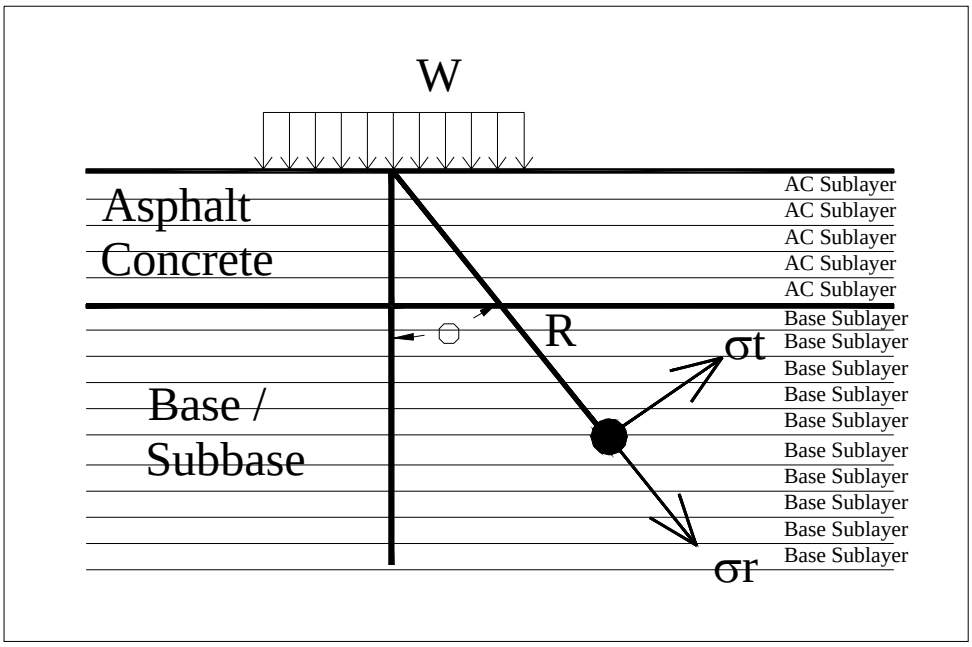


Figure 2.12. SAPSI-M Analysis Model

First, the tensile stresses at the center of the specimen were equated to the transverse tensile stress at the bottom of the AC layer (equation 2.27); however, the obtained vertical load was too high, and caused the sample to fail in local shear near the loading strips as shown in Figure2.13. A typical specimen failing under fatigue is shown in Figures 2.14, 2.15 and 2.16. Additionally, the strains at the center of the specimen under these stresses were much higher than the strains at the bottom of the AC layer. This can be explained by the different confinement provided by the pavement structure in the field (or from a computer modeling of the field) and that provided by the unconfined specimen at its center. Clearly, the confinement in a pavement structure is much higher

than that in a cylindrical specimen, and thus, the high values of the strains. Given the above considerations, the load pulse was determined by equating the transverse tensile strains at the bottom of the AC layer to the tensile strains at the center of the specimen as shown in equation 2.28. Equating the strains seemed to be the logical way to go, regardless of local shear failure near the loading strips. After all, the strain value is what causes the asphalt concrete to fail in tension and not the stress value. When comparing two identical pavement structures with only the AC stiffness being different, the stresses at the bottom of both asphalt layers would be almost the same; however, the strains at the bottom of the stiffer layer will be much lower. Thus the difference in the fatigue life between the two pavements would show that strains are what cause the fatigue failure and not the stresses. Figure 2.17 shows a comparison between the response at the bottom of the AC layer from SAPSI-M modeling and the response at the center of the specimen under the load pulse obtained from the procedure mentioned above.

As for the rest period, a constant ratio of 1 to 4 was used for loading and rest periods. Since the effect of the rest period on the fatigue life is not a part of this study, the constant ratio was used. For single axles, the loading/unloading duration was found to be 0.1 second using the response calculated from SAPSI-M due to a moving load at 40 mph; therefore a rest period of 0.4 seconds was used. For the different axle configurations and trucks, the loading time is taken as the time from the beginning of response due to the first axle until the time when the response of the axle dies, as calculated from SAPSI-M.

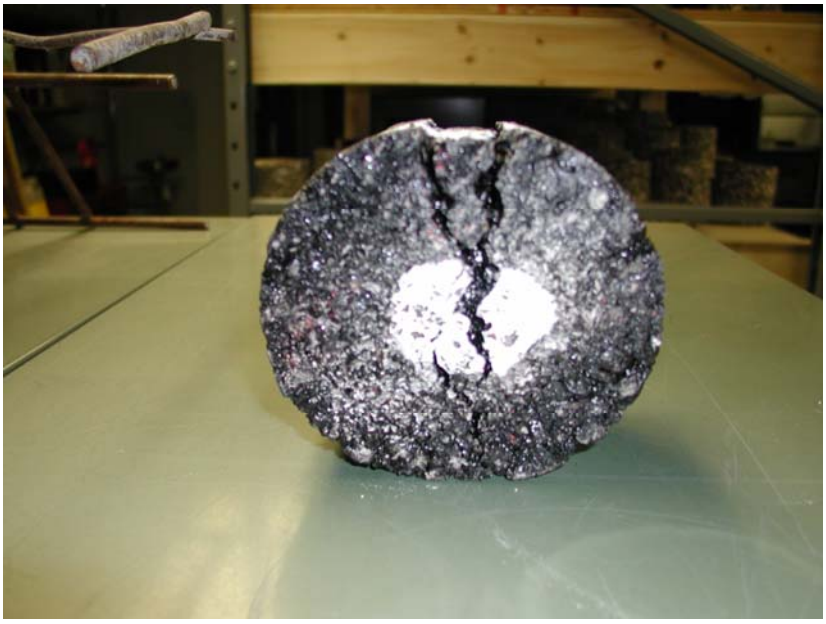

Figure 2.13. Local Shear Failure

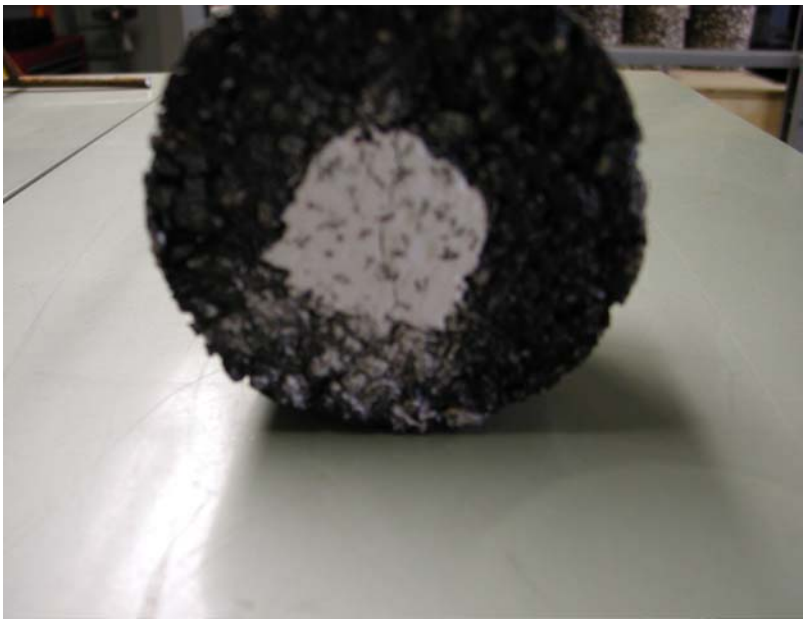

Figure 2.14. Fatigue Cracking in lab Specimen at Early Stages

Figure 2.15. Fatigue Cracking in lab Specimen at Intermediate Stages

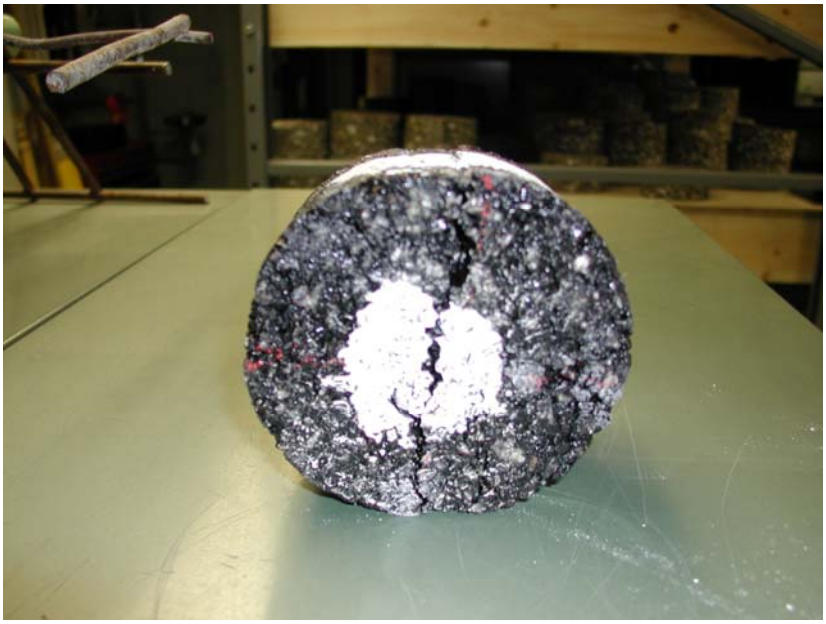

Figure 2.16. Fatigue Cracking in lab Specimen at Final Stages

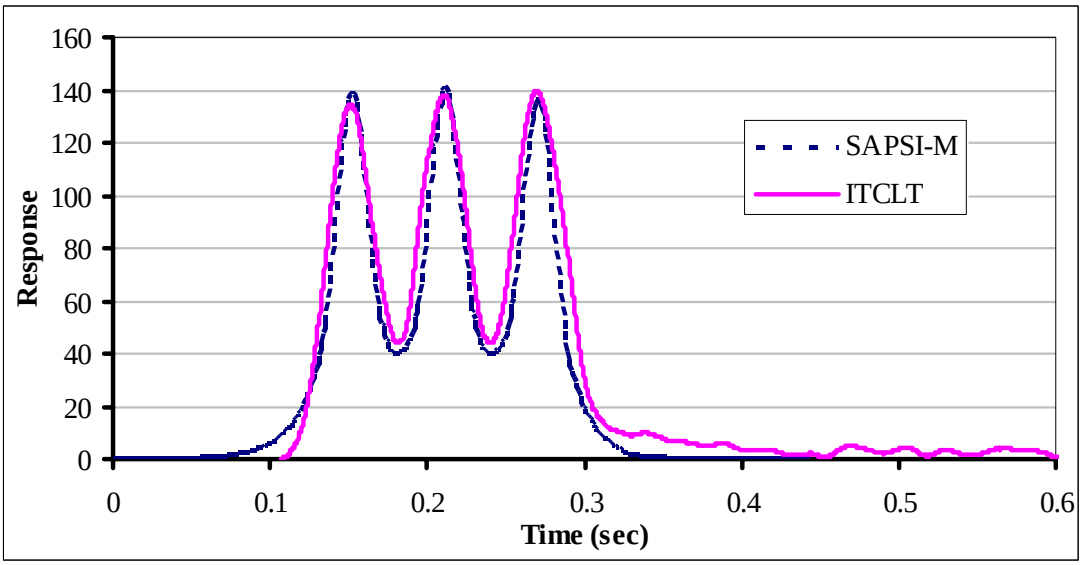


Figure 2.17. SAPMSI-M vs ITCLT Pulses

### 2.3.5 Comparison between ITCLT and Field Conditions

When considering a stationary wheel load on the surface of a pavement structure, three strains/stresses are generated at the bottom of the AC layer. These are the longitudinal strain and stress ($\varepsilon_L$ & $\sigma_L$: parallel to the traffic direction), transverse strain and stress ($\varepsilon_t$ & $\sigma_t$: perpendicular to the traffic direction) and vertical strain and stress ($\varepsilon_v$ & $\sigma_v$: in the vertical plane). As the wheel moves on the surface along the road axis, the

values of the stresses and strains at a given point vary. Typical graphs of longitudinal, transverse and vertical stress time histories are shown in Figures 2.18, 2.19 and 2.20, respectively.

The peak values of the stresses are reached when the wheel is exactly above the point where the response is measured. The positive values represent tensile stresses while negative values correspond to compressive stresses. As can be seen from these graphs, the vertical stresses are not critical. Their magnitude is just above 10% of the longitudinal and transverse stresses. The following tensors show peak values of stresses and strains at the bottom of the AC layer obtained from SAPSI-M analysis under a single load to compare with the stresses and strains at the center of a lab specimen.

$$\begin{pmatrix} L \\ t \\ v \end{pmatrix} \begin{pmatrix} 130.14 & 0 & -8.21 \\ 0 & 133.26 & 0 \\ -8.21 & 0 & -14.8 \end{pmatrix}$$

Stress Tensor

$$\begin{pmatrix} L \\ t \\ v \end{pmatrix} \begin{pmatrix} 1.35E-4 & 0 & -1.33E-5 \\ 0 & 1.4E-4 & 0 \\ -1.33E-5 & 0 & -1.33E-4 \end{pmatrix}$$

Strain Tensor

Recalling equations 2.11, 2.12, 2.19 and 2.20 from section 2.3.1, the stress ratio of the compressive vertical stress to the tensile horizontal stress is 3:1 in the ITT specimen compared with 1:9 in the field. Additionally, the longitudinal stresses are negligible in the lab, while these stresses are the same as the transverse ones in the field. Thus, the stress ratio between the lab and field are totally different and this should be always taken into consideration when analyzing lab results, or calculating load pulses that will be applied to a specimen in the lab. Therefore, only the dissipated energy density from the horizontal tensile stresses and strains was used in determining the fatigue life.

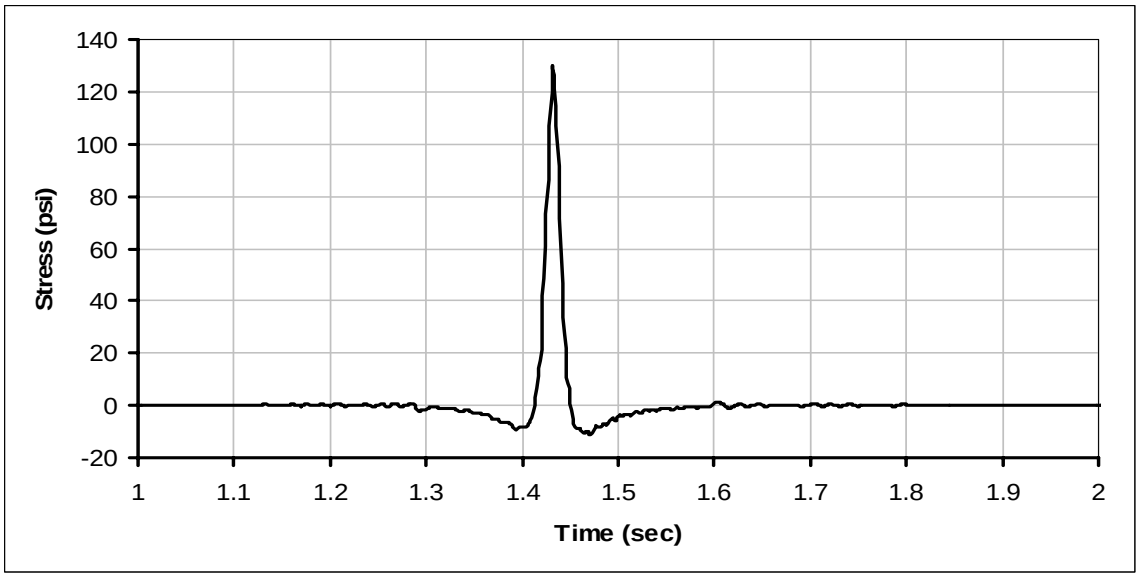


Figure 2.18. Longitudinal Stress Time History at the Bottom of AC Layer

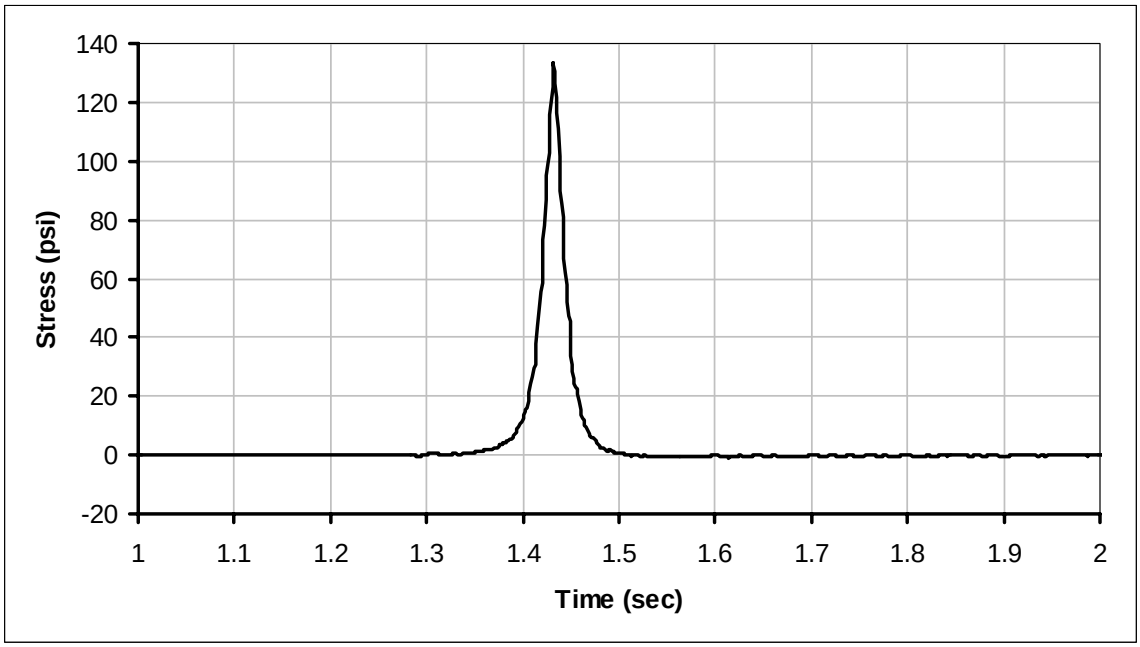


Figure 2.19. Transverse Stress Time History at the Bottom of AC Layer

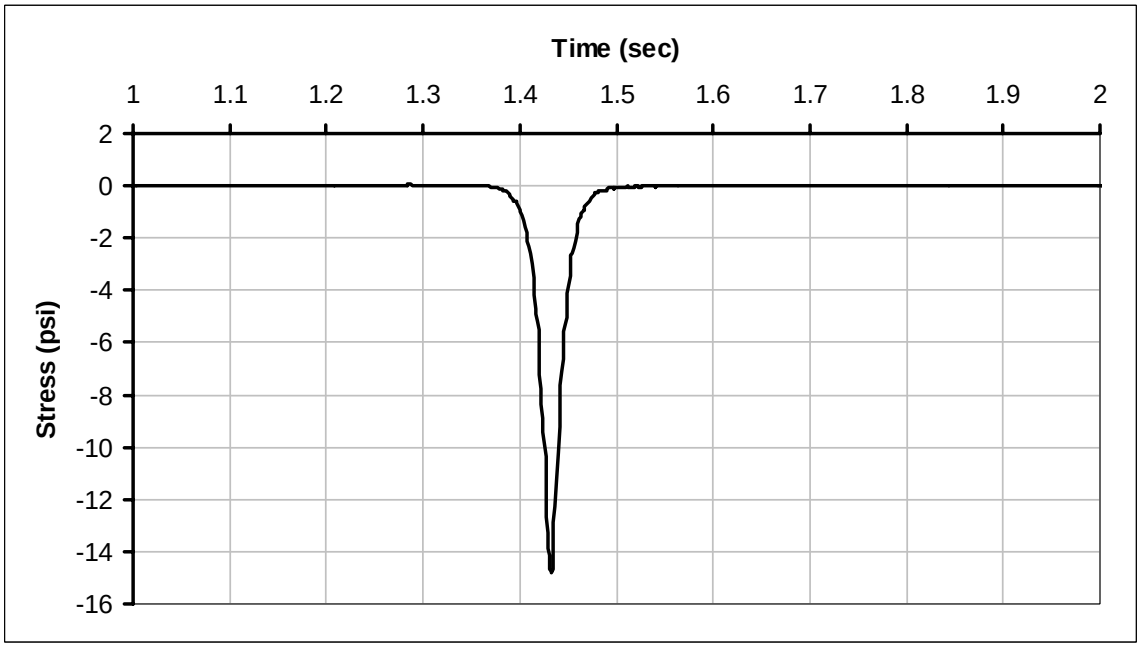


Figure 2.20. Vertical Stress Time History at the Bottom of AC Layer

## 2.4 DISSIPATED ENERGY CONCEPT AND NEW FAILURE CRITERION

Dissipated energy density is defined as the area within a stress-strain hysteresis loop and represents the energy lost at a specific point due to a load application. The tensile stresses and strains at the center of a specimen are used to calculate the dissipated energy density. Figure 2.21 shows a typical stress-strain hysteresis loop.

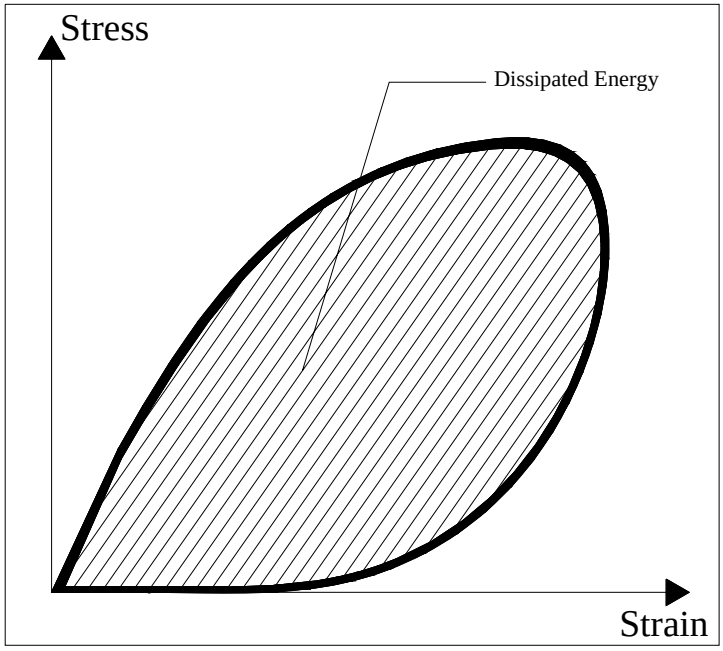


Figure 2.21. Stress-Strain Hysteresis Loop

Energy is dissipated with each cycle and accumulates as the load is repeatedly applied to the specimen. The cumulative dissipated energy density up to a given cycle can be calculated by summing up the dissipated energies in the previous cycles. Initially, the dissipated energy density per cycle is constant for a number of load repetitions, after which it starts to increase rapidly (Figure 2.22). As for the cumulative dissipated energy density, it starts increasing gradually at the beginning, then it starts increasing dramatically as cracking develops (Figure 2.23). Either of the two measures, cumulative or cyclic, can be used as a failure criterion for fatigue testing.

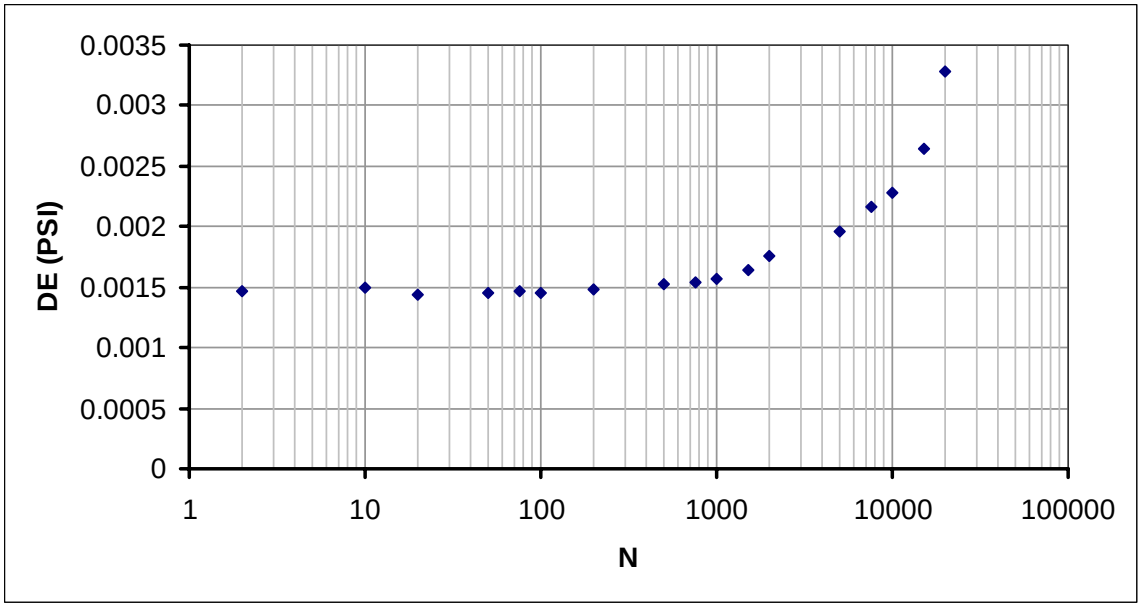


Figure 2.22. Dissipated Energy Density per Cycle

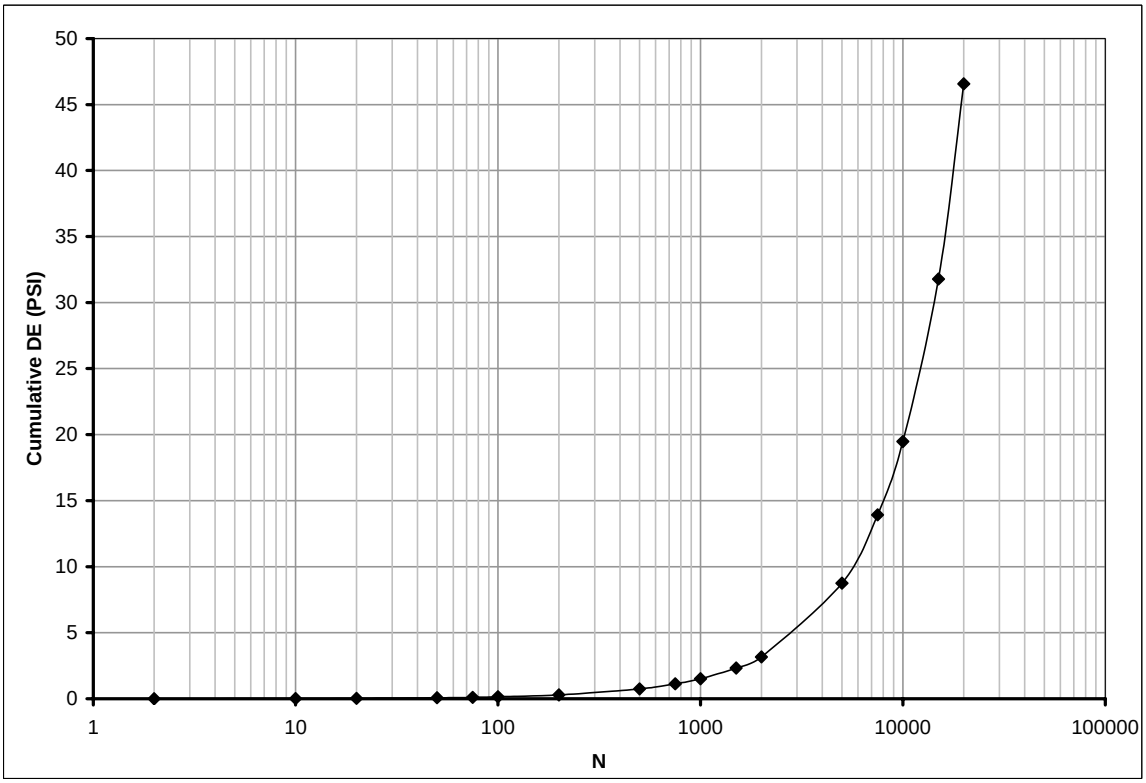


Figure 2.23. Cumulative Dissipated Energy Density

### 2.4.1 Previous Studies on Dissipated Energy

The fatigue of viscoelastic materials subjected to repeated loads has been associated with the energy loss due to these load cycles. Laboratory fatigue tests have showed a unique relation between the fatigue life of an asphalt mixture and the cumulative dissipated energy.

Figure 2.24 shows the values of dissipated energy density per cycle as a function of number of load repetitions [17]. The dissipated energy density per cycle increases with increasing load repetitions in a controlled stress test, while it decreases in a controlled strain test. Additionally, it can be seen that for the initial cycles (before cracks initiation), the values from both tests are equal.

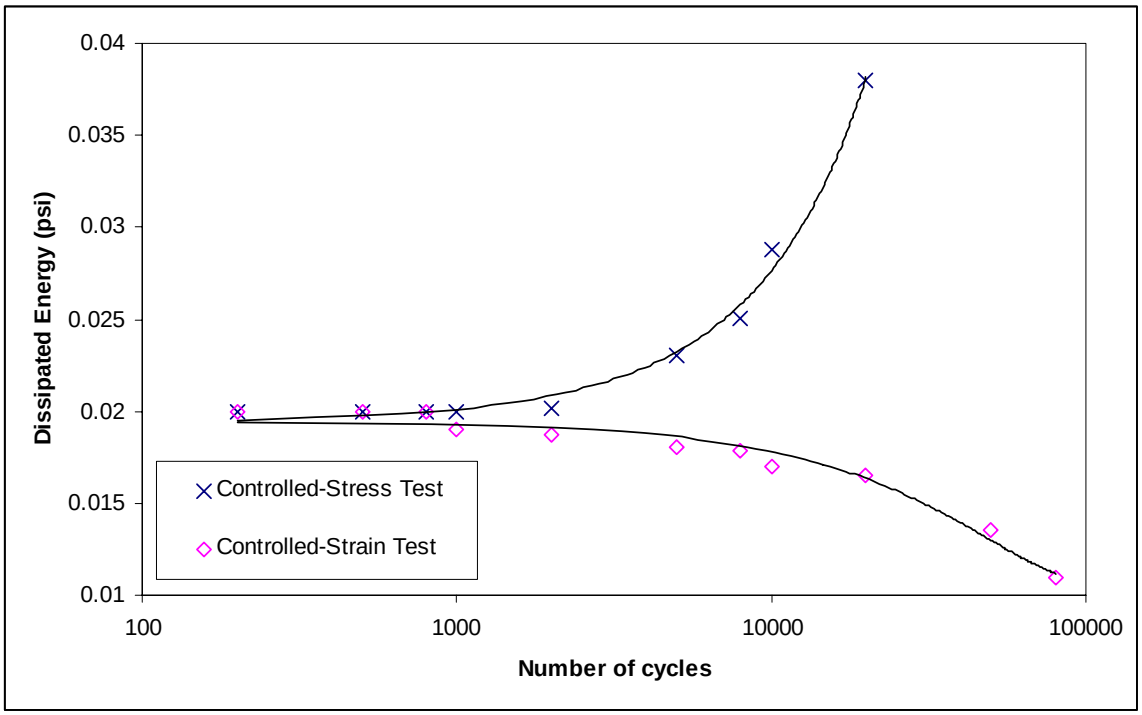


Figure 2.24. Dissipated Energy Density from Controlled-Stress and Controlled-Strain Tests (Sousa, 1992)

Figure 2.25 shows the variation of the cumulative dissipated energy density as the number of load repetitions increase. The cumulative dissipated energy density values obtained from the stress controlled and strain controlled tests are different. However, the two curves are very similar for the first portion (initial cycles).

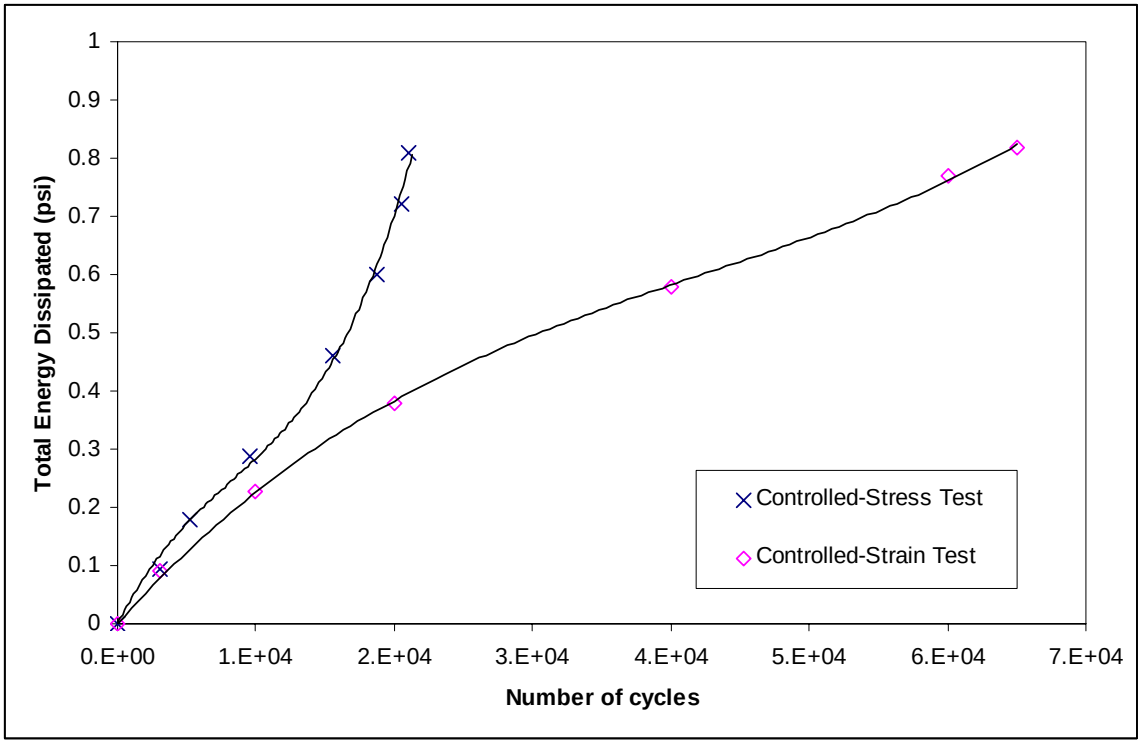


Figure 2.25. Cumulative DE from Controlled-Stress and Controlled-Strain Tests (Van Dijk, 1974)

Van Dijk [6] was one of the first researchers to apply the dissipated energy concept to asphalt concrete fatigue testing. From tests conducted under both stress and strain controlled modes, he concluded that the total amount of dissipated energy density to failure is independent of the testing mode. However, the stress controlled tests dissipate energy much faster than strain controlled tests resulting in lower predicted fatigue life. In another study, Van Dijk [6] reported that the cumulative dissipated energy versus the number of load repetitions is dependent on the mix properties, but independent of test methods (two and three point bending), temperature ($50^{o}$F to $104^{o}$F), mode of loading (stress controlled and strain controlled) and load frequency (10 to 50 Hz).

Monismith et al. [8] indicated that the uniqueness of the cumulative dissipated energy for different types and conditions of testing cannot be sustained. Further investigations showed that the total dissipated energy varies depending on the testing mode, temperature and mix type. Ghuzlan and Carpenter [4] introduced a new failure criterion using the change in dissipated energy between two cycles divided by the dissipated energy per cycle. This criterion is very similar to using the dissipated energy per cycle. They reported that when using this failure criterion, the mode of testing is taken care of, and the results from strain controlled, or stress controlled match well.

Tangella et al. [18] summarized the advantages and disadvantages of the dissipated energy approach in fatigue analysis. The major advantages are:

i) According to Van Dijk, loading mode, temperature, frequency of loading and occurrence of rest period do not have a significant effect on the cumulative dissipated energy.
ii) This procedure is based on a physical phenomenon: the accumulation of the dissipated energy from the repeated load cycles causes the fatigue in a visco-elastic material.
iii) Prediction of fatigue life is possible as a first approximation if initial stiffness and phase angles are known.
iv) For both stress controlled and strain controlled tests, there is a unique relationship between the total dissipated energy and the number of load repetitions to failure.

The major disadvantages of this method include:

i) Accurate prediction of fatigue behavior is not possible without conducting detailed fatigue testing.
ii) The procedure proposed in this method can not be considered as a design technique; rather, it serves to indicate the general magnitude of the fatigue life of a given asphalt mix.

An additional advantage of the dissipated energy approach is its applicability to simulating multi axles and whole trucks at once. This will be discussed later in detail in the next chapter.

### 2.4.2 Dissipated Energy Fatigue Models

As mentioned in the previous sections, the dissipated energy density is determined as the area inside the hysteresis loop. To calculate this area, the trapezoidal rule is used where the area is calculated over a stress/strain interval corresponding to 0.005 seconds. And thus, the dissipated energy density at a given cycle is determined as:

$$Wo = \sum_{1}^{n} \frac{\sigma_{i+1} - \sigma_i}{\frac{1}{2}(\varepsilon_{i+1} + \varepsilon_i)} \tag{2.29}$$

The cumulative dissipated energy density is determined as the integral of the dissipated energy density per cycle:

$$W = \int_{0}^{Nf} w_i di = \sum_{1}^{n} w_i \tag{2.30}$$

Van Dijk presented his fatigue model in terms of the cumulative dissipated energy per unit volume ($W_{fatigue}$) and number of load repetitions to [6] failure ($N_f$). The model is of the form:

$$W_{fatigue} = AN_f^z \quad (2.31)$$

Where A and z are material parameters. For asphalt concrete, Van Dijk suggested that z was equal to 0.63 and A was equal to $6.76 * 10^4$ J/m$^3$.
Sousa et al. [17] suggested two fatigue models, one for the stress controlled test and another for the strain controlled test. The failure criteria were when the dissipated energy reaches 2.1 times the value of the initial dissipated energy for the stress controlled test and half the initial dissipated energy for strain controlled tests. The equations are:

$$N_f = Ln(2.1) / (0.0071\ A^{1.43}) \quad \text{for controlled stress test} \quad (2.32)$$

$$N_f = Ln(0.5) / (-0.00247\ A^{1.43}) \quad \text{for controlled strain test} \quad (2.33)$$

Where: A is the initial dissipated energy.

Monismith et al. [9] evaluated the performance of a thin pavement at the FHWA Accelerated Loading Facility. Tests were run in a strain control mode under a continuous sinusoidal loading with no rest period. The final model related the fatigue life (Nf) to the initial dissipated energy per cycle.

$$Nf = 425.81\ (w_o)^{-1.846} \quad (2.34)$$

### 2.4.3 New Suggested Failure Criterion

Whether using the strain or dissipated energy approach in determining the fatigue life of an asphalt concrete mix, an objective failure criterion based on the actual damage occurring during a fatigue test needs to be established. The most common failure criterion is the 50% reduction in the resilient modulus where failure is defined as the cycle at which the resilient modulus value is half the initial value. However, this is an arbitrary criterion with no exact relationship with the actual amount of damage occurring in the sample. Additionally, this criterion is dependent on the loading mode.

Sousa et al. [17] performed a flexural beam test series that consisted of a ½ factorial experimental design for mixtures composed of two aggregates, two asphalt binders, two asphalt contents, two temperatures, two compaction levels and two loading modes. They used the least squares technique to determine the value of the ratio ($R_f$) of energy dissipated at failure to that of the first cycle. They reported an $R_f$ value of 2.1 for controlled stress tests and 0.5 for controlled strain test. These results indicate that in a stress controlled test, the failure occurs when the area of the hysteresis loop becomes double the area of the first loop. While in a strain controlled test, the failure is defined when the hysteresis loop area becomes half of the initial loop area. The same disadvantages mentioned for the 50% reduction in the resilient modulus apply to this failure definition.

Ghuzlan and Carpenter [4] defined fatigue life as the number of load cycles at which the ratio of the change in the dissipated energy between cycles "i" and "i+1" divided by the total dissipated energy of load cycle "i" begins to increase rapidly. Although this criterion overcomes the testing mode limitation, using this ratio (ΔDE / DE) might be misleading when dealing with experimental results. A small change in the value of the DE will lead to a large change in slope and thus, a negligible noise in the results might be magnified when calculating the slope. Additionally, the failure point when the plateau value starts to increase is still visually picked, introducing a subjective assessment, which depends on the scatter in the lab data. More importantly, the plateau value can not be used in any mechanistic design.

The failure criterion should relate to the damage occurring in the tested specimen. As shown in Figure 2.26, the dissipated energy density remains constant and then suddenly starts increasing. The point when the dissipated energy density starts increasing is basically the initiation of failure, and the corresponding cycle number is the number of repetitions to crack initiation. This is very similar to what Ghuzlan and Carpenter presented with their plateau value and the point where it starts changing. However, it is hard to visually determine the number of cycles at which the dissipated energy density value starts to increase. To overcome the subjectivity in this process, the results obtained from the indirect tensile strength test, and the fatigue test (both dissipated energy density per cycle and cumulative dissipated energy density) were combined.

Figure 2.27 shows the stress strain curve from an indirect tensile strength test. The shaded area represents the stored energy density until cracking (SEC). Previous studies showed that the dissipated energy until crack initiation is the same regardless of the loading mode, and thus, a specimen tested under indirect tensile cyclic load test should start cracking when the total dissipated energy density reaches the same value as SEC. The new fatigue failure criterion is therefore defined by equating the cumulative dissipated energy density under cyclic loading to the SEC value from the indirect tensile strength test. It should be noted that this criterion can be applied to other test modes provided the fatigue and strength tests are conducted under the same test setup. For example, if one is to extend this criterion to flexural beam testing, then the SEC value would be the flexural strength obtained by loading a beam to failure under a constant rate of deformation.

To verify this, three samples were tested using the ITST and the average SEC was determined. Then, triplets were tested under different load pulses and stress levels until fatigue failure. The dissipated energy density per cycle was determined, and integrated to obtain the cumulative dissipated energy density. From the cumulative dissipated energy density, the number of load repetitions ($N_f$) required to reach the SEC was determined.

Figure 2.28 shows the SEC value plotted on the cumulative dissipated energy density curve. The intersection of the SEC line with the cumulative dissipated energy density curve is the fatigue life ($N_f$). The values of $N_f$ was then plotted as a vertical line on the dissipated energy density plot per cycle to check if it matches with the region where the initial dissipated energy density value start to increase. Figure 2.29 shows the

$N_f$-value on the dissipated energy density per cycle plot. As expected, the dissipated energy density value starts to increase in the neighborhood of $N_f$. Figures 2.28 and 2.29 show the same trend from a sample tested at a lower stress level. The value of $N_f$ increase by a ratio of 10, but the same failure criterion still applies. A total of 31 samples tested at three stress levels (4.375, 8.75 and 17.5 psi) and 5 different load pulses (single, tandem, tridem, 4-axles and 8-axles) were used to verify the applicability of this procedure for determining the fatigue failure.

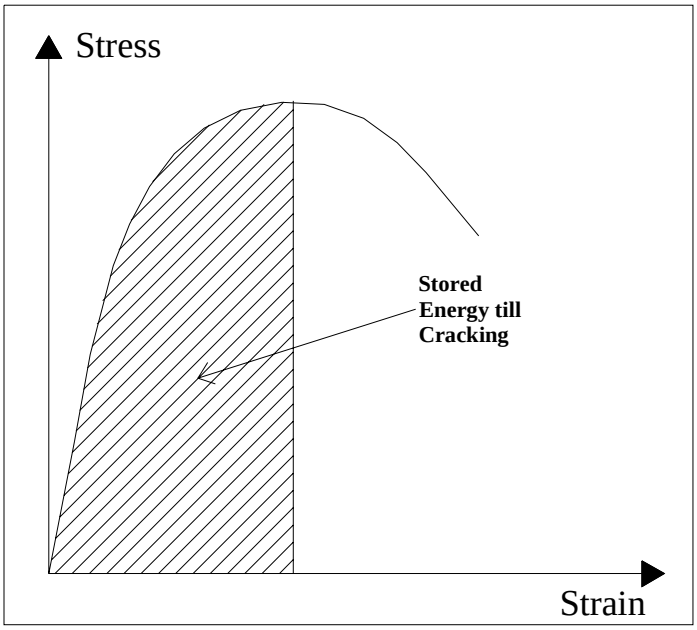


Figure 2.26. (Repeated): Stored Energy Density until Failure

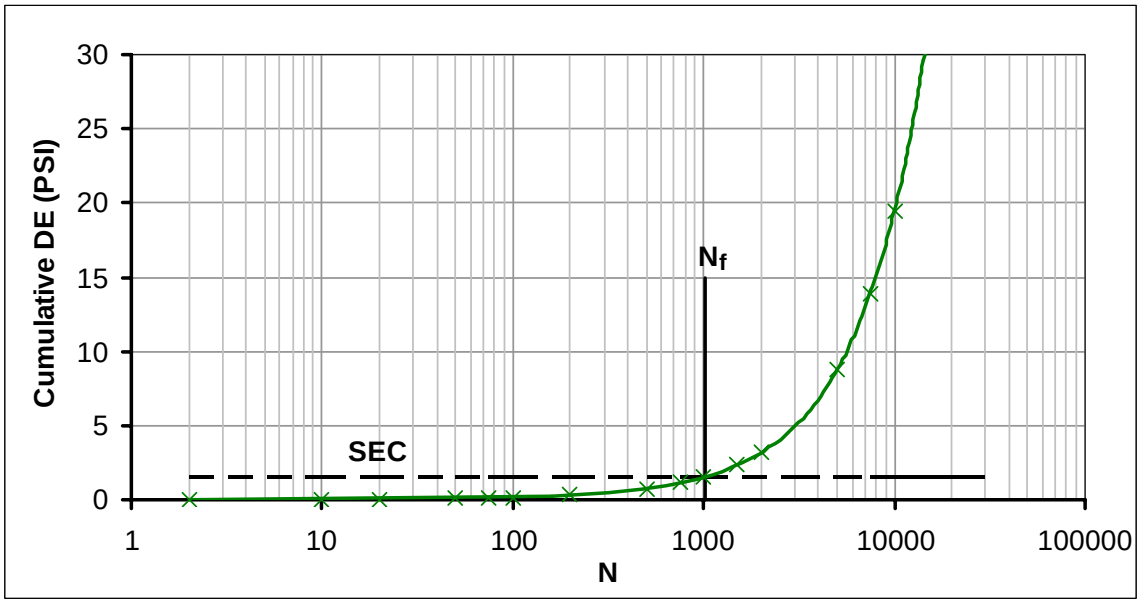


Figure 2.27. Determining $N_f$ from Cumulative Dissipated Energy Density and SEC (Sample 1)

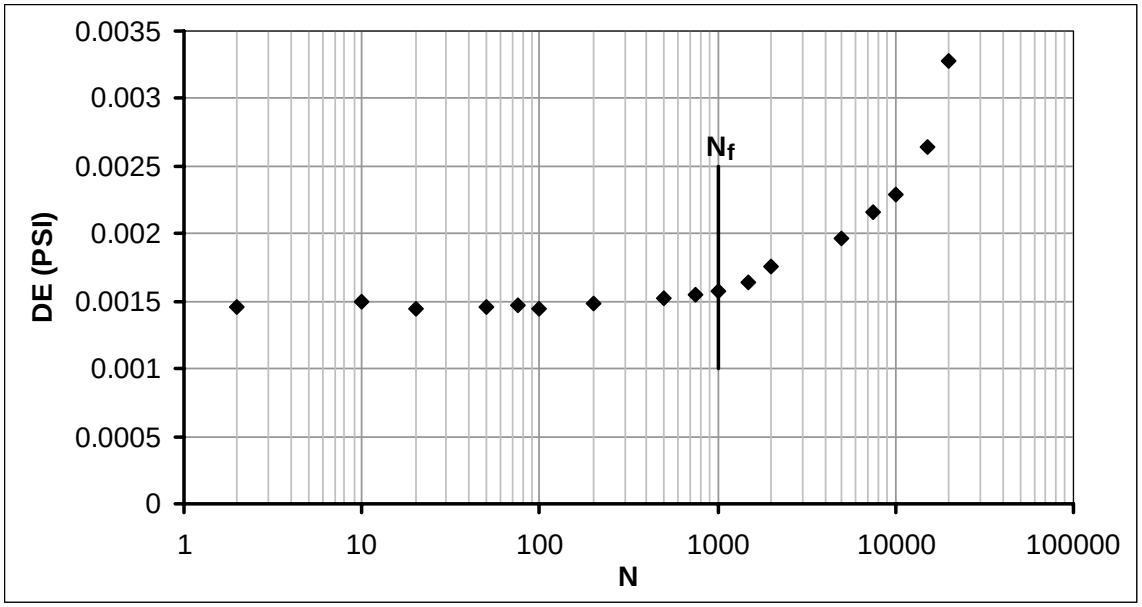


Figure 2.28. Dissipated Energy Density per Cycle Curve with $N_f$ Superimposed on it (Sample 1)

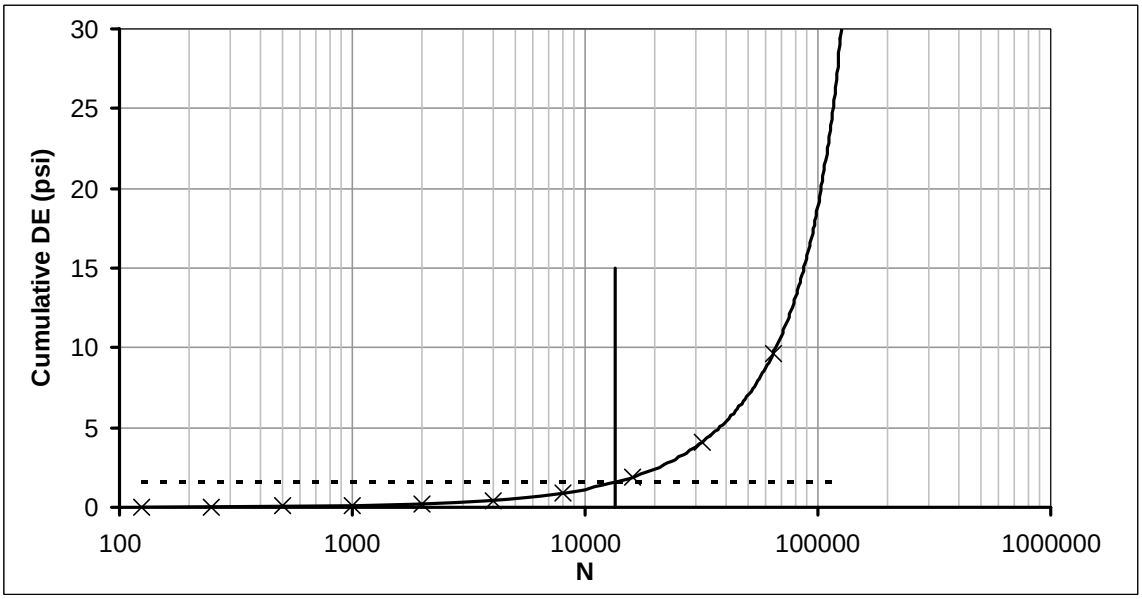


Figure 2.29. Determining $N_f$ from Cumulative Dissipated Energy Density and SEC (Sample 2)

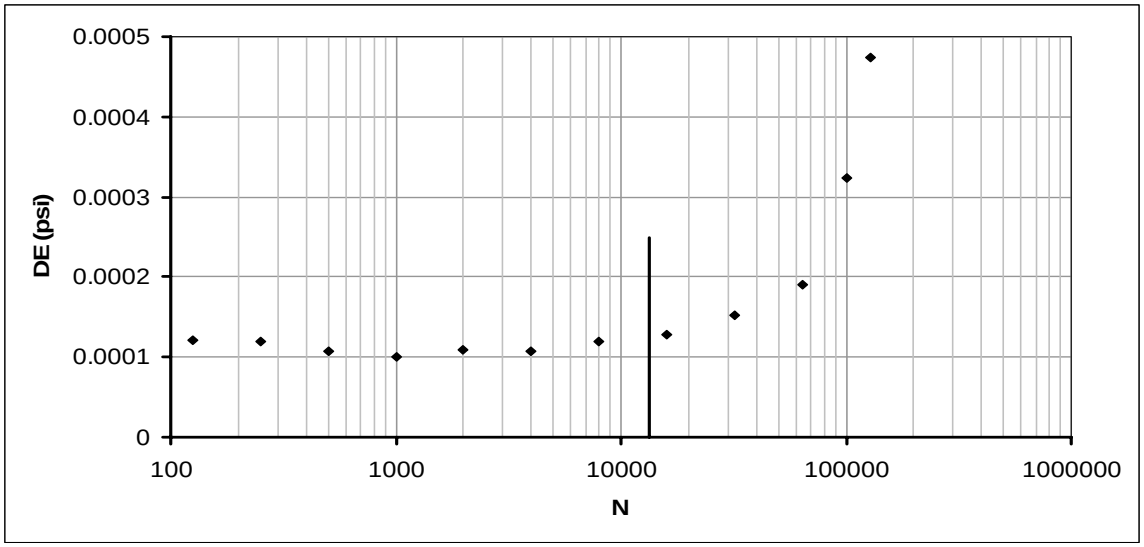


Figure 2.30. Dissipated Energy Density per Cycle Curve with $N_f$ Superimposed on it (Sample 2)

Due to equipment limitations, controlled strain tests were not performed to check whether this criterion is dependent on the loading mode or not. However, from the previous study by Ghuzlan and Carpenter [4] where a similar failure criterion was adopted, it was found to be independent of loading mode. Therefore, it is expected that this procedure should be independent of loading mode as well. In their definition of failure, Ghuzlan and Carpenter found out that using the change in the value of (ΔDE/DE) between two consecutive cycles is an indicator of failure initiation. Since the dissipated energy per cycle was used in determining this ratio, the sudden increase (ΔDE/DE) corresponds basically to the increase in the initial value of the dissipated energy. Thus, the only difference between the failure point presented here and that of Ghuzlan and Carpenter is the procedure used to determine this point. While Ghuzlan and Carpenter use the ratio (ΔDE/DE) and visually pick the failure point, the procedure presented above use the cumulative dissipated energy density and the SEC value from the indirect tensile strength test.

## 2.5 Test Results and Corresponding Fatigue Curves

Two asphalt concrete mixes were tested in this study: I) 4E3 mix and II) 4E10 mix. The mixes were obtained from actual batches that were used by the Michigan DOT on projects in the summer of 2002. A total of 73 samples were compacted using the gyratory compactor (57 from mix I and 16 from mix II). Forty samples were tested for fatigue (35 samples from mix I and 5 from mix II). Three samples from each mix were tested under the indirect tensile test. Mix I was tested first, followed by mix II. The results obtained from mix II were very similar to those of mix I, and thus, the fatigue tests were stopped. Checking results from a previous study at Michigan State University performed by Baladi and Crince [20], their results also showed that there was no clear

difference between the two mixes. The mix used in this study was a super-pave 4E3 mix with a top aggregate size of ½ inch and a target asphalt content of 5.9%. The volumetric properties of mix I are presented in Table 2.2 below.

Table 2.2 Volumetric Properties of Mix I

| Property | $G_{mm}$ | $G_{mb}$ | $G_{se}$ | $G_{sb}$ | VMA | VFA | $G_b$ |
|---|---|---|---|---|---|---|---|
| Value | 2.487 | 2.388 | 2.731 | 2.661 | 15.6% | 74.4% | 1.026 |

## 2.5.1 Preliminary Tests Results

Several tests were performed before the actual fatigue tests started. Tests such as specific gravity, indirect tensile strength and indirect tensile cyclic load tests were performed to determine sample air void content, indirect tensile strength and stored energy density till cracking, and resilient modulus respectively.

### *2.5.1.1 Specific Gravity Test Results*

After the samples were compacted using the gyratory compactor, a bulk specific gravity test was performed on each specimen, and the air void content was determined. The average air void content and its standard deviation for the samples used are 3.9 and 0.2 for mix I, and 3.74 and 0.24 for mix II respectively. Specimens with high or low air voids were not tested. The detailed specific gravity results are included in the appendix.

### *2.5.1.2 Indirect Tensile Strength Test Results*

Three samples (129, 143 and 154) were tested to determine the indirect tensile strength and the stored energy density until cracking. The vertical force at failure was recorded to be used as a reference for the fatigue test vertical loads. The vertical load applied in the fatigue test should be much lower than the peak vertical force from the strength test, or else, the test performed cannot be considered a fatigue test. Results are summarized in Table 2.3Table .

Table 2.3. ITST Results

| Specimen No | 143 | 129 | 154 | Average |
|---|---|---|---|---|
| Tensile Strength (psi) | 170.4 | 167.9 | 174.2 | 170.9 |
| Max. Compressive Stress (psi) | 511.3 | 503.8 | 522.6 | 512.6 |
| Vert. Load at Failure (Lbs.) | 2677.2 | 2637.8 | 2736.2 | 2683.7 |
| Stored Energy Density Until Failure (psi) | 1.547 | 1.553 | 1.568 | 1.556 |

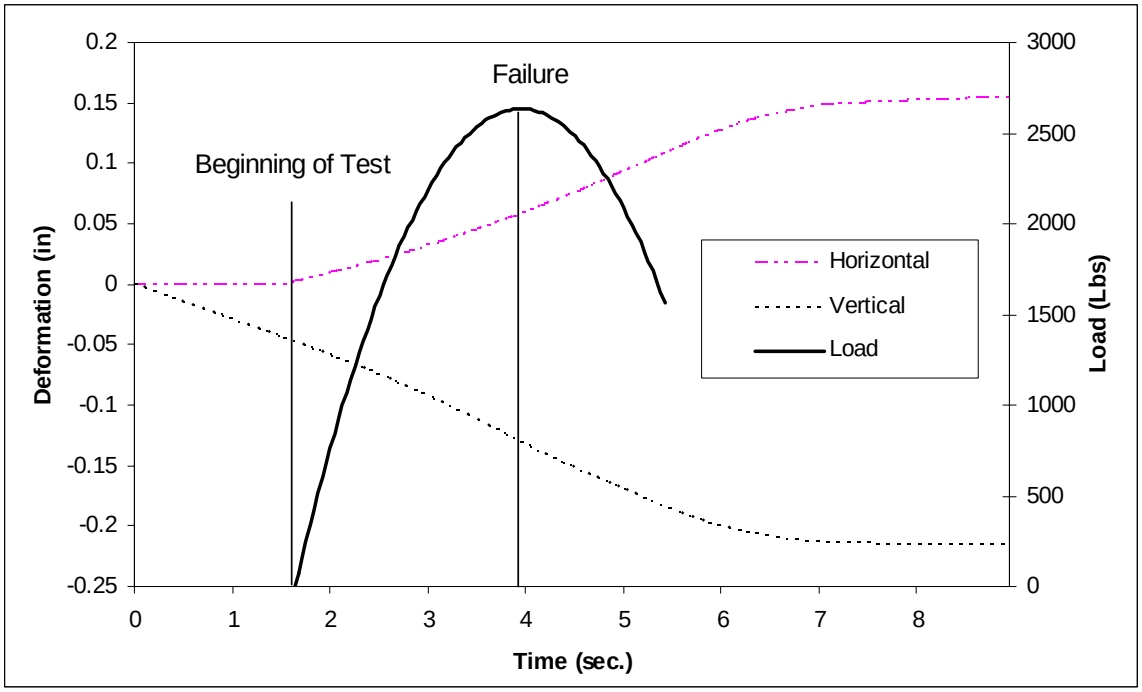


Figure 2.31. Output from ITST (specimen 154)

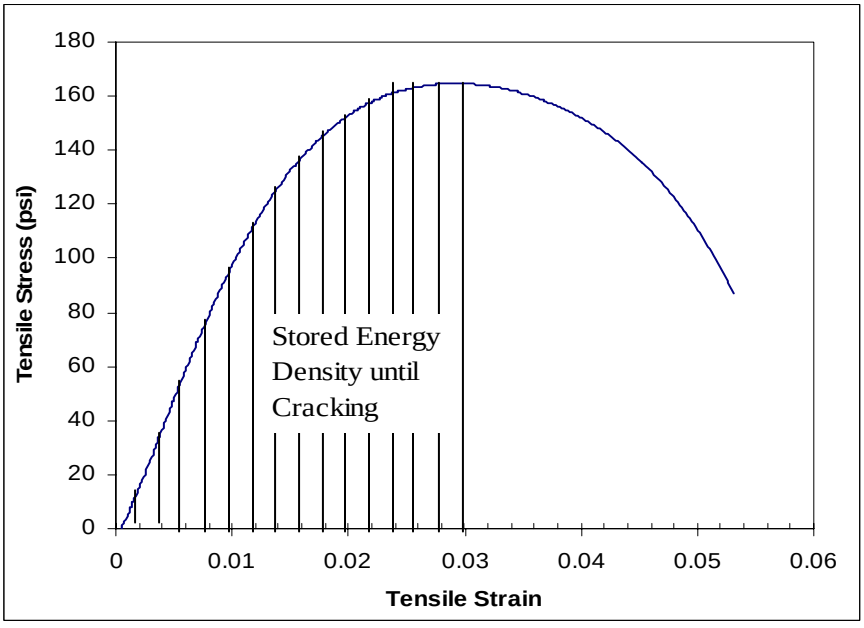


Figure 2.32. Stored Energy Density till Cracking (specimen 154)

Figure 2.31 shows a typical output from the ITST. The vertical deformation is linear until the test ends; this is due to the constant ramping rate of 2 inches per minute at which the test is performed. The test starts when both the load and horizontal deformation

starts picking up. All the vertical deformation before this point is neglected. The specimen fails when the load reaches its peak. This is the point when cracks start to initiate. (Note that the last portion of the load curve is extrapolated. The test is usually stopped after the load starts decreasing. Figure 2.32 shows the stress strain curve and the stored energy density until cracking calculated for the same specimen. (Refer to section 0 for details on calculating the stresses and strains).

### *2.5.1.3 Resilient Modulus*

Two samples (12 and 146) were tested under Indirect Tensile Cyclic Load to determine the "Lab" resilient modulus of the 4E3 mix. Three tests were run on each sample, and the average of the deformations measured at the 499, 500 and 501 cycles were used to determine the resilient modulus. A sustained load of 50 pounds and a cyclic load of 300 pounds were used. The cyclic load was applied at a frequency of 2 hertz with 0.1 seconds of loading and unloading and 0.4 seconds of rest period. The resilient modulus was calculated from the equation (2.35) [1]:

$$MR = \frac{P(3.58791 - 0.062745 * \nu)}{L * Dv} \tag{2.35}$$

where: $P$ is the vertical load (Lbs.)
$L$ is the specimen thickness (in)
$Dv$ is the vertical deformation (in)
$\nu$ is Poisson's ratio.

The results are summarized in Table 2.4 below. The resilient modulus from the laboratory is used to calculate the elastic modulus of the asphalt concrete layer used in the SAPSI-M analysis for obtaining the response of a pavement structure under a given load.

Table 2.4. Resilient Modulus Results

| Sample | | MR (psi) | Mean (psi) | Std. Dev. | COV |
|---|---|---|---|---|---|
| 102 | 102-1 | 243491 | 252575 | 18706 | 7.41% |
| | 102-2 | 250906 | | | |
| | 102-3 | 234016 | | | |
| 146 | 146-1 | 264571 | | | |
| | 146-2 | 238582 | | | |
| | 146-3 | 283883 | | | |

## 2.5.2 Fatigue Curves

The main purpose of this study was to determine a fatigue curve that can be used to determine the fatigue life of an asphalt mix subjected to a multi-axle load pulse. To do

so, specimens were tested under different load pulses representing different axle configurations. Table 2.5 shows the fatigue testing matrix.

Table 2.5. Fatigue Testing Matrix

| Stress Level | Axle no. / Interaction | 1 | 2 | 3 | 4 | 8 |
|---|---|---|---|---|---|---|
| Low | Low (25%) | x x | | x x | | x x |
| | Medium (50%) | | | | | |
| | High (75%) | | | | | |
| Medium | Low (25%) | x x x | | x x x | x x x | x x x |
| | Medium (50%) | | x x x | | | |
| | High (75%) | | | | | x x |
| High | Low (25%) | x x | x x | x x | | x x |
| | Medium (50%) | | | | | |
| | High (75%) | | | | | |

No. of 'x's represents the number of samples tested.

Three tensile stress levels where used: 4.375, 8.75 and 17.5 psi. The medium stress level is the stress required to produce a strain at the center of the specimen equal to those at the bottom of the AC layer modeled in SAPSI-M. The 5 axle configurations tested for fatigue life are: single, tandem, tridem, 4-axles and 8 axles. The spacing between the axles is 3.5 feet and each axle carries 13 kips (medium stress). The interaction level is defined as the ratio of the peak stress to that of the valley (also known as midway) and is shown in Figure 2.33. The high interaction level represents a thicker asphalt concrete layer (about 10 inches) while the lower interaction level represents a thinner pavement (about 6 inches).

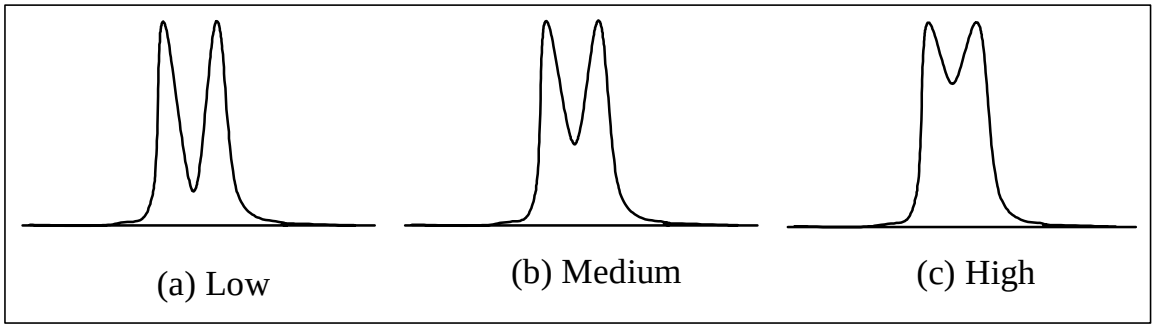


Figure 2.33. Different Interaction Levels

For all fatigue test load pulses, a twenty (20) pound sustained load was used to guarantee contact between the loading strips and the specimens at all times. The twenty pound load was applied first to the specimen, and a rest period of ninety (90) seconds was used before the actual load cycles started. This rest period is applied to make sure that the deformation due to the sustained load is not included in the response recorded for the first

cycle. The average of three consecutive cycles was taken as the value of the intermediate one. Thus, the data presented as cycle number 5 is basically the average of cycles 4, 5 and 6. Collected data were filtered using the moving point average to reduce the noise. A twenty point moving average correction was applied. This is acceptable given that the data was collected at a rate of 2000 readings per second, meaning that in a 0.1 second loading, 200 readings are taken.

Table 2.6. Fatigue Tests Results

| Axle Configuration | Sample No. | Intial DE | Nf | Tensile strains | | Tensile Stresses (psi) |
|---|---|---|---|---|---|---|
| | | | | First Peak | Last Peak | |
| 1 - axle Low Stress(25% Int.) | 119 | 3.00E-05 | 46135 | 2.00E-05 | | 4.062 |
| | 157 | 2.00E-05 | 52137 | 2.50E-05 | | 4.062 |
| 3 - axles Low Stress(25% Int.) | 140 | 1.00E-04 | 15119 | 2.50E-05 | 3.50E-05 | 4.375 |
| | 133 | 1.10E-04 | 11725 | 3.00E-05 | 4.00E-05 | 4.375 |
| 8 - axles Low Stress(25% Int.) | 150 | 1.80E-04 | 8267 | 2.80E-05 | 5.00E-05 | 4.375 |
| | 127 | 2.20E-04 | 6983 | 3.00E-05 | 6.00E-05 | 4.375 |
| 1 - axle Medium Stress(25% Int.) | 139 | 1.10E-04 | 13378 | 3.30E-05 | | 8.125 |
| | 142 | 1.30E-04 | 12209 | 4.00E-05 | | 8.125 |
| | 130 | 1.00E-04 | 14867 | 3.30E-05 | | 8.125 |
| 2 - axle Medium Stress(50% Int.) | 122 | 2.50E-04 | 6122 | | 6.00E-05 | 8.749 |
| | 128 | 2.50E-04 | 5770 | | 6.00E-05 | 8.749 |
| | 124 | 2.80E-04 | 5219 | | 6.00E-05 | 8.749 |
| 3 - axle Medium Stress(25% Int.) | 116 | 3.75E-04 | 4316 | 4.00E-05 | 5.50E-05 | 8.749 |
| | 156 | 4.00E-04 | 3692 | 5.50E-05 | 7.30E-05 | 8.749 |
| | 147 | 3.00E-04 | 4511 | 4.50E-05 | 5.70E-05 | 8.749 |
| 4 - axle Medium Stress(25% Int.) | 141 | 4.25E-04 | 3499 | | 8.00E-05 | 8.749 |
| | 144 | 4.25E-04 | 3772 | | 7.00E-05 | 8.749 |
| | 117 | 4.50E-04 | 4097 | | 6.50E-05 | 8.749 |
| 8 - axle Medium Stress(25% Int.) | 111 | 6.00E-04 | 3215 | 4.00E-05 | 7.50E-05 | 8.749 |
| | 109 | 5.00E-04 | 2650 | 3.30E-05 | 6.50E-05 | 8.749 |
| | 121 | 6.00E-04 | 2269 | 4.00E-05 | 7.00E-05 | 8.749 |
| 8 - axles Medium Stress(75% inter.) | 136 | 7.50E-04 | 2052 | | 1.20E-04 | 4.375 |
| | 114 | 6.00E-04 | 2359 | | 1.00E-04 | 4.375 |
| 1 - axles High Stress(25% Int.) | 112 | 5.25E-04 | 2692 | 8.00E-05 | | 15.624 |
| | 151 | 4.80E-04 | 3020 | 7.00E-05 | | 15.624 |
| 2 - axles High Stress(25% Int.) | 145 | 1.10E-03 | 1533 | | 1.40E-04 | 16.874 |
| | 137 | 1.60E-03 | 891 | | 1.80E-04 | 16.874 |
| 3 - axles High Stress(25% Int.) | 149 | 1.40E-03 | 1105 | 9.00E-05 | 1.30E-04 | 17.499 |
| | 138 | 1.50E-03 | 1020 | 8.40E-05 | 1.30E-04 | 17.499 |
| 8 - axles High Stress(25% Int.) | 118 | 2.50E-03 | 620 | 8.00E-05 | 1.70E-04 | 17.499 |
| | 106 | 2.80E-03 | 568 | 8.00E-05 | 1.70E-04 | 17.499 |

The pavement responses under the actual axle configurations were obtained using the SAPSI-M program. A 6 inch AC layer with an elastic modulus of 700 ksi was used

and typical values for base thickness and modulus and subgrade modulus were input. The load pulse is obtained by equating the tensile strains (time history) at the bottom of the AC layer to the tensile strains at the center of the lab specimen.

The number of repetitions to failure was determined as mentioned in section 2.4.3. The stored energy density until cracking (SEC) was calculated from the indirect tensile strength test and was found to be 1.556 psi. For each tested specimen, the initial dissipated energy density, initial strain and $N_f$ were recorded for later use in developing the fatigue curves. These results are tabulated in Table 2.6.

### *2.5.2.1 Dissipated-Energy-Based Fatigue Curves*

For the dissipated energy fatigue curve, the initial dissipated energy density is plotted versus the number of repetitions to failure. Figure 2.34 shows cumulative dissipated energy density curves for different axle configurations tested under the different stress levels. The overall behavior is as expected: Higher stresses (HS) caused higher dissipated energies, and more axles in a configuration lead to more dissipated energy as well.

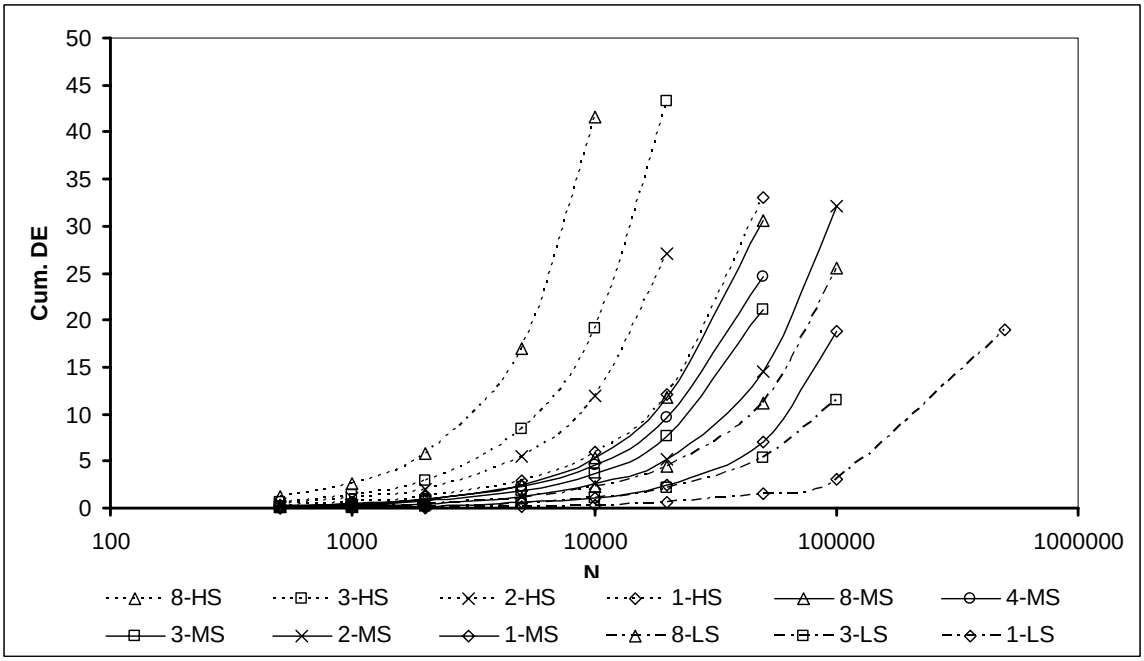


Figure 2.34. Cumulative DE Curves for Different Axle Configurations

Figure 2.35 shows the dissipated energy fatigue curve. It can be seen that this curve is unique. All the different axle configurations with the different interaction and stress levels are presented. Thus, using this fatigue curve would allow for determining the

number of repetitions till failure for any axle configuration in one step without the need to build up an axle group from its components. The fatigue model obtained is:

$$N_f = 2.12 \ \ Wo^{-0.955} \tag{2.36}$$

where *Wo* is the initial dissipated energy density (in psi) of the whole axle group.

However, with the failure criterion used, the failure is assumed when cracks initiate in the specimen. This might not be the best representation of actual failure in the field, where cracks have already initiated and propagated from the bottom of the AC to the top. So, different failure criteria were assumed to check its effect on the dissipated energy fatigue curves. Figure 2.36 shows the curves obtained when considering different dissipated energy levels as the failure criteria.

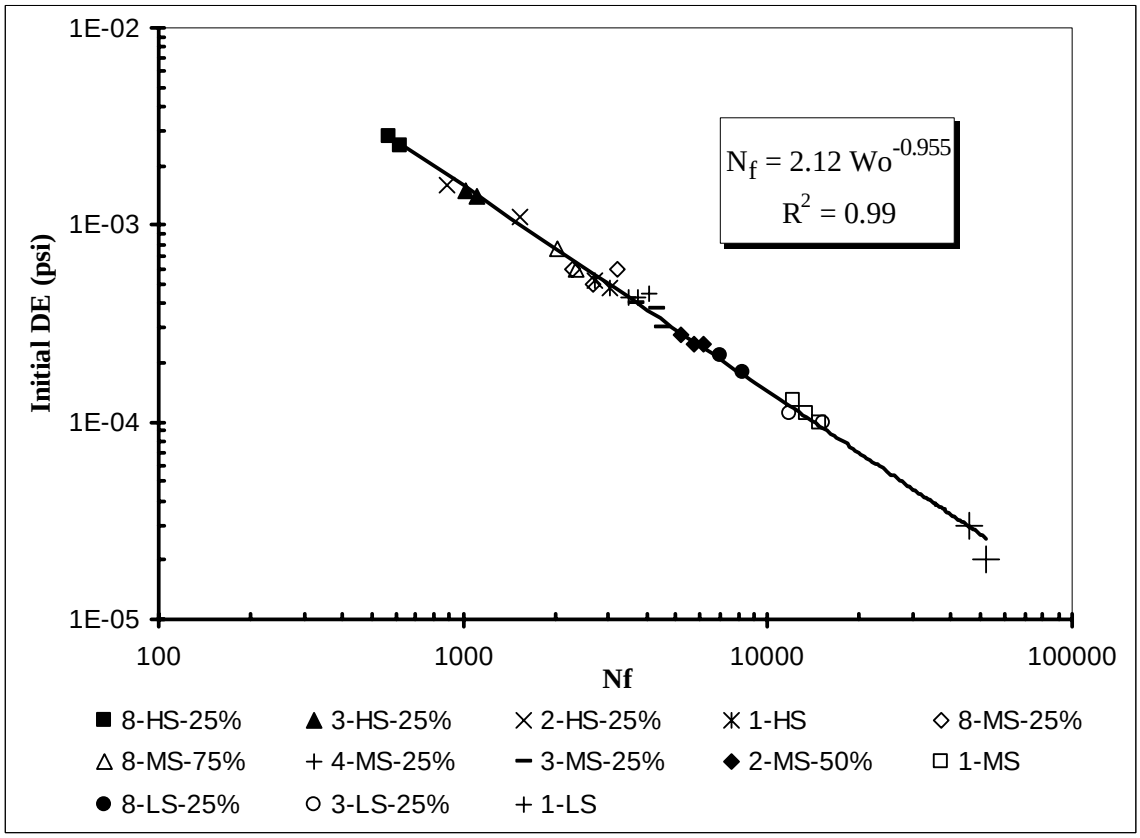


Figure 2.35. Dissipated Energy Fatigue Curve

The curves obtained are all parallel; thus, a shift factor is sufficient to make up for the later cracking stages. Since this was not the main focus of the study, no further analyses were performed to determine what each dissipated energy level corresponded to in terms of crack development and propagation.

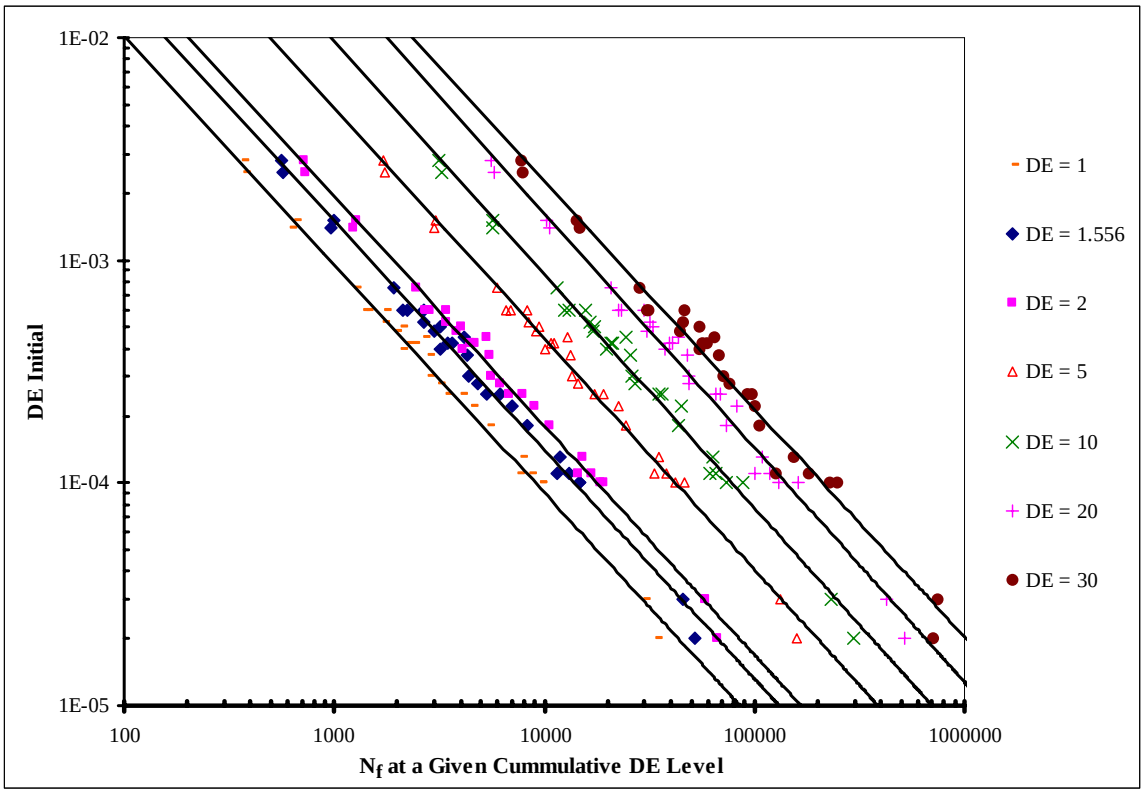


Figure 2.36. Fatigue Curves at Different DE Levels

Two samples were tested under a continuous (i.e., without rest period) haversine load at medium stress level. The same failure criterion was used to define failure, and the dissipated energy density for one cycle corresponded to the load value going from 20 pounds (the sustained load value) to the peak, then back to the 20 pound level. The results were plotted on the same graph with the dissipated energy fatigue curve and are shown in Figure 2.37. The initial dissipated energy density and number of repetitions to failure from this test was found to be matching with the dissipated energy fatigue curve.

Another two samples were tested under a load pulse simulating a whole truck. The truck used, truck number 13 in the Michigan Trucks table (check appendix), consists of a steering axle, front tandem axle, a tridem axle, and a rear tandem and tridem axles consecutively from front to end. The truck with its axle loads is shown in Figure 2.38. The whole truck is treated as one load pulse, and the dissipated energy density is determined for the whole truck. The rest period was determined based on the same ratio used for the axle groups (1 loading to 4 rest period). The loading duration was taken from the point when the influence of the steering axle started till the response due to the final axle died. The results are presented in Figure 2.37Figure  below, and it can be seen that it matches with the dissipated energy fatigue curve. Therefore, no further fatigue testing was performed for trucks or axle groups since the dissipated energy fatigue curve was

found to be unique regardless of the load pulse. The procedure used to determine the truck factors of the rest of the trucks will be presented later.

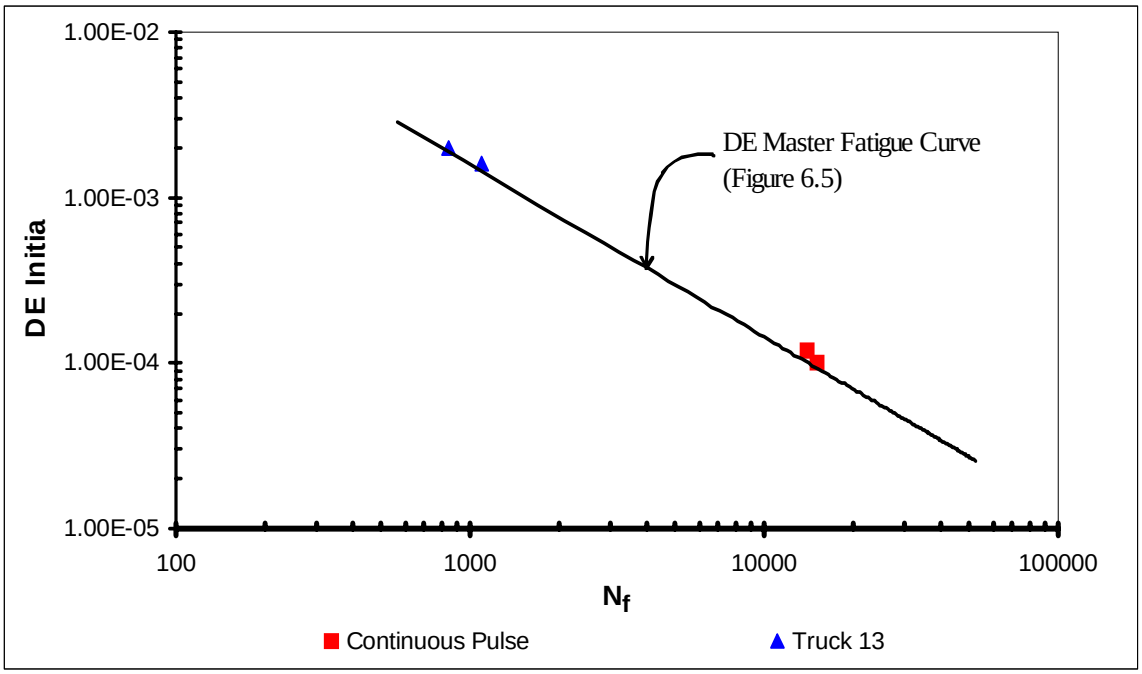


Figure 2.37. Continuous Load Pulse and Truck 13 Results

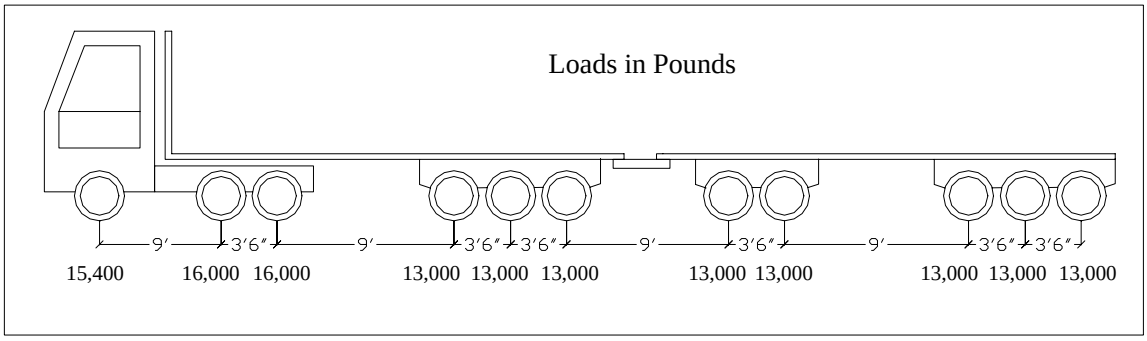


Figure 2.38. Truck Number 13

### *2.5.2.2 Stress Based Fatigue Curves*

Three axle configurations (single, tridem and 8 axles) were tested under three different stress levels (Low, Medium and High). The stress fatigue curves were obtained by plotting the stress level versus the number of load repetitions to failure. The number of repetitions to failure was determined using the same failure criterion as that for the dissipated energy fatigue curve (based on dissipated energy). As expected, at a constant stress level, the number of single axle repetitions to failure was higher than that of a tridem, which in turn, was higher than that of the 8-axle group. Note that for multi-axles

and truck analysis, a stress-based fatigue curve would need to be determined for each configuration separately. The stress fatigue models are:

$$1-axle: N_f = 21.25 \quad (\sigma)^{-2.1304} \tag{2.37}$$

$$3-axles: N_f = 36.76 \quad (\sigma)^{1.8457} \tag{2.38}$$

$$8-axles: N_f = 27.815 \quad (\sigma)^{1.888} \tag{2.39}$$

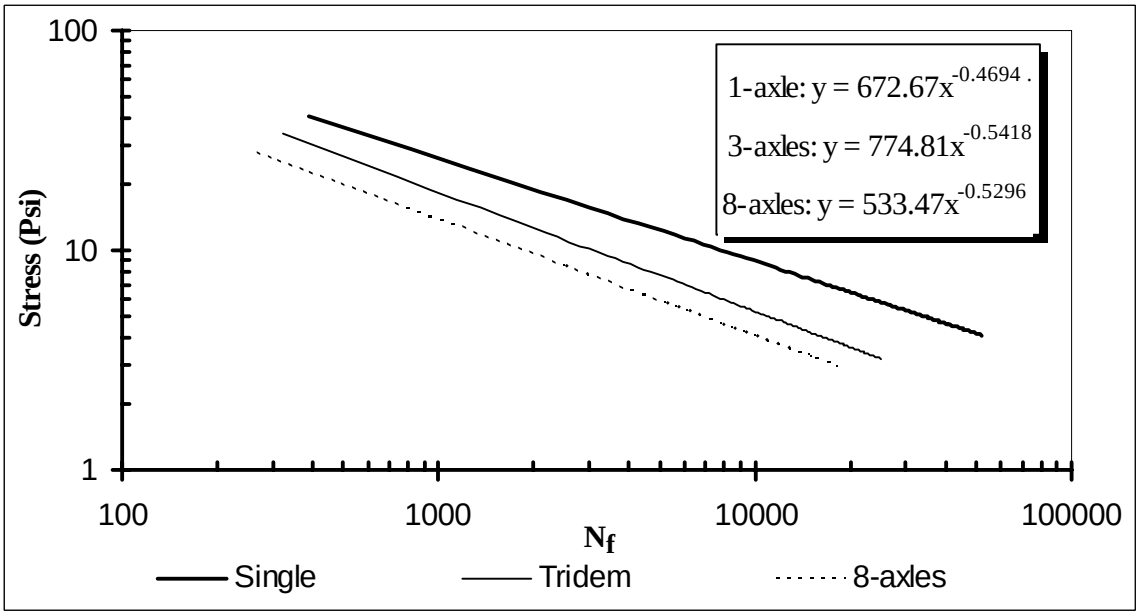


Figure 2.39. Stress Fatigue Curves

### *2.5.2.3 Strain-Based Fatigue Curves*

Strain fatigue curves are the most used fatigue curves for asphalt concrete. However, the way failure is defined varies from researcher to researcher. In general, when using a strain controlled test, the strain level is plotted versus the number of load repetitions to failure; on the other hand, in a stress controlled test, the initial strain is plotted versus the number of load repetitions to failure. In this study, the indirect tensile test performed runs in a stress controlled mode, and thus the initial strains were plotted versus the number of load cycles at which the value of the cumulative dissipated energy density reached the SEC value.

When testing specimens under a multi axle configuration, it was noticed that the strain peak value increased significantly from the first peak, to subsequent peaks (Figure 2.40). This is due to the strain accumulation from one axle response to another and the fact that the test is a stress controlled test. Two strain fatigue curves were generated based on: 1) first strain peak fatigue curves, and 2) last strain peak fatigue curve. The single pulse load results were the same for both fatigue curves since the response has only one peak.

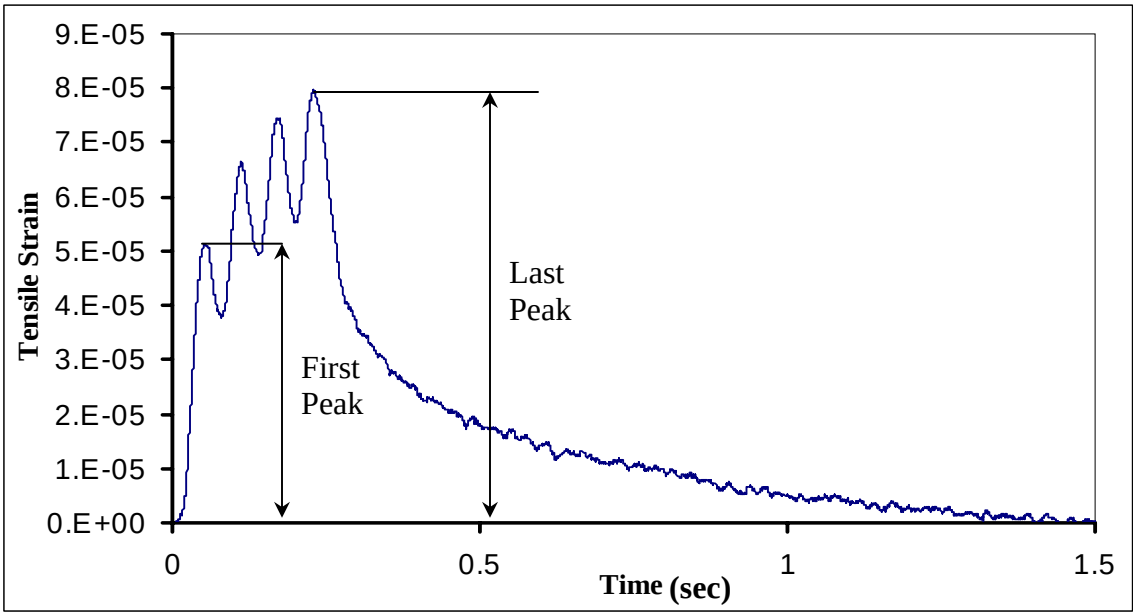


Figure 2.40. Typical Tensile Strain Response from ITT Under Multi Axle Load Configuration

i) Fatigue Curves based on First Peak Strain: Figure 2.41 shows the fatigue curves obtained from plotting the first strain peak ($\varepsilon_{oF}$) versus the number of repetitions to failure (same failure criterion used as above). For a constant stress level, the first peak strain values are the same for single, tridem and 8 axles. This is expected since for the first peak, there is still no accumulation of strains due to the multiple axles. Thus, at a constant strain level, the number of repetitions to failure increases as the number of axles decreases. This means that a fatigue curve needs to be established for each axle configuration. The fatigue models obtained are:

$$1-axle: N_f = 0.0733\ (\varepsilon_{oF})^{-2.342} \quad (2.40)$$

$$3-axles: N_f = 0.0597\ (\varepsilon_{oF})^{-2.172} \quad (2.41)$$

$$8-axles: N_f = 0.0616\ (\varepsilon_{oF})^{-2.479} \quad (2.42)$$

ii) Fatigue Curve Last Peak Strain: To overcome the need of a separate fatigue curve for each axle configuration, the last peak strains ($\varepsilon_{oL}$) were plotted versus the number of repetitions to failure (Figure 2.42). When considering the last peak strain instead of the first, the number of axles and their spacing is taken into account leading to a unique curve for different axle groups, as shown in Figure 2.42. The fatigue model obtained is:

$$N_f = 0.00003777\ (\varepsilon_{oL})^{-1.92802} \quad (2.43)$$

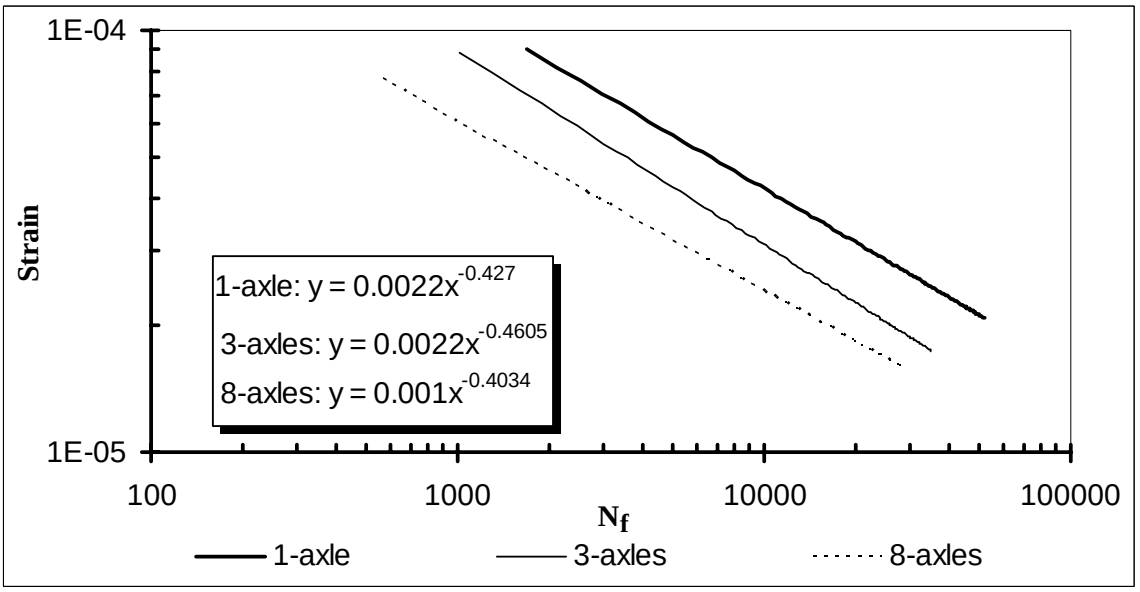


Figure 2.41. Fatigue Curves based on First Peak Strain

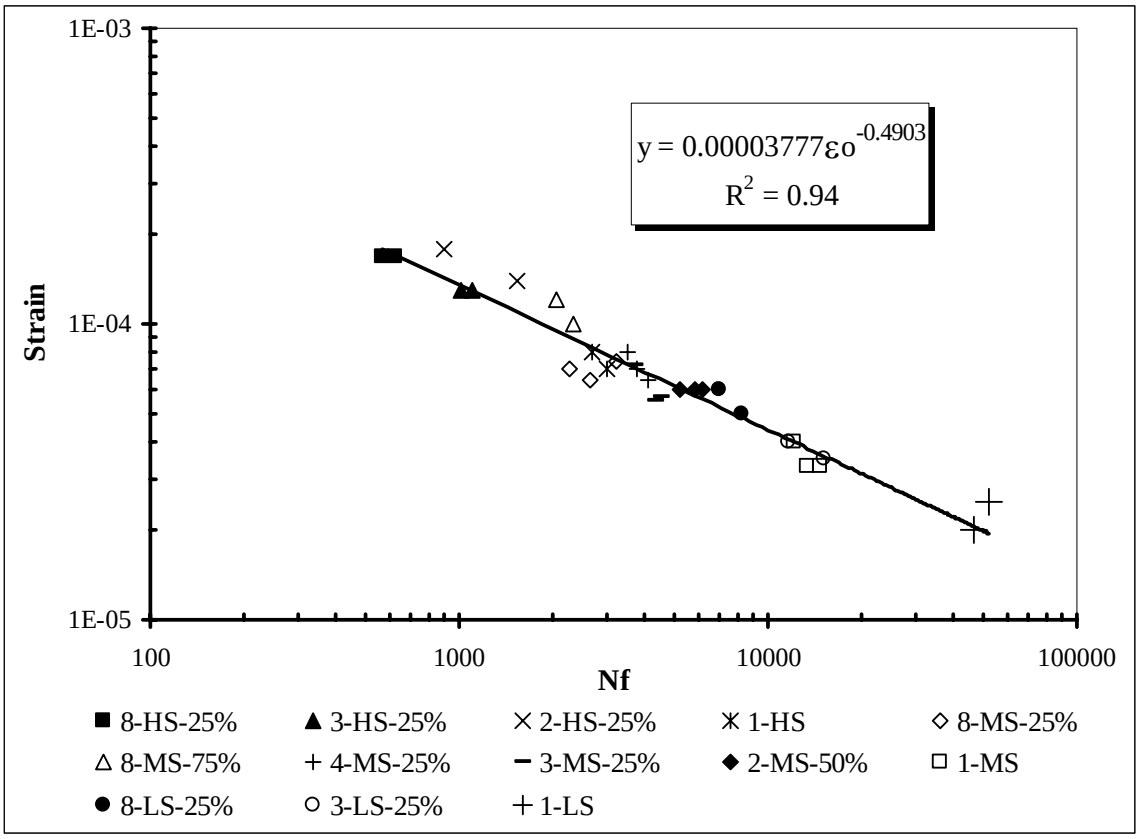


Figure 2.42. Fatigue Curve for All Axle Configurations based on Last Peak Strain

### *2.5.2.4 Comparison between the Different Fatigue Curves*

The stress and the first peak strain fatigue curves are not the best prediction models when analyzing multi-axle configurations or trucks since any axle configuration would need to have its own fatigue curve. On the other hand, using the last peak strain fatigue curve dictates using stress controlled fatigue tests since in a strain-controlled test, there will not be any accumulation of strains from the first axle to the following one (although a similar stress curve might be obtained in a strain-controlled test, but since no strain controlled tests were performed in this study, such curves could not be established). When using the dissipated energy fatigue curve, all these problems can be overcome. Additionally, the last peak strain fatigue curve cannot be used to determine truck factors because the relatively long rest period between the axle groups in a truck reduces the interaction between these groups, and therefore, under estimates the last peak strain. Moreover, there is less scatter in the data when using the initial dissipated energy density versus using the last peak strain. This can be visually seen when comparing Figure 2.41 to Figure 2.42. It is shown as well in the "$R^2$" values for both curves. (Note that when using the last peak strain, the strain values used are still considered as initial strains). Therefore, the dissipated energy fatigue curve is recommended to be used when analyzing multiple axles and truck configurations.

## 2.6 LOAD EQUIVALENCY, AXLE AND TRUCK FACTORS

In this section, the values of Load Equivalency (LEF), Truck (TF) and Axle Factors (AF) values are determined using the fatigue curves established in the previous section, and using the mechanistic prediction models mentioned in section 2.3. When calculating LEFs, TFs and AFs from the fatigue curves, the initial values of dissipated energy and strain were determined for each axle combination as a whole, and used in the fatigue models (based on DE or based on strain) to determine the fatigue life from the combination under study. For the mechanistic prediction models, 1) the initial dissipated energy and strains from single pulses representing peak and peak-midway values were obtained; 2) these values were then used to determine the fatigue life, and 3) Miner's hypothesis is applied to determine the fatigue life of each axle configuration as a whole from its components. Some of the terms used in this section are defined below.

The Load Equivalency Factor (LEF) is defined as the relative damage of an axle group or a truck to that of a standard axle, where damage is the inverse of the number of repetitions to failure.

$$LEF = \frac{Damage\,(axle\ configuration)}{Damage\,(18\text{-}kip\ standard\ axle)} = \frac{Nf\ (axle\ configuration)}{Nf\ (standard)} \qquad (2.44)$$

The Axle Factor (AF) is defined as the relative damage of an axle group to that of a single axle carrying the same load as any of the axle group components. For example, a 39-kip tridem AF is determined as:

$$AF = \frac{Damage\,(39\text{ - kip tridem})}{Damage\,(13 - \text{kip single})} = \frac{Nf\ (13\text{ - kip single})}{Nf\ (39\text{ - kip tridem})} \tag{2.45}$$

The Truck Factor (TF) is defined as the sum of LEF from the axles within a given truck configuration.

The LEF, AF and TF per tonnage are defined as the LEF, AF and TF normalized by the total legal maximum load carried by the axle configuration, respectively. Using the per tonnage values allow for a better understanding of the relative damage caused by the different axle configuration while carrying the same total gross weight, and thus allow for determining the most efficient configuration to carry a certain load.

The initial procedures used to determine these values consist basically of building up the truck or axle group from its axle components and computing the damage based on Miner's hypothesis. However, in this study, the LEFs, AFs and TFs are calculated directly by simulating the whole truck/axle group as one load pulse in an indirect tensile cyclic test.

Both initial dissipated energies and strains were used with their corresponding fatigue curves to determine the number of repetitions to failure. The main advantage of using this approach is eliminating, or at least significantly reducing, the error in the results due to the variability in specimen and testing conditions. The same specimen was used to determine the initial dissipated energy density for all axle groups and trucks studied, and thus eliminating the variability of air void content and the asphalt concrete internal structure. Additionally, performing all the tests while the specimen was still in the same position in the loading frame decreased any errors due to specimen misalignment with the loading strips. Trucks consisting of up to 11 axles and axle groups of up to 8 axles were studied. Three samples from mix I were tested under different load combinations for 15 cycles each to determine the initial dissipated energy density and strains. The results obtained are presented in the following sections.

### 2.6.1 Axle Factors

As mentioned previously, the Axle Factor (AF) is defined as the relative damage of an axle group to that of a single axle carrying the same load as any of the axle group components. The effects of thickness, and thus interaction level, and speed (load duration) on the axle factors were studied using 13-kip axles.

#### *2.6.1.1 AF for Different AC Thickness*

Thin, intermediate and thick asphalt concrete layers were modeled through high (75%), medium (50%) and low (25%) interaction levels between the axle components of an axle group (see section 2.5.2 for proper definitions). Figure 2.43 shows the AF for single, tandem, tridem, quad and 8-axles at the different interaction levels. The results

showed that there is no significant effect of the interaction level on the axle factor. Figure 2.44 shows the axle factors per tonnage. The AF/Tonnage is defined as the axle factors divided by the total weight carried by all the axle group components. Similarly, there is no significant effect of the interaction level on the AF/Tonnage. Therefore, it can be concluded that the thickness of the AC layer has no effect on the relative damage between different axle configurations. Note that the number of repetitions to failure changes as the thickness change for each of the axle groups.

### *2.6.1.2 AF for Different Vehicle Speeds*

To simulate different axle speed values, the duration of the load cycles was modified. However, the same ratio of the loading/unloading to rest period was maintained. Three velocities were studied: 27 mph, 40 mph and 60 mph. Again, the AF and AF/Tonnage were calculated. Figure 2.45 shows that the fatigue life of different axle configurations increases as the speed increases. Figure 2.46 shows that the change in the AF is not as significant as the change in the fatigue life. Figures 2.47 and 2.48 show the effect of speed on the hysteresis loop, and thus the value of dissipated energy density, for single and 8-axles. This increase in the dissipated energy density explains the increase in the fatigue life with an increase in the velocity.

### *2.6.1.3 Summary of Effect of Axle Groups*

Figures 2.43, 2.44 and 2.45 show that using multi axles increases the total fatigue life of an asphalt mix. The increase in fatigue life is much more significant when going from a single to tandem and tridem axles; whereas the value of AF/Tonnage starts to even out as the number of axles reaches 7 and 8. This implies that using an 8-axle configuration to carry 104 kips is much better that using 8 separate axles carrying 13 kips each.

To compare the results obtained from this study with those from the AASHTO findings, the LEF values of the 13-kip single, 26-kip tandem and 39-kip tridem were used to calculate the corresponding axle factors. The AF was calculated as:

$$AF = \frac{LEF(\text{tandem or tridem})}{LEF(\text{single})} \tag{2.46}$$

The AASHTO AF values for the tandem and tridem axles were calculated to be 1.38 and 1.49, respectively. The AF values for the tandem and tridem from this study were found to be 1.57 and 1.95, respectively. It should be noted that the LEFs from the AASHTO study are based on Pavement Serviceability Index (PSI) from the AASHO road test and not from laboratory fatigue tests; therefore, the difference between the two is expected.

## 2.6.2 Load Equivalency Factors

The Load Equivalency Factor (LEF) is defined as the relative damage of an axle group to that of a standard axle. The same results were obtained for the LEFs as the AFs. The only difference is that the values of the AF and AF/Tonnage are lower since the standard 18 kip single axle will have a lower fatigue life than the 13 kip single axle. However, all the results were presented in the form of AF in this study since the effect of the usage of axle groups would be more obvious when compared to a similar single axle instead of a single axle with a different weight. The results are summarized in Table 2.7 below.

Table 2.7. LEF Results

| Nf | | $N_f$ | LEF | LEF/Tonnage |
|---|---|---|---|---|
| 1 axle 18-kip | | 5388 | 1.00 | 1.00 |
| 1 axle 13-kip | | 7750 | 0.70 | 0.96 |
| 25% Interaction | 2 axles | 4889 | 1.10 | 0.76 |
| | 3 axles | 3876 | 1.39 | 0.64 |
| | 4 axles | 2889 | 1.87 | 0.65 |
| | 5 axles | 2377 | 2.27 | 0.63 |
| | 7 axles | 1893 | 2.85 | 0.56 |
| | 8 axles | 1707 | 3.16 | 0.55 |
| 50% Interaction | 2 axles | 5987 | 0.90 | 0.62 |
| | 3 axles | 4592 | 1.17 | 0.54 |
| | 4 axles | 3577 | 1.51 | 0.52 |
| | 5 axles | 2992 | 1.80 | 0.50 |
| | 7 axles | 2477 | 2.18 | 0.43 |
| | 8 axles | 2289 | 2.35 | 0.41 |
| 75% Interaction | 2 axles | 5644 | 0.95 | 0.66 |
| | 3 axles | 4155 | 1.30 | 0.60 |
| | 4 axles | 3431 | 1.57 | 0.54 |
| | 5 axles | 3058 | 1.76 | 0.49 |
| | 7 axles | 2549 | 2.11 | 0.42 |
| | 8 axles | 2439 | 2.21 | 0.38 |

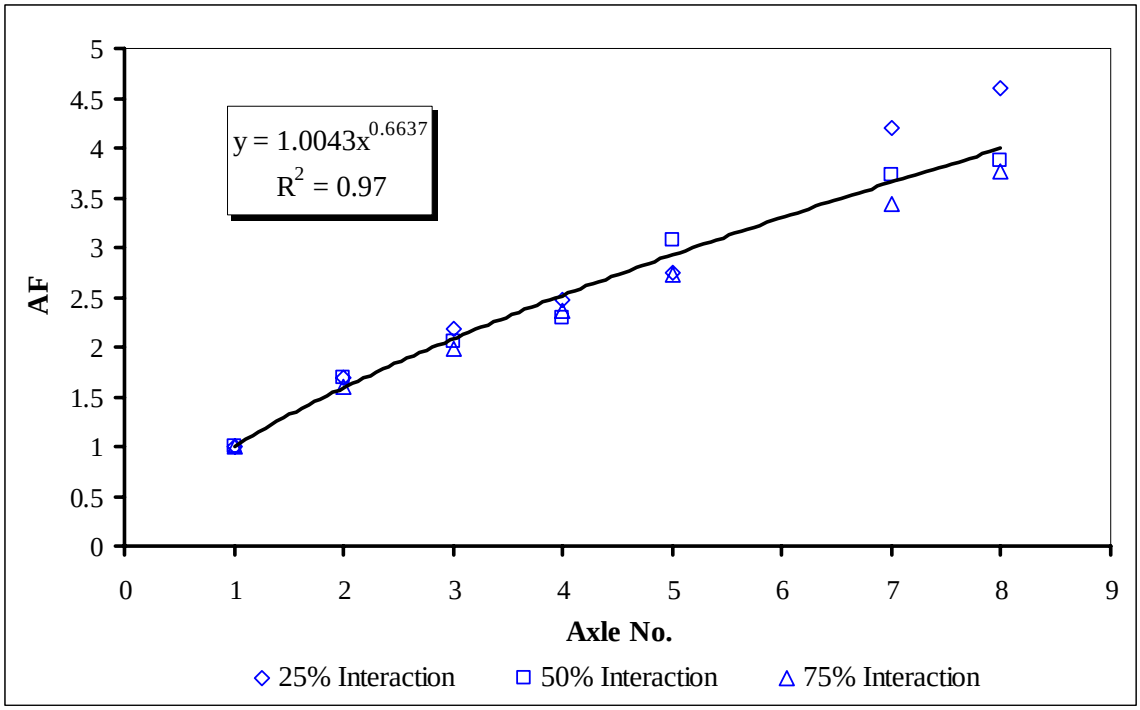


Figure 2.43. Axle Factor for Different Interaction Levels

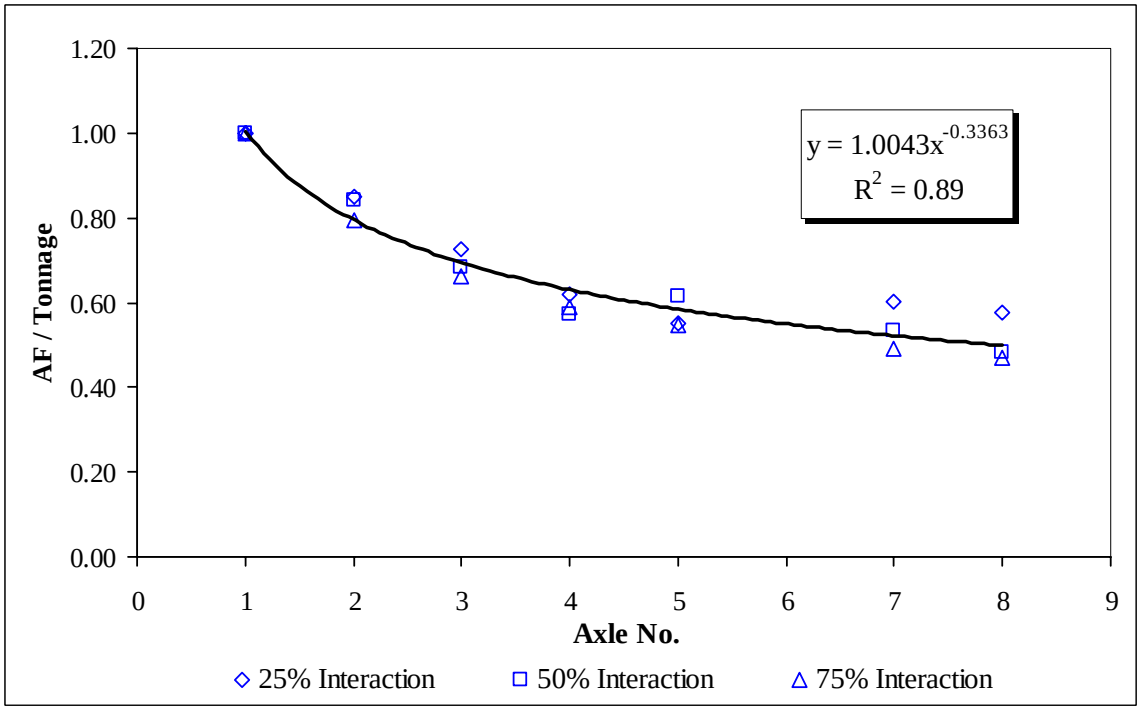


Figure 2.44. Axle Factor per Tonnage for Different Interaction Levels

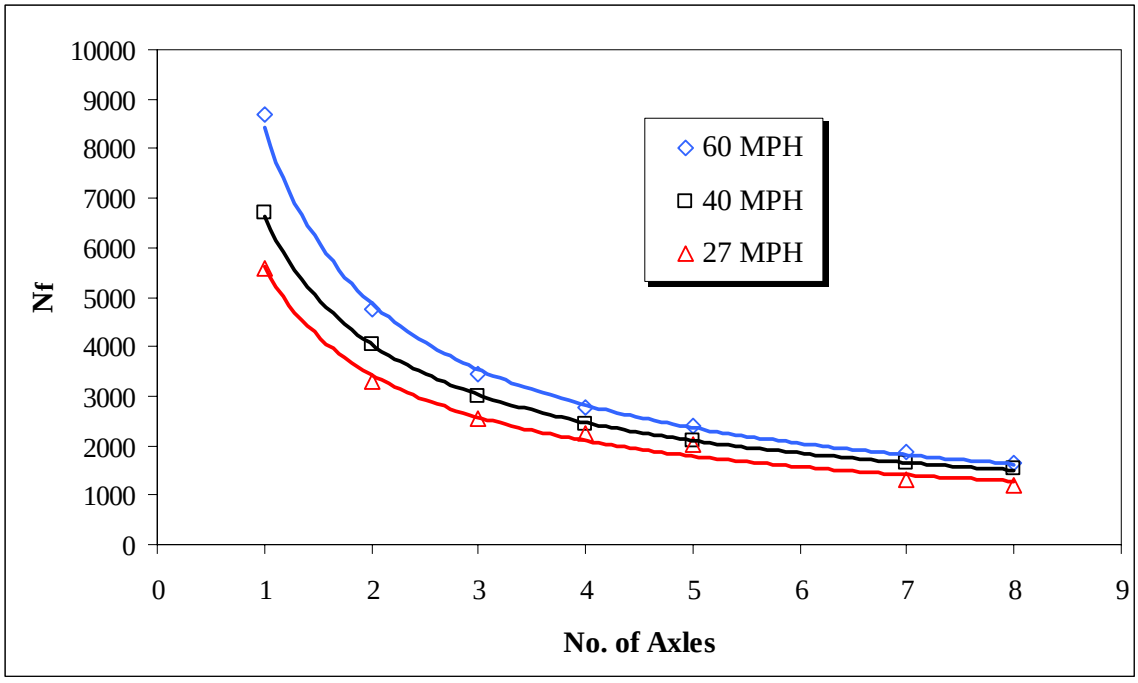


Figure 2.45. Nf Vs No. of Axles for Different Speed Values

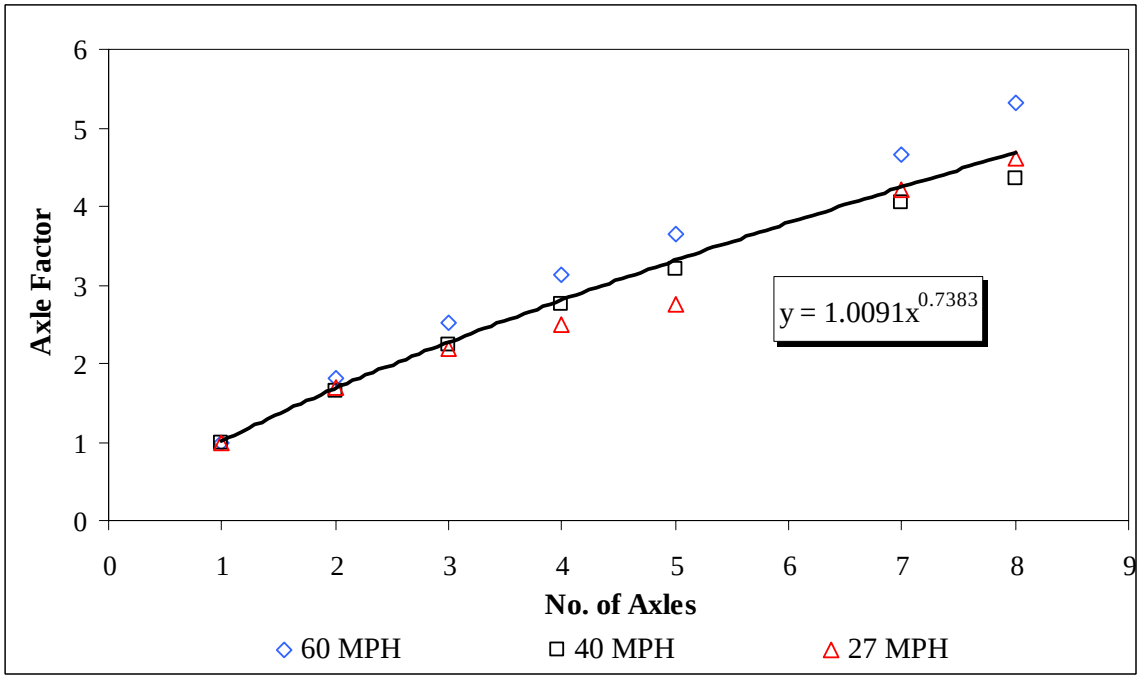


Figure 2.46. Axle Factor for Different Speed Values

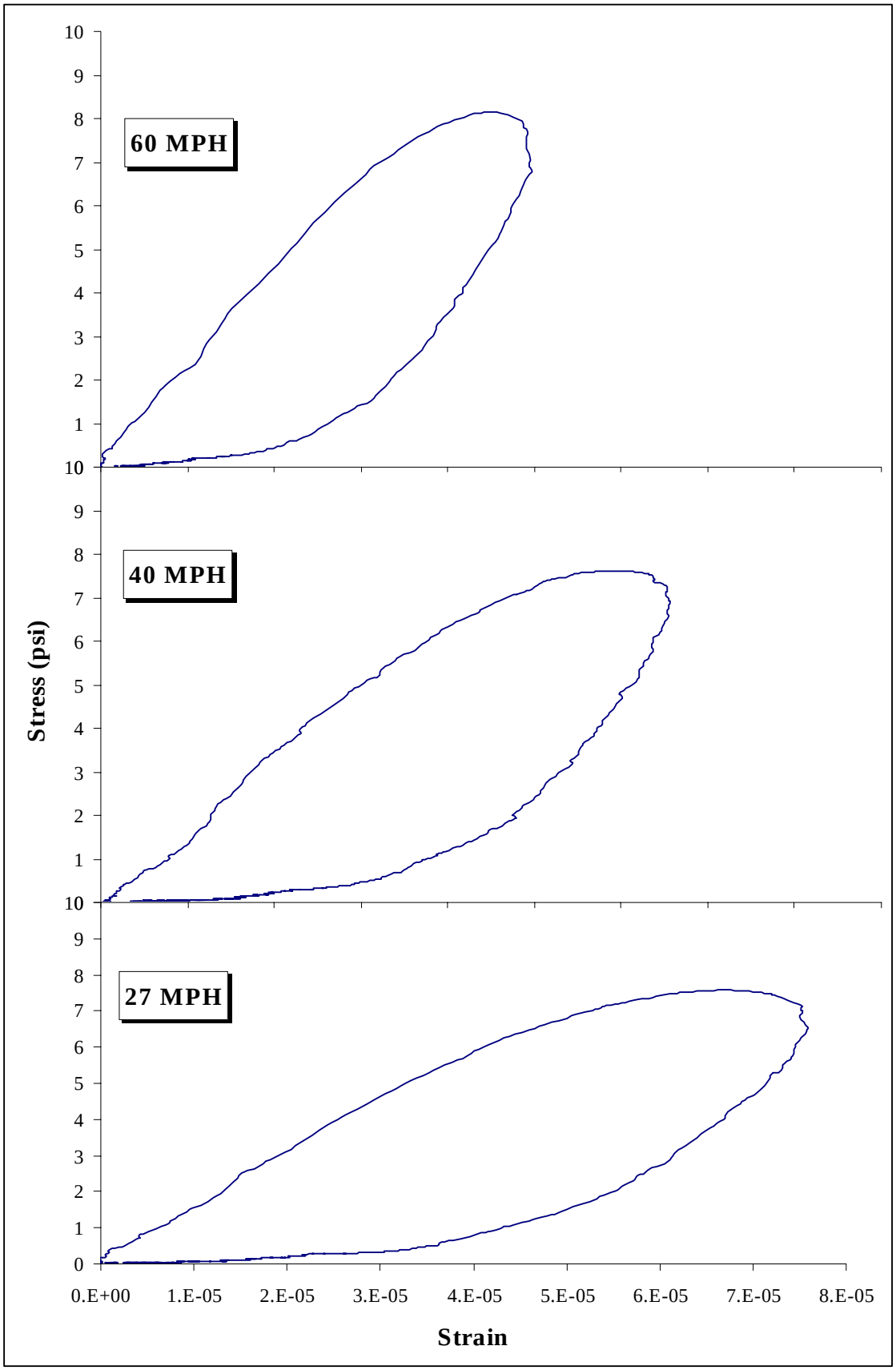


Figure 2.47. Effect of Speed on Dissipated Energy of a Single Axle

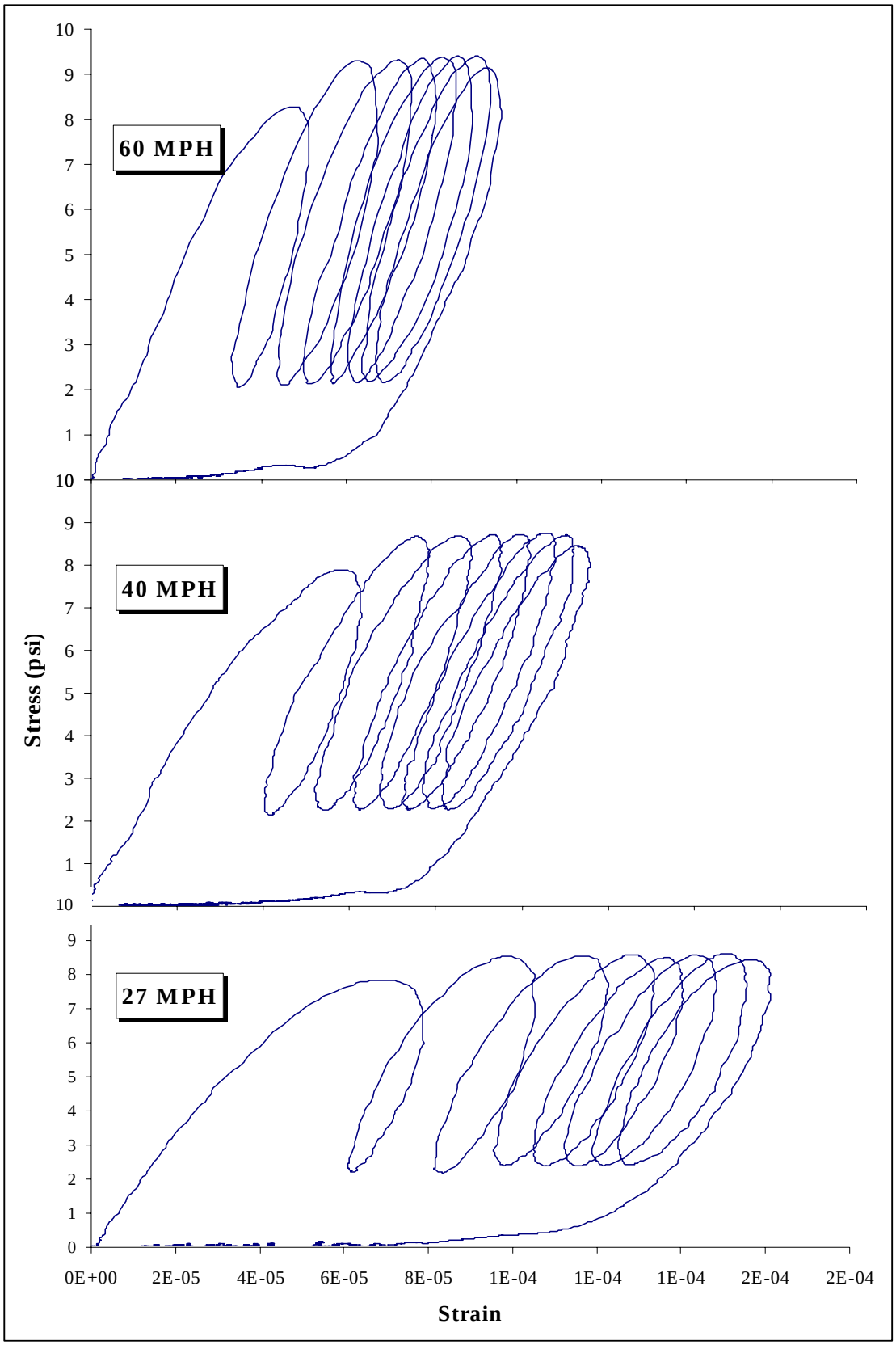


Figure 2.48. Effect of Speed on Dissipated Energy of an 8-Axle Group

## 2.6.3 Truck Factors

### *2.6.3.1 TF from Laboratory Measurements*

Truck Factor (TF) is defined as the relative damage of a truck to that of a standard axle. Ten trucks were selected for laboratory testing. The trucks were chosen to cover the axle configurations that are used in Michigan. The trucks used are: Truck 1, Truck 2, Truck 3, Truck 4, Truck 10, Truck 13, Truck 14, Truck 17, Truck 19, Truck 20, and Truck 21 (Check Table 2.8 for truck details). The initial dissipated energy density for all the trucks and the standard axle was determined twice, each time from a different sample. The fatigue life for each truck was determined using the dissipated energy fatigue curve, and the corresponding truck factors and truck factors per tonnage were calculated.

Table 2.8. Truck Axles and Axle Groups

| Truck No | No. of Axle Groups | No. of Axles | Truck Configuration |
|---|---|---|---|
| 1 | 2 | 2 | 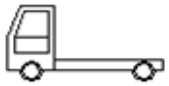 |
| 2 | 2 | 3 |  |
| 3 | 2 | 4 | 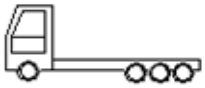 |
| 4 | 2 | 5 | 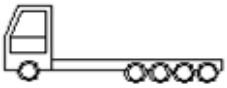 |
| 10 | 6 | 7 | 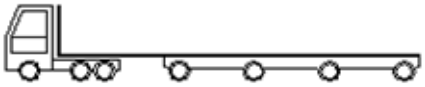 |
| 13 | 5 | 11 |  |
| 14 | 6 | 11 |  |
| 17 | 3 | 10 | 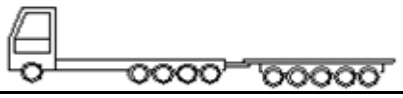 |
| 19 | 3 | 10 |  |
| 20 | 3 | 11 |  |
| 21 | 3 | 5 | 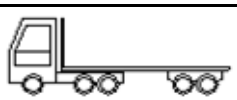 |

Figure 2.49 shows the truck factors, and Figure 2.50 shows the truck factors per tonnage. From the latter figure, it can be seen that Truck 1 is the most damaging per tonnage. Truck 1 is a 2-axle single body truck that consists of a 15.4 kip front steering axle and a

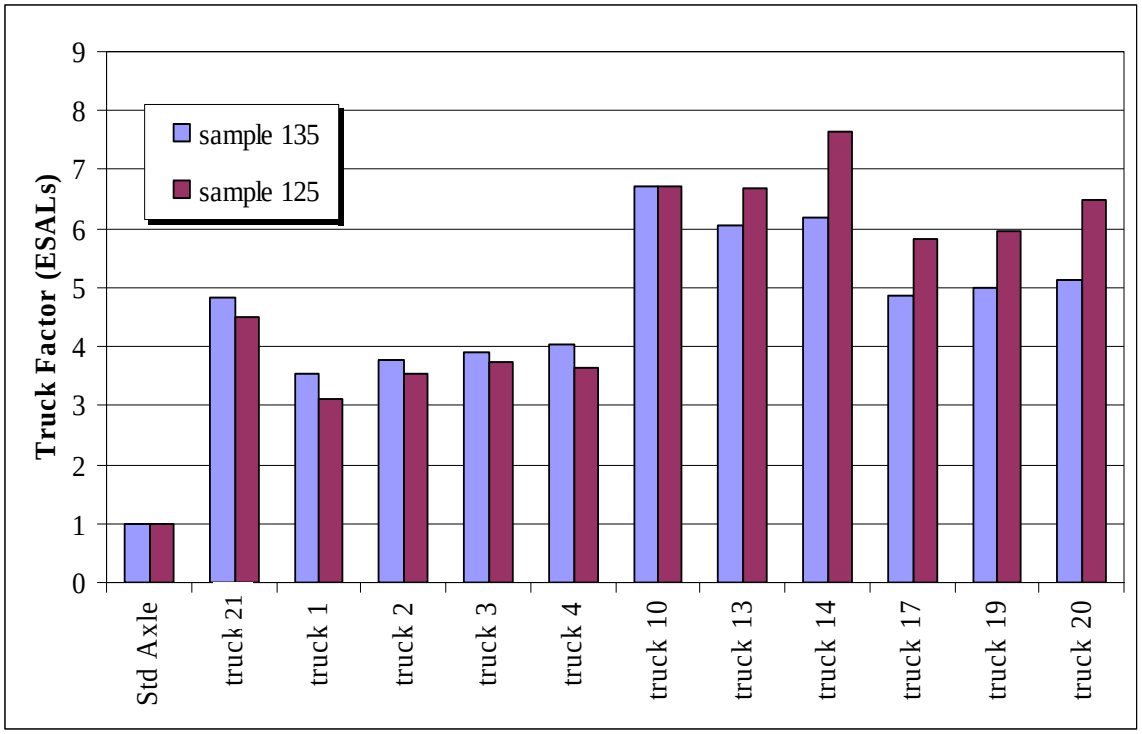


Figure 2.49. Truck Factors

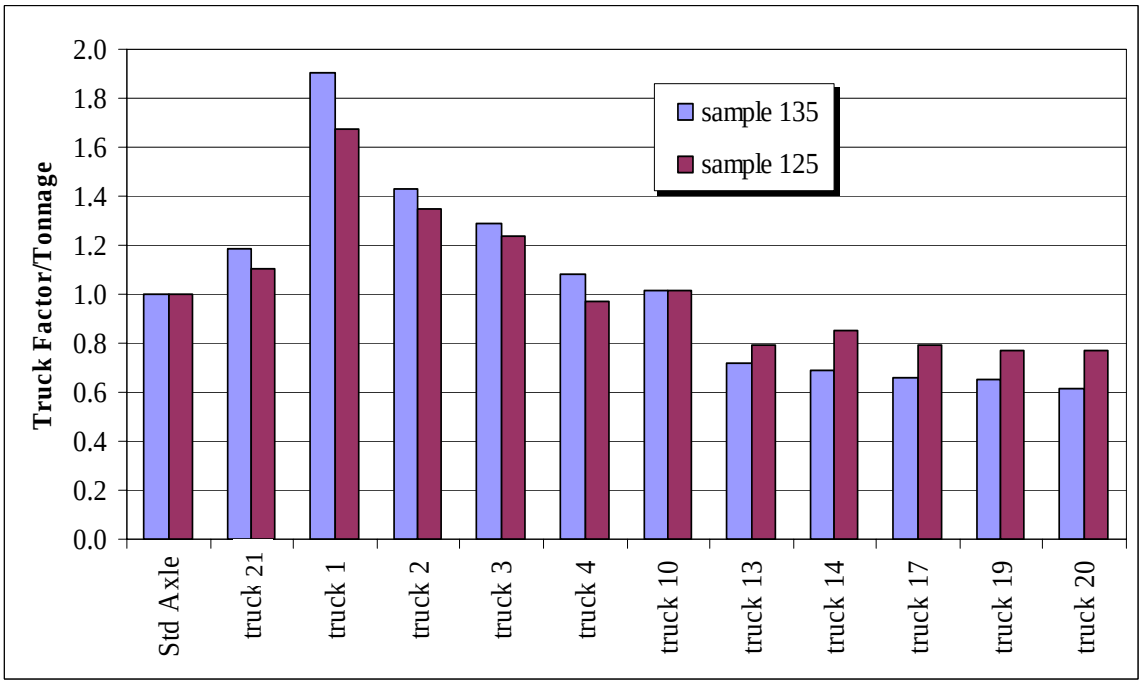


Figure 2.50 Truck Factors per Tonnage

single 18 kip standard axle in the rear. Trucks 13, 14, 17, 19, and 20 have very similar low truck factors per tonnage because their total load is distributed over larger axle groups (Table 2.8). The decrease in the truck factor per tonnage when going from Truck 1 to Truck 4 emphasizes the same finding mentioned in section 0 that multi-axle groups are less damaging than individual axles when considering the load they carry. Truck 20, which has the most axles and least axle groups, is the most efficient between all the trucks investigated.

#### *2.6.3.2 TF from Laboratory AF and AASHTO LEF*

This study was charged with determining the relative damage caused by multiple axles within an axle group; i.e., how much damage is caused by grouping multiple axles into one axle group. The scope of the study did not include verifying the AASHTO's "Fourth Power" damage law; i.e., we were not charged with determining how much damage is caused by increasing the load of a given axle relative to the standard 18-kip single axle. To do so would require extensive full-scale testing similar to what had been done in the original AASHO road test. Therefore, the TF's were obtained by converting multiple axle groups within each truck configuration into an equivalent number of single axles using the AF's obtained in this study, calculating the LEF of each axle group by multiplying the AF values obtained from the laboratory (Figure 2.43) with the Load Equivalency Factor (LEF) from AASHTO corresponding to the single axle at the legal load limit, and then summing the LEF of the different axle groups within a truck. This was done for different pavement cross-sections varying in AC layer thickness and modulus. Table 2.9 summarizes the results.

### 2.6.4 Evaluating Different Mechanistic Approaches for Determining AF and TF

In the mechanistic fatigue prediction of asphalt pavements due to different axle groups and trucks, the common practice is to build up the truck or axle group from its axle components and compute the damage based on Miner's hypothesis. Two approaches are typically adopted for axle groups: (1) Using the peak values, and (2) using the difference between the peak and midway values of the response. As for trucks, the damage is calculated by summing up the damage from the individual axles. These approaches use the fatigue curves obtained from single haversine or continuous sinusoidal load pulses to determine the damage/fatigue life of the individual axles. In this study, the fatigue life of an asphalt mixture under different trucks and axle groups was determined directly from the indirect tensile cyclic load test by using load pulses that are equivalent to the passage of an entire axle group or truck. Additionally, the fatigue life under individual axles was determined for the purpose of predicting the damage based on the procedures mentioned above. The predicted and measured fatigue lives were compared for the different axle groups and trucks. Both dissipated energy and strain fatigue curves were used to determine the axle factors, while only the dissipated energy fatigue curve was used for determining truck factors.

Table 2.9 Truck Factors from Laboratory AF and AASHTO LEF

| | | | Truck Factors | | | | | |
|---|---|---|---|---|---|---|---|---|
| | | | Eac = 350 ksi | | | Eac = 700 ksi | | |
| Truck | Truck No. | Total Wt. | 3.5 in | 8 in | 12 in | 3.5 in | 8 in | 12 in |
|  | 1 | *33.4* | 1.533 | 1.507 | 1.499 | 1.524 | 1.501 | 1.497 |
| 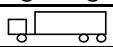 | 2 | *47.4* | 1.523 | 1.459 | 1.440 | 1.501 | 1.445 | 1.434 |
| 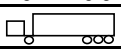 | 3 | *54.4* | 1.082 | 1.009 | 0.989 | 1.057 | 0.995 | 0.983 |
| 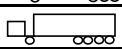 | 4 | *67.4* | 1.198 | 1.115 | 1.092 | 1.169 | 1.099 | 1.085 |
| 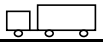 | 5 | *51.4* | 2.533 | 2.507 | 2.499 | 2.524 | 2.501 | 2.497 |
|  | 6 | *65.4* | 2.523 | 2.459 | 2.440 | 2.501 | 2.445 | 2.434 |
| 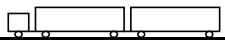 | 7 | *87.4* | 4.533 | 4.507 | 4.499 | 4.524 | 4.501 | 4.497 |
| 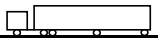 | 8 | *83.4* | 3.523 | 3.459 | 3.440 | 3.501 | 3.445 | 3.434 |
| 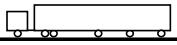 | 9 | *101.4* | 4.523 | 4.459 | 4.440 | 4.501 | 4.445 | 4.434 |
| 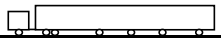 | 10 | *119.4* | 5.523 | 5.459 | 5.440 | 5.501 | 5.445 | 5.434 |
| 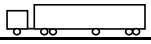 | 11 | *91.4* | 2.942 | 2.843 | 2.815 | 2.908 | 2.823 | 2.805 |
|  | 12 | *117.4* | 3.362 | 3.227 | 3.189 | 3.316 | 3.200 | 3.176 |
|  | 13 | *151.4* | 3.041 | 2.848 | 2.795 | 2.974 | 2.810 | 2.777 |
| 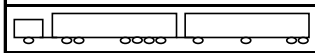 | 14 | *161.4* | 4.607 | 4.451 | 4.408 | 4.553 | 4.420 | 4.393 |
| 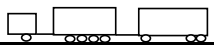 | 15 | *117.4* | 3.188 | 3.067 | 3.034 | 3.146 | 3.043 | 3.022 |
| 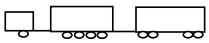 | 16 | *125.4* | 2.607 | 2.451 | 2.408 | 2.553 | 2.420 | 2.393 |
| 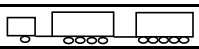 | 17 | *132.4* | 1.969 | 1.821 | 1.781 | 1.917 | 1.792 | 1.767 |
| 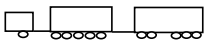 | 18 | *143.4* | 2.711 | 2.542 | 2.496 | 2.652 | 2.509 | 2.480 |
| 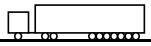 | 19 | *138.4* | 2.487 | 2.341 | 2.300 | 2.436 | 2.312 | 2.287 |
|  | 20 | *151.4* | 2.576 | 2.423 | 2.380 | 2.523 | 2.392 | 2.366 |
| 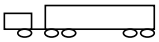 | 21 | *79.4* | 2.513 | 2.411 | 2.381 | 2.479 | 2.390 | 2.371 |

### *2.6.4.1 AF from Strain Fatigue Curve*

Single, tandem, tridem, 4-axle, 5-axle, 7-axle and 8-axle load pulses were tested to determine their initial strains (last peak) on the same specimen. Additionally, single pulses with peak magnitudes equal to 25%, 50% and 75% of the single peak stress were applied on the same specimen and their corresponding initial strains were determined. The strains from the latter pulses were used in the peak-midway method of building axle groups.

Figures 2.51 and 2.53 show the measured and calculated using peak-midway and peak methods respectively for the six axle groups at three interaction levels. Figures 2.52 and 2.54 show the percentage difference between measured and calculated $N_f$-values as well as to this difference divided by the number of axles in each axle group, using peak-midway and peak-peak methods, respectively.

It can be seen from these figures that the peak-midway method results vary widely depending on the interaction level. While for 25% interaction, the peak-midway method over estimates the damage, the same method under estimates the damage for higher interaction levels. Additionally, the percentage difference per N does not follow any obvious trend whether between the different axle groups within an interaction level or between the interaction levels in general. Therefore, it is hard to correct for the error resulting from using this method. On the other hand, the peak-peak method is more consistent regardless of the interaction level. Moreover, there is an obvious trend between the percentage difference and the number of axles. A linear correction factor of the form shown in equation (2.47) below can be used to correct the calculated Nf using the peak-peak method.

$$C_f = -0.0116\,(N) + 0.1748 \qquad (2.47)$$

where: $C_f$ is the correction factor per axle.
N is the number of axles in the axle group

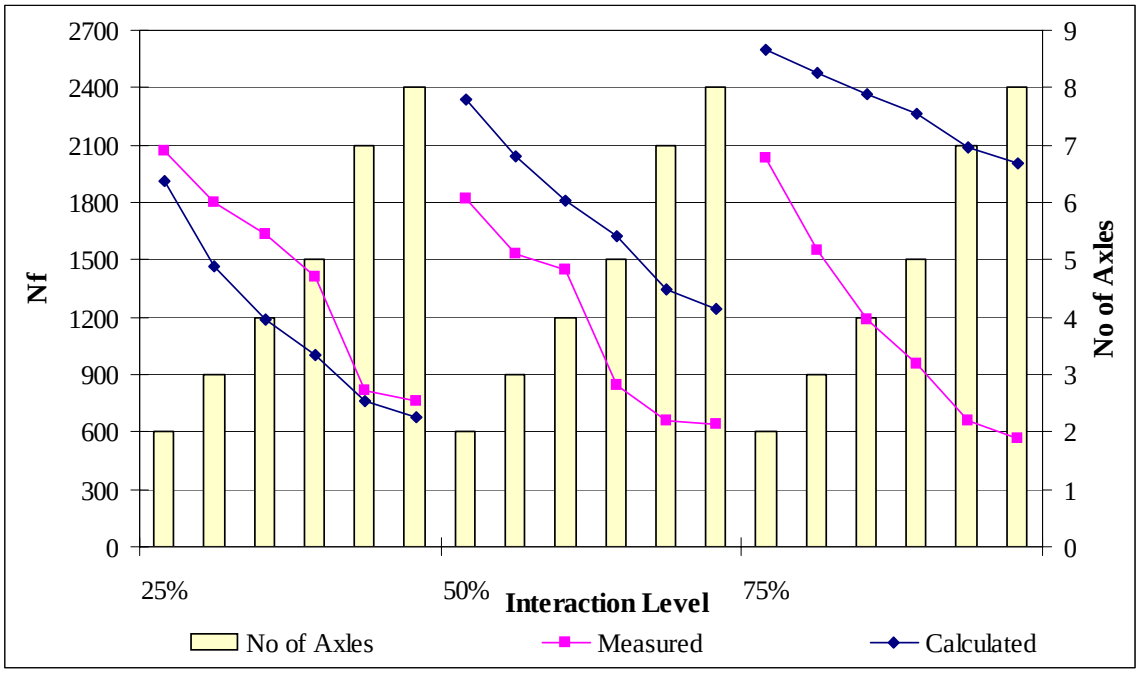


Figure 2.51. Fatigue Lives under Different Axle Groups Using Peak-Midway Method from Strain Fatigue Curve

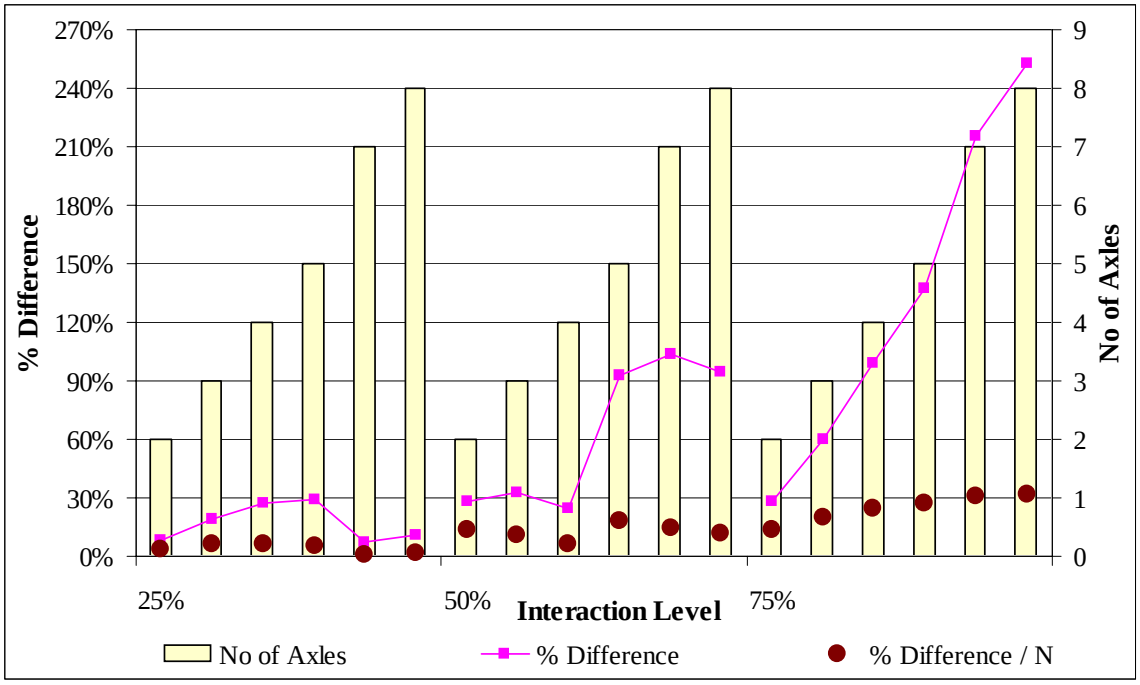


Figure 2.52. Percent Difference between Measured and Calculated Fatigue Lives under Different Axle Groups Using Peak-Midway Method from Strain Fatigue Curve

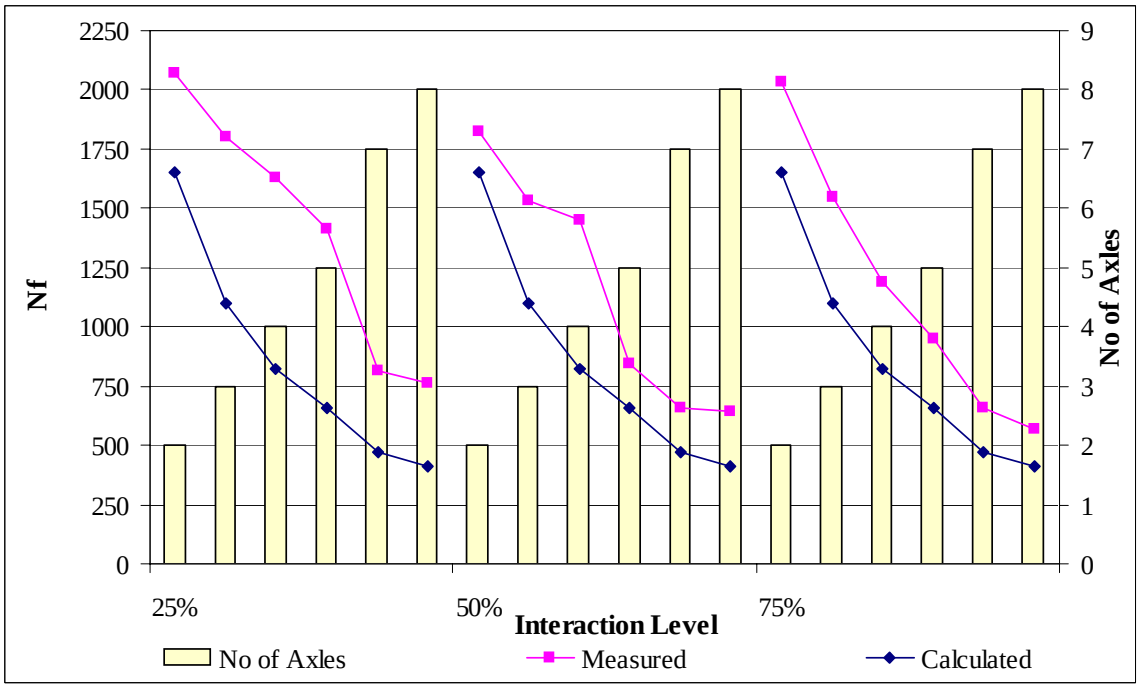


Figure 2.53. Fatigue Lives under Different Axle Groups Using Peak Method from Strain Fatigue Curve

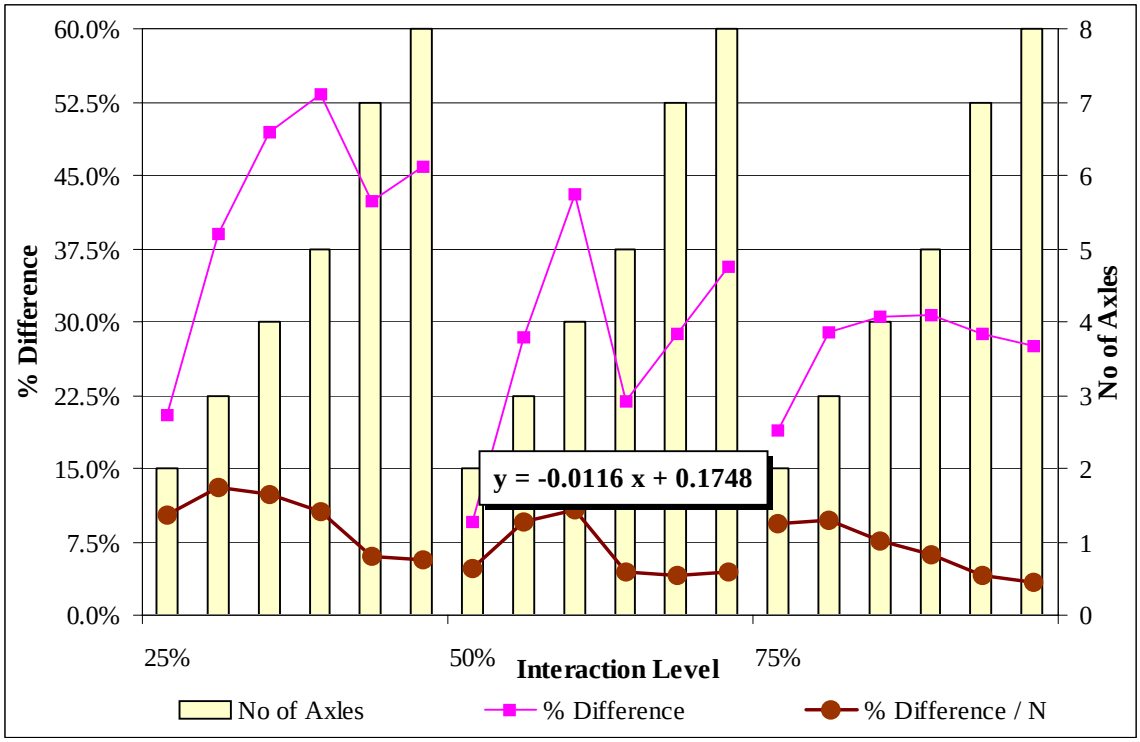


Figure 2.54. Percent Difference between Measured and Calculated Fatigue Lives under Different Axle Groups Using Peak Method from Strain Fatigue Curve

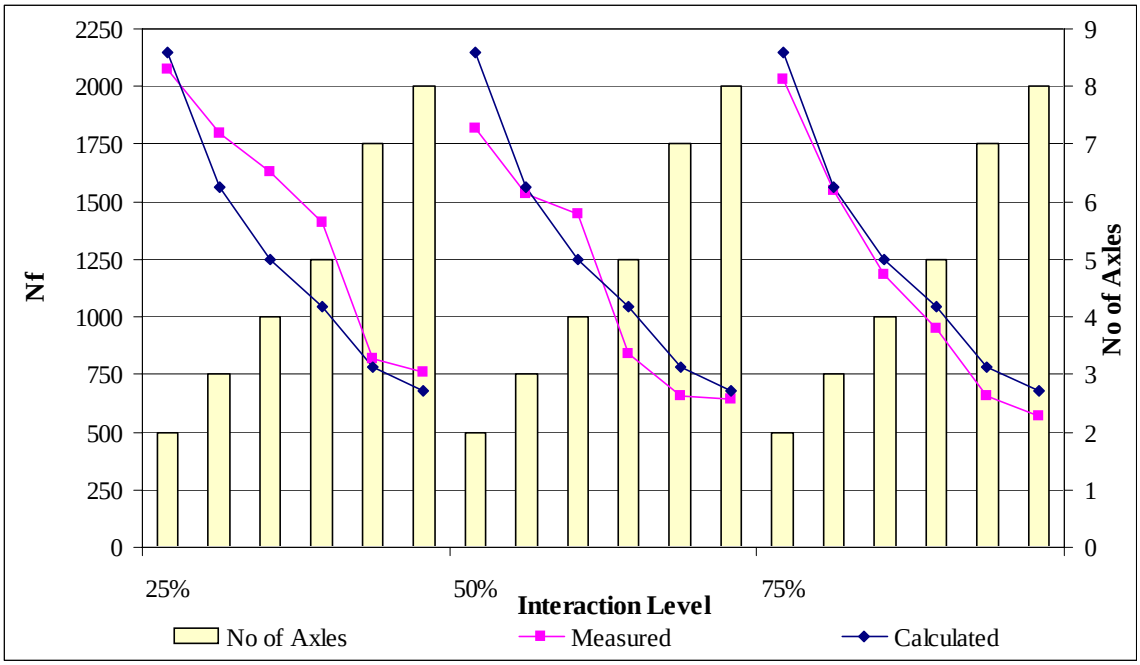


Figure 2.55. Fatigue Lives under Different Axle Groups Using Peak Method from Strain Fatigue Curve (After Correction)

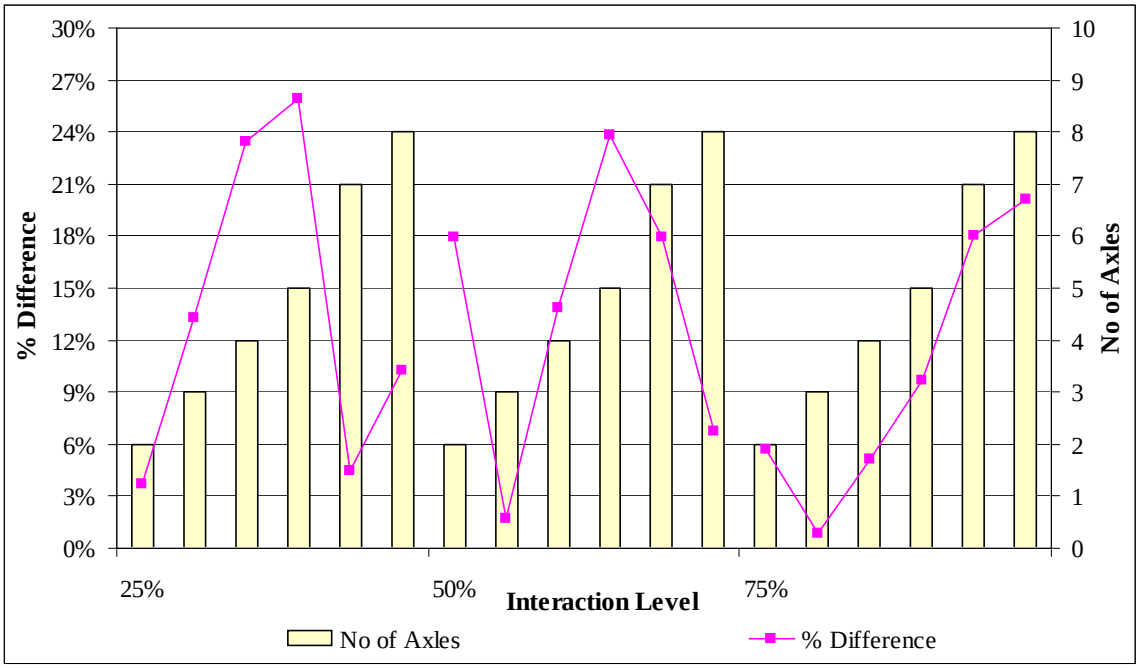


Figure 2.56. Percent Difference between Measured and Calculated Fatigue Lives under Different Axle Groups Using Peak-Peak Method from Strain Fatigue Curve (After Correction)

The final $N_f$ can be calculated as:

$$(N_f)_{final} = (N_f)_{calculated} * (1 + N * C_f) \quad (2.48)$$

where: $(N_f)_{calculated}$ is the calculated $N_f$ using Miner's Hypothesis.

Figure 2.55 shows the calculated $N_f$ using peak-peak method with the correction factor versus the measured ones from the fatigue curves for the six axle groups at the three interaction levels. By comparing Figures 2.51, 2.43 and 2.55, the increase in the prediction accuracy is very obvious. This can be also seen from Figure 2.56 where the percentage difference was reduced to less than 16% for all axle configurations and interaction levels.

### *2.6.4.2 AF from Dissipated Energy Fatigue Curve*

Single, tandem, tridem, 4-axle, 5-axle, 7-axle and 8-axle load pulses were tested to determine their initial dissipated energy on the same specimen. Additionally, single pulses with peak magnitudes equal to 25%, 50% and 75% of the single peak stress were applied on the same specimen and their corresponding initial dissipated energies were

determined. The dissipated energies from the latter pulses were used in the peak-midway method of building axle groups. The same procedure mentioned in the previous section was used for determining $N_f$ of an axle group.

Figures 2.57 and 2.59 show the measured and calculated $N_f$-values using peak-midway and peak methods respectively versus the measured ones from the fatigue curves for the six axle groups at three interaction levels. Figures 2.58 and 2.60 show the percentage difference between measured and calculated $N_f$-values as well as this difference divided by the number of axles in each axle group using peak-midway and peak-peak methods, respectively.

It can be seen from these figures that the peak-midway method results vary widely depending on the interaction level. For 25% and 50% interaction, the peak-midway method over-estimates the damage. The same method under estimates the damage for 75% interaction level for some axles and over estimates it for others. On the other hand, the peak-peak method is more consistent regardless of the interaction level. Moreover, there is an obvious trend between the percentage difference and the number of axles. A linear correction factor of the form shown in equation (2.49) below can be used to correct the calculated $N_f$-values using the peak method.

$$C_f = 0.137\,(N) \tag{2.49}$$

where: $C_f$ is the correction factor per axle.
N is the number of axles in the axle group

It should be noted that when calculating the percentage difference to check accuracy of the prediction models, it is calculated as the difference between the measured and calculated $N_f$-values divided by the measured one. However, to calculate the correction factor, this should be modified to: measured minus calculated divided by calculated since when using the correction factor, the only known term is going to be the calculated $N_f$ only. This explains the difference between the average value of percentage difference per N shown in Figure 2.62 and the correction factor shown in the equation. The final $N_f$ can be calculated as shown in equation (2.48) in the previous section.

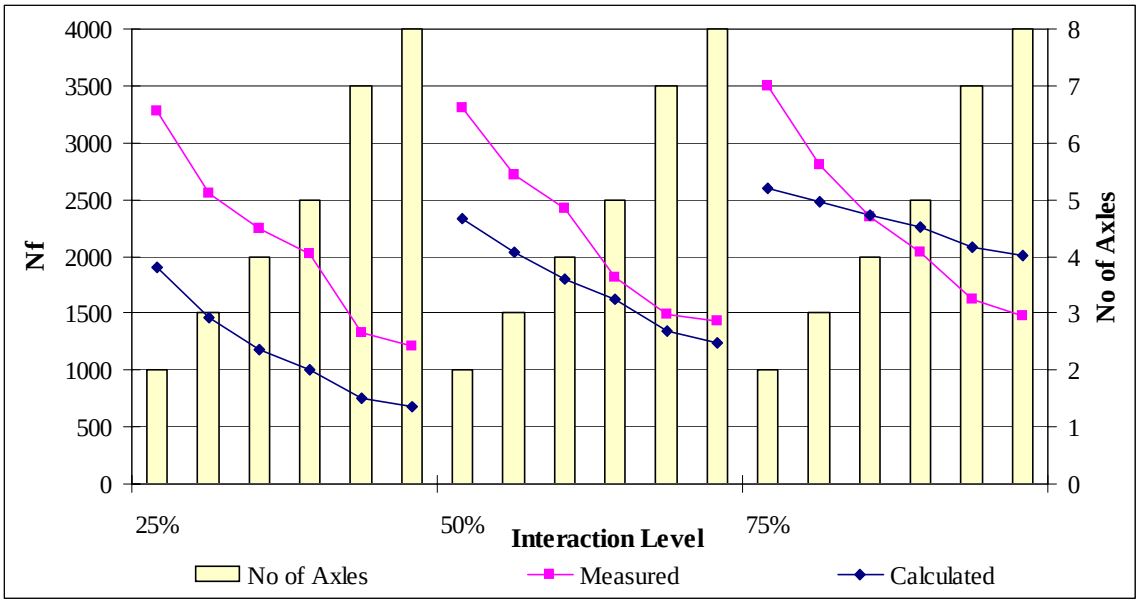


Figure 2.57. Fatigue Lives under Different Axle Groups Using Peak-Midway Method from DE Fatigue Curve

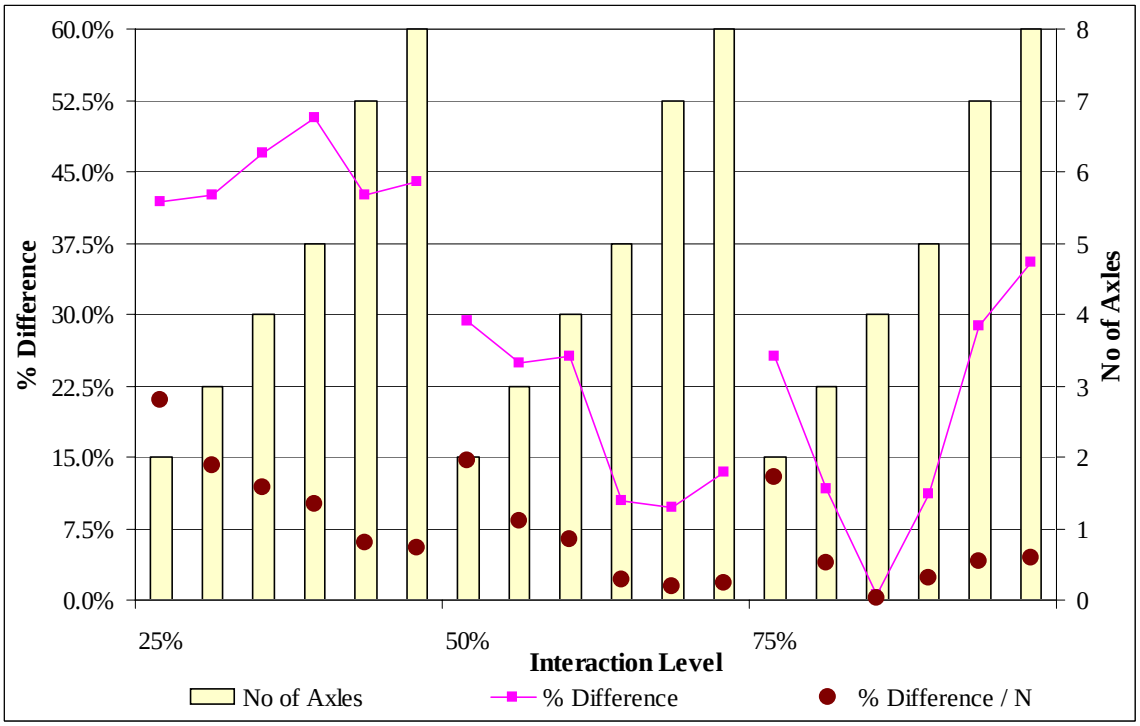


Figure 2.58. Percent Difference between Measured and Calculated Fatigue Lives under Different Axle Groups Using Peak-Midway Method from DE Fatigue Curve

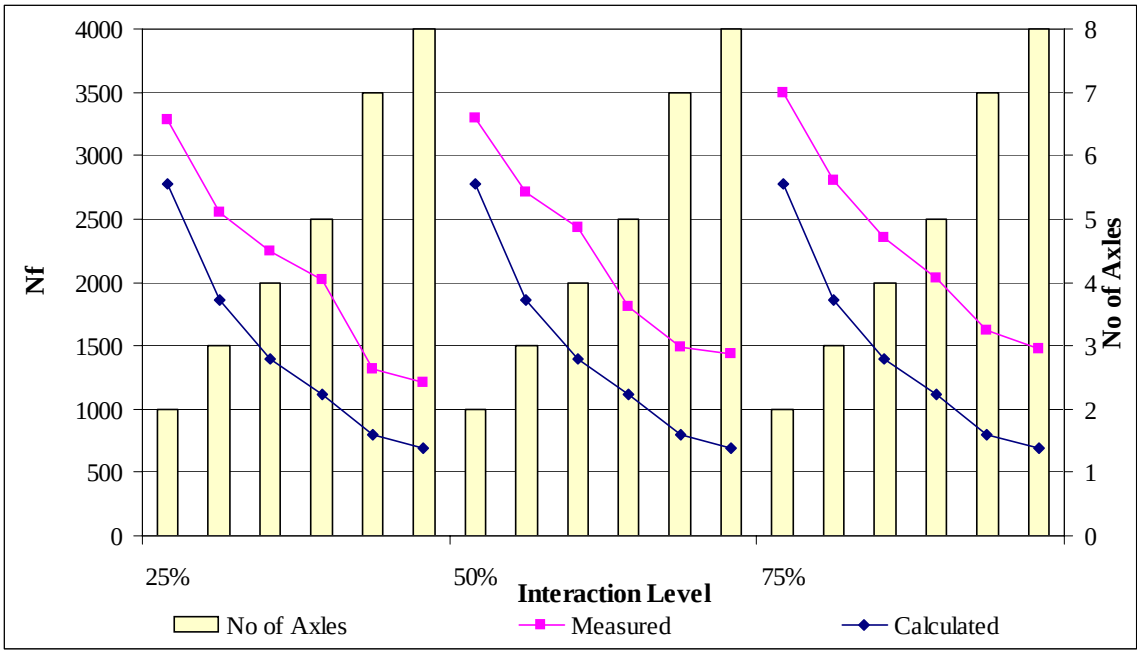


Figure 2.59. Fatigue Lives under Different Axle Groups Using Peak Method from DE Fatigue Curve

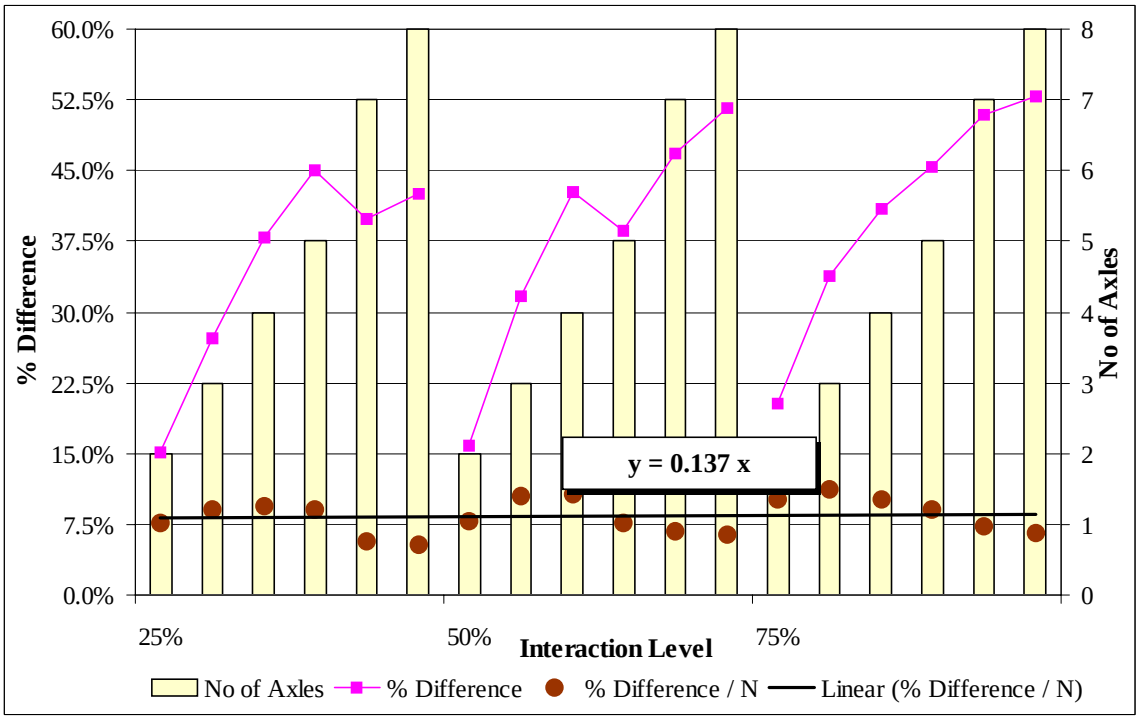


Figure 2.60. Percent Difference between Measured and Calculated Fatigue Lives under Different Axle Groups Using Peak Method from DE Fatigue Curve

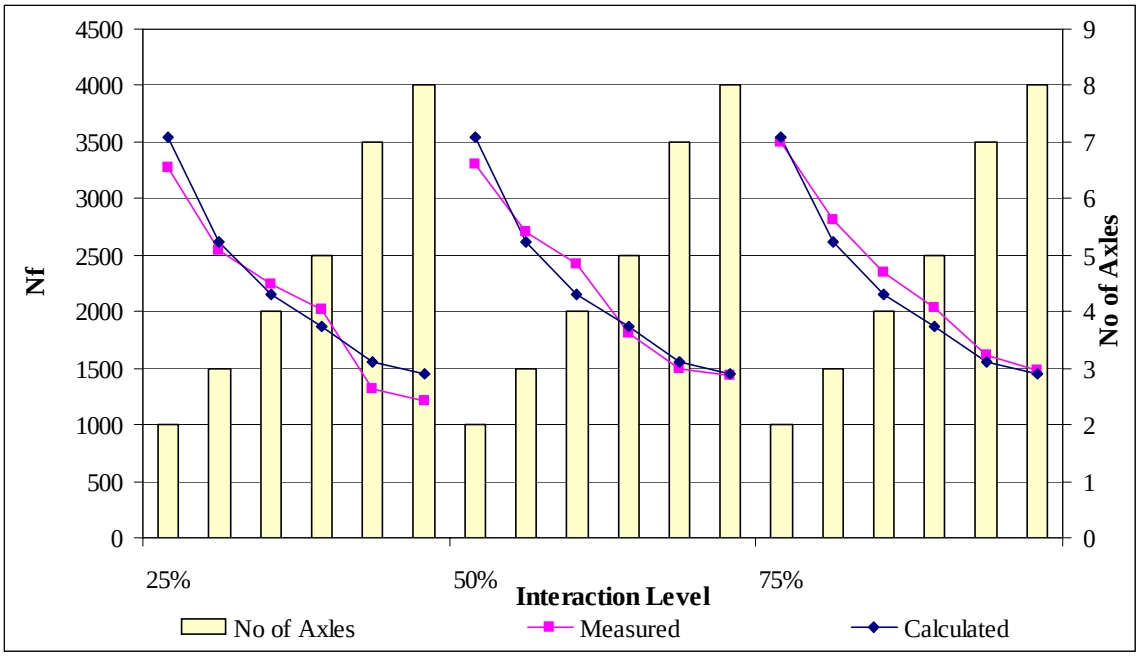


Figure 2.61. Fatigue Lives under Different Axle Groups Using Peak Method from DE Fatigue Curve (After Correction)

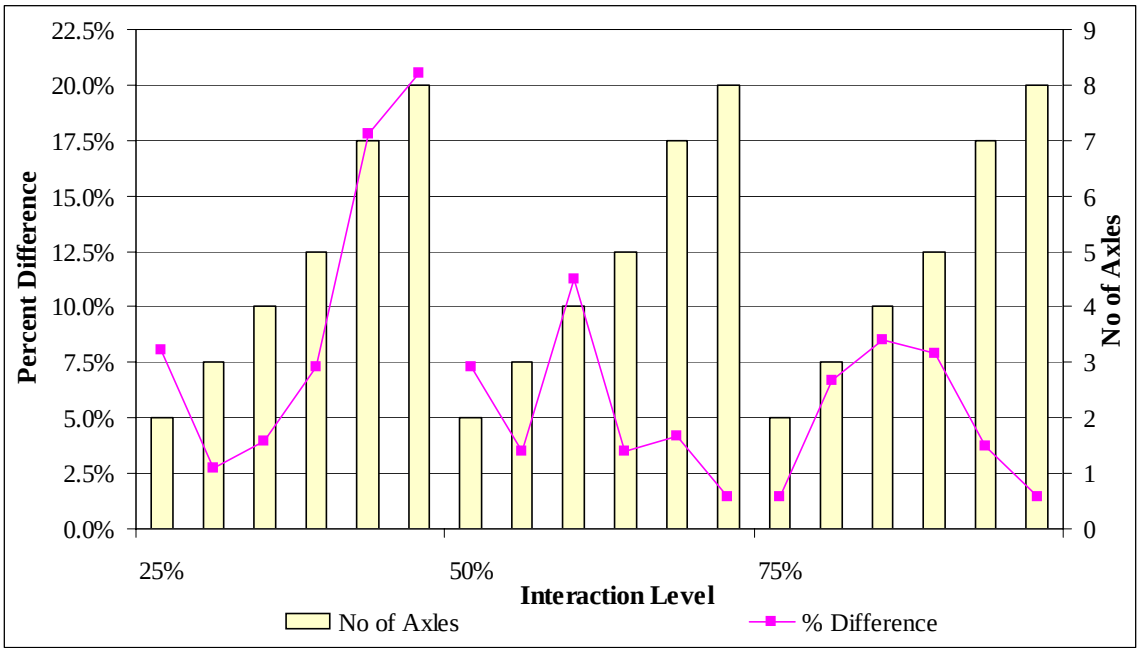


Figure 2.62. Percent Difference between Measured and Calculated Fatigue Lives under Different Axle Groups Using Peak Method from DE Fatigue Curve (After Correction)

### *2.6.4.3 Summary of Mechanistic Approaches for Determining AF*

The peak-peak method under-predicted the fatigue life regardless of the interaction level, the number of axles and the fatigue curve used. Therefore, a correction factor was calculated to reduce the errors obtained from this method and reach more reasonable results. On the other hand, the peak-midway method results were inconsistent, and varied with the interaction level, fatigue prediction model and number of axles, making it harder to correct the results obtained. Therefore, whenever it is not possible to use the fatigue curves to determine the damage of the whole axle at once, the peak-peak method is recommended to predict the fatigue life of an axle group with the correction factors mentioned in equations (2.47) and (2.49).

### *2.6.4.4 TF from Dissipated Energy Fatigue Curves*

Load pulses equivalent to Trucks 0, 1, 2, 3, 4, 10, 13, 14, 17, 19, 20, single (13 kips, 15.4 kips, 16 kips and 18 kips), tandem (2-13 kips and 2-16 kips), tridem (3-13 kips), 4-axle (4-13 kips), 5-axle (5-13 kips), 7-axle (7-13 kips) and 8-axle (8-13 kips) were applied to the same specimen and their corresponding initial dissipated energies were obtained. Using the dissipated energy fatigue curve, the fatigue life was determined for all these axle configurations. The $N_f$ values obtained for the trucks were considered as the measured fatigue life, and thus used as a reference to check the accuracy of building up trucks. Two procedures were used for calculating the $N_f$ of a truck:

i) Using individual axle method. In this case, $N_f$ of Truck 13, for example (Figure 2.63), was calculated from $N_f$-values of a single 15.4-kip axle, a two 16-kip single axles and eight 13-kip single axles. Note that this is the common practice in mechanistic design procedures.

ii) Using axle groups. In this case, $N_f$ of Truck 13 was calculated from $N_f$-values of the single 15.4-kip axle, a 32-kip tandem axle, two 39-kip tridem axles and a 26-kip tandem axle.

Figure 2.63 shows the measured and calculated $N_f$-values using individual axles and axle groups for the eleven trucks at three interaction levels. Figure 2.64 shows the percentage difference between measured and calculated $N_f$-values from both methods. Additionally, the percentage difference divided by the number of axles in each truck is also shown in the same figure for the methods using axle groups.

It can be seen from these figures that the method using axle groups gives more accurate results than the method using single axles. For Truck 1, the $N_f$ calculated from both methods coincide since this truck has only two single axles. Additionally, as the ratio of the number of axles to axle groups increases, the error obtained from the individual axles increases as well. Figure 2.64 shows that there is an obvious trend between the percentage difference from the method using axle groups and the number of

axles. The percentage difference per N is constant, and thus a correction factor can be applied when using the method with axle groups. The correction factor is of the form:

$$C_f = 0.038\ (N) \tag{2.50}$$

where: $C_f$ is the correction factor per axle.
N is the number of axles in the axle group

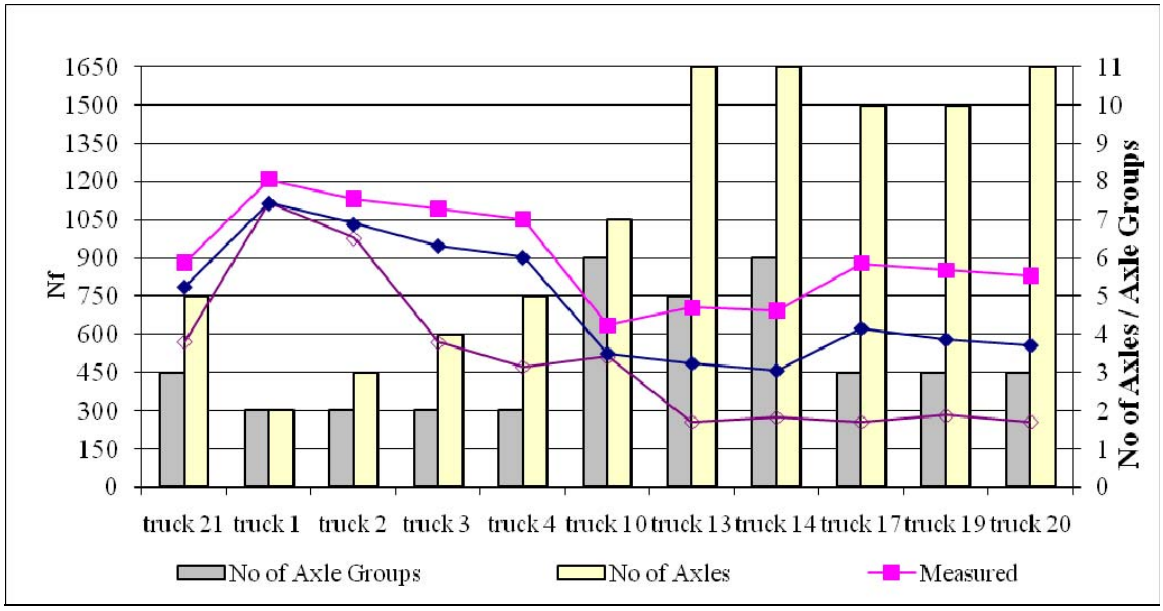


Figure 2.63. Trucks Fatigue Lives Using Axle Groups and Individual Axles from DE Fatigue Curve

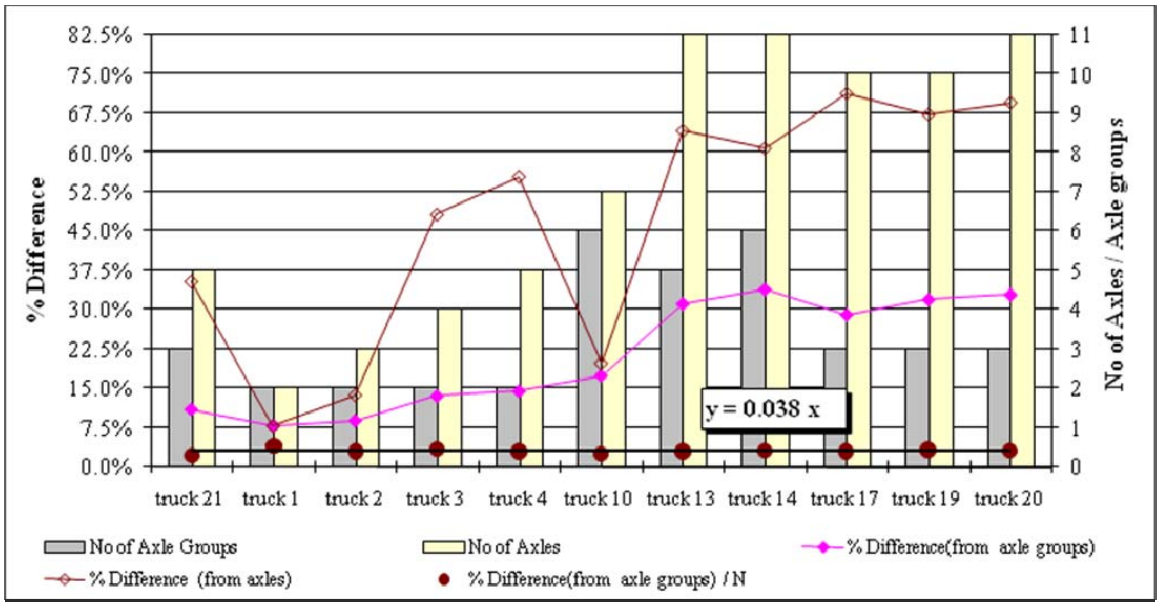


Figure 2.64. Percent Difference between Measured and Calculated Trucks Fatigue Lives from DE Fatigue Curve

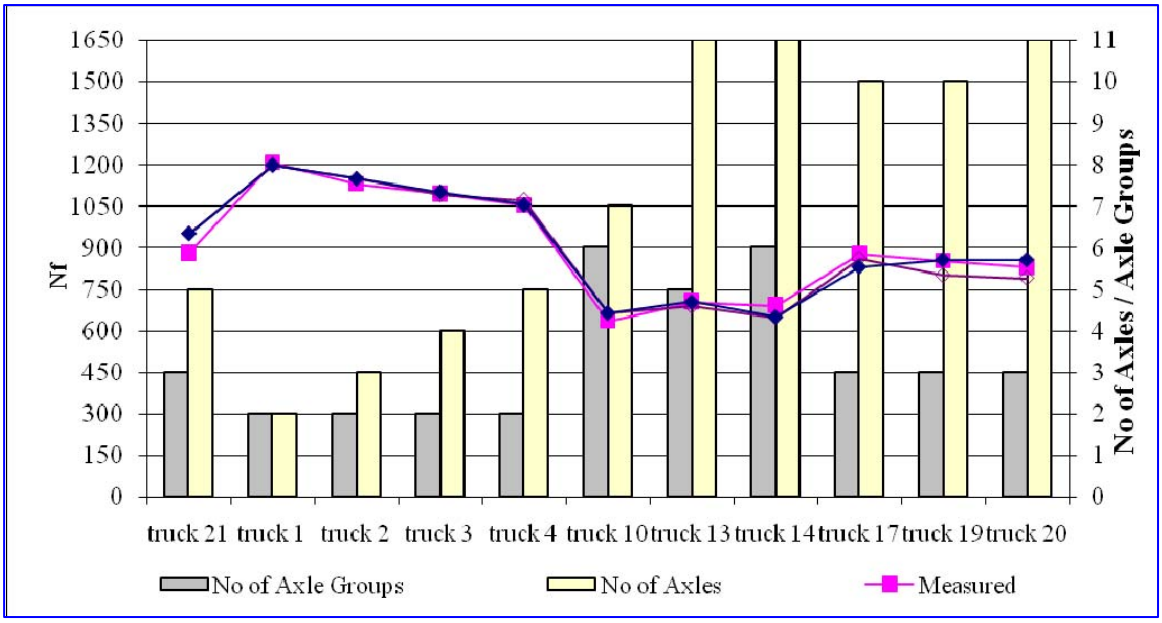


Figure 2.65. Truck Fatigue Lives Using Axle Groups and Individual Axles from DE Fatigue Curve (After Correction)

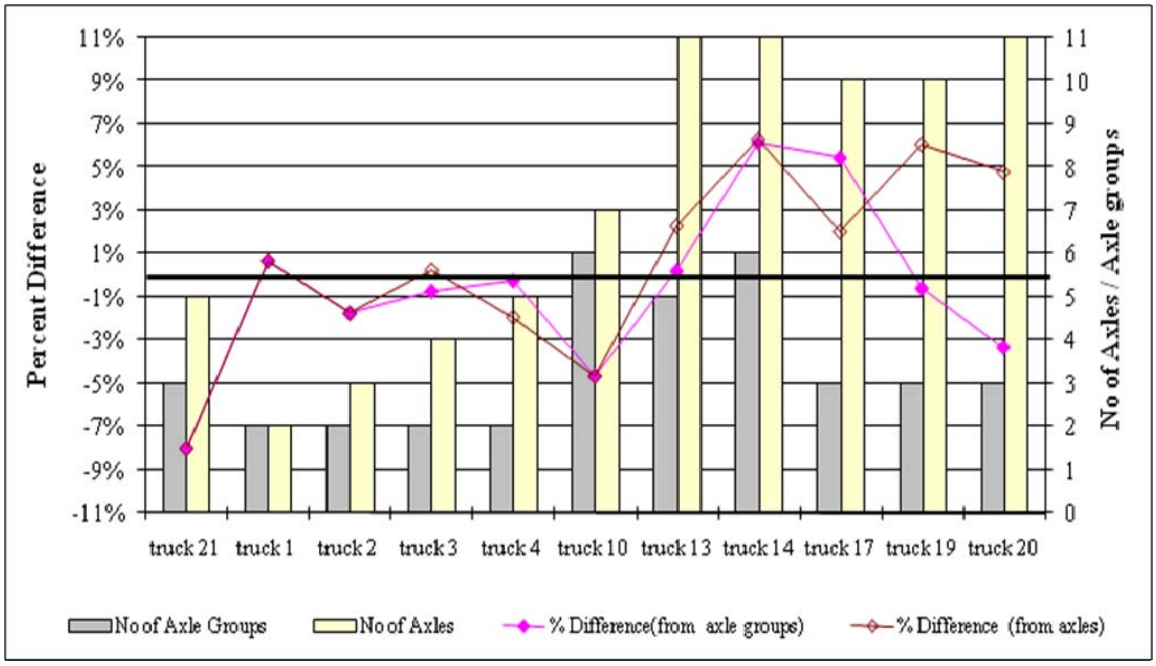


Figure 2.66. Percent Difference between Measured and Calculated Trucks Fatigue Lives from DE Fatigue Curve (After Correction)

Figures 2.65 and 2.66 show the $N_f$ obtained from the two methods after correction and the percentage difference between these values and the measured ones. The reduction in error is very obvious. It should be noted that for the method using individual axle, the axle groups were calculated first using the peak-peak method and corrected using equations (2.47) and (2.49), then these axle groups were used to determine the $N_f$-values for the trucks using the correction factor presented in equation (2.50). Therefore, whenever determining the Nf for the whole truck in one step is not possible, it is recommended to use the method using axle groups with the corresponding correction factor, or else, use individual axles to calculate $N_f$-values of axle groups and then calculate the trucks $N_f$-values from these results with applying the corresponding correction factors at each step.

## 2.7 LABORATORY CONCLUSIONS AND RECOMMENDATIONS

### 2.7.1 Conclusions

Based on the experimental results from fatigue testing of asphalt concrete mixes in an indirect tensile cyclic load test, the following conclusions were drawn:

i) The stored energy density criterion (SEC), developed in this study, was found to be as a good failure criterion for fatigue life of asphalt concrete mixes when using the dissipated energy approach. This failure criterion indicates crack initiation in the specimen.

ii) The fatigue curves obtained using the SEC value as failure criterion does not represent field conditions where cracking at failure is at more developed stages. Nevertheless, similar fatigue curves were obtained at higher dissipated energy levels indicating that a shift factor might be enough to obtain fatigue performance at later crack propagation levels.

iii) The initial dissipated energy-based fatigue curve was found to be unique for different axle and truck configurations at different stress levels, making it useful for predicting the fatigue life of an axle group or a truck at once without the need for summing up the damage from individual axles.

iv) Multi axles were found to be less damaging per tonnage compared to single axles. Increasing the number of axles carrying the same load results in less damage. This decrease in damage was found to be more significant between single, tandem and tridem axles, while it starts to level off at higher axle numbers. Similar results were obtained for trucks where trucks having more axles and axle groups had lower truck factors per tonnage than those with single axles.

v) Both speed and AC thickness (expressed through the interaction level between consecutive axles) had no significant effect on the axle factor values for the different axle configurations investigated, although changes in either of them did affect the fatigue life.

vi) Using the peak-midway method for predicting the fatigue life of an axle group was found to be inconsistent and the results varied depending on the interaction level between consecutive axles and the number of axles in an axle group.

vii) Using the peak method for predicting the fatigue life of an axle group was found to be more consistent regardless of the interaction level and the number of axles. A correction factor as a function of the number of axles was developed to correct for fatigue life calculated from the peak method.

viii) Summing the damage from the axle groups composing a truck was found to yield a better prediction of truck fatigue life from trucks than using the individual axles. A correction factor based on the number of individual axles in a truck was developed to improve the results obtained from using axle groups. It was also found that using the fatigue life from individual axle to determine the fatigue life from an axle group then using the latter in determining the fatigue life of a truck could be used if the corresponding correction factors were applied in each stage.

### 2.7.2 Recommendations

The results of this study have led to many interesting conclusions. However, more mixes need to be tested to be able to generalize the conclusions reached. Additionally, similar tests should be performed at different temperatures to study its effect on the results. Finally, it is highly recommended that a different testing setup (flexural beam preferably) be used to check the consistency of the results under different loading modes and stress states. The flexural beam test could allow for stress reversals, which are relevant for longitudinal stresses and strains. This will allow for checking the peak and peak-midway methods of predicting the fatigue life using longitudinal stress/strain.

# CHAPTER 3
# FATIGUE CRACKING – MECHANISTIC ANALYSIS

## 3.1 INTRODUCTION

Different trucks consist of different axle groups and cause different damage levels to pavement systems. The Equivalent Single Axle Load (ESAL) concept has been widely used to compare the damage caused by different trucks and axle groups. This concept allows the engineer to describe the damage caused by the passage of a truck or an axle group in terms of the damage caused by the passage of a standard axle. This standard axle is a single axle with dual tires, and is loaded to 18 kip with a tire pressure of 70 psi. The relative damage of an axle group to the damage of a standard axle is called Load Equivalency Factor (LEF) and is expressed in ESALs. Similarly, Truck Factor (TF) is defined by the relative damage of a truck to the damage of a standard axle. TF is calculated by summing up the LEFs of axle groups that make up a truck.

However, there are various methods of calculating pavement damage. Different methods of damage calculation would result in different values of damage for a given axle type. When the LEF is calculated, the damage of a given axle is normalized to the damage of the standard axle calculated within the same method. Therefore, comparison of the LEFs from different methods may not highlight the differences between the various methods of damage calculation.

In this chapter, the damage and the LEFs/TFs are calculated using three different methods: (1) peak strains, (2) difference between peak and midway strains, and (3) dissipated energy. Both longitudinal and transverse responses were studied for several different flexible (asphalt) pavement systems. Twenty Michigan trucks and their axle groups were used to calculate the damage and the LEFs/TFs. The only mode of failure considered is fatigue.

The objectives of this analysis are:

- To calculate the LEFs and TFs of the axle groups and trucks using different methods.
- To compare pavement fatigue damage calculated from different methods.
- To investigate the effect of thickness, modulus and damping ratio of asphalt concrete on pavement fatigue damage.

## 3.2 METHODS USED

The methods used in this study are well documented by Hajek (Hajek and Agarwal, 1990) and Chatti (Chatti et al, 2000). However, the methods are defined herein to discuss some issues.

### 3.2.1 Strain Methods

The strain methods use the horizontal strains at the bottom of the AC layer to calculate the fatigue life of the pavement system, using laboratory derived fatigue equations of the form:

$$N_f = \alpha \varepsilon^{\beta} \tag{3.1}$$

The damage is calculated as the inverse of the fatigue life as shown in equation 3.2.

$$Damage = 1 / N_f \tag{3.2}$$

where Nf is the fatigue life of the pavement.

The LEF is the relative damage of an axle group to that of a standard axle.

$$LEF_{axle} = \frac{Damage_{axle}}{Damage_{standard\ axle}} \tag{3.3}$$

For multiple axles, the damage is calculated from several critical strains individually and then summed. The difference between the two strain methods lies in the strain values that are input into the fatigue equations. In this analysis, only the peak and peak-midway strain methods are considered.

Figure 3.1 shows typical longitudinal strain time histories under single and tandem axles. The peak method takes only the peak tension part of the strains (designated as $\varepsilon_p$ in the figure) to calculate the fatigue life of the pavement system.

The peak-midway strain method accounts for both the peak tensile strain and the peak compressive strain of the longitudinal strain time histories. The difference of the peak tensile and compressive strains (designated as $\varepsilon_{pm}$ in Figure 3.1) is input in empirical fatigue equations to calculate the fatigue life and the damage of the pavement. It should be noted that there is no fatigue testing done with this type of loading pulse.

Figure 3.2 shows typical transverse strain time histories under single and tandem axles. This method is theoretically identical to the peak-midway strain method for the transverse strain under a single axle. However, for transverse strains under multiple axles, this method neglects the interaction between the adjacent axles and treats them as two separate single axles. In other words, it considers the two peak strain values ($\varepsilon_1$ and $\varepsilon_{p1}$ in

Figure 3.2 (b)) separately such that it does not differentiate between the tandem axle and two separate single axles.

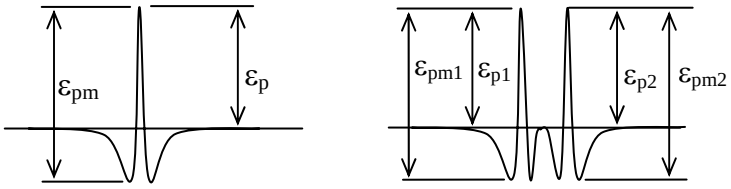


(a) Single axle (b) Tandem axle

Figure 3.1. Typical longitudinal strain time histories

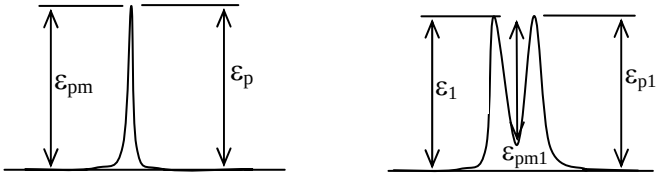


(a) Single axle (b) Tandem axle

Figure 3.2. Typical transverse strain time histories

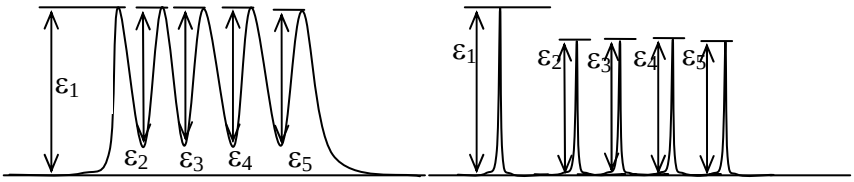


(a) Peak-midway method for 5 axle group (b) Five separate single axles

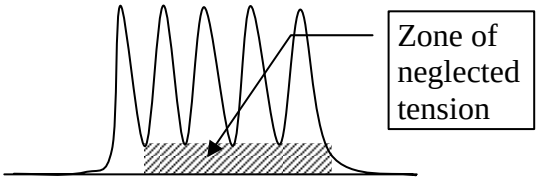


(c) Zone of neglected tension from peak-midway strain method

Figure 3.3. Transverse strain time history under a 5 axle group

The peak-midway method, on the other hand, takes the peak tensile strain due to the first axle (shown as $\varepsilon_1$ in Figure 3.2 (b)) and the difference of the second peak and the valley in between (shown as $\varepsilon_{pm1}$ in Figure 3.2 (b)). Thus, this method considers the interaction between the two axles of the tandem axle. However, consider the transverse strain time history shown in Figure 3.3 (a). The peak-midway method takes the strains $\varepsilon_1$ through $\varepsilon_5$ separately and calculates the fatigue damage. As a result, this method treats the response of a 5 axle group as that of 5 different single axles shown in Figure 3.3 (b). Also, notice that the midway strains between the 5 peak strains are still in tension. The peak-midway method does not account for the portion that remains in tension during the passage of the 5 axle group. Thus, this method creates a zone of neglected tension as shown in Figure 3.3 (c). As the level of interaction between the adjacent axles and the number of axles in an axle group increase, the zone of neglected tension will increase.

### 3.2.2 Dissipated Energy Method

Dissipated energy is defined as the area within a stress-strain hysteresis loop. It represents the energy lost in the pavement due to the passage of an axle group. Figures 3.4 and 3.5 show the longitudinal and transverse stress-strain loops, respectively, for a single and a tridem axle.

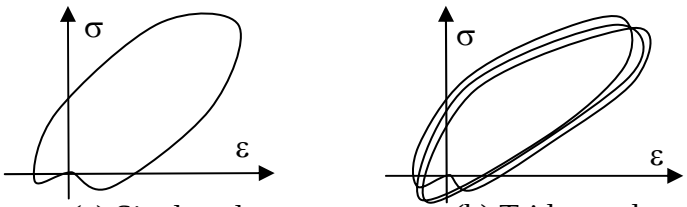


(a) Single axle (b) Tridem axle

Figure 3.4. Longitudinal stress-strain hysteresis loop

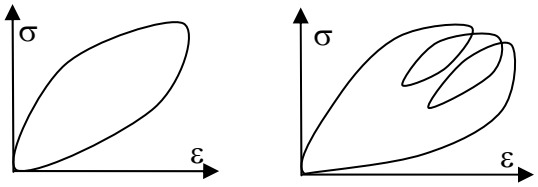


(a) Single axle (b) Tridem axle

Figure 3.5. Transverse stress-strain hysteresis loop

The advantage of the dissipated energy concept is that the dissipated energy can be calculated as a single scalar value and put into the fatigue equations to calculate the damage directly. This procedure eliminates the summation of damage due to several critical strain values that is necessary for the strain methods. Furthermore, the dissipated

energy value captures the totality of the stress-strain response during the passage of the load(s) while the strain values correspond to only one point in time. The method also differentiates between multi axles and several independent single axles naturally. As a result, the dissipated energy method should be the most desired method to be used.

## 3.3 FATIGUE EQUATIONS

Fatigue equations that relate the dissipated energy due to a single axle to the fatigue life are available in the literature. However, no literature was found for fatigue testing under multiple axle loadings. To overcome this problem, fatigue tests using the Indirect Tensile Cyclic Load Test (ITCLT) have been performed at Michigan State University (Mohtar, 2003). The laboratory tests were based on the transverse loading pulses of several axle types. The results suggest the following equation regardless of the axle type:

$$N_f = 1.498 \times w_0^{-0.998} \tag{3.4}$$

where $N_f$ is the fatigue life and $w_0$ is the initial dissipated energy density (in psi).

For comparison, the strain-based fatigue equation was also developed from the test data. This equation is based on the single pulse and transverse strain.

$$N_f = 1.647 \times 10^{-6} \times \varepsilon_0^{-2.237} \tag{3.5}$$

where $N_f$ is the fatigue life and $\varepsilon_0$ is the initial strain.

Fatigue equations based on longitudinal strains or compression-tension loading could not be developed due to the limitations of the testing apparatus. The above equations were, nonetheless, used for both transverse and longitudinal stress and strain pulses.

## 3.4 ANALYSIS

### 3.4.1 Pavement Profiles and Axle/Truck Configurations

The pavement profiles used in this chapter are summarized in Table 3.1. The configurations and gross weights of typical Michigan trucks are presented in Table 3.2. The axle types of the trucks are listed in Table 3.3 along with their load magnitudes. All axles presented here are composed of dual tires except for the front steering axle.

The tire pressure was held constant at 689 kPa (100 ksi). As a result, the tire-pavement contact area was varied as the load of the axle varied. To calculate the LEFs/TFs, the fatigue life of a standard axle with dual tires and a tire pressure of 483 kPa (70 ksi) was also calculated.

Table 3.1. Pavement profiles used

| Pavement Profile Type | AC Thickness, mm(in) | AC Modulus, MPa (ksi) | AC Damping Ratio |
|---|---|---|---|
| Thin, Soft, Low Damping | 90 (3.5) | 2410 (350) | 0.05 |
| Thin, Soft, High Damping | 90 (3.5) | 2410 (350) | 0.10 |
| Thin, Stiff, Low Damping | 90 (3.5) | 4830 (700) | 0.05 |
| Medium, Soft, Low Damping | 203 (8) | 2410 (350) | 0.05 |
| Medium, Soft, High Damping | 203 (8) | 2410 (350) | 0.10 |
| Medium, Stiff, Low Damping | 203 (8) | 4830 (700) | 0.05 |
| Thick, Soft, Low Damping | 305 (12) | 2410 (350) | 0.05 |
| Thick, Soft, High Damping | 305 (12) | 2410 (350) | 0.10 |
| Thick, Stiff, Low Damping | 305 (12) | 4830 (700) | 0.05 |

Table 3.2. Trucks used and their gross weights

| Truck No. | Shape | Gross Weight kN (kips) | Truck No. | Shape | Gross Weight kN (kips) |
|---|---|---|---|---|---|
| 1 | 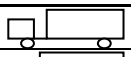 | 149 (33.4) | 11 | 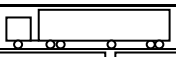 | 407 (91.4) |
| 2 | 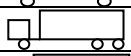 | 211 (47.4) | 12 |  | 522 (117.4) |
| 3 | 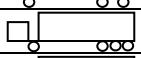 | 242 (54.4) | 13 | 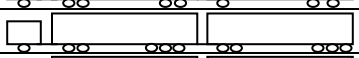 | 674 (151.4) |
| 4 | 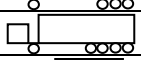 | 300 (67.4) | 14 | 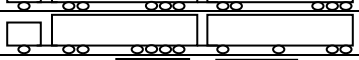 | 718 (161.4) |
| 5 |  | 229 (51.4) | 15 |  | 522 (117.4) |
| 6 | 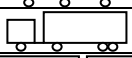 | 291 (65.4) | 16 |  | 558 (125.4) |
| 7 | 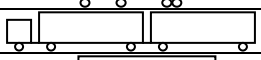 | 389 (87.4) | 17 |  | 589 (132.4) |
| 8 | 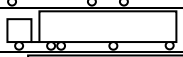 | 371 (83.4) | 18 | 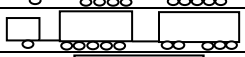 | 674 (151.4) |
| 9 | 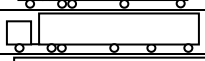 | 451 (101.4) | 19 | 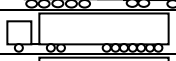 | 616 (138.4) |
| 10 | 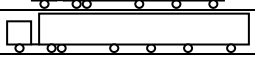 | 531 (119.4) | 20 | 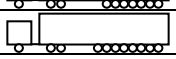 | 674 (151.4) |

Table 3.3. Axle types and loads

| Axle type | Load per axle, kN (kips) |
|---|---|
| Standard axle | 80 (18) |
| Front steering axle | 69 (15.4) |
| Single axle | 80 (18) |
| Tandem axle | 71 (16) |
| Tandem' axle | 58 (13) |
| Tridem axle | 58 (13) |
| Quad axle | 58 (13) |
| 5 axles | 58 (13) |
| 7 axles | 58 (13) |
| 8 axles | 58 (13) |

### 3.4.2 Generating the Stress and Strain Time Histories

The stress and strain time histories for all axle types were generated using SAPSI-M computer program (Chatti and Yun, 1995). Since the only mode of failure considered was fatigue, all responses were generated for the bottom of the asphalt concrete layer. Figure 3.6 shows longitudinal and transverse strain time histories of soft, high damping and thin AC pavement under a tandem axle generated by SAPSI-M. The details of shape and characteristics of the time histories are well described elsewhere (Chatti et al, 2000), and therefore are not included herein. The strains as well as the dissipated energy calculated from the program were then input into the above fatigue equations 3.4 and 3.5 to predict the fatigue damage and to calculate the LEFs/TFs.

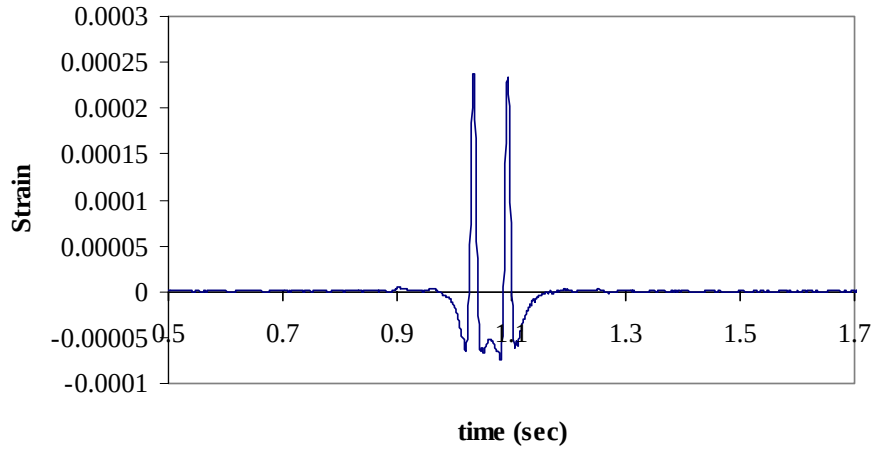


(a) Longitudinal

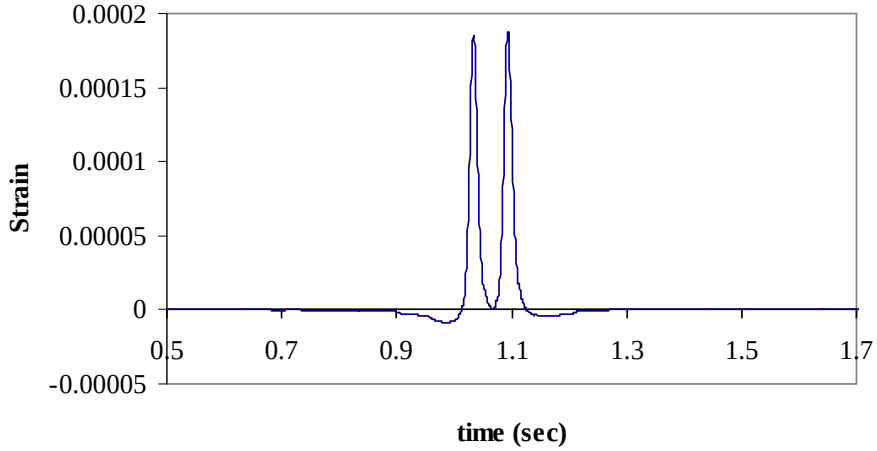


(b) Transverse

Figure 3.6. Longitudinal and transverse strain time histories generated by SAPSI-M

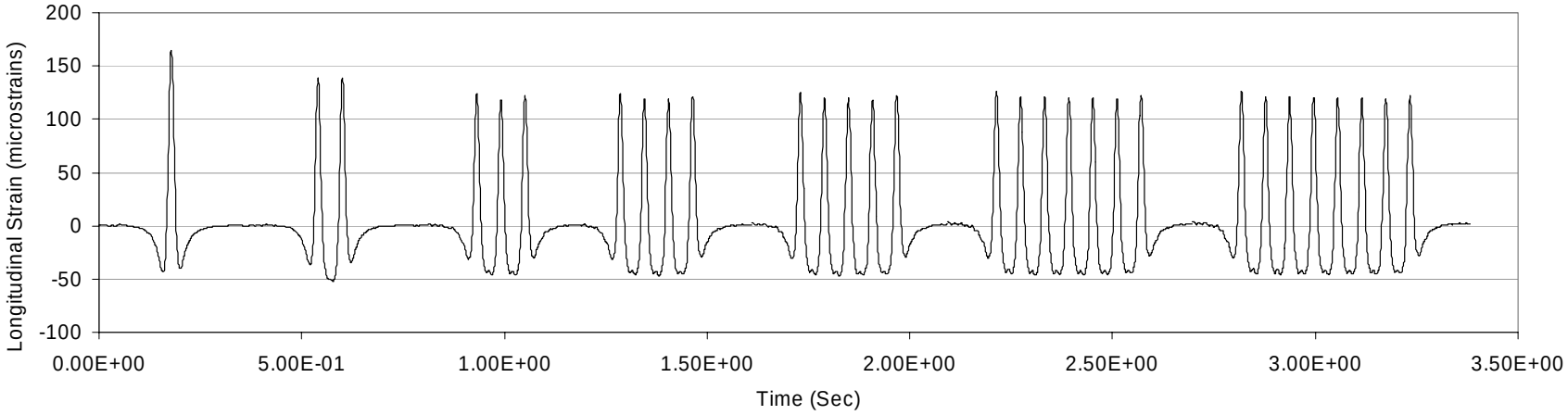


Figure 3.7 Longitudinal strain pulses for different axle configurations – Thin pavement

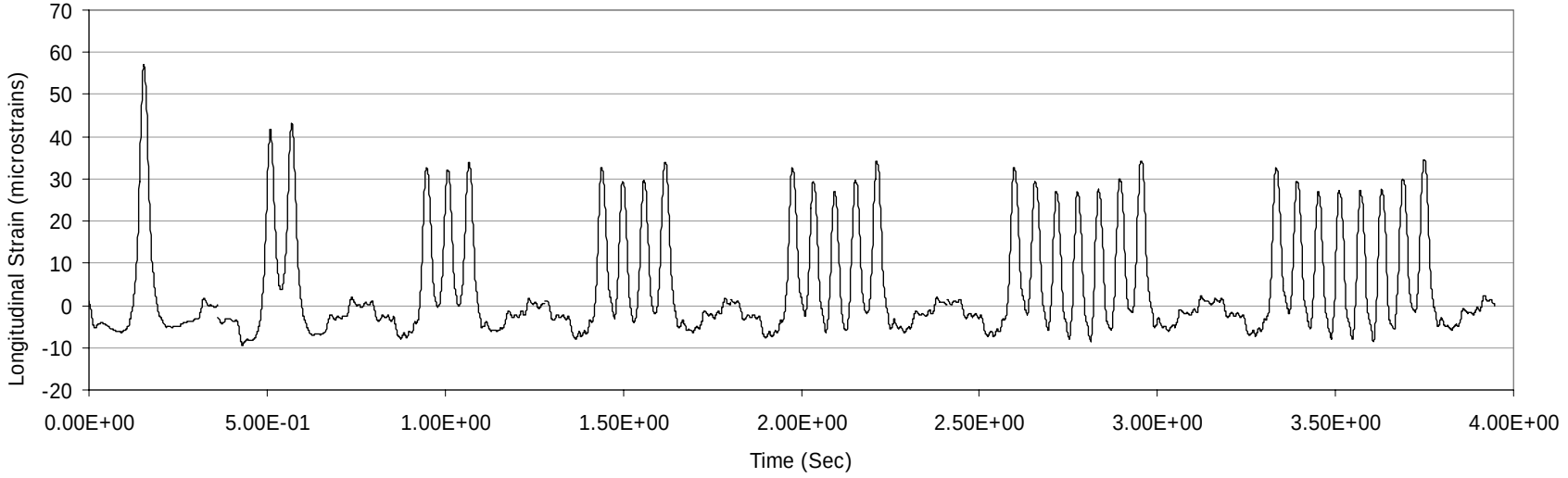


Figure 3.8 Longitudinal strain pulses for different axle configurations – Thick pavement

Figures 3.7 and 3.8 show the longitudinal strains under different axle configurations for thin and thick pavements, respectively. The plots show a significant reduction in strain, as the number of axles within an axle group increases, with this reduction being more severe in the case of a thick pavement. This is because of the increased interaction between axles within an axle group.

## 3.5 RESULTS

From the outputs of the SAPSI-M computer program, the fatigue damage per passage and the LEFs/TFs values were calculated. Figure 3.9 shows the damage based on dissipated energy for longitudinal and transverse stresses and strains in the soft, low damping AC pavement. Based on this figure, the damage due to longitudinal stresses and strains is always critical (i.e. the dissipated energy due to the longitudinal stress-strain relationship is always greater than that due to the transverse stress-strain relationship). This is also true for all pavement profiles analyzed in this study. This confirms that the response in the longitudinal direction is more critical than that in the transverse direction. Therefore, only the longitudinal results are presented in this chapter.

Figures 3.10 through 3.12 show the LEF values of the axles. The following can be observed:

- For thin AC pavements, all three methods agree with each other. The percent difference between the peak and peak-midway strain methods and the dissipated energy method ranges approximately from -11 % to 9 %.
- For medium-thick and thick AC pavements, the peak-midway strain method is matching better with the dissipated energy method than the peak strain method. The percent difference of peak and peak-midway strain methods ranges from -4 % to 40 % and from -10 % to 20 %, respectively.
- For thick AC pavements, both strain methods under predict the LEF values of multi axles relative to the dissipated energy method, with the under prediction being worse for the peak strain method.

Figures 3.13 through 3.15 show the fatigue damage values due to the passage of different axle groups. The following observations can be made:

- For thin AC pavements, the percent difference of the peak and peak-midway strain methods to the dissipated energy method ranges approximately from -52 % to 30 % and from -170 % to 50 %, respectively.
- For medium thick AC pavements, the percent difference of the peak and peak-midway strain methods to the dissipated energy method ranges approximately from -80 % to 50 % and from -150 % to -3 %, respectively; for thick AC pavements the percent differences vary from -70 % to 50 % and from -110 % to 20 %.
- The damage calculated from the peak-midway strain method is the highest for all cases except for the stiff and thick pavement.

- For soft, low damping AC pavements, the peak strain method matches the dissipated energy well, compared to the peak-midway strain method, which predicts higher damage values than the other two methods. The agreement is better as the thickness of the asphalt layer increases. This trend is the reverse of what is observed for the LEF values.
- For soft, high damping thick AC pavements and stiff, low damping medium-thick AC pavements, the peak-midway strain method matches well with the dissipated energy method.

Figures 3.16 through 3.18 show the truck factors of the 20 Michigan trucks calculated by the three methods. The TFs from the peak-strain method agree well with those from the other two methods for thin pavements, where the level of interaction between axles is low. For thicker pavements, the peak strain method under predicts the TFs, with the under predictions worsening for trucks with multiple-axles with more than two axles (i.e. tridems, quads and higher axles). The TFs from the peak-midway strain method are in good agreement with those from the dissipated energy method except for stiff, thick AC pavements and trucks with multiple axles with more than two axles (i.e. tridems, quads and higher axles).

Figures 3.19 through 3.21 show the damage values calculated by the 3 methods. The damage values per passage of the various trucks are different using the three methods, with the peak-midway strain method giving the highest damage values, except for the case of stiff, low damping thick AC pavements.

The dissipated energy method gives the lowest damage values for soft, low damping AC pavements. Increasing AC stiffness and damping increases the energy-based damage values. For thick AC pavements with stiff modulus or high damping ratios, the dissipated energy method gives the highest damage values, while for thin and medium-thick AC pavements with soft, high damping or stiff, low damping, the dissipated energy method gives damage values in-between the strain-based methods.

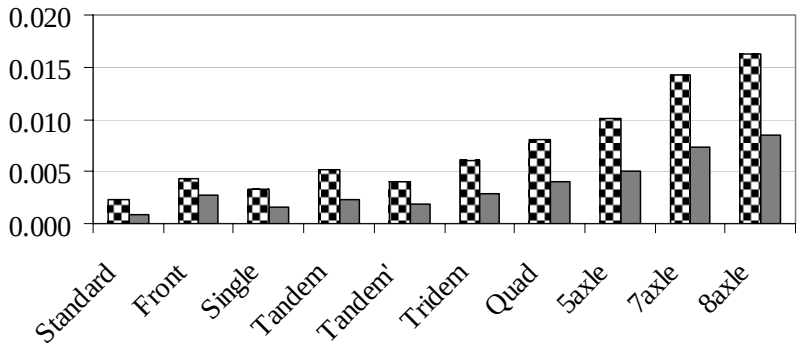


(a) 90mm (3.5in) AC

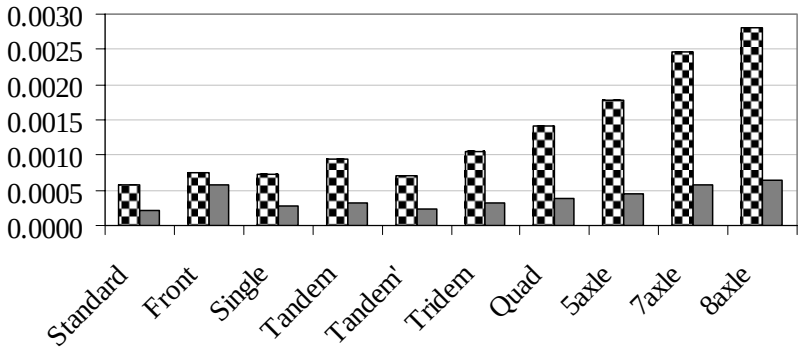


(b) 203mm (8in) AC

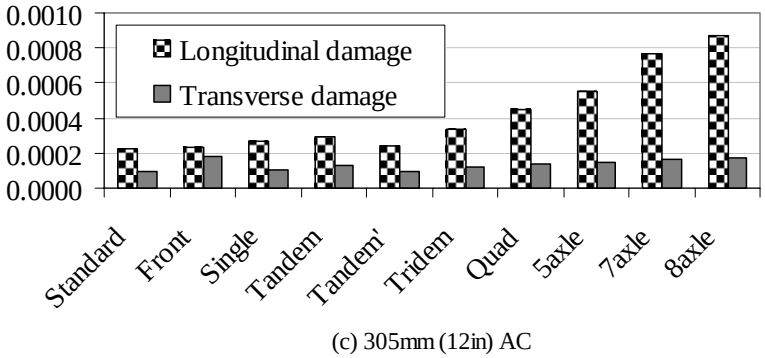


(c) 305mm (12in) AC

Figure 3.9. Comparison of pavement damage from longitudinal and transverse stresses and strains (soft AC, low damping).

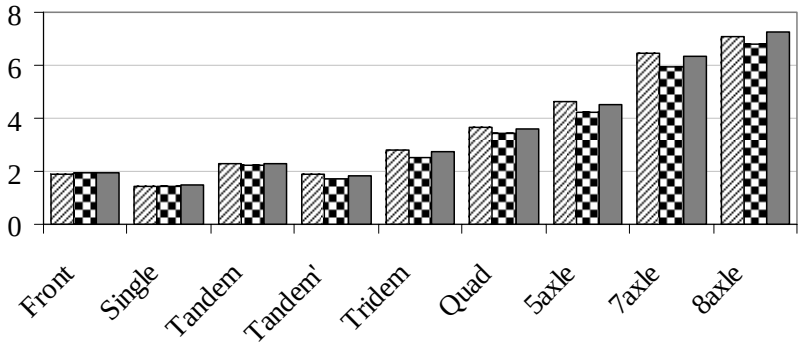


(a) 90 mm (3.5 in) AC

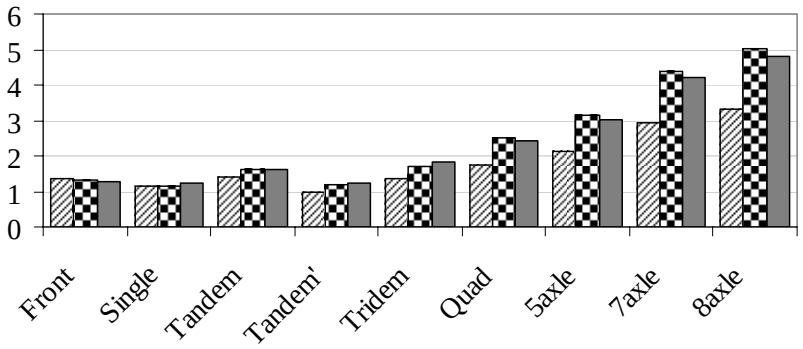


(b) 203 mm (8 in) AC

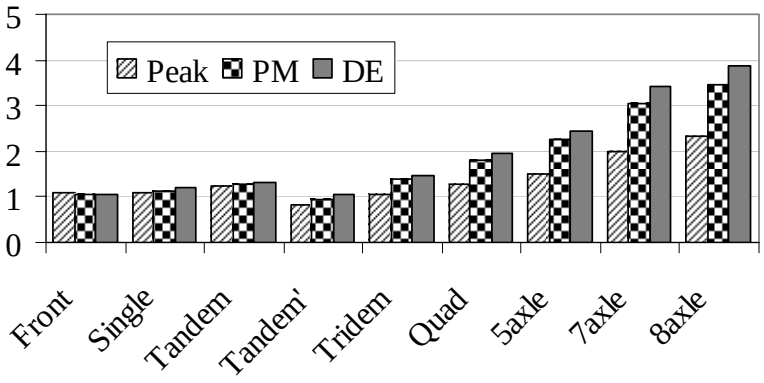


(c) 305 mm (12 in) AC

Figure 3.10. LEF of the axles for soft, low damping AC

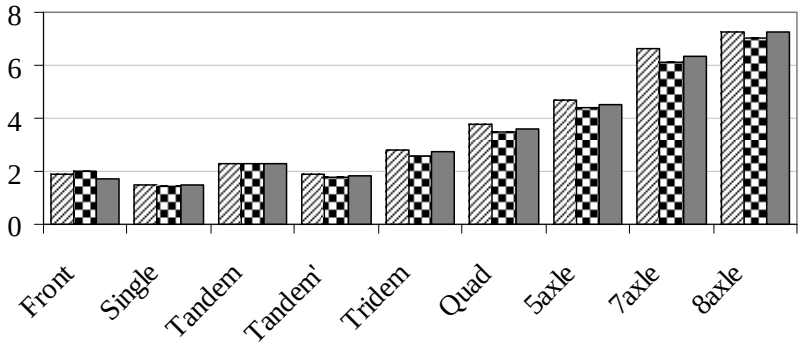


(a) 90 mm (3.5 in) AC

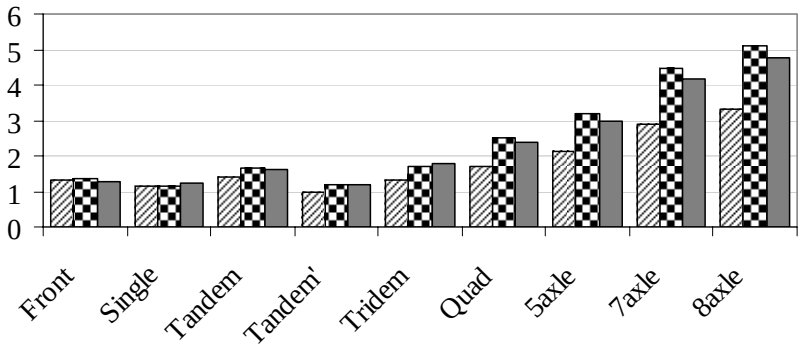


(b) 203 mm (8 in) AC

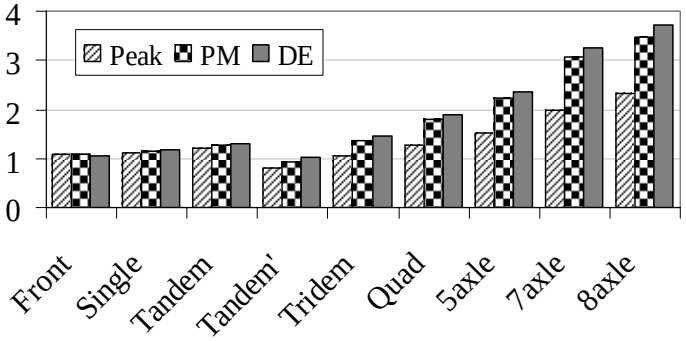


(c) 305 mm (12 in) AC

Figure 3.11. LEF of the axles for soft, high damping AC

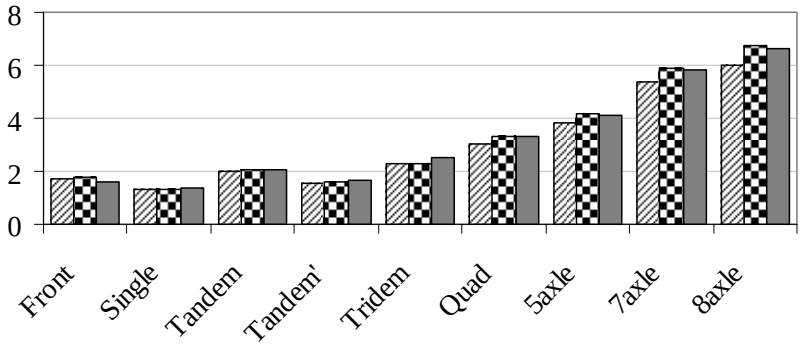


(a) 90 mm (3.5 in) AC

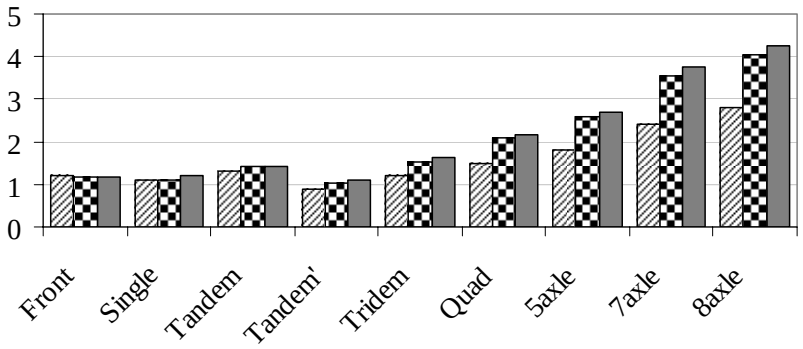


(b) 203 mm (8 in) AC

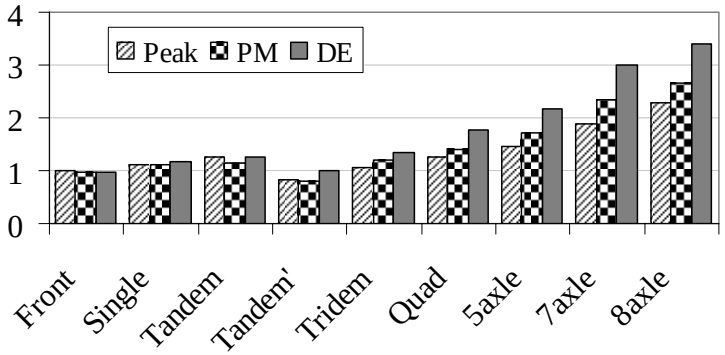


(c) 305 mm (12 in) AC

Figure 3.12. LEF of the axles for stiff, low damping AC

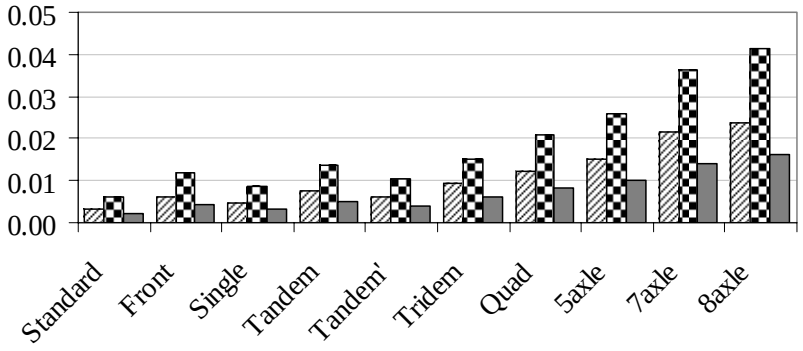


(a) 90mm (3.5in) AC

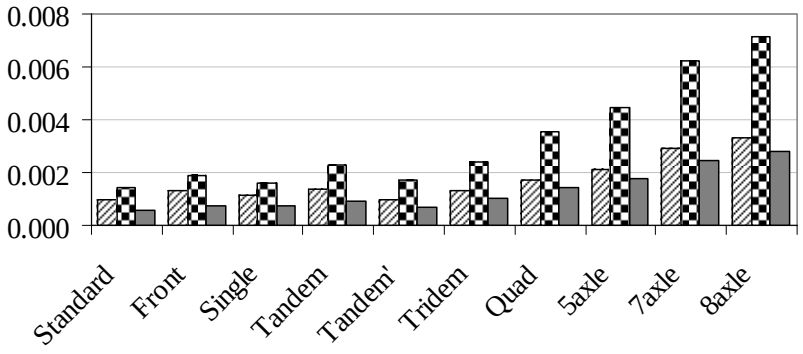


(b) 203mm (8in) AC

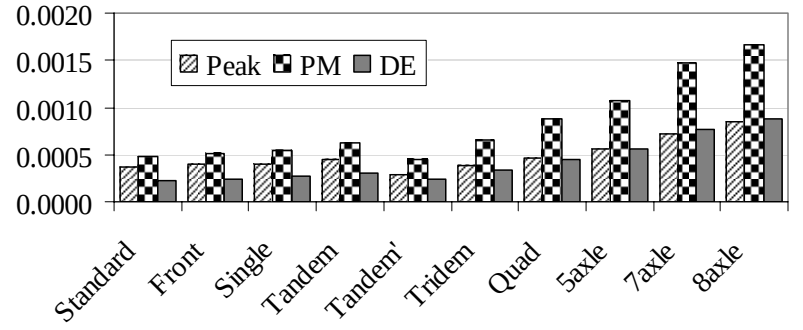


(c) 305mm (12in) AC

Figure 3.13. Fatigue damage from axles for soft, low damping AC

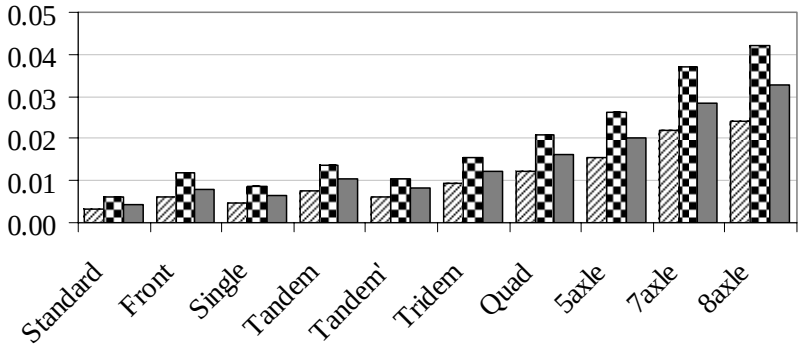


(a) 90mm (3.5in) AC

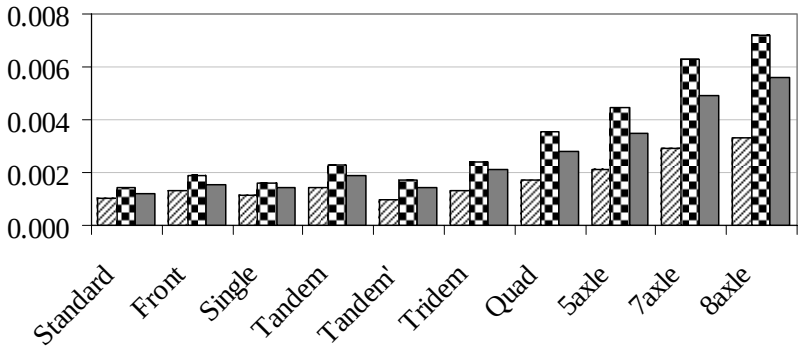


(b) 203mm (8in) AC

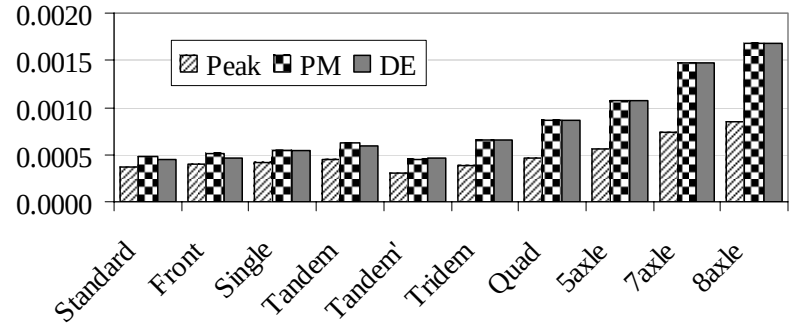


(c) 305mm (12in) AC

Figure 3.14. Fatigue damage from axles for soft, high damping AC

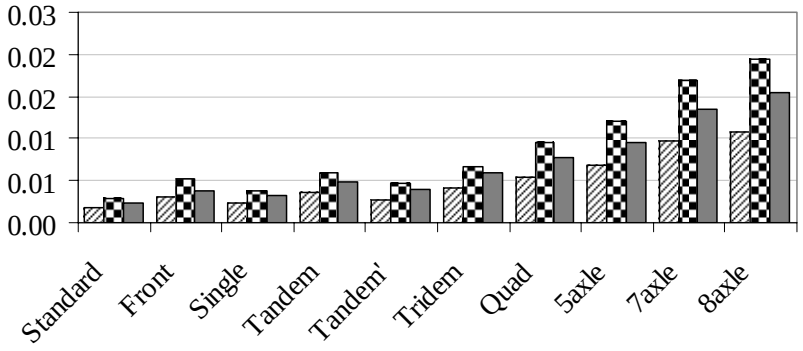


(a) 90mm (3.5in) AC

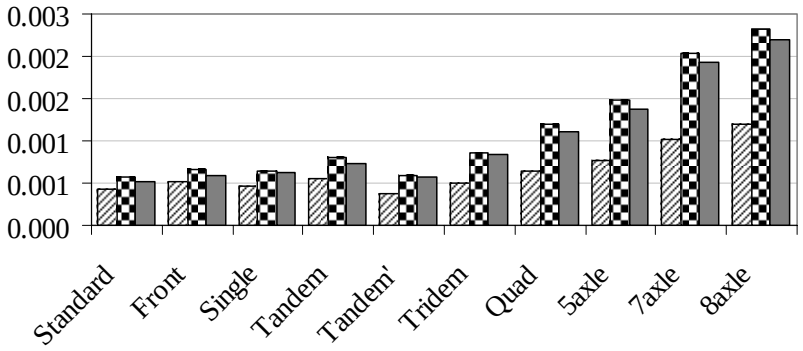


(b) 203mm (8in) AC

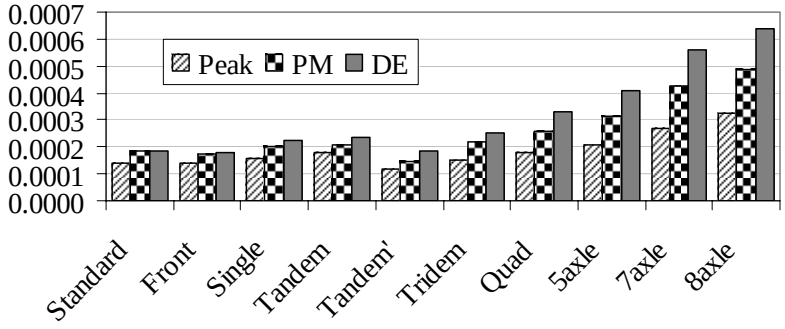


(c) 305mm (12in) AC

Figure 3.15. Fatigue damage from axles for stiff, low damping AC

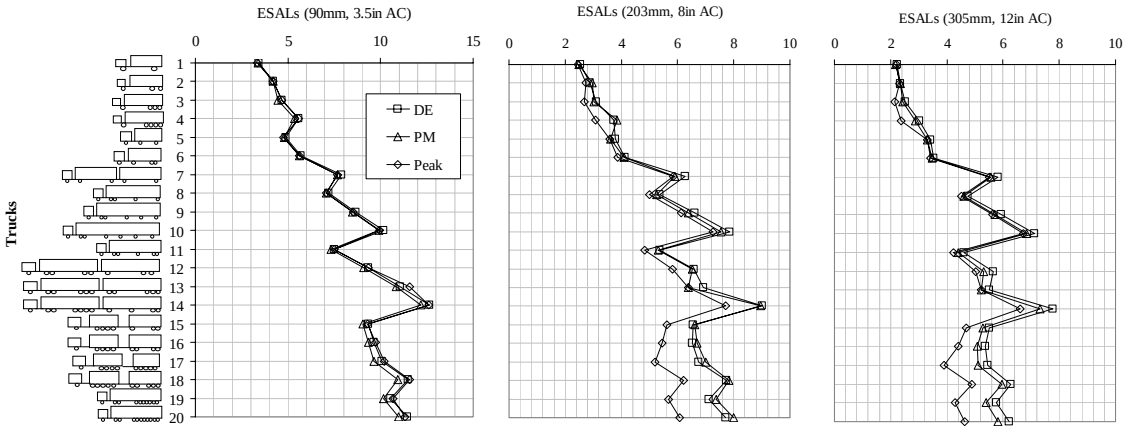


Figure 3.16. Truck factors for soft, low damping AC

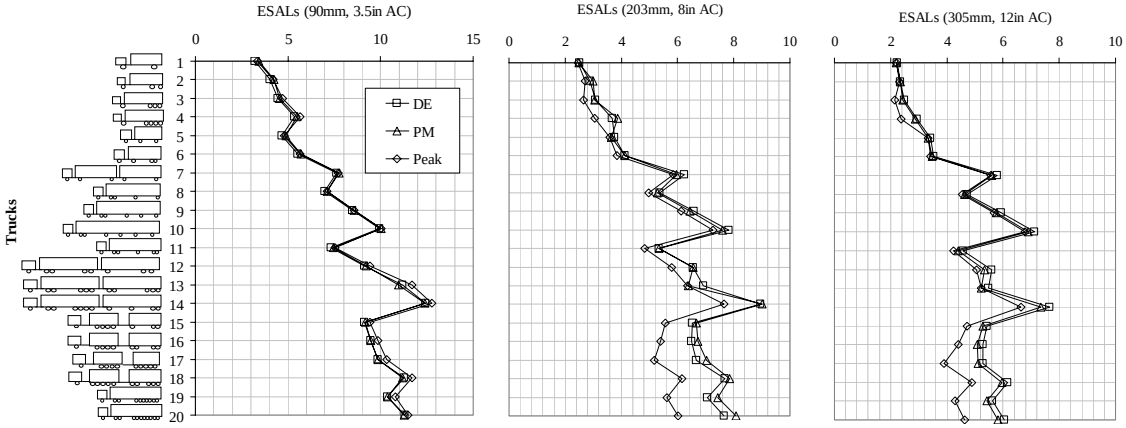


Figure 3.17. Truck factors for soft, high damping AC

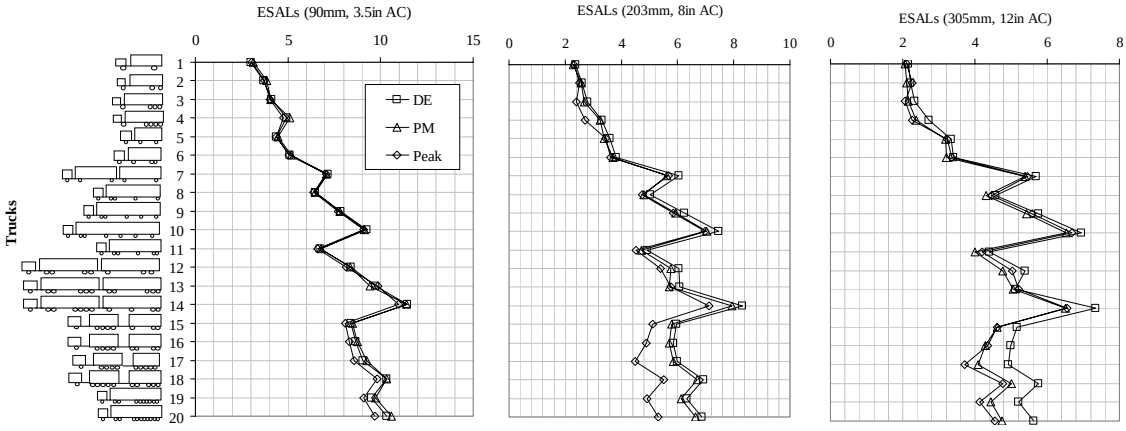


Figure 3.18. Truck factors for stiff, low damping AC

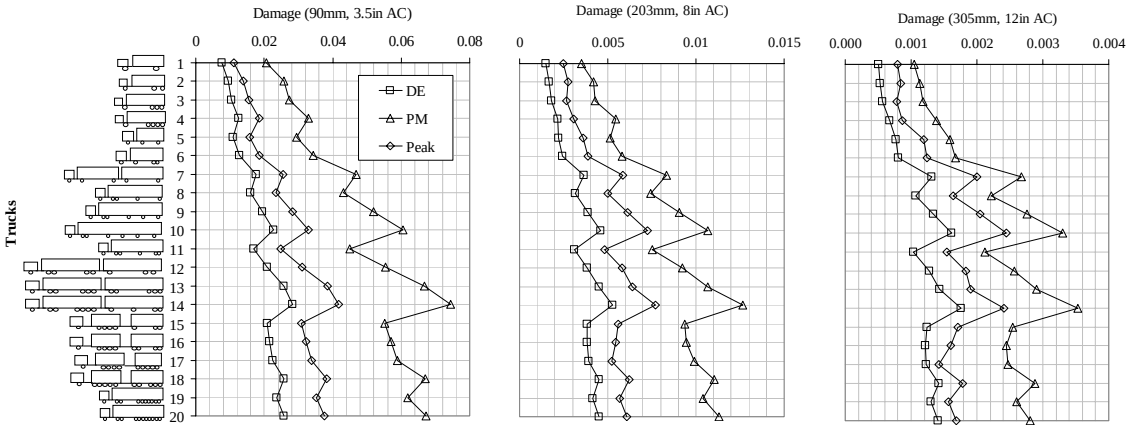


Figure 3.19. Fatigue damage from trucks for soft, low damping AC

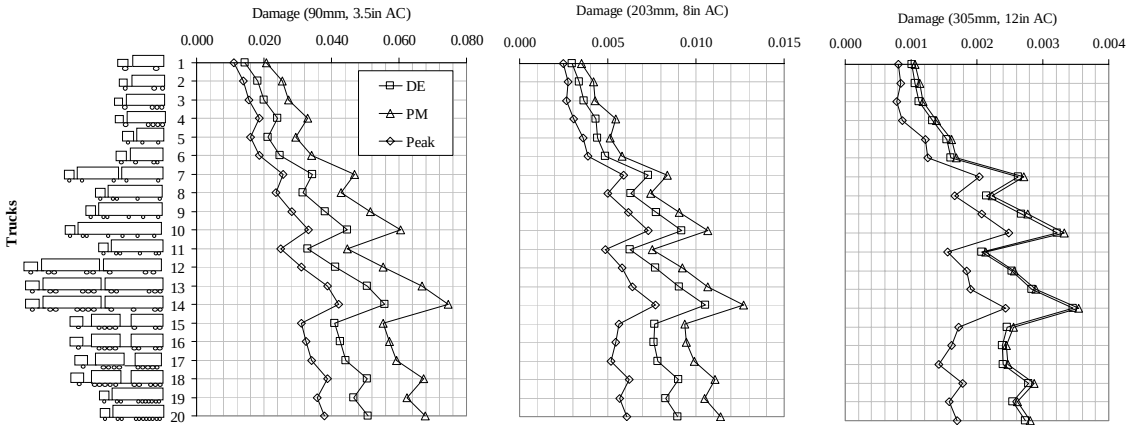


Figure 3.20. Fatigue damage from trucks for soft, high damping AC

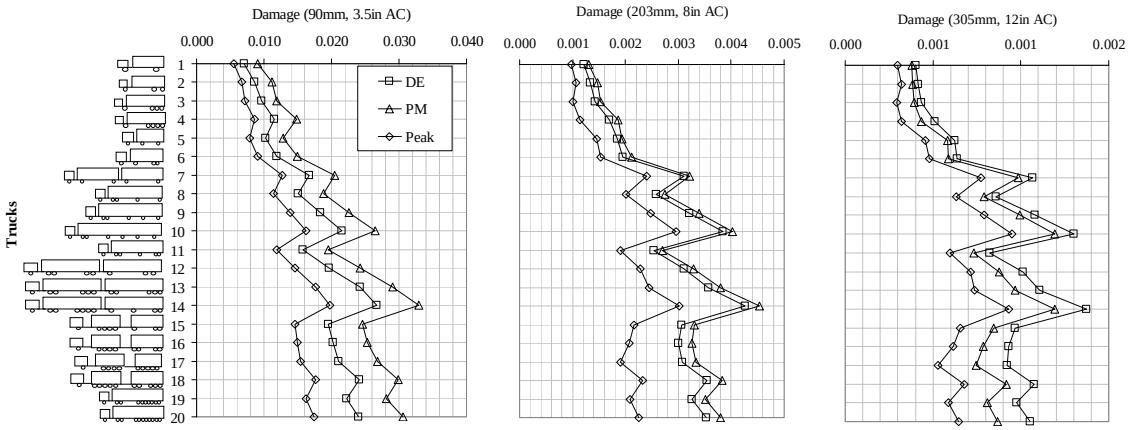


Figure 3.21. Fatigue damage from trucks for stiff, low damping AC

## 3.6 CONCLUSION

In this chapter, three methods of estimating axle Load Equivalency Factors (LEF) and Truck Factors (TF) were compared: (1) peak strains, (2) difference between peak and midway strains, and (3) dissipated energy. The results based on the dissipated energy method confirm that the response in the longitudinal direction is more critical than that in the transverse direction. The results also reveal that, in general, the LEFs/TFs based on the peak-midway strain method agree well with those from the dissipated energy method. The peak strain method usually under predicts the LEFs and TFs compared to the other two methods except for thin pavements. In terms of pavement damage per passage, the peak-midway strain method agrees better with the dissipated energy method than the peak strain method except for soft, low damping AC pavements.

The dissipated energy method is recommended for estimating pavement fatigue damage because the strain methods are limited to “peak” responses, and do not provide a rationale for selecting which “peak” value to use, while the dissipated energy method captures the totality of the stress-strain response during the passage of the load(s), thus eliminating the uncertainty about which strain value to use. However, the dissipated energy method still needs to be calibrated with field data.

The truck factors for various levels of AC damping were averaged for the six profiles and compared with the AASHTO truck factors. The results are summarized in table 3.4. The results indicate that the AASHTO factors are significantly lower that the mechanistic-based values, especially for the thinner pavements.

Table 3.4 Comparison of Truck Factors from mechanistic analysis and AASHTO

| | | | AASHTO Truck Factors | | | | | | ME Truck Factors | | | | | | Ratio of ME to AASHTO Truck Factors | | | | | |
|---|---|---|---|---|---|---|---|---|---|---|---|---|---|---|---|---|---|---|---|---|
| | | | Eac = 350 ksi | | | Eac = 700 ksi | | | Eac = 350 ksi | | | Eac = 700 ksi | | | Eac = 350 ksi | | | Eac = 700 ksi | | |
| Truck | Truck No. | Total Wt. (kips) | 3.5 in | 8 in | 12 in | 3.5 in | 8 in | 12 in | 3.5 in | 8 in | 12 in | 3.5 in | 8 in | 12 in | 3.5 in | 8 in | 12 in | 3.5 in | 8 in | 12 in |
|  | 1 | *33.4* | 1.53 | 1.51 | 1.50 | 1.52 | 1.50 | 1.50 | 2.21 | 2.04 | 1.87 | 2.16 | 1.96 | 1.84 | 1.44 | 1.36 | 1.25 | 1.42 | 1.30 | 1.23 |
| 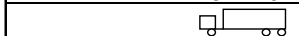 | 2 | *47.4* | 1.39 | 1.33 | 1.31 | 1.37 | 1.32 | 1.31 | 2.76 | 2.34 | 1.97 | 2.66 | 2.14 | 1.89 | 1.98 | 1.76 | 1.50 | 1.94 | 1.62 | 1.45 |
|  | 3 | *54.4* | 0.97 | 0.91 | 0.89 | 0.95 | 0.89 | 0.88 | 3.04 | 2.50 | 2.09 | 2.92 | 2.26 | 1.95 | 3.14 | 2.75 | 2.35 | 3.08 | 2.53 | 2.20 |
|  | 4 | *67.4* | 1.12 | 1.04 | 1.02 | 1.09 | 1.03 | 1.01 | 3.65 | 2.98 | 2.47 | 3.50 | 2.68 | 2.27 | 3.27 | 2.86 | 2.42 | 3.21 | 2.62 | 2.24 |
|  | 5 | *51.4* | 2.53 | 2.51 | 2.50 | 2.52 | 2.50 | 2.50 | 3.21 | 3.04 | 2.87 | 3.16 | 2.96 | 2.84 | 1.27 | 1.21 | 1.15 | 1.25 | 1.18 | 1.14 |
| 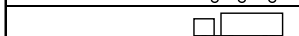 | 6 | *65.4* | 2.39 | 2.33 | 2.31 | 2.37 | 2.32 | 2.31 | 3.76 | 3.34 | 2.97 | 3.66 | 3.14 | 2.89 | 1.57 | 1.43 | 1.29 | 1.54 | 1.35 | 1.25 |
| 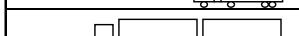 | 7 | *87.4* | 4.53 | 4.51 | 4.50 | 4.52 | 4.50 | 4.50 | 5.21 | 5.04 | 4.87 | 5.16 | 4.96 | 4.84 | 1.15 | 1.12 | 1.08 | 1.14 | 1.10 | 1.08 |
|  | 8 | *83.4* | 3.39 | 3.33 | 3.31 | 3.37 | 3.32 | 3.31 | 4.76 | 4.34 | 3.97 | 4.66 | 4.14 | 3.89 | 1.40 | 1.30 | 1.20 | 1.38 | 1.25 | 1.18 |
|  | 9 | *101.4* | 4.39 | 4.33 | 4.31 | 4.37 | 4.32 | 4.31 | 5.76 | 5.34 | 4.97 | 5.66 | 5.14 | 4.89 | 1.31 | 1.23 | 1.15 | 1.30 | 1.19 | 1.14 |
| 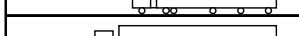 | 10 | *119.4* | 5.39 | 5.33 | 5.31 | 5.37 | 5.32 | 5.31 | 6.76 | 6.34 | 5.97 | 6.66 | 6.14 | 5.89 | 1.25 | 1.19 | 1.12 | 1.24 | 1.15 | 1.11 |
|  | 11 | *91.4* | 2.75 | 2.66 | 2.64 | 2.72 | 2.64 | 2.63 | 4.97 | 4.31 | 3.84 | 4.82 | 4.04 | 3.72 | 1.81 | 1.62 | 1.46 | 1.77 | 1.53 | 1.41 |
| 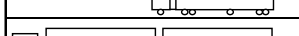 | 12 | *117.4* | 3.11 | 2.99 | 2.96 | 3.07 | 2.97 | 2.95 | 6.19 | 5.29 | 4.70 | 5.98 | 4.94 | 4.54 | 1.99 | 1.77 | 1.59 | 1.95 | 1.66 | 1.54 |
|  | 13 | *151.4* | 2.63 | 2.46 | 2.42 | 2.57 | 2.43 | 2.40 | 7.64 | 6.22 | 5.26 | 7.33 | 5.66 | 4.94 | 2.91 | 2.53 | 2.18 | 2.85 | 2.33 | 2.06 |
| 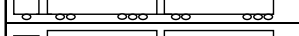 | 14 | *161.4* | 4.34 | 4.20 | 4.16 | 4.29 | 4.17 | 4.14 | 8.41 | 7.25 | 6.43 | 8.16 | 6.77 | 6.15 | 1.94 | 1.73 | 1.55 | 1.90 | 1.62 | 1.48 |
|  | 15 | *117.4* | 2.97 | 2.86 | 2.83 | 2.93 | 2.84 | 2.82 | 6.19 | 5.27 | 4.57 | 6.00 | 4.86 | 4.32 | 2.08 | 1.84 | 1.61 | 2.04 | 1.71 | 1.53 |
|  | 16 | *125.4* | 2.34 | 2.20 | 2.16 | 2.29 | 2.17 | 2.14 | 6.41 | 5.25 | 4.43 | 6.16 | 4.77 | 4.15 | 2.75 | 2.39 | 2.05 | 2.69 | 2.20 | 1.94 |
|  | 17 | *132.4* | 1.85 | 1.71 | 1.67 | 1.80 | 1.68 | 1.66 | 6.70 | 5.40 | 4.45 | 6.42 | 4.84 | 4.04 | 3.63 | 3.16 | 2.66 | 3.57 | 2.88 | 2.44 |
| 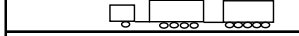 | 18 | *143.4* | 2.34 | 2.46 | 2.16 | 2.29 | 2.17 | 2.15 | 7.63 | 6.21 | 5.16 | 7.33 | 5.60 | 4.77 | 3.26 | 2.52 | 2.39 | 3.20 | 2.58 | 2.22 |
| 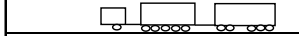 | 19 | *138.4* | 2.41 | 2.26 | 2.22 | 2.36 | 2.24 | 2.21 | 7.03 | 5.71 | 4.72 | 6.76 | 5.13 | 4.31 | 2.92 | 2.52 | 2.12 | 2.87 | 2.29 | 1.95 |
| 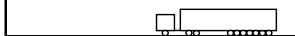 | 20 | *151.4* | 2.56 | 2.40 | 2.35 | 2.50 | 2.37 | 2.34 | 7.64 | 6.18 | 5.10 | 7.34 | 5.55 | 4.64 | 2.99 | 2.58 | 2.16 | 2.94 | 2.34 | 1.98 |
|  | 21 | *79.4* | 2.24 | 2.15 | 2.13 | 2.21 | 2.13 | 2.12 | 4.30 | 3.63 | 3.07 | 4.16 | 3.32 | 2.94 | 1.92 | 1.69 | 1.44 | 1.88 | 1.55 | 1.39 |

# CHAPTER 4
# CALIBRATION OF MECHANISTIC-EMPIRICAL RUTTING MODEL

## 4.1 INTRODUCTION

Since rutting is a major failure mode in flexible pavements, researchers have been trying to predict rut depth for future rehabilitation and budget allocation. There are two main approaches for the prediction of rutting: 1) subgrade strain model (i.e. AI and Shell models) and 2) permanent deformation within each layer. The first approach assumes that most of the rutting results from the subgrade layer only, and is no longer valid based on observations from the field. The second approach considers the rutting contribution from all pavement layers, and is not widely used due to the difficulties of determining the elasto-plastic characteristics of pavement materials. Due to increased tire pressures and new axle configurations as well as observations from the field, researchers began to investigate the rutting contribution from all pavement layers. This approach is also implemented in the new mechanistic-empirical (ME) pavement design guide.

One of the main models related to this approach is the VESYS rutting model that relates the plastic strain to the elastic strain through the permanent deformation parameters (PDPs) $\mu$ and $\alpha$ as follows:

$$\varepsilon_p(n) = \mu * \varepsilon_e * n^{-\alpha} \tag{4.1}$$

The most essential task in using this model is to accurately calculate PDPs ($\mu$ and $\alpha$) for each pavement layer within the pavement system. As mentioned in Chapter 2 of Volume I, several attempts have been made to estimate these parameters; however agreement between studies varies. Yet, the previous research provides a common, but wide range for these parameters. As can be seen in Equation 4.1, $\alpha$ is an exponent and therefore prediction of rutting is very sensitive to small changes in the $\alpha$-value. In this research, PDPs were backcalculated by matching the rut time series data from the SPS-1 experiment in the LTPP program. The most novel aspect of this backcalculation process involved the application of the approach developed in NCHRP 468 (White et. al., 2002), which uses transverse surface profiles to locate the layer causing most of the rutting.

In this chapter, a unique solution for these parameters was attained for each pavement section within the SPS-1 experiment using the above process. PDPs were then related to pavement material properties, climatic conditions, and particular pavement cross-sections through regression analysis of SPS-1 experiment data.

## 4.2 SPS-1 EXPERIMENT

The Specific Pavement Study-1 (SPS-1) experiment includes eighteen sites with twelve pavement sections each, for a total of 216 sections located in all four LTPP climatic

regions: Wet Freeze (WF), Wet-No-Freeze (WNF), Dry Freeze (DF), and Dry-No-Freeze (DNF). The locations of SPS-1 sites within the United State are shown in Figure 4.1. The SPS-1 experiment includes a wide range of pavement structures (different HMA/base/subbase thickness and base types) in various site conditions (traffic level, subgrade type and climate). Table 4.1 shows the descriptive statistics for the SPS-1 variables.

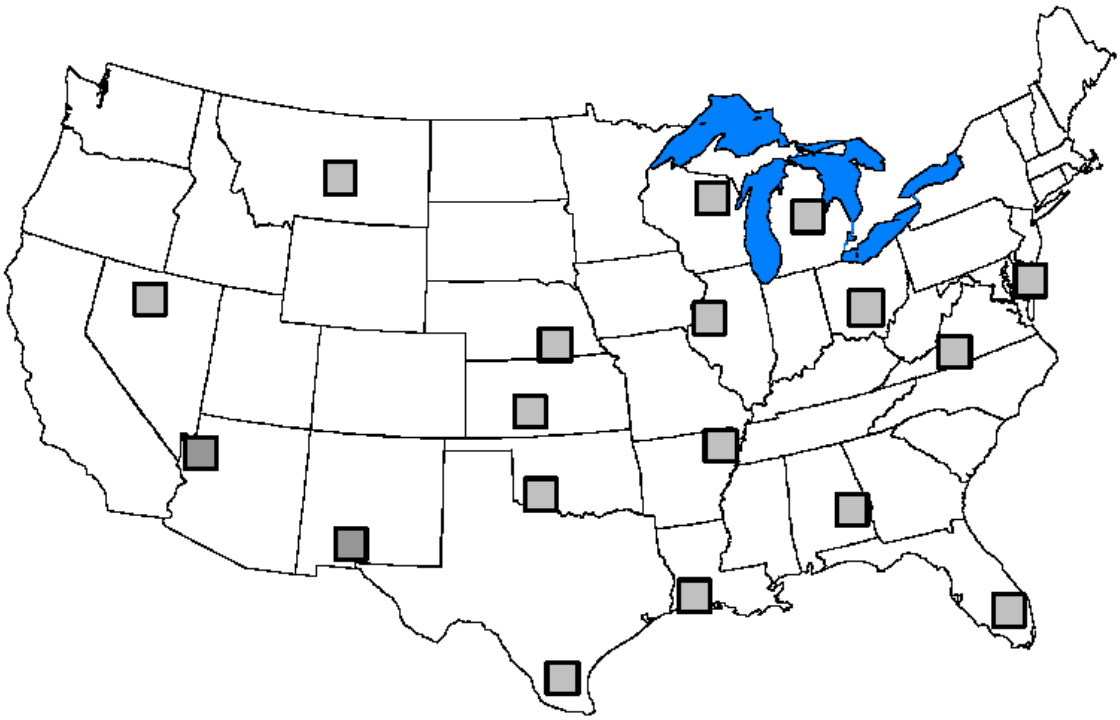

Figure 4.1 Location of the SPS-1 sites

Table 4.1 Descriptive statistics for SPS-1 experiment (LTPP database release 18)

| Variables | Minimum | Maximum | Average | St. dev. | COV % |
|---|---|---|---|---|---|
| HMA thickness, in | 3.4 | 9.5 | 5.75 | 1.5 | 26 |
| Base thickness, in | 7.1 | 17.9 | 11.14 | 2.88 | 25.8 |
| Rut depth, mm | 3 | 30 | 8.62 | 5.31 | 61.6 |
| KESAL/year | 113 | 524 | 279 | 126 | 45.2 |
| Age, year | 0.83 | 10.2 | 6.5 | 2.34 | 36 |
| FI*, $^{o}$C-day | 0 | 988 | 226 | 276 | 121.7 |
| AARF**, mm | 221 | 1539 | 846 | 402 | 47.5 |

* Freezing index
** Average annual rain fall
1 inch = 2.54 cm

### 4.2.1 SPS-1 Data Used In The Analysis

The SPS-1 data used in this research are as follows:

- Initial Falling Weight Deflectometer ( FWD) data for backcalculation of pavement layer moduli,
- Time series rutting data for minimizing the error between predicted and measured rut depth,
- Transverse profile data to locate rutting within individual pavement layers,
- Traffic data for rutting prediction,
- Pavement layer thicknesses for backcalculation of material properties and regression analysis to predict permanent deformation parameters,
- Climatic data for regression analysis to predict permanent deformation parameters, and
- Material properties for regression analysis to predict permanent deformation parameters.

## 4.3 VESYS MODEL

The original form of VESYS rutting model is based on the assumption that the permanent strain is proportional to the resilient strain so that:

$$\varepsilon_p(n) = \mu\varepsilon_e n^{-\alpha} \tag{4.2}$$

where

$\varepsilon_p(n)$ = the permanent or plastic strain due to a single load application,

$\varepsilon_e$ = the elastic or resilient strain at 200 repetitions,

$n$ = the number of load applications,

$\alpha$ = permanent deformation parameter indicating the rate of decrease in permanent deformation as the number of load applications increases (hardening effect),

$\mu$ = permanent deformation parameter representing the constant of proportionality between plastic and elastic strain.

The total permanent deformation can be obtained by integrating Equation 4.2 as follows:

$$\varepsilon_p = \int_0^n \mu\varepsilon_e n^{-\alpha} dn = \frac{\mu}{1-\alpha}\varepsilon_e n^{1-\alpha} \tag{4.3}$$

The cumulative permanent deformation, $\rho_p$ in all pavement layers from all load groups can be calculated from the following equation:

$$\rho_p = \sum_{j=1}^{L} h_j \frac{\mu_j}{1-\alpha_j} \left( \sum_{i=1}^{k} \varepsilon_{e_{i,j}} n_i^{1-\alpha_j} \right) \tag{4.4}$$

where

$\varepsilon_{e_{i,j}}$ = the vertical compressive strain at the middle of layer *j* due to load group *i*,

$\alpha_j$ and $\mu_j$ = PDPs for layer *j*.

Determining the actual values for the PDPs for each pavement layer is the most challenging task to achieve an accurate rutting prediction. The flow chart in Figure 4.2 shows the process used to predict the values of α and μ from in-service pavements in the SPS-1 experiment.

## 4.4 BACKCALCULATION OF PAVEMENT LAYER MODULI

In this analysis, the initial layer moduli for each SPS-1 pavement section were backcalculated using Falling Weight Deflectometer (FWD) data obtained after the initial construction of the test sections. The MICHBACK computer program was used for the (static) backcalculation.

### 4.4.1 MICHBACK Computer Program

There are several computer programs that can be used for backcalculation of the pavement layer moduli such as MICHBACK, MODCOMP, MODULUS, and EVERCALC. Backcalculation analysis was performed for two pavement sections, which have known layer moduli (from the forward analysis), using the four backcalculation programs (Svasdisant, 2003). The MICHBACK computer program produced similar, and in some cases better results over other backcalculation programs. Moreover, each SPS-1 section has 11 or more FWD measurements, and each point location requires backcalculation of the layer moduli. The MICHBACK computer program can carry out backcalculation of all these point locations at once, which simplifies the analysis and makes it more efficient.

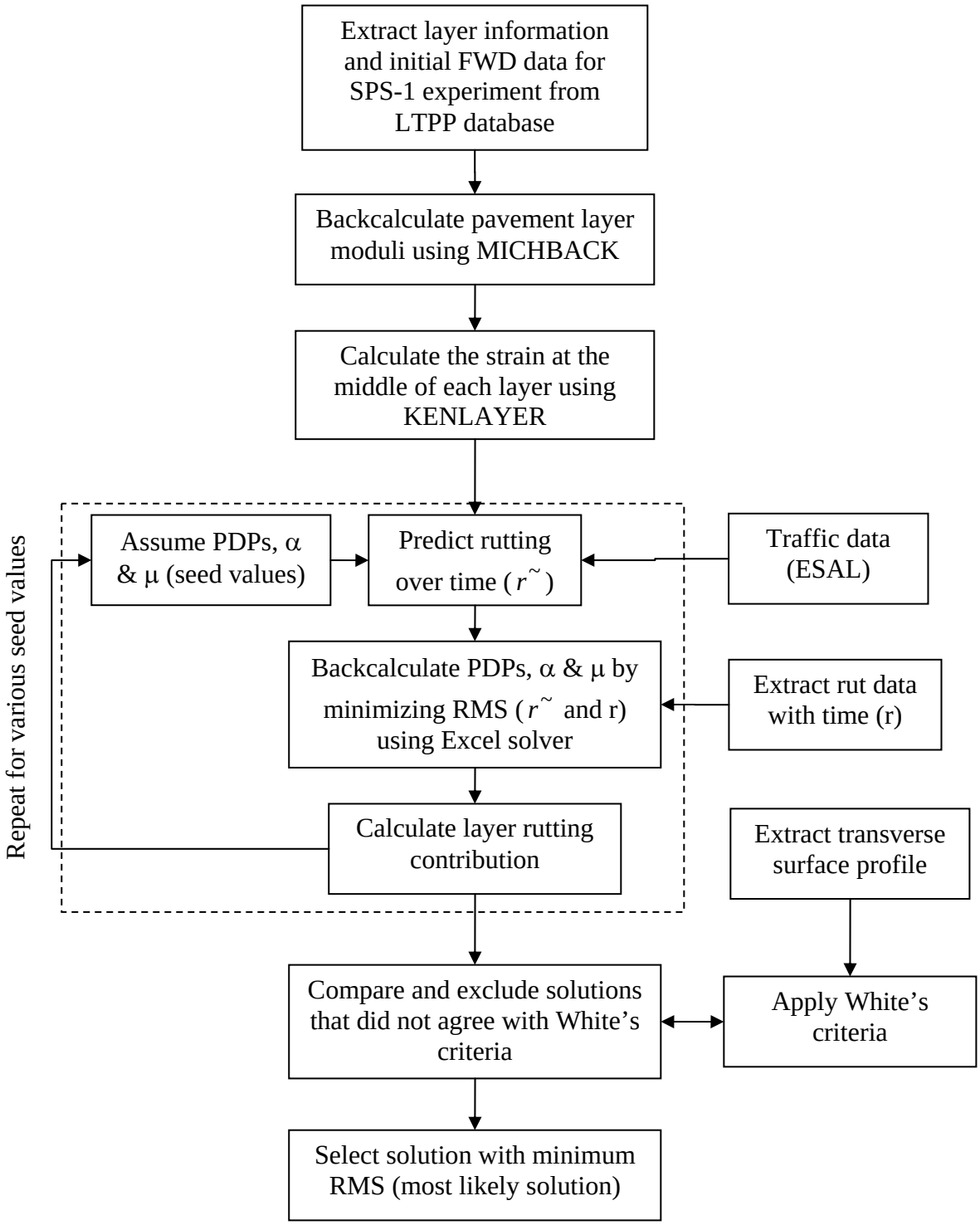


Figure 4.2 Flow chart for calibration of mechanistic-empirical rutting model

In this study, the backcalculation of layer moduli for all SPS-1 sections was conducted in order to calculate the vertical compressive strain at the middle of each pavement layer. The process of layer moduli backcalculation yields a variety of possible values, some of which are highly improbable (i.e. sub-layers with higher moduli than the HMA layer). Therefore, the following section will highlight the procedures used during the backcalculation to insure accurate estimation of pavement layer moduli.

### 4.4.2 Quality control of the backcalculation procedures

Several steps were used to ensure accurate and reliable backcalculation of pavement layer moduli as follows (Schorsch, 2003):

- The solutions converge, which means the difference between two consecutive solutions is smaller than a specified tolerance limit. This criterion was used to eliminate any unacceptable results. If the solution did not converge several trials were made to combine or separate (subgrade) layers and/or introduce a stiff layer. The sections with convergent moduli values were used in the later analysis of this research, while all others were eliminated.
- Low RMS values provide high accuracy backcalculation results and assure close matches of the measured and calculated deflection basins. Figure 4.3 shows the distribution of RMS (%) for all point locations within the SPS-1 experiment. Though all data were initially included, later procedural steps eliminated those with unacceptable RMS% values.
- HMA layer moduli > base layer moduli > roadbed soil moduli. This criterion is based on the principles of pavement design which call for decreasing the pavement modulus with depth. This was held as a general rule, but if the solution did not meet this criterion other trials with pavement layer combinations or stiff layers were introduced.
- A roadbed modulus criterion of < 60000 psi was employed to eliminate unreasonable moduli for natural subgrade soil.

In parallel with the above criteria, examining the presence of a stiff layer for each SPS-1 section was taken into consideration to improve the backcalculation procedure. The deflection data can be utilized to calculate the surface modulus which represents the weighted mean modulus of the half space. The surface modulus calculated using Boussinesq's equations [Ullidtz, 1987].

$$E_o(0) = 2 * (1 - \mu^2) * \sigma_o * \frac{a}{d(0)} \tag{4.5}$$

$$E_o(r) = (1 - \mu^2) * \sigma_o * \frac{a^2}{(r * d(r))} \tag{4.6}$$

Where,

$E_o(r)$ = surface modulus at a distance r from the center of the FWD loading plate

$\mu$ = Poisson's ratio

$\sigma_o$ = contact stress under the loading plate

$d(r)$ = deflection at a distance r

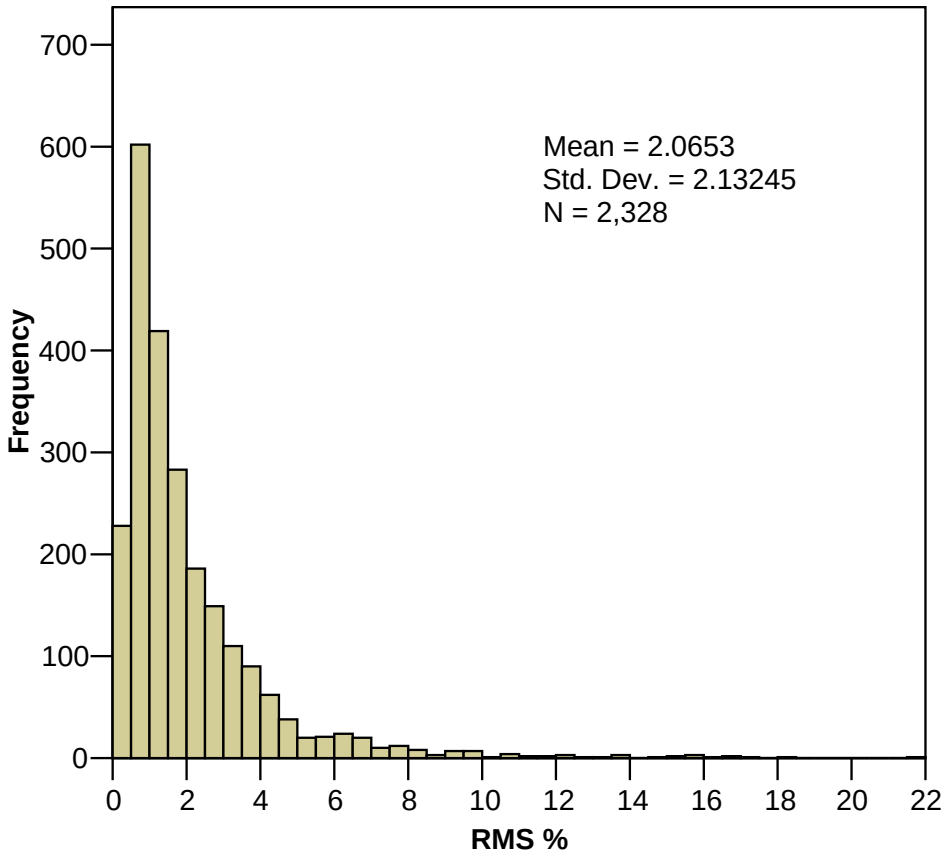


Figure 4.3 Distribution of RMS (%) for all point locations within SPS-1 experiment

Figure 4.4 shows an example of the relationship between the equivalent modulus and the distance from the center of the FWD loading plate at different point locations within the section. If the equivalent modulus value at the tail of the curve remains constant with increasing distance, it indicates a deep or non-existent stiff layer and linear elastic behavior of subgrade as shown in Figure 4.4 (a) . If the equivalent modulus value at the tail of the curve increases with increasing distance, it indicates the presence of a shallow stiff layer and nonlinear elastic behavior of subgrade as shown in Figure 4.4 (b). If the equivalent modulus value at the tail of the curve decreases with increasing distance, it indicates no presence of stiff layer and nonlinear elastic behavior of subgrade as shown in Figure 4.4 (c). Taking into account an existing stiff layer helps the solution to converge; however the exact depth of the stiff layer was determined by trials according to the minimum RMS. In this study, only linear elastic backcalculation analyses were considered (Ullidtz, 1987).

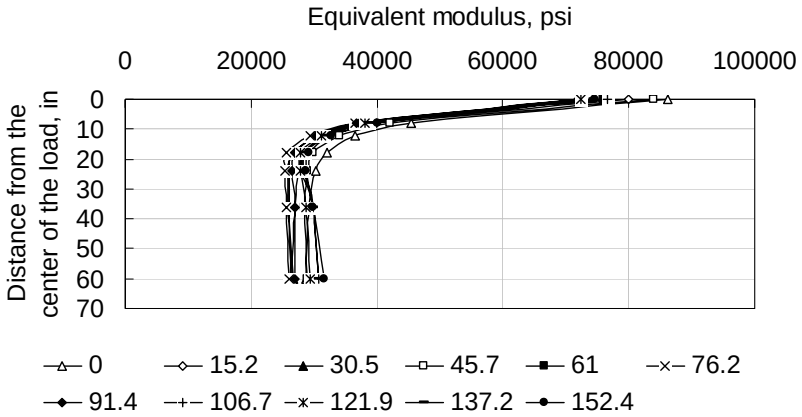


(a) Section 550121 – deep or no stiff layer and linear elastic behavior of subgrade

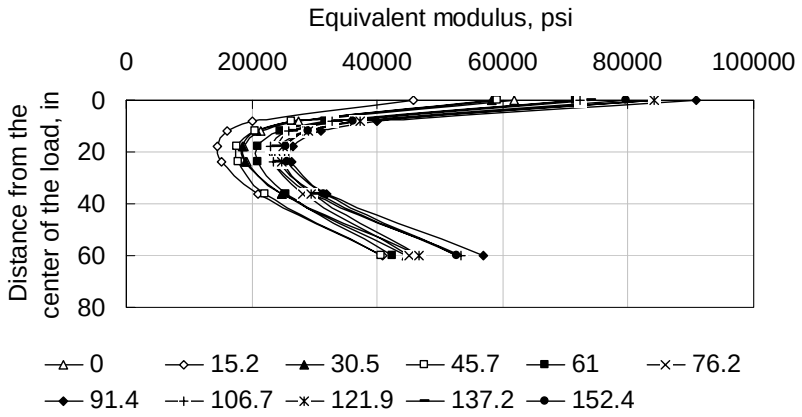


(b) Section 260120 – shallow stiff layer and nonlinear elastic behavior of subgrade

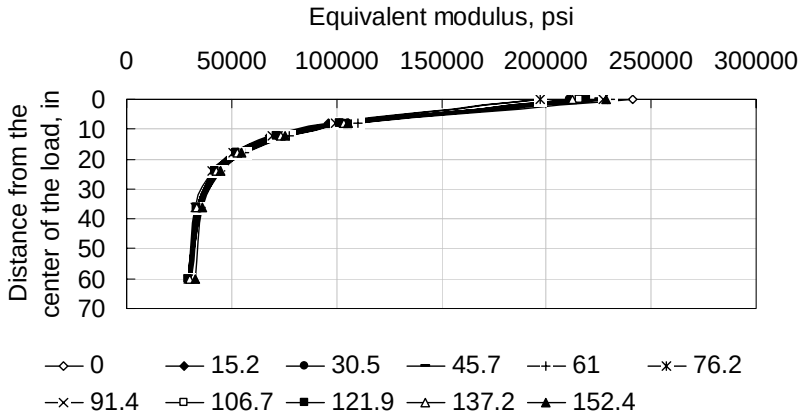


(c) Section 50115 – no stiff layer and nonlinear elastic behavior of subgrade

Figure 4. 4 Equivalent pavement modulus versus the distance from the center of the load at different point locations within the section.

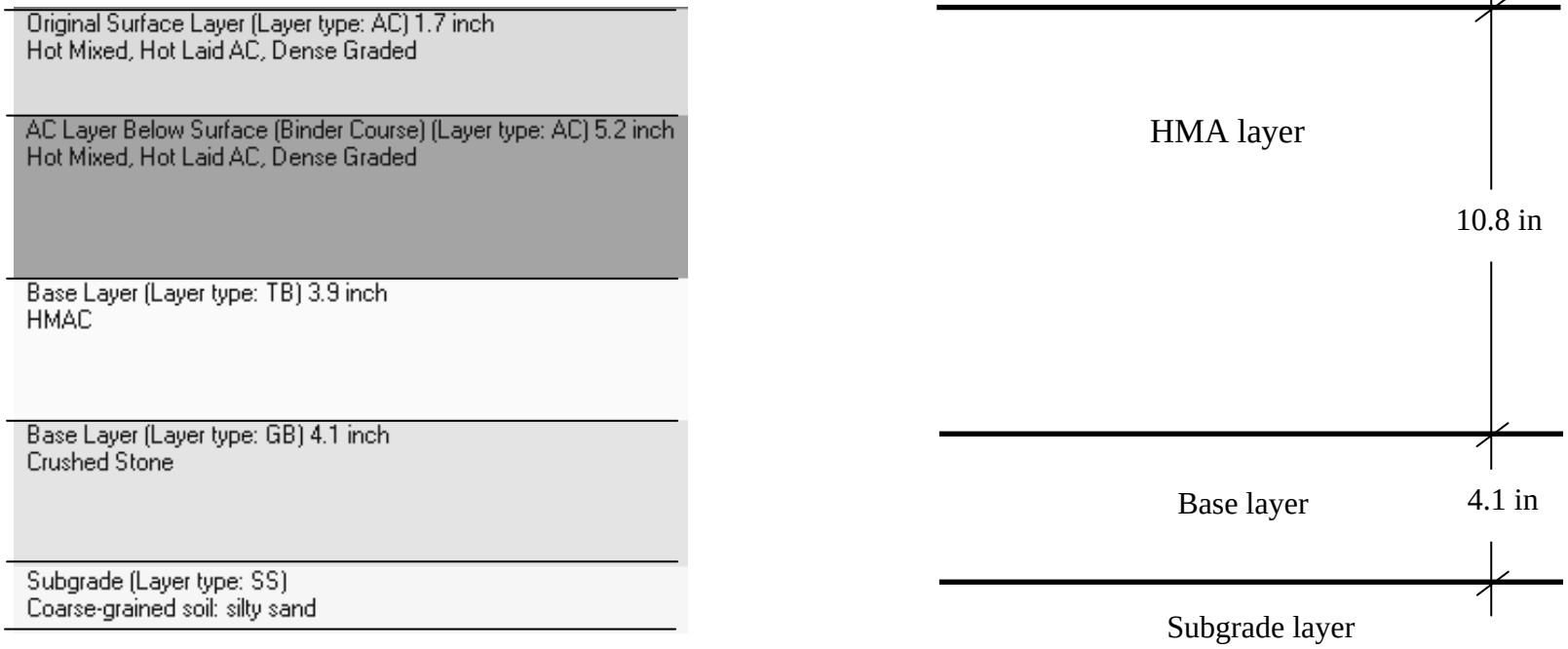


(a) Section 5-0117

(b) Backcalculated layers

Figure 4.5 Pavement layer thicknesses for conventional pavement

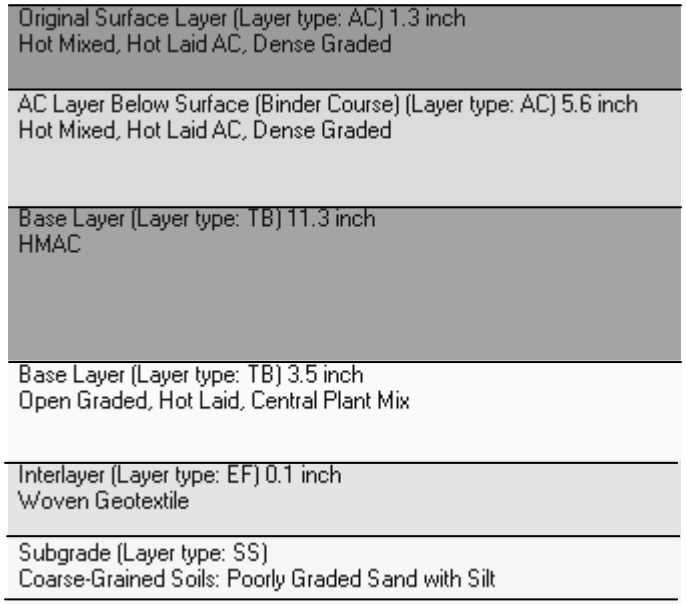


(a) Section 5-0124

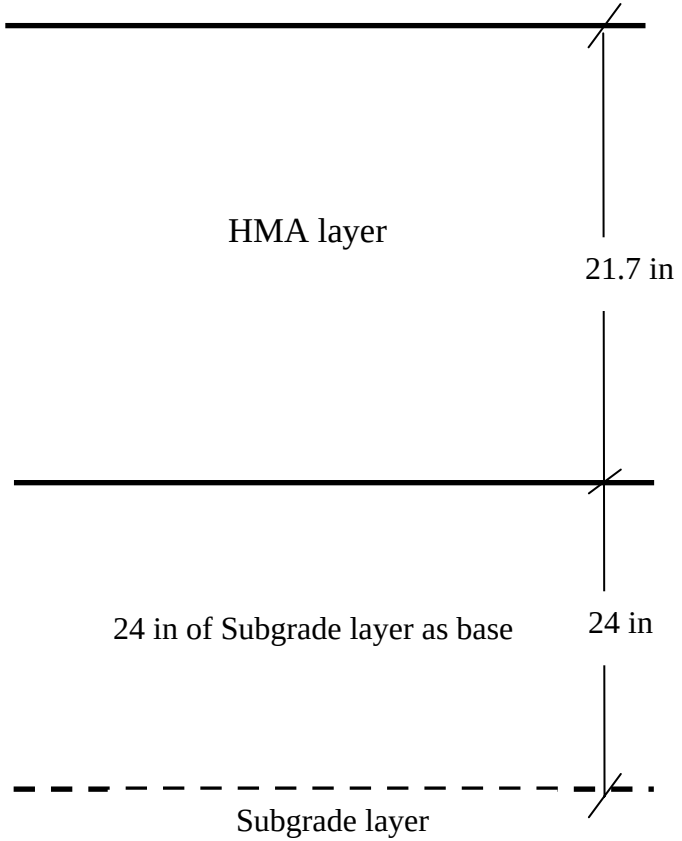


(b) Backcalculated layers

Figure 4.6 pavement layer thicknesses for full depth asphalt

### 4.4.3 Combination /Separation of Pavement Layers

MICHBACK computer program can backcalculate the layer moduli for 3 to 5 layers, however the backcalculation for 5 layers is less accurate. Also, increasing the number of layers will increase the number of PDPs since each layer has two unknown parameters. In most cases, the SPS-1 sections have more than 4 pavement layers. Therefore, the combination of similar pavement layers or division of the subgrade into two layers was taken into consideration in order to treat the pavement structure as a 3- layers system. This allowed the highest accuracy backcalculation and minimized the number of unknown permanent deformation parameters. Figure 4.5 shows an example of pavement section with (a) as constructed layers and (b) pavement layer thicknesses used in the backcalculation procedure. The HMA layers and the treated base layer were combined together as one HMA layer (as shown in Figure 4.5 (b)) and an average modulus was used for forward analysis. On the other hand, when no granular base existed in the design the treated base layer was used as a separate layer in the backcalculation. If this solution did not converge, the treated base was assumed to be part of the overall HMA layer and a 24-inch layer of the subgrade was treated as a base layer, with the rest of the subgrade below considered as the third layer as shown in Figure 4.6.

### 4.4.4 Modulus Variation in the Longitudinal Direction

The length of each SPS-1 pavement section is 500 ft with 11 or more point locations for collecting FWD data. Sometimes, the inconsistency of pavement layer thickness, material variability, and computational quality among other factors cause large variations in the backcalculated moduli between point locations. Hence, the layer moduli variability in the longitudinal direction of each section was tested. All pavement layer (HMA, base, subgrade) moduli were normalized to the first point location, and other point locations were checked against this point for all pavement sections. Figure 4.7 shows two example modulus variations for the pavement layers along the longitudinal direction of two sections. Figure 4.7 (a) shows the modulus variations for section 50113 where there are acceptable modulus variations along the longitudinal direction. Figure 4.7 (b) shows huge variations in the base modulus which might be due to inconsistency in the base thickness.

### 4.4.5 Summary of the Backcalculation Procedure

As explained above, there are many steps in determining layer moduli that extend beyond the simple backcalculation output. The results of the backcalculation procedure as output from programs often require additional attention and discrimination. Great effort went into the backcalculation procedure through several trials and checking steps to ensure the backcalculated moduli are the most suitable ones. After applying all the quality control steps, the number of sections reduced from 216 to 159 sections. All sections with HMA, granular base, and subgrade layers (conventional pavements) were categorized as one group (120 sections). These sections will have a subset of PDP combinations with 6 unknown PDPs (two for each layer) for each section. Sections with HMA and subgrade layers (full-depth asphalt pavements) were categorized as another group (39 sections). This group will have a second subset of PDP combinations with 4 unknown PDPs (2 for the HMA layer and 2 for the subgrade layer) for each section. Table 4.2 shows the descriptive statistics of HMA and base

thicknesses as well as layer moduli (AC, base and subgrade) for the final 109 sections that were used in the backcalculation of PDPs.

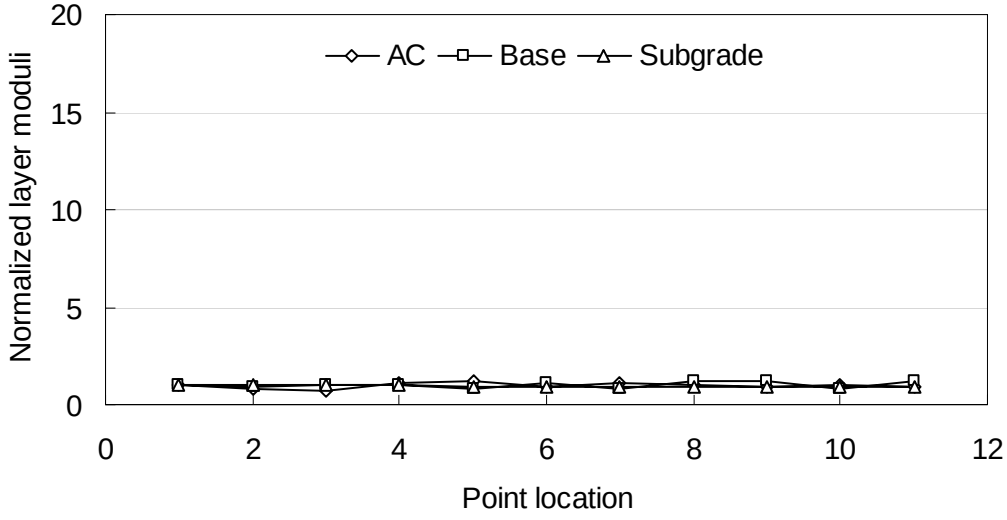


(a) section 5-0113

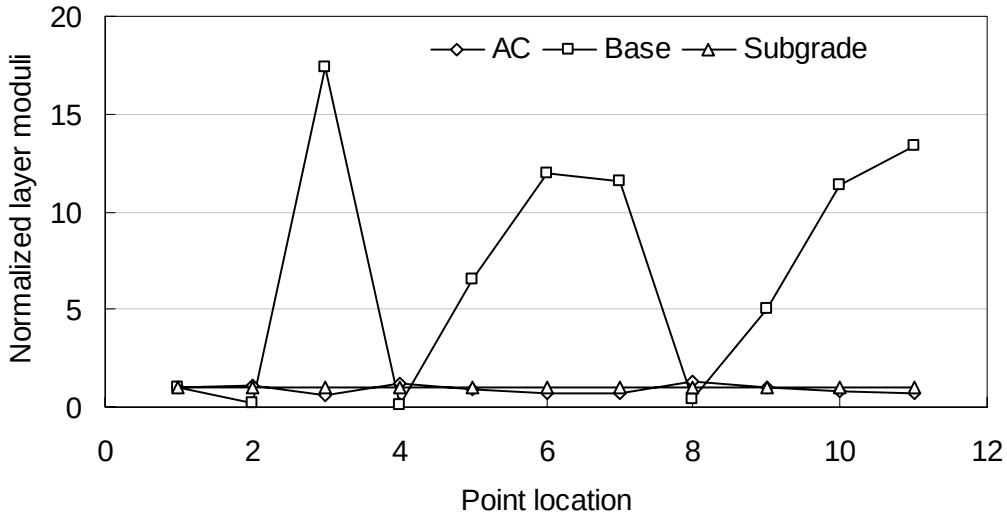


(b) section 30-0123

Figure 4.7 Modulus variations for the pavement layers along the longitudinal direction

Table 4.2 Descriptive statistics for final backcalculation procedures (109 sections)

| Variables | Minimum | Maximum | Average | St. dev. | COV % |
|---|---|---|---|---|---|
| HMA thickness, in | 4.0 | 22.2 | 11.56 | 4.27 | 36.94 |
| Base thickness, in | 3.5 | 46.1 | 18.77 | 11.62 | 61.91 |
| HMA modulus, psi | 69,201 | 2,778,015 | 686,030 | 567,971 | 82.79 |
| Base modulus, psi | 4,599 | 2,499,710 | 118,191 | 345,501 | 292.32 |
| Subgrade modulus, psi | 15,099 | 57,984 | 29,980 | 8,757 | 29.21 |

### 4.4.6 HMA Modulus Temperature Correction

The FWD test temperature varies with time and space even between point locations within the same section. Therefore, the FWD backcalculation results need to be brought to the same temperature in order to compare them. The backcalculated HMA modulus for each pavement section was corrected to the reference temperature of 68°F (20°C) by multiplying it with a temperature correction factor (CF) developed by Park (2000):

$$E_{HMA}(T_r) = CF\ E_{HMA}(T)$$

$$CF = 10^{0.0224(T - T_r)} \tag{4.7}$$

where

$CF$ = Temperature correction factor
$T$ = Mid-depth temperature (°C)
$T_r$ = Reference temperature of 20°C

The mid-depth temperature within the HMA layer was predicted using an empirical equation developed by Park (2000) as a function of the measured surface temperature.

$$T_h = T_{surf} + (-0.3451h - 0.0432h^2 + 0.00196h^3) * \sin(-6.3252t + 5.0967) \tag{4.8}$$

where

$T_h$ = HMA temperature at depth h in °C
$T_{surf}$ = HMA temperature at the surface in °C
$h$ = mid-depth of HMA at which temperature is to be determined in cm
$t$ = time when the HMA surface temperature was measured in days (0<t<1, e.g., 1:30 pm = 13.5/24=0.5625 days)

## 4.5 FORWARD ANALYSIS

The VESYS model relates the plastic strain occurring in each pavement layer to the vertical elastic compressive strain in that layer. There are several computer programs for conducting the forward analysis such as ELYSYM5, VESYS, MICH-PAVE, ILLI-PAVE, and DAMA. The KENLAYER computer program was developed by Huang (1993). He compared the forward analysis of all of these computer programs with KENLAYER results. The solution of the KENLAYER program gave similar or better results for all types of analyses. Therefore, the KENLAYER computer program was used to calculate the vertical compressive strain at the middle of each pavement layer, assuming that the mid-depth strain represented the average layer strain.

To calculate the total rut depth resulting from all layers, it is essential to calculate the strain in the sub-layers until the strain is no longer detectable. Based on the assumption that there is no deformation beyond a certain depth in the subgrade, the subgrade was divided into six 40-inch layers and the calculation of vertical compressive strain performed until the strain approached zero. Figure 4.8 shows the division of the subgrade layer into six 40-inch sub-layers. Also, Figure 4.9 shows the strain values at the middle of each pavement layer for 5 different SPS-1 sections caused by one standard 18-kips single axle. As shown in the figure the strain at the middle of the sixth layer has a very small value, as expected.

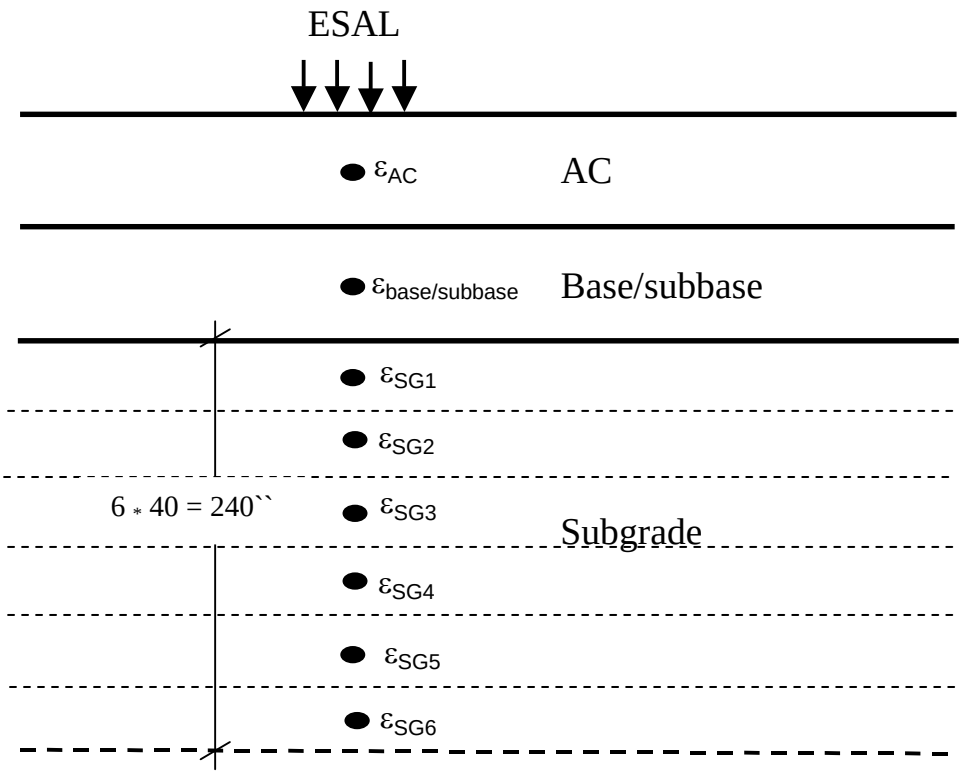


Figure 4.8 Division of the subgrade layer into several sub-layers

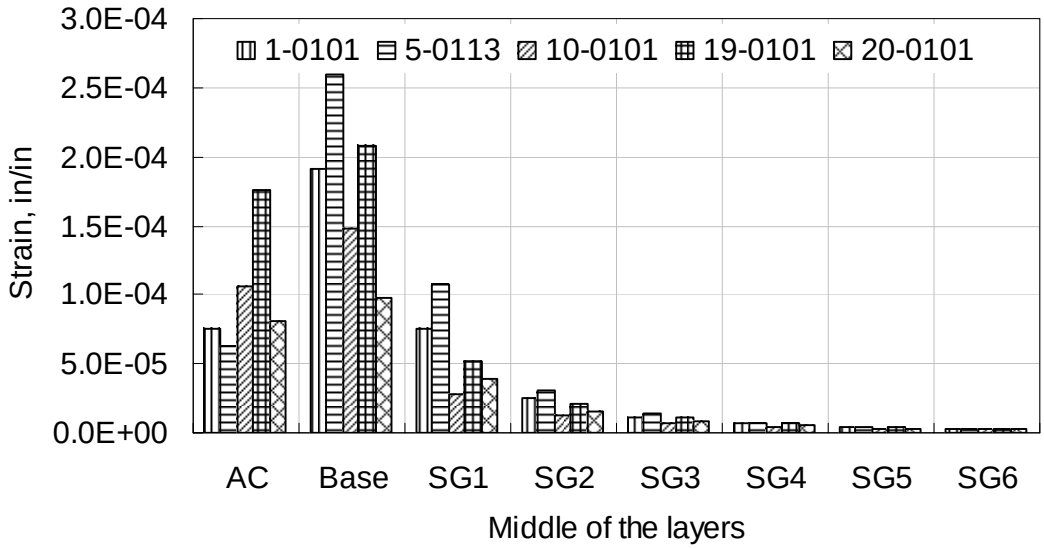


Figure 4.9 Strain at the middle of pavement layers for 5 different SPS-1 sections

## 4.6 MEASURED RUT DATA FROM IN-SERVICE (SPS-1) PAVEMENTS

The Long Term Pavement Performance (LTPP) database includes time series rutting data for all SPS-1 sections. Figure 4.10 shows the progression of rutting with time for all SPS-1 sections. As shown in the figure some of these sections showed premature rutting due to material- or construction-related problems. These sections were excluded from the analysis since the VESYS model cannot predict premature rutting. More detailed analysis regarding premature rutting due to material- or construction-related problems and structural rutting can be found in NCHRP 20-50 (10/16) report (Chatti et al., 2005).

### 4.6.1 Filtering the Measured Rut Data

Due to the inconsistency of field measurements with time, there was some variability of the measured rut depth. Therefore, in order to have a consistent time series trend, the rut depths which were believed to be caused by the measurement variability/error were removed from the original data, especially where no maintenance action was carried out. Making the time series trend smoother helped in achieving a better optimization (minimizing the RMS between measured and predicted) as explained in section 4.7. Figure 4.11 (a) shows an example of a pavement section (1-0105) where only two points at year 8 and 10 have shown a lower rut depth compared to the existing time series trend. However, no maintenance was performed at that time; therefore, these two points were considered as faulty measurements and were deleted for this section. Figures 4.11 (b) and (c) show the cleaned rut data with time and load with the time series trend. A similar procedure to clean the time series rut depth data was adopted for all the pavement sections in the SPS-1 experiment. The VESYS rutting model was used to determine the PDPs for each section by minimizing the error between the actual field data and the predictions. This is explained in detail in the following sections.

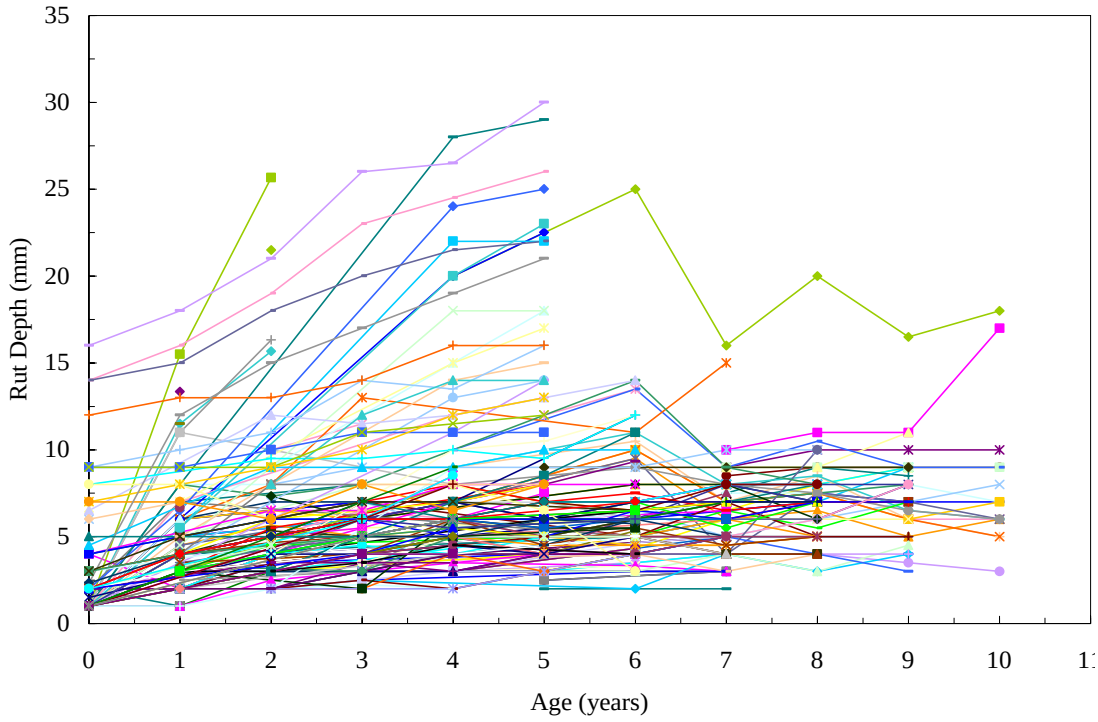


Figure 4.10 Rutting with time for SPS-1 pavements - All sections

## 4.7 BACKCALCULATION OF PERMANENT DEFORMATION PARAMETERS

The backcalculation was performed based on three layers, HMA, base, and subgrade. Each layer has two PDPs (α and μ); therefore a total of six parameters need to be backcalculated for each SPS-1 section. The parameter α represents the rate of decrease in permanent deformation as the number of load applications increase (hardening/densification effect). The parameter μ represents the constant of proportionality between plastic and elastic strain due to the repetition of each load. As shown in equation 4.2, the number of load repetitions (n) is raised to the power -α, therefore α is site-specific and has to be backcalculated by changing the number of load repetitions (i.e. using time series rutting data for each section). Rutting can be predicted by using seed values for α and μ, such as those provided in Chapter 2 of Volume I (Table 2-4).

These six PDPs were backcalculated for each pavement section using Microsoft Excel "Solver," by minimizing the Root Mean Square (RMS) difference between the measured and the predicted rutting. The following equation shows the optimization procedure:

$$\text{minimize } F = \sum_{i=1}^{s} (\rho_i - RD_i)^2 \tag{4.9}$$

where:

$F$ = function to be minimized by changing α and μ,

$\rho_i$ = predicted rut depth from equation 4.4,

$RD_i$ = measured rut depth in the field,

$s$ = total number of rutting measurements in the field over time.

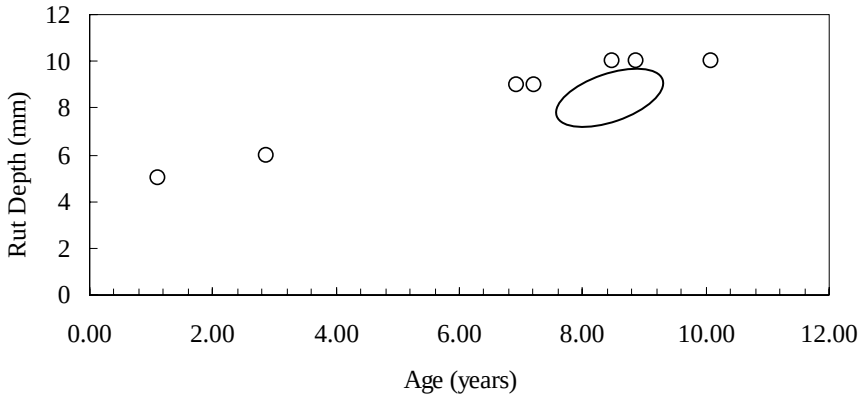


(a) original rut data versus time

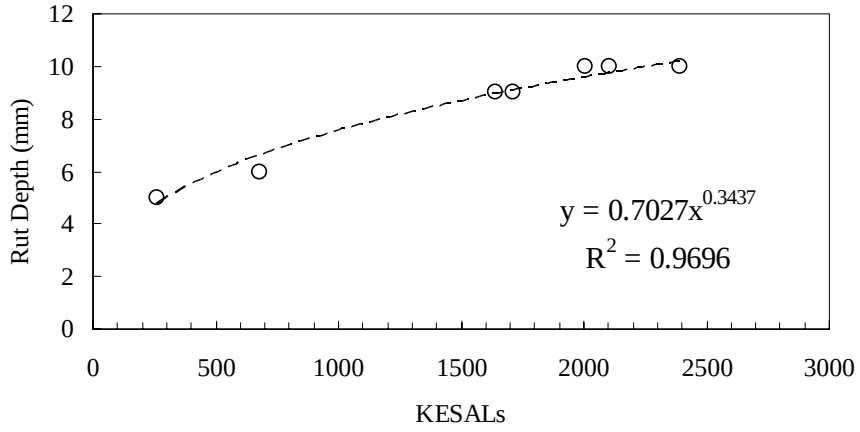


(a) cleaned rut data versus load

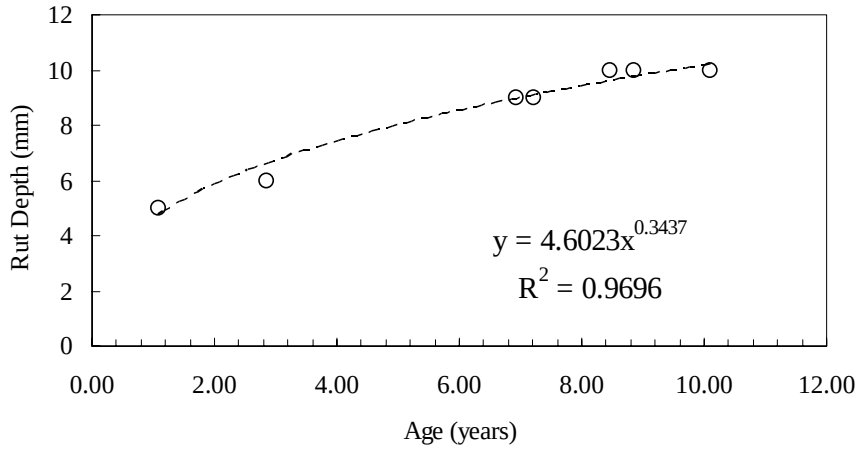


(b) cleaned rut data versus time

Figure 4.11 Measured time series rutting data for section 1-0105

### 4.7.1 Backcalculation Parameters Constraints

Investigating the VESYS rutting model (Equation 4.4) showed that $\alpha$ represents the rate (progression) of permanent deformation and operates within the exponent of the number of load applications as $(1-\alpha)$. Increasing the number of load applications will increase the rutting rate, meaning the exponent must be a positive value. So $\alpha$ is constrained to a range of values between 0 and 1. Lower values of $\alpha$ indicate higher rutting rates, and vice versa. The parameter $\mu$ represents the constant of proportionality between plastic and elastic strains in Equation 4.4. Since rut depth is defined as a positive value, the value of $\mu$ has to be positive. Low values of $\mu$ indicate low initial rutting while higher $\mu$ values (>1) indicate premature rutting. These constraints were taken into consideration in the optimization procedure.

### 4.7.2 Initial Backcalculation Results

Table 4.3 shows the backcalculation of PDPs using different seed values. In the first ten solutions, the same seed values were used for all six parameters, while the remaining solutions have different seed values (according to results from previous research, see Table 2-4 in Chapter 2 of Volume I) for each parameter. It can be seen that a good agreement (small RMS) between measured and predicted rutting can be achieved; however the solution is not unique. In other words, the backcalculated parameters are dependent on the seed values. This is due to the various possible distributions of rutting throughout the multiple pavement layers which still match the total surface rutting, and yet did not match the actual rutting percentage for each individual layer. The RMS values, after the third solution, were very small (less than 1%) and close to each other which indicate good agreement between the measured and predicted rut depth. However, each solution gives completely different rut percentage for each pavement layer, yet the total rutting for all layers matches well with the measured surface rutting. The question now is which solution is closest to the actual pavement behavior?

The most logical way to solve this problem involves knowing the rut percentage within each pavement layer, such that only two parameters can be calculated at one time. There are several ways to determine the percent rutting for each pavement layer:

- Assume the percent rutting within each pavement layer based on other studies. However these percentages are section-specific and depend on the pavement material properties, load, and climatic conditions. Therefore, it is not suitable to generalize this assumption for different pavement sections,
- Cut trenches and measure the rutting contribution from each layer. However, the inconsistency of the pavement layer thicknesses along with the noise caused by the erratic sub-layer boundary make the measurement of layer contribution difficult to determine (Chen *et al.*, 2003).
- Install Linear Variable Differential Transformer (LVDT) instruments (e.g., a device such as the Multi-Depth Deflectometer, MDD). However, these instruments are very expensive and not suitable for long-term investigation due to durability issues (they may be suitable for accelerated pavement tests) (Zhou and Scullion, 2002 and Huang, 1993).
- Measure the transverse surface profile of the pavement. Using transverse surface profiles, the contribution of each pavement layer can be identified as a percentage of the total rutting. The required data are available for each section, require less complicated and non-destructive procedures to collect, and can be easily monitored

Table 4.3 Backcalculation of PDPs using different seed values for section 1-0105

| Solution # | Seed parameter | $\mu_{HMA}$ | $\mu_{Base}$ | $\mu_{SG}$ | $\alpha_{HMA}$ | $\alpha_{Base}$ | $\alpha_{SG}$ | RMS% | HMA rut % | Base rut % | SG rut % |
|---|---|---|---|---|---|---|---|---|---|---|---|
| 1 | 0.01 | 0.010 | 0.011 | 0.010 | 0.346 | 0.363 | 0.999 | 7.860 | 27% | 73% | 0% |
| 2 | 0.1 | 0.014 | 0.015 | 0.011 | 0.297 | 0.469 | 0.646 | 7.660 | 68% | 26% | 6% |
| 3 | 0.2 | 0.010 | 0.113 | 0.081 | 0.681 | 0.544 | 0.693 | 1.055 | 0% | 74% | 25% |
| 4 | 0.3 | 0.303 | 0.282 | 0.295 | 0.597 | 0.632 | 0.999 | 0.713 | 35% | 65% | 0% |
| 5 | 0.4 | 0.368 | 0.356 | 0.412 | 0.670 | 0.633 | 0.999 | 0.661 | 18% | 82% | 0% |
| 6 | 0.5 | 0.406 | 0.391 | 0.427 | 0.630 | 0.657 | 0.999 | 0.668 | 32% | 68% | 0% |
| 7 | 0.6 | 0.515 | 0.532 | 0.523 | 0.584 | 0.758 | 0.999 | 0.642 | 68% | 32% | 0% |
| 8 | 0.7 | 0.559 | 0.320 | 0.010 | 0.723 | 0.622 | 0.842 | 0.656 | 16% | 84% | 1% |
| 9 | 0.8 | 0.024 | 0.010 | 0.448 | 0.346 | 0.999 | 0.982 | 0.499 | 60% | 0% | 40% |
| 10 | 0.9 | 0.010 | 0.486 | 0.010 | 0.904 | 0.657 | 0.553 | 0.658 | 0% | 85% | 15% |
| 11 | Lower Limits of Kenis and Wang* | 0.571 | 0.185 | 0.012 | 0.584 | 0.688 | 0.830 | 0.761 | 76% | 23% | 1% |
| 12 | Middle limits of Kenis and Wang | 0.480 | 0.199 | 0.056 | 0.636 | 0.609 | 0.983 | 0.639 | 35% | 60% | 5% |
| 13 | Upper limits of Kenis and Wang | 0.539 | 0.301 | 0.015 | 0.605 | 0.680 | 0.732 | 0.657 | 56% | 41% | 3% |
| 14 | Lower Limits of Bonaquist** | 0.044 | 1.582 | 0.010 | 0.411 | 0.838 | 0.631 | 0.564 | 48% | 46% | 6% |
| 15 | Middle limits of Bonaquist | 0.218 | 0.146 | 0.154 | 0.583 | 0.769 | 0.667 | 0.671 | 29% | 8% | 63% |
| 16 | Upper limits of Bonaquist | 0.679 | 0.015 | 0.134 | 0.967 | 0.988 | 0.619 | 0.639 | 5% | 1% | 94% |

* Kenis and Wang, 1997
** Bonaquist, 1996

over time while the pavement is in-service. The LTTP database includes transverse surface profile data for all SPS-1 sections as part of the monitoring data. In addition, agencies are increasingly collecting transverse surface profiles instead of measuring only the maximum rut depth.

Given the above considerations, it was decided to use the fourth approach; i.e., measured transverse surface profiles, to solve the problem of non-unique parameter solutions. The extensive LTPP data were used for this purpose.

### 4.7.3 Transverse surface profile analysis criteria

Several researchers have analyzed the transverse surface profile (Simpson, et al., 1995, White, et al., 2002 and Villiers, et al., 2005). The shape of the transverse surface profile is a good indication of where the rutting originated within the pavement structure. Simpson, et al., 1995 developed criteria for analyzing the transverse surface profile such that one can locate the individual failed layer (the most probable contributor to the rutting). Furthermore, White et al., 2002 refined these criteria by applying finite element analysis. Based on the refined criteria, Figures 4.12, 4.13, and 4.14 show examples of transverse surface profiles for failed HMA, base, and subgrade layers, respectively. The criteria used for this research are discussed next.

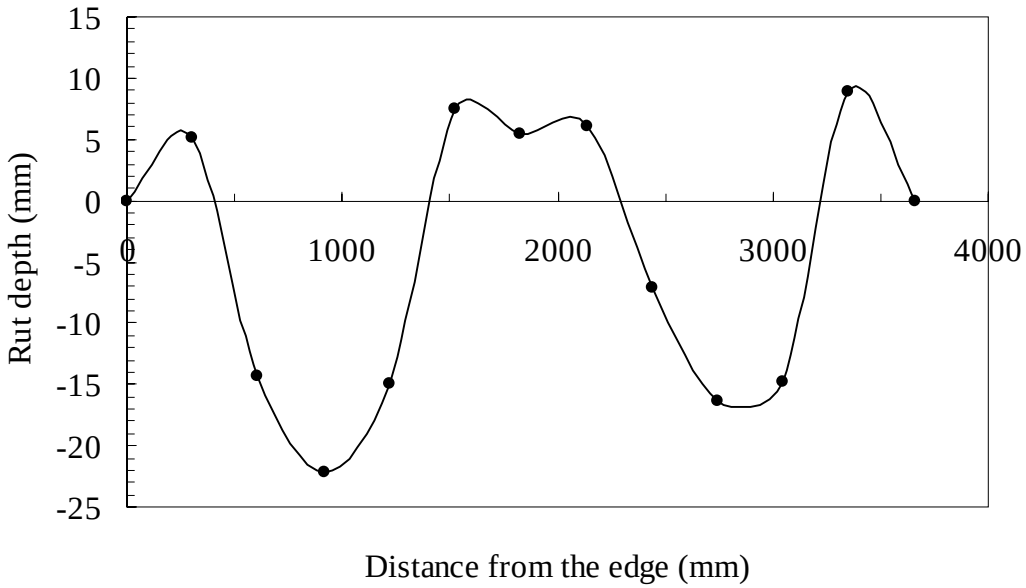


Figure 4.12 Transverse surface profile for HMA layer rutting— Section 31-0113

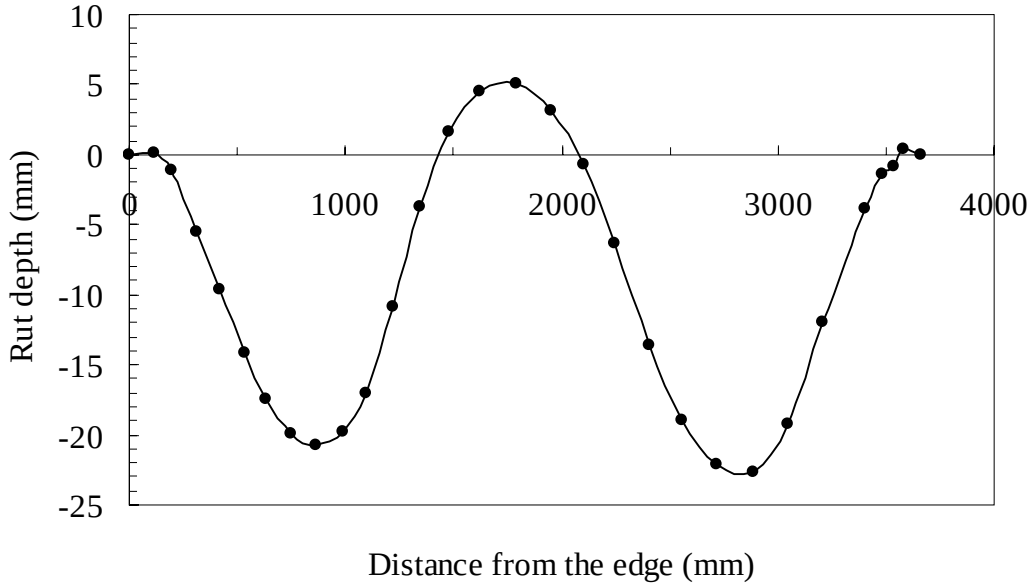


Figure 4.13 Transverse surface profile for base rutting—Section 20-0102

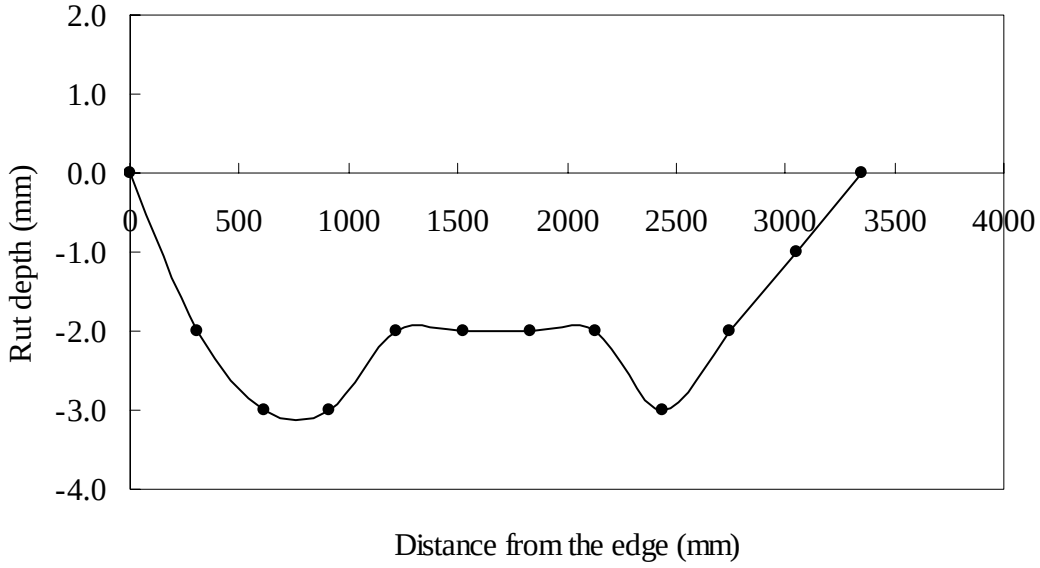


Figure 4.14 Transverse surface profile for subgrade rutting—Section 32-0110

The following equations represent the criteria developed by White et.al. to determine the failed layer identity using transverse surface profile data:

$$A = A_p + A_n \tag{4.10}$$

$$R = \left| \frac{A_p}{A_n} \right| \tag{4.11}$$

$$C_1 = (-858.21)D + 667.58 \tag{4.12}$$

$$C_2 = (-1509)D - 287.78 \tag{4.13}$$

$$C_3 = (-2{,}120.1)D - 407.95 \tag{4.14}$$

Where,

$A$ = total area

$A_p$ = positive area (see Figure 4.15)

$A_n$ = negative area (see Figure 4.15)

$R$ = area ratio

$C_1$ = theoretical average total area for HMA failure, $mm^2$

$C_2$ = theoretical average total area for base/subbase failure, $mm^2$

$C_2$ = theoretical average total area for subgrade failure, $mm^2$

$D$ = maximum rut depth, mm (see Figure 4.16)

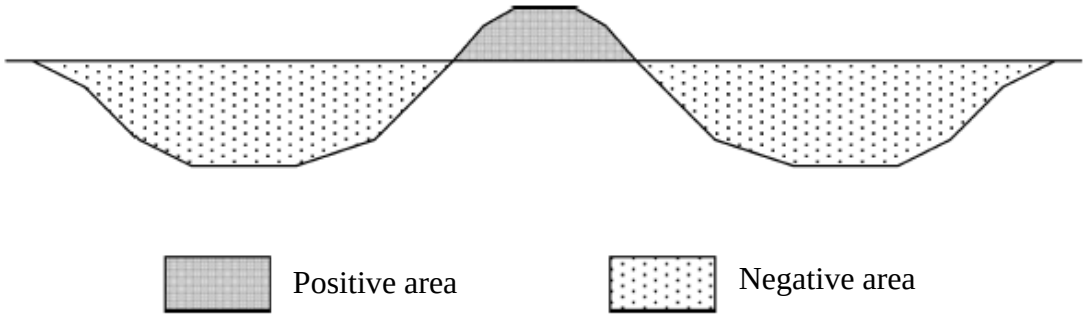


Figure 4.15 Definition of positive and negative area in transverse surface profile (White, et al., 2002)

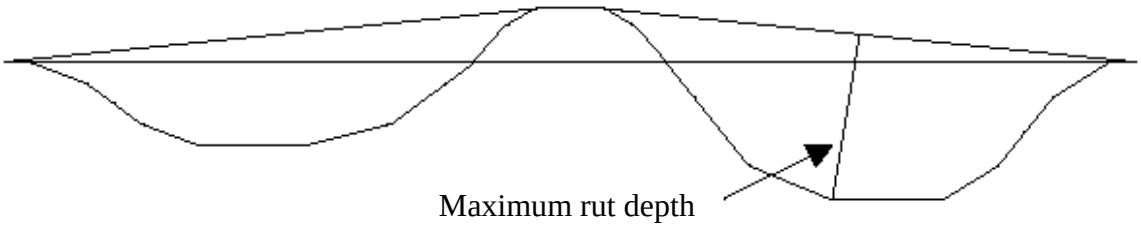


Figure 4.16 Definition of maximum rut depth (White, et al., 2002)

Based on the characteristics of a given surface profile and the criteria described above, the following outcomes can be predicted:

(a) Failure will occur in the HMA layer if:

$$R > 0.05 \quad \text{and} \quad A > (C_1+C_2)/2$$

(b) Failure will occur in the base/subbase layer if:

$$R < 0.05 \quad \text{and} \quad A > (C_2+C_3)/2$$

(c) If none of the above criteria are satisfied, that suggests subgrade layer failure.

### 4.7.4 Unique Solution for Backcalculation of Permanent Deformation Parameters

The problem of parameter uniqueness described previously can be dealt with by combining backcalculation strategies with transverse surface profile analysis. This combination of procedures overcomes the uniqueness problem for the backcalculation of the PDPs by limiting the number of realistic candidates. In applying this technique to section 1-0105 (as shown in Table 4.3), the following steps are required:

- Backcalculate the parameters using different typical seed values.
- For each solution calculate the RMS error and the percent rutting from each layer as shown in Table 4.3. Since the RMS error is minimized when there is a good match with the field measurement, solutions 1, 2, 3, and 4 are excluded because they have higher RMS compared to other solutions.
- Assume that each layer will share some portion of the total rutting, unless premature rutting occurred due to construction-related issues. Based on this assumption, one can exclude solutions 1, 3, 4, 5, 6, 7, 8, 9, 10 and 11 since they have negligible detected rutting in at least one layer.
- Apply the criteria from section 4.7.3 for available transverse surface profiles at different times (with more consideration for the latest available data) and point locations within the pavement section to determine where the rutting originated. Figure 4.17 shows the transverse surface profile for section 1-0105 at one point location from the latest observation. The shape suggests that the rutting originated in both HMA and base layers (see discussion in section 4.7.3).
- To further verify this initial visual assessment, Table 4.4 shows the frequency of layer failure over 9 years along the 11 point locations (making a total of 99 surface profiles available for analysis). Based on this, solutions 12, 13, and 14 are probable candidates; however the most likely solutions are 13 and 14. This is based on their close agreement with the transverse surface profile analysis and relatively low RMS errors. Furthermore, a solution with minimal RMS error comes closer to representing the actual pavement behavior in the field. In this case, solution number 14 satisfies all of these criteria, and can therefore be considered as the most likely solution for the permanent deformation parameters.

This same procedure was applied to the surface profiles for all sections in order to backcalculate the unique permanent deformation parameters; out of 120 three-layer sections, 109 sections (91%) had a most likely solution. In the remaining 11 sections, rutting measurements were too low for layer-identification. Figure 4.18 shows the measured versus predicted (from equation 4.4) rut depth for all sections included in the backcalculation of PDPs.

The ability to obtain a unique solution for each section's PDPs allows for many advantages in rutting prediction. These will be discussed in the following section.

Table 4. 4 Number of point locations with corresponding failed layer-section 1-0105

| Number of surface profiles | Failed layer |
|---|---|
| 56 | HMA |
| 37 | Base |
| 3 | Subgrade |
| 3 | NA* |

* White's criteria failed to recognize them

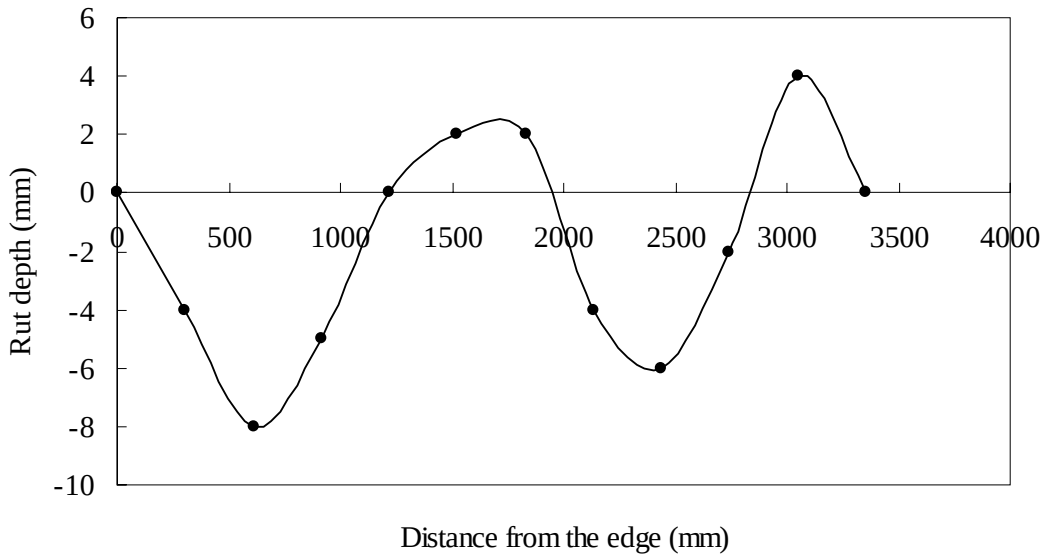


Figure 4.17 Transverse profile section 1-0105

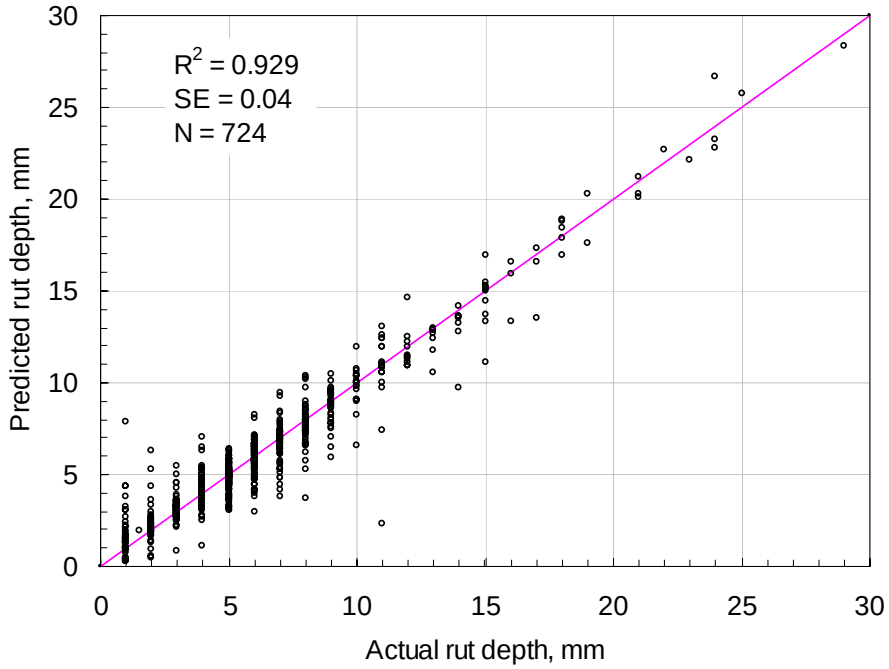


Figure 4.18 Measured versus predicted rut depth for sections used in the backcalculation

### 4.7.5 Advantages of Using Backcalculated Parameters

There are several advantages of using the field-derived PDPs as follows:

- Determine accurate parameters for pavement layers, since they are specific for each section,
- Determine the contribution (percentage) of each layer to the total pavement rutting without any destructive means such as trenching,
- Characterize existing rutting as either premature ($\mu>1$) or structural ($\mu<1$)
- Based on the above information, a correct remedial action can be taken for pavement rehabilitation,
- These procedures also can be used as diagnostic/prediction tools for rutting,
- Compare these parameters as well as the rutting percentage with the previously developed parameters of accelerated loading facilities, ALFs to describe the difference in behavior between the actual field performance and ALFs,
- These parameters can be predicted based on the material parameters, cross sections, environmental conditions (from actual field data) of each section,
- These procedures can be incorporated into a spreadsheet such that from the transverse surface profile data the layer rutting contribution can be calculated quickly.

### 4.7.6 Summary Statistics for Backcalculation of Permanent Deformation Parameters

By applying the above procedures to distinguish the most likely solution, the backcalculated PDPs and the rutting contribution of each pavement layer were determined for all (109) sections. Excluding the sections that have:

- $\mu > 1$ which represents high initial rutting (premature rutting),
- $\alpha = 0.99$ which represents no progression of rutting with time because the majority of the rutting occurred at the initial stage,
- 100% of the rutting in the HMA layer, in order to eliminate any rut failure due to specific material problems within the HMA layer,

The number of sections with normal structural rutting reduced from 109 to 43 sections. Figure 4.19 shows the time series rutting data for both categories, and Table 4.5 shows their respective descriptive statistics. Also, the distribution of $\alpha$ and $\mu$ as well as the rutting percentages for both categories are shown in Figures 4.20, 4.21, and 4.22, respectively. Figures 4.20 and 4.22 show that excluding the abnormal sections, $\alpha$-values and the rutting percentage become normally distributed. On the other hand, $\mu$-values showed either uniform or lognormal distribution even after excluding the abnormal sections.

### 4.7.7 Comparison of Current Results with Those from Previous Work

There were several trials in the past to backcalculate the permanent deformation parameters, some of them from field data and the others from ALF. The first study predicted overall average parameters for GPS-1 sections and was not based on time series rutting data to predict the parameters for each section (Ali et al., 1998). The second study predicted the parameters for only one section using the transverse surface profile (Ali and Tayabji, 2000). Other researchers used ALF (FHWA and Texas DOT) data to backcalculate the permanent deformation parameters. Figure 4.23 shows comparison of the average predicted PDPs with the previous studies. A good agreement exists between this study's SPS-1 predicted parameters with those of the ALF studies especially the $\alpha$ values.

Also, there were several methods to measure the rutting contribution from each pavement layer. The results from the above developed procedure for predicting the rut percentages from each layer was compared with the measured rut depths from previous studies (AASHO and ALFs). Figure 4.23 shows the average rut percentage of the normal behavior group (43 sections) with AASHO and ALF. The results showed a good agreement between the predicted rutting percentages of the SPS-1 sections and the ALF-TxMLS. It is important to note that the developed procedure (a non-destructive method for analyzing rutting by layer) compares quite favorably with the trenching technique for measuring the same rut layer contribution used in the other studies (Zhou and Scullion, 2002).

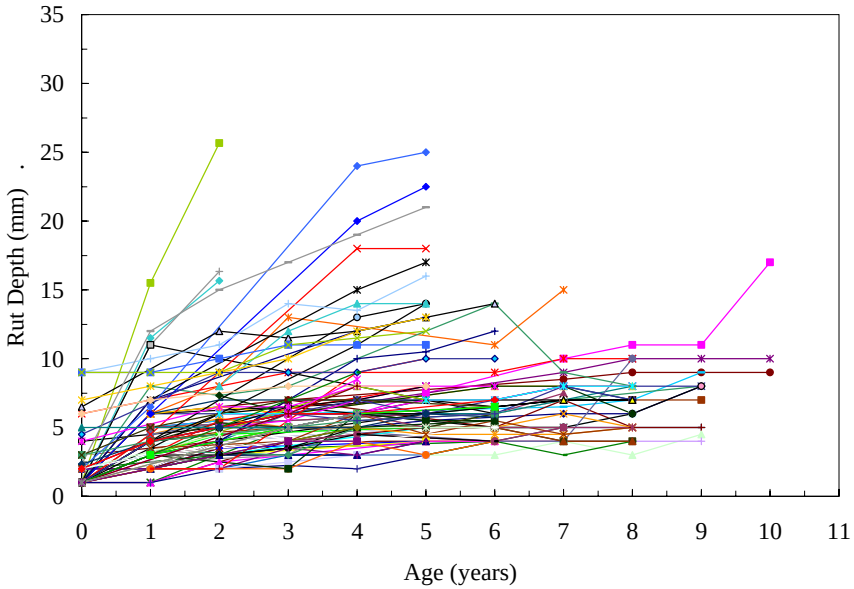


(a) time series rutting data for 109 sections

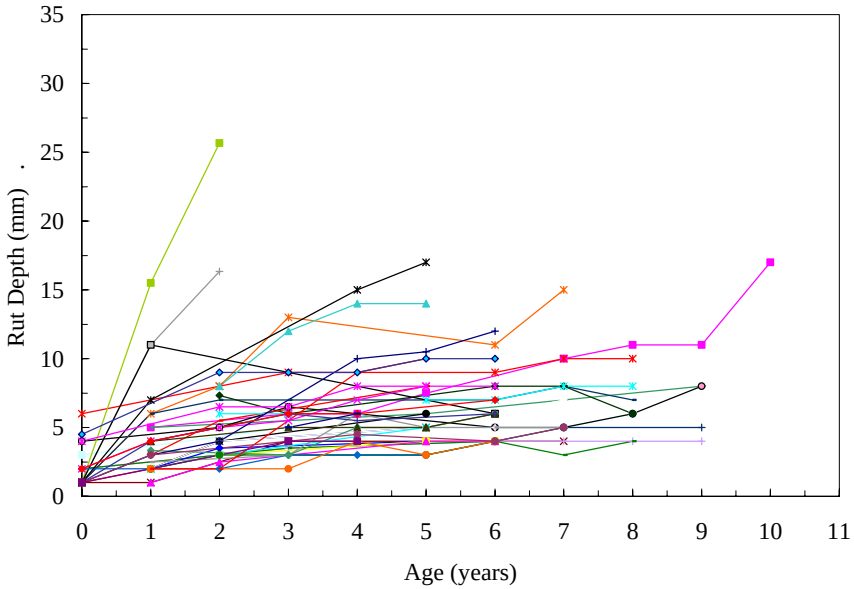


(b) time series rutting data for 43 sections

Figure 4.19 Time series rutting data for three layers system

Table 4.5 Descriptive statistics of PDPs and rutting percentage

| Number of sections | | $\alpha_{HMA}$ | $\alpha_{base}$ | $\alpha_{SG}$ | $\mu_{ac}$ | $\mu_{base}$ | $\mu_{SG}$ | HMA rut % | Base rut % | SG rut % |
|---|---|---|---|---|---|---|---|---|---|---|
| 109 | Minimum | 0.207 | 0.258 | 0.410 | 0.010 | 0.010 | 0.010 | 0.0 | 0.0 | 0.0 |
| | Maximum | 0.999 | 0.999 | 0.999 | 9.962 | 10.123 | 2.085 | 100.0 | 71.7 | 99.2 |
| | Average | 0.611 | 0.771 | 0.843 | 0.947 | 0.700 | 0.302 | 63.3 | 25.6 | 11.2 |
| | St. dev. | 0.211 | 0.187 | 0.163 | 1.355 | 1.473 | 0.440 | 24.4 | 17.1 | 17.1 |
| | COV | 34.57 | 24.22 | 19.36 | 143.06 | 210.38 | 145.71 | 38.59 | 66.71 | 152.97 |
| 43 | Minimum | 0.272 | 0.258 | 0.410 | 0.010 | 0.010 | 0.010 | 7.5 | 02.9 | 0.5 |
| | Maximum | 0.955 | 0.990 | 0.986 | 0.993 | 0.927 | 0.824 | 95.6 | 66.2 | 54.6 |
| | Average | 0.551 | 0.682 | 0.739 | 0.381 | 0.245 | 0.130 | 57.0 | 27.5 | 15.5 |
| | St. dev. | 0.175 | 0.148 | 0.137 | 0.340 | 0.263 | 0.219 | 2.0 | 12.8 | 15.0 |
| | COV | 31.83 | 21.69 | 18.49 | 89.15 | 107.38 | 168.70 | 35.05 | 46.55 | 96.75 |

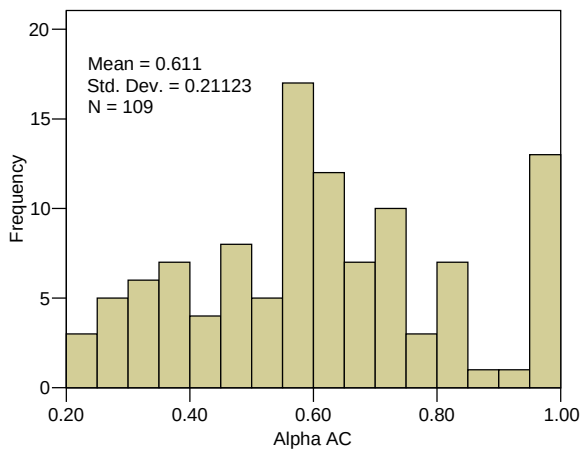


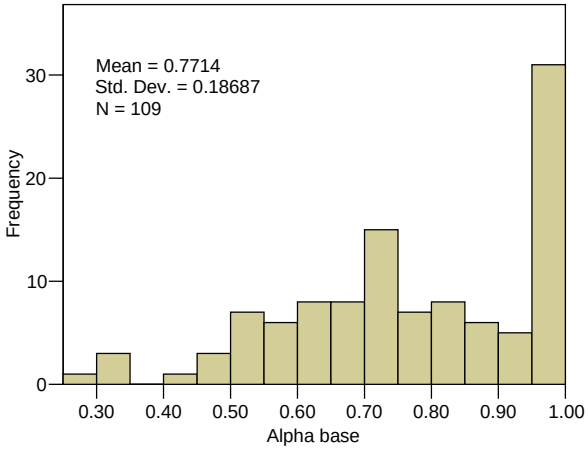


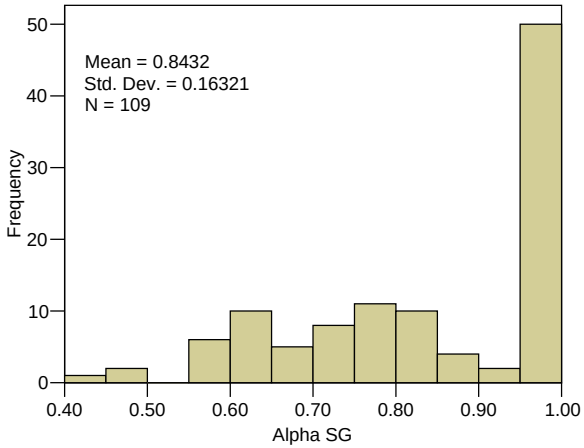


(a) data from all sections

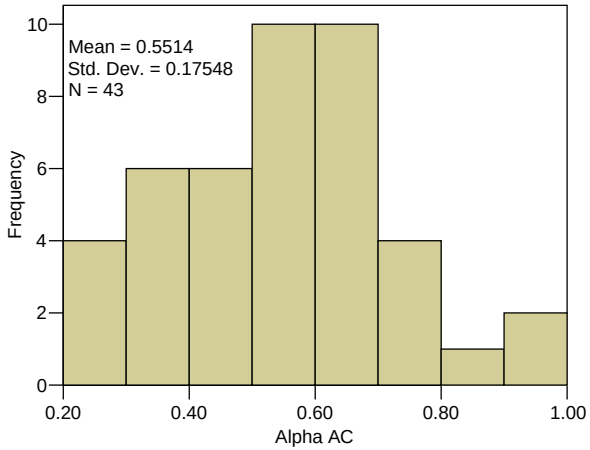


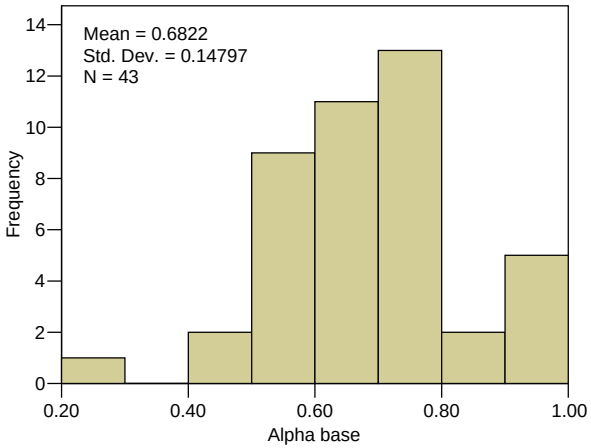


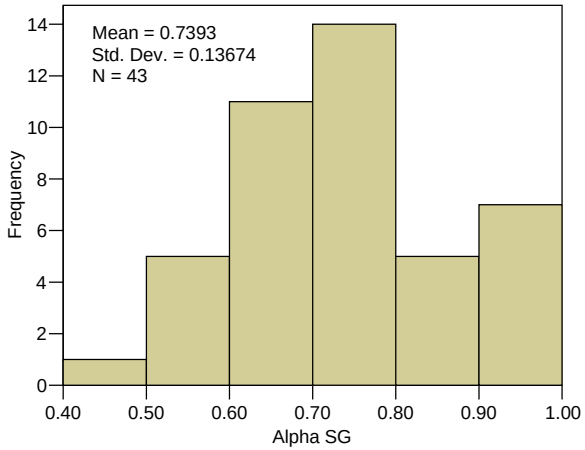


(b) Data from sections with structure rutting

Figure 4.20 α–value histograms

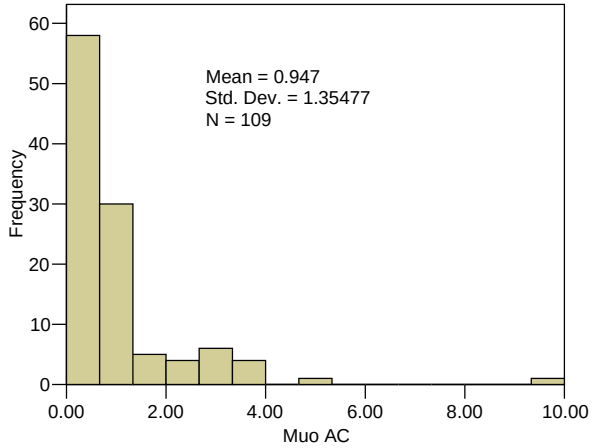


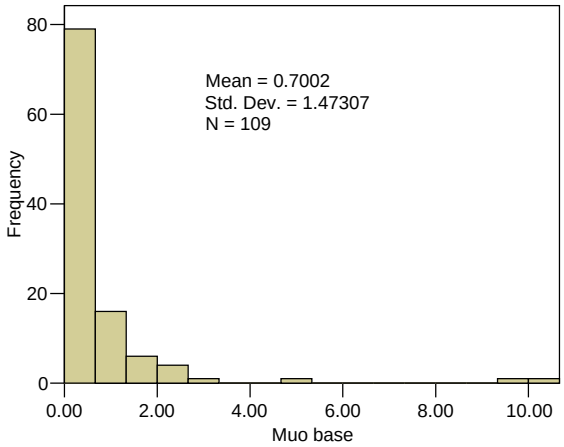


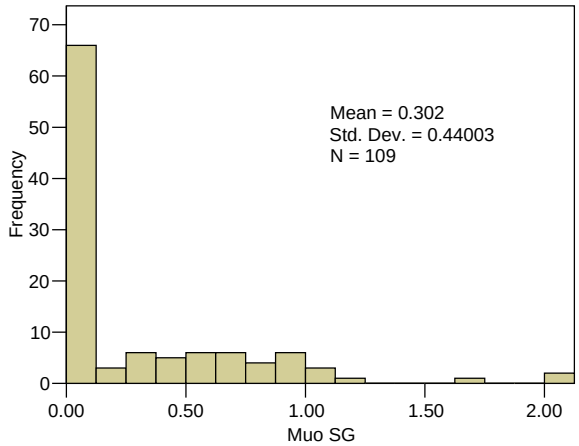


(a) data from all sections

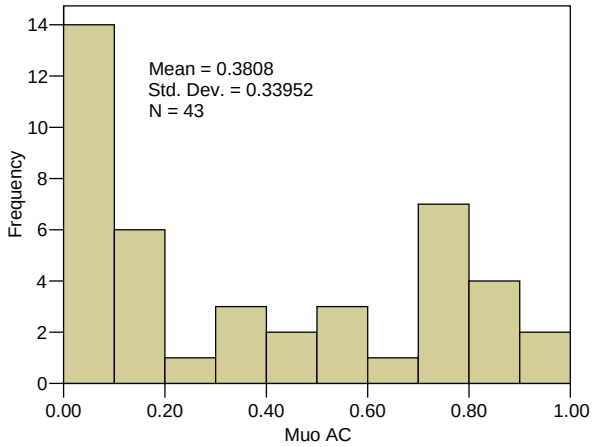


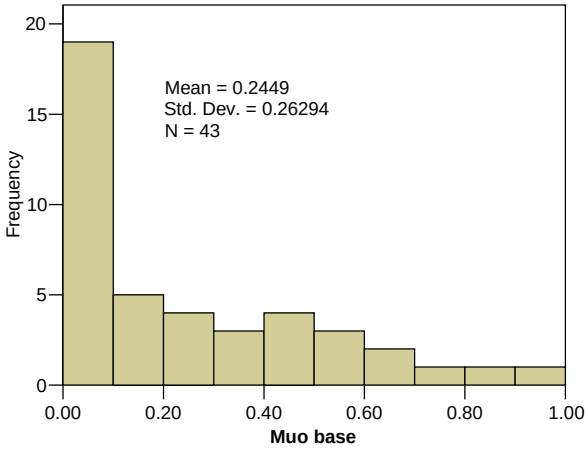


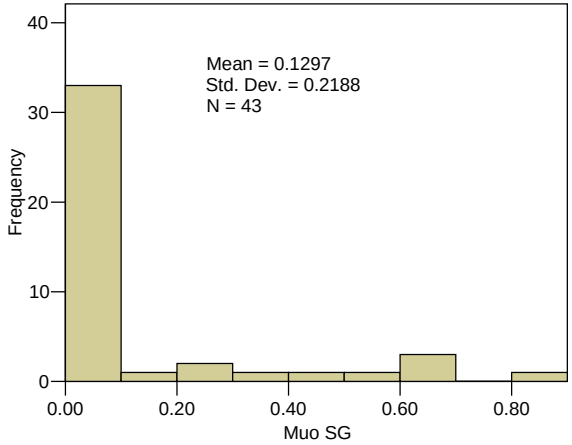


(b) Data from sections with structure rutting

Figure 4.21 μ-value histograms

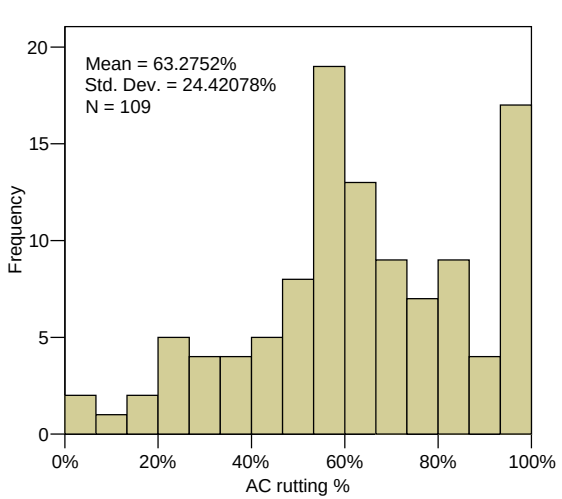


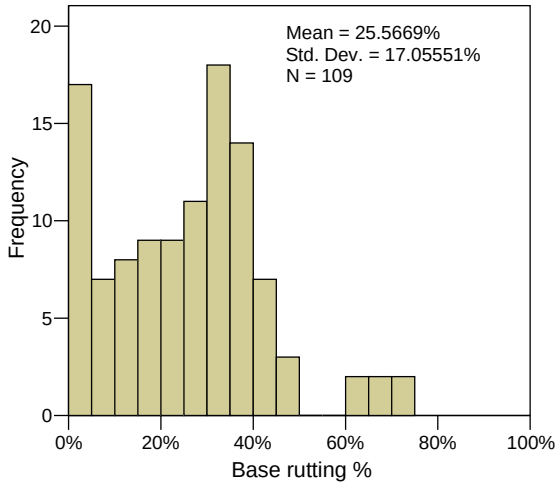


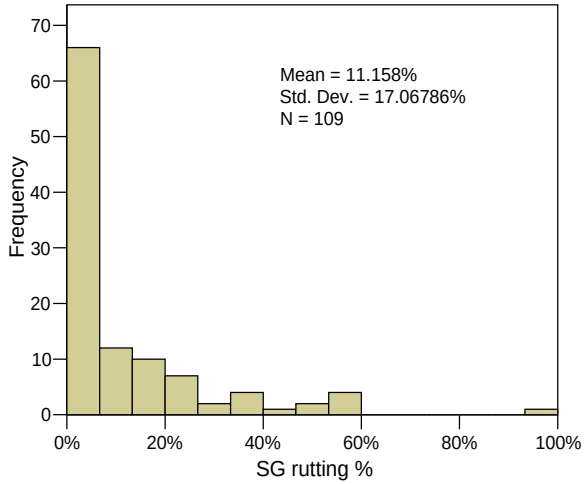


(a) data from all sections

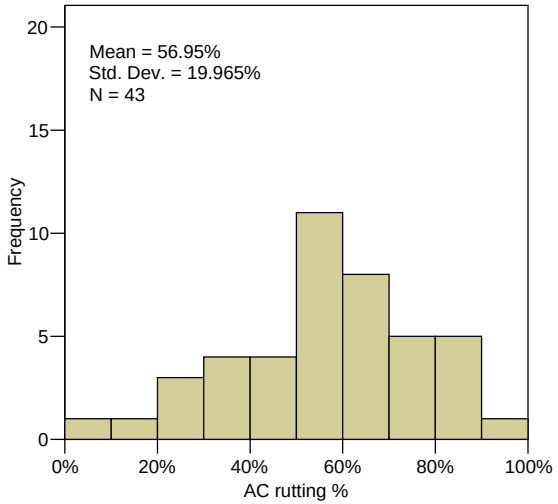


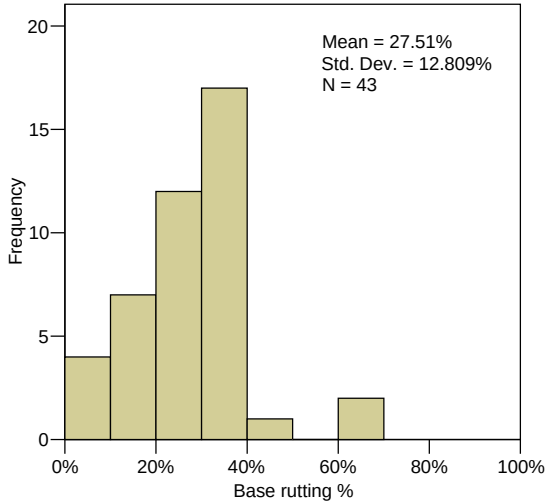


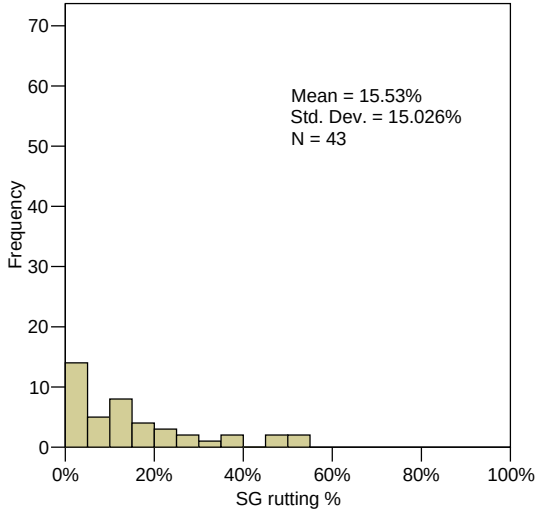


(b) Data from sections with structure rutting

Figure 4.22 Layer rutting contribution histograms

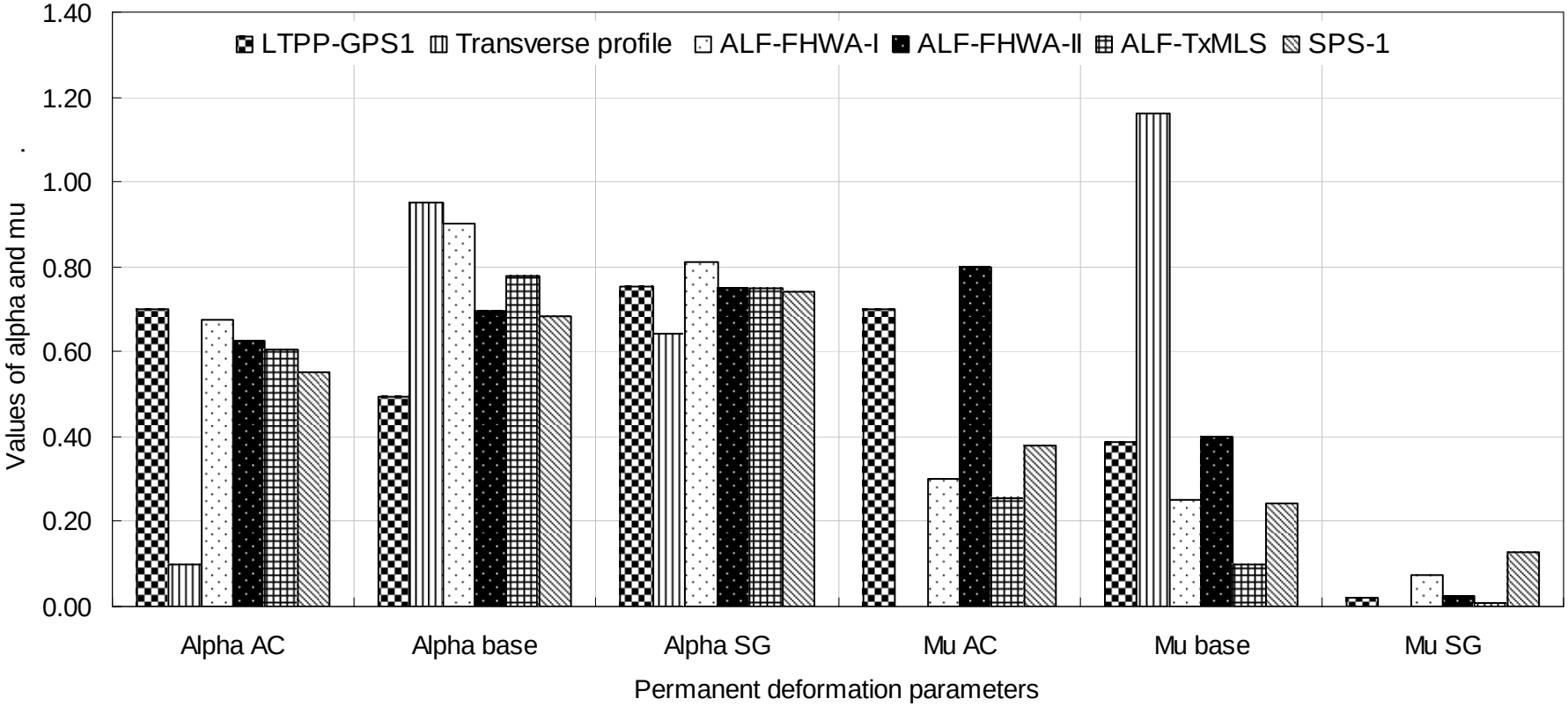


Figure 4.23 Comparison of permanent deformation parameters

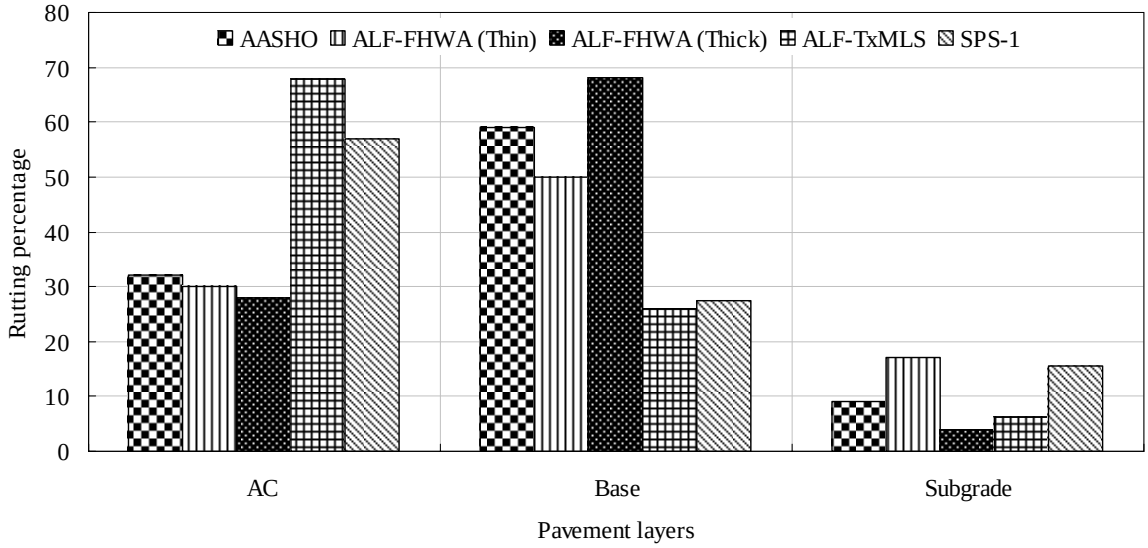


Figure 4.24 Comparison of rutting contribution of pavement layer

## 4.8 PREDICTION OF PERMANENT DEFORMATION PARAMETERS

A majority of the previous studies give a wide range of values for the permanent deformation parameters. Compared with the multiplicative constant, $\mu$, even slight changes in the exponential constant, $\alpha$, produce large differences in predicted rutting over the lifetime of the pavement. Moreover, these parameters are section-specific according to material properties, layer cross section, and climatic condition. In the past, there were some trials to predict these parameters in the laboratory for HMA-layer material; yet predicted values need to be shifted to account for actual field behavior. The next sections explain the regression analysis used to predict the PDPs from in-service pavements (considering material properties, layer cross section, and climatic conditions) in the SPS-1 experiment.

### 4.8.1 Available Material Properties

The LTPP database provides information for the pavement layers of all SPS-1 experiment sections, structural, material as well as climatic variables. Several data elements were extracted for each pavement layer from release 17 of the LTPP database (Datapave.com) as follows:

- HMA layer
    - The gradation of the fine and coarse aggregate,
    - Bulk specific gravity of fine and coarse aggregate,
    - Bulk specific gravity of the asphalt mixture from field cores,
    - Maximum theoretical specific gravity of the mix,
    - HMA binder content,
    - Kinematic and absolute viscosity of the asphalt binder
    - Indirect tensile strength of the mixture,
    - Resilient modulus of the mixture.

- Base layer
    - The gradation of the fine and coarse aggregate.
    - Atterberg limits (liquid and plastic limits)

- Subgrade layer
    - Gradation,
    - Moisture content and dry density,
    - Atterberg limits (liquid and plastic limits)
    - Unconfined strength test.

Using the HMA layer data, the voids in total mix (VTM), voids in mineral aggregate (VMA), and voids filled with asphalt (VFA) were calculated as follows:

$$VTM = \left(1 - \frac{G_{mb}}{G_{mm}}\right) * 100 \tag{4.15}$$

$$VMA = \left[1 - \frac{G_{mb}\left(1 - P_b\right)}{G_{sb}}\right] * 100 \tag{4.16}$$

$$VFA = \left(\frac{VMA - VTM}{VMA}\right) * 100 \tag{4.17}$$

Bulk specific gravity of the combined aggregate, $G_{sb}$, can be calculated from the following equation:

$$G_{sb} = \frac{P_F + P_C}{\frac{P_F}{G_F} + \frac{P_C}{G_C}} \tag{4.18}$$

where

$VTM$ = voids in total mix
$VMA$ = voids in mineral aggregates
$VFA$ = voids filled with asphalt
$G_{mb}$ = bulk specific gravity of the cores
$G_{mm}$ = maximum theoretical specific gravity
$G_{sb}$ = aggregate bulk specific gravity
$P_b$ = percent asphalt content
$P_F$ = weight percentages of fine aggregates (percent passing sieve # 4)
$P_C$ = weight percentages of coarse aggregates (1- percent passing sieve # 4)
$G_F$ = bulk specific gravity of fine aggregate
$G_C$ = bulk specific gravity of coarse aggregate

Several climatic variables were extracted from the SPS-1 data, and Table 4.6 explains those that are considered in the regression analysis.

Table 4.6 Climatic variables considered

| **Climatic variables** | **Description** |
|---|---|
| Mean annual temperature | Average of daily mean air temperatures for year, $^{o}$C |
| Maximum annual temperature | Average of daily maximum air temperatures for year, $^{o}$C |
| Minimum annual temperature | Average of daily minimum air temperatures for year, $^{o}$C |
| Days above 32 $^{o}$C | Number of days where daily maximum air temperature is above 32.2 $^{o}$C for year |
| Days below 0 $^{o}$C | Number of days where daily minimum air temperature is below 0 $^{o}$C for year |
| Freeze index | Calculated freezing index for year |
| Freeze thaw cycle | Number of freeze/thaw cycles for year. |
| Total annual precipitation | Total precipitation for year |
| Wet days | Number of days for which precipitation was greater than 0.25 mm for the month. |
| Intense precipitation days/year | Number of days for which precipitation was greater than 12.7 mm for year |

The pavement layer thicknesses from the backcalculation procedure and the strain at the middle of each pavement layer were considered as independent variables in the regression analysis.

Since the independent variables are many, not all are introduced in the multiple linear regression analysis. Based on the previous studies along with the simple univariate linear regression of each variable, the independent variables that have reasonable relationships with the PDPs were selected and introduced in the model. Additionally, the backward regression analysis selects the most statistically significant variables for each permanent deformation parameter.

### 4.8.2 Regression Analysis

Possible forms of multiple linear regression models are shown in Equations 4.19 through 4.23. Equation 4.19 shows the general form of multiple regression; Equation 4.20 is a mathematical form for multiple linear regression; Equation 4.21 is similar to Equation 4.20 except that it includes additional interactive effects; Equation 4.22 is a multiplicative form of regression which can consider the non-linear effects of the variables; and Equation 4.23 shows the log-linear regression form for multiple variables.

$$Y = f\left(x_1, x_2, x_3, .....\right) + \varepsilon_{\text{model}} \tag{4.19}$$

$$Y = \beta_0 + \sum_{i}^{n} \beta_i x_i + \varepsilon_{\text{model}} \tag{4.20}$$

$$Y = \beta_0 + \sum_{i}^{n} \beta_i x_i + \sum_{i}^{n} \sum_{j}^{n} \beta_i x_i x_j + \varepsilon_{\text{model}} \tag{4.21}$$

$$Y = \beta_0 \prod_i^n x_i^{\beta_i} \varepsilon_{\text{model}} \tag{4.22}$$

$$\log Y = \log \beta_0 + \sum_i^n \beta_i \log x_i + \varepsilon_{\text{model}} \tag{4.23}$$

The multi-linear regression analysis with variable selection offers two major advantages:

- It provides relationships with explicit terms, and
- Allows for accuracy assessment of permanent deformation parameter predictions.

In this study, the multiplicative form of multiple linear regression (Equation 4.22) was utilized to model the nonlinear relationship between the PDPs and the independent variables. Several precautions were taken into consideration to ensure integrity of the model as follows:

- The signs of the multiple linear regression coefficients agree with the signs of the simple linear regression of the individual independent variables,
- The signs of the multiple linear regressions for each independent variable agree with intuitive engineering judgment. For example, higher annual temperature should increase the rate of the rutting in HMA layer, and therefore create more positive values for (1-$\alpha$) and $\mu$.
- There should be no multicollinearity among the final selected independent variables. For example, two independent variables having the same effect (high bivariate correlation) on the dependent variable should not be included in one model at the same time.
- One of several variable selection algorithms, such as stepwise, forward, and backward regression analyses, is used in regression to eliminate the statistically insignificant independent variables.
- The model is selected with the smallest number of independent variables, minimum standard error, and highest $R^2$ value.

In addition, after finalizing the model for each permanent deformation parameter, the regression models were tested to ensure there were no assumption violations. These tests are:

- Normality distribution,
- Constant variance,
- Cook's distance.

### 4.8.3 HMA Layer Regression Analysis

The rutting in the HMA layer is characterized by $\alpha_{HMA}$ and $\mu_{HMA}$. The parameter, $\alpha_{HMA}$, represents the rate of decrease in HMA rutting as the number of load applications increases (since there is a natural limit to the amount of permanent deformation) and as the

material becomes stiffer (the hardening effect due to environmental conditions). The parameter, $\mu_{HMA}$, represents the constant of proportionality between plastic and elastic strain within the HMA layer.

There are several factors affecting HMA rutting. All available material and climatic data used to explain HMA rutting were extracted from the LTPP database, as per the existing literature (see chapter 2 of Volume I). Using simple linear regression, these independent variables were regressed on $\alpha_{HMA}$ and $\mu_{HMA}$. The variables that have reasonable relationships (relatively higher $R^2$) were introduced into the multiple linear regression models. The backward regression analysis was utilized to select the statistically significant variables for the final model. A total of 15 sections were used for predicting $\alpha_{HMA}$ and $\mu_{HMA}$. This is due to the limited amount of available data to calculate VTM, VFA, and VMA, which are important for explaining the rate of the HMA rutting. Equations 4.24 and 4.25 show the final model for $\alpha_{HMA}$ and $\mu_{HMA}$.

$$\alpha_{HMA} = 5105.124 * (Strain)^{0.555} * P_{10}^{-1.013} * (VFA)^{-0.58} * (Max\ AT)^{0.732} \quad (4.24)$$

$$\mu_{HMA} = 6.746 * \alpha_{HMA}^{4.102} * FI^{-0.213} \quad (4.25)$$

where:

*Strain* = strain at the middle of HMA layer due to ESAL
$P_{10}$ = % passing sieve number 10 of the most upper HMA layer
*VFA* = % voids filled with asphalt of the most upper HMA layer
*Max A T* = Average of daily maximum air temperatures for year, $^oC$
*FI* = freezing index

Table 4.7 ANOVA for $\alpha_{HMA}$ and $\mu_{HMA}$

| Variable | | Sum of Squares | df | Mean Square | F | Sig. |
|---|---|---|---|---|---|---|
| α | Regression | 1.675 | 4 | .419 | 33.604 | 0.000 |
| | Residual | 0.125 | 10 | 0.012 | - | - |
| | Total | 1.800 | 14 | - | - | - |
| μ | Regression | 16.675 | 2 | 8.338 | 26.065 | 0.000 |
| | Residual | 3.519 | 11 | 0.320 | - | - |
| | Total | 20.194 | 13 | - | - | - |

It can be seen from the equations that $\alpha_{HMA}$ is a function of $P_{10}$ and VFA (both material-related properties), strain (structure-related), and Max AT (environment-related), while $\mu_{HMA}$ is a function of $\alpha_{HMA}$ (rate of rutting) and FI (environment-related). This implies that, in order to predict $\mu_{HMA}$, an estimate for $\alpha_{HMA}$ must be predicted first.

Attempts were made to predict $\mu_{HMA}$ from variables other than $\alpha_{HMA}$ (mainly those listed below Equations 4.24 and 4.25), but all alternatives to using $\alpha_{HMA}$ were found to have much lower $R^2$ values. Figures 4.26 and 4.27 show the individual relationship between these independent variables and $\alpha_{HMA}$ and $\mu_{HMA}$, respectively. Table 4.7 shows the analysis of variance of the multiple linear regression of $\alpha_{HMA}$ and $\mu_{HMA}$. The results show that the overall models for $\alpha$ and $\mu$ are statistically significant. Table 4.8 shows that 90% and 79 % of the variance for $\alpha_{HMA}$ and $\mu_{HMA}$, respectively, is explained by the independent variable.

Table 4. 8 Model summary for $\alpha_{HMA}$ and $\mu_{HMA}$

| Variable | R | $R^2$ | Adjusted $R^2$ | Std. Error of the Estimate |
|---|---|---|---|---|
| $\alpha$ | 0.965 | 0.931 | 0.903 | 0.112 |
| $\mu$ | 0.909 | 0.826 | 0.794 | 0.565 |

Table 4.9 shows the non-standardized and standardized model coefficients, t-test, statistical significance, and collinearity statistics for both $\alpha_{HMA}$ and $\mu_{HMA}$. It can be seen from the table that all independent variables included in the model for both $\alpha_{HMA}$ and $\mu_{HMA}$ are statistically significant. Also, there was no concern about the multicollinearity (small VIF). Moreover, there is a good agreement between the multiple linear regression coefficient signs and the univariate relationship of the individual variables as shown in Figures 4.26 and 4.27. The standardized regression coefficients show that:

- The higher the initial strain and/or the yearly average of daily maximum air temperatures, the higher the $\alpha_{HMA}$ value, which means a lower rate of rutting progression with time (the exponent is $1-\alpha_{HMA}$). In other words, if the HMA layer is soft (higher initial strain) or the climatic region is hot (higher temperatures); the majority of the rutting will occur at the initial stage and taper off with the remaining life of the pavement.
- The higher the percent passing sieve number 10 and/or the percent of voids filled with asphalt, the lower the $\alpha_{HMA}$ value, which means a higher rate of rutting progression with time. In other words, rutting will be more pronounced if the HMA layer is composed of a finer mix or it contains more voids.
- The higher the $\alpha_{HMA}$, the higher the $\mu_{HMA}$, as can be seen in Figure 4.27. This means that pavements with lower initial rutting (lower $\mu_{HMA}$ value) will show rutting over a longer period of time (lower $\alpha_{HMA}$ value).
- The higher the freezing index for a region, the lower its $\mu_{HMA}$ values. This indicates that unlike hotter regions, pavements constructed in colder regions will show lower initial rutting.

Table 4.9 shows the standardized regression coefficients used to rank the importance of the independent variables to $\alpha_{HMA}$ and $\mu_{HMA}$ values, as shown in Figure 4.25.

Table 4.9 Model coefficients for $\alpha_{HMA}$ and $\mu_{HMA}$

| Variables | | Unstandardized Coefficients | | Standardized Coefficients | t | Sig. | Collinearity Statistics | |
|---|---|---|---|---|---|---|---|---|
| | | Beta | Std. Error | Beta | | | Tolerance | VIF |
| $\alpha$ | Constant | 8.538 | 1.220 | - | 6.997 | 0.000 | - | - |
| | Strain | 0.555 | 0.071 | 0.727 | 7.820 | 0.000 | 0.802 | 1.247 |
| | % passing # 10 | -1.013 | 0.156 | -0.611 | -6.485 | 0.000 | 0.781 | 1.281 |
| | VFA | -0.580 | 0.238 | -0.213 | -2.439 | 0.035 | 0.907 | 1.103 |
| | Max A T | 0.732 | 0.105 | 0.589 | 6.951 | 0.000 | 0.966 | 1.036 |
| $\mu$ | Constant | 1.909 | 0.419 | - | 4.550 | 0.001 | - | - |
| | $\alpha_{HMA}$ | 4.102 | 0.658 | 0.786 | 6.229 | 0.000 | 0.995 | 1.005 |
| | FI | -0.213 | 0.066 | -0.406 | -3.219 | 0.008 | 0.995 | 1.005 |

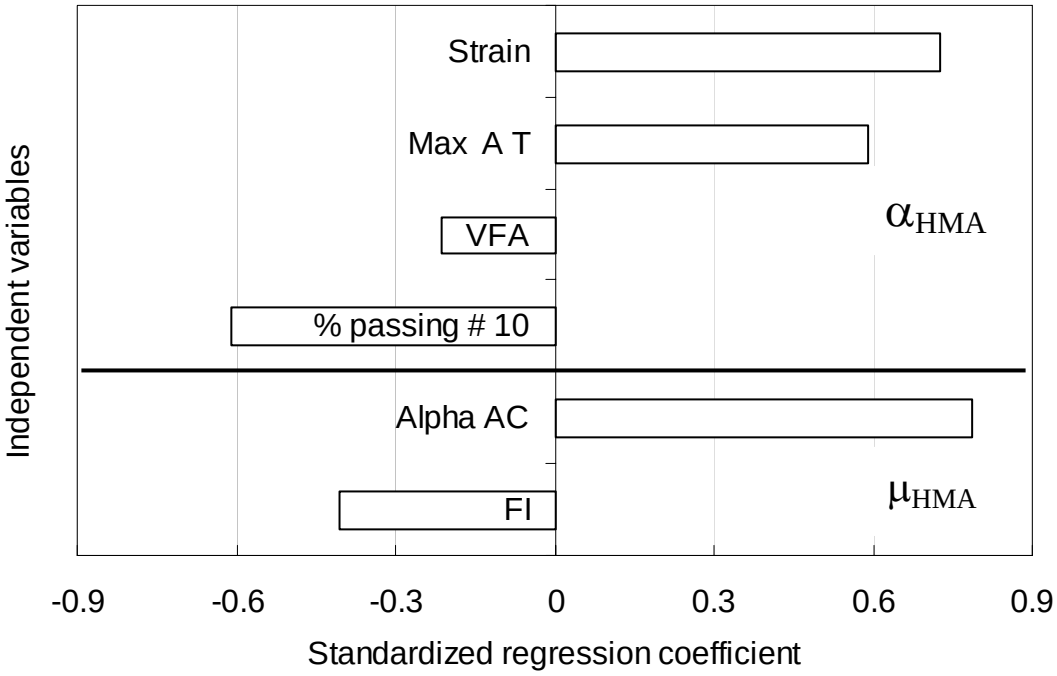


Figure 4.25 Ranking the importance of the independent variables for $\alpha_{HMA}$and $\mu_{HMA}$

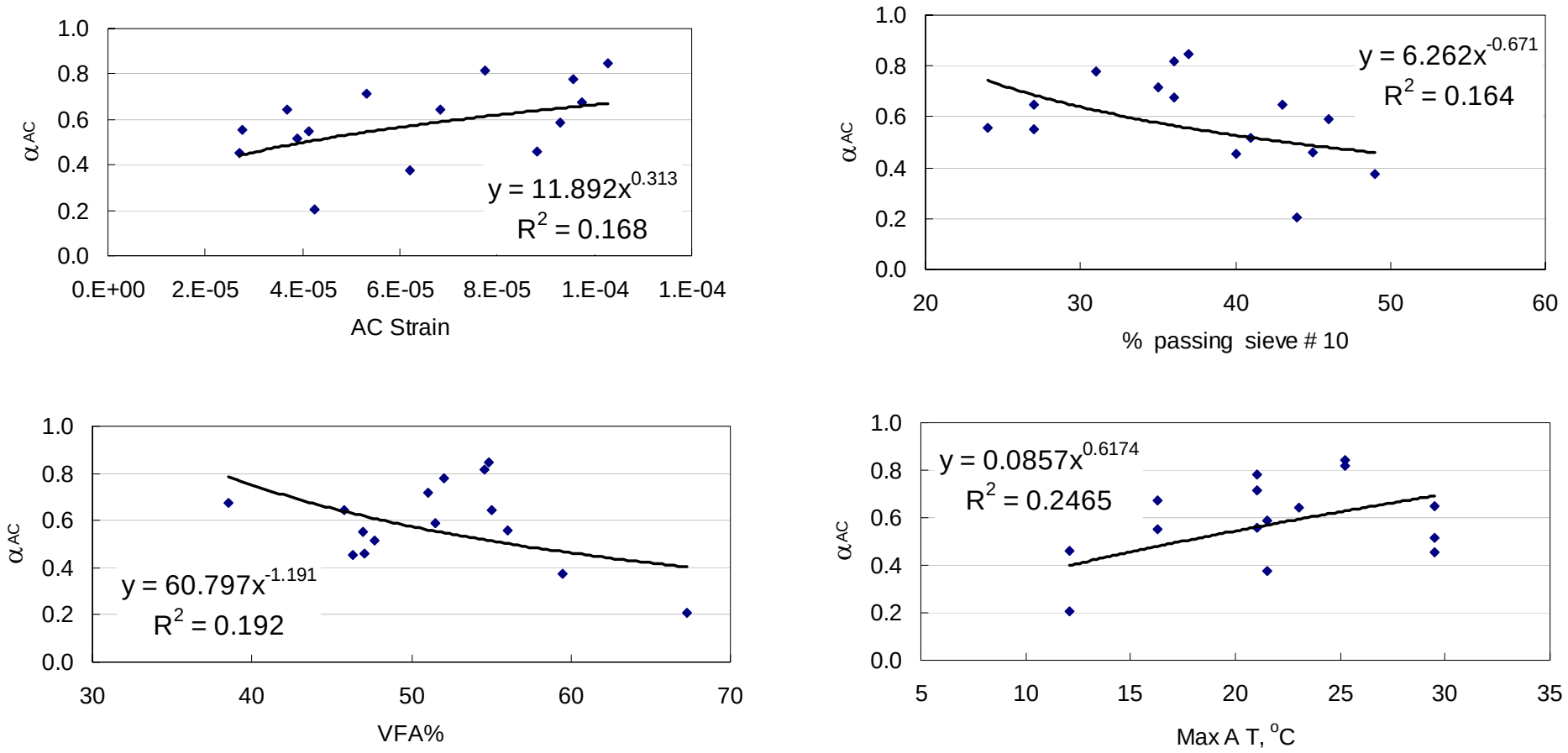


Figure 4.26 Relationship of $\alpha_{HMA}$ versus strain at the middle of the HMA, % passing sieve number 10, VFA% and Max AT

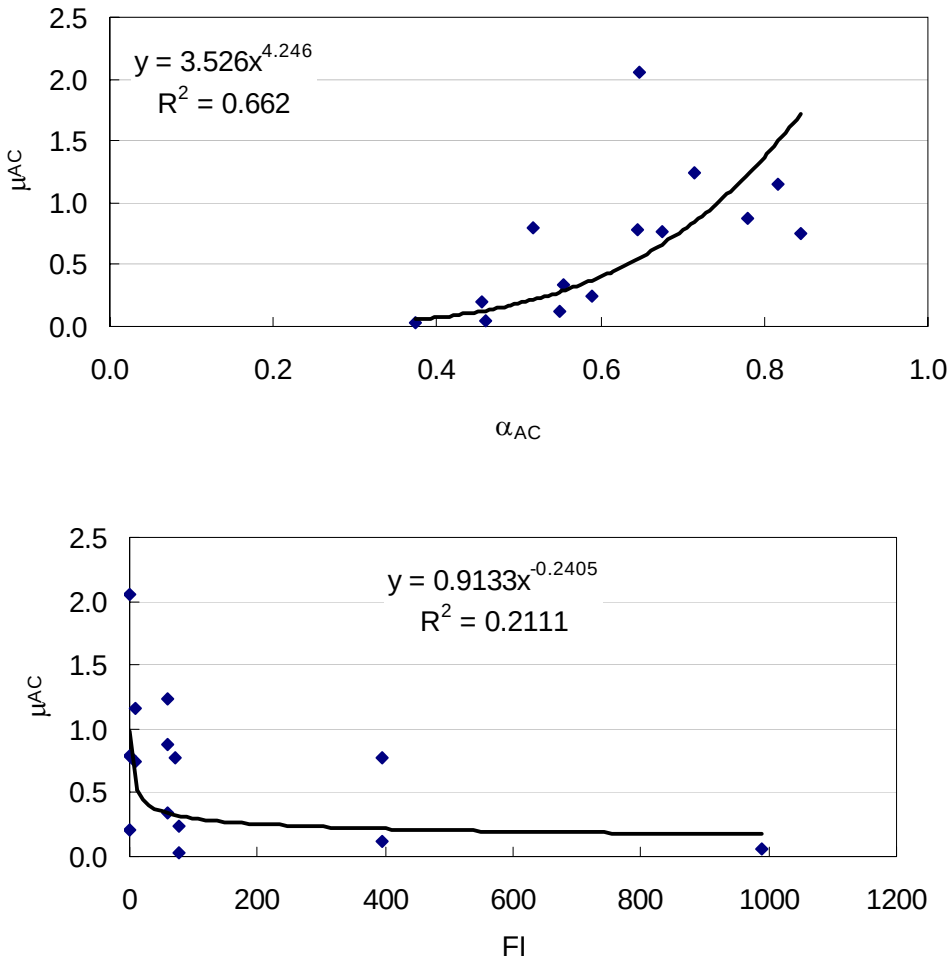


Figure 4.27 Relationship of $\alpha_{HMA}$ versus $\mu_{HMA}$ and FI

Figure 4.28 shows a reasonable prediction of $\alpha_{HMA}$ and $\mu_{HMA}$ in logarithmic and arithmetic scales. A reduction in $R^2$ (small for $\alpha_{HMA}$ and quite large for $\mu_{HMA}$) occurs due to the transformation from logarithmic to arithmetic scale. This dramatic reduction for $\mu_{HMA}$ implies:

- Prediction of $\mu_{HMA}$ is very sensitive to $\alpha_{HMA}$ (standardized $\beta$ =0.786), so small changes in $\alpha_{HMA}$ prediction affect the predicted value of $\mu_{HMA}$ to a great degree.
- There is large scatter in the relationship between $\alpha_{HMA}$ and $\mu_{HMA}$ (Figure 4.26) especially when $\mu_{HMA}$ is greater than 0.7.
- Good prediction of $\mu_{HMA}$ at higher values (>1) is not expected since higher $\mu_{HMA}$ values represent higher initial HMA rutting due to specific problems (material, construction and/or environment).

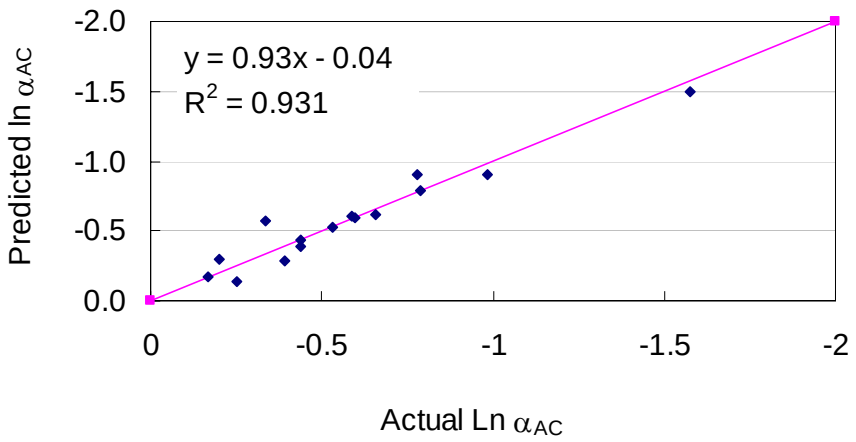


(a) Actual versus predicted α (ln scale)

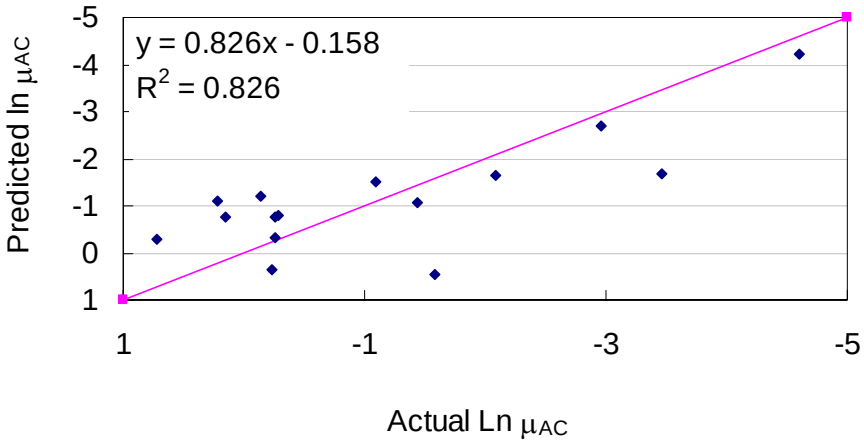


(c) Actual versus predicted μ (ln scale)

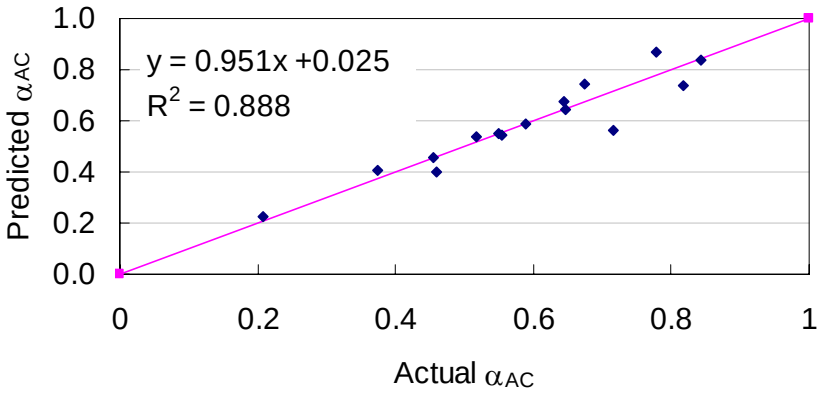


(b) Actual versus predicted α

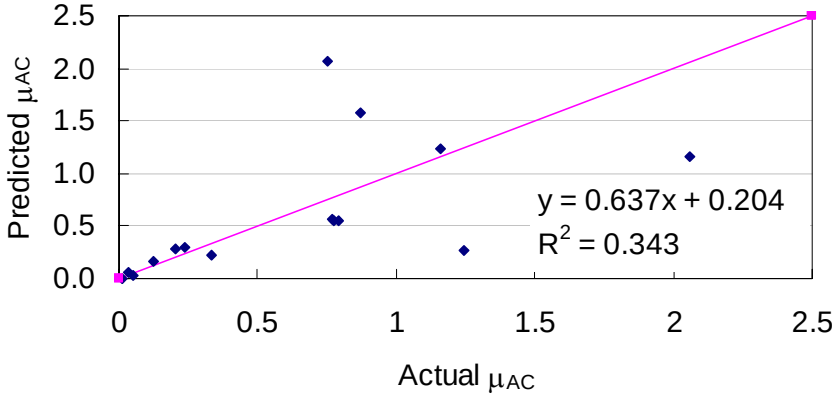


(d) Actual versus predicted μ

Figure 4.28 Actual versus predicted α and μ for HMA layer

Table 4.10 shows the descriptive statistics for $\alpha_{HMA}$, $\mu_{HMA}$ and their independent variables used in the regression analyses. It should be noted that Equations 4.24 and 4.25 should be used within the range for each variable listed in Table 4.10 in order to obtain reasonable predictions.

Table 4.10 Descriptive statistics of $\alpha_{HMA}$, $\mu_{HMA}$, and their independent variables

| | $\alpha_{HMA}$ | $\mu_{HMA}$ | Strain | $P_{10}$ | VFA | Max AT | FI |
|---|---|---|---|---|---|---|---|
| Mean | 0.589 | 0.649 | 6.35E-05 | 37 | 51.6 | 22 | 158 |
| St. Dev. | 0.173 | 0.675 | 2.73E-05 | 8 | 6.8 | 6 | 273 |
| Minimum | 0.207 | 0.010 | 2.69E-05 | 24 | 38.5 | 12 | 1 |
| Maximum | 0.844 | 2.059 | 1.03E-04 | 49 | 67.3 | 29 | 988 |

### 4.8.4 Base Layer Regression Analysis

For base layer, the only data available were the gradation, base thickness used in the backcalculation, and the calculated strain at the middle of the base due to one standard axle. Unlike the HMA layer, in which the materials are highly controlled, the base and subgrade layers of flexible pavements are frequently more dissimilar from one section to another. This becomes evident when examining sieve analyses. Since the content of HMA material is highly controlled, a particular sample can be uniquely identified by an individual sieve measurement, that is, the percent material passing through one particular sieve (see Figure 4.29). This is not the case for the base layer material, since base materials from two different sections might have the same percent passing through one sieve and different gradations for the other sieves, as shown in Figure 4.30. Therefore, a new index termed, Gradation Index (GI) is introduced in this analysis to represent the gradation of the base layer such that using the GI alone or with the percent passing of any given sieve (such as sieve 4, 10, or 200) will be more representative of an individual base layer's material. The GI can be calculated from the following equation:

$$GI = \frac{\Sigma P * \log SS}{\Sigma \log SS} \tag{4.26}$$

where

$p$ = log % passing of the individual sieve, and
$\log SS$ = sieve size in mm.

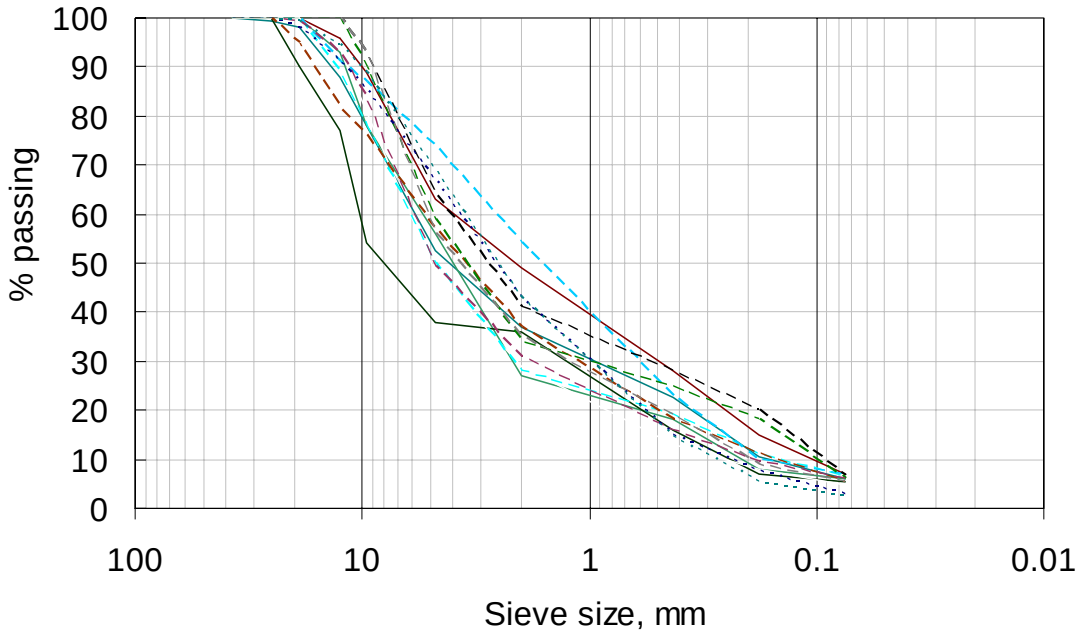


Figure 4.29 Sieve analysis of HMA layer

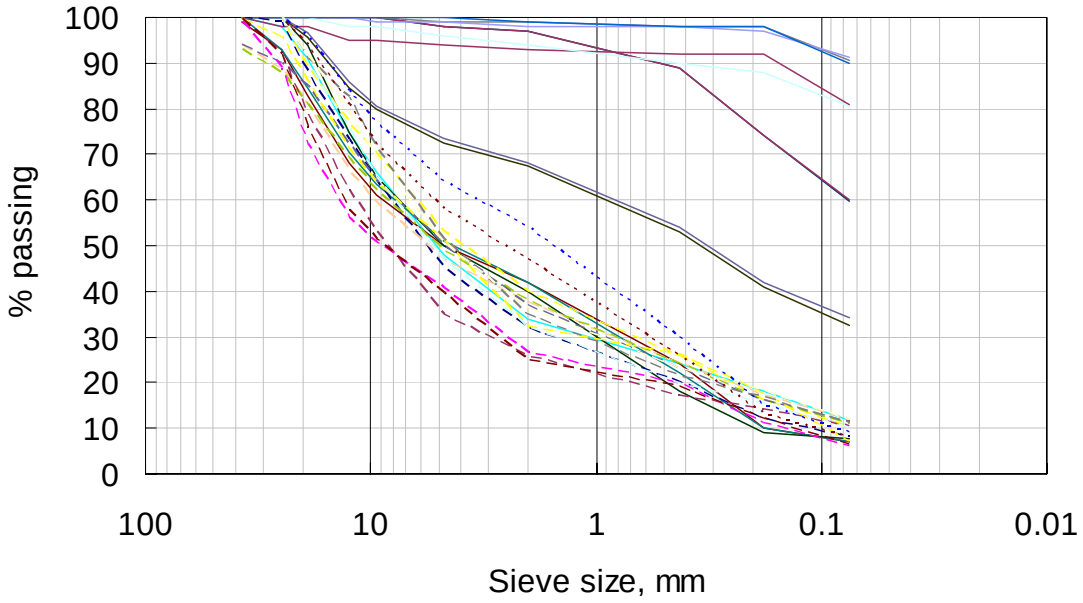


Figure 4.30 Sieve analysis of base layer

For the base regression analysis, only sections that have base rutting of 10 percent or more out of the total surface rutting and available base gradations were considered, these total 27 sections. The final regression equations for predicting the αbase and μbase are shown below:

$$\alpha_{base} = 2.724 * 10^{-5} * \mathrm{mod}ulus^{0.102} * Thickness^{0.066} * P_{200}{}^{-0.098} * GI^{1.982} \quad (4.27)$$

$$\mu_{base} = 7.1977 * 10^{-3} * \alpha^{6.256} * Thickness^{-0.808} * strain^{-0.809} \quad (4.28)$$

where

| | |
|---|---|
| Modulus | = backcalculated base modulus, psi |
| Thickness | = Thickness of base layer used in the backcalculation, in |
| $P_{200}$ | = % passing sieve number 200 |
| GI | = Gradation index |
| Strain | = Strain at the middle of the base layer due to one standard axle |

Table 4.11 shows the analysis of variance of the multiple linear regression for αbase and μbase. The results show that the overall models for αbase and μbase are statistically significant. Table 4.12 shows that 50.6 % and 68.7 % of the variance for αbase and μbase, respectively, is explained by the independent variable.

Table 4.13 shows the non-standardized and standardized model coefficients, t-test, statistical significance, and collinearity statistics for both αbase and μbase. It can be seen from the table that all independent variables included in the model for both αbase and μbase are statistically significant except for the base thickness in the αbase model. Excluding the base thickness from the model causes dramatic reduction of $R^2$, therefore base thickness was kept in the model. Also, there was no concern about multicollinearity (small VIF). Moreover, there is a good agreement between the multiple linear regression coefficient signs and the univariate relationship of the individual variables as shown in Figures 4.31 and 4.32. The standardized regression coefficients show that:

- The higher the initial modulus, the higher the $\alpha_{base}$ value, which means a lower rate of rutting progression with time (the exponent is $1-\alpha_{base}$).
- The thicker the base with higher GI (coarser material), the higher the $\alpha_{base}$, which means a lower rate of base rutting with time.
- The higher the percent passing sieve 200, the lower the $\alpha_{base}$, which leads to a higher rate of rutting with time.
- Similar to the HMA layer, there is a strong relationship between $\alpha_{base}$ and $\mu_{base}$ ($R^2$ = 0.5949); the higher the $\alpha_{base}$ the higher the $\mu_{base}$ as can be seen in Figure 4.32. This means that a pavement with lower initial rutting (lower $\mu_{base}$ value) will show rutting over a longer period of time (lower $\alpha_{base}$ value).
- The thicker the base layer with higher initial strain value, the lower the $\mu_{base}$, which indicates that rutting will keep progression with time.

Table 4.13 shows the standardized regression coefficients used to rank the importance of the independent variables in the αbase and μbase models, as shown in Figure 4.33.

Table 4.11 ANOVA for $\alpha_{base}$ and $\mu_{base}$

| Variables | | Sum of Squares | df | Mean Square | F | Sig. |
|---|---|---|---|---|---|---|
| $\alpha$ | Regression | 0.674 | 4 | 0.169 | 7.653 | 0.001 |
| | Residual | 0.485 | 22 | 0.022 | - | - |
| | Total | 1.159 | 26 | - | - | - |
| $\mu$ | Regression | 59.631 | 3 | 19.877 | 20.000 | 0.000 |
| | Residual | 22.859 | 23 | .994 | - | - |
| | Total | 82.490 | 26 | - | - | - |

Table 4.12 Model summary for $\alpha_{base}$ and $\mu_{base}$

| Variables | R | $R^2$ | Adjusted $R^2$ | Std. Error of the Estimate |
|---|---|---|---|---|
| $\alpha$ | 0.763 | 0.582 | 0.506 | 0.148 |
| $\mu$ | 0.850 | 0.723 | 0.687 | 0.997 |

Table 4.13 Model coefficients for $\alpha_{base}$ and $\mu_{base}$

| Variables | | Unstandardized Coefficients | | Standardized Coefficients | t | Sig. | Collinearity Statistics | |
|---|---|---|---|---|---|---|---|---|
| | | Beta | Std. Error | Beta | | | Tolerance | VIF |
| $\alpha$ | Constant | -10.511 | 3.519 | - | -2.987 | 0.007 | - | - |
| | Modulus | 0.102 | 0.037 | 0.447 | 2.751 | 0.012 | 0.721 | 1.387 |
| | Thickness | 0.066 | 0.051 | 0.205 | 1.303 | 0.206 | 0.771 | 1.297 |
| | P200 | -0.098 | 0.032 | -0.462 | -3.094 | 0.005 | 0.854 | 1.172 |
| | GI | 1.982 | 0.715 | 0.429 | 2.774 | 0.011 | 0.794 | 1.259 |
| | Constant | -4.934 | 2.083 | - | -2.369 | 0.027 | - | - |
| $\mu$ | $\alpha$ | 6.256 | 0.942 | 0.742 | 6.639 | 0.000 | 0.966 | 1.035 |
| | Thickness | -0.808 | 0.355 | -0.298 | -2.280 | 0.032 | 0.707 | 1.415 |
| | Strain | -0.809 | 0.254 | -0.417 | -3.182 | 0.004 | 0.700 | 1.428 |

Figure 4.34 shows the prediction of $\alpha_{HMA}$ and $\mu_{HMA}$ in logarithmic (ln) and arithmetic scales. Similar to $\alpha_{HMA}$ and $\mu_{HMA}$, the figure shows a reasonable prediction of $\alpha$base in the actual scale. A reduction in $R^2$ for $\mu$base occurs due to the transformation from ln to actual scale, similar to $\mu_{HMA}$ (as mentioned previously).

Table 4.14 shows the descriptive statistics of $\alpha$base, $\mu$base and their independent variables used in the regression analysis. It should be noted that Equations 4.27 and 4.28 are used within the range of the data in Table 4.14 to obtain reasonable predictions.

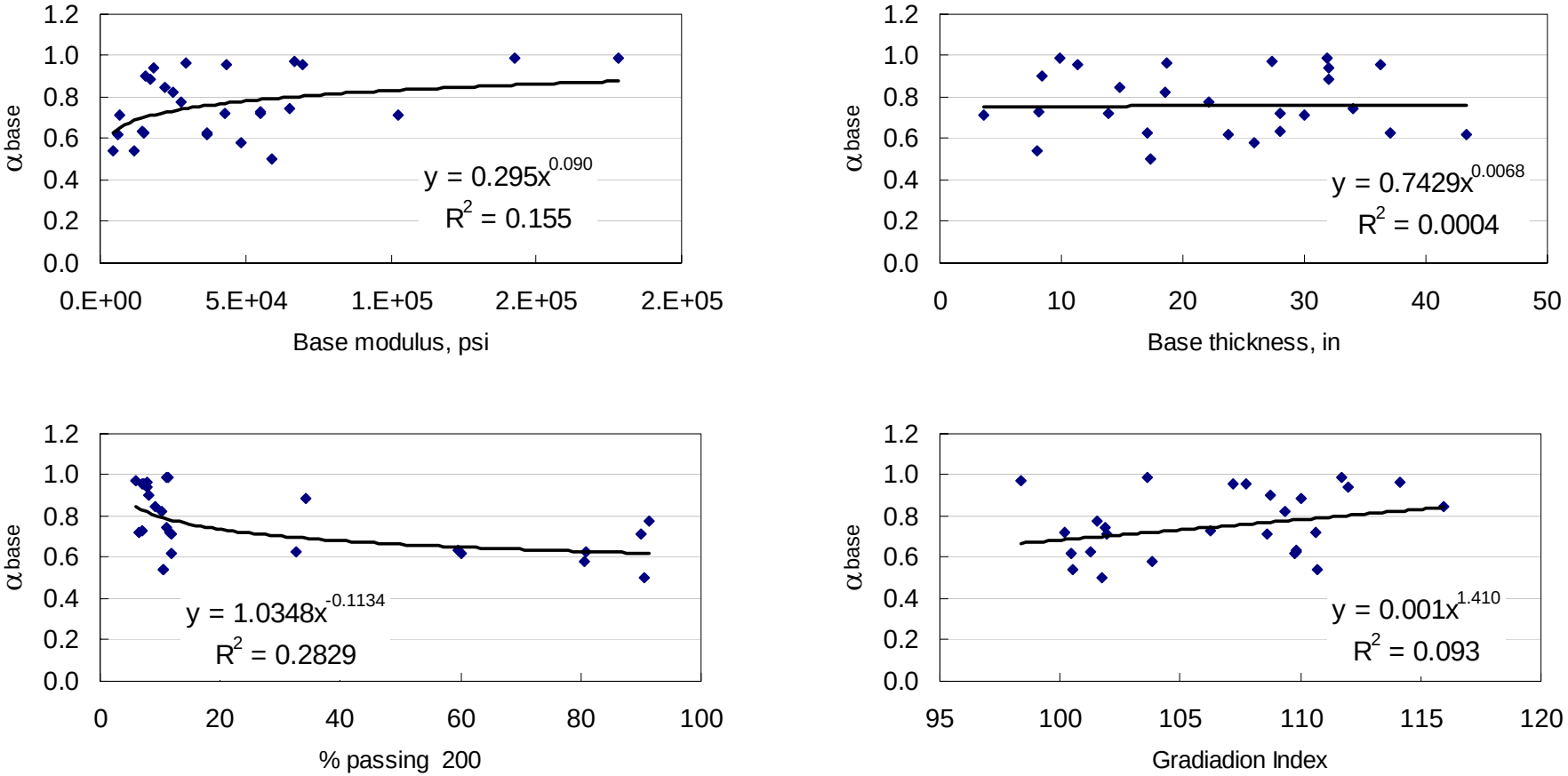


Figure 4.31 Relationship between $\alpha_{base}$ and base modulus, base thickness, % passing sieve number 200, and GI

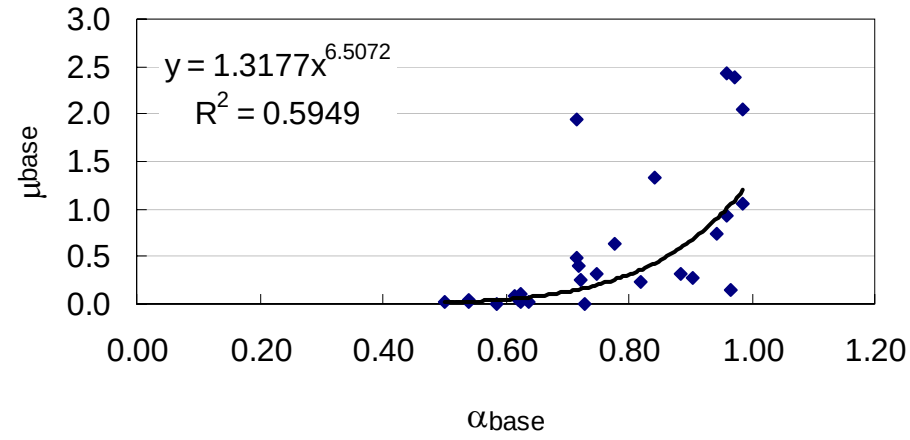


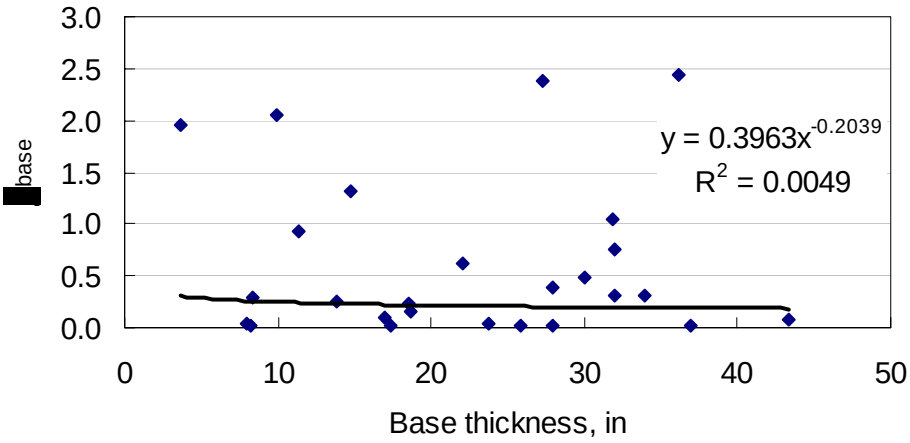


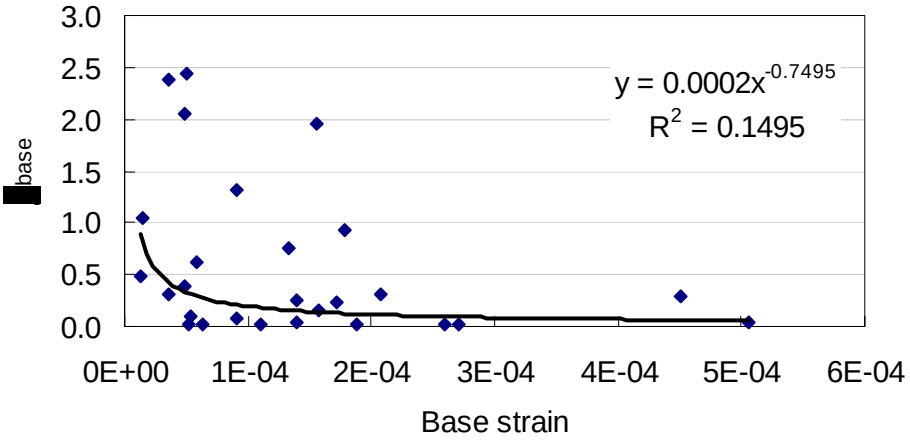


Figure 4.32 Relationship between $\mu_{base}$ and $\alpha_{base}$, base thickness, and base strain

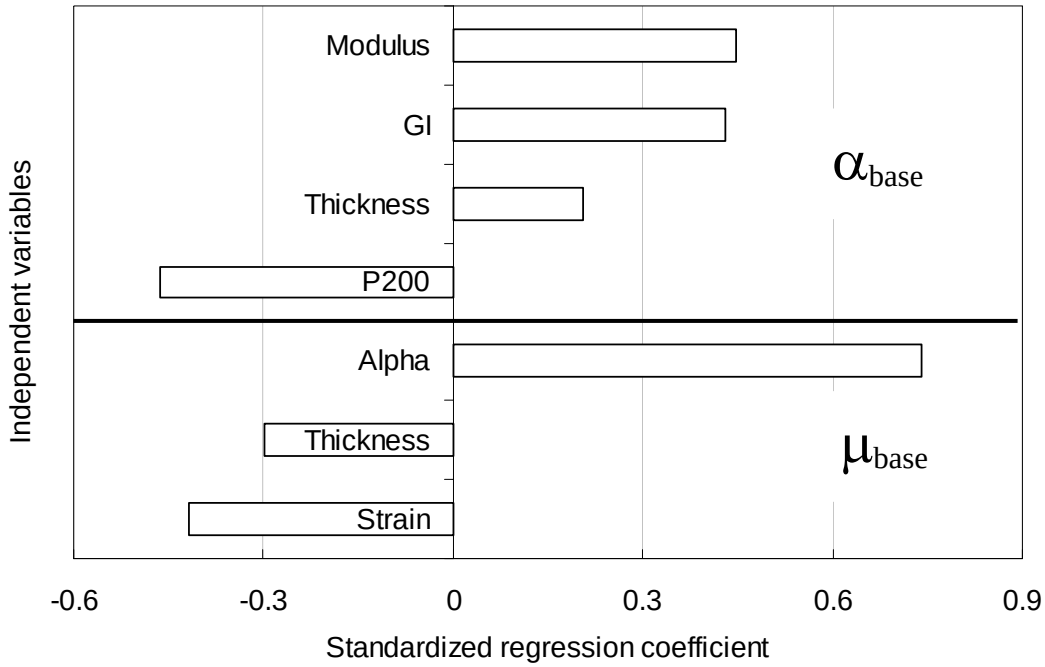


Figure 4.33 Ranking the importance of the independent variables for $\alpha_{base}$ and $\mu_{base}$

Table 4.14 Descriptive statistics of $\alpha_{base}$, $\mu_{base}$, and their independent variables

| Item | $\mu_{base}$ | $\alpha_{base}$ | modulus | thickness | Strain | $P_{200}$ | GI |
|---|---|---|---|---|---|---|---|
| Mean | 0.60 | 0.76 | 45058 | 21.7 | 1.38E-04 | 29.1 | 106.59 |
| ST. DEV. | 0.77 | 0.16 | 41131 | 11.0 | 1.21E-04 | 31.5 | 4.86 |
| Minimum | 0.01 | 0.50 | 4599 | 3.6 | 1.29E-05 | 5.9 | 98.38 |
| Maximum | 2.44 | 0.99 | 178098 | 43.3 | 5.07E-04 | 91.3 | 115.99 |

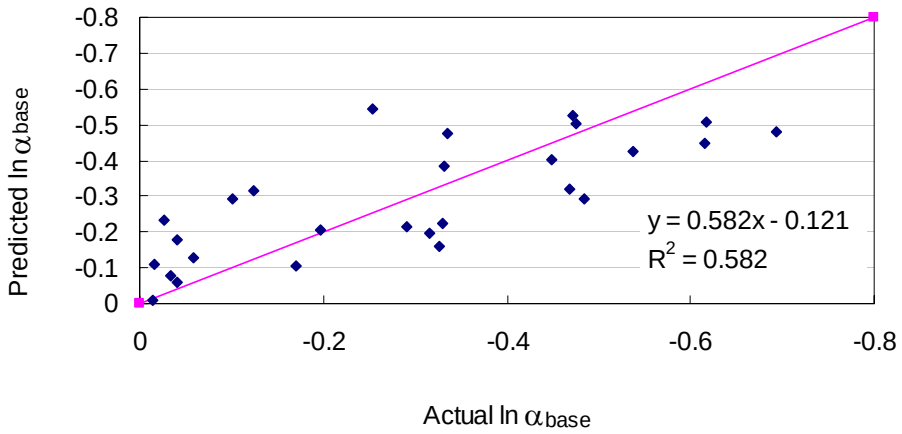


(a) Actual versus predicted α – ln scale

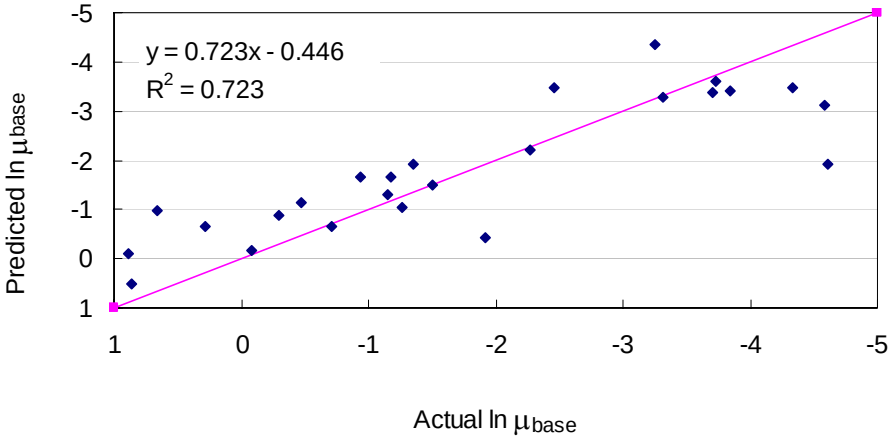


(c) Actual versus predicted μ – ln scale

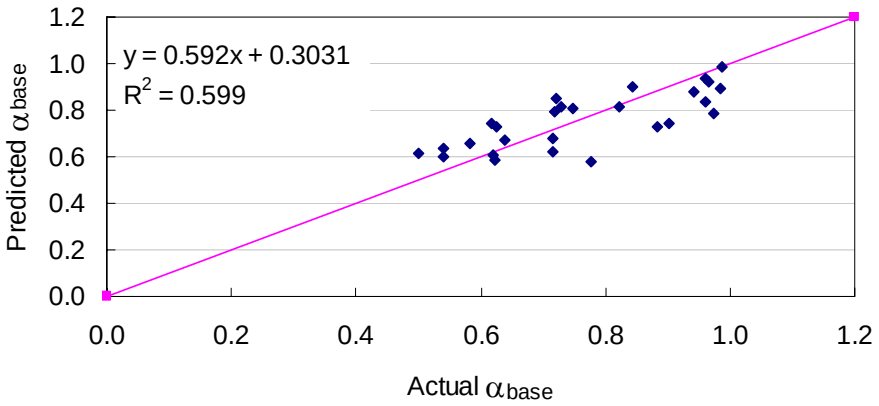


(b) Actual versus predicted α

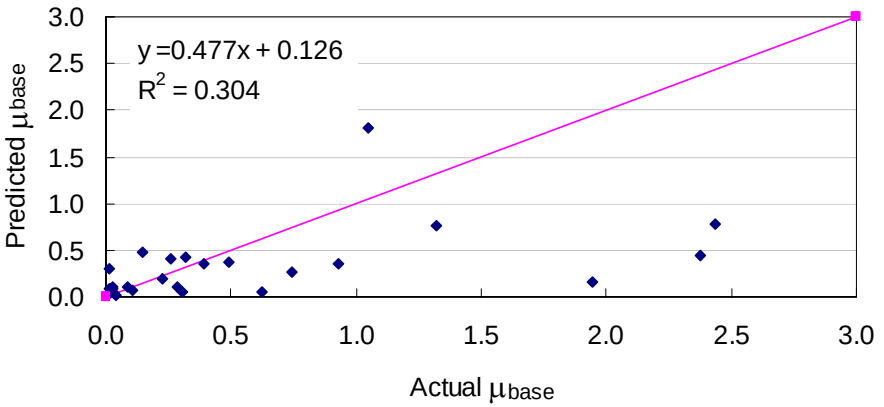


(d) Actual versus predicted μ

Figure 4.34 Actual versus predicted α and μ for base layer

### 4.8.5 Subgrade Regression Analysis

Similar to the base layer and even more pronounced, the percent subgrade material passing through one sieve is not enough to characterize the subgrade materials, as shown in Figure 4.35. Therefore, the need for the GI (Equation 4.26) is at least as great for the subgrade regression analysis as it was for the base layer.

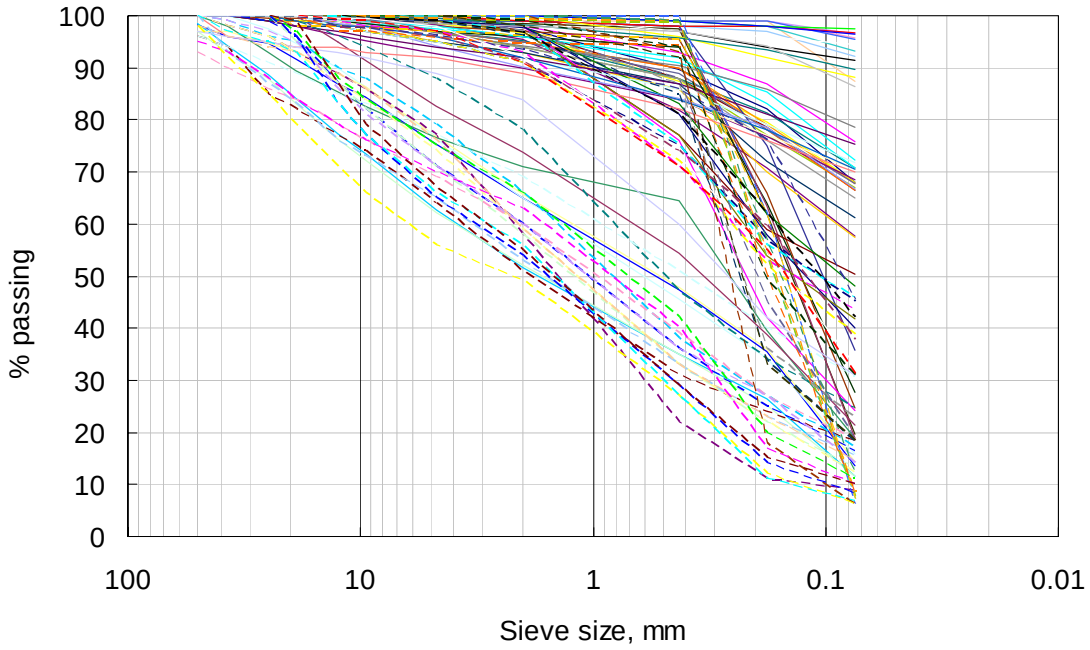


Figure 4.35 Sieve analysis of subgrade layer

For subgrade analysis, only those sections that show rutting in the subgrade and have $\alpha_{SG}$ values less than 0.9 were considered, which totals 17 sections. The final regression equations for predicting the $\alpha_{SG}$ and $\mu_{SG}$ are shown below:

$$\alpha_{SG} = 1.385 \times 10^{-5} * strain^{0.043} * GI^{1.89} * PI^{0.116} * D_{32}{}^{0.14} * FI^{0.036} * \text{wet days}^{0.326} \quad (4.29)$$

$$\mu_{SG} = 2.575 * 10^{-63} * \text{modulus}^{2.41} * strain^{-0.764} * GI^{22.594} * PI^{1.304} \quad (4.30)$$

where

| | |
|---|---|
| Strain | = Strain at the middle of the first 40 inches of subgrade layer due to one ESAL |
| GI | = Gradation index (as calculated from equation 4.26) |
| PI | = Plasticity index of subgrade layer |
| $D_{32}$ | = Number of days where daily maximum air temperature is above 32.2 $^{o}$C for year |
| Wet days | = Number of days for which precipitation was greater than 0.25 mm for year. |
| Modulus | = backcalculated subgrade modulus, psi |

Table 4.15 shows the analysis of variance for $\alpha_{SG}$ and $\mu_{SG}$. The results show that the overall models for $\alpha_{SG}$ and $\mu_{SG}$ are statistically significant. Table 4.16 shows that 47.3% and 84.8% of the variance for $\alpha_{SG}$ and $\mu_{SG}$, respectively, is explained by the independent variables.

Table 4.15 ANOVA for $\alpha_{SG}$ and $\mu_{SG}$

| Variables | | Sum of Squares | df | Mean Square | F | Sig. |
|---|---|---|---|---|---|---|
| $\alpha$ | Regression | 0.152 | 6 | 0.025 | 3.389 | 0.043 |
| | Residual | 0.075 | 10 | 0.007 | - | - |
| | Total | 0.227 | 16 | - | - | - |
| $\mu$ | Regression | 33.212 | 4 | 8.303 | 23.344 | 0.000 |
| | Residual | 4.268 | 12 | 0.356 | - | - |
| | Total | 37.480 | 16 | - | - | - |

Table 4.16 Model summary for $\alpha_{SG}$ and $\mu_{SG}$

| | R | $R^2$ | Adjusted $R^2$ | Std. Error of the Estimate |
|---|---|---|---|---|
| $\alpha$ | 0.819 | 0.670 | 0.473 | 0.08660 |
| $\mu$ | 0.941 | 0.886 | 0.848 | 0.59640 |

Table 4.17 shows the non-standardized and standardized model coefficients, *t*-test, statistical significance, and collinearity statistics for both $\alpha_{SG}$ and $\mu_{SG}$. It can be seen from the table that all independent variables included in the model for both $\alpha_{SG}$ and $\mu_{SG}$ are statistically significant except for the strain and FI in the $\alpha_{SG}$ model. Excluding either of these variables from the model causes a dramatic reduction of the $R^2$ value, therefore, similar to the base layer, they were kept in the model since the backward regression analysis selects them. Also, there was no concern about multicollinearity (small VIF). Moreover, there is a good agreement between the multiple linear regression coefficient signs and the univariate relationship of the individual variables as shown in Figures 4.36, 4.37 and 4.38. The standardized regression coefficients as depicted in Figure 4.39 show that:

- The higher the PI, GI, D32, wet days, FI, and vertical compressive strain at the middle of the first 40 in of the subgrade, the higher the $\alpha_{SG}$, which means a lower rate of rutting progression with time (the exponent is $1-\alpha_{SG}$). This is what the multiple linear regression analysis showed; however the univariate relationship of these variables with $\alpha_{SG}$ supports this result with a weak trend. Hence, the resulting $\alpha_{SG}$ relationships can not be generalized since the statistical evidence is not strong enough.
- The higher the PI, GI, and subgrade modulus, the higher the $\mu_{SG}$, which means a majority of the resulting rutting will occur at the first stage of pavement life with very little progression with time. Similar to the base layer, higher initial strain value in the subgrade indicates that rutting will keep progressing with time.

Table 4.17 Model Coefficients for $\alpha_{SG}$ and $\mu_{SG}$

| Variables | | Unstandardized Coefficients | | Standardized Coefficients | t | Sig. | Collinearity Statistics | |
|---|---|---|---|---|---|---|---|---|
| | | Beta | Std. Error | Beta | | | Tolerance | VIF |
| $\alpha$ | Constant | -11.187 | 3.965 | - | -2.822 | 0.018 | - | - |
| | Strain | 0.043 | 0.031 | 0.283 | 1.391 | 0.194 | 0.798 | 1.252 |
| | GI | 1.890 | 0.805 | 0.955 | 2.348 | 0.041 | 0.199 | 5.020 |
| | PI | 0.116 | 0.035 | 1.271 | 3.342 | 0.007 | 0.228 | 4.387 |
| | $D_{32}$ | 0.140 | 0.061 | 0.914 | 2.269 | 0.047 | 0.203 | 4.924 |
| | FI | 0.036 | 0.020 | 0.656 | 1.796 | 0.103 | 0.247 | 4.047 |
| | Wet days | 0.326 | 0.105 | 0.853 | 3.109 | 0.011 | 0.438 | 2.281 |
| $\mu$ | Constant | -144.12 | 21.825 | - | -6.603 | 0.000 | - | - |
| | SG modulus | 2.410 | 0.956 | 0.403 | 2.521 | 0.027 | 0.371 | 2.692 |
| | Strain | -0.764 | 0.274 | -0.388 | -2.786 | 0.016 | 0.490 | 2.043 |
| | GI | 22.594 | 5.006 | 0.890 | 4.513 | 0.001 | 0.244 | 4.096 |
| | PI | 1.304 | 0.211 | 1.118 | 6.191 | 0.000 | 0.291 | 3.436 |

Figure 4.40 shows the prediction of $\alpha_{SG}$ and $\mu_{SG}$ in logarithmic (ln) and arithmetic scales. Table 4.18 shows the discriptive statistics of $\alpha_{SG}$, $\mu_{SG}$ and the independent variables used in the regression analysis. Similar to the HMA and base layers, Equations 4.29 and 4.30 are used within the range of the data in Table 4.18 to obtain reasonable predictions. Figure 4.41 shows the measured (field), calculated (backcalculated PDPs), and predicted (regression equations) rut depth for one of the sections that have data for HMA, base, and subgrade layers (section 50113).

Finally, it should be noted that, as shown in Figure 4.24, a majority of the total rutting occurs within the HMA layer (on average, 57%), followed by the base layer (27.5%), and the subgrade layer (15.5%). The decay in PDP prediction is justifiable when correlated with the decay in successive layers' overall rutting percentages. This is primarily due to two analytical/data factors. First, with a smaller percentage of the total rutting to predict, the base and subgrade models are more constrained by available data and the smaller magnitude of the rutting effect measured within these layers. Secondly, the base and subgrade layers have successively fewer variables available within the predictive models than the HMA layer; therefore, it is more difficult to explain the rutting in these layers with a decreased number of variables. The results of this analysis agree with the expectation that prediction of the PDPs decays as the rutting percentage decreases. HMA regression analysis showed that the overall model for $\alpha_{HMA}$ and $\mu_{HMA}$ are statistically significant, as are all variables included. On the other hand, the overall models for $\alpha_{base}$ and $\mu_{base}$ are statistically significant, with only one insignificant variable (base thickness). Following the same pattern of decreased significance with decreased rutting percentage, the overall models for $\alpha_{SG}$ and $\mu_{SG}$ are statistically significant, yet contain two insignificant variables (strain and FI). This understandable pattern suggests the need for more study and further theorizing of variables to explain rutting within the base and subgrade layers.

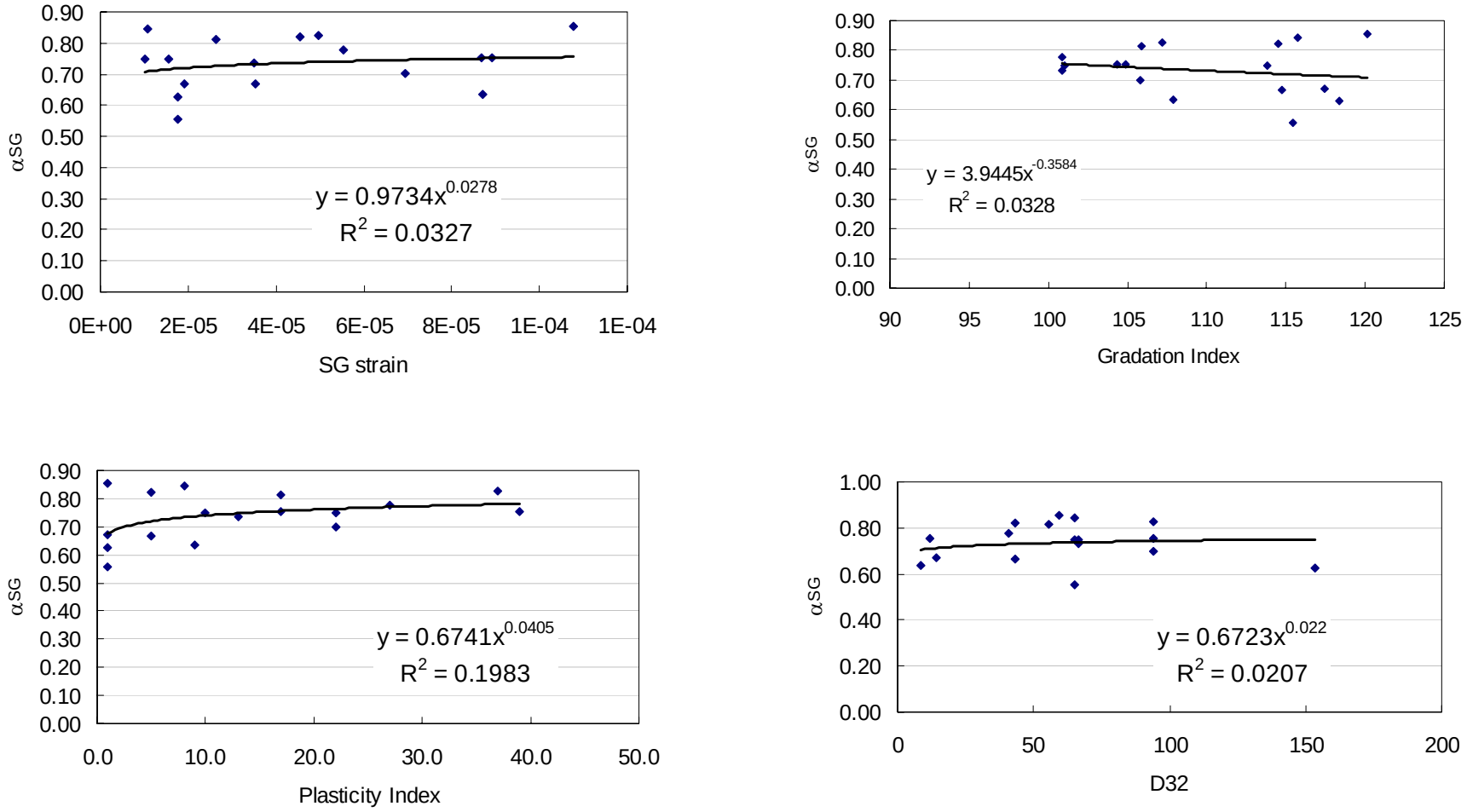


Figure 4.36 Relationship between $\alpha_{SG}$ and strain at the middle of the top 40 inches of SG, GI, PI, and $D_{32}$

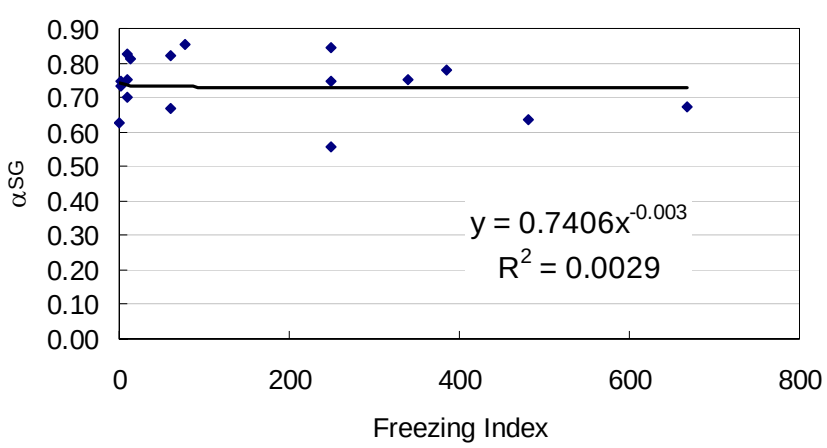


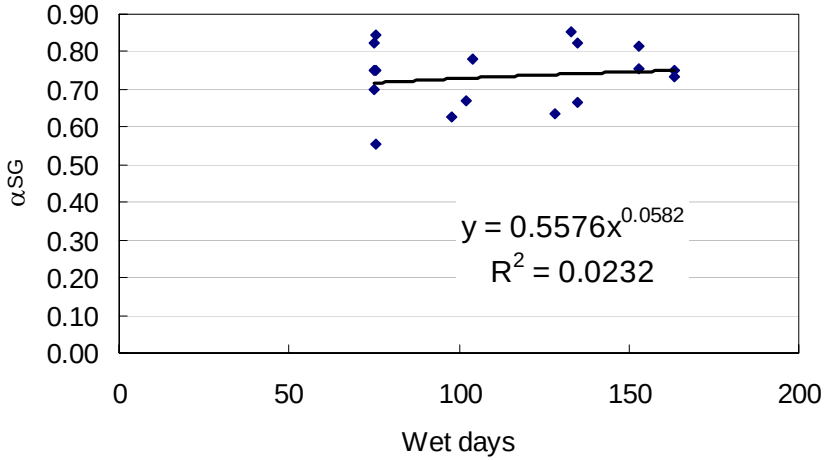


Figure 4.37 Relationship between $\alpha_{SG}$ and FI and wet days

Table 4.18 Descriptive statistics of $\alpha_{SG}$, $\mu_{SG}$, and the independent variables

| | $\mu_{SG}$ | $\alpha_{SG}$ | modulus | strain | GI | PI | D32 | FI | Wet days |
|---|---|---|---|---|---|---|---|---|---|
| Average | 0.22 | 0.74 | 31189 | 4.578E-05 | 109.94 | 13.82 | 61.12 | 168.31 | 112.87 |
| Minimum | 0.01 | 0.56 | 16846 | 1.014E-05 | 100.86 | 1.00 | 8.43 | 0.74 | 75.04 |
| Maximum | 1.67 | 0.85 | 48495 | 1.077E-04 | 120.13 | 39.00 | 153.43 | 667.27 | 163.43 |
| St. dev. | 0.41 | 0.08 | 7827 | 3.171E-05 | 6.62 | 12.21 | 35.66 | 202.53 | 34.34 |
| COV | 54.55 | 871.78 | 398 | 144.35 | 1661.89 | 113.24 | 171.39 | 83.10 | 328.71 |

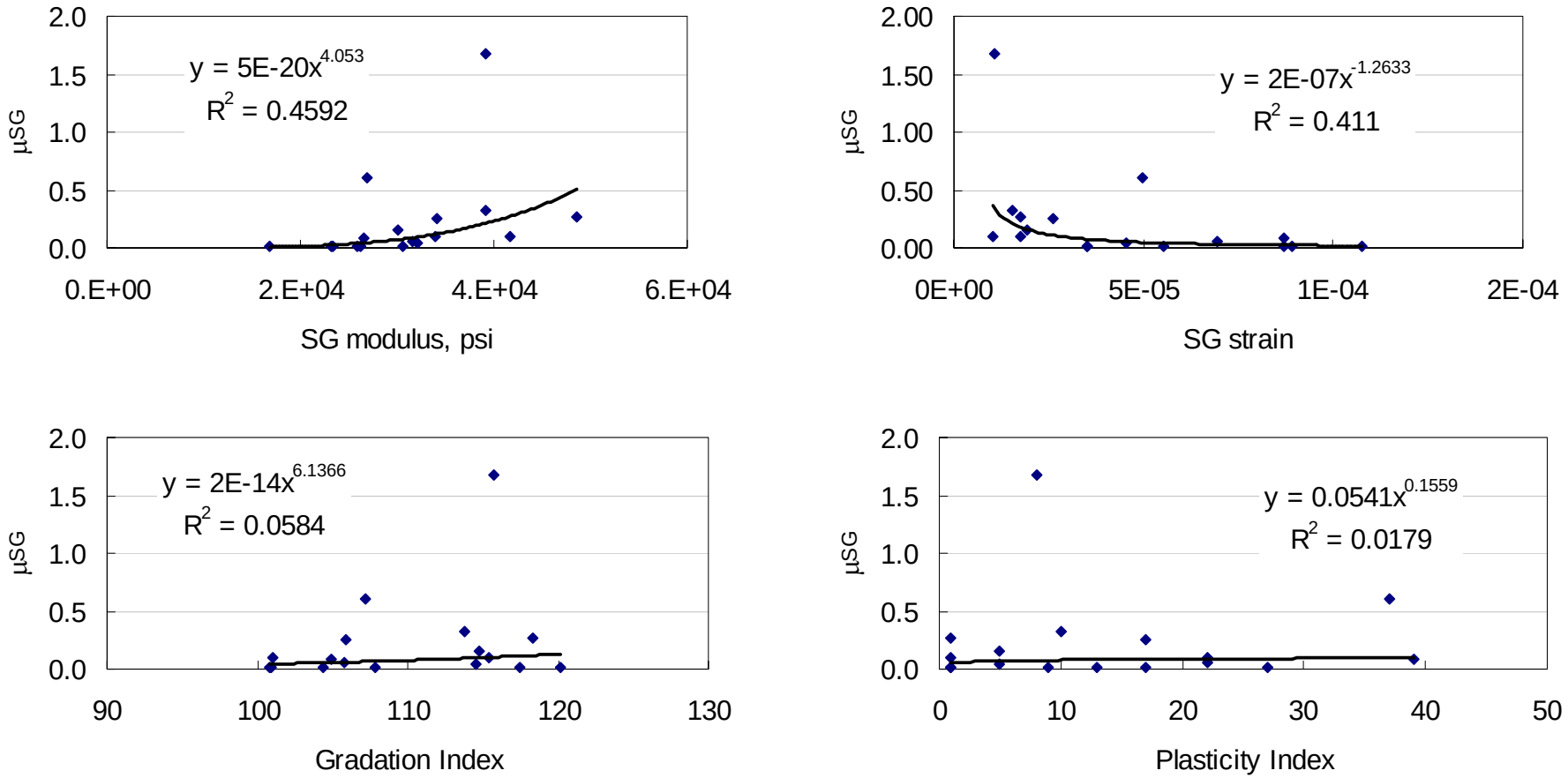


Figure 4.38 Relationship between $\mu_{SG}$ and modulus, strain at the middle of the top 40 inches of SG, GI, and PI

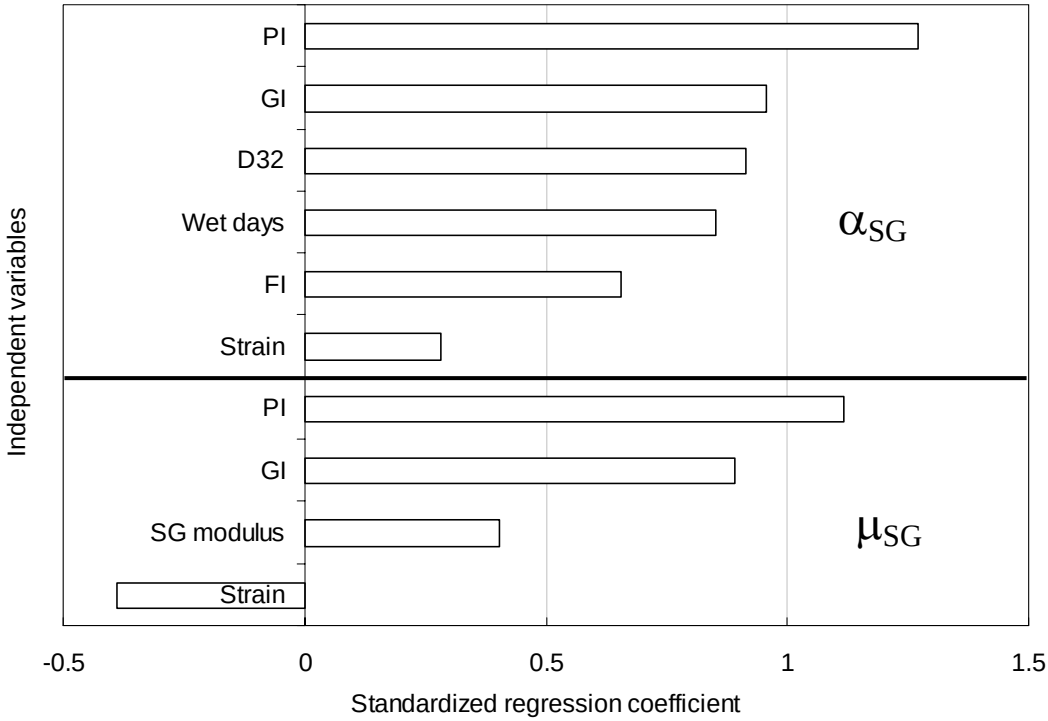


Figure 4.39 Ranking the importance of the independent variables for $\alpha_{SG}$ and $\mu_{SG}$

## 4.9 SUMMARY

This chapter addresses several procedural difficulties that were major concerns within previous PDP backcalculations such as: 1) PDPs are site specific rather than average values that can be generalized, 2) the backcalculated PDPs are based on time series data of rutting for each section instead of one rutting value, 3) $\alpha$−values should be backcalculated based on a varying traffic level ($\alpha$ is within the exponent of *n*, which is the number of load repetitions) rather than one rut value which corresponds to one traffic level, 4) choosing the backcalculated PDP values that match the sectional transverse surface profiles solves the uniqueness problem. The resulting calibrated rutting model will be utilized in the mechanistic analysis (Chapter 6) for relative comparison of different axle/truck configurations and their effects on rutting. The following section summarizes the main conclusions and the recommended future research related to this analysis.

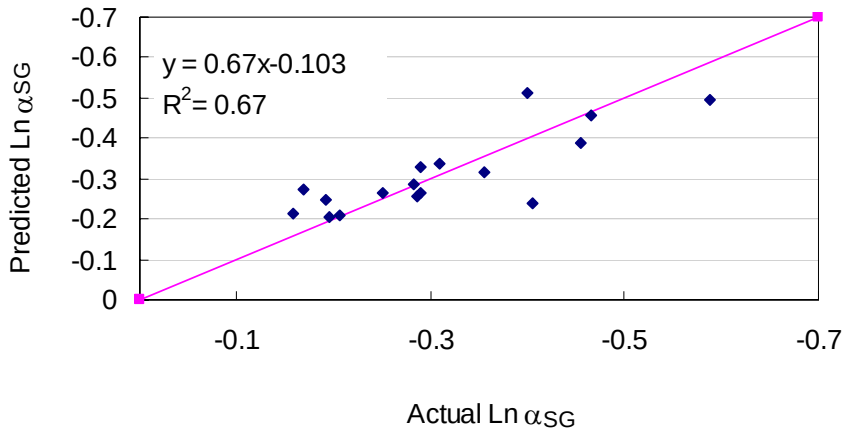


(a) Actual versus predicted α – ln scale

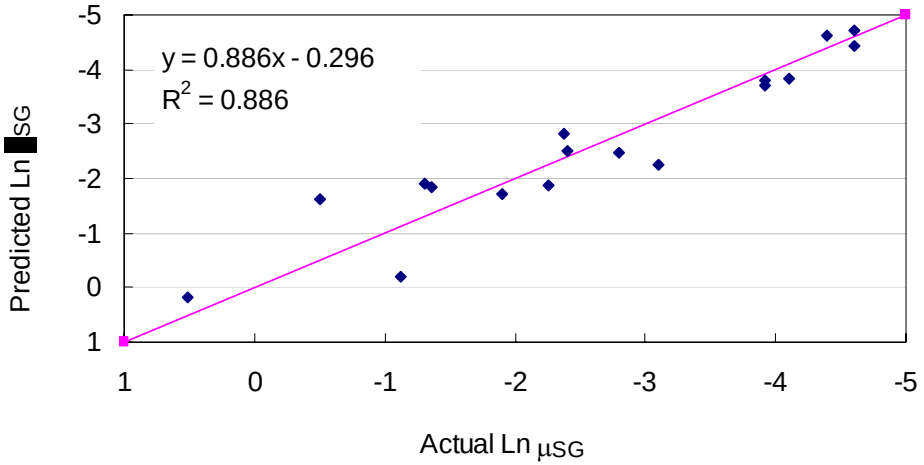


(c) Actual versus predicted μ – ln scale

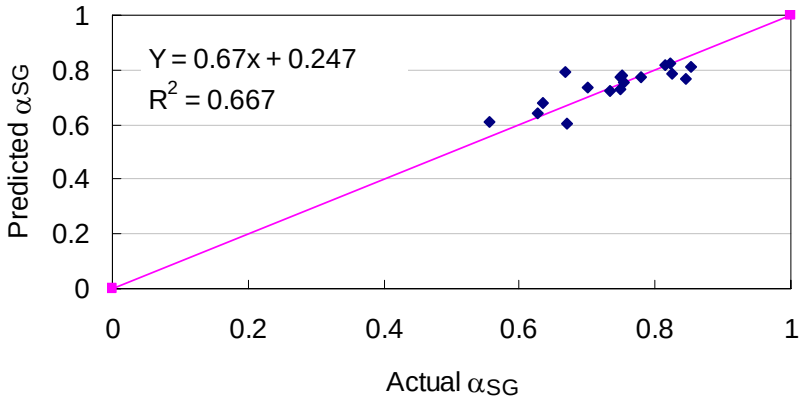


(b) Actual versus predicted α

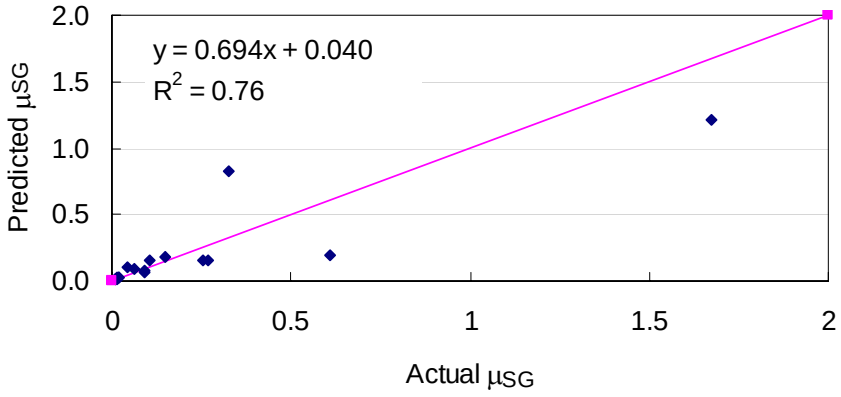


(d) Actual versus predicted μ

Figure 4.40 Actual versus predicted α and μ for subgrade layer

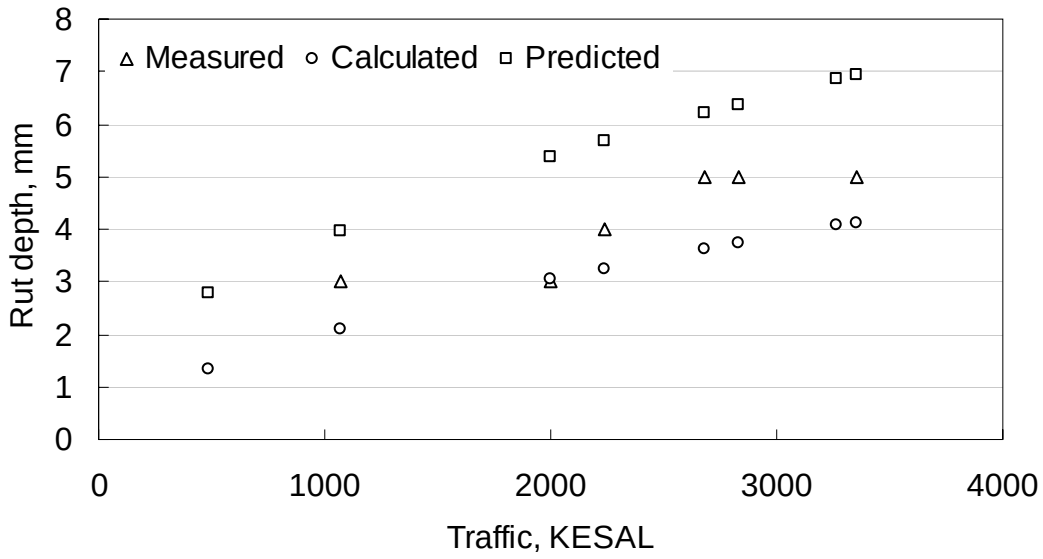


Figure 4.41 Measured, calculated, and predicted total rut depth for section 50113

### 4.9.1 Conclusion

Within this chapter, the following items were accomplished:

- Backcalculation of the PDPs from in-service pavement rut data;
- A remedy for uniqueness of backcalculation of PDPs was developed by selecting the solution that produces layer rutting percentages matching the individual transverse surface profile;
- A developed procedure allowing for calculation of the layer rutting contribution through non-destructive means, which also can be used as a diagnostic/ prediction tool;
- A good agreement between the backcalculated PDPs, as well as layer rutting percentage, with the previously developed parameters of ALFs; and
- Parameters were predicted based on the material properties, cross sections, environmental conditions (actual field data) of each section.

### 4.9.2 Future Research

Though the improved methodology outlined in this chapter yields promising results, there are several areas of the current study open for future improvement.

- The same analysis can be conducted again when there are more material properties available, such as *VTM*, *VMA*, and *VFA* for the HMA layer; compaction data (moisture content and dry density) and unconfined compression strength for the base layer; and more aggregate gradation for all pavement layers.
- The same analysis procedures can be performed for ALFs where more data and more controlled environments are available.

- Further validation of the calibrated rutting model can be conducted using other data sets outside of the SPS-1 experiment, such as GPS-1 and ALFs.
- The rutting model was calibrated based on the calculated strain due to one standard axle; however, either validation or calibration can be done based on axle load spectra to eliminate the error due to converting the actual load distribution to ESALs based on load equivalency factors, LEF.
- In this analysis, the rutting model was calibrated for conventional flexible pavements (three layer system); the amount of the data two-layer systems (full depth pavements) was very small. So, similar procedures for full depth asphalt pavements can be done wherever there are data for two layer pavement systems. Fortunately, the uniqueness problem will be less severe since there will be four PDPs instead of the six values in a three layer system.

# CHAPTER 5
# RUTTING - LABORATORY INVESTIGATION

## 5.1 INTRODUCTION

Since the end of the SHRP research program, several research studies were conducted to select a fundamentals-based laboratory Simple Performance Test (SPT) for permanent deformation. The candidate tests were evaluated and validated using three different experimental sites: 1) the Minnesota Test Road (MnROAD), 2) the Federal Highway Administration's (FHWA) Accelerated Loading Facility (ALF) test sections, and 3) the West Track FHWA test road facility. The candidate test parameters had good to excellent correlation with actual measured rut depths. The test methods and their parameters were ranked as follows: 1) the dynamic modulus measured through triaxial compression tests at high temperature; 2) the flow time measured through triaxial creep tests; 3) the flow number measured through confined or unconfined repeated load tests; and 4) the permanent shear strain measured at 1000 loading cycles using repeated shear load tests (Kaloush and Witczak, 2002). More recently, there seems to be a consensus on using the flow number as the best indicator of rutting potential.

The main purpose of the experiment in this research study is to investigate the relative rut damage caused by different axle types (single, tandem, tridem, quad etc.) as well as different truck configurations on hot mix asphalt (HMA). For this purpose, the unconfined cyclic load test was used to determine the effect of multiple loading pulses on the rutting performance of an asphalt mixture. The test enables a direct comparison of the effect of axle/truck configurations on rut performance of HMA.

## 5.2 SAMPLE PREPARATION

This section details the sample preparation procedure including how to determine the exact sample weight for the target air voids and gyratory compaction. Twenty 66-lb asphalt concrete bags of 4E3-MDOT mix (4E3 represents the $4^{th}$ layer from the bottom, with a design traffic of 3 million ESAL repetitions) were obtained during the summer of 2004 from the Spartan Asphalt mix plant (Lansing, Michigan), labeled and stored at room temperature. Table 5.1 shows the aggregate gradation of the mix. The volumetric properties of the mix are shown in Table 5.2.

A 6-inch (diameter) by 7-inch (height) cylindrical sample required approximately 15.4 lb of the mixture. Since there is no simple relationship between the sample weight and percent air voids, the required sample weight for the target air voids (5.5 % and 4.2% before and after coring, respectively) was determined through trials. Initial calculations estimated the approximate sample weight to be 15.84 lb. Knowing the target percent air voids ($V_a$ %) and the maximum theoretical specific gravity of the asphalt concrete

mixture ($G_{mm}$), the bulk specific gravity of the compacted sample can be calculated using the following equation:

$$G_{mb} = G_{mm}(100 - Va\%) \tag{5.1}$$

Knowing the expected bulk specific gravity and volume of the sample, the approximate required weight of the sample was calculated using the following equation:

$$W = G_{mb} * \rho_w * V \tag{5.2}$$

where:

$W$ = weight of the sample,
$\rho_w$ = the density of water, and
$V$ = the final volume of the compacted specimen.

Table 5.1 Aggregate gradation of the mix

| Sieve Number (opening, mm) | % passing |
|---|---|
| 3/4 in (19.00) | 100 |
| 1/2 in (12.50) | 99.5 |
| 3/8 in (9.50) | 88.6 |
| 4 (4.75) | 58.7 |
| 8 (2.36) | 35.2 |
| 16 (1.18) | 23.7 |
| 30 (0.60) | 17.3 |
| 50 (0.30) | 11 |
| 100 (0.15) | 6.5 |
| 200 (0.075) | 4.7 |

Table 5.2 Volumetric properties of the asphalt mix

| Property | $G_{mm}$ | $G_{mb}$ | $G_{se}$ | $G_{sb}$ | *VMA* | *VFA* | $G_b$ |
|---|---|---|---|---|---|---|---|
| Value | 2.487 | 2.386 | 2.714 | 2.641 | 14.7% | 72.7% | 1.028 |

where:

$G_{mm}$ = maximum theoretical specific gravity
$G_{se}$ = effective specific gravity of aggregates
*VMA* = voids in mineral aggregate
$G_b$ = specific gravity of the bitumen
$G_{mb}$ = bulk specific gravity
$G_{sb}$ = bulk specific gravity of aggregates
*VFA* = voids filled with asphalt

By using this approximated theoretical weight in the first compaction trial, the number of trials to determine the targeted sample weight was minimized. The Superpave gyratory compactor was used to compact samples in the laboratory with a target air voids content of 5.5 %, as shown in Figure 5.1. Table 5.3 shows the specific gyratory compactor parameters used during the compaction procedures.

Table 5.3 Gyratory compactor setup

| Setup | Value |
|---|---|
| Angle of tilt | $1.25^{o}$ |
| Loading ram | 600 kPa |
| Rotation speed | 30 rpm |
| Specimen height | 7 inch |

Figure 5.1 Compacted test specimen (6-inch diameter, 7-inch height)

For each sample, a specific gravity test (ASTM D-2726) was used to determine the actual specific gravity, volume, and air void content. The bulk specific gravity of the mix, $G_{mb}$, was calculated using the following equation:

$$G_{mb} = \frac{W_{dry\ in\ air}}{(W_{SSD} - W_{Submerged}) * \rho_w} \tag{5.3}$$

where:

$W_{dry\ in\ air}$ = dry weight of the specimen,
$W_{SSD}$ = saturated surface dry specimen weight,
$W_{Submerged}$ = weight of the specimen submerged in water, and
$\rho_w$ = density of water.

The volume of the specimen and its air voids content were calculated using the following equations:

$$V_{sample} = (W_{SSD} - W_{Submerged}) * \rho_w \tag{5.4}$$

$$Va\% = \frac{G_{mm} - G_{mb}}{G_{mm}} * 100 \tag{5.5}$$

where:

$Va\%$ = the air voids content, and
$G_{mm}$ = the maximum theoretical specific gravity of the asphalt mix.

The air void tolerance for the test specimens was ±0.5% variation from the mean air voids content.

### 5.2.1 Samples Coring, Sawing, and Capping

After gyratory compaction and the specific gravity test, the samples were cored from the center to produce a 3.7-inch diameter specimen. Figure 5.2 shows the coring device used. The sample holder shown in the figure was fabricated in-house and used to restrain the sample during the coring process. 0.5 inch was trimmed from each side of the cored specimen to achieve 6-inch height sample, using a saw as shown in Figure 5.3. Figure 5.4 shows the final cored and sawed sample. The cored samples were capped with sulfur capping compound according to ASTM 617-98 (2003). There are three main reasons for using smaller capped test specimens obtained from larger gyratory specimens in this experiment [Monismith, C.L. et. al.( 2000) and Leahy, R.B. et. al. (1994)]:

(a) Coring machine

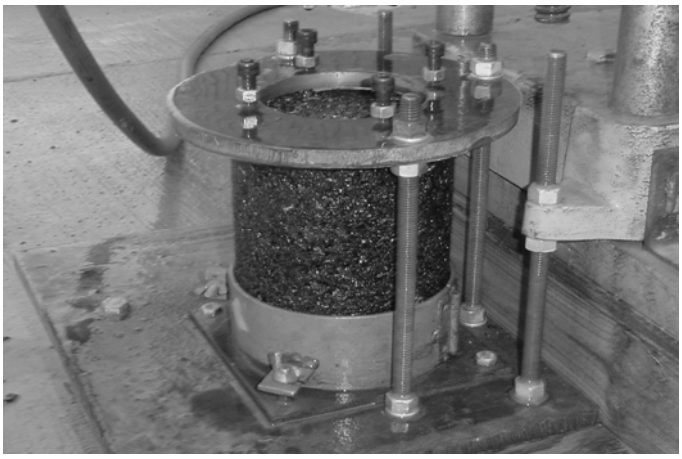

(b) Sample holder

Figure 5.2 Coring of test specimens

Figure 5.3 Sawing operation

- To obtain an appropriate aspect ratio for the test specimens – A minimum H/L ratio of 1.5 was needed (6/3.7 = 1.62) in order to ensure that the response of a tested sample using unconfined uniaxial compression test represents a fundamental engineering property.

- To eliminate areas of high air voids in the gyratory specimens – As numerous studies have illustrated, gyratory compacted specimens of this size typically have a large degree of non-homogeneity of air voids near the ends and the circumference of the specimen.
- To eliminate end friction and violation of the theoretical boundary effects – Relatively smooth, parallel specimen ends were achieved in the testing.

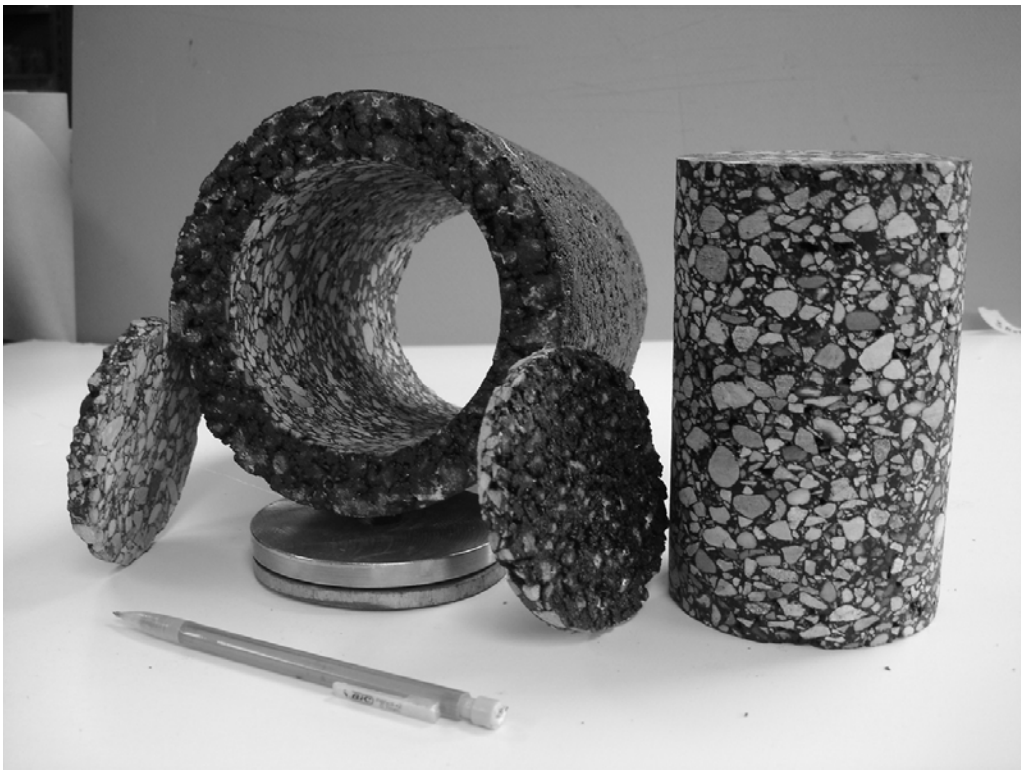

Figure 5.4 Cored sample

### 5.2.2 Air Voids Before and After Coring

The bulk specific gravities and air void contents for each test specimen were measured before and after the specimens were cored. The air void tolerance used to accept or reject the test specimens was a ±0.5% variation from the mean air voids content for both before and after coring. Figure 5.5 shows the air voids content before and after coring. As shown in the figure the average the percent air void was 5.47 before coring, with a standard deviation of 0.09, and 4.22 after coring, with a standard deviation of 0.15 respectively.

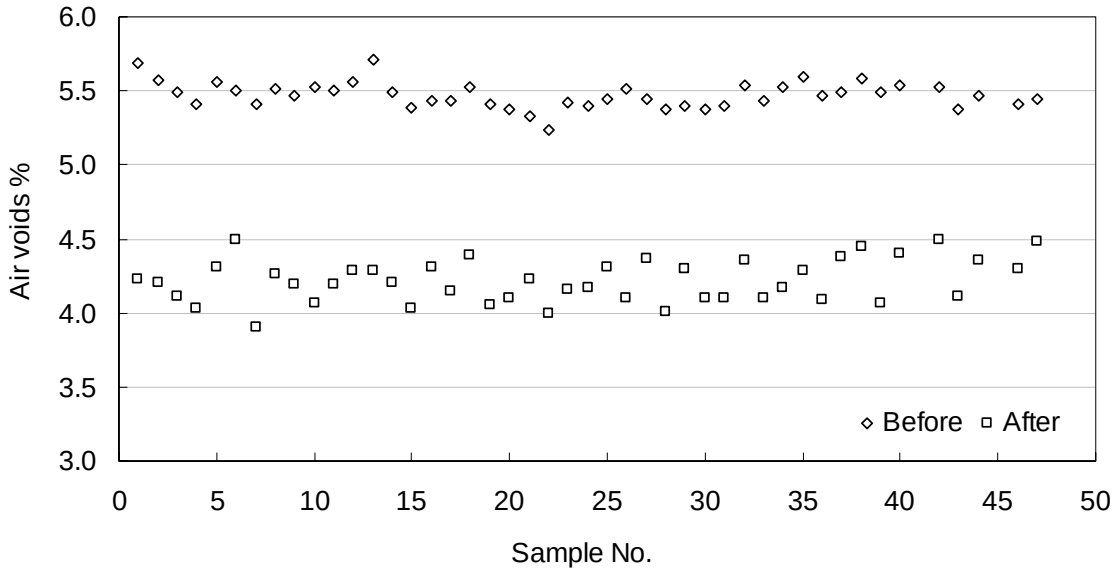


Figure 5.5 Air voids before and after coring

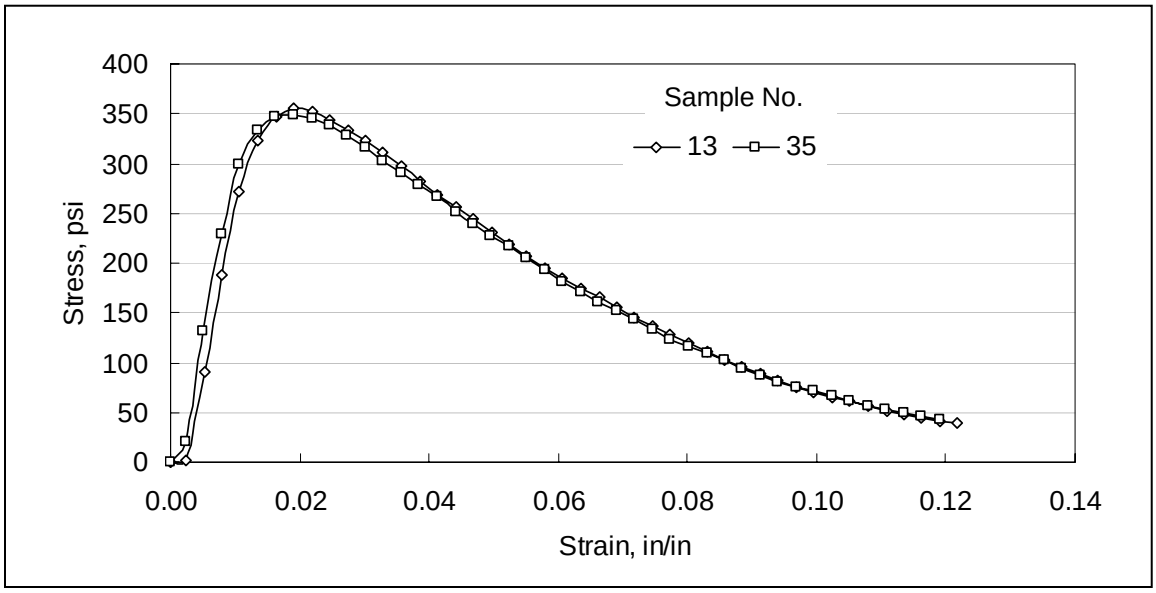


Figure 5.6 Stress versus strain for unconfined compression strength tests at 100$^{o}$F

## 5.3 UNCONFINED UNIAXIAL COMPRESSION STRENGTH TEST

Unconfined uniaxial compression strength tests were conducted, at first, for two samples at 100$^{o}$F to determine the maximum compression strength of the asphalt concrete cylinder. The vertical load and deformation were recorded during each test. The vertical load applied in the uniaxial cyclic load test should be much lower than the peak vertical

force from the compression strength test (stress ratio from 0.3 to 0.1) to ensure that failure is not due to shear. Figure 5.6 shows the relationship between the stress and strain of samples 13 and 35. The maximum unconfined compressive strength at 100$^{o}$F was 355 and 349 psi for samples 13 and 35, respectively. The stored energy (the area under the stress-strain curve in Figure 5.6) until total failure was 22.16 and 20.98 psi for the samples, respectively.

## 5.4 UNCONFINED CYCLIC COMPRESSION LOAD TEST

The objective of this experiment is to investigate the effect of different axle configurations and truck types on the rutting of an asphalt mixture. The results of this experiment provide a relative assessment of HMA rut damage from different axle/truck combinations, and not a (universal) predictive rut model. The specimens were subjected to cyclic pulses in an Unconfined Cyclic Compression Load Test (UCCLT). The series of cyclic uniaxial compression tests were conducted using different multiple load pulses. The pulses were designed to simulate different axle/truck configurations. The ratio of loading/unloading duration to rest period was held constant at (1:9). For single axles (as an example), the loading duration was found to be 0.08 s to simulate a load moving at 30 mph; therefore a rest period of 0.72 s was used. For multiple axle configurations and trucks, the loading time was taken as the time from the beginning of response due to the first axle until the time when the response of the last axle dies as shown in Figure 5.7.

Laboratory testing of both axle and truck configurations were performed at identical temperature (100$^{o}$F) and average air void (4.22%) levels, and had the same number (2) of replications. The experimental test factorial for axle configurations is shown in Table 5.4. All axle configurations were tested at 25% and 75% interaction levels and at high stress level (corresponding to trucks tire pressure), while single and tridem axles were also tested at the 0% interaction level and the additional stress levels of low and medium (corresponding to passenger cars and light weight trucks tire pressure).

Table 5.4 Experimental test factorial for axle configurations

| Variable | Level of treatment | | | | |
|---|---|---|---|---|---|
| | (1) | (2) | (3) | (4) | (5) |
| Axles | Single | Tandem | Tridem | Quad | 8-axles |
| Interactions | 25% and 75% | 25% and 75% | 25% and 75% | 25% and 75% | 25% and 75% |
| Stress level* | H, M, and L | H | H, M, and L | H | H |

* Stress level: H =87.88 psi, M = 60.13psi, L = 32.38 psi

After testing axle configurations at variable interaction levels (25% and 75%), the results (to be discussed in more detail later) showed no significant difference. This influenced the subsequent design of the truck configuration testing. As a result, all truck

configurations were tested at the 0% interaction level and at the high stress level (corresponding to truck tire pressure) (see Table 5.5).

Table 5.5 Experimental test factorial for axle configurations

| Variable | Level of treatment | | | | |
|---|---|---|---|---|---|
| | (1) | (2) | (3) | (4) | (5) |
| Trucks* | S5**  | S1T2  | S1T2Tr2**  | S3T2Q1  | S1T1E1**  |
| Interactions | 0% | 0% | 0% | 0% | 0% |
| Stress level | H | H | H | H | H |

* Trucks defined by their axle configuration

** S5 = Truck with five single axles, S1T2Tr2 = Truck with one single axle + 2 tandem axle + 2 tridem axles, and SIT1E1= truck with one single axle + one tandem axle + one eight axle

## 5.5 TESTING PROCEDURES

The unconfined cyclic compression load tests were conducted using an MTS electro-hydraulic test machine, as shown in Figure 5.8. Since the pavements are more likely to rut at higher temperature, the tests were performed at controlled temperature ($100^oF \pm 1$). The samples were raised to a temperature of $100^oF$ inside the test chamber over the course of 12 hours before starting the actual test to insure uniform temperature throughout the mass of the specimen. Two steel plates (one at the top and another at the bottom) were used to distribute the load evenly over the cross-sectional area of the specimen. Two linear variable displacement transducers (LVDTs) were connected to the sample to measure vertical deflection. The samples took from 4 to 5 hours until total failure at high stress level for all axle and truck configurations, 9 to 11 hours at medium stress level, and 45 to 50 hours at low stress level.

### 5.5.1 Typical Test Results

A typical example of uniaxial cyclic compression load tests results is shown in Figure 5.9 (a). As shown in the figure, the cumulative vertical permanent deformation (CVPD) can be divided into three major zones:

- The primary zone—the portion in which the strain rate decreases with loading time;
- The secondary zone—the portion in which the strain rate is constant with loading time; and
- The tertiary flow zone—the portion in which the strain rate increases with loading time.

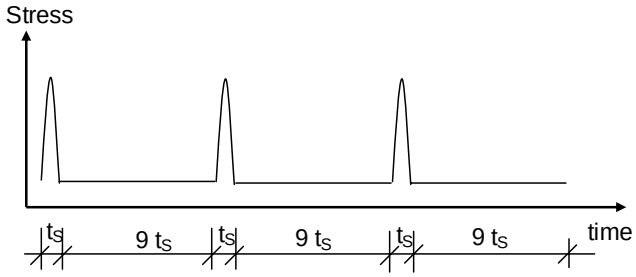


(a) Single axle

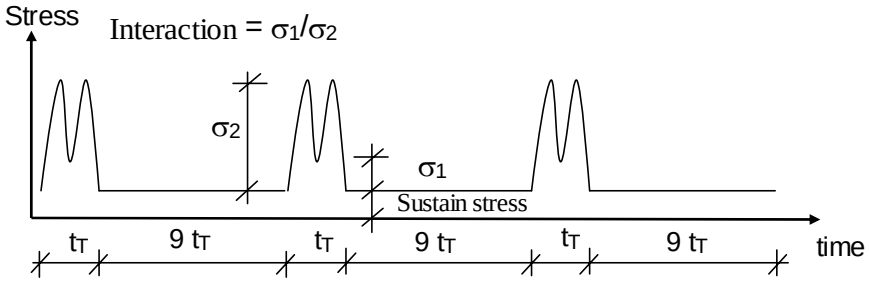


(b) Tandem axle

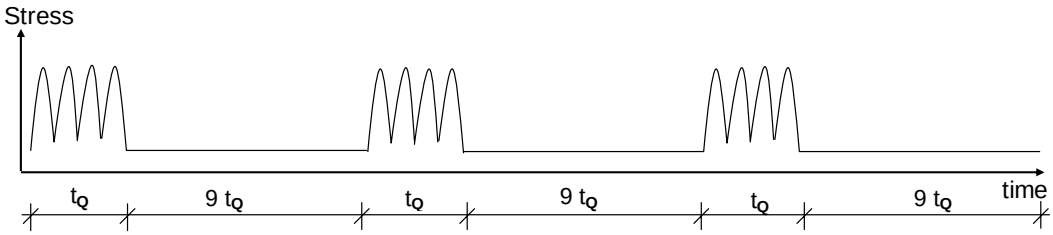


(c) 4-axles


(d) Truck S1T1E1

Figure 5.7 Loading and unloading time for axle and truck configurations

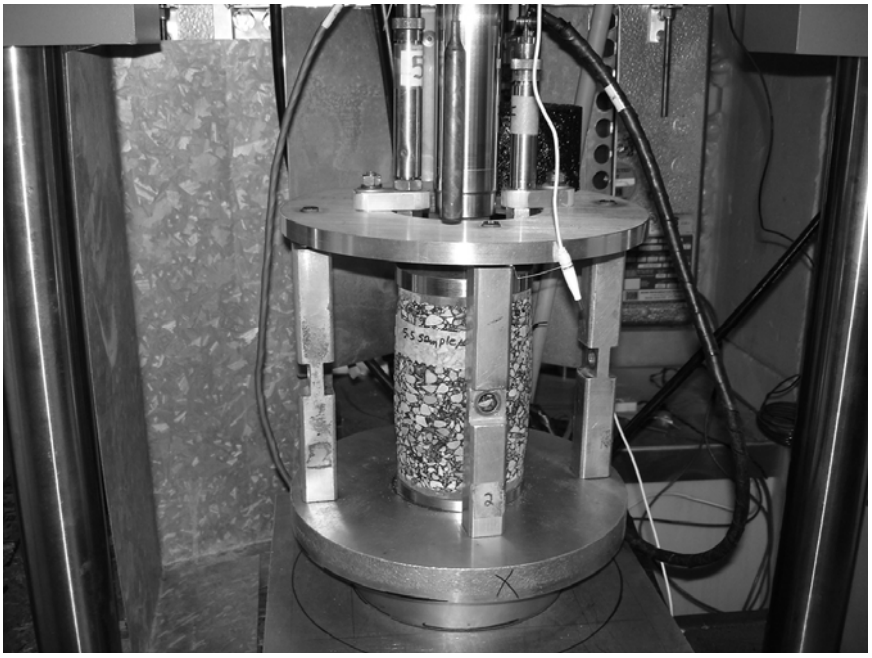

Figure 5.8 Unconfined cyclic compression load test set up

The starting point of tertiary deformation is defined as the flow number ($N_f$), which has been found to be a significant parameter in evaluating an HMA mixture's rutting resistance (Kaloush and Witczak, 2002). The rate of change in *CVPD* was obtained by calculating the incremental slope with respect to the number of load repetitions as shown below:

$$\text{Slope} = \frac{\Delta\, CVPD}{\Delta N} = \frac{(CVPD)_{N_i} - (CVPD)_{N_{i-1}}}{N_i - N_{i-1}} \tag{5.6}$$

where:

$CVPD$ = cumulative vertical permanent deformation at cycle $N_i$ or $N_{i-1}$
$N$ = number of cycles

The slope of the *CVPD* curve first decreases (primary zone), reaches a valley or plateau (at the end of the secondary zone), and then starts to increase (throughout the tertiary zone). The decrease in the slope at the beginning of the test is due to densification and sample seating. When cracks are initiated, the rate of *CVPD* increases. Hence, in this procedure, the rutting life of a sample is defined as the number of load repetitions at which the rate of accumulation of *CVPD* starts to increase, as shown in Figure 5.9 (b).

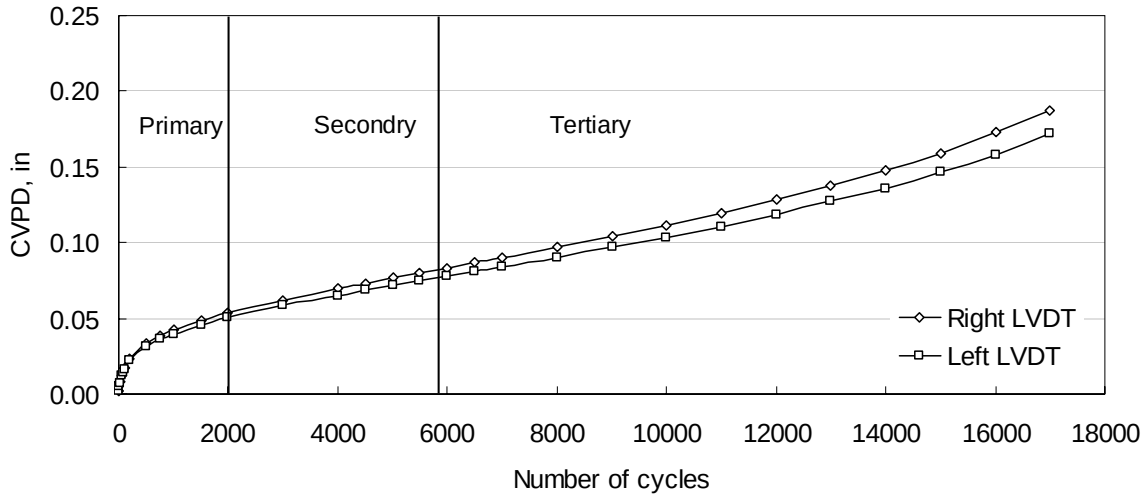


(a) Relationship between cumulative vertical permanent deformation and number of cycles

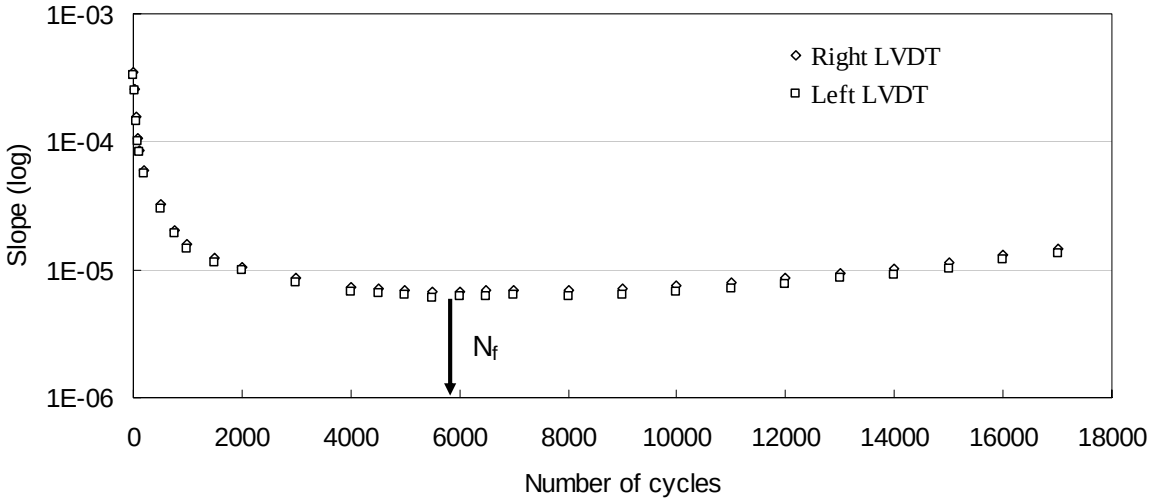


(b) Rate of change in cumulative vertical permanent deformation vs. number of cycles

Figure 5.9 Typical experimental results from uniaxial cyclic compression load tests (single axle-sample number 10)

## 5.6 EXPERIMENTAL TEST RESULTS

The main objective of this experiment is to study the relative effect of different axle and truck configurations on asphalt pavement rutting. Several factors were included in the experiment, and the following sections discuss these factors and show the experimental results.

### 5.6.1 Effect of Interaction Level

The applied load from a truck axle group at the surface of the pavement is distributed downward through the pavement over a triangular pattern, when viewed along a longitudinal cross-section. At the tire-pavement interface, the stress is close to the tire pressure value and there is no interaction between the responses caused by the individual axles. The load from the axle tire is distributed over a larger area at increasing depth within the pavement as shown in Figure 5.10. The amount of the interaction level depends on the thickness and the stiffness of the asphalt concrete layer, among other factors.

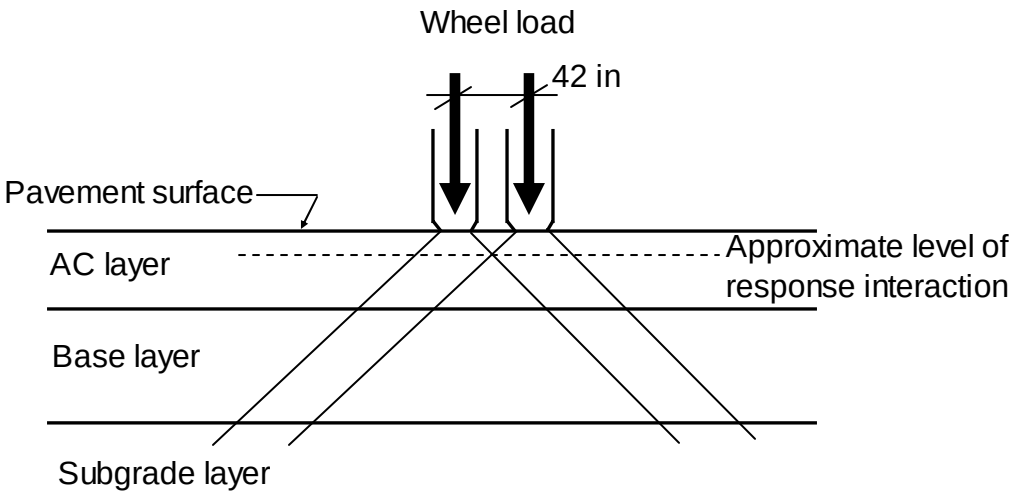


Figure 5.10 Distribution of wheel load (Deen, *et al.*, 1980)

All axle configurations used in this experiment were simulated at 25% and 75% interactions. Figure 5.11 shows an example of the interaction levels for the quad axle configurations. The number of cycles to failure ($N_f$) for all tested axles configurations were determined. Figure 5.12 shows the effect of the interaction level of different axle configuration on pavement rutting. The results show that there is no significant effect of the interaction level on the number of cycles to rutting failure for different axle configurations. These results indicate that the most important two factors that characterize the sample failure are the stress level and the loading pulse duration.

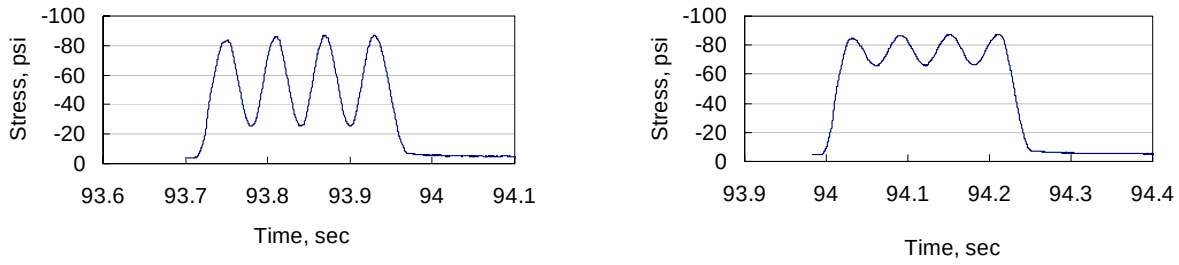


(a) 25% interaction (b) 75% interaction

Figure 5.11 Interaction levels for the quad axle configuration

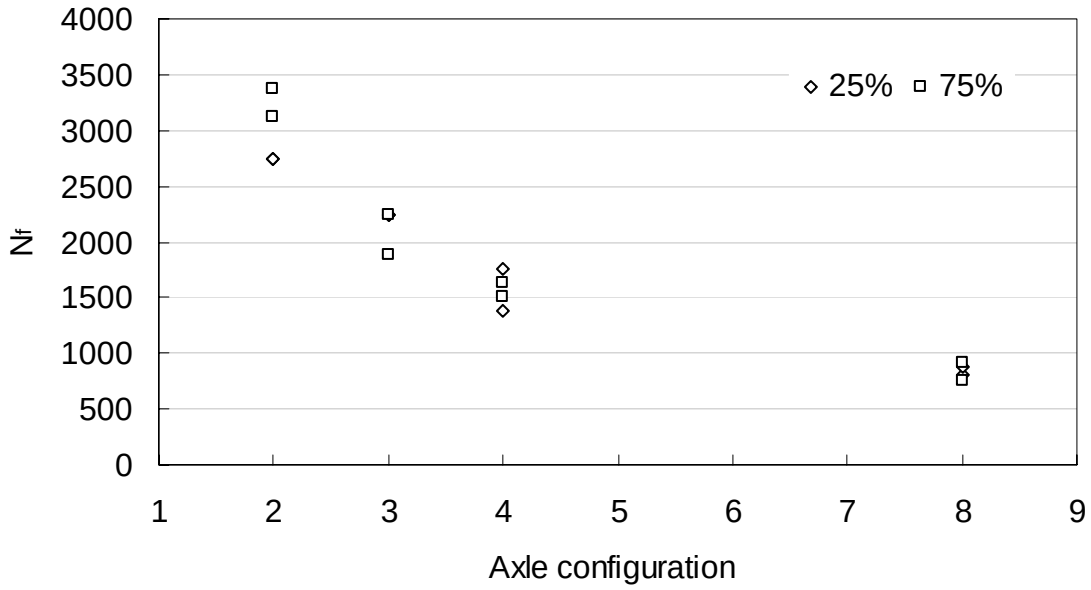


Figure 5.12 Effect of the interaction level of different axle configuration on pavement rutting

### 5.6.2 Axle Factors

The axle factor (AF) is defined as the damage of an axle group normalized to that of a single axle carrying the same load as any of the individual axles within the axle group. The *AF* can be calculated from the following equation:

$$AF = \frac{\text{Damage of the axle group}}{\text{Damage of the single axle}} = \frac{\dfrac{1}{N_{f\ \text{axle group}}}}{\dfrac{1}{N_{f\ \text{single axle}}}} = \frac{N_{f\ \text{single axle}}}{N_{f\ \text{axle group}}} \tag{5.7}$$

Figure 5.13 shows the *AF*s for different axle configurations (single, tandem, tridem, quad, and 8-axles). The results show that the *AF*s are approximately in proportion to the number of axles within an axle group. In other words, rutting damage is

proportional to axle load. A similar mechanistic finding for rutting damage was reported by Gillespie *et al*, 1993; however, the study was done for limited axle configurations. As a confirmation of this finding, the rutting damage normalized per axle load is shown in Figure 5.14. The results show that the rut damage per axle is constant for both interaction levels.

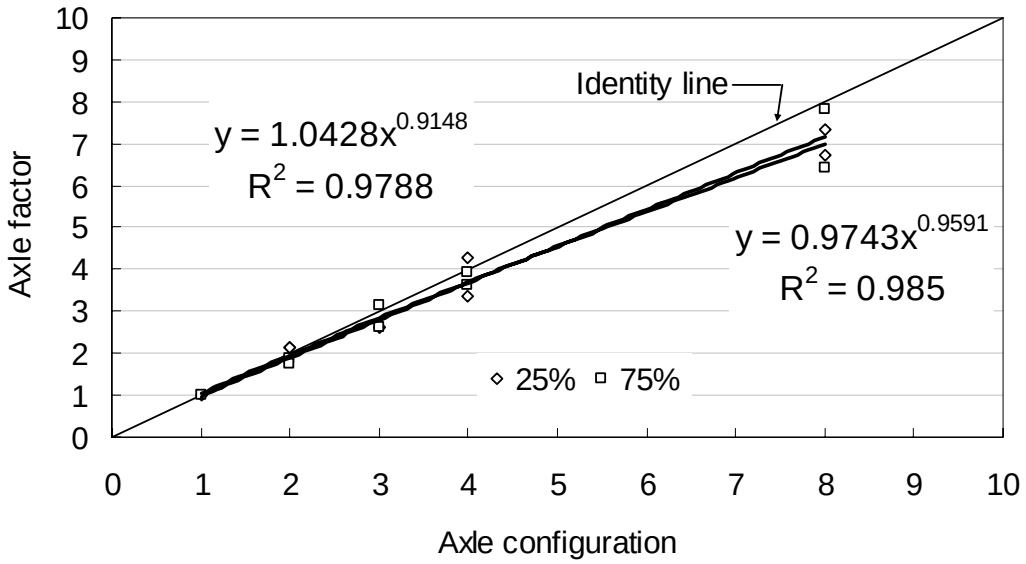


Figure 5.13 Axle factors for different axle configurations and interaction levels

The results from this experiment provide evidence that multiple axles cause rutting at the same relative rate as single axles. They produce similar or even slightly less (the 8-axle result is 7.07 times the damage of a single axle) rutting damage than single axle loads. Additionally, comparing *AF*s that were previously developed for fatigue damage due to the same axle configurations at Michigan State University (El Mohtar, 2003), it appears that the multiple axles impose far less fatigue damage (the 8-axle result is 4.5 times the damage of a single axle) relative to rutting damage. To compare the results obtained from this study with those from the AASHO findings, when compared to the 13-kip single axle configuration, the *AF* values of the 26-kip tandem and 39-kip tridem configurations were calculated to be 1.38 and 1.49, respectively. The *AF* values for the tandem and tridem configurations from this study were found to be 1.97 and 2.74, respectively. It should be noted that the *AF*s from the AASHO study are based on Pavement Serviceability Index (PSI) values from the AASHO road test and not from laboratory rutting tests; therefore, a significant difference between the two is understandable. The fact that the AASHO *AF*s fall between the *AF*s from this study and those of the previously cited fatigue study, suggests that axle factors need to be developed for each pavement distress rather than expecting a single axle factor to speak for all distresses. Furthermore, since pavement fatigue and rutting rarely occur at extreme levels within the same pavement, the environmental conditions of the site (i.e., average yearly temperature, seasonal variation in temperature and precipitation, etc.) must be taken into consideration when selecting the most appropriate *AF* to use in pavement design.

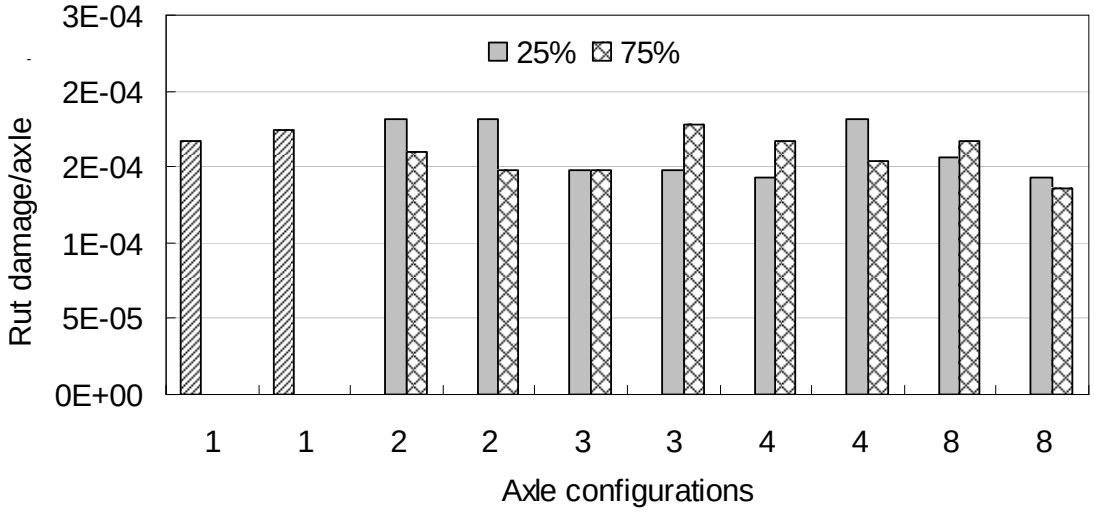


Figure 5.14 Rut damage per axle for two replications of each axle configuration/interaction level pair

### 5.6.3 Truck Factors

As mentioned previously, after testing axle configurations at various interaction levels (25% and 75%), the results showed no significant difference between the two levels. This influenced the subsequent design of the truck configuration testing. As a result, all truck configurations were tested at 0% interaction and high stress levels (conservative case). Similar to the axle factor, the truck factor is calculated as follows:

$$TF = \frac{\text{Damage of the truck}}{\text{Damage of the single axle}} = \frac{\dfrac{1}{N_{f\ \text{truck}}}}{\dfrac{1}{N_{f\ \text{single axle}}}} = \frac{N_{f\ \text{single axle}}}{N_{f\ \text{truck}}} \tag{5.8}$$

Figure 5.15 shows the truck factors for the five truck configurations. The results show more variations, with the truck factors for the five-axle truck ranging from 6 (S1T2 truck) to 8 (S5 truck), and those of the 11-axle trucks from 10 (S1T1E1 truck) to 14 (S1T2Tr2 and S3T2Q1 trucks). These variations may be partly explained by the following reasons: (i) the rest period between axles within a given truck configuration is not the same as that for the individually tested axles; (ii) the sequence of axles varies from one truck configuration to another.

Figure 5.16 shows the rut damage per axle for these trucks. The results do indicate that grouping of axles resulted in reduced damage per load carried. The 5-axle trucks with two tandem axles (S1T2) produced less damage than the truck with only single axles (S5). Also, the truck with the 8-axle group (S1T1E1) produced less rut damage per load carried than the other 11-axle trucks. It should be noted that the truck that has a quad axle (S3T2Q1) as a maximum axle group shows a similar or slightly higher truck factor than

the one with tandems and tridems (S1T2Tr2). This is due to the fact that it has 3 single axles.

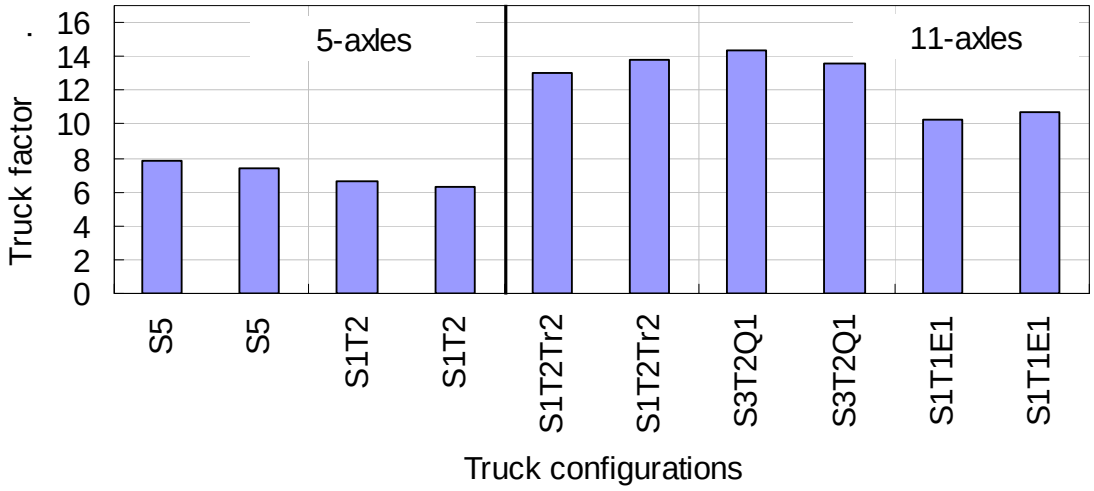


Figure 5.15 Truck factor vs. total number of axles within truck (two replicates each)

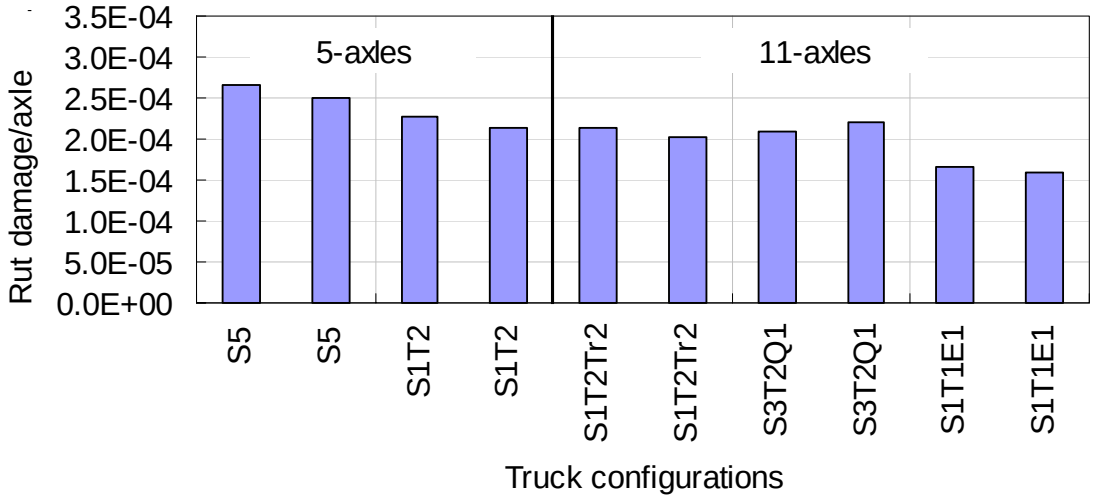


Figure 5.16 Relationship between total number of truck axles, maximum axle group, and truck factor (two replications each)

The above results presented rut damage in terms of axle and truck factors, which were obtained using separate tests for individual axle groups and different truck configurations, respectively. This provides an opportunity to relate the rut damage caused by a given truck to that from individual axle groups. An attempt was made to compose a truck's CVPD from the values of its constituent axle configurations. Figure 5.17 shows an example of summing up the CVPD from single, tandem and eight-axle groups for the S1T1E1 truck. The figure shows that the sum of the rut values obtained from individual axle cyclic load testing does not match the value obtained cyclic testing using truck load

pulses. This difference is the result of summing rut values from different (mismatched) zones; i.e., primary versus secondary and tertiary zones. For example, Figure 5.17 shows that the 8-axle configuration and the S1T1E1 truck both reach the tertiary zone at a cycle number that is still within the primary zone of both the single and tandem axle configurations. Since the vertical deformation taking place within these two zones is qualitatively different, it is unreasonable to consider summing them. Therefore, using direct summation from individual axle groups to predict truck rutting damage would be erroneous.

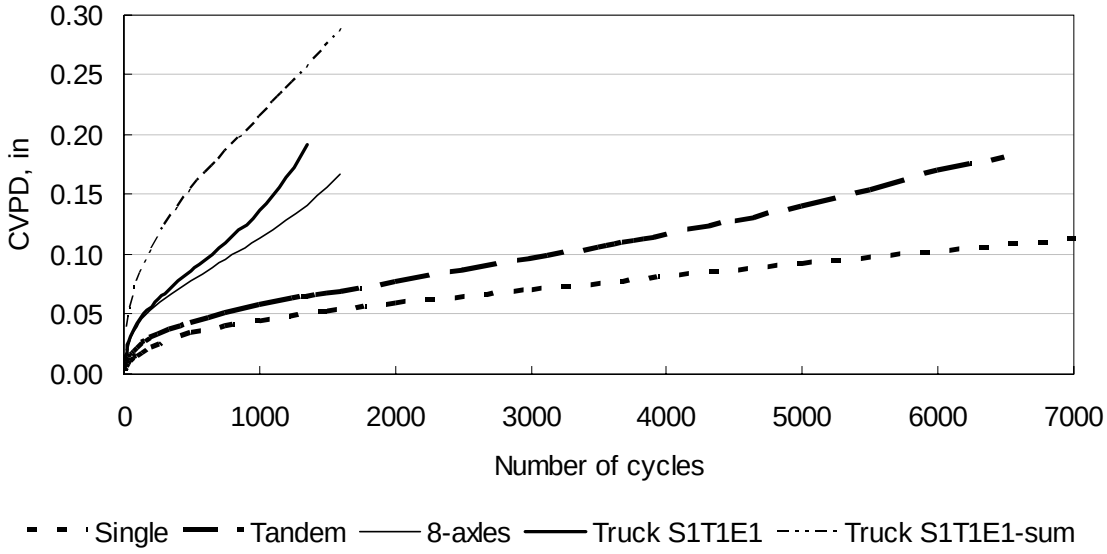


Figure 5.17 Prediction of the truck rutting damage from its constituent axle configurations

*5.6.3.1 Using Miner's Rule*

Since prediction of the truck damage from the simple summation of its individual axle rutting damage is erroneous, one could use the most common method of summing damage for a loading spectrum; i.e., Miner's rule (Miner, 1924).

$$D = \Sigma \frac{n_i}{N_i} \tag{5.9}$$

where:

$n_i$ = Number of cycles to failure for the truck

$N_i$ = Number of cycles to failure for the individual axle

This method is widely understood and easy to implement and is the foundation for many other cumulative damage theories that have been proposed. Ideally, the summation of damage ratios would equal one at failure. The parameter $D$ has been documented in the literature; it is usually found in the range $0.7 < D < 2.2$ with an average value near unity

(Shigley and Mischke, 1989). Therefore, the truck damage was calculated from its constituent axles that were tested separately. The following steps show the calculation for truck S3T2Q1.

- Using Equation 5.9, $n_i$ is the number of cycles to failure for the truck,
- Each truck configuration and its constituent axles have duplicate rut tests,
- Table 5.6 shows the possible combinations of summing the truck damage from its constituent axles (from both axle replications); it shows 8 different possible combinations to compose the truck from its axle groupings using the number of cycles to failure from the first truck sample,
- The same equations can be applied using the number of cycles to failure from the second truck sample,
- The above steps are applied at different values of *CVPD* (0.04, 0.05, 0.06, 0.07, 0.08, 0.09, 0.1, 0.11 inch) which are within the secondary zone of permanent deformation,
- These steps produce 8 (possible combinations) *2 (truck samples) *8 (values of *CVPD*) = 128 possible combinations,
- It should be noted that these are not all the possible combinations, however the rest will give damage values within the range defined by the considered combinations.

The distribution of the calculated damage for each truck is shown in Figure 5.18. The average value of the damage and the standard deviation is illustrated in Figure 5.19. The results show that damage is underestimated for trucks with smaller axle groups, and as the size of the maximum axle groups increases, the rutting damage increases. The range of the mean damage is 0.67 for the single axle truck (S5) to 1.075 for the eight-axle truck (S1T1E1); however, the overall mean damage from all truck configurations is close to unity (0.873). The accuracy of Miner's rule in calculating the rutting damage depends on the axle load spectra. In other words, if the axle loads are mixed and have all axle configurations (single to eight axles) the damage predictions will be very close to unity. Where as, if the majority of the axles are small axle groups, the predicted damage will be underestimated. On the other hand, if the majority of the axles are within larger axle groups, the predicted damage will be overestimated. There are two significant drawbacks to using Miner's rule that cause the damage values to have a wide range. First, the influence of the order of application of various axle configurations is not considered. Second, the damage is assumed to accumulate at the same rate (linear) at a given axle configuration (Oh, 1991). Though both of these need further study, developing a non-linear damage model is outside the scope of this study.

Table 5.6 Possible combinations of the truck damage from its constituent axles

| | |
|---|---|
| 1 | $D1 = 3\frac{n_1}{N_{s1}} + 2\frac{n_1}{N_{T1}} + \frac{n_1}{N_{Q1}}$ |
| 2 | $D2 = 3\frac{n_1}{N_{s2}} + 2\frac{n_1}{N_{T2}} + \frac{n_1}{N_{Q2}}$ |
| 3 | $D3 = 3\frac{n_1}{N_{s1}} + 2\frac{n_1}{N_{T2}} + \frac{n_1}{N_{Q2}}$ |
| 4 | $D4 = 3\frac{n_1}{N_{s2}} + 2\frac{n_1}{N_{T1}} + \frac{n_1}{N_{Q2}}$ |
| 5 | $D5 = 3\frac{n_1}{N_{s2}} + 2\frac{n_1}{N_{T2}} + \frac{n_1}{N_{Q1}}$ |
| 6 | $D6 = 3\frac{n_1}{N_{s1}} + 2\frac{n_1}{N_{T1}} + \frac{n_1}{N_{Q2}}$ |
| 7 | $D7 = 3\frac{n_1}{N_{s1}} + 2\frac{n_1}{N_{T2}} + \frac{n_1}{N_{Q1}}$ |
| 8 | $D8 = 3\frac{n_1}{N_{s2}} + 2\frac{n_1}{N_{T1}} + \frac{n_1}{N_{Q1}}$ |

where:

$n_1$ = number of cycles to reach certain *CVPD* for truck S3T1Q1 for the first sample

$N_{s1}$ = number of cycles to reach certain *CVPD* for single axle for the first sample

$N_{s2}$ = number of cycles to reach certain *CVPD* for single axle for the second sample

$N_{T1}$ = number of cycles to reach certain *CVPD* for tandem axle for the first sample

$N_{T2}$ = number of cycles to reach certain *CVPD* for tandem axle for the second sample

$N_{Q1}$ = number of cycles to reach certain *CVPD* for quad axle for the first sample

$N_{Q2}$ = number of cycles to reach certain *CVPD* for quad axle for the second sample

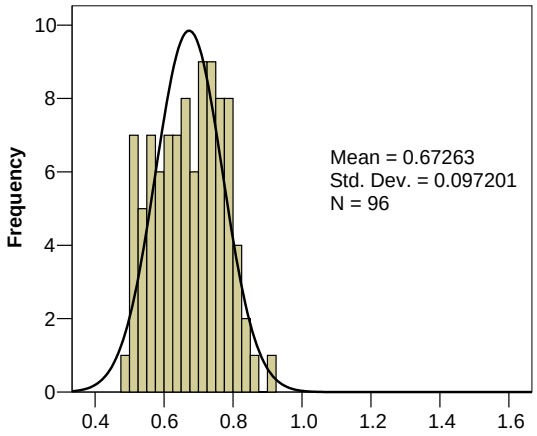


(a) Truck S5

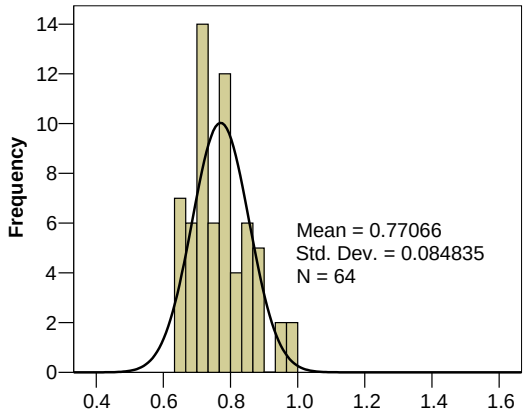


(b) Truck S1T2

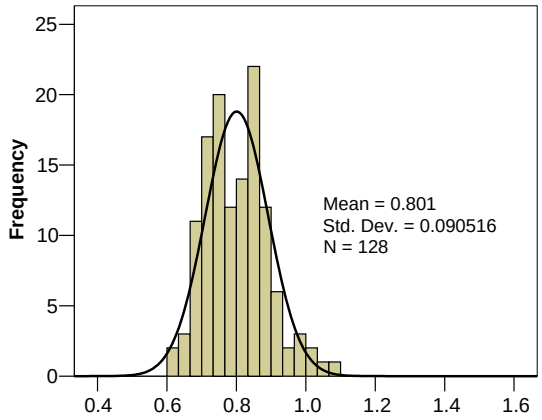


(c) Truck S1T2Tr2

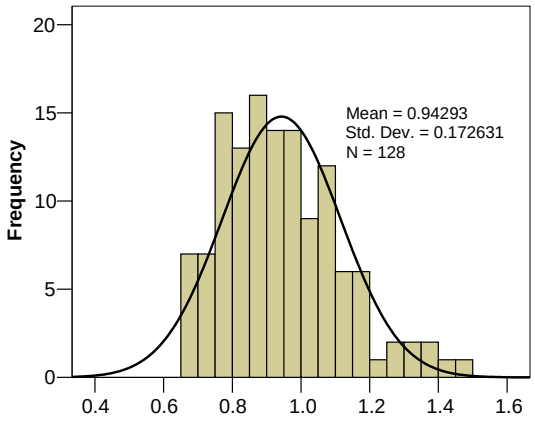


(d) Truck S3T2Q1

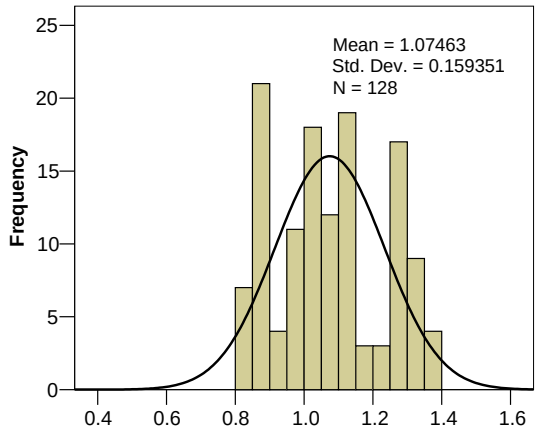


(e) Truck S1T1E1

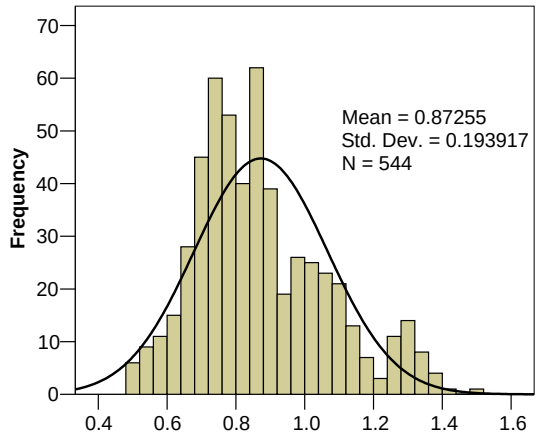


(f) Overall

Figure 5.18 Damage distribution for different truck configurations

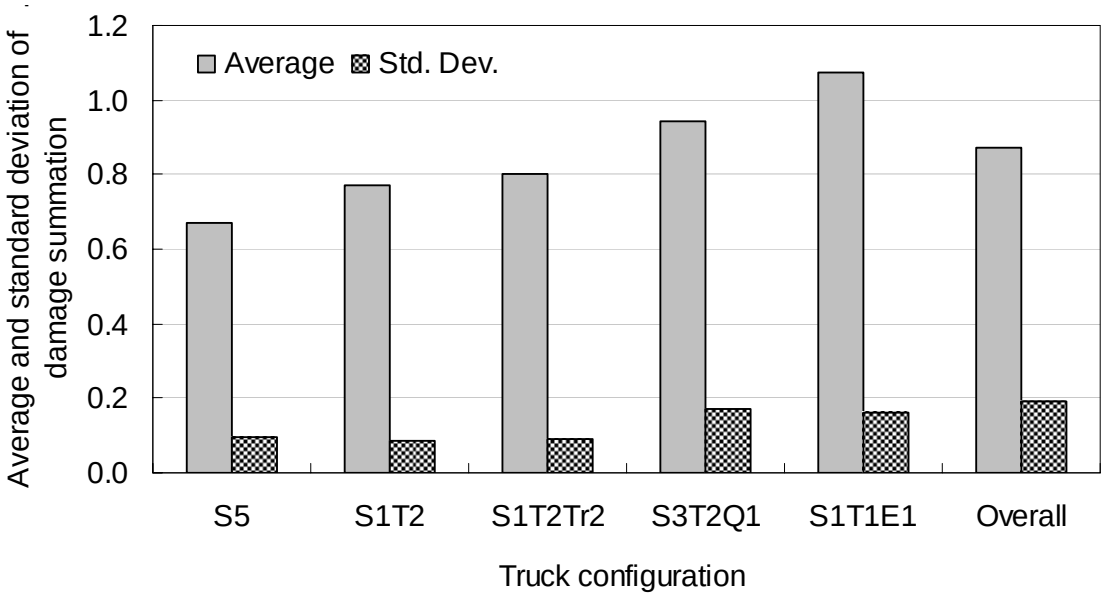


Figure 5.19 Average and standard deviation of the rutting damage for different truck configurations

*5.6.3.2 Combining Results from Individual Axles, Trucks and Different Stress Levels*

In this procedure, we derive a simple equation by using the individual axle groups and the rest period between them as independent variables:

$$TF = a_0 n_{rest-period} + a_1 n_1 + a_2 n_2 + a_3 n_3 + a_4 n_4 + a_5 n_5 + a_7 n_7 + a_8 n_8$$

The axle factors ($a_1$, $a_2$, $a_3$, $a_4$, $a_5$, $a_5$, $a_7$ and $a_8$) were obtained from figure 5.13 (individual axle load testing), and the weighting factor for rest period ($a_0$) was found by minimizing the error between the measured and calculated Truck Factors (TF) using the Excel Solver (Standard error = $10^{-12}$). Table 5.7 summarizes these values. The value for $a_0$ was 0.64, meaning that the effect of the reduced rest period within a truck configuration on rutting damage is equivalent to about 64% of that caused by a single axle load. In other words, the fact that the rest period between axle groups within a truck configuration during the "truck tests" is less than that between individual axles during "axle tests" causes an increase in rut damage equivalent to adding 0.64 single axle to a given truck configuration for each rest period between axle groups. The n-values correspond to the number of equivalent axle loads at the legal load limits (15.4 kips for steer, 18 kips for single, 32 kips for tandem, 39 kips for tridem, 52 kips for quad and 104 kips for eight-axle). These were obtained using the equation from Figure 5.25 (see table 5.8). The TF were calculated for all truck configurations. Table 5.9 summarizes these results.

Table 5.7 Summary of the rest period and individual axle factors

| $a_0$ | $a_1$ | $a_2$ | $a_3$ | $a_4$ | $a_5$ | $a_7$ | $a_8$ |
|---|---|---|---|---|---|---|---|
| 0.64 | 1.00 | 1.93 | 2.83 | 3.77 | 4.61 | 6.25 | 7.05 |

Table 5.8 Summary of axle load equivalency factors adjusted for legal load limits

| Steer | Single | Tandem | Tridem | Quad | Five-axle | Seven-axle | Eight-axle |
|---|---|---|---|---|---|---|---|
| 0.69 | 1.00 | 0.75 | 0.46 | 0.46 | 0.46 | 0.46 | 0.46 |

Table 5.9 Truck factors from rutting analysis

| Truck | Truck No. | Total Wt.(kips) | Truck Factor |
|---|---|---|---|
| 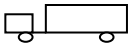 | 1 | *33.4* | 2.34 |
| 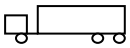 | 2 | *47.4* | 2.79 |
| 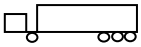 | 3 | *54.4* | 2.63 |
| 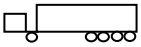 | 4 | *67.4* | 3.06 |
| 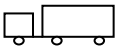 | 5 | *51.4* | 3.98 |
| 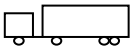 | 6 | *65.4* | 4.43 |
|  | 7 | *87.4* | 7.27 |
| 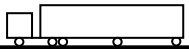 | 8 | *83.4* | 6.08 |
| 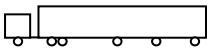 | 9 | *101.4* | 7.72 |
| 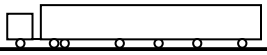 | 10 | *119.4* | 9.37 |
| 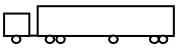 | 11 | *91.4* | 5.96 |
| 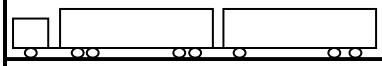 | 12 | *117.4* | 7.48 |
| 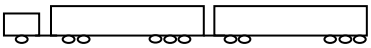 | 13 | *151.4* | 8.18 |
| 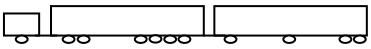 | 14 | *161.4* | 9.97 |
| 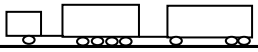 | 15 | *117.4* | 6.80 |
| 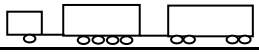 | 16 | *125.4* | 6.68 |
| 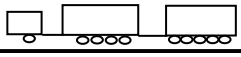 | 17 | *132.4* | 5.86 |
| 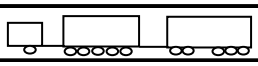 | 18 | *143.4* | 7.02 |
| 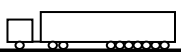 | 19 | *138.4* | 6.29 |
|  | 20 | *151.4* | 6.65 |
| 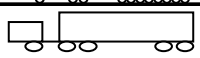 | 21 | *79.4* | 4.88 |

*5.6.3.3 TF from Laboratory AF and AASHTO LEF*

In this analysis, TF's were calculated by multiplying the AF values obtained from the laboratory (Figure 5.13) with the Load Equivalency Factor (LEF) from AASHTO corresponding to the single axle at the legal load limit. This was done for different pavement cross-sections varying in AC layer thickness and modulus. Table 5.10 summarizes the results.

Table 5.10 Truck Factors from Laboratory AF and AASHTO LEF

| | | | Truck Factors | | | | | |
|---|---|---|---|---|---|---|---|---|
| | | | Eac = 350 ksi | | | Eac = 700 ksi | | |
| Truck | Truck No. | Total Wt. | 3.5 in | 8 in | 12 in | 3.5 in | 8 in | 12 in |
|  | 1 | *33.4* | 1.533 | 1.507 | 1.499 | 1.524 | 1.501 | 1.497 |
|  | 2 | *47.4* | 1.523 | 1.459 | 1.440 | 1.501 | 1.445 | 1.434 |
|  | 3 | *54.4* | 1.082 | 1.009 | 0.989 | 1.057 | 0.995 | 0.983 |
|  | 4 | *67.4* | 1.198 | 1.115 | 1.092 | 1.169 | 1.099 | 1.085 |
|  | 5 | *51.4* | 2.533 | 2.507 | 2.499 | 2.524 | 2.501 | 2.497 |
|  | 6 | *65.4* | 2.523 | 2.459 | 2.440 | 2.501 | 2.445 | 2.434 |
| 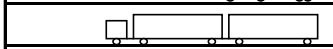 | 7 | *87.4* | 4.533 | 4.507 | 4.499 | 4.524 | 4.501 | 4.497 |
|  | 8 | *83.4* | 3.523 | 3.459 | 3.440 | 3.501 | 3.445 | 3.434 |
|  | 9 | *101.4* | 4.523 | 4.459 | 4.440 | 4.501 | 4.445 | 4.434 |
| 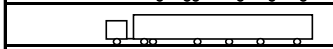 | 10 | *119.4* | 5.523 | 5.459 | 5.440 | 5.501 | 5.445 | 5.434 |
| 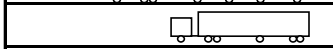 | 11 | *91.4* | 2.942 | 2.843 | 2.815 | 2.908 | 2.823 | 2.805 |
| 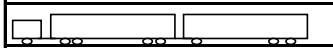 | 12 | *117.4* | 3.362 | 3.227 | 3.189 | 3.316 | 3.200 | 3.176 |
| 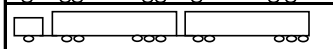 | 13 | *151.4* | 3.041 | 2.848 | 2.795 | 2.974 | 2.810 | 2.777 |
| 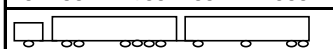 | 14 | *161.4* | 4.607 | 4.451 | 4.408 | 4.553 | 4.420 | 4.393 |
| 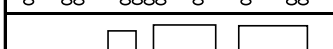 | 15 | *117.4* | 3.188 | 3.067 | 3.034 | 3.146 | 3.043 | 3.022 |
| 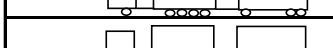 | 16 | *125.4* | 2.607 | 2.451 | 2.408 | 2.553 | 2.420 | 2.393 |
| 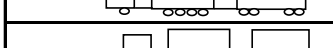 | 17 | *132.4* | 1.969 | 1.821 | 1.781 | 1.917 | 1.792 | 1.767 |
| 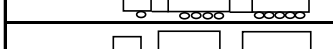 | 18 | *143.4* | 2.711 | 2.542 | 2.496 | 2.652 | 2.509 | 2.480 |
|  | 19 | *138.4* | 2.487 | 2.341 | 2.300 | 2.436 | 2.312 | 2.287 |
| 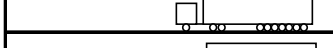 | 20 | *151.4* | 2.576 | 2.423 | 2.380 | 2.523 | 2.392 | 2.366 |
| 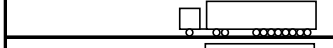 | 21 | *79.4* | 2.513 | 2.411 | 2.381 | 2.479 | 2.390 | 2.371 |

## 5.7 PERMANENT DEFORMATION DAMAGE CURVES

Several permanent deformation damage curves were developed in this study based on: (1) last peak strain, (2) dissipated energy, (3) strain area, and (4) S-N rutting curves. The data from which these rutting damage model curves are calculated are represented in Table 5.11.

### 5.7.1 Last Peak Strain Curve

Strain-based damage curves are the most used curves for asphalt concrete. In this study, the uniaxial compression cyclic load test runs in a stress controlled mode. When testing specimens under a multi axle configuration, it was noticed that the strain peak value increased significantly from the first peak, to the subsequent peaks. The last peak strain has the advantage of representing and identifying the tested axle group or truck as shown in Figure 5.20. The last peaks of the initial strains pulses were plotted versus the number of load repetitions to failure. A strain-based rutting curve was generated based on the last strain peak of the initial cycles for all tested axles and truck configurations, as shown in Figure 5.21. The resulting last peak strain of the initial cycles can characterize the axle or truck configuration which overcomes the need for a separate rutting curve for each axle configuration. When considering the last peak strain instead of the first, the number of axles and their spacing is taken into account leading to a unique curve for different axle groups. All the different axle and truck configurations with the different interaction and stress levels are presented in Figure 5.21. Therefore, using this strain-based rutting curve allows for determining the number of repetitions until failure for any axle and truck configuration in one step, without the need to conduct testing until the total failure of the sample.

The last peak strain rutting damage model is as follows:

$$N_f = 0.00027\varepsilon_o^{-2.398} \tag{5.10}$$

where:

$\varepsilon_o$ = is the last peak strain of the initial cycle, and

$N_f$ = is the number of cycles to failure.

The developed strain-based rutting equation can be used to calculate the axle or truck factor as follows:

$$AF \text{ or } TF = \frac{\text{Damage of axle or truck}}{\text{Damage of the single axle}} = \frac{N_{f\ \text{single axle}}}{N_{f\ \text{axle or truck}}} = \left( \frac{\varepsilon_{o\text{single axle}}}{\varepsilon_{o\text{axle or truck}}} \right)^{2.398} \tag{5.11}$$

Table 5.11 Experimental test results

| Axle configurations | # of Axles | Interaction level | Stress* level | AV % | Flow number ($N_f$) | IDE, psi | Last Peak Strain ($\varepsilon_o$) | Initial strain area |
|---|---|---|---|---|---|---|---|---|
| 1-axles | 1 | NA | H | 4.2 | 6000 | 0.02572 | 0.00092 | 0.00025 |
| 1-axles | 1 | | | 4.07 | 5750 | 0.02715 | 0.00092 | 0.00025 |
| 2-axles | 2 | 25% | | 4.2 | 2750 | 0.04182 | 0.00118 | 0.00055 |
| 3-axles | 3 | | | 4.19 | 2250 | 0.04950 | 0.00114 | 0.00109 |
| 4-axles | 4 | | | 4.23 | 1750 | 0.06223 | 0.00148 | 0.00145 |
| 8-axles | 8 | | | 4.23 | 800 | 0.09877 | 0.00199 | 0.00415 |
| 2-axles | 2 | | | 4.35 | 2750 | 0.04486 | 0.00130 | 0.00068 |
| 3-axles | 3 | | | 4.36 | 2250 | 0.05594 | 0.00146 | 0.00112 |
| 4-axles | 4 | | | 4.38 | 1375 | 0.06852 | 0.00183 | 0.00190 |
| 8-axles | 8 | | | 4.39 | 875 | 0.09904 | 0.00203 | 0.00432 |
| 2-axles | 2 | 75% | | 4.1 | 3125 | 0.04836 | 0.00144 | 0.00078 |
| 3-axles | 3 | | | 4.11 | 2250 | 0.05550 | 0.00162 | 0.00128 |
| 4-axles | 4 | | | 4.11 | 1500 | 0.06374 | 0.00188 | 0.00191 |
| 8-axles | 8 | | | 4.12 | 750 | 0.07804 | 0.00205 | 0.00409 |
| 2-axles | 2 | | | 4.3 | 3375 | 0.04305 | 0.00127 | 0.00066 |
| 3-axles | 3 | | | 4.3 | 1875 | 0.05999 | 0.00175 | 0.00139 |
| 4-axles | 4 | | | 4.31 | 1624 | 0.06465 | 0.00182 | 0.00196 |
| 8-axles | 8 | | | 4.31 | 917 | 0.08345 | 0.00227 | 0.00484 |
| 1-axle | 1 | NA | L | 4.49 | 74500 | 0.00301 | 0.00028 | 0.00004 |
| 1-axle | 1 | | | 4.5 | 57500 | 0.00351 | 0.00038 | 0.00008 |
| 1-axle | 1 | | M | 4.4 | 13500 | 0.01267 | 0.00063 | 0.00017 |
| 1-axle | 1 | | | 4.5 | 10500 | 0.01420 | 0.00072 | 0.00020 |
| 1-axle | 1 | | | 4.45 | 7500 | 0.01349 | 0.00067 | 0.00016 |
| 3-axle | 3 | 0% | | 4.17 | 4500 | 0.02887 | 0.00098 | 0.00089 |
| 3-axle | 3 | | | 4.17 | 3125 | 0.03050 | 0.00097 | 0.00075 |
| 3-axle | 3 | | L | 4.16 | 25000 | 0.00708 | 0.00049 | 0.00043 |
| 3-axle | 3 | | | 4.14 | 19750 | 0.00773 | 0.00052 | 0.00046 |
| Truck S1T2 | 5 | | H | 4.08 | 933 | 0.11798 | 0.00190 | 0.00662 |
| Truck S1T2 | 5 | | | 4.09 | 883 | 0.11086 | 0.00182 | 0.00629 |
| Truck S5 | 5 | | | 4.1 | 800 | 0.11807 | 0.00180 | 0.00495 |
| Truck S5 | 5 | | | 4.1 | 750 | 0.14000 | 0.00162 | 0.00415 |
| Truck S5 | 5 | | | 4.26 | 750 | 0.12449 | 0.00173 | 0.00916 |
| Truck S1T2Tr2 | 11 | | | 3.91 | 450 | 0.21985 | 0.00226 | 0.03430 |
| Truck S1T2Tr2 | 11 | | | 3.99 | 425 | 0.22077 | 0.00257 | 0.01756 |
| Truck S1T1E1 | 11 | | | 4.01 | 575 | 0.18627 | 0.00208 | 0.01106 |
| Truck S1T1E1 | 11 | | | 4.03 | 550 | 0.18959 | 0.00230 | 0.01281 |
| Truck S3T2Q1 | 11 | | | 4.05 | 411 | 0.22742 | 0.00189 | 0.01573 |
| Truck S3T2Q1 | 11 | | | 4.07 | 434 | 0.21491 | 0.00176 | 0.01441 |

* Stress level: H =87.88 psi, M = 60.13psi, L = 32.38 psi

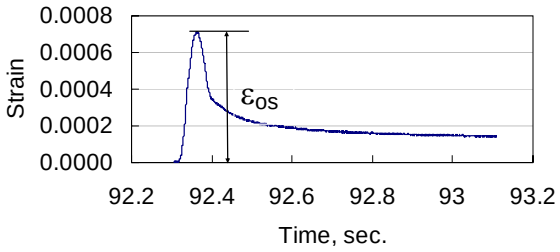


(a) single axle

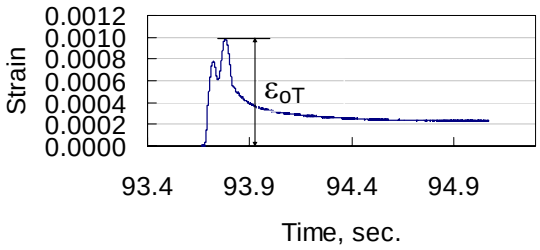


(b) Tandem axle

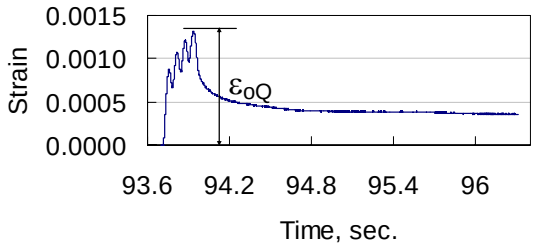


(c) Quad axle

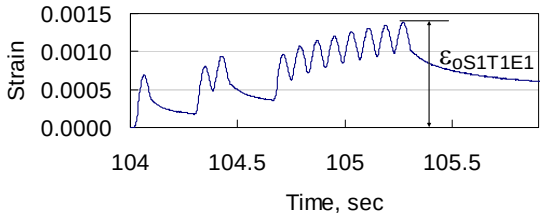


(d) Truck S1T1E1

Figure 5.20 Examples of the last peak of the initial strain pulse

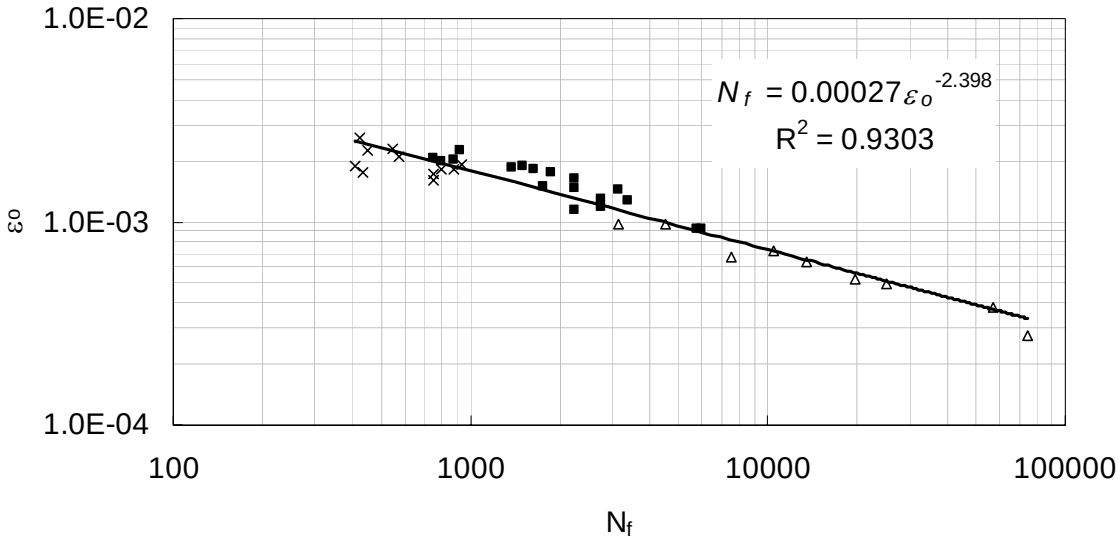


- Individual axles (S, T, Tr, Q, E) - 25% and 75% Interaction - High stress level
- Single and tridem (0% interaction) axles-Low and Medium stress level
- Trucks - 0% interaction - High stress level

Figure 5.21 Last peak strain rutting curve

### 5.7.2 Dissipated Energy-Based Curve

The dissipated energy (area within the stress-strain relationship) was calculated for all tested samples as well as the number of cycles to failure (as mentioned earlier, Figure 5.9). Figure 5.22 shows an example of the relationship between the dissipated energy and number of cycles. For the dissipated energy rutting damage curve, the initial dissipated energy density is plotted versus the number of load repetitions to failure. Figure 5.23 shows the dissipated energy rutting curve (for all individual axles, trucks, and individual axles and different stress levels).

Similar to the last peak strain rutting curve, the dissipated energy-based curve is unique. All the different axle and truck configurations with the different interaction and stress levels are presented. Therefore, using this rutting curve would allow for determining the number of repetitions until failure for any axle and truck configuration without conducting testing a sample to failure. In fact, considering the stronger correlation between *IDE* and $N_f$, this may be a more precise model for predictive purposes. Yet, the application of the dissipated energy model in mechanistic analyses would require visco-elastic analysis, which is limited by existing software (especially for larger axle groups). The dissipated energy rutting damage model is as follows.

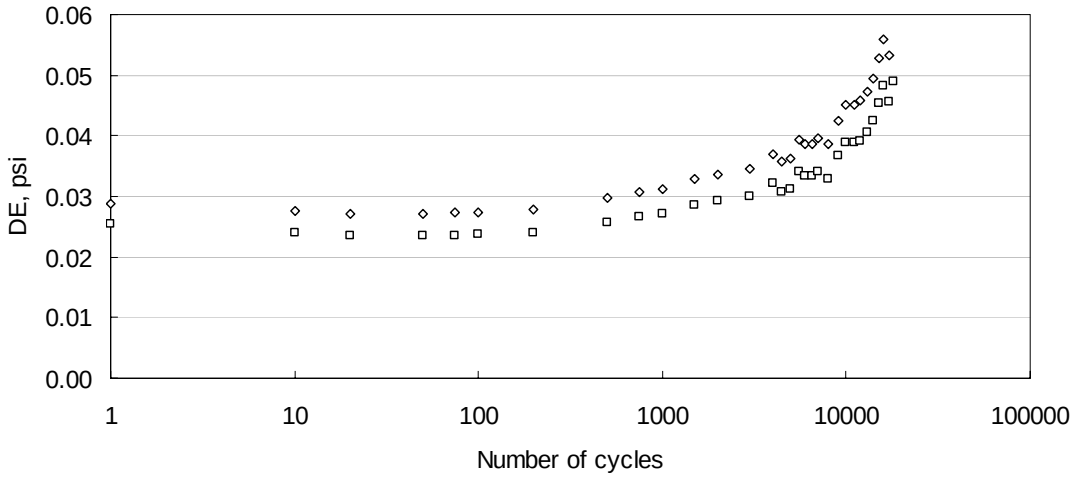


Figure 5.22 Example of Dissipated energy versus number of load repetitions for one sample (two LVDT)

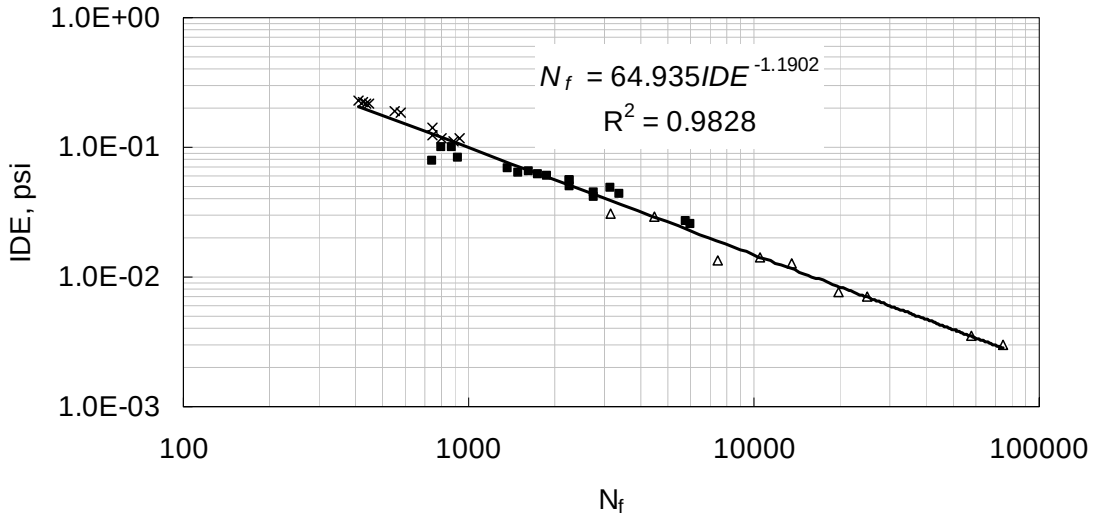


Figure 5.23 Dissipated energy-based rutting damage curve

$$N_f = 64.935 \quad IDE^{-1.1902} \tag{5.12}$$

where:

$IDE$ = is the initial dissipated energy density in psi of the whole axle or truck group, and

$N_f$ = is the number of cycles to failure.

Equation 5.12 can be used to calculate the axle or truck factors as follow:

$$AF \text{ or } TF = \frac{\text{Damage of axle or truck}}{\text{Damage of the single axle}} = \frac{N_{f\ \text{single axle}}}{N_{f\ \text{axle or truck}}} = \left( \frac{IDE_{\text{single axle}}}{IDE_{\text{axle or truck}}} \right)^{1.19} \tag{5.13}$$

### 5.7.3 Strain Area-Based Curve

The area under the initial strain curves (Figure 5.20) were calculated for all tested axle and truck configurations as well as different stress levels, and plotted against the number of cycles to failure, as shown in Figure 5.24. The strain area-based rutting damage model obtained from this procedure is as given by equation 5.14.

$$N_f = 14.857\ A_o^{-0.777} \tag{5.14}$$

where:

$A_o$ = is the initial area under the strain curve, and

$N_f$ = Number of cycles to failure.

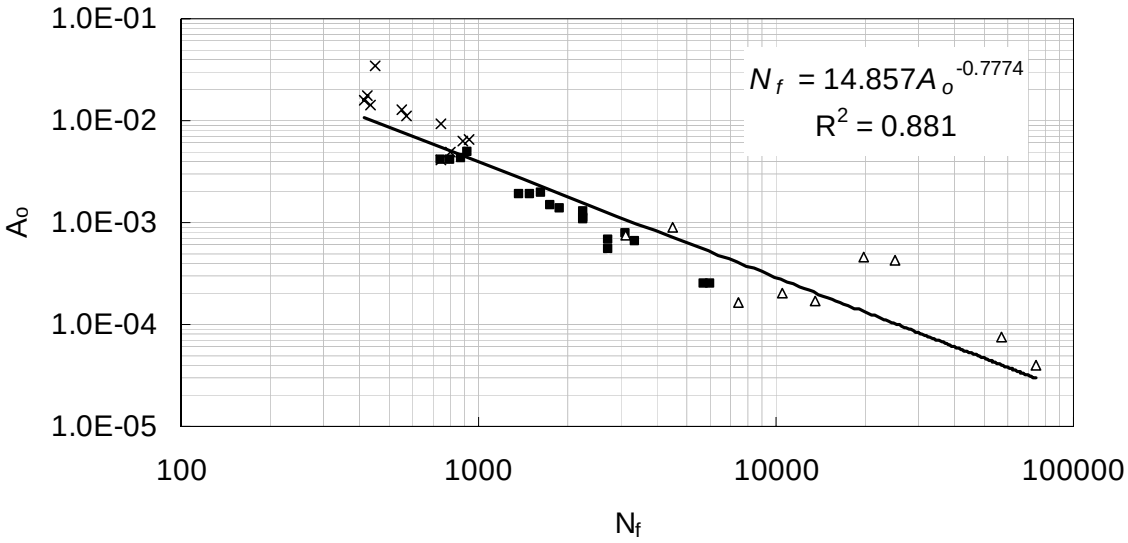


Figure 5.24 Strain area-based rutting damage curve

Axle and truck factors can be calculated using the area-based rutting damage as follows:

$$AF \text{ or } TF = \frac{\text{Damage of axle or truck}}{\text{Damage of the single axle}} = \frac{N_{f\ \text{single axle}}}{N_{f\ \text{axle or truck}}} = \left( \frac{A_{o\text{single axle}}}{A_{o\text{axle or truck}}} \right)^{0.777} \tag{5.15}$$

The dissipated energy method and the strain area method are recommended for estimating pavement rutting damage, rather than the last peak strain method. This is simply because the initial last peak strain in the laboratory includes not only the effect of the individual axle load, but also the sample's "memory" of previous axle loads within an axle group. Since all peaks are of equal strain value in a mechanistic analysis, especially when elasticity of the pavement system is assumed, a mechanistic application of this method can not adequately represent the system's response to an entire axle group. Since rutting damage depends not only on the discrete strain value, but also the duration of the

pulse, the additional advantage of the dissipated energy and strain area methods is that both utilize a more complete representation of the values and duration of the axle group response.

### 5.7.4 Stress-Based Curve

All axles and trucks were tested at high stress level except for single and tridem axles; these were additionally tested at medium and low stress levels. Figure 5.25 shows the relationship between the stress levels (H = 87.88 psi, M = 60.13 psi, L = 32.38 psi) and the number of cycles to failure. The results show that the two relationships for single and tridem are approximately parallel (slope of single = -2.45 and slope of tridem = -2.35) with an average factor of 2.7 for high stress level, 3.2 for medium stress level, and 2.9 for low stress level (overall 2.9) between them. These results confirm the proportionality, even at different stress levels, of rut damage with respect to axle gross weight.

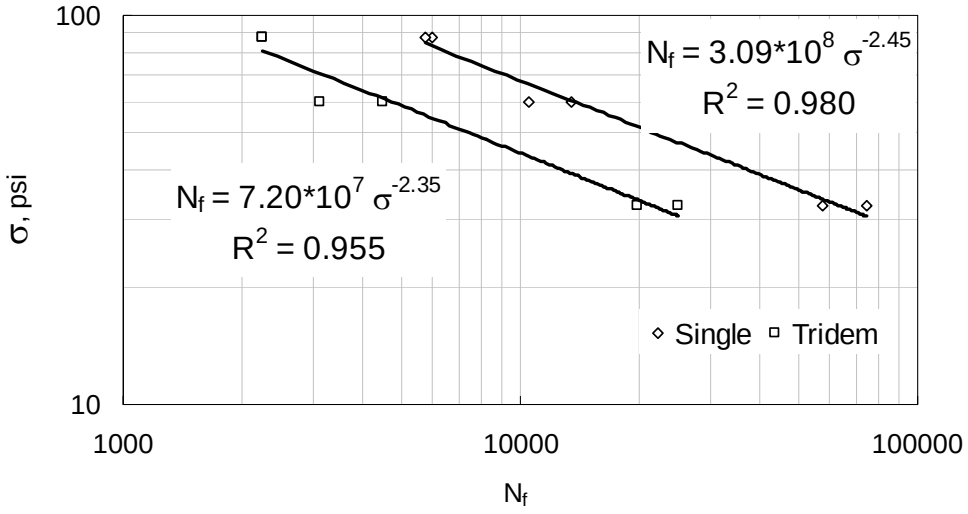


Figure 5.25 Stress level versus number of cycles to failure (S-N curve) for single and tridem axles

## 5.8 CALIBRATION OF PERMANENT DEFORMATION DAMAGE MODELS

Characterizing the flexible pavement damage caused by multiple axle loads requires quantification and summation of the pavement responses. Two different approaches can be used: (1) discrete methods (Hajek and Agarwal, 1990) and (2) integration (Hajek and Agarwal, 1990) or strain rate methods (Govind, 1988). The discrete methods are applicable only for single pulses, so when it comes to multiple axles their usefulness is debated within the research community since most do not account for

the pavement response rate due to the passage of multiple axles. On the other hand, the integration method proposed with an arbitrary exponent, $n_i$, is incompatible with the other methods. Similarly, the strain rate method was developed for fatigue damage and there is not enough information to apply it to rutting damage. In this research, axle factors for pavement rutting due to multiple axle pulses were developed in the laboratory using Uniaxial Compression Cyclic Load Tests (UCCLT). These axle factor were used to facilitate the calibration of all of these methods in order to determine a suitable exponent for each.

### 5.8.1 Peak Method

This method was developed and used mainly for the mechanistic analysis of asphalt pavement fatigue. This method relates the damage of single or multiple axles and truck configurations to the damage of a standard axle based on peak strains (Figure 5.26) as follows:

$$AF \text{ or } TF = \frac{\text{Damage of axle or truck}}{\text{Damage of the standard axle}} = \frac{N_{f\ \text{std.}}}{N_{f\ \text{axle or truck}}} = \sum_{i=1}^{m} \left( \frac{\varepsilon_{std}}{\varepsilon_i} \right)^{n_p} \qquad (5.16)$$

where:

$\varepsilon_{std}$ = peak strain caused by the standard axle,
$\varepsilon_i$ = peak strain from multiple axle or truck,
$M$ = number of axles in an axle group or truck, and
$n_p$ = the exponent of the peak method.
$N_f$ = number of cycles to failure

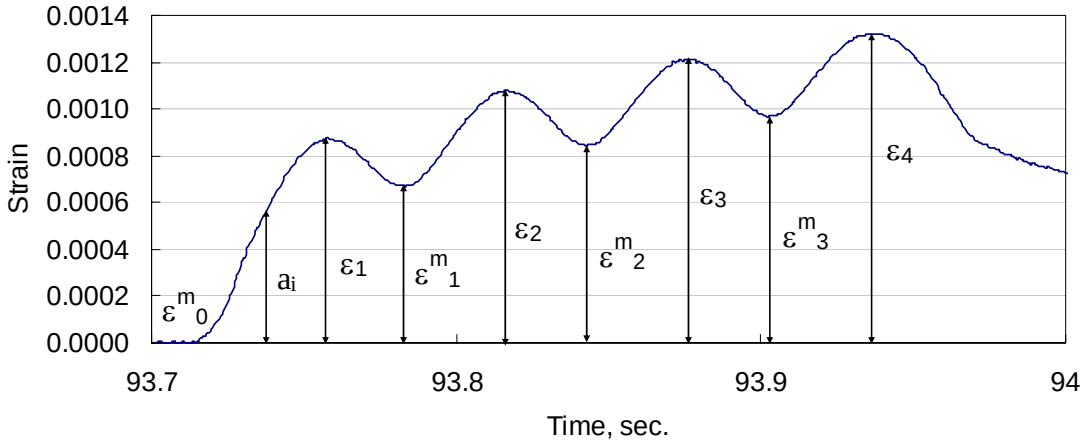


Figure 5.26 Peak and peak midway strain for 4-axle group

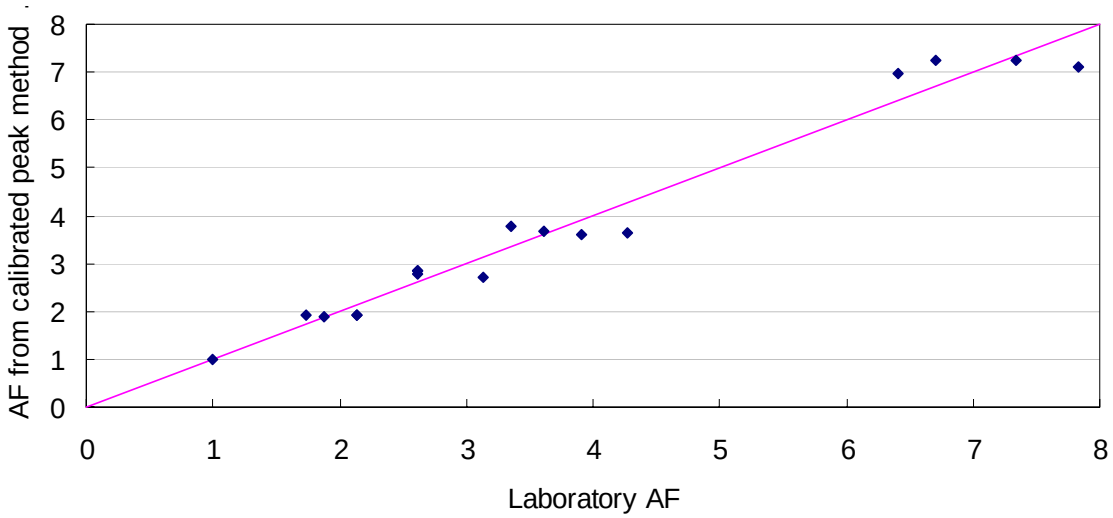


Figure 5.27 Axle factor from calibrated peak method versus laboratory axle factor

This method is calibrated by assuming an arbitrary exponent, $n_p$, and minimizing the sum of the square error between the predicted and the laboratory axle factor using Excel solver. The calibrated exponent ($n_p$) was 0.2061 with a square error sum of 2.279. Figure 5.27 shows the axle factor from the calibrated peak method versus laboratory axle factor for different axle configurations.

### 5.8.2 Peak-Midway Method

Similar to the peak method, the peak-midway strain method was developed and used mainly for the mechanistic analysis of asphalt concrete fatigue. This method relates the first peak and the subsequent valley-to-peak difference (Figure 5.26) to the peak of a standard axle raised to the exponent, $n_{p\text{-}m}$, as follows.

$$AF \text{ or } TF = \frac{\text{Damage of axle or truck}}{\text{Damage of the standard axle}} = \frac{N_f \text{ std.}}{N_f \text{ axle or truck}} = \sum_{i=1}^{p} \left( \frac{\varepsilon_{std}}{\varepsilon_i - \varepsilon^m_{i-1}} \right)^{n_{p-m}} \quad (5.17)$$

where:

$\varepsilon_{std}$ = peak strain of the standard axle,
$\varepsilon_i$ = peak strain of multiple axle or truck,
$\varepsilon^m$ = midway strain,
$P$ = number of axles in an axle group or truck, and
$n_{p\text{-}m}$ = the exponent of the peak-midway method.
$N_f$ = number of cycles to failure

The peak-midway method was calibrated using the laboratory axle factor values to determine the exponent for rutting damage. The calibrated exponent ($n_{p\text{-}m}$) was -0.1069 with a square error sum of 2.47. Figure 5.28 shows the axle factor of the calibrated peak-midway method versus the laboratory axle factor values for different axle configurations.

Both peak and peak-midway methods do not take into account the duration of the strain pulse since both consider the discrete values of the peak or peak and midway strains. However, rutting damage is highly influenced not only by the strain value but also by the duration of the loading pulse. Therefore, the integration and strain rate methods are examined in the following sections.

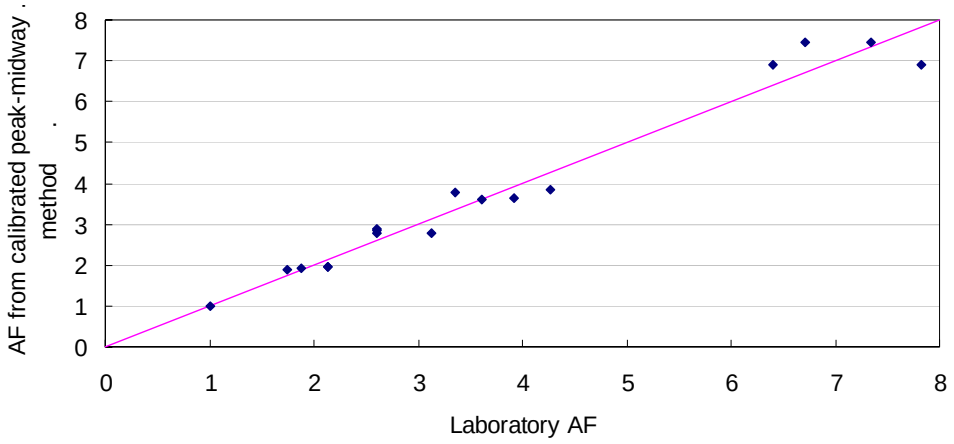


Figure 5.28 Axle factor from calibrated peak-midway method versus laboratory axle factor values

### 5.8.3 Integration Method

The integration method was proposed by Hajek and Agarwal, 1990. Even though the method takes into account both the magnitude and duration of the pavement response due to multiple axles, the arbitrary nature of the exponent, $n_i$, makes it incompatible with the other methods. The developed laboratory axle factors facilitate the calibration of this method, and allow for an empirical determination of a suitable exponent. The axle and truck factor can be calculated from the integration method as follows:

$$AF \text{ or } TF = \frac{N_{f\ \text{std.}}}{N_{f\ \text{axle or truck}}} = \frac{\int_0^t \left| a_i^{n_i} \right| dt}{\int_0^t \left| a_s^{n_i} \right| dt} \tag{5.18}$$

where:

$a_i$ = the strain values of an axle or truck within the strain time history as shown in Figure 5.26,

$a_s$ = the strain values of standard axle within the strain time history,

$t$ = time if the strain is expressed in the time domain and distance if the strain is expressed in the space domain,

$n_i$ = is the integration method exponent, and

$N_f$ = number of cycles to failure.

The calibrated exponent for this rutting-oriented application of the integration method is 0.1303, compared to 3.8 for the fatigue discrete methods (peak and peak-midway). The square error sum is 2.387. This large difference can be explained by the following observations.

- The previous exponent (3.8) was not calibrated for the integration method; it was borrowed from the discrete methods.
- The previous exponent (3.8) was based on fatigue, which has a fundamentally different failure mechanism than rutting (0.1303).
- The exponent in the integration method is inside the integrand, which is expected to require, even for fatigue, a dramatically different value due to its location in the equation. Therefore, the usual "power law" explanation does not apply when the exponent is within an integration.

The resulting exponent offers a promising solution to the problem of multi-axle damage prediction, since the integration method accounts for not only the peak values but also for the duration of the strain pulse. Figure 5.29 shows the relationship between the axle factors of the calibrated integration method versus the laboratory axle factor values.

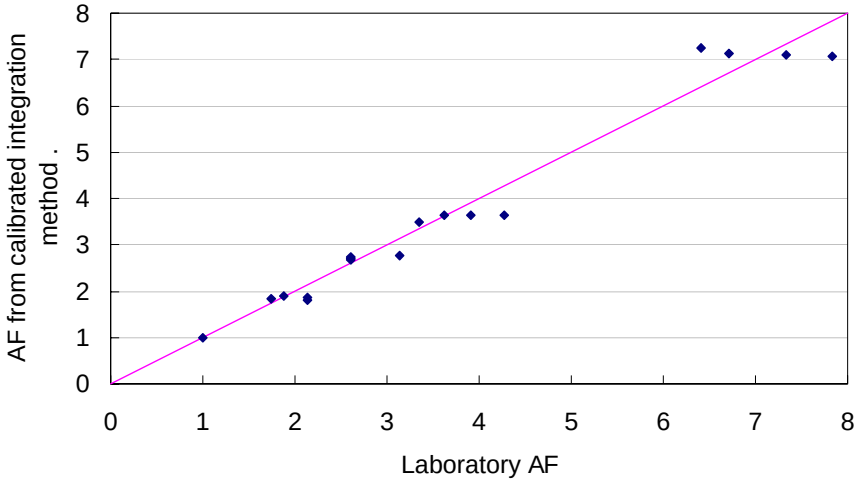


Figure 5.29 Axle factor from the integration method versus laboratory axle factor values

### 5.8.4 Strain Rate Method

The strain rate method was developed to determine the damage transform from stress fields as shown in Equation 5.19 (Govind, 1988). The method was developed for fatigue and calibrated using AASHO road test data. The calibration has an excellent agreement with the AASHTO load equivalency factors. The strain rate method is adapted in this study to the strain field as shown in Equation 5.20. Figure 5.30 depicts the elements of the strain rate method.

$$\sum_{i=1}^{m} D_i^{\,n} = \sum_{i=1}^{m} \left( \frac{1}{t_{i+1} - t_i} \int_{t_j}^{t_{j+1}} \left| \frac{d\sigma}{dt} \right| dt \right)^n \tag{5.19}$$

$$AF \text{ or } TF = \frac{\text{Damage of axle group or truck}}{\text{Damage of single axle}} = \frac{N_{f\ \text{std.}}}{N_{f\ \text{axle or truck}}}$$

$$= \frac{\sum_{i=1}^{m} \left( \frac{1}{t_{i+1} - t_i} \sum_{j=1}^{p} \left| \varepsilon_{j+1} - \varepsilon_j \right| \right)^{n_{s-r}}}{\left( \frac{1}{t_1 - t_0} \sum_{j=1}^{p} \left| \varepsilon_{j+1} - \varepsilon_j \right| \right)^{n_{s-r}}} \tag{5.20}$$

where:

$m$ = number of axles (sub-event),

$p$ = number of discrete points within one sub-event,

$t_o$ = the starting time of the sub-event,

$t_1$ = the ending time of the sub-event 1 and starting time for sub-event 2, and

$\varepsilon$ = the discrete strain values within the sub-event, and

$n_{s\text{-}r}$ = is the exponent for the strain rate method.

$N_f$ = number of cycles to failure

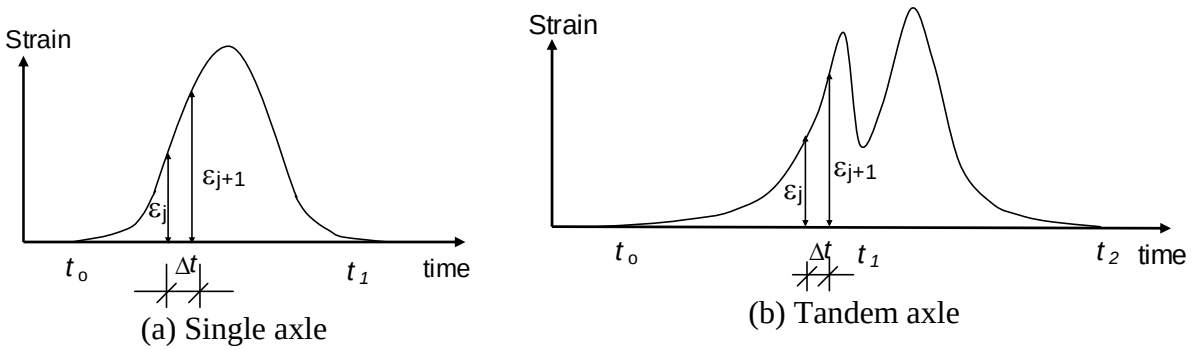


Figure 5.30 Depiction of variables from strain rate method

The laboratory axle factor facilitates the calibration of the strain rate method. Similar to the integration method, the strain rate method is calibrated by iteration of the square error sum minimization process. Due to its computational complexity, an iterative approach was used to minimize the difference between the axle factor of the strain rate method and the laboratory axle factor values by changing the exponent $n_{s\text{-}r}$. The calibrated exponent, $n_{s\text{-}r}$, of the strain rate method is 0.8625 with square error sum of 9.032. Figure 5.31 shows the relationship between the calibrated strain rate method axle factors and the laboratory axle factor values.

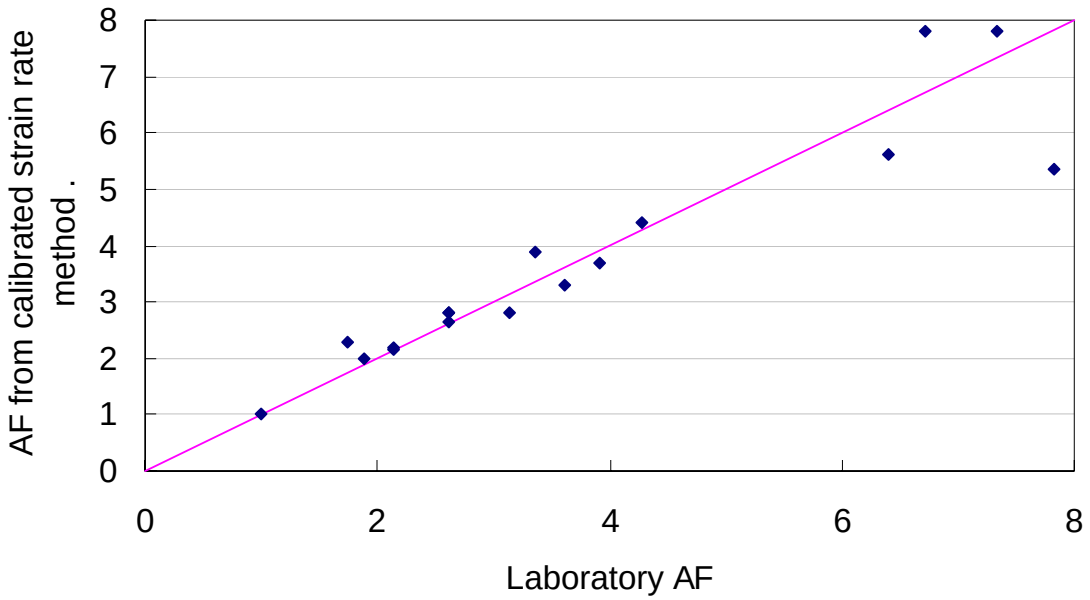


Figure 5.31 Axle factor from strain rate method versus laboratory axle factor values

Figure 5.32 summarizes the exponents and the square error sum of all developed rutting damage models and the calibrated methods.

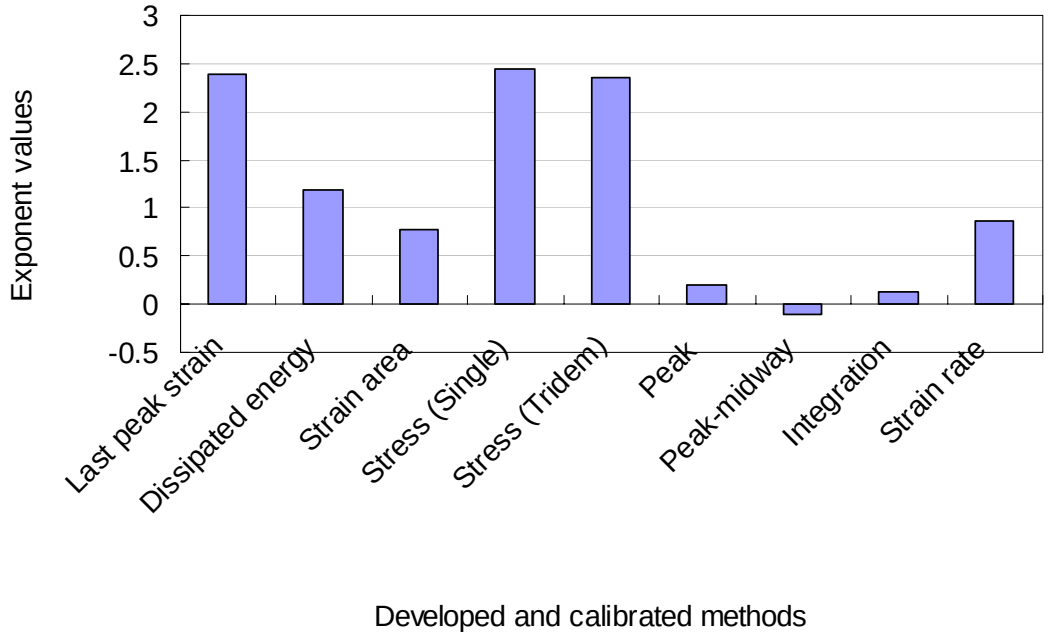


Figure 5.32 Summary of the developed and calibrated rutting damage methods

The last peak initial strain, strain area, and dissipated energy methods were calibrated for the laboratory axle factor values, and their exponent values (*n*'s) were approximately the same as each of the power corresponding to their individual permanent deformation damage curves (section 5.7). The relatively close agreement between these two strategies for calculating each method's *n* value is evidence of consistency in the calibration procedure. However, the exponent of each permanent deformation damage curve is more reliable, since it is based on a larger, more diverse data set, containing not only all axle configurations but also the truck configurations and stress levels.

## 5.9 PREDICTION OF PERMANENT STRAIN

It is well known that permanent deformation, whether in the field or in the laboratory, obeys a fractional-power relationship ($0<\alpha<1$); however when a laboratory sample reaches the tertiary zone (failure) this relationship no longer applies ($\alpha>1$). Therefore, the permanent deformation power function within the first two zones can be expressed as shown in equation 5.21.

$$\frac{\varepsilon_p}{\varepsilon_r} = \mu N^{\alpha} \tag{5.21}$$

where:

$\varepsilon_p$ = accumulated permanent strain,

$\varepsilon_r$ = resilient strain,

$\mu$ = permanent deformation parameter representing the constant of proportionality between plastic and elastic strain,

$\alpha$ = permanent deformation parameter indicating the rate of decrease in permanent deformation as the number of load applications increases, and

$N$ = the number of load applications.

The cumulated vertical permanent strains were normalized with the value of the initial last peak strain (as shown in Figure 5.20). As mentioned earlier, the last peak strain has the advantage of representing and uniquely identifying the tested axle group or truck. The normalized accumulated permanent strains with the values of the initial last peak strain were plotted against the number of load repetitions within the primary and secondary zones only, as shown in Figure 5.34. The figure shows samples of the μ and α values for three different axle configurations and one truck configuration. It should be noted that the initial last peak strain from the laboratory includes the resilient, visco-elastic, and the plastic strain.

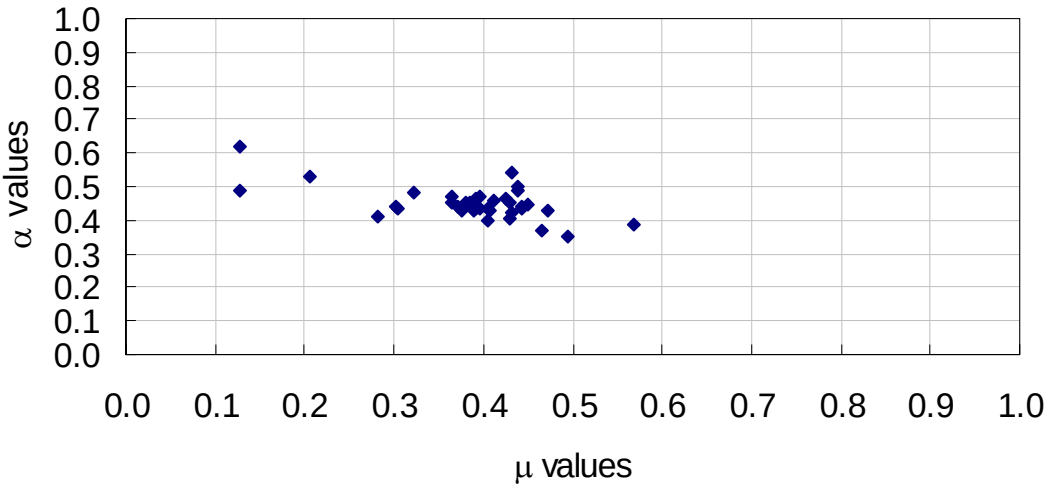


Figure 5.33 Values of μ and α for all tested axle and truck configurations

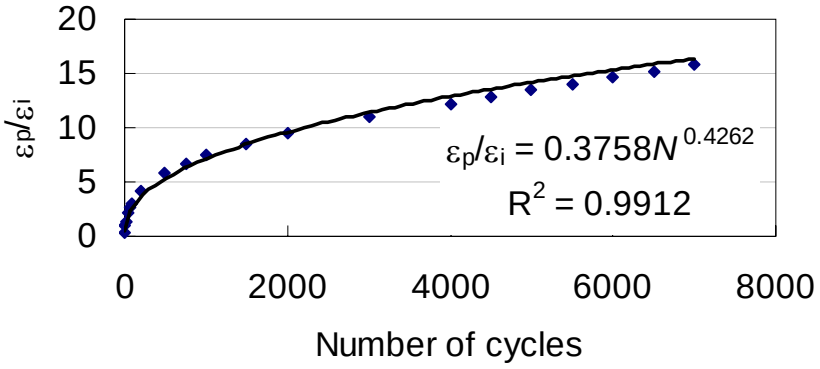


(a) Single axle

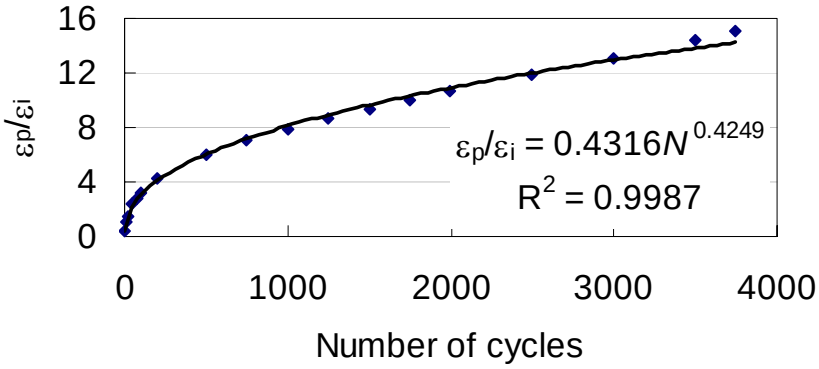


(b) Tandem axle

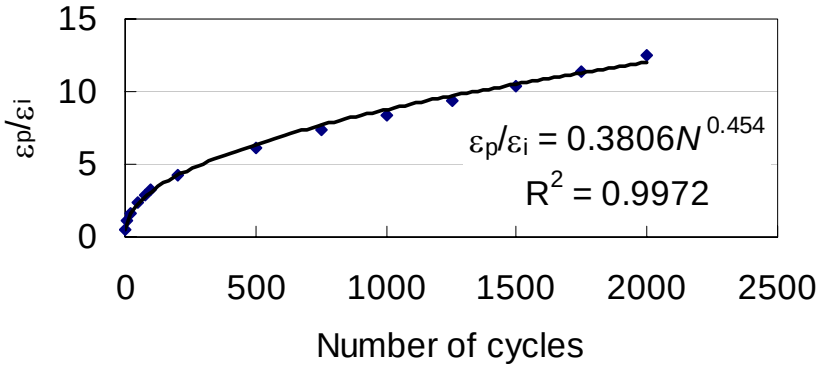


(c) Quad axle

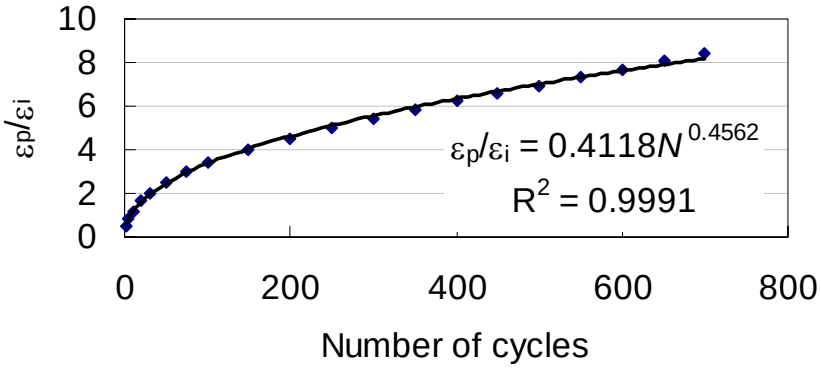


(d) Truck S1T1E1

Figure 5.34 Example of normalized cumulative strain with the initial last peak strain versus number of cycles

The μ and α values for all tested axle and truck configurations were calculated and are displayed in Figure 5.33. As can be seen in the figure the values of α (the rate of change in permanent deformation as the number of load applications increases) cluster tightly in a small range, from 0.35 to 0.61. The values of μ (the proportionality between plastic and elastic strain) cluster more loosely in a wider range, from 0.12 to 0.56. This means that once the sample is compacted and the aggregate is seated, the rate of the accumulated plastic strain, when normalized with its initial strain, will be approximately the same regardless of the load configuration. These results indicate that laboratory samples follow a trend that is consistent with the behavior of field performance, but the predictive power of the laboratory values for α and μ depends upon more detailed calibration from field data. Chapter 4 explains one such method that could be used for field calibration of permanent deformation parameters in further detail.

## 5.10 CONCLUSION

The main achievements of this laboratory experiment are as follows:

- Axle and truck factors for rutting damage were established based on laboratory data.
- Using Miner's rule to calculate the total damage for each truck by summing the damage caused by its constituent axles is dependant on axle configuration.
- Permanent deformation damage curves were developed using empirical data for the following methods: last-peak strain, dissipated energy, strain area, and peak stress.
- Permanent deformation damage models (peak, peak-midway, integration, and strain rate) were calibrated using laboratory axle factor values.
- The need was established for field calibration of permanent deformation parameters for the purpose of rutting prediction.

## 5.11 FUTURE RESEARCH

Though this study successfully accomplished its main goals, there is room to improve and expand knowledge. Future studies may focus on the effect of temperature and percent air void on laboratory axle and truck factors. These test variables, though held constant during this experiment, most likely have significant effects on pavement performance, and are therefore worthy of consideration. Further studies may also investigate the effect of axle group on rutting damage using Miner's rule and develop a nonlinear damage model that takes axle grouping within truck configurations into account. With the diversity of truck configurations on today's highways, this further investigation would be quite useful.

# CHAPTER 6
# RUTTING - MECHANISTIC ANALYSIS

## 6.1 INTRODUCTION

In this chapter, the calibrated mechanistic-empirical rutting model (Chapter 4) as well as laboratory results (Chapter 5) are used to compare mechanistic layer rutting damage for different axle and truck configurations. During the calibration of the VESYS model, an investigation of the contribution of each pavement layer from SPS-1 experiment data showed that, on average, hot mix asphalt concrete (HMA) rutting is 57% of the total, base rutting is 27%, and subgrade rutting is 16% (Figure 4.24). Moreover, the laboratory investigations showed that the axle factors for rutting damage due to different axle configurations follow a trend curve that is slightly below the identity line relating axle factor and the number of axles within an axle group.

The conclusions from the field investigation (Volume I) and the laboratory experiment chapter were further investigated using the mechanistic analysis of axle and truck configuration effects on rutting damage in each individual pavement layer. Since a thick HMA layer will account for a majority of the rutting damage in a pavement system (Chapter 4), and the rutting within such HMA layer is roughly proportional to the number of axles within an axle group (Chapter 5), remaining questions about the effect of axle interaction on the sub-layers are the focus of this chapter. The selection of pavement profiles in this study is designed to further examine the effect of heavy axle trucks on a thick pavement, where there is interaction in the base and subgrade layers (Figure 6.1), and a thin pavement, where there is interaction in the subgrade layer only (Figure 6.2). Table 6.1 shows the layer thicknesses and moduli of the two pavement cross-sections that are used in the mechanistic analysis.

Table 6.1 Pavement cross-sections and moduli

| Cross-section # | HMA | | Base | | Subgrade |
|---|---|---|---|---|---|
| | Thickness, in | Modulus, psi | Thickness, in | Modulus, psi | Modulus, psi |
| 1 | 8 | 450000 | 36 | 30000 | 10000 |
| 2* | 4.1 | 551236 | 8.2 | 55283 | 23205 |

* Section 50113 SPS-1 experiment

## 6.2 FORWARD ANALYSIS

The main goal of this research is to investigate the relative effect of multiple axle and truck configurations on rutting damage. Since there is no available software that can

handle larger than tridem axle groups, the KENLAYER (Huang, 1993) elastic analysis program was used with responses due to larger axle groups being calculated by superposition. As shown previously in Figure 4.8, the vertical compression stress and strain due to standard and single axles at the middle of the HMA, base, and six 40-inch subsequent layers of subgrade were calculated. The standard axle load used in this analysis is 18 kips with a tire pressure of 70 psi, while the single axle load is 13 kips with a tire pressure of 100 psi. For the purposes of consistency, the responses of all multiple axle and truck configurations were compiled from the superposition of the appropriate number of single axles. As an example, Figures 6.1 and 6.2 show the vertical compression strain at the middle of the HMA, base, and six subsequent subgrade (SG) layers due to an 8-axle group for cross-sections number 1 and 2.

## 6.3 RELATIVE COMPARISON OF RUTTING DAMAGE CAUSED BY MULTIPLE AXLES

The calibrated mechanistic-empirical rutting model (Chapter 4), along with the laboratory results (Chapter 5) make it possible to mechanistically compare the resulting rutting damage due to different axle and truck configurations for specific pavement profiles.

### 6.3.1 Calibrated Mechanistic-Empirical Rutting Model

In Chapter 4, The VESYS rutting model was calibrated using field data from the SPS-1 experiment. The calibrated rutting model is utilized in this mechanistic analysis to compare the resulting rutting (HMA, base, and subgrade) from different axle and truck configurations for different pavement profiles (Table 6.1). The calibrated rutting model is as follows:

$$\rho_p = h_{AC}\frac{\mu_{AC}}{1\text{-}\alpha_{AC}}\left(\sum_{i=1}^{K}(n_i)^{1-\alpha_{AC}}\left(\varepsilon_{ei,AC}\right)\right) + h_{base}\frac{\mu_{base}}{1\text{-}\alpha_{base}}\left(\sum_{i=1}^{K}(n_i)^{1-\alpha_{base}}\left(\varepsilon_{ei,base}\right)\right)$$
$$+h_{SG}\frac{\mu_{SG}}{1\text{-}\alpha_{SG}}\left(\sum_{i=1}^{K}(n_i)^{1-\alpha_{SG}}\left(\varepsilon_{ei,SG}\right)\right) \quad (6.1)$$

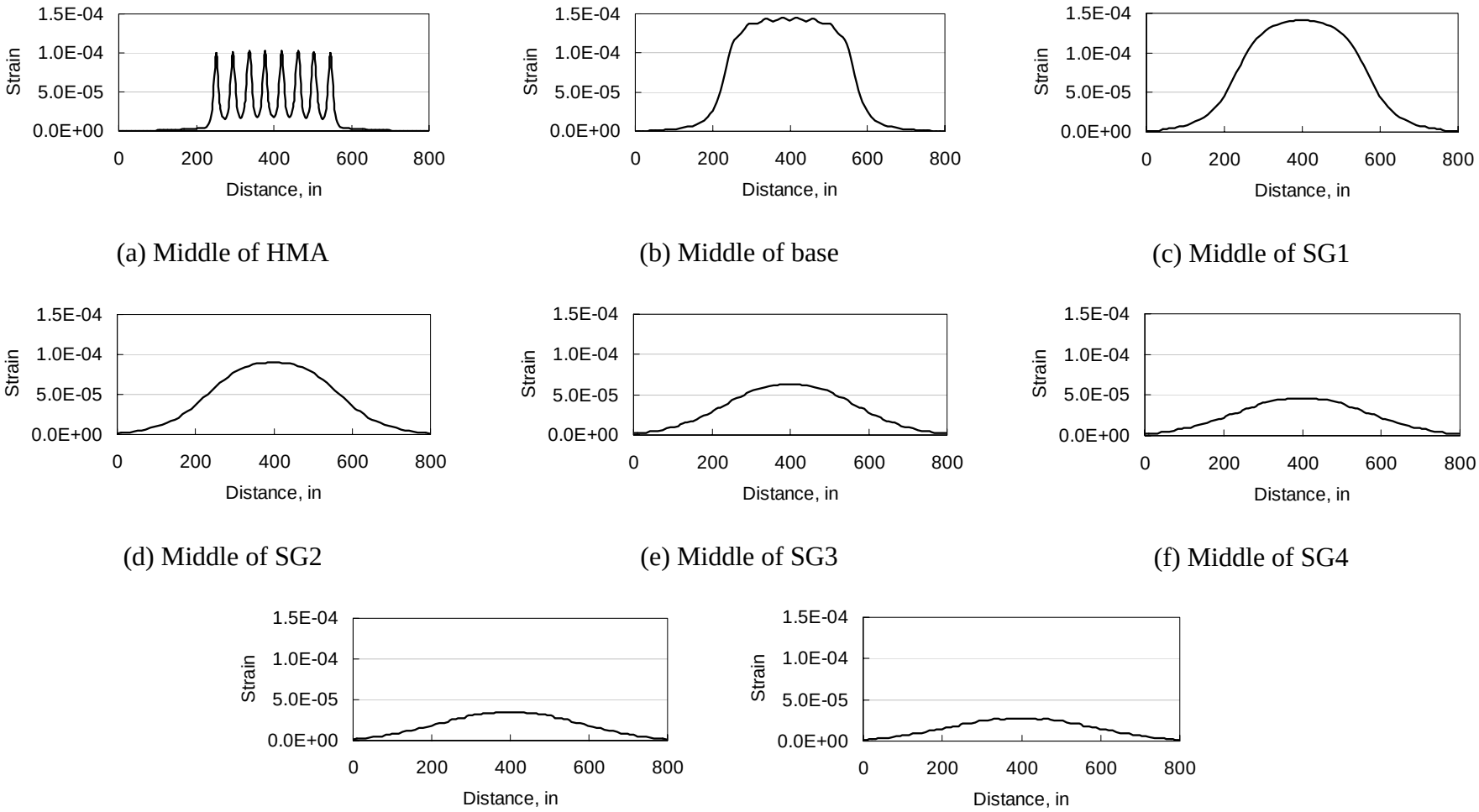


(a) Middle of HMA

(b) Middle of base

(c) Middle of SG1

(d) Middle of SG2

(e) Middle of SG3

(f) Middle of SG4

(g) Middle of SG5

(h) Middle of SG6

Figure 6.1 Vertical compressive strain at the middle of each pavement layer due to an 8-axle group on thick HMA pavement (profile 1)

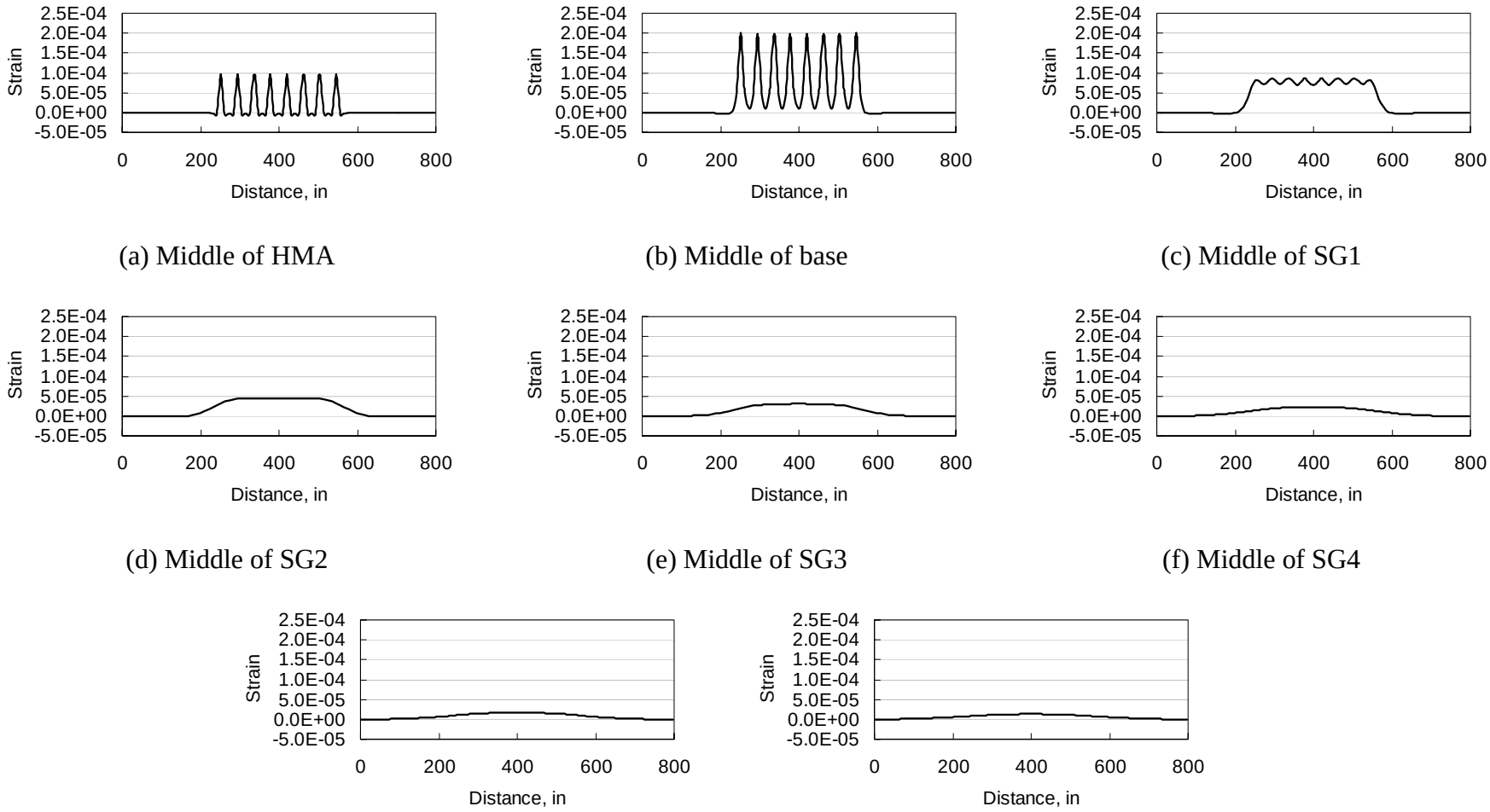


(a) Middle of HMA (b) Middle of base (c) Middle of SG1

(d) Middle of SG2 (e) Middle of SG3 (f) Middle of SG4

(g) Middle of SG5 (h) Middle of SG6

Figure 6.2 Vertical compressive strain at the middle of each pavement layer due to an 8-axle group on thin HMA pavement (profile 2)

where:

$\rho_p$ = total cumulative rut depth (in the same units as the layer thickness),
$i$ = subscript indicating axle group,
$K$ = number of axle group,
$h$ = layer thickness for HMA layer, combined base layer, and subgrade layer, respectively,
$n$ = number of load applications,
$\varepsilon_e$ = compression vertical elastic strain at the middle of the layers,
$\mu$ = permanent deformation parameter representing the constant of proportionality between plastic and elastic strain, and
$\alpha$ = permanent deformation parameter indicating the rate of decrease in rutting as the number of load applications increases.

The permanent deformation parameters for the two cross-sections were calculated from the developed regression equations in Chapter 4 (Equations 4-24, 4-25, 4-27, 4-28, 4-29, and 4-30). It should be noted that the pavement layer thicknesses and moduli shown in Table 6.1 were inputs for these equations, whereas all other variables were assumed at the mean values of the range used to develop the regression equations as shown in Tables 4-10, 4-14, and 4-18. Table 6.2 shows the calculated permanent deformation parameters for these cross-sections.

Table 6.2 Calculated permanent deformation parameters

| | $\alpha_{HMA}$ | $\mu_{HMA}$ | $\alpha_{base}$ | $\mu_{base}$ | $\alpha_{SG}$ | $\mu_{SG}$ |
|---|---|---|---|---|---|---|
| Cross-Section 1 | 0.702 | 0.537 | 0.741 | 0.134 | 0.873 | 0.010 |
| Cross-Section 2 | 0.594 | 0.271 | 0.716 | 0.129 | 0.910 | 0.037 |

As noted in Figure 6.1, the 8-axle responses (vertical compression elastic strain) at the middle of the HMA layer have lower interaction levels, whereas the interaction level increases with depth until the 8-axle response becomes one, wide pulse at deeper sub-layers. To study the effect of the response pulse duration and the interaction on rutting calculation for different axle and truck configurations, the strain value in the calibrated rutting model is employed in two different procedures: 1) sum the rutting damage due to only the strain values underneath each axle within an axle group, and 2) sum the rutting damage due to the strain values underneath the axles (similar to previous) and also include strain values outside the axle group (at the same intervals) until the strain becomes negligible. A diagram illustrating these two procedures for calculating

rutting damage due to an 8-axle group is shown in Figure 6.3. The rutting due to one million repetitions of different axle and truck configurations were calculated using both procedures for each layer for both cross-sections.

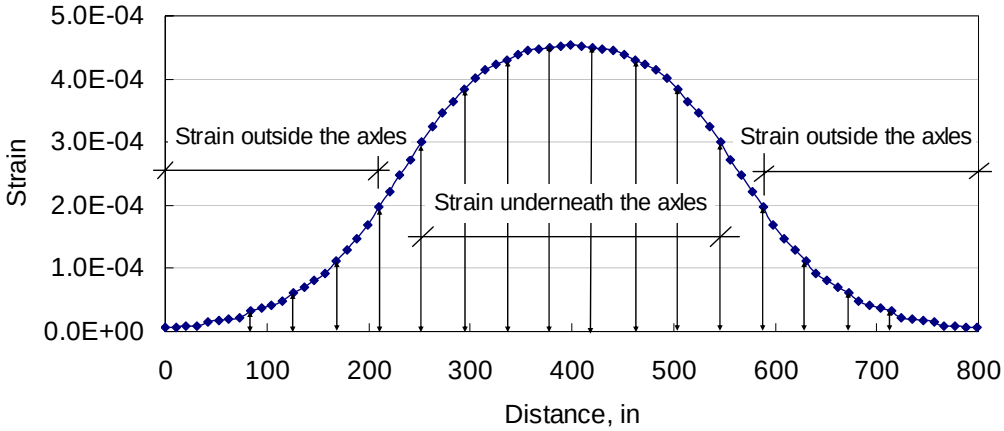


Figure 6.3 Strain values underneath and outside the axle group

## 6.4 RESULTS AND DISCUSSION

The calibrated mechanistic-empirical rutting model (Equation 6.1) is employed to calculate the layer rutting for both thick and thin pavement sections. Figures 6.4 to 6.7 show the per-layer and total rut depth due to one million repetitions for different axle and truck configurations using both procedures. The calculated rutting for the individual layers as well as the total was normalized to the rutting due to a single axle (axle and truck factors) to study the relative effect of these axle and truck configurations on pavement rutting damage.

The results show that when there is no strain interaction between axles, both procedures for calculating the rut depth show rutting damage proportional to the number of axles. This is the case for HMA layer of cross-section 1 and HMA and base layers of cross-section 2. On the other hand, when there is strain interaction between the axles, the first procedure (accounting only for the strain values under the axles) shows that the multiple axles are more damaging relative to the same number of single axles (Figures 6.4, c and d (axles) and Figures 6.5, c and d (trucks)). This result is due to the fact that procedure 1 ignores the strains outside the axles, and the effect of these strain values becomes more severe at higher levels of interaction. Yet, since unaccounted for strain values still result in rutting damage, it is not logical to ignore strain values outside the axles, as shown in Figure 6.3. Calculating the rut depth by accounting for all strain values (strain underneath and outside the axles) shows that whether there is strain interaction or not, the axle and truck factors are proportional to the number of axles. The results of

procedure 2 indicate that the interaction in the sub-layers is not important and does not impose additional relative rutting damage. These results can be further confirmed from the laboratory investigation of the HMA layer. Since interaction between pulses was not significant for the visco-elastic material (HMA layer) it will be even less significant for the granular sub-layers, as indicated by the mechanistic analysis in this study. This conclusion suggests that procedure 2 is more accurate than procedure 1 for calculating the rut depth due to multiple axle and truck configurations. However, the analysis presented here is relative to a unit axle load of 13 kips. This does not represent actual axle loading in a realistic truck configuration. Therefore, the results merely confirmed the proportionality between rut depth and axle load passage, and should not be used for calculating axle load equivalency factors and truck factors.

In a similar mechanistic analysis of the effect of heavy-vehicle characteristics on pavement response and performance, Gillespie *et al.,* 1993 calculated the rut depth for different truck configurations by integrating the influence function, which resulted in rutting damage that is proportional to the axle load. Though Gillespie's analyses include several truck configurations, the maximum axle group among all truck configurations was limited to tandem. Therefore, this current mechanistic analysis, laboratory experiment, and in-service pavement analysis extend these conclusions to a larger number of heavy axle and truck configurations.

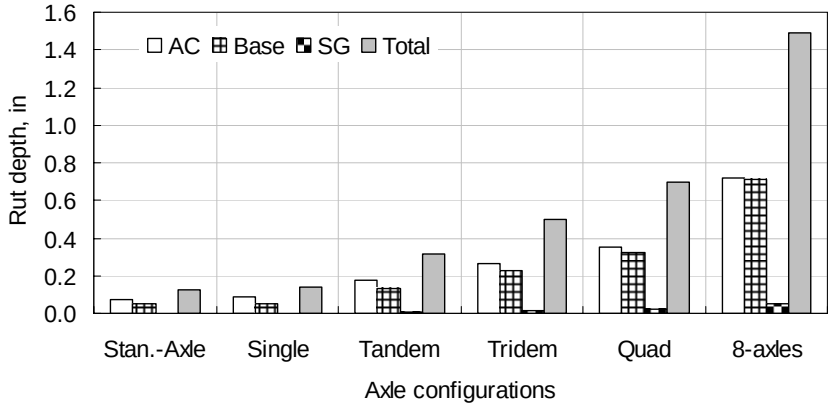


(a) Rut depth for section 1

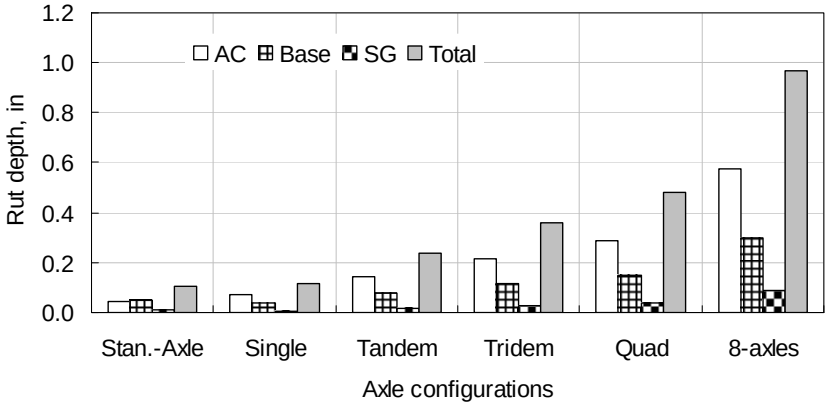


(b) Rut depth for section 2

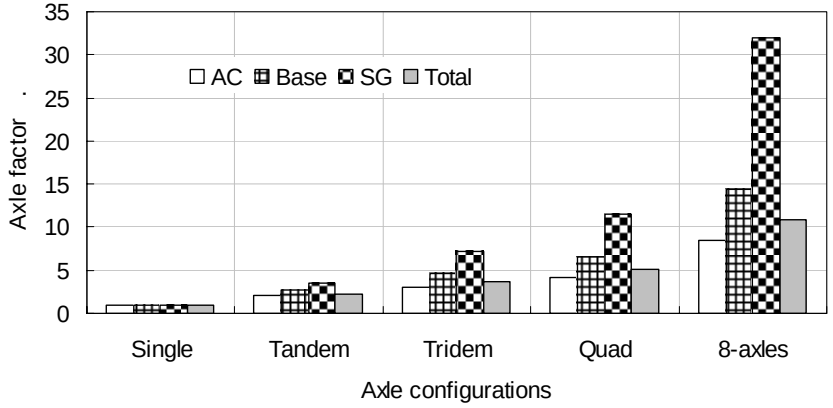


(c) Axle factor for section 1

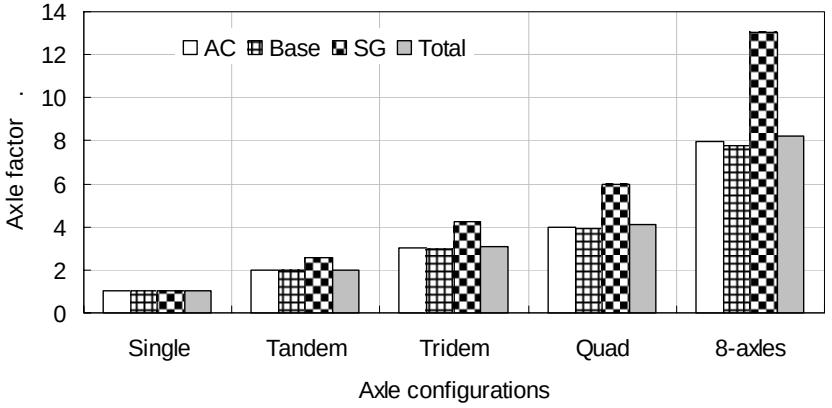


(d) Axle factor for section 2

Figure 6.4 Rut depth for pavement layers and their axle factors at one million repetitions – procedure 1

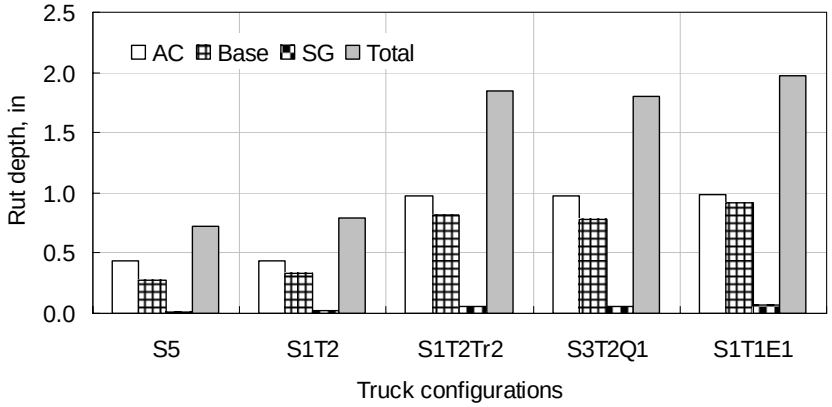


(a) Rut depth for section 1

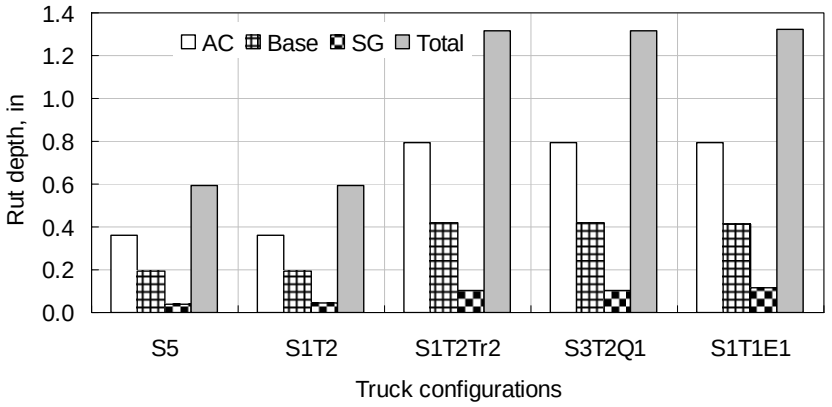


(b) Rut depth for section 2

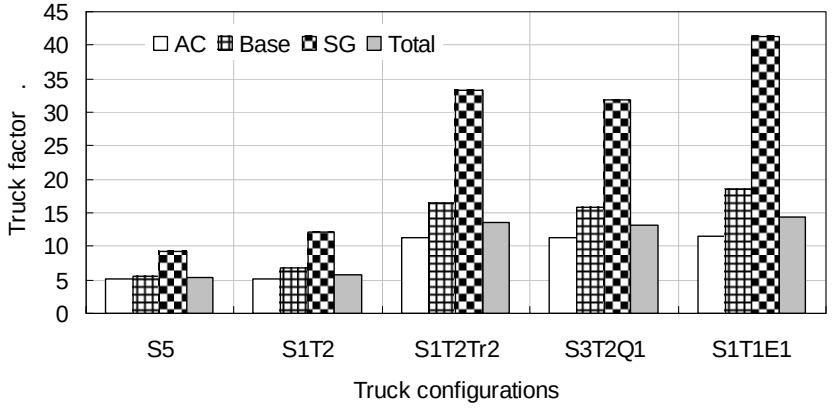


(c) Truck factor for section 1

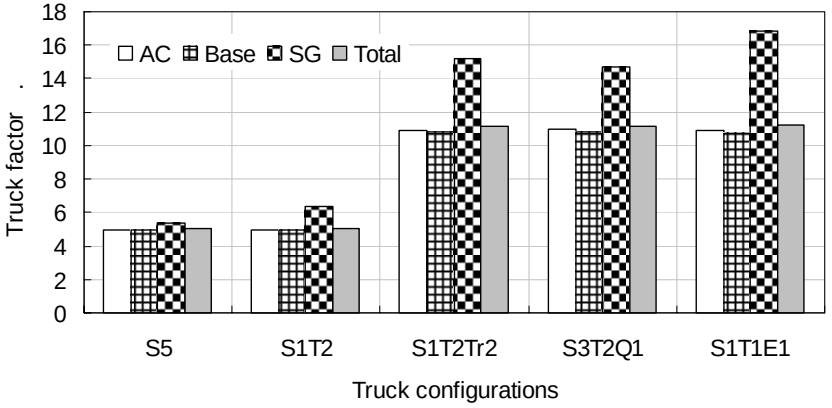


(d) Truck factor for section 2

Figure 6.5 Rut depth for pavement layers and their truck factors at one million repetitions – procedure 1

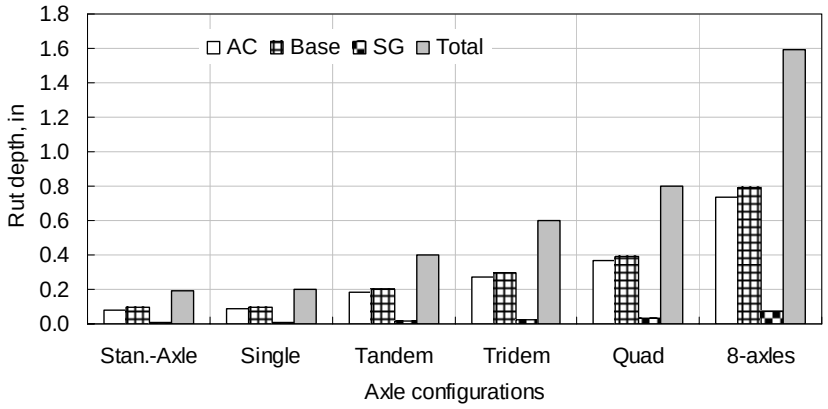


(a) Rut depth for section 1

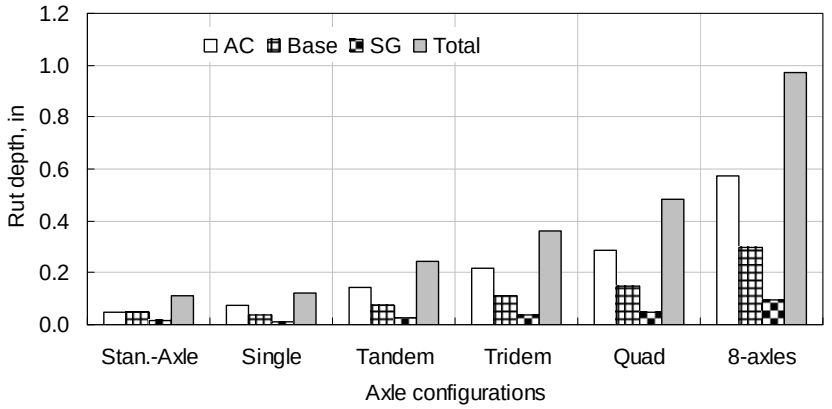


(b) Rut depth for section 2

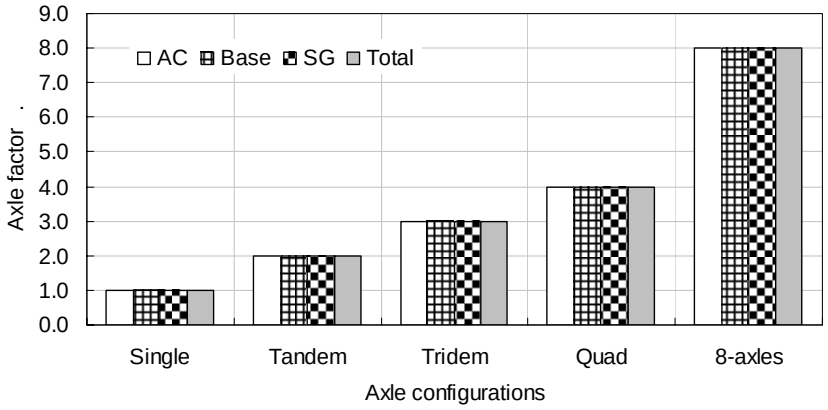


(c) Axle factor for section 1

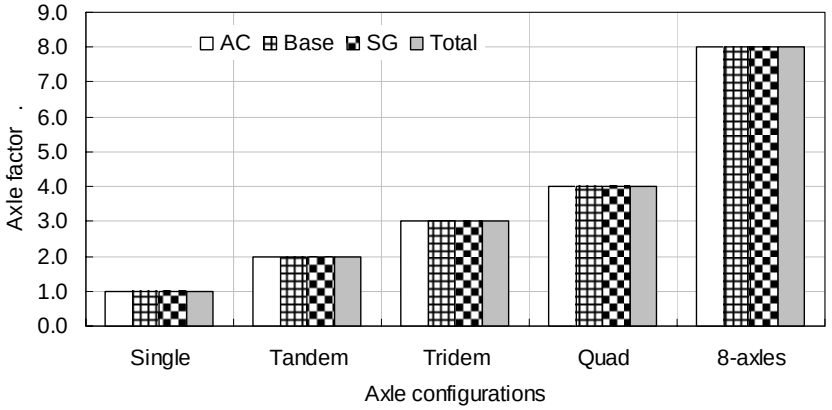


(d) Axle factor for section 2

Figure 6.6 Rut depth for pavement layers and their axle factors at one million repetitions – procedure 2

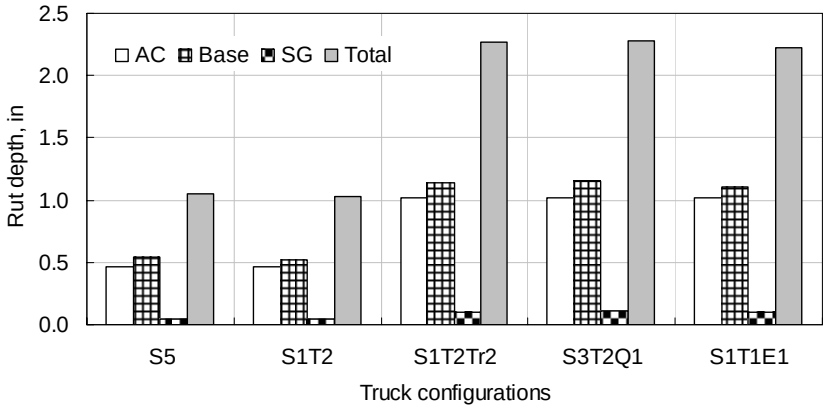


(a) Rut depth for section 1

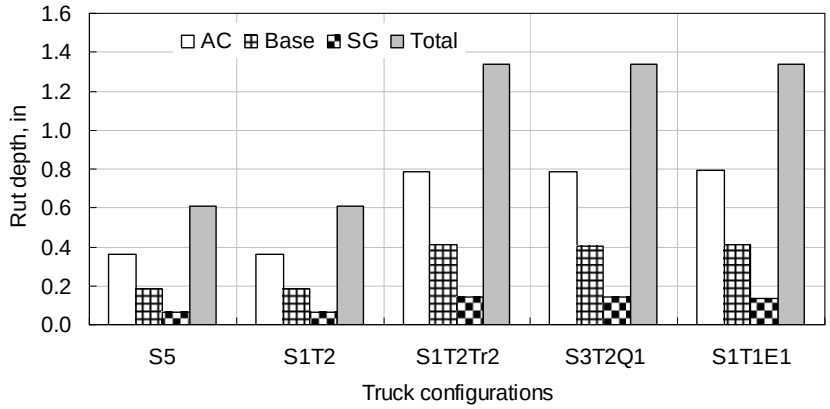


(b) Rut depth for section 2

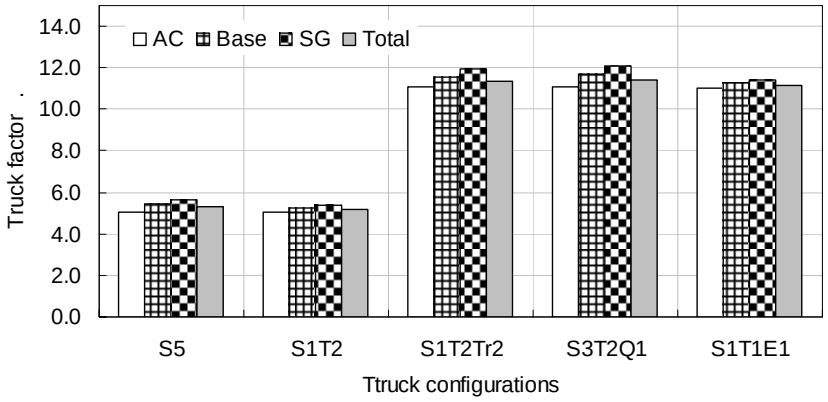


(c) Truck factor for section 1

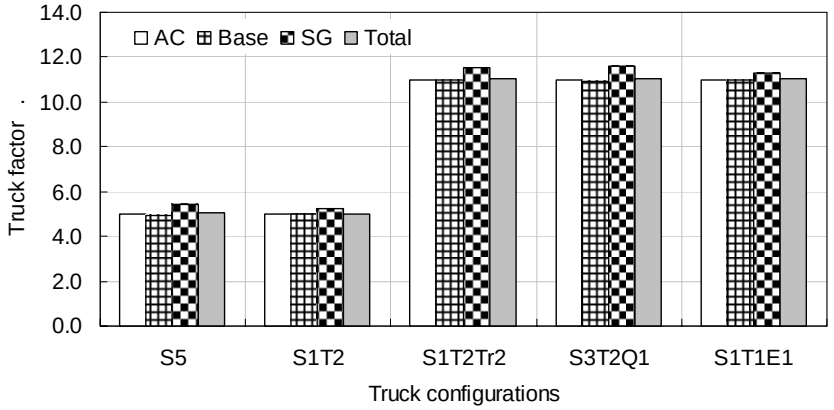


(d) Truck factor for section 2

Figure 6.7 Rut depth for pavement layers and their truck factors at one million repetitions – procedure 2

### 6.4.1 Rutting Prediction Using the New Mechanistic-Empirical Design Guide

The new mechanistic-empirical (ME) design guide (Witczak and El-basyouny, 2004) predicts several forms of distress, including rutting. In particular, the document discusses and predicts rutting for the individual layers as well as the total surface rutting. Unlike the VESYS rutting model, the MEPDG software has two independent equations for predicting rutting: one for rutting within the HMA layer and one for rutting within granular materials (base/subbase) and the subgrade. Moreover, the program can handle trucks with single, tandem, tridem, and quad axle configurations. The rutting due to single and tandem axle configurations was calculated in the present study using the new design guide for a single SPS-1 section. The predicted rutting for each individual pavement layer and the total rutting were not proportional to the number of axles; that is, a tandem axle produced less than twice the rutting damage of a single axle. Figure 6.6 shows the rut depth and axle factor for tandem axles for two SPS-1 sections, thin (50113) and thick sections (190101). This prompted a further investigation of the methods and assumptions that were incorporated into the new MEPDG guide. The two major concerns about the ME rutting models in the new design guide, and the solutions offered by the present study, are summarized below:

- Unlike the procedure described in the current study to calibrate the VESYS rutting model—linking the shape of the transverse surface profile to the layer rutting contributions—the MEPDG research team bases layer rutting on an assumed and statistically idealized percentage that is applied to all LTPP sections equally. In the MEPDG document, it states that a lack of trench data makes section-based layer contributions impossible to calculate. The resulting lack of variation on a section-by-section basis therefore becomes a matter of "practical," rather than statistical significance. By including the transverse surface profile as a means of quantifying the layer contribution of each section to the total rutting, the gap between assuming an individual section's layer contribution and calculating it has been bridged.
- The most significant drawback is that the MEPDG model uses only the maximum strain value within a multiple axle group, as if the axle group can be quantitatively represented by the superposition of the many axles into a single, static pulse. However, this neglects the rutting damage due to those strain values outside the maximum; of which, there are many in a large multiple axle group. This, of course, can be partially accounted for in the calibration procedure, but this adjustment is highly artificial and is not representative of the damage that occurs at an individual point in the pavement as the entire load (up to an 8-axle group) passes over. The present study attempted to validate the MEPDG model, but found that, even with the calibration procedure adjustments, the predicted rutting damage is not proportional to the number of axles within a group. Therefore, the present study provides a more representative model for rutting prediction, based on the summation of rutting damage throughout the entirety of the passage of an axle group, not just the damage produced by the singular, maximum strain value.

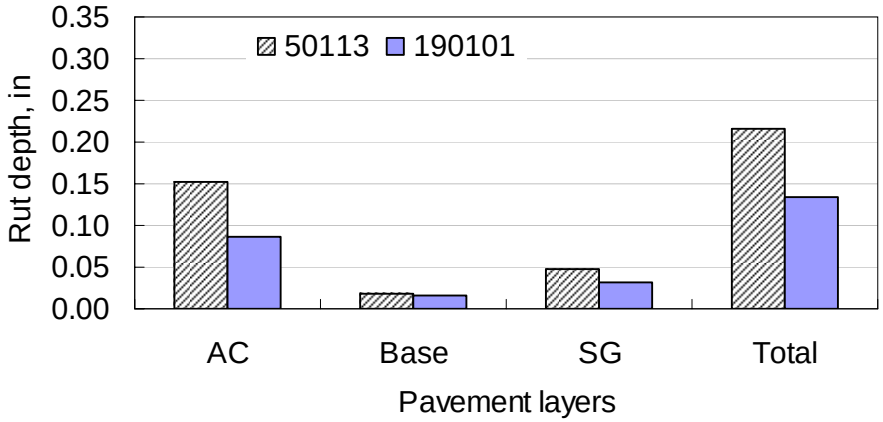


(a) Rut depth due to single axles

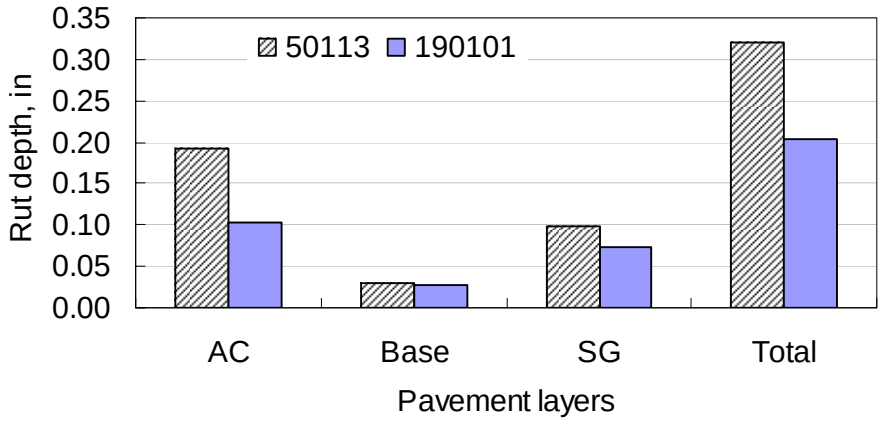


(b) Rut depth due to tandem axles

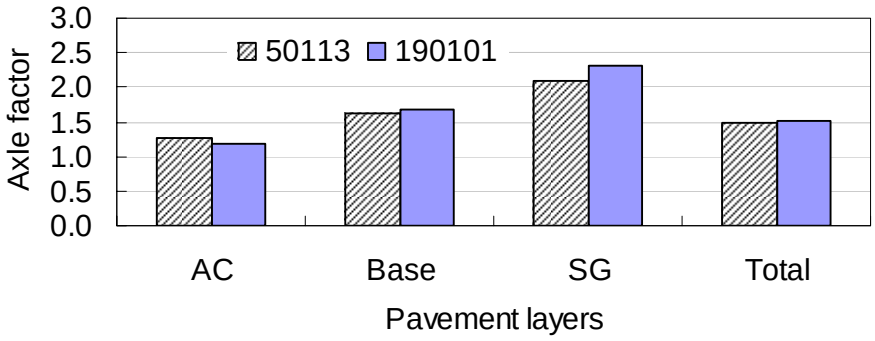


(c) Tandem axle factor

Figure 6.8 Rut depth for single and tandem axles and tandem axle factor using MEPDG

# CHAPTER 7

# TRUCK FACTORS FOR FLEXIBLE PAVEMENT DESIGN

The truck factors (TF) presented in tables 2.9 and 5.10 in chapters 2 and 5 of this volume were calculated using the legal load limits for all the axles and trucks. However, not all the trucks using the roadways are always fully loaded. These truck factors could prove to be very conservative from a design point of view. Therefore, truck factors should also be calculated considering actual loads carried by the trucks in Michigan. Weigh-in-motion (WIM) data were collected from 42 weigh stations in Michigan for the year 2007. The data from these weigh stations were used to determine the axle load spectra for different classes of trucks. The load spectra were then used to calculate the average truck factor for all truck classes. This chapter presents details of this analysis.

## 7.1 WIM DATA

WIM data include weights of the individual axles and distances between them. WIM data from each station were analyzed to identify the axle groups and truck types based on standard axle configurations of trucks of different classes. The FHWA definition of truck class was used for this purpose and the trucks were classified into classes 5 through 13. Figure 7.1 shows the distribution of these trucks for a sample weigh station (File: W26829189) and Figure 7.2 shows the combined truck distribution of all the 42 weigh stations.

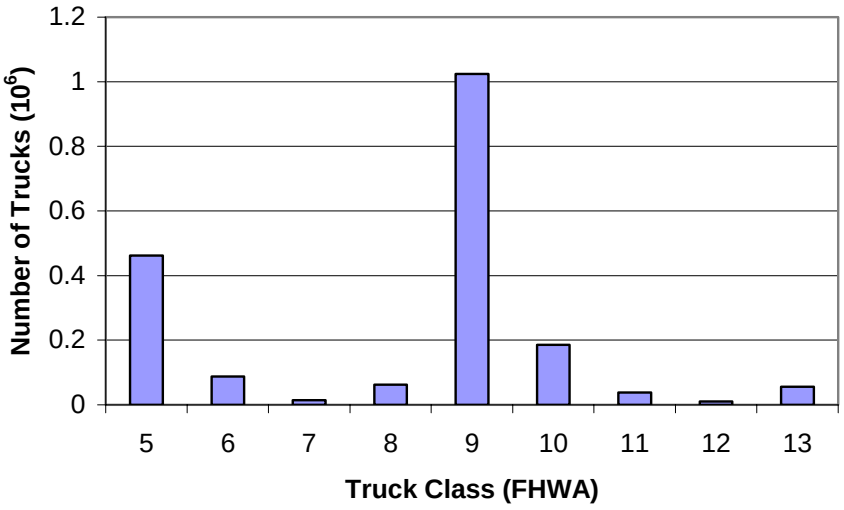


Figure 7.1. Truck distribution for sample weigh station W26829189 (year 2007)

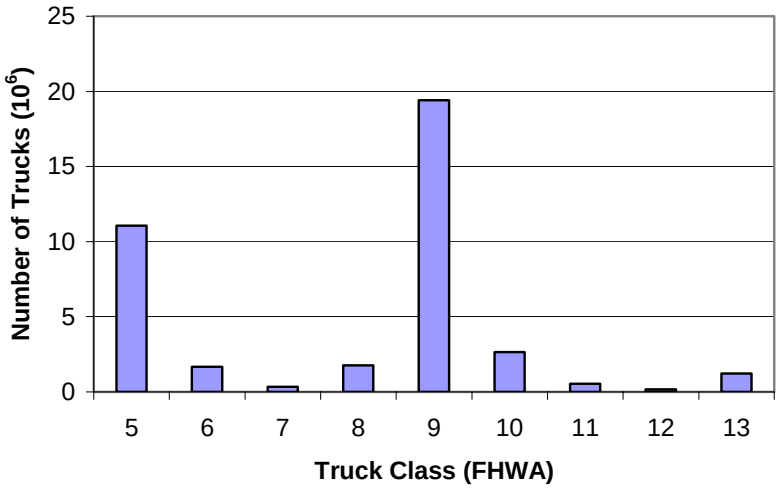


Figure 7.2. Combined truck distribution for all 42 weigh stations (year 2007)

As mentioned earlier, different trucks of the same classification have different loads on their axles. Analysis of the WIM data gave the actual load distribution spectrum for all the axle configurations of different truck classes. For example, Figures 7.3 and 7.4 show the load spectra for tridem- and quad-axle groups, respectively, for class 7 trucks weighed at the 42 WIM stations. The WIM station data had some records with unusually high axle weights. It was also noted that the frequency of loads in excess of the legal load limits was higher than would be expected. Such records were assumed to be in error and were therefore excluded from the analysis. A threshold of 25% higher than the legal maximum load for each axle-group was used for this purpose.

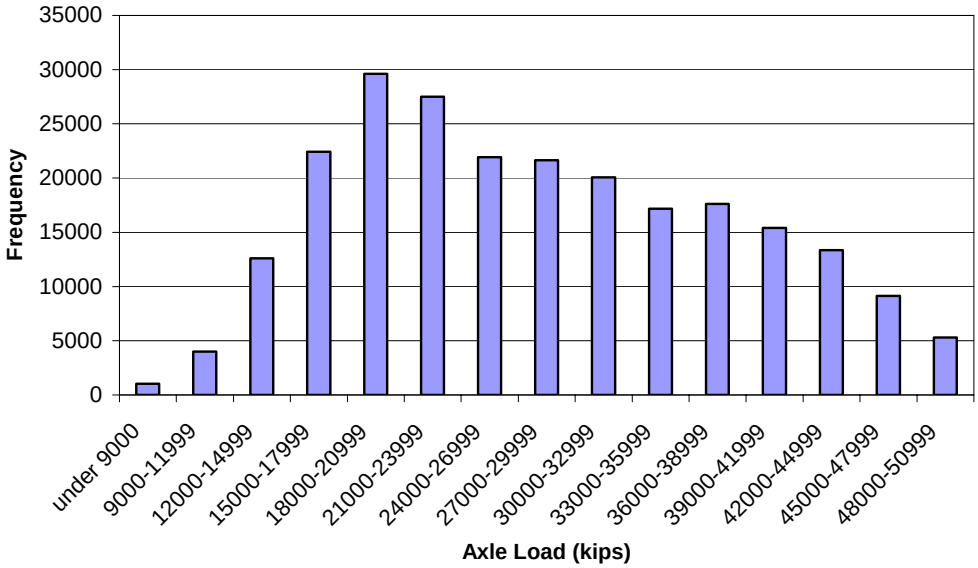


Figure 7.3. Load spectrum of tridem axles for truck class 7

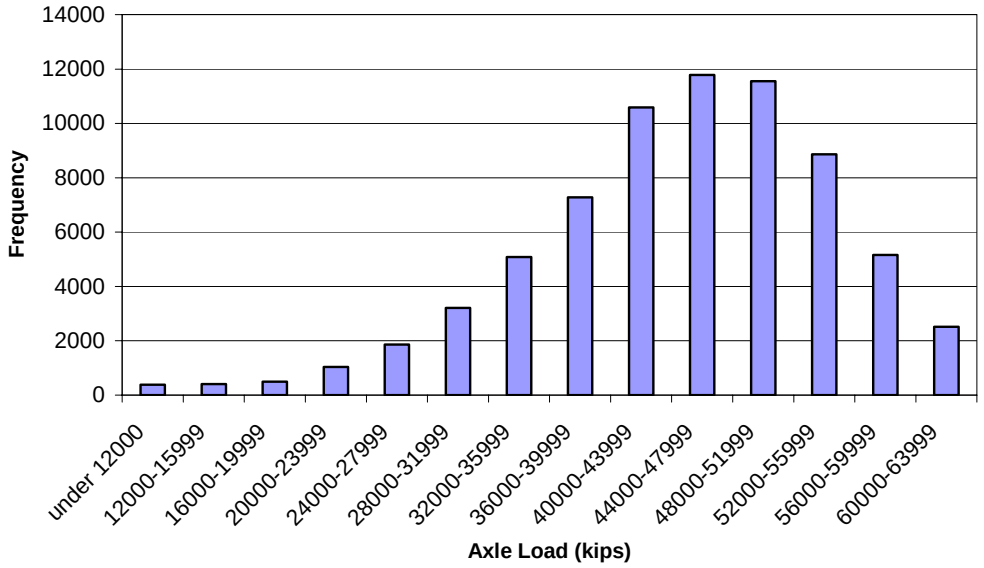


Figure 7.4. Load spectrum of quad axles for truck class 7

Calculation of truck factors for each class is an elaborate process which is presented briefly in the following sections. Details of the method can be found in the MDOT position paper entitled “Method of Calculating 18-kip Axle Equivalencies”.

## 7.2 TRUCK FACTOR CALCULATION

This study was charged with determining the relative damage caused by multiple axles within an axle group; i.e., how much damage is caused by grouping multiple axles into one axle group. The scope of the study did not include verifying the “AASHTO Fourth Power” damage law; i.e., we were not charged with determining how much damage is caused by increasing the load of a given axle relative to the standard 18-kip single axle. To do so would require extensive full-scale testing similar to what had been done in the original AASHO road test.

In this analysis, we used a similar procedure for calculating truck factors as was described in chapters 2 and 5 of this volume, for fatigue cracking and rutting respectively, except that the entire load spectrum for each axle group and each truck class was considered to calculate the truck factor. The reader can refer to Tables 2.9 and 5.10 which present the truck factors for fatigue and rutting, respectively, in the AASHTO framework using laboratory results. The procedure used to calculate TF’s is summarized as follows:

(1) Convert multiple axle groups within each truck configuration into an equivalent number of single axles using the Axle Factors (AF) as defined in this study.

(2) Calculate the Load Equivalency Factor (LEF) of each axle group by multiplying

the AF values obtained from the laboratory with the LEF from AASHTO corresponding to the load carried by an individual axle within each load category of a given axle group (e.g., 10 kip for an individual axle of a 30 kip tridem).

(3) Sum the LEF of the different axle groups within a truck.

Table 7.1 shows a sample calculation of the truck factors for class 7 trucks. Other details corresponding to this example are as follows:

- Pavement type: Flexible
- AC layer thickness: 3.5 inches
- AC layer modulus: 350 ksi
- Base layer thickness: 12 inches
- Base layer modulus: 30 ksi
- Subbase layer thickness: 18 inches
- Subbase layer modulus: 15 ksi
- Structural Number: 5.0
- Distress Type: Fatigue Cracking

These ALEFs were calculated for each of the load subcategories (shown in the first column of table 7.1). Each subcategory of load had a range of 1 kip. Axle groups having loads above the threshold of 25% higher than the legal maximum load (for each axle-group) were excluded from the calculation. The number of axle-groups of each type for each load subcategory were then multiplied with the corresponding ALEF to obtain the cumulative ALEF for all the trucks with that axle group and load subcategory. Finally the cumulative ALEF for all the axles in the truck and for all the load subcategories were calculated. The cumulative ALEF thus obtained was divided by the total number of trucks to obtain the average truck factor for the corresponding truck class.

## 7.3 RESULTS AND DISCUSSION

The example presented here corresponds to class 7 truck and the truck factor has been calculated from fatigue cracking point of view for flexible pavements. This procedure was repeated to obtain truck factors for other truck classes as well from fatigue point of view for flexible pavements with the above mentioned structure which corresponds to a structural number of 5.0. Truck factors for higher AC layer thickness and higher modulus were also calculated using the same procedure. Table 7.2 presents the results for the 9 different classes of trucks and 6 different pavement structures and AC layer moduli (three thicknesses and two moduli). The structural numbers for the 6 different pavement structures have also been listed in table 7.2. Base and subbase thicknesses and moduli were kept constant in all the cases.

Table 7.1. Load spectrum and truck factor calculation for class 7 truck (fatigue cracking)

| Axle load (lb) | EALF | Number of axles | ESAL | Axle load (lb) | EALF | Number of axles |
|---|---|---|---|---|---|---|
| Single axle | | | | Tridem axle | | |
| under 3000 | 0.000 | 1216 | 0.222 | under 9000 | 0.000 | 1029 |
| 3000-3999 | 0.001 | 2375 | 3.014 | 9000-11999 | 0.003 | 4002 |
| 4000-4999 | 0.003 | 2769 | 9.166 | 12000-14999 | 0.007 | 12597 |
| 5000-5999 | 0.007 | 4564 | 33.507 | 15000-17999 | 0.015 | 22424 |
| 6000-6999 | 0.014 | 6089 | 88.266 | 18000-20999 | 0.030 | 29618 |
| 7000-7999 | 0.026 | 15660 | 410.624 | 21000-23999 | 0.054 | 27505 |
| 8000-8999 | 0.044 | 25411 | 1125.242 | 24000-26999 | 0.092 | 21919 |
| 9000-9999 | 0.071 | 44563 | 3152.586 | 27000-29999 | 0.147 | 21655 |
| 10000-10999 | 0.108 | 45430 | 4904.046 | 30000-32999 | 0.224 | 20066 |
| 11000-11999 | 0.158 | 26947 | 4269.784 | 33000-35999 | 0.329 | 17182 |
| 12000-12999 | 0.225 | 25035 | 5632.418 | 36000-38999 | 0.466 | 17614 |
| 13000-13999 | 0.310 | 17256 | 5355.657 | 39000-41999 | 0.643 | 15417 |
| 14000-14999 | 0.417 | 20324 | 8484.560 | 42000-44999 | 0.866 | 13351 |
| 15000-15999 | 0.549 | 14906 | 8185.365 | 45000-47999 | 1.139 | 9134 |
| 16000-16999 | 0.708 | 16455 | 11652.881 | 48000-50999 | 1.468 | 5297 |
| 17000-17999 | 0.897 | 11448 | 10272.334 | 51000-53999 | 1.860 | 0 |
| 18000-18999 | 1.119 | 11867 | 13281.831 | 54000-56999 | 2.321 | 0 |
| 19000-19999 | 1.377 | 7506 | 10332.626 | 57000-59999 | 2.854 | 0 |
| 20000-20999 | 1.672 | 6941 | 11605.756 | 60000-62999 | 3.467 | 0 |
| 21000-21999 | 2.008 | 4740 | 9519.903 | 63000-65999 | 4.164 | 0 |
| 22000-22999 | 2.389 | 0 | 0.000 | 66000-68999 | 4.952 | 0 |
| 23000-23999 | 2.816 | 0 | 0.000 | 69000-71999 | 5.838 | 0 |
| 24000-24999 | 3.293 | 0 | 0.000 | 72000-74999 | 6.828 | 0 |
| 25000-25999 | 3.825 | 0 | 0.000 | 75000-77999 | 7.930 | 0 |
| 26000-26999 | 4.415 | 0 | 0.000 | 78000-80999 | 9.153 | 0 |
| 27000-27999 | 5.068 | 0 | 0.000 | 81000-83999 | 10.507 | 0 |
| 28000-28999 | 5.789 | 0 | 0.000 | 84000-86999 | 12.002 | 0 |
| 29000-34999 | 6.176 | 0 | 0.000 | 87000-104999 | 12.805 | 0 |
| 35000-39999 | 6.176 | 0 | 0.000 | 105000-111999 | 12.805 | 0 |
| 40000-50000 | 6.176 | 0 | 0.000 | 120000-150000 | 12.805 | 0 |

| Axle load (lb) | EALF | Number of axles | ESAL |
|---|---|---|---|
| Quadric axle | | | |
| under 12000 | 0.000 | 391 | 0.179 |
| 12000-15999 | 0.003 | 408 | 1.299 |
| 16000-19999 | 0.008 | 493 | 4.095 |
| 20000-23999 | 0.018 | 1038 | 19.124 |
| 24000-27999 | 0.036 | 1864 | 67.808 |
| 28000-31999 | 0.066 | 3212 | 211.357 |
| 32000-35999 | 0.111 | 5088 | 565.403 |
| 36000-39999 | 0.178 | 7280 | 1292.442 |
| 40000-43999 | 0.271 | 10590 | 2868.765 |
| 44000-47999 | 0.398 | 11789 | 4687.699 |
| 48000-51999 | 0.565 | 11552 | 6522.163 |
| 52000-55999 | 0.779 | 8864 | 6903.822 |
| 56000-59999 | 1.048 | 5165 | 5411.002 |
| 60000-63999 | 1.378 | 2512 | 3461.655 |
| 64000-67999 | 1.777 | 0 | 0.000 |
| 68000-71999 | 2.252 | 0 | 0.000 |
| 72000-75999 | 2.809 | 0 | 0.000 |
| 76000-79999 | 3.455 | 0 | 0.000 |
| 80000-83999 | 4.196 | 0 | 0.000 |
| 84000-87999 | 5.040 | 0 | 0.000 |
| 88000-91999 | 5.994 | 0 | 0.000 |
| 92000-95999 | 7.066 | 0 | 0.000 |
| 96000-99999 | 8.264 | 0 | 0.000 |
| 100000-103999 | 9.598 | 0 | 0.000 |
| 104000-107999 | 11.079 | 0 | 0.000 |
| 108000-111999 | 12.718 | 0 | 0.000 |
| 112000-115999 | 14.527 | 0 | 0.000 |
| 116000-139999 | 15.499 | 0 | 0.000 |
| 140000-159999 | 15.499 | 0 | 0.000 |
| 160000-200000 | 15.499 | 0 | 0.000 |
| ESAL for all trucks weighted : | | | 206354.175 |

$$\text{Truck factor} = \frac{\text{8-kip ESALs for all trucks weighte}}{\text{Number of trucks weighted}} = \frac{2.064E+05}{309775} = 0.666$$

Table 7.2. Final average truck factors for flexible pavements from fatigue cracking point of view (AASHTO framework)

| | Truck Factors - Fatigue (AASHTO Framework) | | | | | |
|---|---|---|---|---|---|---|
| | Eac=350ksi | | | Eac=700ksi | | |
| Truck Class | 3.5 in (SN=5.02) | 8 in (SN=6.83) | 12 in (SN=8.44) | 3.5 in (SN=5.45) | 8 in (SN=7.8) | 12 in (SN=9.89) |
| 5 | 0.196 | 0.188 | 0.186 | 0.193 | 0.186 | 0.185 |
| 6 | 0.525 | 0.499 | 0.492 | 0.516 | 0.494 | 0.490 |
| 7 | 0.666 | 0.634 | 0.626 | 0.654 | 0.628 | 0.623 |
| 8 | 0.420 | 0.401 | 0.396 | 0.413 | 0.397 | 0.394 |
| 9 | 0.874 | 0.831 | 0.819 | 0.858 | 0.823 | 0.816 |
| 10 | 1.437 | 1.372 | 1.356 | 1.414 | 1.360 | 1.350 |
| 11 | 1.138 | 1.092 | 1.080 | 1.122 | 1.084 | 1.077 |
| 12 | 1.126 | 1.106 | 1.104 | 1.118 | 1.104 | 1.103 |
| 13 | 1.696 | 1.608 | 1.585 | 1.665 | 1.591 | 1.577 |

The same procedure was followed for rutting. Truck factors were calculated for the 6 different cases with three AC layer thicknesses and two different AC layer moduli for all the nine truck classes. Table 7.3 presents these results.

Table 7.3. Final average truck factors for flexible pavements from rutting point of view (AASHTO framework)

| | Truck Factors - Rutting (AASHTO Framework) | | | | | |
|---|---|---|---|---|---|---|
| | Eac=350ksi | | | Eac=700ksi | | |
| Truck Class | 3.5 in (SN=5.02) | 8 in (SN=6.83) | 12 in (SN=8.44) | 3.5 in (SN=5.45) | 8 in (SN=7.8) | 12 in (SN=9.89) |
| 5 | 0.197 | 0.188 | 0.186 | 0.193 | 0.187 | 0.186 |
| 6 | 0.589 | 0.560 | 0.552 | 0.578 | 0.554 | 0.549 |
| 7 | 0.795 | 0.752 | 0.741 | 0.779 | 0.744 | 0.738 |
| 8 | 0.433 | 0.412 | 0.407 | 0.425 | 0.408 | 0.405 |
| 9 | 1.019 | 0.969 | 0.956 | 1.001 | 0.960 | 0.952 |
| 10 | 1.776 | 1.691 | 1.669 | 1.746 | 1.675 | 1.661 |
| 11 | 1.141 | 1.095 | 1.083 | 1.124 | 1.086 | 1.079 |
| 12 | 1.132 | 1.112 | 1.109 | 1.124 | 1.110 | 1.108 |
| 13 | 2.096 | 1.985 | 1.956 | 2.057 | 1.964 | 1.946 |

Figure 7.5 graphically compares the current MDOT truck factors with those calculated in this study. These truck factors correspond to flexible pavement with structural number 5.0. The calculated average truck factors for fatigue cracking are comparable to the MDOT truck factors. Trucks belonging to class 5 and 11 have only single axles. Since ALEF for single axle has been obtained using AASHTO equation in this study as well as in MDOT calculations the truck factors should be similar. The slight difference in the truck factor in this class (class 11) is because of different load spectrum used by MDOT as compared to that in this study. The load spectrum used in this study is much more recent. In the case of trucks having multiple-axle groups truck factors for rutting are relatively higher, for example for class 13 trucks. This is because laboratory results show that amount of rutting is almost directly proportional to the number of axles in the axle group.

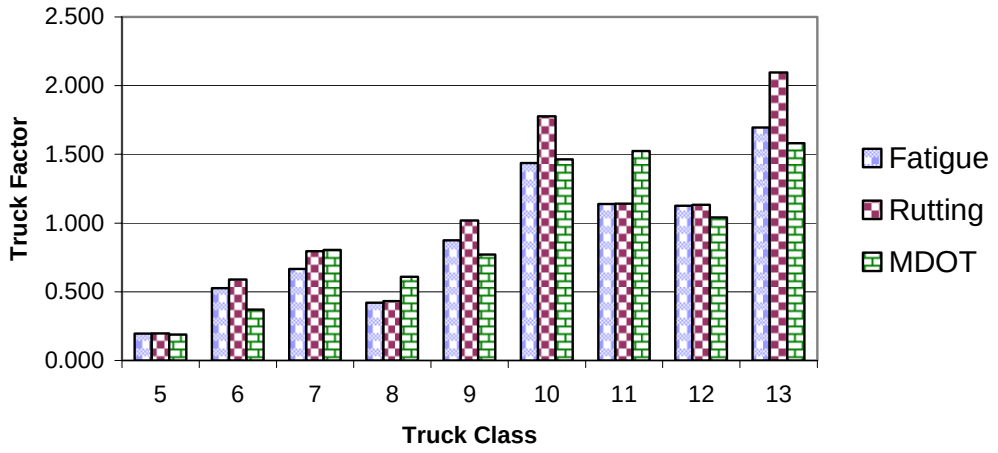


Figure 7.5. Comparing current MDOT truck factors with calculated average truck factors for SN = 5

# CHAPTER 8
# CONCLUSIONS AND RECOMMENDATIONS

Considering the increases in truck traffic and fuel prices, demands for heavier gross truck weights with larger axle groups should make this study relevant to policy–makers and pavement designers. The findings from the study are valuable for both truck weight and size policy purposes as well as pavement design protocols. The study provides updated truck factors taking into account multiple axle group effects and compatible with the AASHTO load equivalency framework for:

- Maximum legal loads for each truck type (useful for weight and size policy)
- Axle load spectra for each truck class (useful for pavement design)

The following summarizes the conclusions from the analyses of asphalt concrete pavements, and lists recommendations for truck factors of various axle configurations.

## 8.1 CONCLUSIONS

### 8.1.1 Analysis of In-service Flexible Pavement Performance Data

Based on the analyses of in-service pavement performance data to determine the effect of heavy multiple axle trucks on flexible pavement damage (Volume I of this report), the following main conclusions can be drawn:

1. Trucks with single and tandem axles affect pavement cracking (DI) more than those with multiple axles (tridem and higher).
2. Conversely, heavier trucks with multiple axles have more effect on rutting than those with single and tandem axles.
3. RQI results did not show enough evidence to draw a firm conclusion.

However, the above findings cannot be considered as definitive conclusions that can be implemented in a quantitative manner. Rather, they have highlighted general apparent trends that need to be confirmed with mechanistic analyses, controlled laboratory testing, or better yet, accelerated pavement testing (APT). The main findings of the analyses conducted in this volume (Volume II- Flexible Pavements) are summarized below. Full-scale accelerated pavement testing (APT) was outside the scope of this study. However, it is recommended that such tests be conducted in a future study. Since MDOT does not have an APT facility, it is recommended that MDOT consider joining other State Highway Agencies (SHA) in conducting a pooled fund study to support the findings of this study using full-scale APT tests.

### 8.1.2 Laboratory Fatigue and Rut Testing

Based on the experimental results from fatigue and rut testing of asphalt concrete mixes using the indirect tensile cyclic load test and the uniaxial cyclic load test, respectively, the following main conclusions can be drawn:

1. Multiple axles were found to be less damaging in fatigue per load carried compared to single axles. Increasing the number of axles carrying the same load results in less fatigue damage. This decrease in fatigue damage was found to be more significant between single, tandem and tridem axles, while it starts to level off at higher axle numbers. Similar results were obtained for trucks where trucks having more axles and axle groups had lower truck factors per tonnage than those with single axles.
2. Rutting damage due to different axle configurations is approximately proportional to the number of axles within an axle group. In other words, rutting damage is proportional to the gross weight of the axle group or truck, with multiple axles causing slightly less damage than a combination of smaller axle groups, for the same load carried. This was due mainly to the effect of rest period between the axle load cycles.

### 8.1.3 Mechanistic Analyses

Results from mechanistic analyses confirm the experimental findings; i.e., that:

1. Multiple axles are less damaging in fatigue per load carried compared to single axles.
2. Rutting damage due to different axle configurations is approximately proportional to the number of axles within an axle group.

However, load equivalency factors (LEF) derived from mechanistic analyses can be significantly higher than those from AASHTO, with the differences being higher for thinner flexible pavements. These results suggest that the AASHTO based fourth power law may need to be revised in the future.

## 8.2 RECOMMENDATIONS

Figure 8.1 summarizes the axle factors obtained from laboratory fatigue and rut testing and compares them to the AASHTO axle factors (extrapolated for axles larger than the tridem based on a best fit curve using the axle factors from single, tandem and tridem axles).

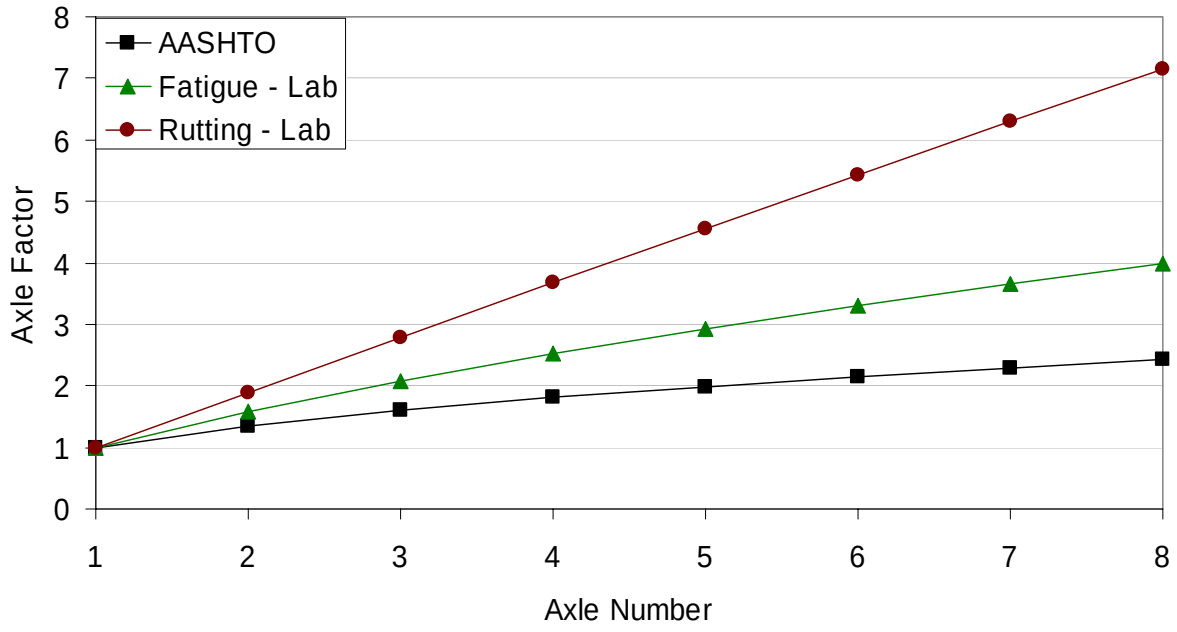


Figure 8.1 Flexible pavement axle factors for various axle configurations

### 8.2.1 Truck Factors Using Legal Load Limits for Weight and Size Policy

Tables 8.1 and 8.2 summarize recommended Truck Factors based on multiplying the axle factors for fatigue and rutting, respectively, by the AASHTO LEF value for a given legal load per axle (e.g., for a 39 kip tridem use 13 kip legal axle load). These truck factors are therefore based on fatigue and rutting considerations, but are provided within the AASHTO LEF framework.

Figures 8.2 and 8.3 show the same fatigue and rutting based Truck Factors for different pavement structures. Theses factors are ranked in descending order of relative damage caused to a flexible pavement with SN=5 (AC layer modulus of 350 ksi and thickness of 3.5 in) to better show the most/least damaging truck configurations.

Table 8.1 Fatigue-based Truck Factors for Legal Load Limits - AASHTO LEF Framework

| | | | Truck Factors | | | | | |
|---|---|---|---|---|---|---|---|---|
| | | | Eac = 350 ksi | | | Eac = 700 ksi | | |
| Truck | Truck No. | Total Wt. | 3.5 in | 8 in | 12 in | 3.5 in | 8 in | 12 in |
| 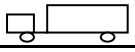 | 1 | *33.4* | 1.533 | 1.507 | 1.499 | 1.524 | 1.501 | 1.497 |
| 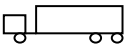 | 2 | *47.4* | 1.523 | 1.459 | 1.440 | 1.501 | 1.445 | 1.434 |
| 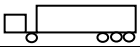 | 3 | *54.4* | 1.082 | 1.009 | 0.989 | 1.057 | 0.995 | 0.983 |
| 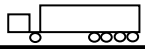 | 4 | *67.4* | 1.198 | 1.115 | 1.092 | 1.169 | 1.099 | 1.085 |
| 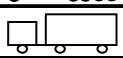 | 5 | *51.4* | 2.533 | 2.507 | 2.499 | 2.524 | 2.501 | 2.497 |
| 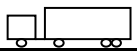 | 6 | *65.4* | 2.523 | 2.459 | 2.440 | 2.501 | 2.445 | 2.434 |
|  | 7 | *87.4* | 4.533 | 4.507 | 4.499 | 4.524 | 4.501 | 4.497 |
| 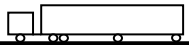 | 8 | *83.4* | 3.523 | 3.459 | 3.440 | 3.501 | 3.445 | 3.434 |
| 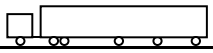 | 9 | *101.4* | 4.523 | 4.459 | 4.440 | 4.501 | 4.445 | 4.434 |
| 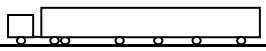 | 10 | *119.4* | 5.523 | 5.459 | 5.440 | 5.501 | 5.445 | 5.434 |
| 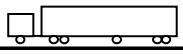 | 11 | *91.4* | 2.942 | 2.843 | 2.815 | 2.908 | 2.823 | 2.805 |
|  | 12 | *117.4* | 3.362 | 3.227 | 3.189 | 3.316 | 3.200 | 3.176 |
| 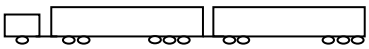 | 13 | *151.4* | 3.041 | 2.848 | 2.795 | 2.974 | 2.810 | 2.777 |
| 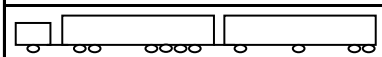 | 14 | *161.4* | 4.607 | 4.451 | 4.408 | 4.553 | 4.420 | 4.393 |
| 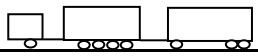 | 15 | *117.4* | 3.188 | 3.067 | 3.034 | 3.146 | 3.043 | 3.022 |
| 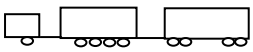 | 16 | *125.4* | 2.607 | 2.451 | 2.408 | 2.553 | 2.420 | 2.393 |
| 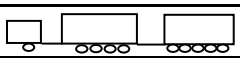 | 17 | *132.4* | 1.969 | 1.821 | 1.781 | 1.917 | 1.792 | 1.767 |
| 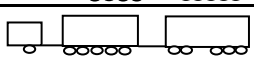 | 18 | *143.4* | 2.711 | 2.542 | 2.496 | 2.652 | 2.509 | 2.480 |
| 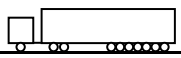 | 19 | *138.4* | 2.487 | 2.341 | 2.300 | 2.436 | 2.312 | 2.287 |
| 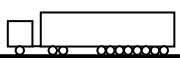 | 20 | *151.4* | 2.576 | 2.423 | 2.380 | 2.523 | 2.392 | 2.366 |
|  | 21 | *79.4* | 2.513 | 2.411 | 2.381 | 2.479 | 2.390 | 2.371 |

Table 8.2 Rutting-based Truck Factors for Legal Load Limits - AASHTO LEF Framework

| | | | Truck Factors | | | | | |
|---|---|---|---|---|---|---|---|---|
| | | | Eac = 350 ksi | | | Eac = 700 ksi | | |
| Truck | Truck No. | Total Wt. | 3.5 in | 8 in | 12 in | 3.5 in | 8 in | 12 in |
| 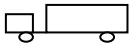 | 1 | *33.4* | 1.533 | 1.507 | 1.499 | 1.524 | 1.501 | 1.497 |
| 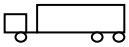 | 2 | *47.4* | 1.734 | 1.663 | 1.642 | 1.710 | 1.648 | 1.634 |
| 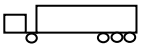 | 3 | *54.4* | 1.279 | 1.189 | 1.165 | 1.248 | 1.172 | 1.157 |
| 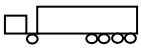 | 4 | *67.4* | 1.529 | 1.418 | 1.388 | 1.490 | 1.396 | 1.378 |
| 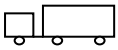 | 5 | *51.4* | 2.533 | 2.507 | 2.499 | 2.524 | 2.501 | 2.497 |
| 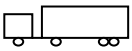 | 6 | *65.4* | 2.734 | 2.663 | 2.642 | 2.710 | 2.648 | 2.634 |
| 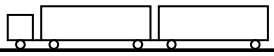 | 7 | *87.4* | 4.533 | 4.507 | 4.499 | 4.524 | 4.501 | 4.497 |
| 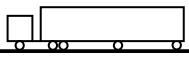 | 8 | *83.4* | 3.734 | 3.663 | 3.642 | 3.710 | 3.648 | 3.634 |
| 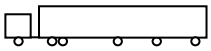 | 9 | *101.4* | 4.734 | 4.663 | 4.642 | 4.710 | 4.648 | 4.634 |
| 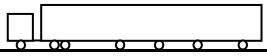 | 10 | *119.4* | 5.734 | 5.663 | 5.642 | 5.710 | 5.648 | 5.634 |
| 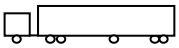 | 11 | *91.4* | 3.244 | 3.129 | 3.096 | 3.205 | 3.105 | 3.085 |
| 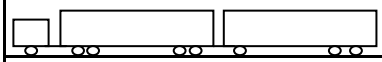 | 12 | *117.4* | 3.754 | 3.595 | 3.551 | 3.699 | 3.563 | 3.536 |
|  | 13 | *151.4* | 3.737 | 3.494 | 3.428 | 3.652 | 3.446 | 3.405 |
| 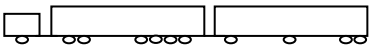 | 14 | *161.4* | 5.240 | 5.040 | 4.985 | 5.171 | 5.001 | 4.966 |
| 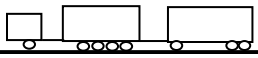 | 15 | *117.4* | 3.731 | 3.574 | 3.530 | 3.677 | 3.543 | 3.516 |
| 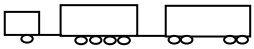 | 16 | *125.4* | 3.240 | 3.040 | 2.985 | 3.171 | 3.001 | 2.966 |
|  | 17 | *132.4* | 2.747 | 2.532 | 2.475 | 2.672 | 2.491 | 2.455 |
| 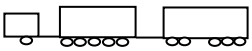 | 18 | *143.4* | 3.335 | 3.123 | 3.064 | 3.261 | 3.081 | 3.045 |
| 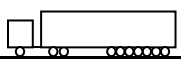 | 19 | *138.4* | 3.384 | 3.172 | 3.114 | 3.311 | 3.130 | 3.094 |
| 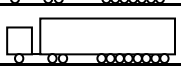 | 20 | *151.4* | 3.595 | 3.365 | 3.302 | 3.515 | 3.320 | 3.280 |
| 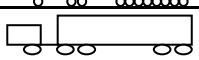 | 21 | *79.4* | 2.936 | 2.819 | 2.784 | 2.897 | 2.794 | 2.772 |

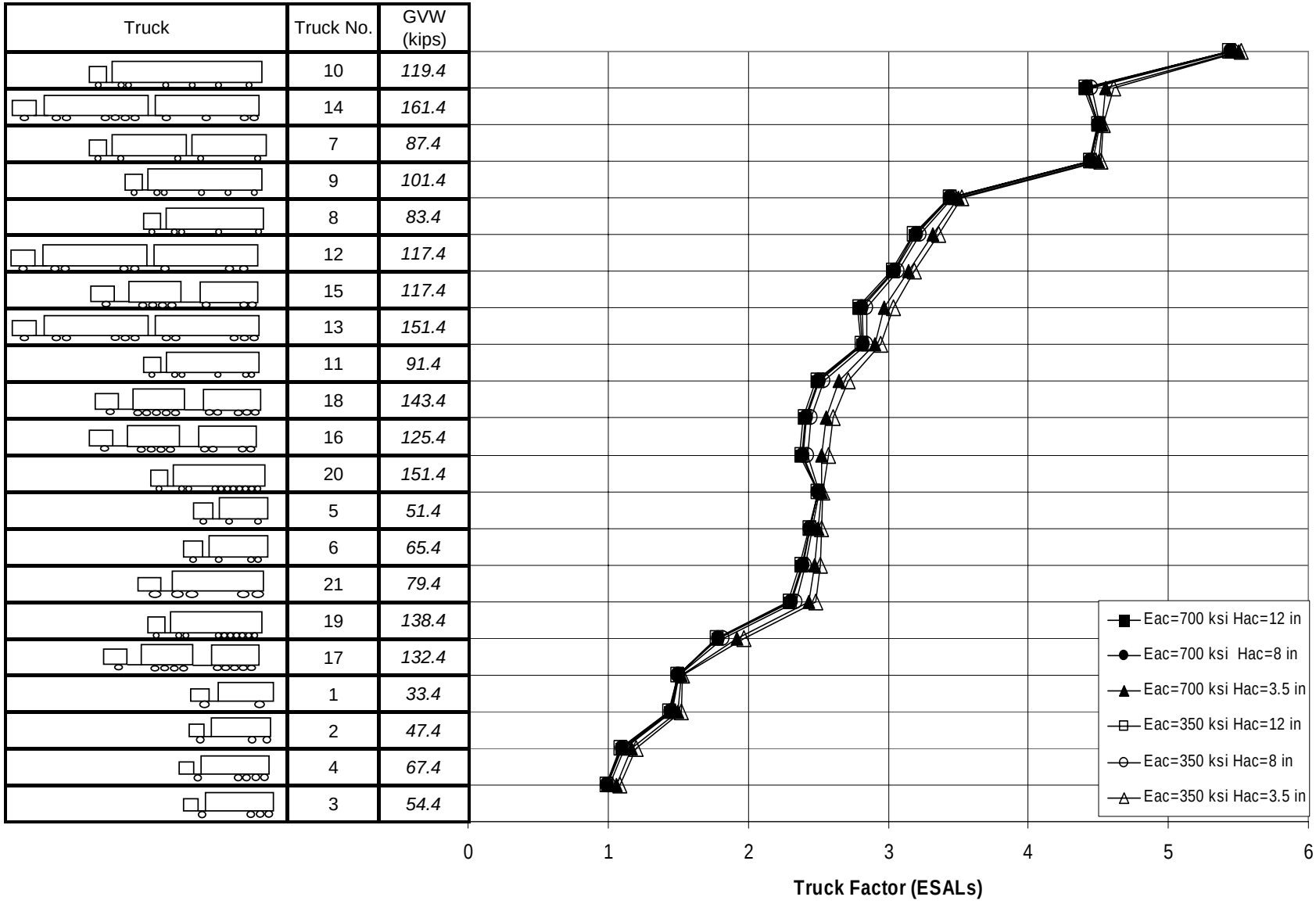


Figure 8.2 Fatigue-based Truck Factors within AASHTO LEF framework

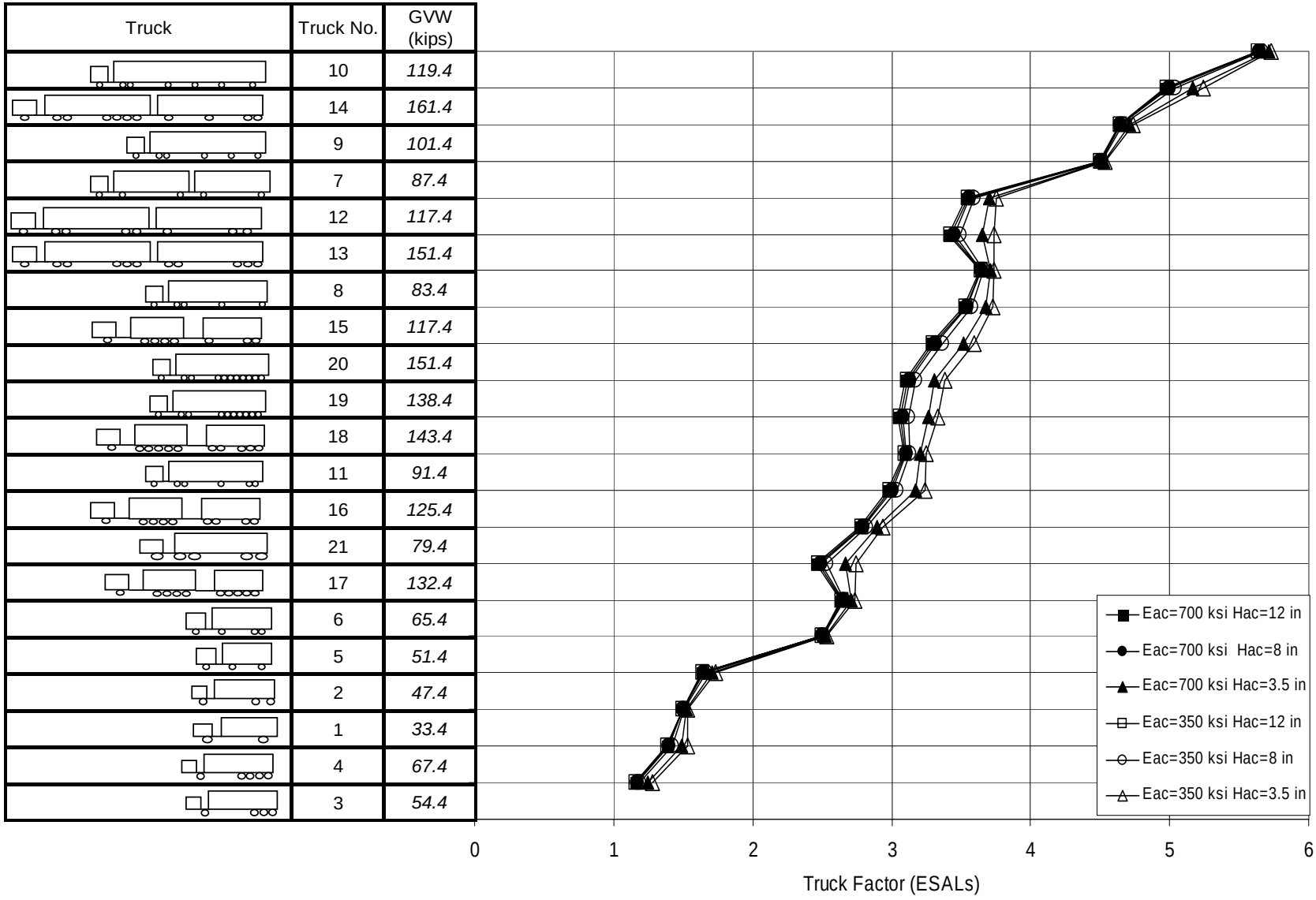


Figure 8.3 Rutting-based Truck Factors within AASHTO LEF framework

### 8.2.2 Truck Factors Using Axle Load Spectra for Pavement Design

Tables 8.3 and 8.4 summarize recommended Truck Factors based on multiplying the axle factors for fatigue and rutting, respectively, by the AASHTO LEF value using the axle load spectra from 42 WIM stations in Michigan. These truck factors are therefore useful for pavement design, taking into account fatigue and rutting considerations, and are provided within the AASHTO LEF framework. Table 8.5 and Figure 8.4 compare the TFs from this study to those currently used by MDOT.

Table 8.3. Fatigue-based Truck Factors for Flexible Pavement Design - AASHTO LEF Framework

| | Truck Factors - Fatigue (AASHTO Framework) | | | | | |
|---|---|---|---|---|---|---|
| | Eac=350ksi | | | Eac=700ksi | | |
| Truck Class | 3.5 in (SN=5.02) | 8 in (SN=6.83) | 12 in (SN=8.44) | 3.5 in (SN=5.45) | 8 in (SN=7.8) | 12 in (SN=9.89) |
| 5 | 0.196 | 0.188 | 0.186 | 0.193 | 0.186 | 0.185 |
| 6 | 0.525 | 0.499 | 0.492 | 0.516 | 0.494 | 0.490 |
| 7 | 0.666 | 0.634 | 0.626 | 0.654 | 0.628 | 0.623 |
| 8 | 0.420 | 0.401 | 0.396 | 0.413 | 0.397 | 0.394 |
| 9 | 0.874 | 0.831 | 0.819 | 0.858 | 0.823 | 0.816 |
| 10 | 1.437 | 1.372 | 1.356 | 1.414 | 1.360 | 1.350 |
| 11 | 1.138 | 1.092 | 1.080 | 1.122 | 1.084 | 1.077 |
| 12 | 1.126 | 1.106 | 1.104 | 1.118 | 1.104 | 1.103 |
| 13 | 1.696 | 1.608 | 1.585 | 1.665 | 1.591 | 1.577 |

Table 8.4. Rut-based Truck Factors for Flexible Pavement Design - AASHTO LEF Framework

| | Truck Factors - Rutting (AASHTO Framework) | | | | | |
|---|---|---|---|---|---|---|
| | Eac=350ksi | | | Eac=700ksi | | |
| Truck Class | 3.5 in (SN=5.02) | 8 in (SN=6.83) | 12 in (SN=8.44) | 3.5 in (SN=5.45) | 8 in (SN=7.8) | 12 in (SN=9.89) |
| 5 | 0.197 | 0.188 | 0.186 | 0.193 | 0.187 | 0.186 |
| 6 | 0.589 | 0.560 | 0.552 | 0.578 | 0.554 | 0.549 |
| 7 | 0.795 | 0.752 | 0.741 | 0.779 | 0.744 | 0.738 |
| 8 | 0.433 | 0.412 | 0.407 | 0.425 | 0.408 | 0.405 |
| 9 | 1.019 | 0.969 | 0.956 | 1.001 | 0.960 | 0.952 |
| 10 | 1.776 | 1.691 | 1.669 | 1.746 | 1.675 | 1.661 |
| 11 | 1.141 | 1.095 | 1.083 | 1.124 | 1.086 | 1.079 |
| 12 | 1.132 | 1.112 | 1.109 | 1.124 | 1.110 | 1.108 |
| 13 | 2.096 | 1.985 | 1.956 | 2.057 | 1.964 | 1.946 |

Table 8.5. Comparison of Truck Factors for Flexible Pavement Design

Flexible Pavement with SN = 5

| Truck Class | Truck Factors | | |
|---|---|---|---|
| | Fatigue Cracking | Rutting | MDOT |
| 5 | 0.196 | 0.197 | 0.1881 |
| 6 | 0.525 | 0.589 | 0.3710 |
| 7 | 0.666 | 0.795 | 0.8047 |
| 8 | 0.420 | 0.433 | 0.6092 |
| 9 | 0.874 | 1.019 | 0.7705 |
| 10 | 1.437 | 1.776 | 1.4640 |
| 11 | 1.138 | 1.141 | 1.5254 |
| 12 | 1.126 | 1.132 | 1.0410 |
| 13 | 1.696 | 2.096 | 1.5819 |

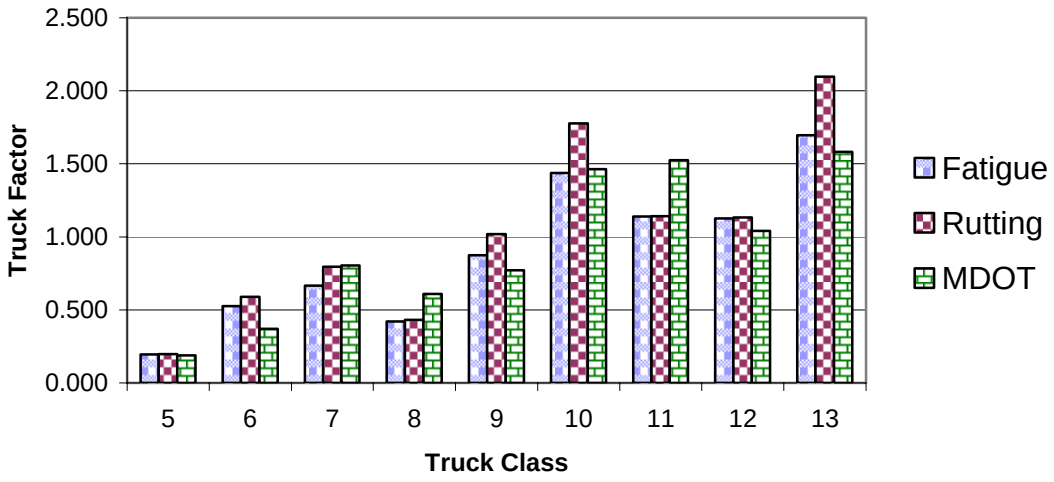


Figure 8.4. Comparison of current MDOT truck factors with those from this study for flexible pavement with SN = 5

# REFERENCES


Ali, H. A., and S. D. Tayabji (2000), "Using transverse profile data to compute plastic deformation parameters for asphalt concrete pavements." *Transportation Research Record*(1716), pp 89-97.

Ali, H. A., S. D Tayabji., and, F. La Torre (1998), "Calibration of mechanistic-empirical rutting model for in-service pavements." *Transportation Research Record*(1629), pp159-168.

Allen, J.C. (2001), "Species-Habitat Relationships For The Breeding Birds of A Long leaf Pine Ecosystem" Master of Science in Ecology, Faculty of the Virginia Polytechnic Institute and State University.

ARA, Inc., ERES Division (2004), "Guide for mechanistic- empirical design of new and rehabilitated pavement structures" NCHRP report No. 1-37A, appendix ii-1and appendix gg-1.

Aryes, M. Jr. (2002), "Unbound Material Rut Model Modification". Development of the 2002 Guide for the Design of New and Rehabilitated Pavement Structures. NCHRP 1-37A. Inter Team Technical Report.

ASTM D 2726 – 96a Test Method for Bulk Specific Gravity and Density of Non-Absorptive Compacted Bituminous Mixtures.

ASTM D 4123-82 (1995) Test Method for Indirect Tensile Test for Resilient Modulus of Bituminous Mixtures.

Baladi G. Y., (1988) '*Integrated Material and Structural Design Method for Flexible Pavements*', Vol. 1: Technical Report, FHEA.

Baladi G. Y., (1989) '*Fatigue Life and Permanent Deformation Characteristics of Asphalt Concrete Mixes*', Transportation Research Record 1227, TRB, Notional research Council, Washington, D.C..

Belsley, D. A., Edwin Kuh, and Roy E. Welsch. (1980), *Regression diagnostics : identifying influential data and sources of collinearity*, New York : Wiley.

Bonaquist, R. F. (1996), "Development and application of a comprehensive constitutive model for granular materials in flexible pavement structures." Ph. D. thesis, University of Maryland at Collage park.

Bonaquist, R.F., D.W. Christensen, and William Stump (2003), "Simple Performance Tester for Superpave Mix Design: First-Article Development and Evaluation" NCHRP report 513, Transportation Research Board, Washington, D.C.

Chatti, K., D. Lee., and T. Kim (2000) "Truck Damage Factors Using Dissipated Energy vs. Peak Strains" 6th International Symposium on Heavy Vehicle Weights and Dimensions. pp. 175-184. June 18-22.

Chatti, K., Iftikhar, A., and Kim, H. B., (2001) '*Comparison of Energy Based Fatigue Curves for Asphalt Mixtures Using Cyclic Indirect Tensile and Flexural Tests*'. 2nd International Conference on Engineering Materials, pp. 271-282.

Chatti, K. and H.S. Lee, (2003) *'Comparison of Mechanistic Fatigue Prediction Methods for Asphalt Pavements'*, Proceedings, International Conference on Computational and Experimental Engineering and Sciences, Corfu, Greece, July 24-29.

Chatti, K., H. Salama, and C. El Mohtar (2004), "Effect of heavy trucks with large axle groups on asphalt pavement damage" 8th International Symposium on Heavy Vehicle Weights and Dimensions, South Africa.

Chatti, K., N. Buch, S. W. Haider, A. S. Pulipaka, R. W. Lyles, D. Gilliland, and P. Desaraju (2005), "LTPP Data Analysis: Influence of Design and Construction Features on the Response and Performance of New Flexible and Rigid Pavements," NCHRP report No. 20-50 [10/16].

Chatti, K. and H. S. Lee ( 2004), "Evaluation of Strain and Energy Based Fatigue prediction Methods for Asphalt Pavement Subjected to Multiple Axle Loading" International Journal of Pavements, Vol. 3 No. 1& 2.

Chatti, K. and El Mohtar, C. (2004), "Effect of Different Axle Configurations on Fatigue Life of Asphalt Concrete Mixture" Transportation Research Record, n 1891, p 121-130

Chen, D.H., J. Bilyeu, T. Scullion, D. F. Lin, and F. Zhou, (2003), "Forensic Evaluation of Premature Failures of Texas Specific Pavement Study–1 Sections" ASCE Journal of Performance of Constructed Facilities, 2003, pp 67-74.

Claussen, A. I. M., J. M. Edwwareds, P. Sommer, and P. Uge (1977), "Asphalt Pavement Design -The Shell Method." *Proceedings, 4th International Conference on the Structural Design of Asphalt Pavement*, 39-74.

Crince, J.E., (2000) *'The Engineering Characteristics of Michigan's Asphalt Mixtures'*, Masters Project, Michigan State University.

Datapave website http://www.datapave.com/

Deen, C. Robert, Herbert F. Southgate, and Jesse G. Mayes (1980), "The Effect of Truck Design on Pavement Performance." Asphalt Paving Technology, Vol. 49, PP 606-632.

Dillon, W. and M. Goldstein (1984), “Multivariate Analysis Method and Applications” John Wiley & Sons.

El Mohtar, C. (2003), "The Effect of Different Axle Configurations on the Fatigue Life of an Asphalt Concrete Mixtures," MS., Michigan State University, E. Lansing MI 48824.

Federal Highway Administration Website http://fhwapap07.fhwa.dot.gov/vtris/

Fernando, E and, C. Bertrand (2002), “Application of profile data to detect localized roughness”, Transportation Research Record, n 1813, 02-4050, p 55-61

Ghuzlan K. A. and Carpenter S. H., ‘*Energy-Derived, Damage-Based Failure Criterion for Fatigue Testing*’.

Gillespie, Thomas D., S. M. Karamihas, M. W. Sayers, and, D. Cebon (1993), "Effects of Heavy-Vehicle Characteristics on Pavement Response and Performance." *NCHRP Report 353*, The University of Michigan, Transportation Research Institute, Ann Arbor, Michigan.

Golub, G. H., M. Heath and, G. Wahba (1979), "Generalized Cross-Validation as a Method for Choosing a Good Ridge Parameter." *Technometrics*, Vol. 21 pp.215-223(No. 2), pp.215-223.

Govind, S. (1988), “A dynamic Analysis of pavement systems to Determine a Damage Transform from Stress Fields.” Ph.D. dissertation, Department of Civil Engineering, University of Texas at Austin, Austin, Tex.

Graus, J., Deacon, J.A., Monismith, C.L., Tangella, R., (1990) ‘*Summary Report on Fatigue Response of Asphalt Mixtures*’, SHRP Project A-003-A, University of California, Berkeley.

Hajek, J. J., and A. C. Agarwal (1990), “Influence of Axle Group Spacing on Pavement Damage” Transportation Research Record, No. 1286, pp. 138-149.

Hanna, A.N., S.D. Tayabji, and J.S. Miller (1994), “SHRP-LTPP Specific Pavement Studies,” Five-Year Report, Strategic Highway Research Program, National Research Council.

Harold L. Von Quintus and Amy L. Simpson (2003), “Structural Factors for Flexible Pavements—Initial Evaluation of the SPS-1 Experiment” FHWA-RD-01-166.

Harvey, John and Lorina Popescu (2000), “Rutting of Caltrans Asphalt Concrete and Asphalt- Rubber Hot Mix Under Different Wheels, Tires and Temperatures – Accelerated Pavement Testing Evaluation” Report Prepared for California Department of Transportation.

Huang, Y. H., (1993), “Pavement analysis and design.” Prentice Hall.

Huang, H. Y., ‘*Pavement Analysis and Design*’. Prentice Hall.

Ilves, G. J., and Majidzadeh, K. (1991), "Reevaluation of the Methods for Calculation of Load Equivalency and Damage Ratios."

Kenis, W. and W. Wang (1997), "Calibrating Mechanistic Flexible Pavement Rutting Model from Full Scale Accelerating Tests." *8th International conference on asphalt pavement*, Seattle, Washington, 663-672.

Kim, H. B. (1999), "Framework for incorporating rutting prediction model in the reliability-based design of flexible pavements," Ph.D., Michigan State University, East Lansing.

Kaloush, K.E and M. W. Witczak (2002), “Tertiary flow characteristics of asphalt mixtures”, Journal of the Association of Asphalt Paving Technologists, Vol. 71, pp 249-280.

Kaloush, K. E. and Witczak, M. W. (2000), “Development of a Permanent to Elastic Strain Ratio Model for Asphalt Mixtures” Development of the 2002 Guide for the Design of New and Rehabilitated Pavement Structures. NCHRP 1-37A. Inter Team Technical Report.

Leahy, R.B. (1989), “Permanent Deformation Characteristics of Asphalt Concrete”, Ph.D. Dissertation, University of Maryland, College Park.

Leahy, R.B., E.T. Harrigan, and H. Von Quintus (1994), “Validation of Relationships Between Specification Properties and Performance” Report No. SHRP-A-409. Transportation Research Board, National Research Council, Washington, DC.

Matthews, J. M., Monismith, C. L., and Craus, J. (1993), "Investigation of laboratory fatigue testing procedures for asphalt aggregate mixtures," *Journal of Transportation Engineering*, 119(4), 634-654.

Miner, M. A. (1945), "Cumulative Damage in Fatigue," *Transactions of the ASME*, 67, A159-A164.

Moavenzadeh, F., J. E. Soussou, H. K. Findakly, and B. Brademeyer (1974), "Synthesis for rational design of flexible pavement," *FH 11-776*, Federal Highway Administration.

Monismith, C. L. (1981). Proc. ‘*Fatigue Characteristics of Asphalt Paving Mixtures and Their Use in Pavement Design*’. 18th Paving Conf., Univ. of New Mexico, Albuquerque, N. M.

Monismith, C. L. (1994), “Fatigue Response of Asphalt-Aggregate Mixes. Strategic Highway Research Program,” Project A-404, National Research Council.

Monismith, C.L, J.T. Harvey, and F. Long, S. Weissman (2000), “Tests to Evaluate the Stiffness and Permanent Deformation Characteristics of Asphalt/Binder-Aggregate Mixes” Technical memorandum, TM-UCB PRC.

Mukhtar, Hamid., (19993) ‘*Reduction of Pavement Rutting and Fatigue Cracking*’, Ph.D. thesis, Michigan State University.

Neter, J. and W. Wasserman (1996), “Applied Linear Statistical Models” Chicago: Irwin.

Oh, B. Hwan (1991), “Cumulative Damage Theory of Concrete under Variable-Amplitude Fatigue Loadings.” ACI Materials Journal, Vol. 88, No. 1.

Park, Dong-Yeob (2000), “Effect of Temperature and Loading Time on the Stiffness Properties of HMAC in Flexible Pavements” Ph. D. thesis, Department of Civil and Environmental Engineering, Michigan State University, East Lansing Michigan.

Pell, P. S., and Cooper, K. E. (1975). Proc. ‘*The Effect of Testing and Mix Variables on the Fatigue Performance of Bituminous Materials’*. AAPT, 44, 1-37.

Qi, X. and M. W. Witczak (1998), “Time-Dependent Permanent Deformation Models for Asphaltic Mixtures” Transportation Research Record, No. 1639, pp. 83-93.

Rao Tangella, S. C. S., J. Craus, J. A. Deacon, C. L. Monismith, (1990), "Summary Report on Fatigue Response of Asphalt Mixtures." SHRP Project A-003-A, University of California, Berkeley.

Saraf, C. L., Ilves, G. J., and Majidzadeh, K (1995), "Effect of Heavy Vehicle Weight on Pavement Performance." Road Transport Technology-4 Proceeding of the Fourth International Symposium on Heavy Vehicle Weights and Dimensions.

Schorsch, M. R. (2003) “Determining the causes of top-down cracks in bituminous pavements.” Master Thesis, Department of Civil and Environmental Engineering, Michigan State University, East Lansing Michigan.

Sebaaly, P. E., and Tabatabaee, N. (1992), "Effect of Tire Parameters on Pavement Damage and Load-Equivalency Factors." *Journal of Transportation Engineering*, 118(6), 805-819.

Shook, J. F., F. N. Finn, M. W. Witczak, and C. L. Monismith (1982), "Thickness Design of Asphalt Pavement - The Asphalt Institute Method." *Proceedings, 5th International Conference on the Structural Design of Asphalt Pavement*, 17-44.

Shigley, J. and Mischke, C. (1989), "Mechanical Engineering Design," 5th ed. p. 310. McGraw-Hill, Inc.

Simpson, A. L., J. F. Daleiden, and W. O. Hadley (1995), " Rutting analysis from a different perspective" Transportation research record 1473, pp 9-16.

Simpson A. L., J. B. Rauhut, P. R. Jordahl, E. Owusu-Antwi, M. I. Darter, R. Abroad, O. J. Pendleton, and Y. Lee (1994), "Sensitivity Analyses for Selected Pavement Distresses" SHRP report No. SHRP-P-393.

Sousa, J.B., Rowe G., Tayebali, A.A., (1992) *'Dissipated Energy and Fatigue of asphalt Aggregate Mixtures'*, Paper prepared for the Annual Meeting of Association of Asphalt Paving Technologists, University of California, Berkeley, Feb.

Svasdisant, T. (2003), "Analysis of top-dawn cracking in rubblized and flexible pavements" Ph. D. thesis, Department of Civil and Environmental Engineering, Michigan State University, East Lansing Michigan.

Tangella, S.R., Craus, J., Deacon, J.A., and Monismith, C.L., (1990) *'Summary Report on Fatigue response of Asphalt Mixtures'*, Report for Strategic Highway Research Program, TM-UCB-A003A-89-3. University of California, Berkley, Feb.

Ullidtz, P. (1987), "Pavement Analysis," Elsevier.

Villiers, C., R. Roque, and B. Dietrich (2005), "Interpretation of Transverse Profiles to Determine the Source of Rutting within Asphalt Pavement System" 84th TRB Annual Meeting, January 9-13, TRB paper no: 05-1841.

Von Quintus, H. and Killingsworth, B., (1998) *'Analyses Relating to Pavement Material Characterizations and Their Effects on Pavement Performance'*, FHWA-RD-97-085.

W. Van Dijk, (1975) '*Practical Fatigue Characterization of Bituminous Mixes*', Proceeding of the Association of Asphalt Paving Technologists, Phoenix, Arizona, Vol. 44.

W. Van Dijk, Visser, W., (1997) *'The Energy Approach to Fatigue for Pavement Design'*, AAPT, N0. 46.

White, T. D., J. E. Haddock, A. J. T. Hand, and H. Fang (2002), "Contributions of Pavement Structural Layers to Rutting of Hot Mix Asphalt Pavements" NCHRP report No.468.

Witczak, M. W., K. Kaloush, T. Pellinen, M. El-basyouny, and H. Von Quintus (2002), "Simple Performance Test for Superpave Mix Design" NCHRP report 465, National Academy Press, Washington, D.C.

Witczak, M. W. and M. El-basyouny (2004), “Calibration of Permanent Deformation Models for Flexible Pavements” appendix gg-1 of guide for mechanistic-empirical design of new and rehabilitated pavement structures, ARA, inc., ERES division, 505 west University Avenue, Champaign, Illinois 61820

Zhou, F. and Tom Scullion (2002), “VESYS5 Rutting Model Calibrations with Local Accelerated Pavement Test Data and Associated Implementation,” Report No. FHWA/TX-03/9-1502-01-2

# APPENDIX A - Hysteresis Loops and Trucks

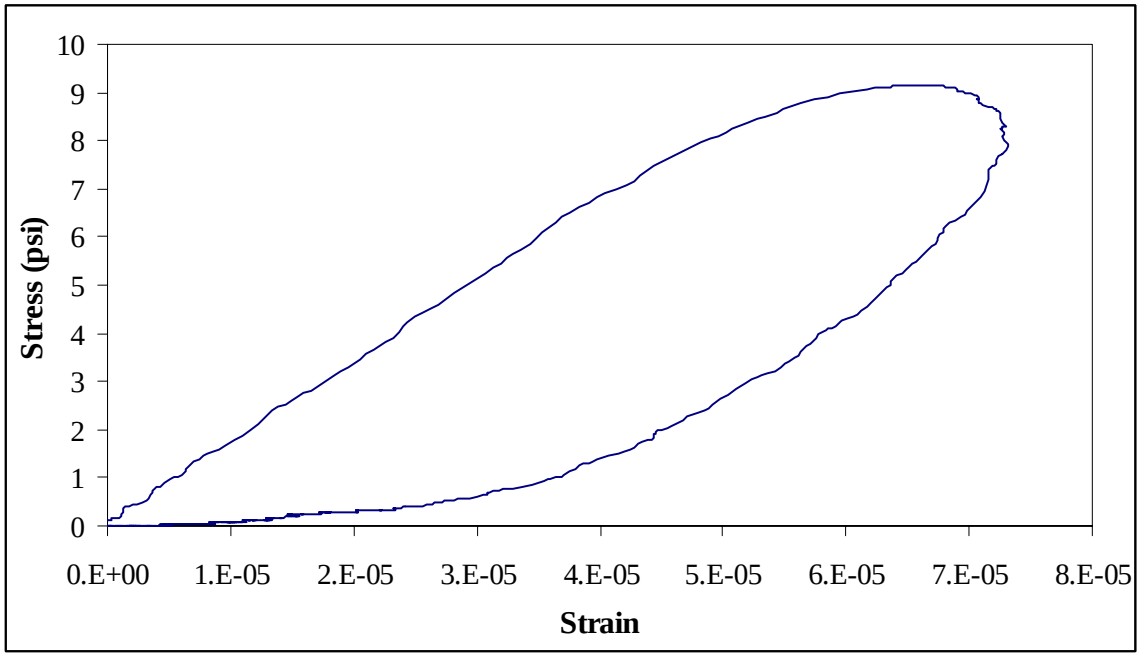


**Figure A.1 Hysteresis Loop for Single Axle**

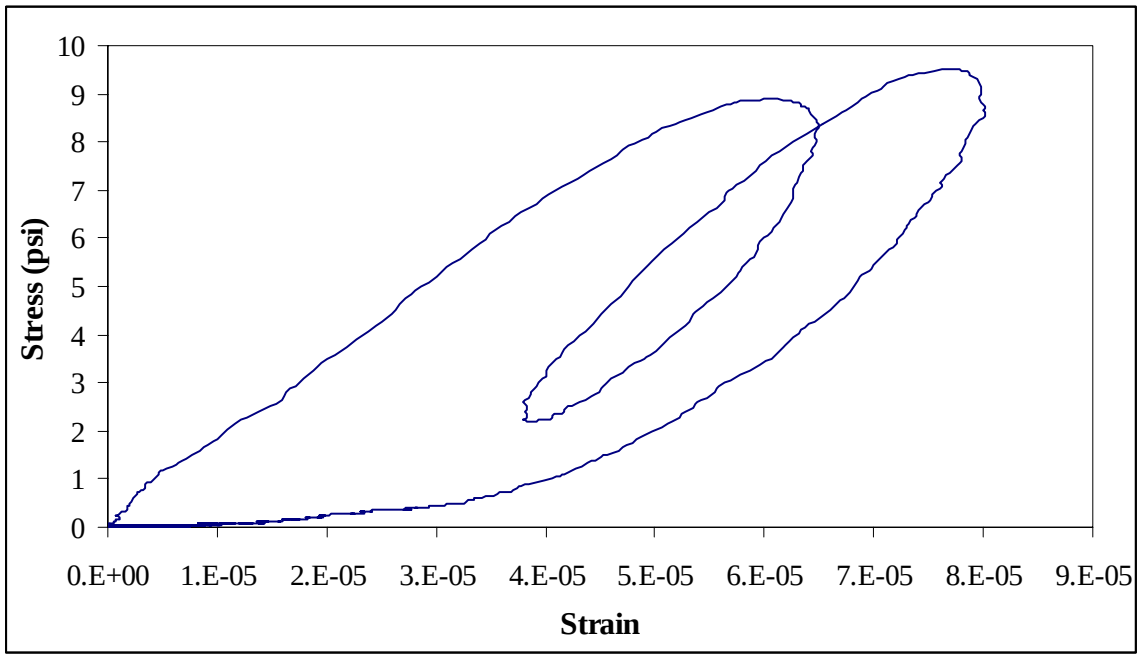


**Figure A.2 Hysteresis Loop for Tandem Axle 25% Interaction**

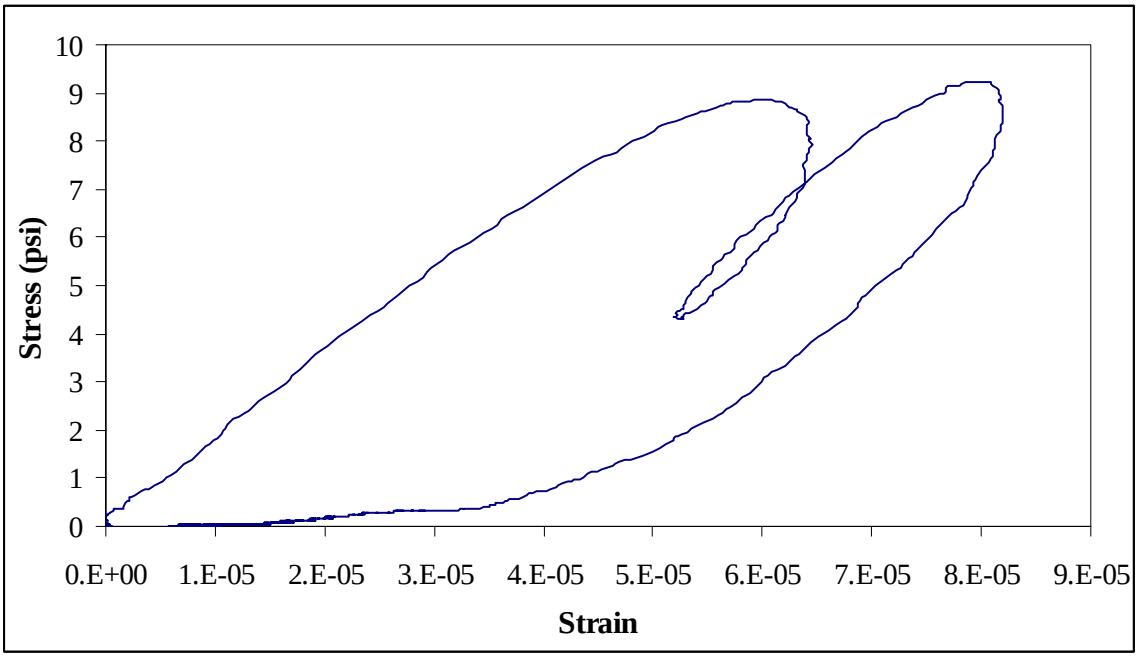


**Figure A.3 Hysteresis Loop for Tandem Axle 50% Interaction**

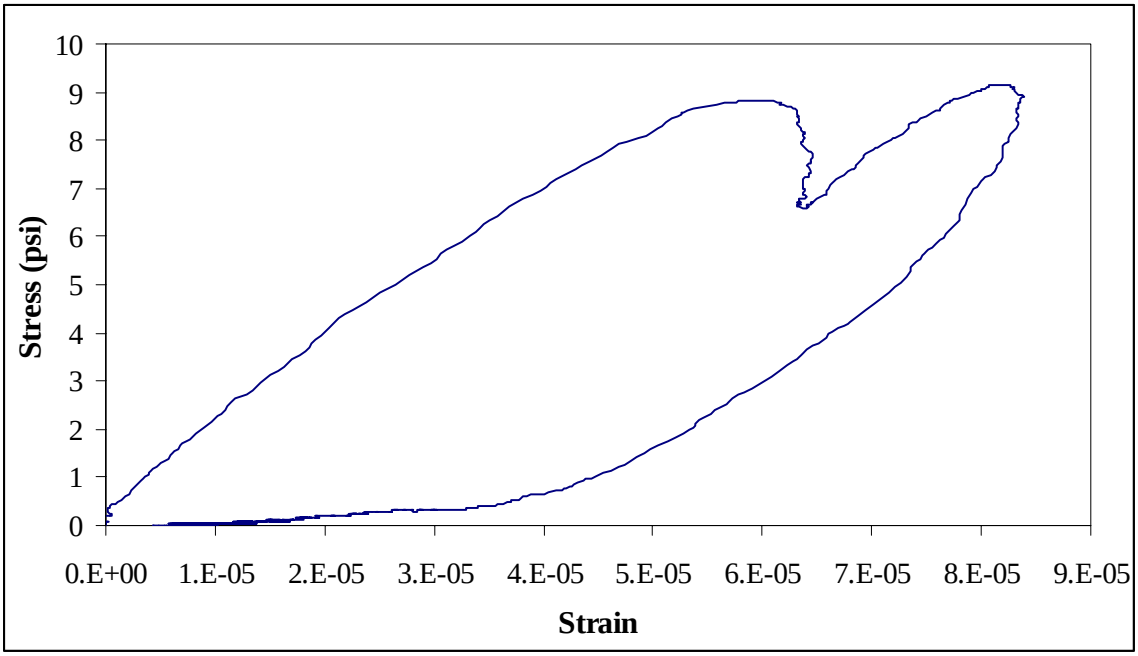


**Figure A.4 Hysteresis Loop for Tandem Axle 75% Interaction**

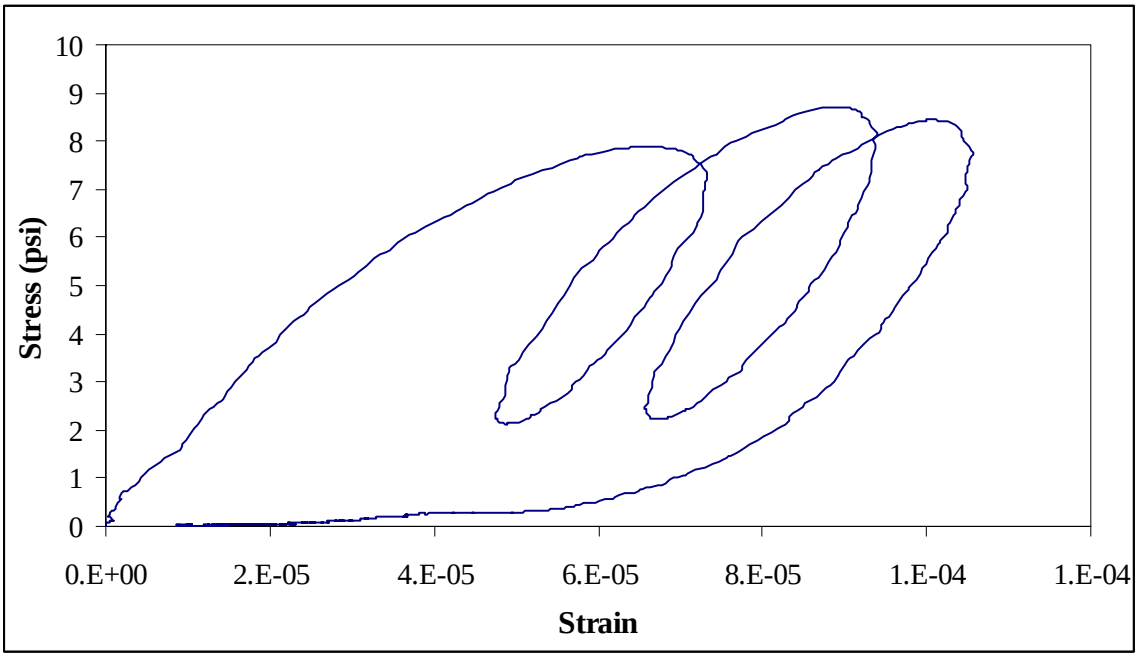


**Figure A.5 Hysteresis Loop for Tridem Axle 25% Interaction**

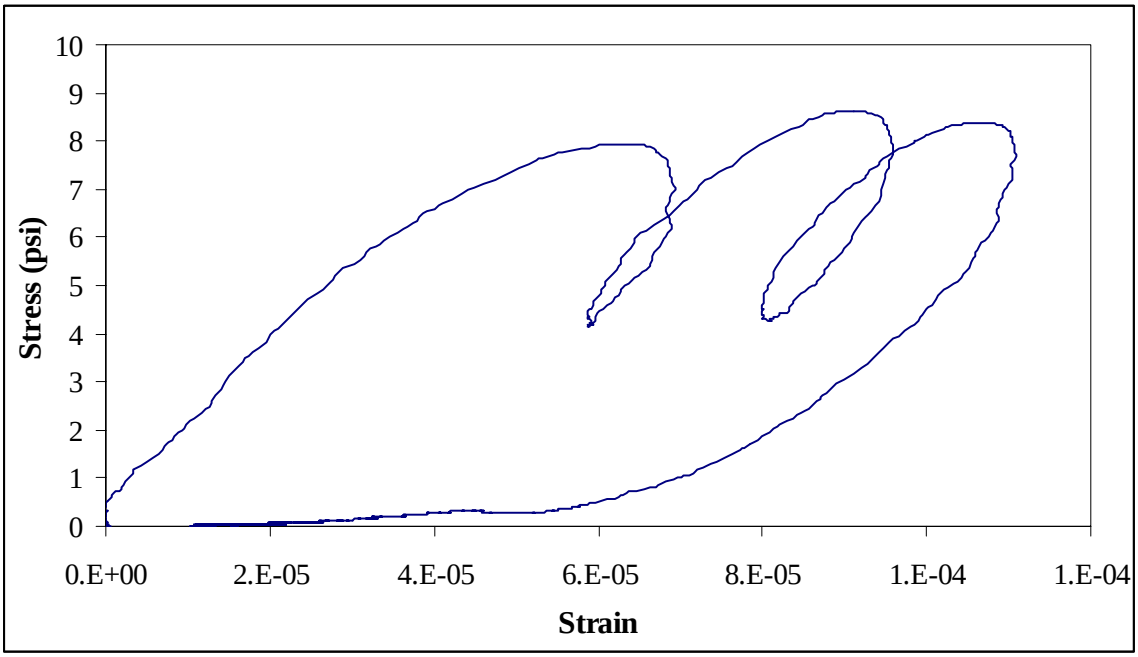


**Figure A.6 Hysteresis Loop for Tridem Axle 50% Interaction**

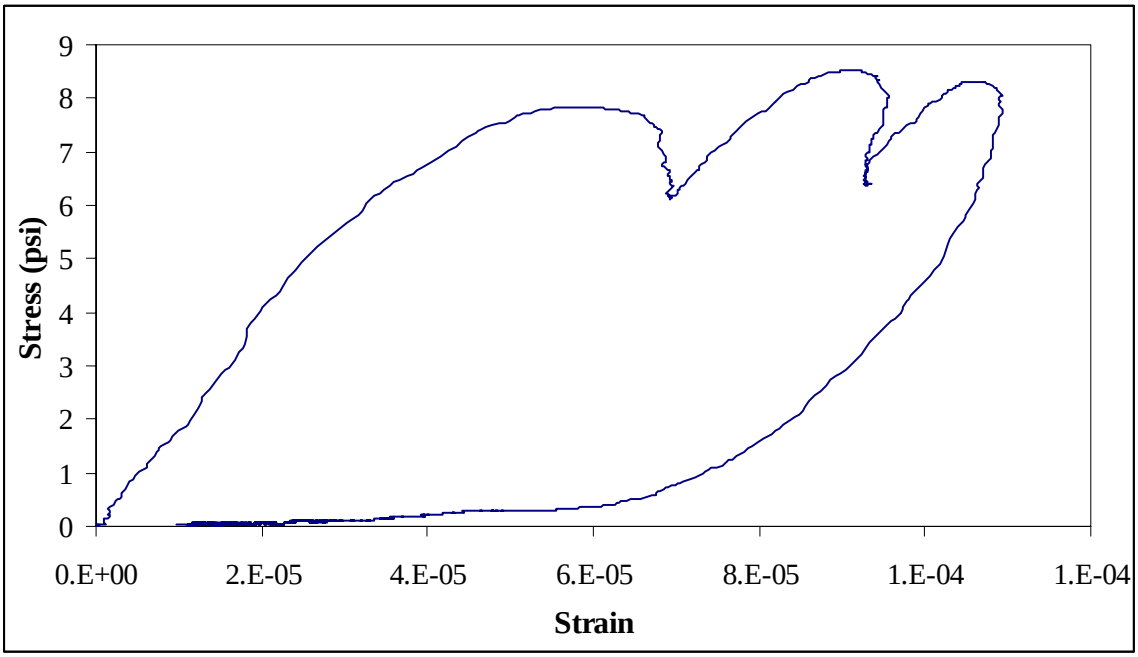


**Figure A.7 Hysteresis Loop for Tridem Axle 75% Interaction**

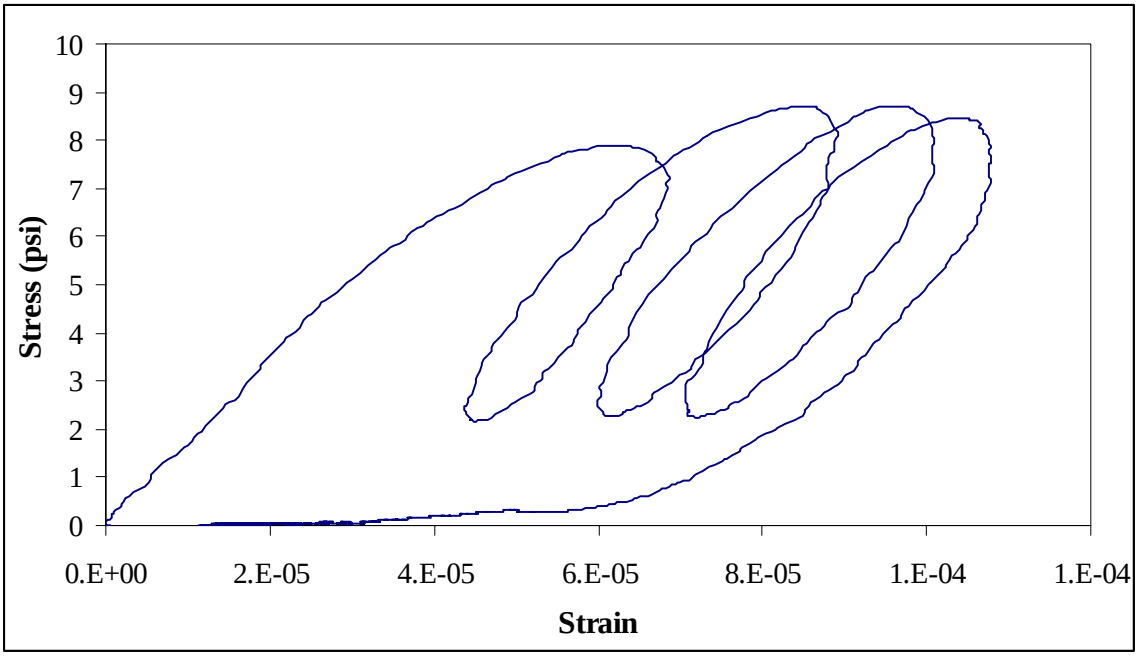


**Figure A.8 Hysteresis Loop for 4-Axle 25% Interaction**

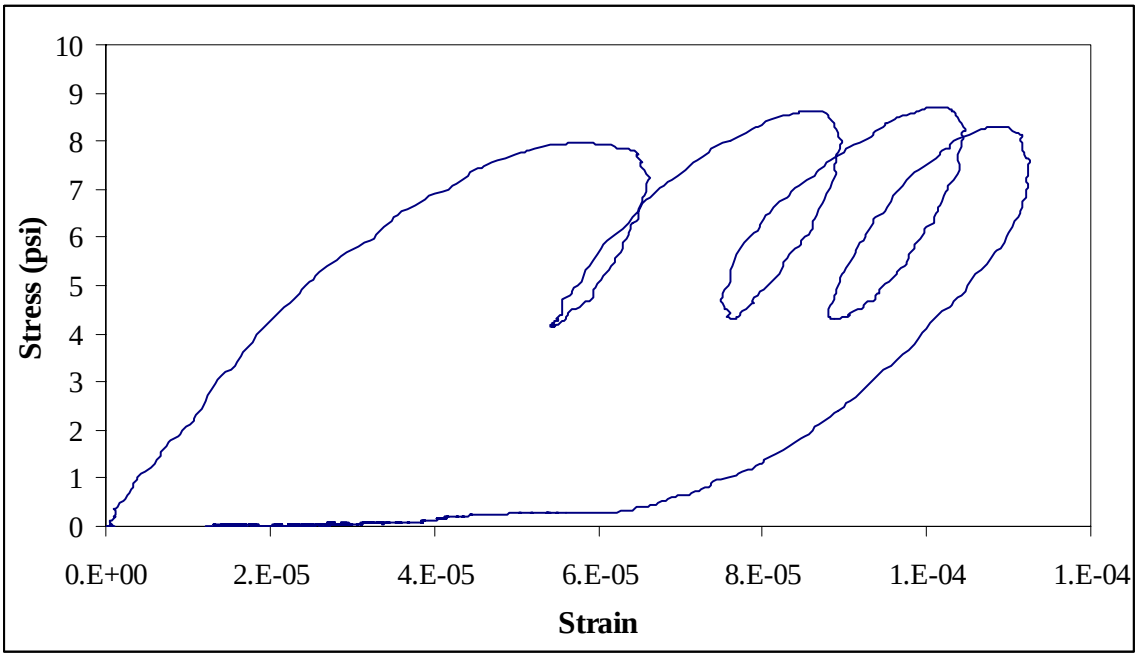


**Figure A.9 Hysteresis Loop for 4-Axle 50% Interaction**

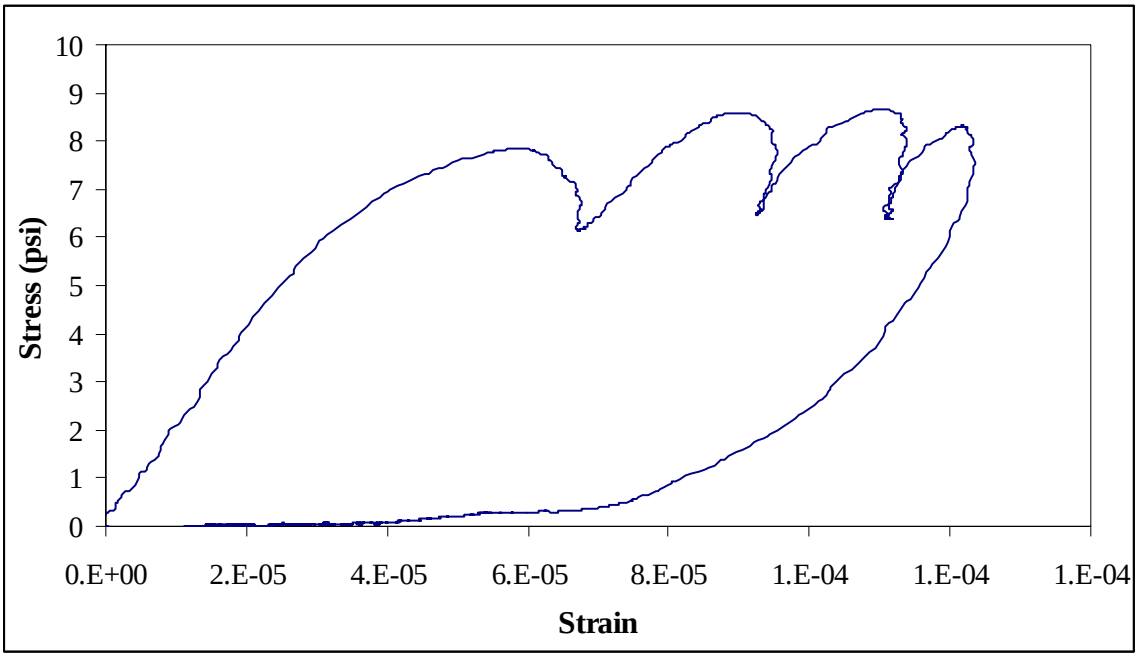


**Figure A.10 Hysteresis Loop for 4-Axle 75% Interaction**

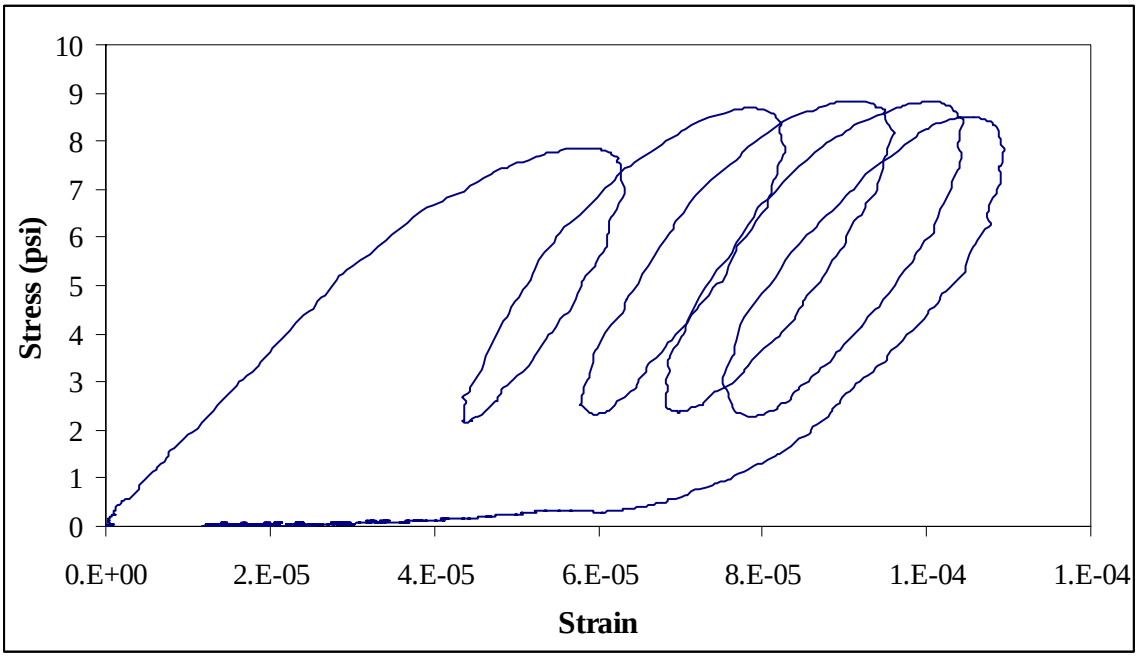


**Figure A.11 Hysteresis Loop for 5-Axle 25% Interaction**

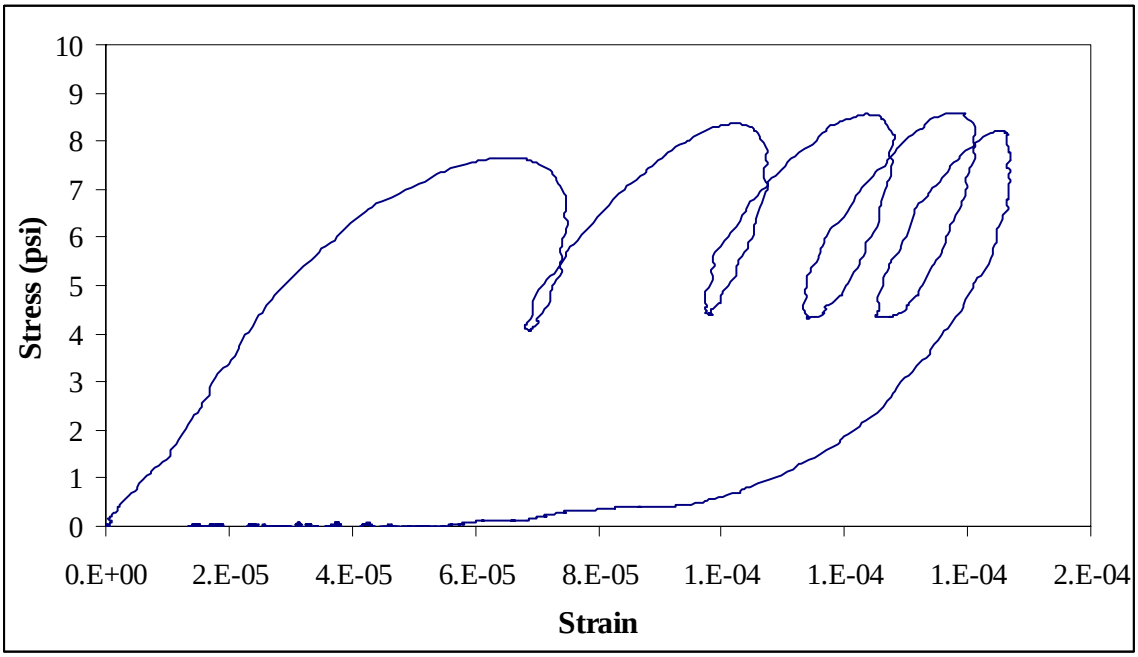


**Figure A.12 Hysteresis Loop for 5-Axle 50% Interaction**

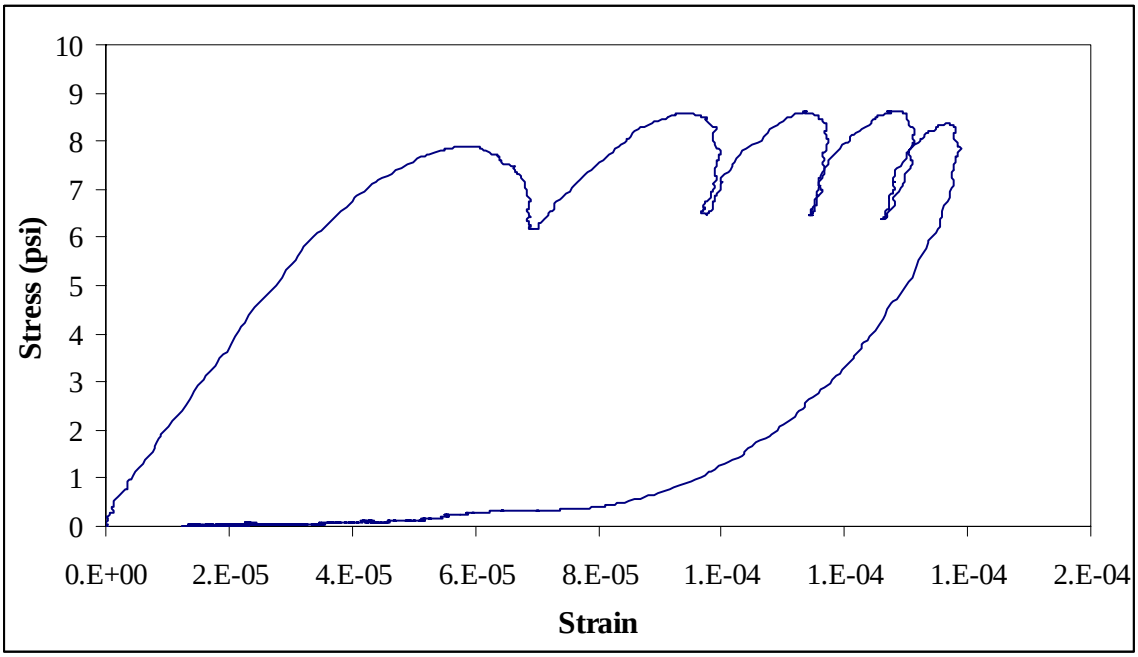


**Figure A.13 Hysteresis Loop for 5-Axle 75% Interaction**

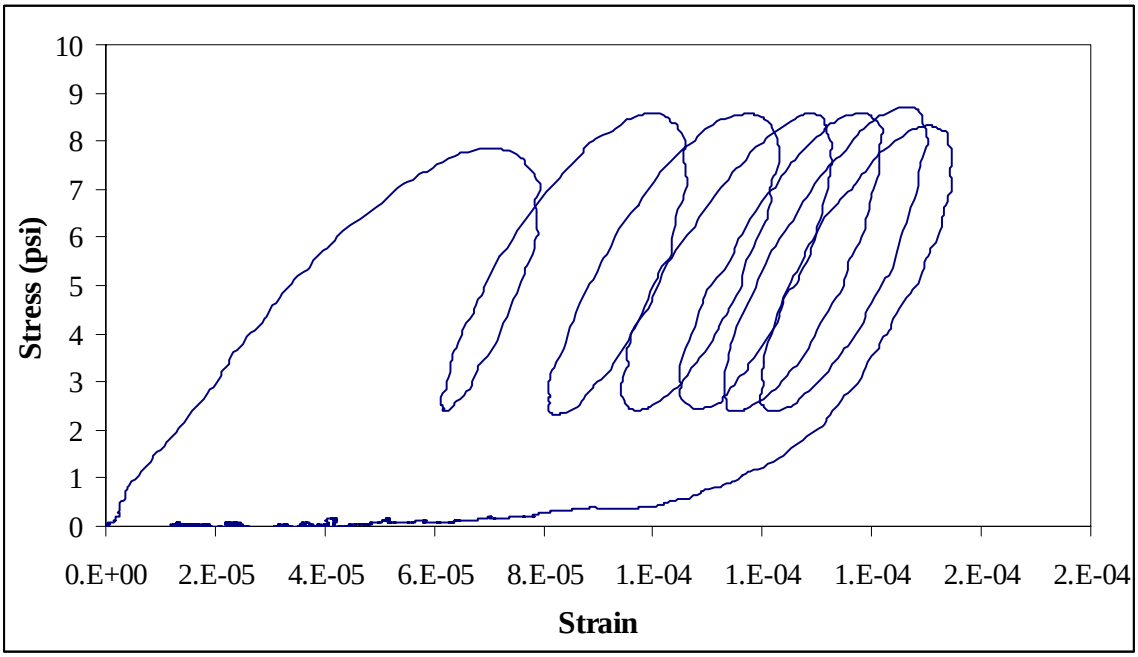


**Figure A.14 Hysteresis Loop for 7-Axle 25% Interaction**

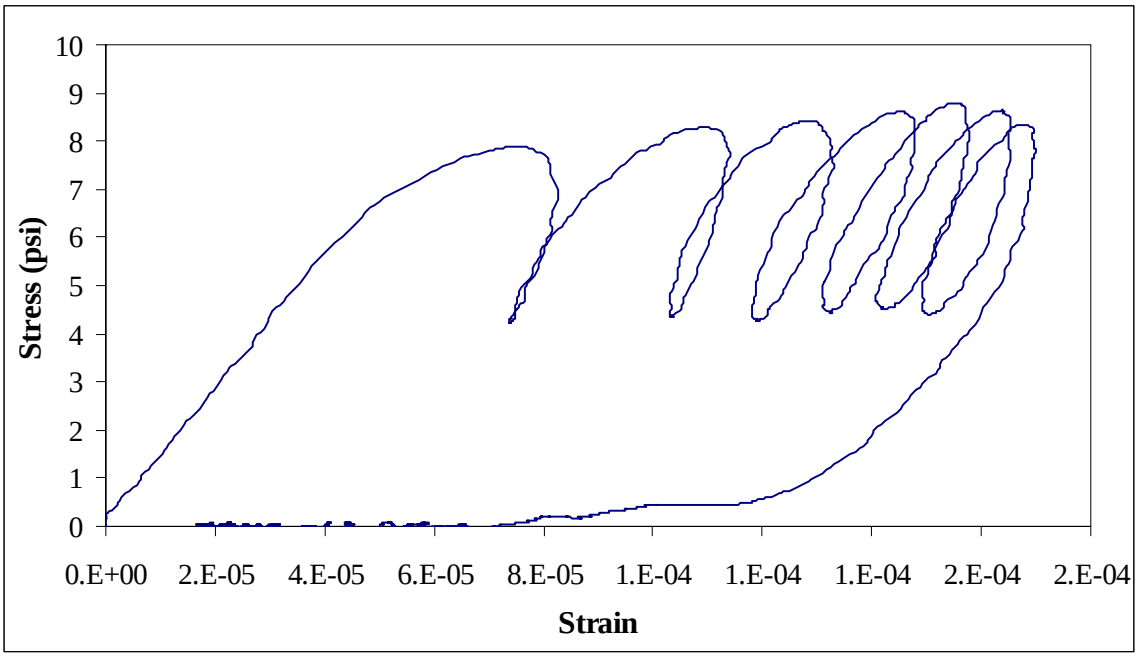


**Figure A.15 Hysteresis Loop for 7-Axle 50% Interaction**

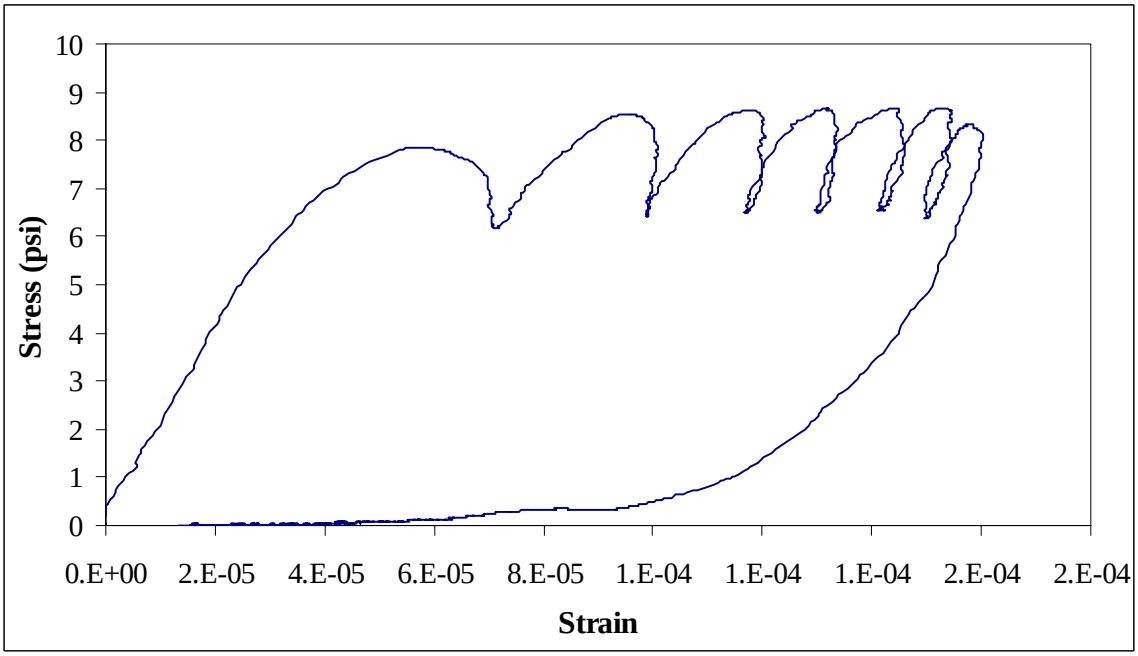


**Figure A.16 Hysteresis Loop for 7-Axle 75% Interaction**

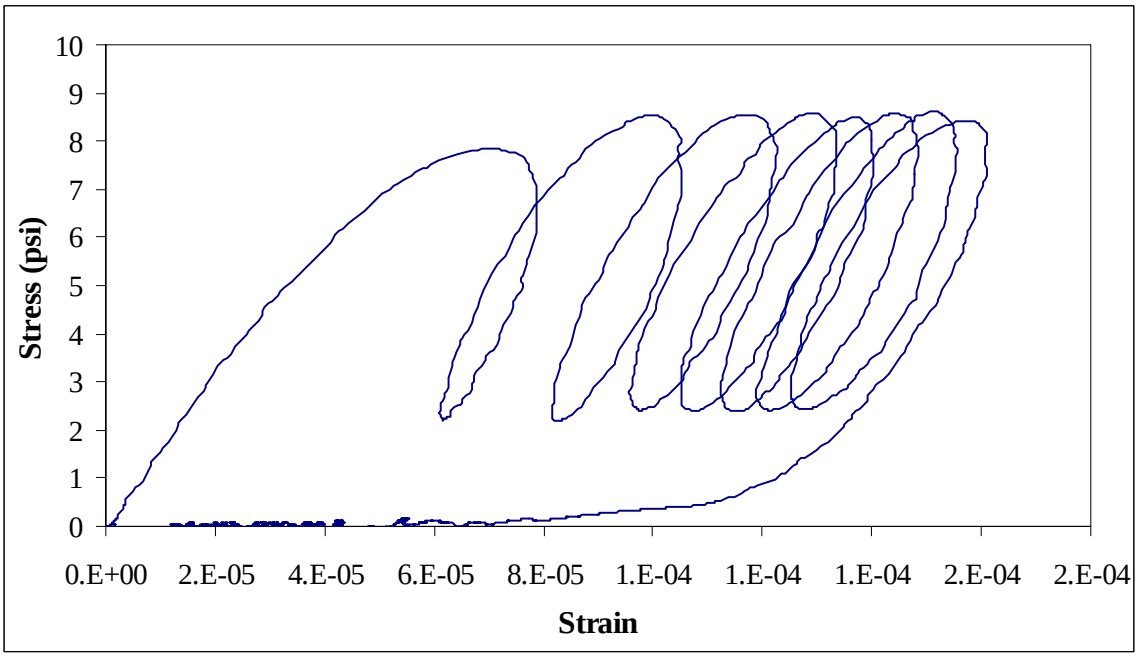


**Figure A.17 Hysteresis Loop for 8-Axle 25% Interaction**

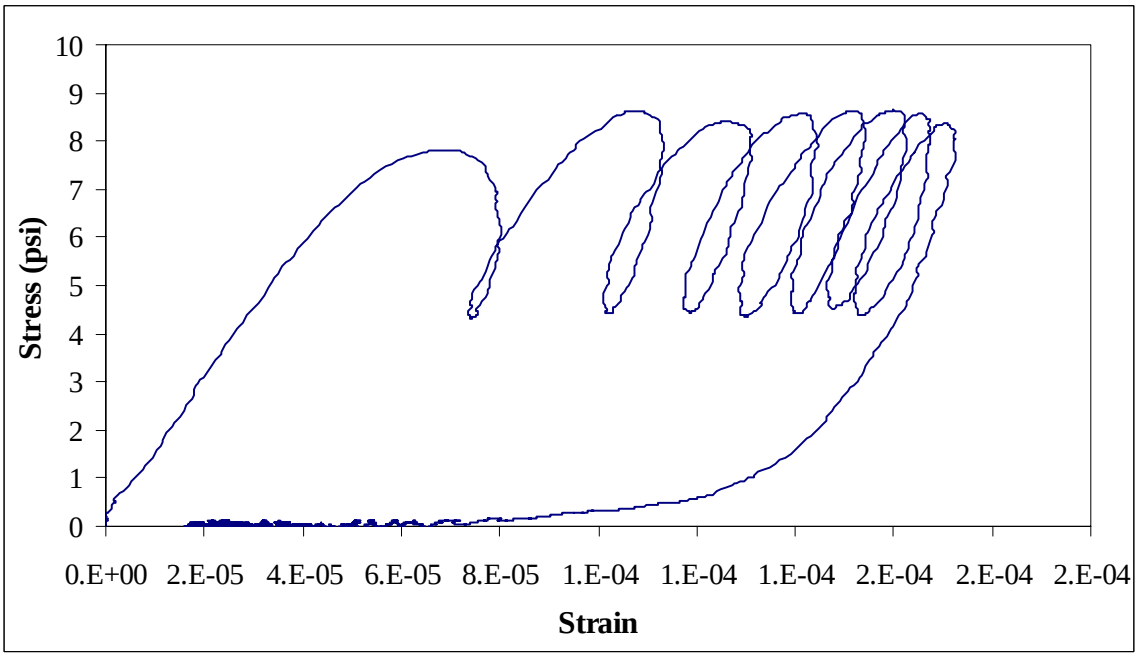


**Figure A.18 Hysteresis Loop for 8-Axle 50% Interaction**

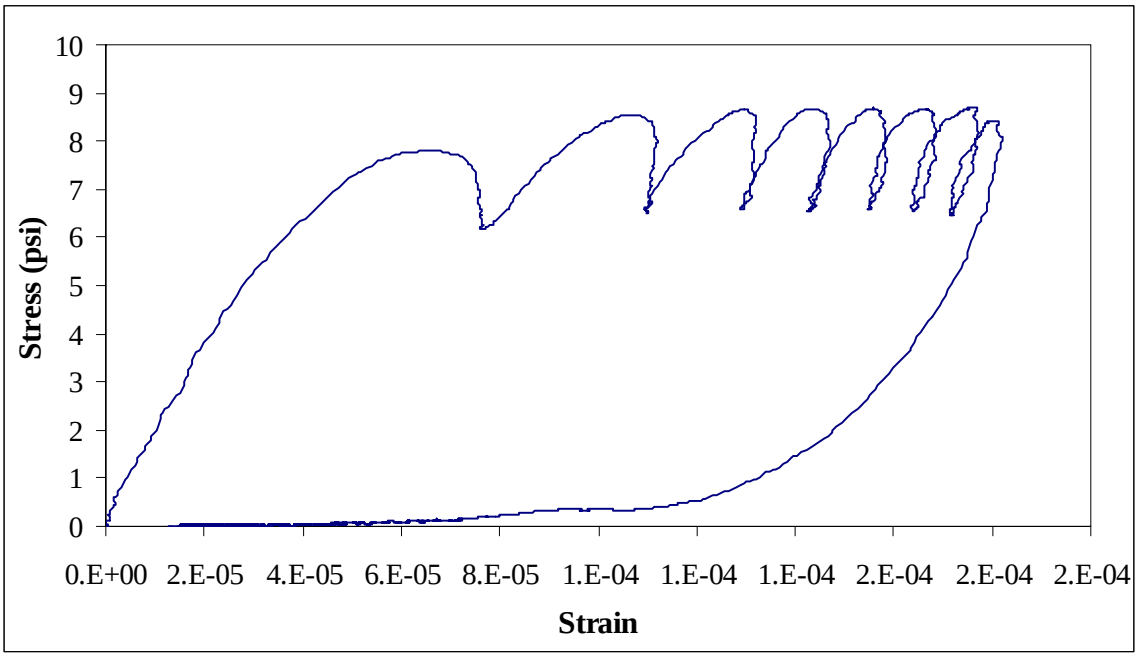


**Figure A.19 Hysteresis Loop for 8-Axle 75% Interaction**

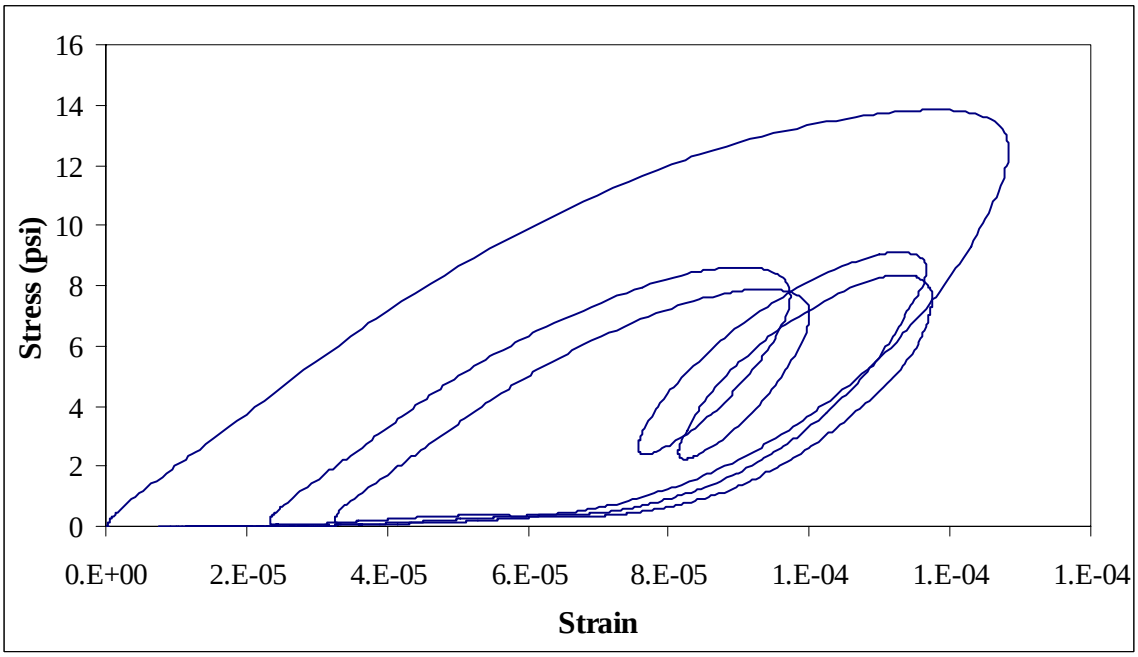


**Figure A.20 Hysteresis Loop for Truck 0**

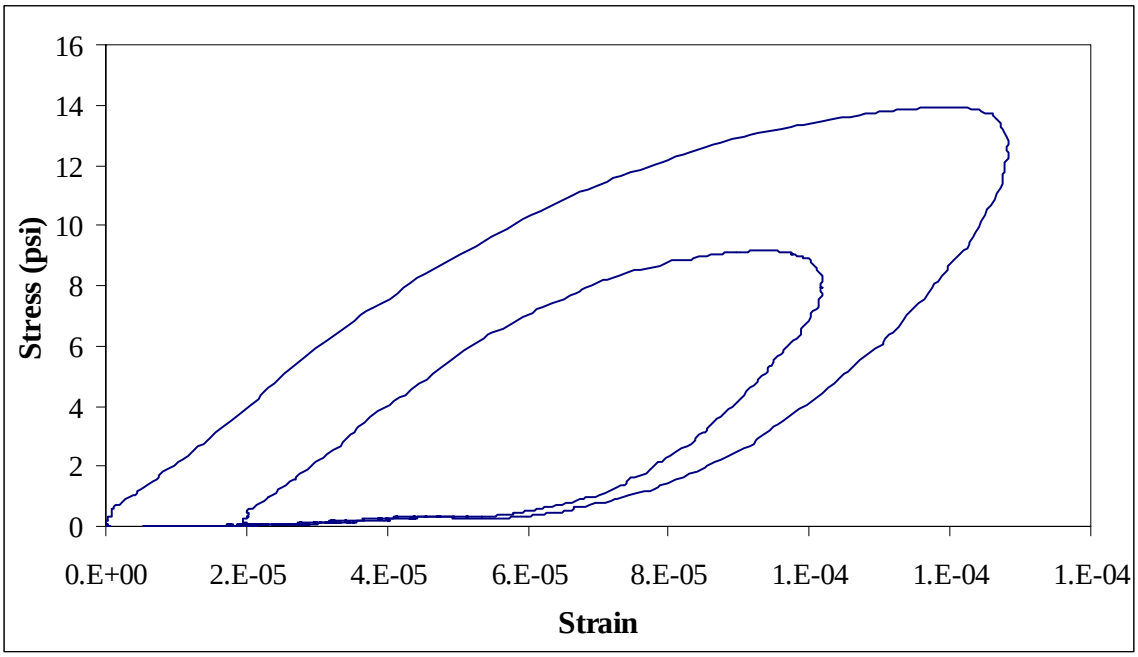


**Figure A.21 Hysteresis Loop for Truck 1**

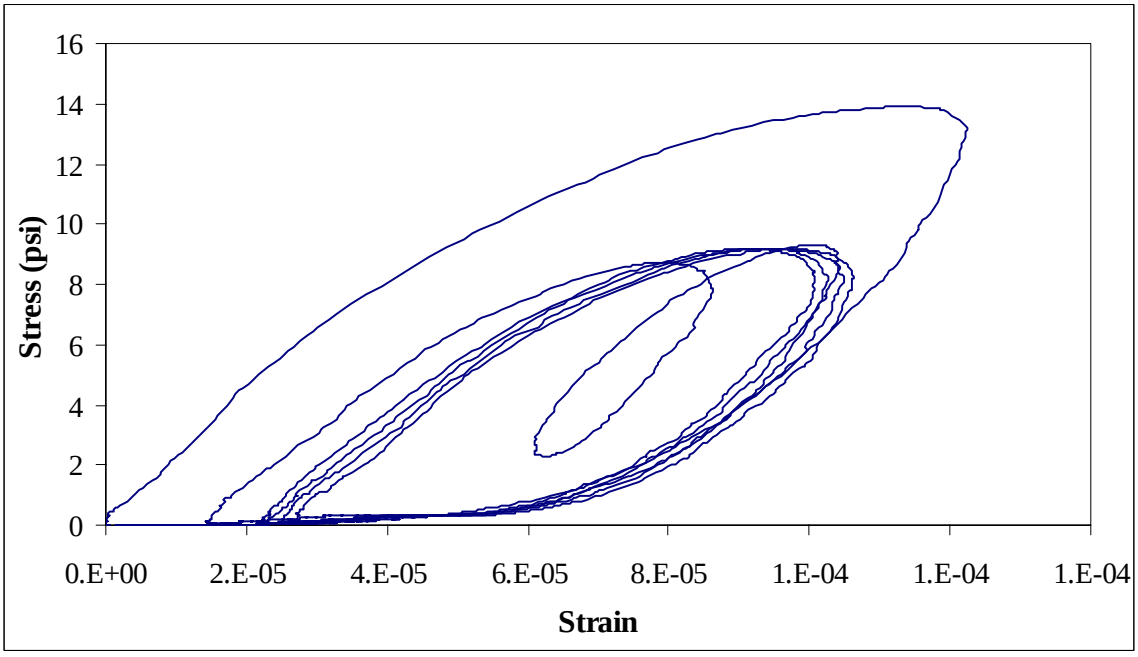


**Figure A.22 Hysteresis Loop for Truck 10**

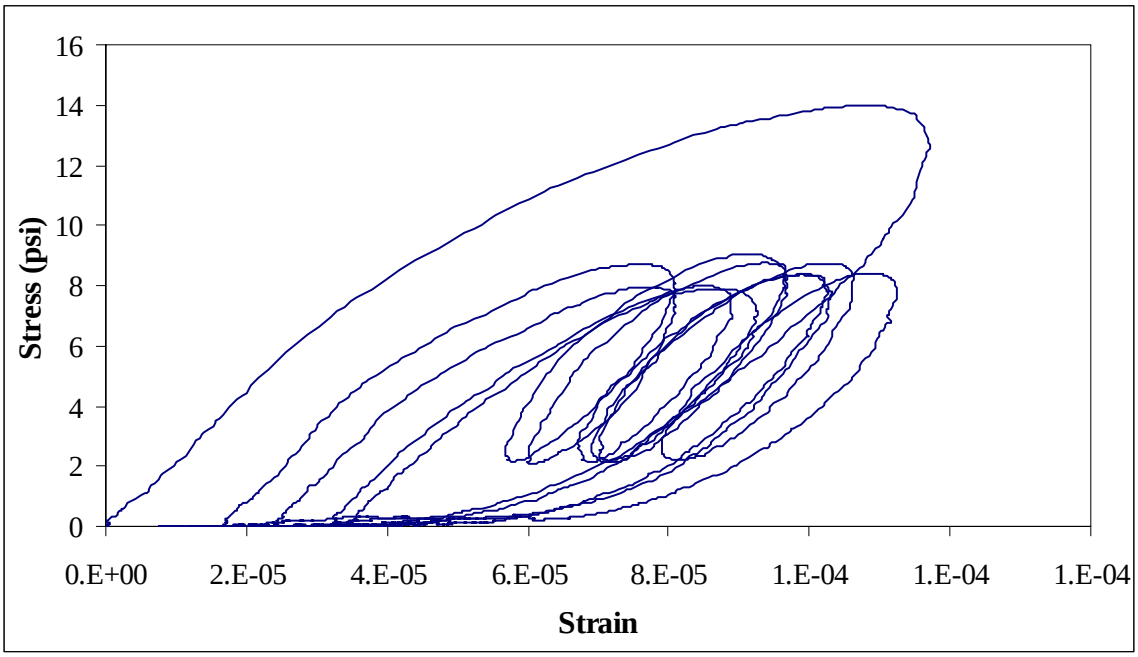


**Figure A.23 Hysteresis Loop for Truck 13**

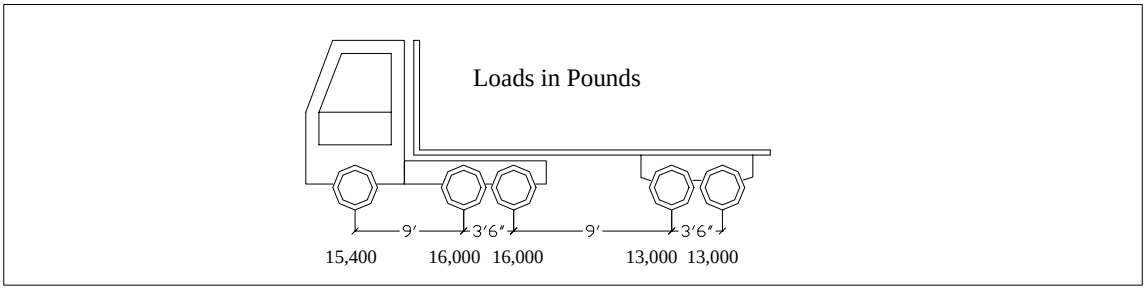


**Figure A.24 Truck 0**

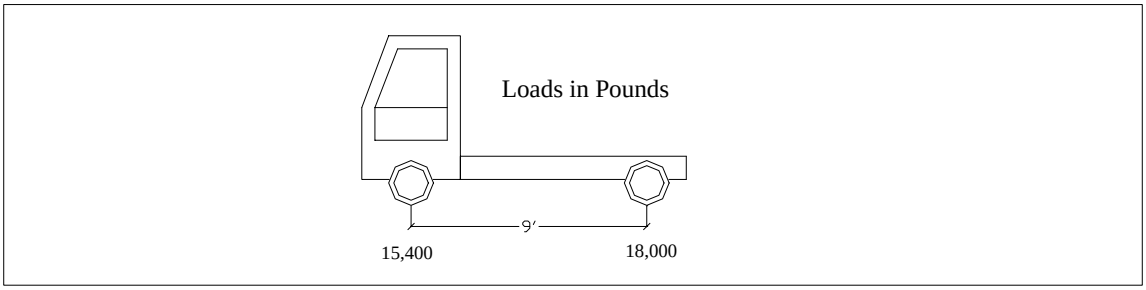


**Figure A.25 Truck 1**

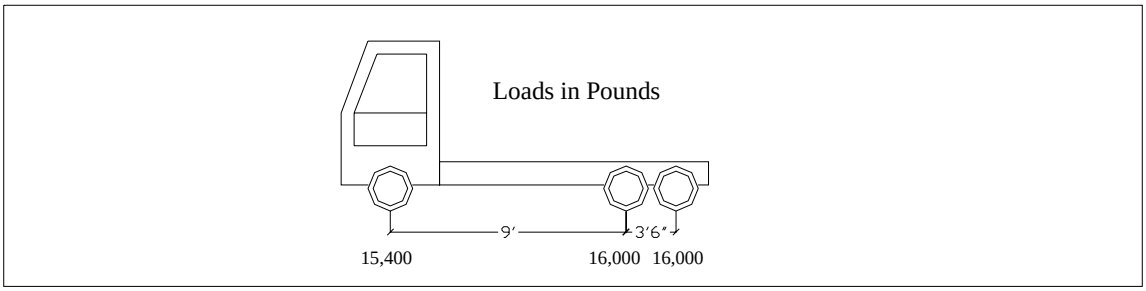


**Figure A.26 Truck 2**

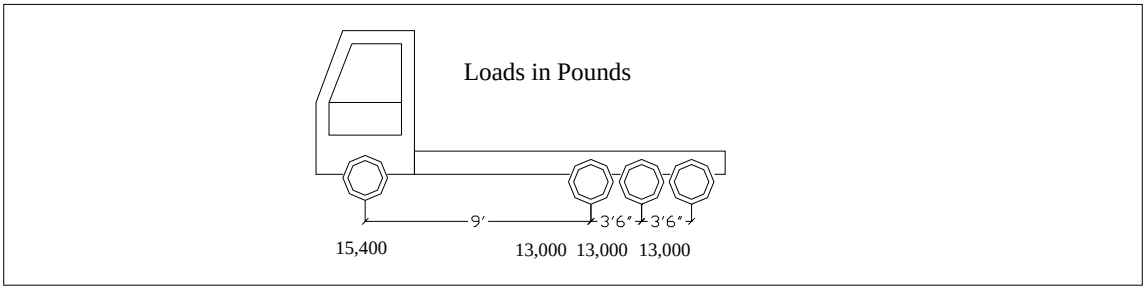


**Figure A.27 Truck 3**

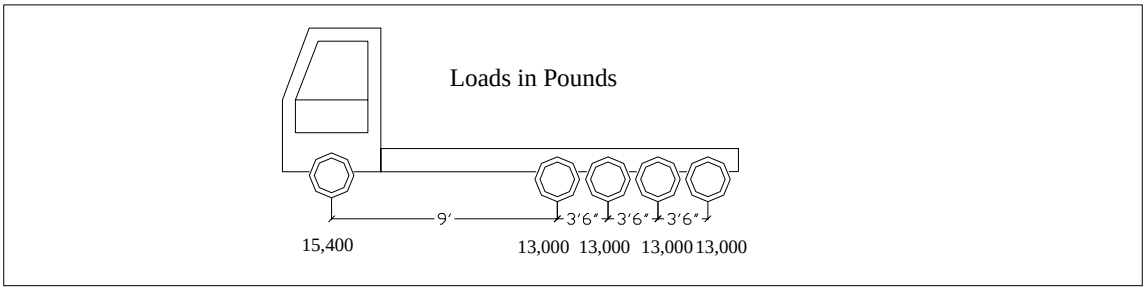


**Figure A.28 Truck 4**

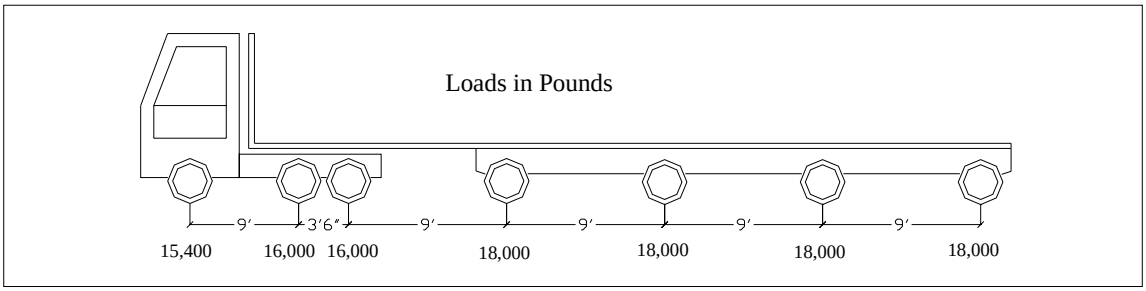


**Figure A.29 Truck 10**

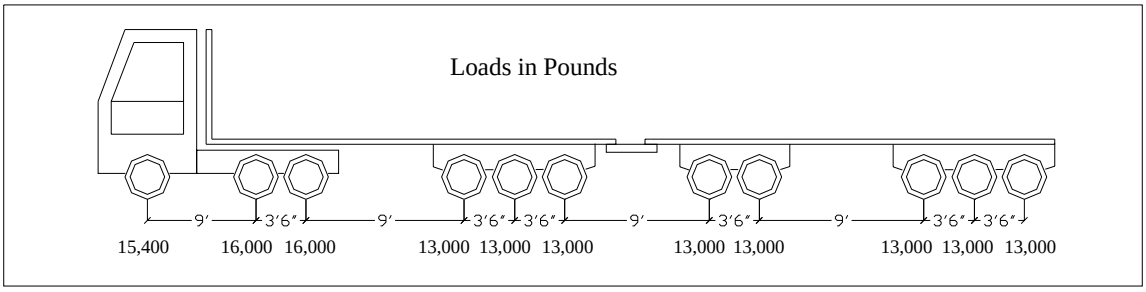


**Figure A.30 Truck 13**

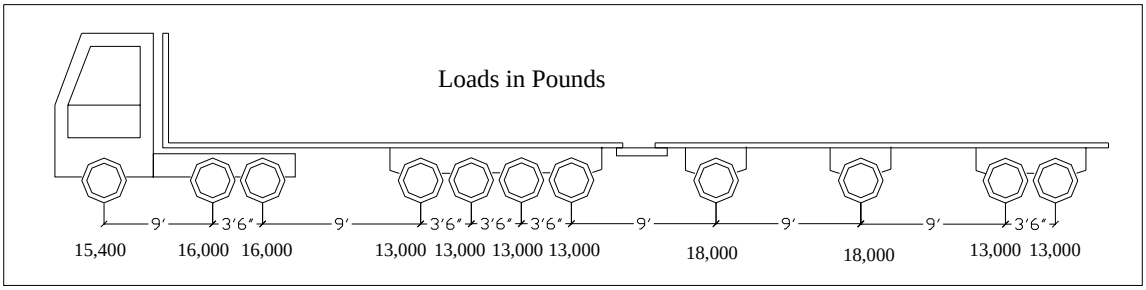


**Figure A.31 Truck 14**

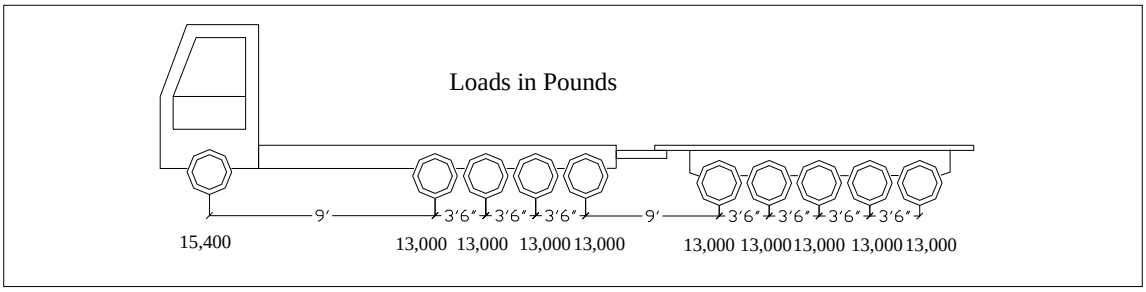


**Figure A.32 Truck 17**

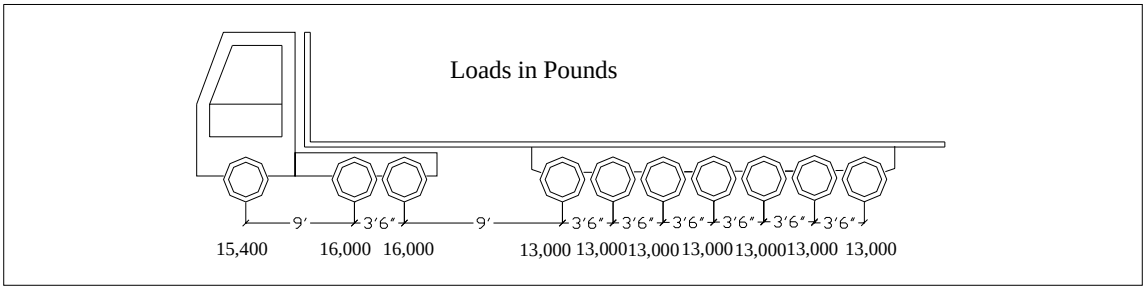


**Figure A.33 Truck 19**

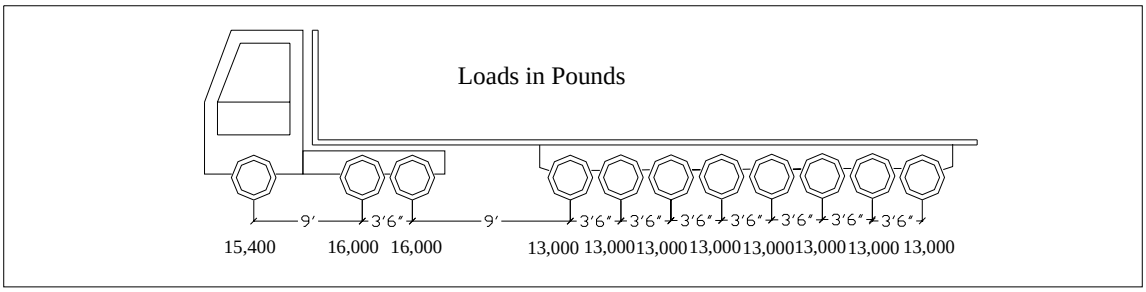


**Figure A.34 Truck 20**

# APPENDIX B - Fatigue and Specific Gravity Tests Results

**Table B.1 Specific Gravity Results for Tested Specimens of Mix I**

| Specimen # | Gmm | Wt in air (gr.) | Wt sub. (gr.) | Wt SSD (gr.) | Volume ($cm^3$) | SG SSD | SG air | Va % |
|---|---|---|---|---|---|---|---|---|
| 104 | 2.489 | 1141.30 | 664.20 | 1142.90 | 478.7 | 2.388 | 2.384 | 4.212 |
| 106 | 2.489 | 1144.80 | 667.70 | 1145.80 | 478.1 | 2.397 | 2.394 | 3.798 |
| 107 | 2.489 | 1144.80 | 668.50 | 1146.20 | 477.7 | 2.399 | 2.396 | 3.717 |
| 109 | 2.489 | 1144.80 | 667.10 | 1145.40 | 478.3 | 2.395 | 2.393 | 3.838 |
| 110 | 2.489 | 1142.90 | 665.30 | 1144.50 | 479.2 | 2.388 | 2.385 | 4.178 |
| 111 | 2.489 | 1142.60 | 666.60 | 1144.50 | 477.9 | 2.395 | 2.391 | 3.942 |
| 112 | 2.489 | 1142.00 | 667.10 | 1143.60 | 476.5 | 2.400 | 2.397 | 3.711 |
| 113 | 2.489 | 1144.40 | 669.00 | 1146.70 | 477.7 | 2.400 | 2.396 | 3.751 |
| 114 | 2.489 | 1143.20 | 665.80 | 1145.00 | 479.2 | 2.389 | 2.386 | 4.153 |
| 116 | 2.489 | 1143.60 | 667.30 | 1145.00 | 477.7 | 2.397 | 2.394 | 3.818 |
| 117 | 2.489 | 1144.70 | 668.10 | 1146.90 | 478.8 | 2.395 | 2.391 | 3.947 |
| 118 | 2.489 | 1143.90 | 667.80 | 1145.40 | 477.6 | 2.398 | 2.395 | 3.773 |
| 119 | 2.489 | 1143.90 | 669.00 | 1146.30 | 477.3 | 2.402 | 2.397 | 3.712 |
| 120 | 2.489 | 1143.90 | 665.60 | 1145.70 | 480.1 | 2.386 | 2.383 | 4.274 |
| 121 | 2.489 | 1143.90 | 667.00 | 1145.40 | 478.4 | 2.394 | 2.391 | 3.933 |
| 122 | 2.489 | 1144.70 | 667.40 | 1146.00 | 478.6 | 2.394 | 2.392 | 3.906 |
| 124 | 2.489 | 1144.80 | 668.20 | 1146.70 | 478.5 | 2.396 | 2.392 | 3.878 |
| 125 | 2.489 | 1143.80 | 665.40 | 1145.20 | 479.8 | 2.387 | 2.384 | 4.222 |
| 126 | 2.489 | 1144.30 | 666.10 | 1146.20 | 480.1 | 2.387 | 2.383 | 4.240 |
| 127 | 2.489 | 1145.40 | 667.10 | 1146.90 | 479.8 | 2.390 | 2.387 | 4.088 |
| 128 | 2.489 | 1145.70 | 668.90 | 1147.70 | 478.8 | 2.397 | 2.393 | 3.863 |
| 129 | 2.489 | 1143.40 | 668.30 | 1145.50 | 477.2 | 2.400 | 2.396 | 3.734 |
| 130 | 2.489 | 1143.30 | 666.90 | 1144.80 | 477.9 | 2.395 | 2.392 | 3.883 |
| 131 | 2.489 | 1141.90 | 664.30 | 1143.60 | 479.3 | 2.386 | 2.382 | 4.282 |
| 133 | 2.489 | 1143.40 | 665.90 | 1144.90 | 479.0 | 2.390 | 2.387 | 4.096 |
| 135 | 2.489 | 1145.60 | 667.00 | 1147.60 | 480.6 | 2.388 | 2.384 | 4.231 |
| 136 | 2.489 | 1143.80 | 668.50 | 1145.40 | 476.9 | 2.402 | 2.398 | 3.640 |
| 137 | 2.489 | 1143.60 | 668.10 | 1145.00 | 476.9 | 2.401 | 2.398 | 3.657 |
| 138 | 2.489 | 1144.10 | 667.90 | 1145.60 | 477.7 | 2.398 | 2.395 | 3.776 |
| 139 | 2.489 | 1144.00 | 667.90 | 1146.10 | 478.2 | 2.397 | 2.392 | 3.885 |
| 140 | 2.489 | 1145.80 | 669.60 | 1147.60 | 478.0 | 2.401 | 2.397 | 3.693 |
| 141 | 2.489 | 1144.50 | 667.40 | 1146.20 | 478.8 | 2.394 | 2.390 | 3.963 |
| 142 | 2.489 | 1145.20 | 668.40 | 1147.10 | 478.7 | 2.396 | 2.392 | 3.885 |
| 143 | 2.489 | 1142.10 | 666.10 | 1144.20 | 478.1 | 2.393 | 2.389 | 4.024 |
| 144 | 2.489 | 1143.10 | 666.80 | 1145.00 | 478.2 | 2.394 | 2.390 | 3.961 |
| 145 | 2.489 | 1144.00 | 666.40 | 1145.80 | 479.4 | 2.390 | 2.386 | 4.126 |
| 147 | 2.489 | 1143.60 | 667.20 | 1144.90 | 477.7 | 2.397 | 2.394 | 3.818 |
| 148 | 2.489 | 1144.90 | 669.70 | 1146.70 | 477.0 | 2.404 | 2.400 | 3.567 |
| 149 | 2.489 | 1144.40 | 668.40 | 1146.20 | 477.8 | 2.399 | 2.395 | 3.771 |
| 150 | 2.489 | 1145.20 | 669.40 | 1147.20 | 477.8 | 2.401 | 2.397 | 3.704 |
| 151 | 2.489 | 1144.10 | 666.20 | 1145.10 | 478.9 | 2.391 | 2.389 | 4.017 |
| 152 | 2.489 | 1143.20 | 667.30 | 1143.90 | 476.6 | 2.400 | 2.399 | 3.630 |
| 154 | 2.489 | 1144.70 | 668.20 | 1145.90 | 477.7 | 2.399 | 2.396 | 3.725 |
| 155 | 2.489 | 1142.40 | 666.60 | 1143.70 | 477.1 | 2.397 | 2.394 | 3.798 |
| 156 | 2.489 | 1145.70 | 668.20 | 1147.60 | 479.4 | 2.394 | 2.390 | 3.983 |
| 157 | 2.489 | 1144.00 | 667.70 | 1145.00 | 477.3 | 2.399 | 2.397 | 3.704 |

**Table B.2 Specific Gravity Results of Mix II**

| Specimen # | Gmm | Wt in air (gr.) | Wt sub. (gr.) | Wt SSD (gr.) | Volume ($cm^3$) | SG SSD | SG air | Va % |
|---|---|---|---|---|---|---|---|---|
| 201 | 2.498 | 1150.00 | 669.30 | 1151.00 | 481.7 | 2.389 | 2.387 | 4.428 |
| 202 | 2.498 | 1147.60 | 669.70 | 1148.10 | 478.4 | 2.400 | 2.399 | 3.970 |
| 203 | 2.498 | 1148.30 | 671.70 | 1149.80 | 478.1 | 2.405 | 2.402 | 3.851 |
| 204 | 2.498 | 1152.70 | 676.70 | 1154.00 | 477.3 | 2.418 | 2.415 | 3.321 |
| 205 | 2.498 | 1147.90 | 670.80 | 1149.00 | 478.2 | 2.403 | 2.400 | 3.905 |
| 206 | 2.498 | 1150.80 | 672.80 | 1152.10 | 479.3 | 2.404 | 2.401 | 3.883 |
| 207 | 2.498 | 1153.40 | 677.20 | 1155.10 | 477.9 | 2.417 | 2.413 | 3.384 |
| 208 | 2.498 | 1149.50 | 672.60 | 1151.00 | 478.4 | 2.406 | 2.403 | 3.811 |
| 209 | 2.498 | 1147.10 | 671.80 | 1148.20 | 476.4 | 2.410 | 2.408 | 3.609 |
| 210 | 2.498 | 1147.30 | 669.80 | 1148.90 | 479.1 | 2.398 | 2.395 | 4.135 |
| 211 | 2.498 | 1149.40 | 673.90 | 1150.90 | 477.0 | 2.413 | 2.410 | 3.537 |
| 212 | 2.498 | 1151.80 | 672.50 | 1153.00 | 480.5 | 2.400 | 2.397 | 4.040 |
| 213 | 2.498 | 1148.90 | 671.60 | 1149.90 | 478.3 | 2.404 | 2.402 | 3.841 |
| 214 | 2.498 | 1149.50 | 673.70 | 1150.80 | 477.1 | 2.412 | 2.409 | 3.549 |
| 215 | 2.498 | 1148.40 | 672.10 | 1149.70 | 477.6 | 2.407 | 2.405 | 3.742 |
| 216 | 2.498 | 1151.20 | 674.60 | 1152.20 | 477.6 | 2.412 | 2.410 | 3.507 |

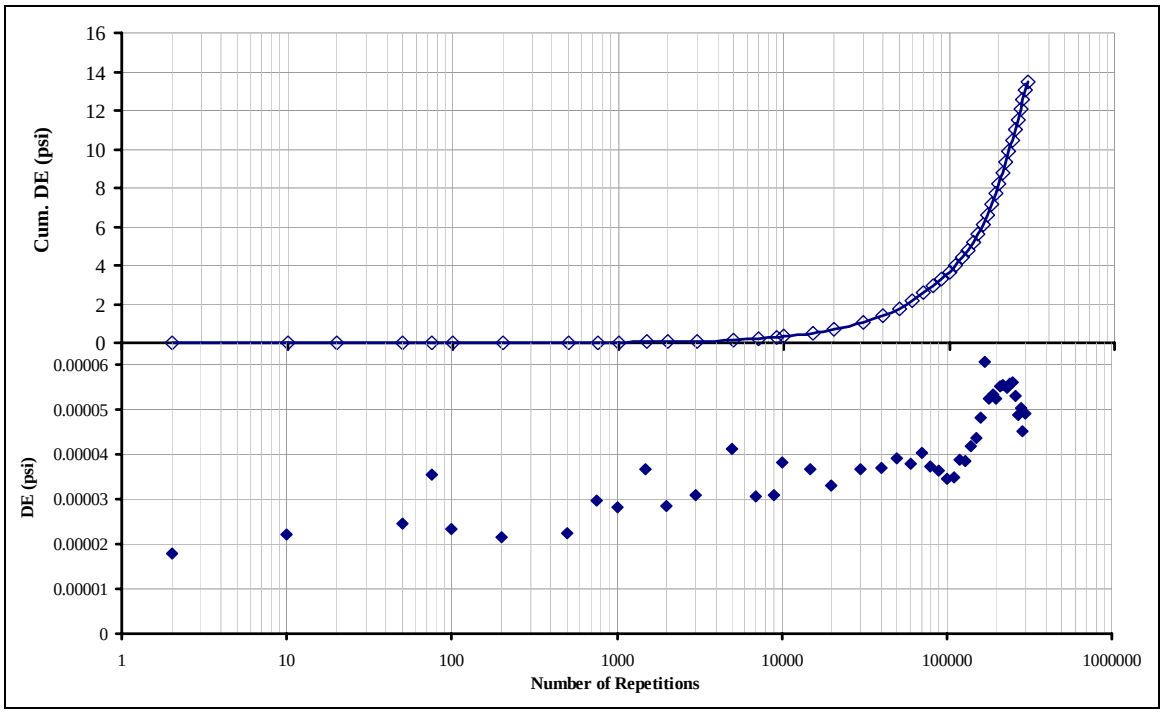


**Figure B.1 Single Axle Low Stress (Specimen 112)**

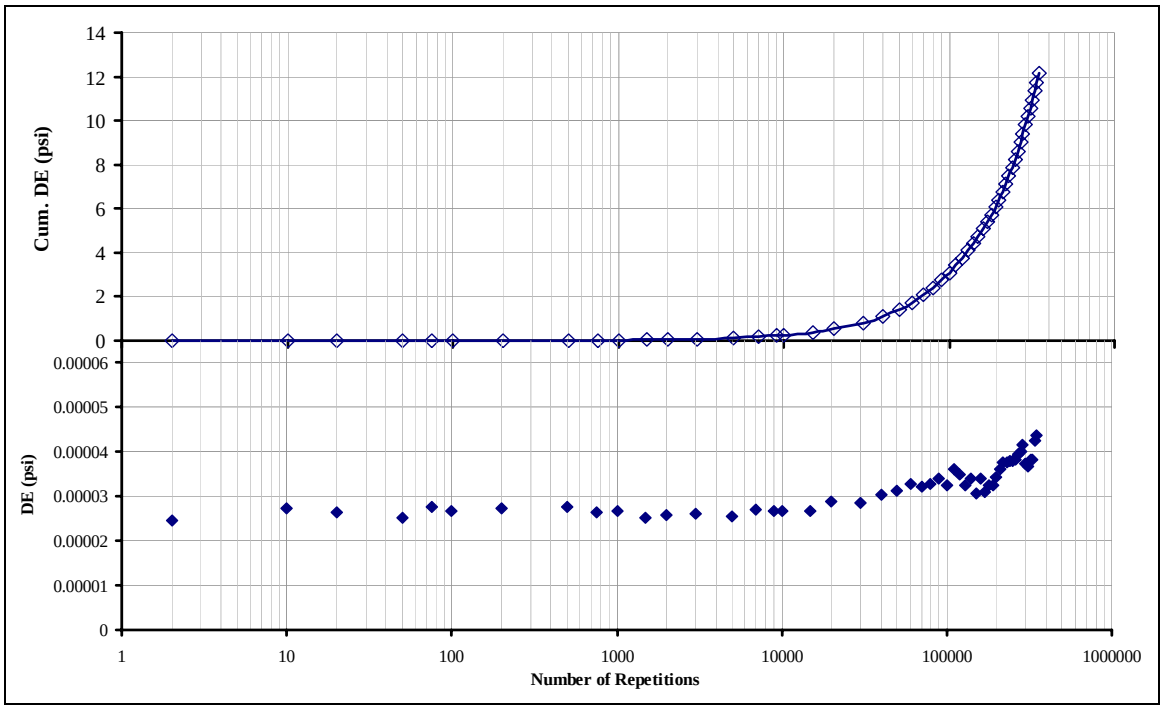


**Figure B.2 Single Axle Low Stress (Specimen 157)**

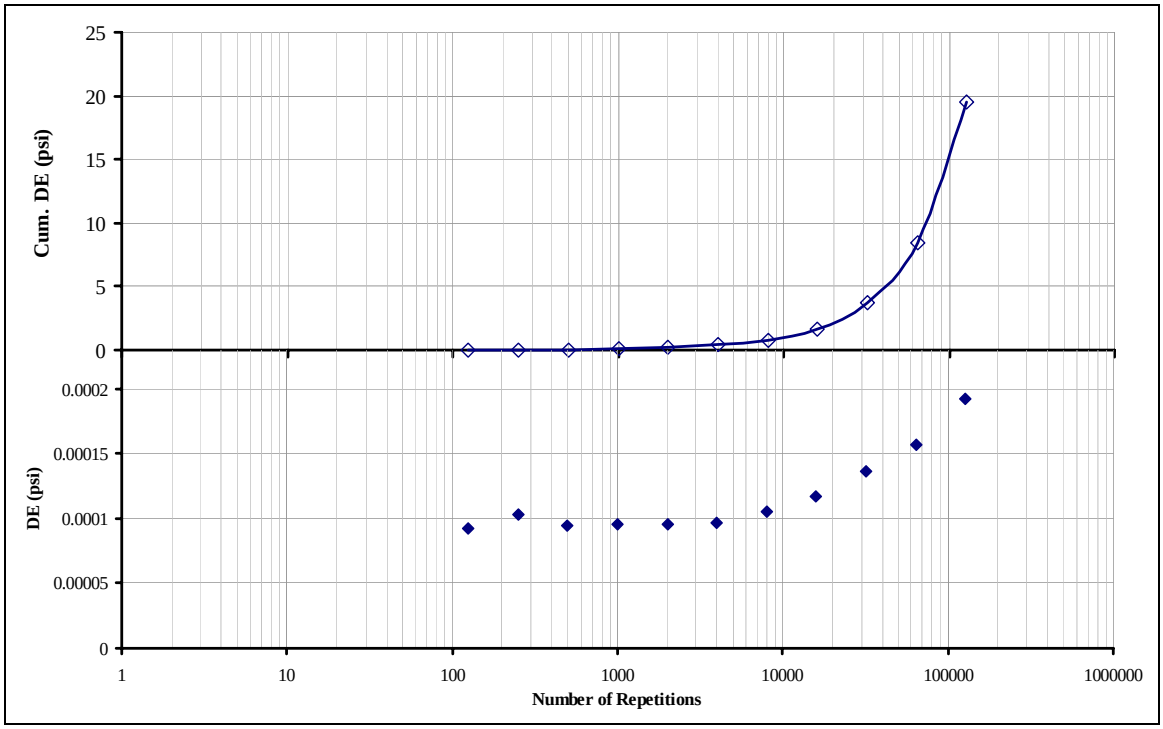


**Figure B.3 Single Axle Medium Stress (Specimen 130)**

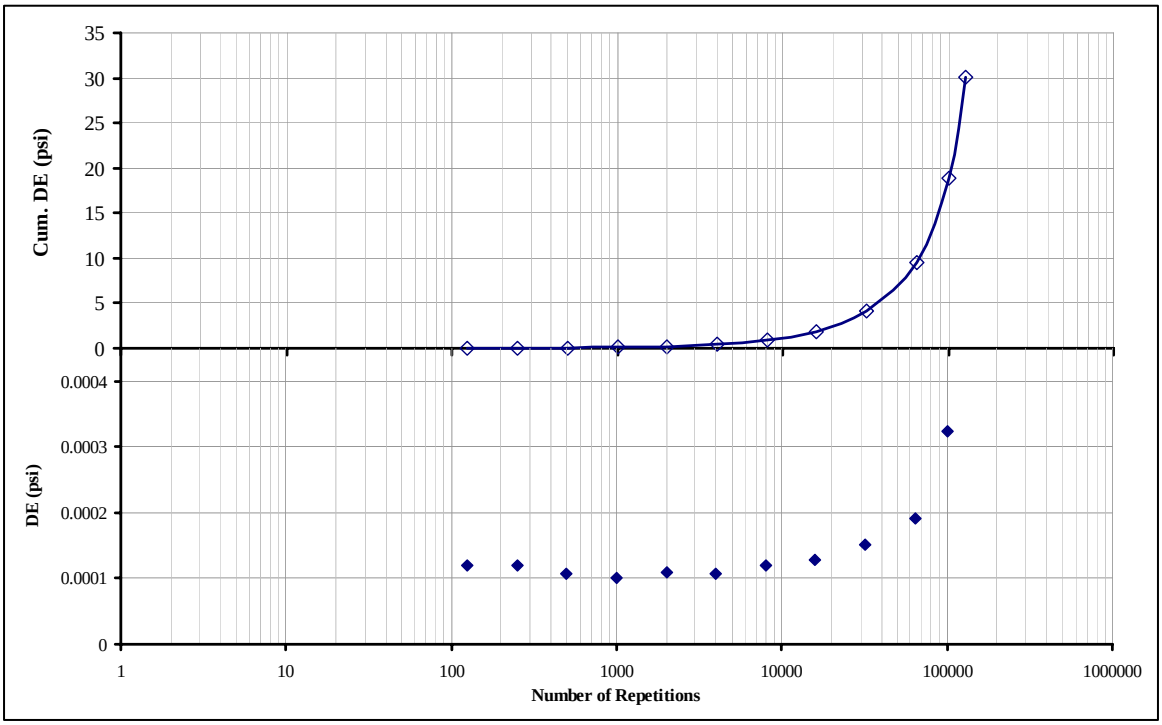


**Figure B.4 Single Axle Medium Stress (Specimen 139)**

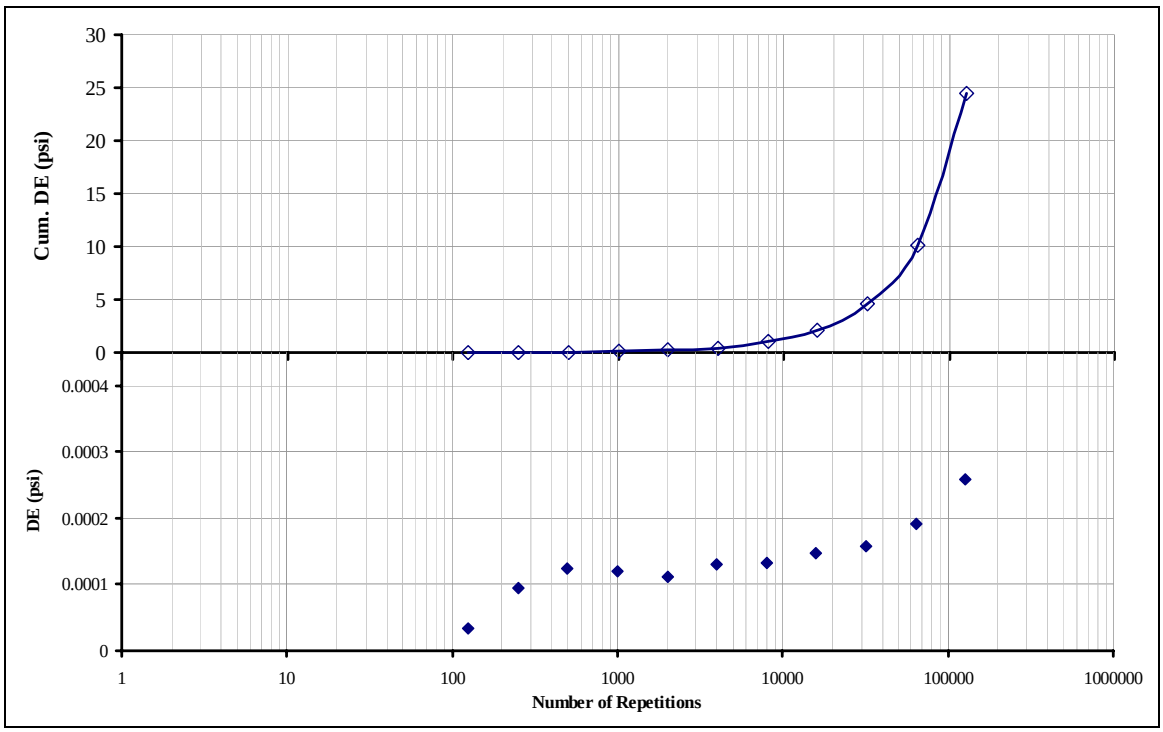


**Figure B.5 Single Axle Medium Stress (Specimen 142)**

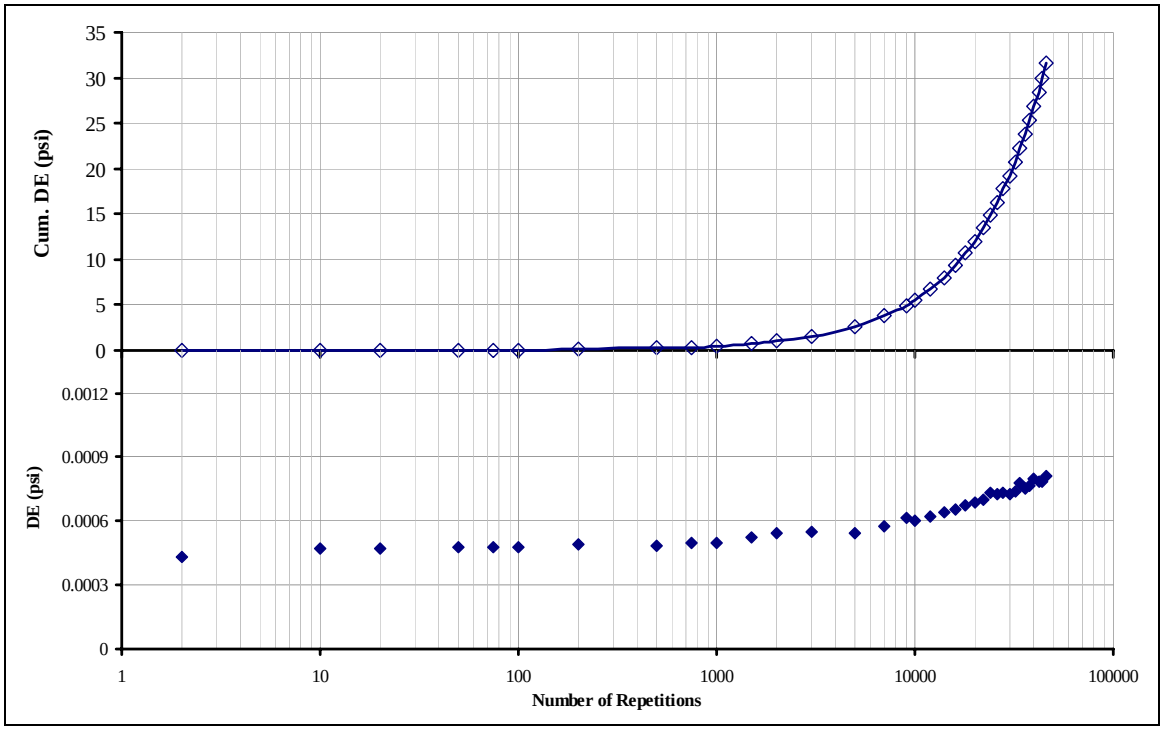


**Figure B.6 Single Axle High Stress (Specimen 119)**

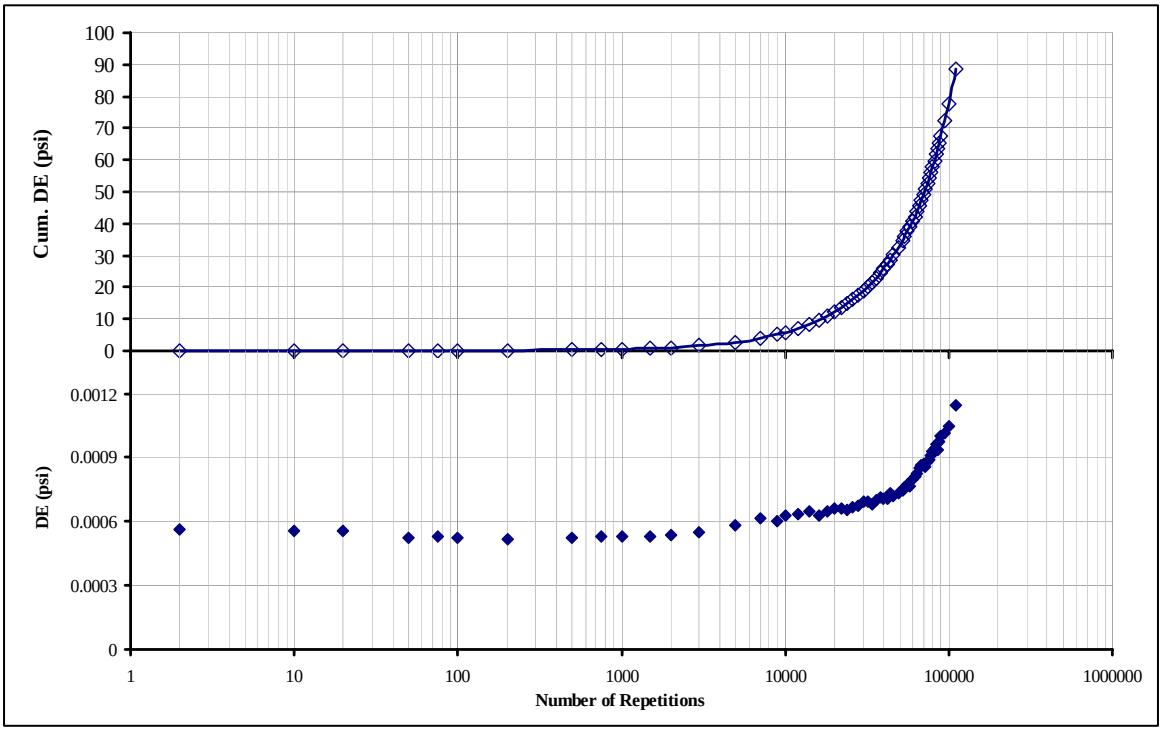


**Figure B.7 Single Axle High Stress (Specimen 151)**

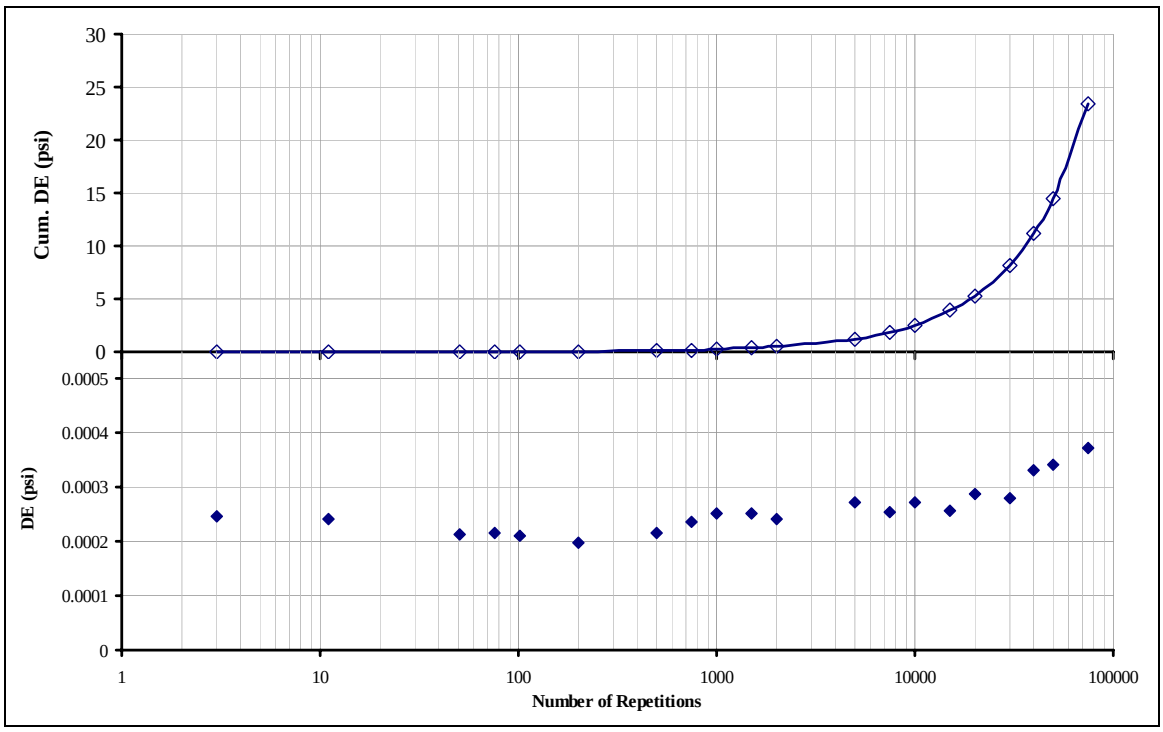


**Figure B.8 Tandem Axle Medium Stress (Specimen 122)**

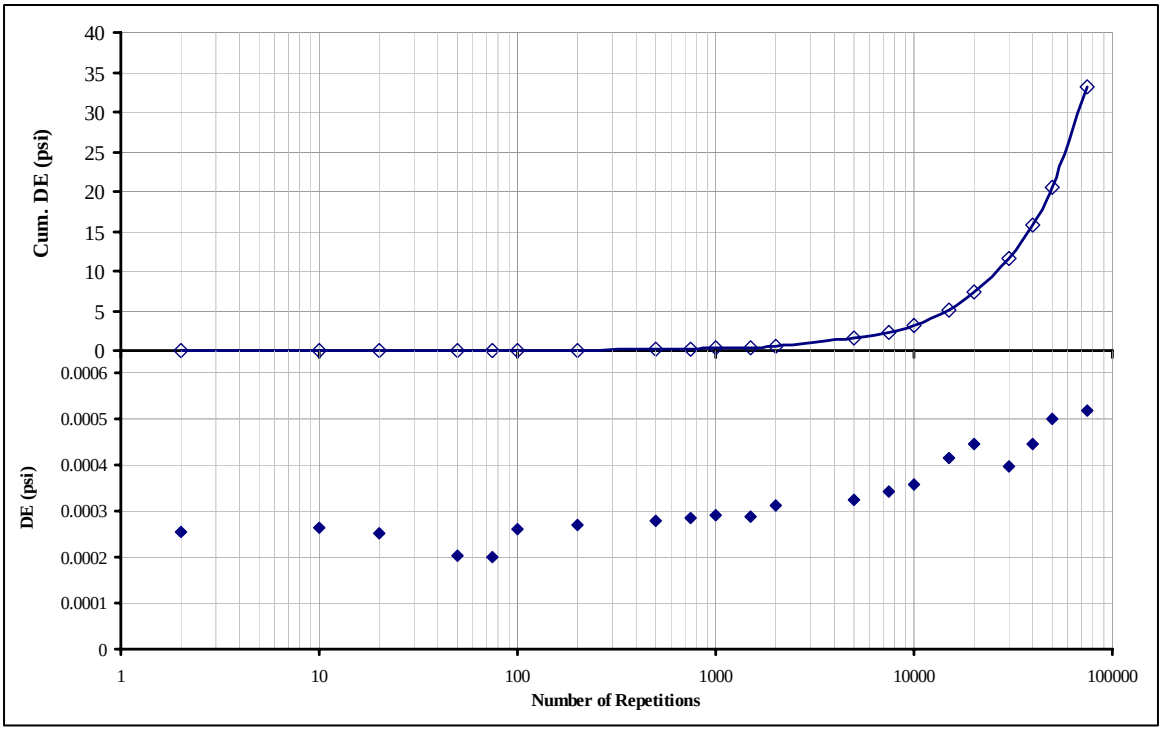


**Figure B.9 Tandem Axle Medium Stress (Specimen 124)**

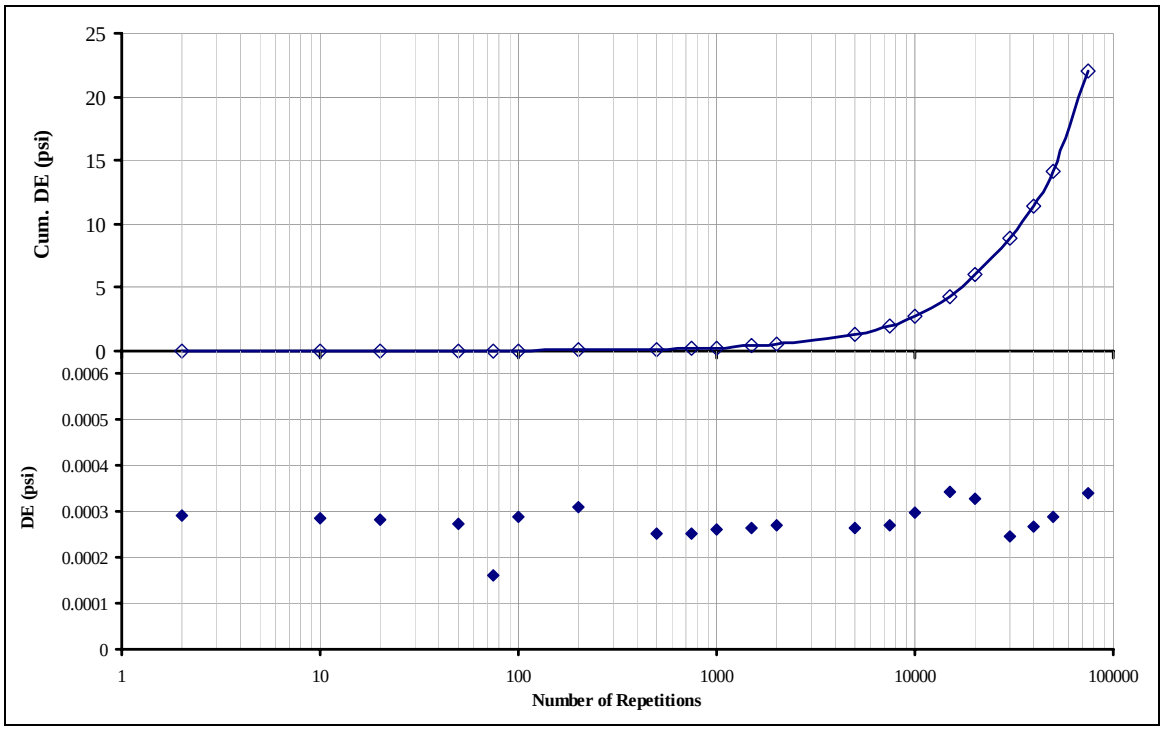


**Figure B.10 Tandem Axle Medium Stress (Specimen 128)**

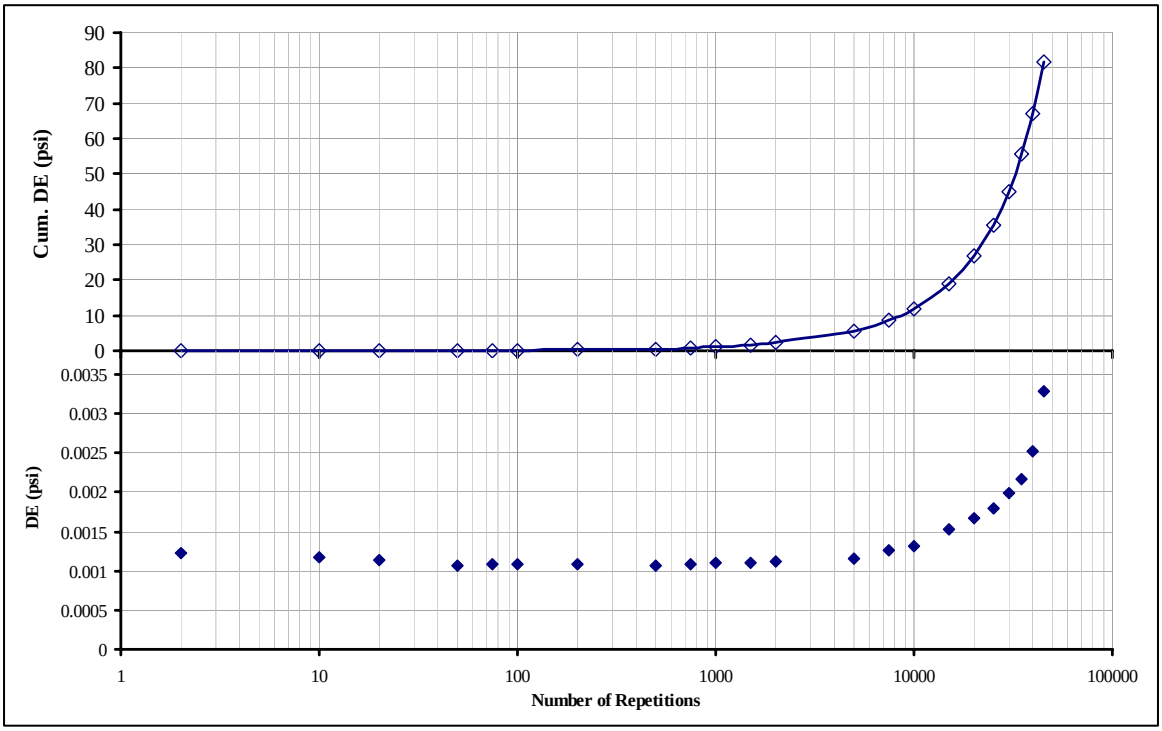


**Figure B.11 Tandem Axle High Stress (Specimen 145)**

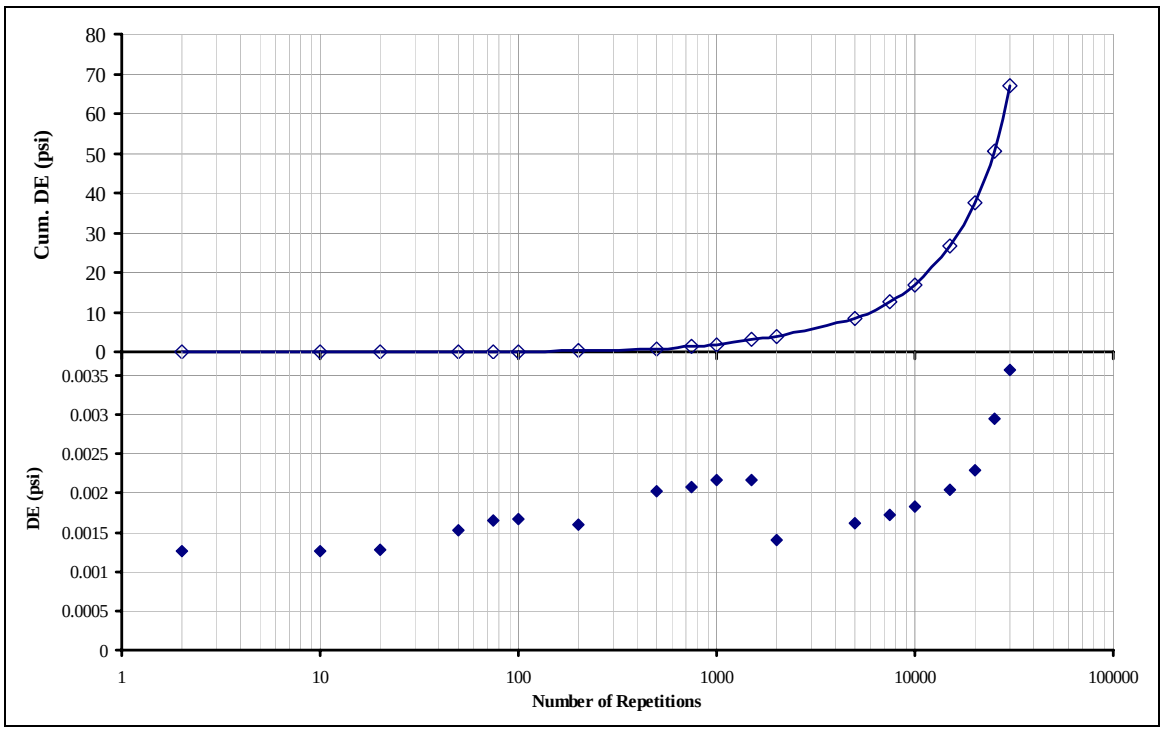


**Figure B.12 Tandem Axle High Stress (Specimen 137)**

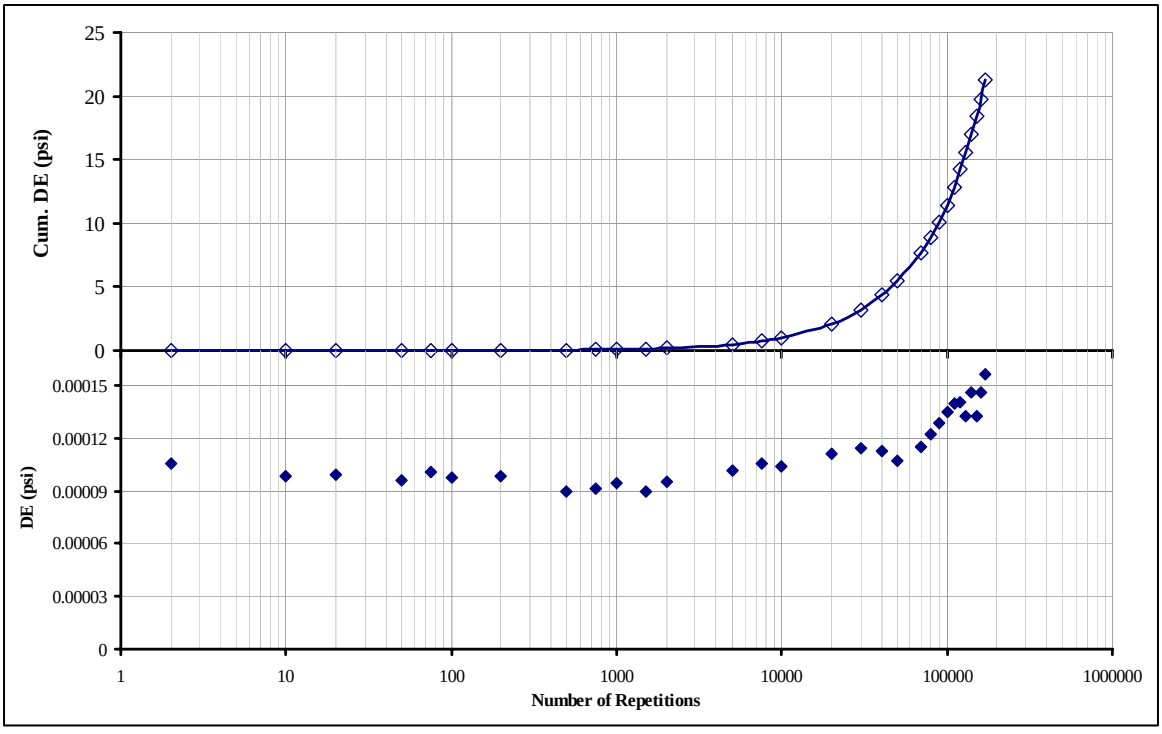


**Figure B.13 Tridem Axle Low Stress (Specimen 140)**

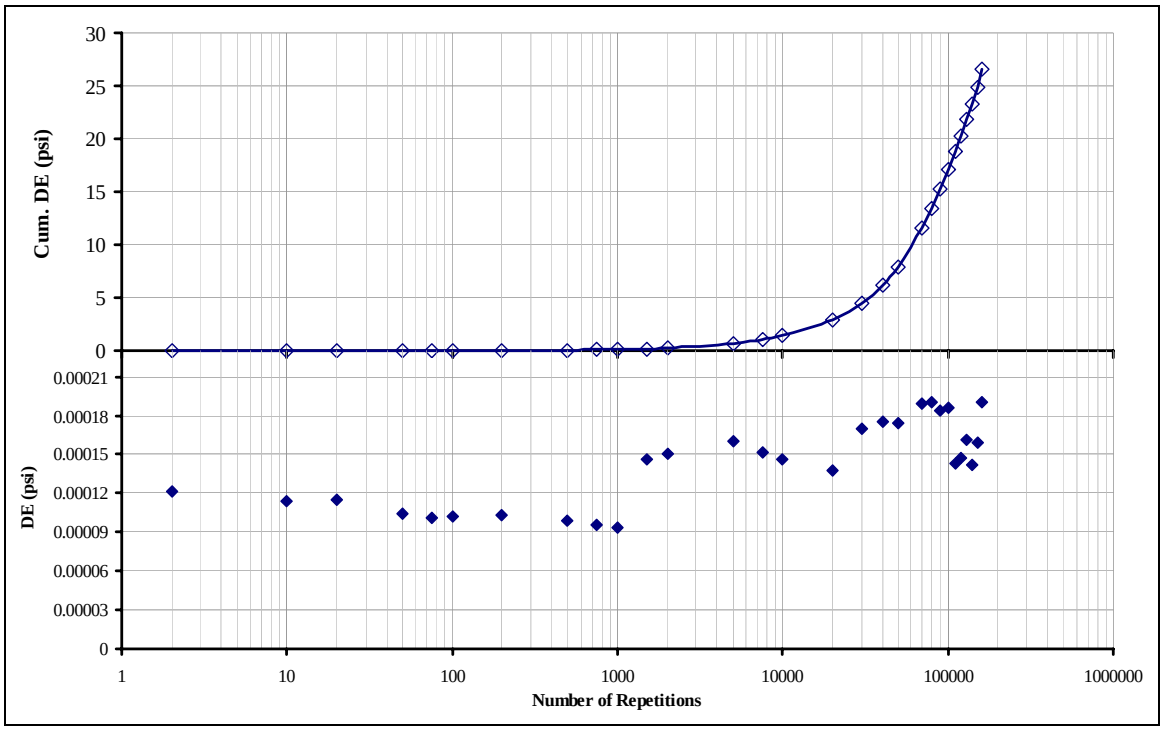


**Figure B.14 Tridem Axle Low Stress (Specimen 133)**

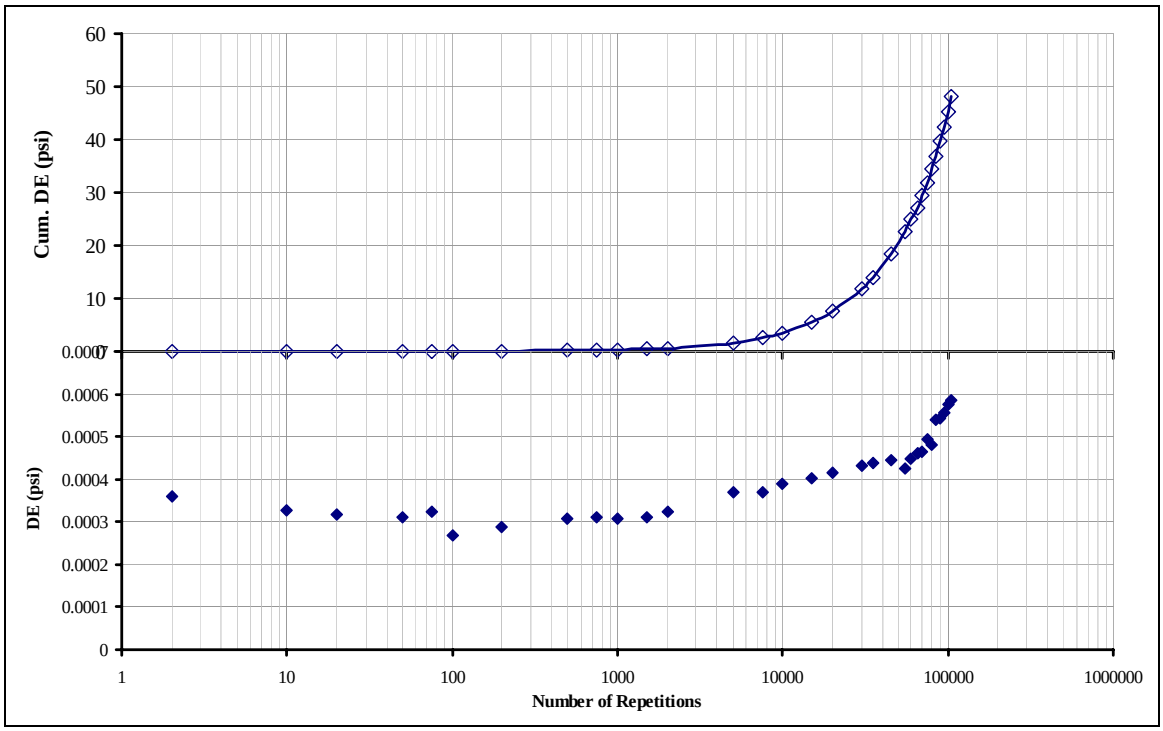


**Figure B.15 Tridem Axle Medium Stress (Specimen 147)**

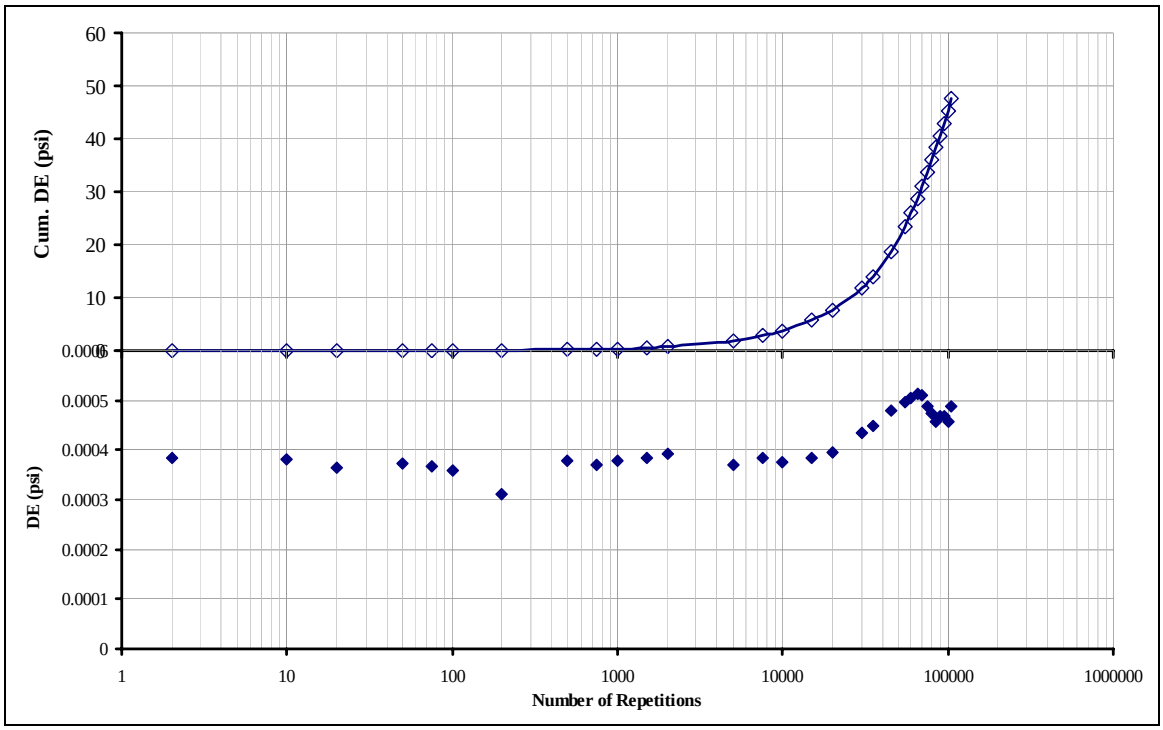


**Figure B.16 Tridem Axle Medium Stress (Specimen 116)**

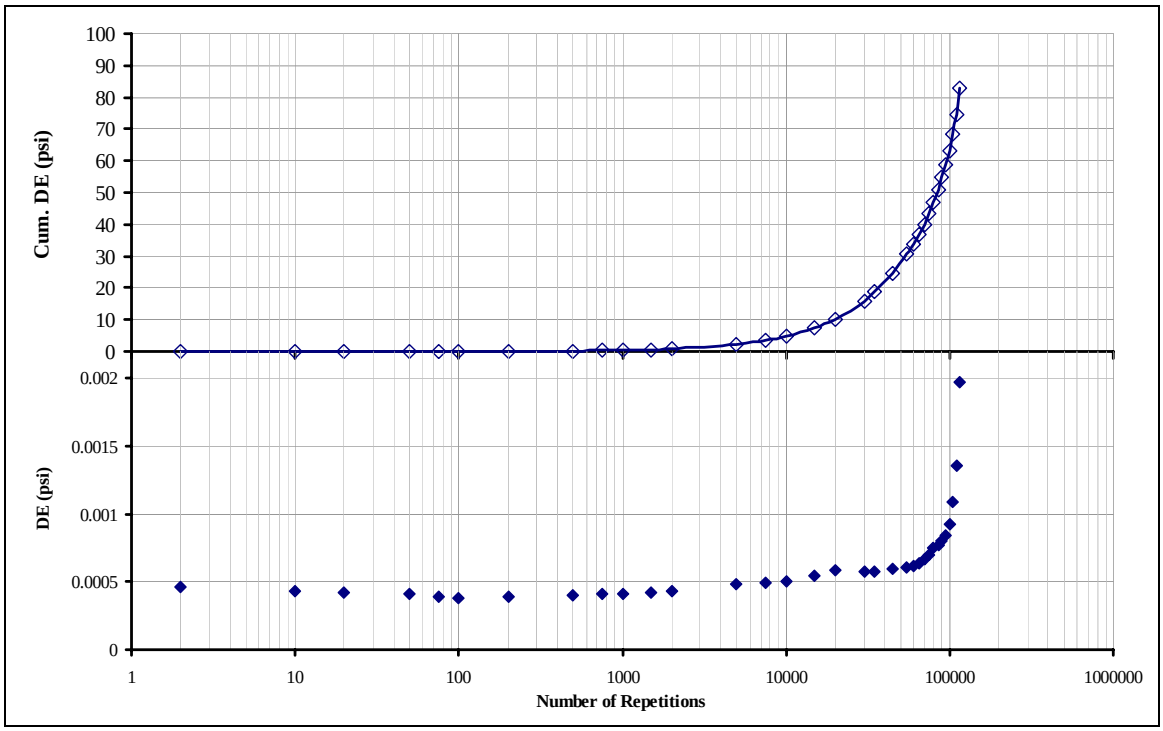


**Figure B.17 Tridem Axle Medium Stress (Specimen 156)**

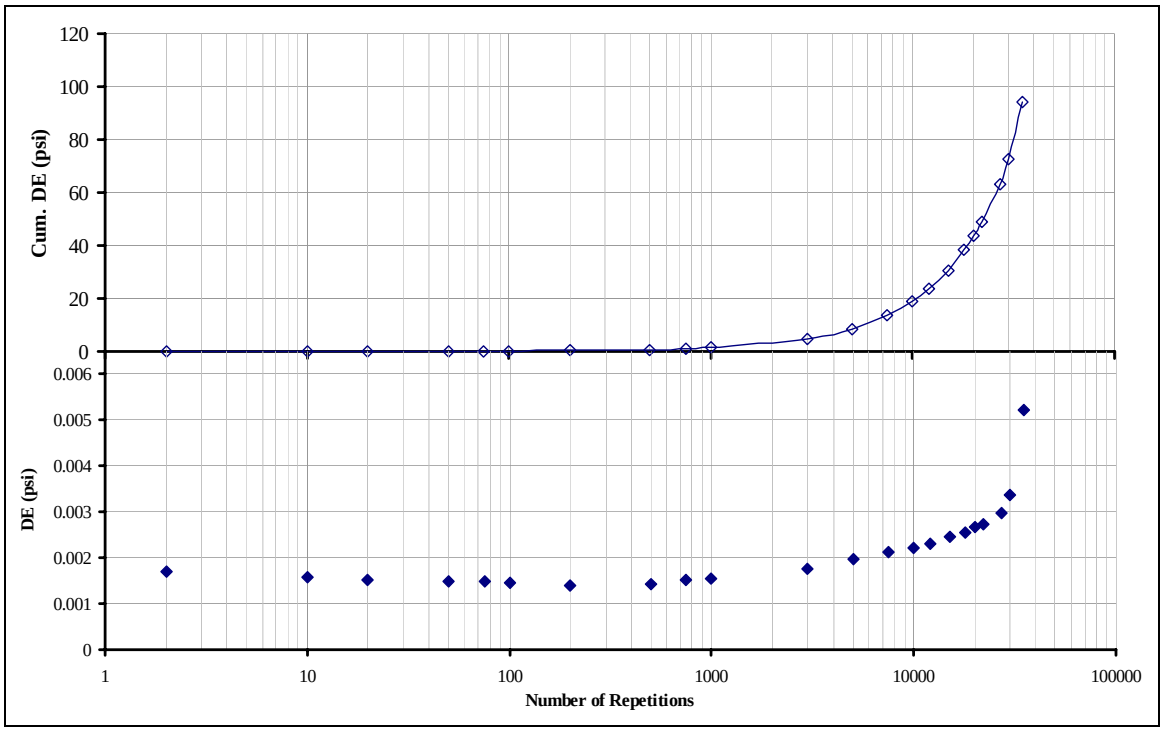


**Figure B.18 Tridem Axle High Stress (Specimen 149)**

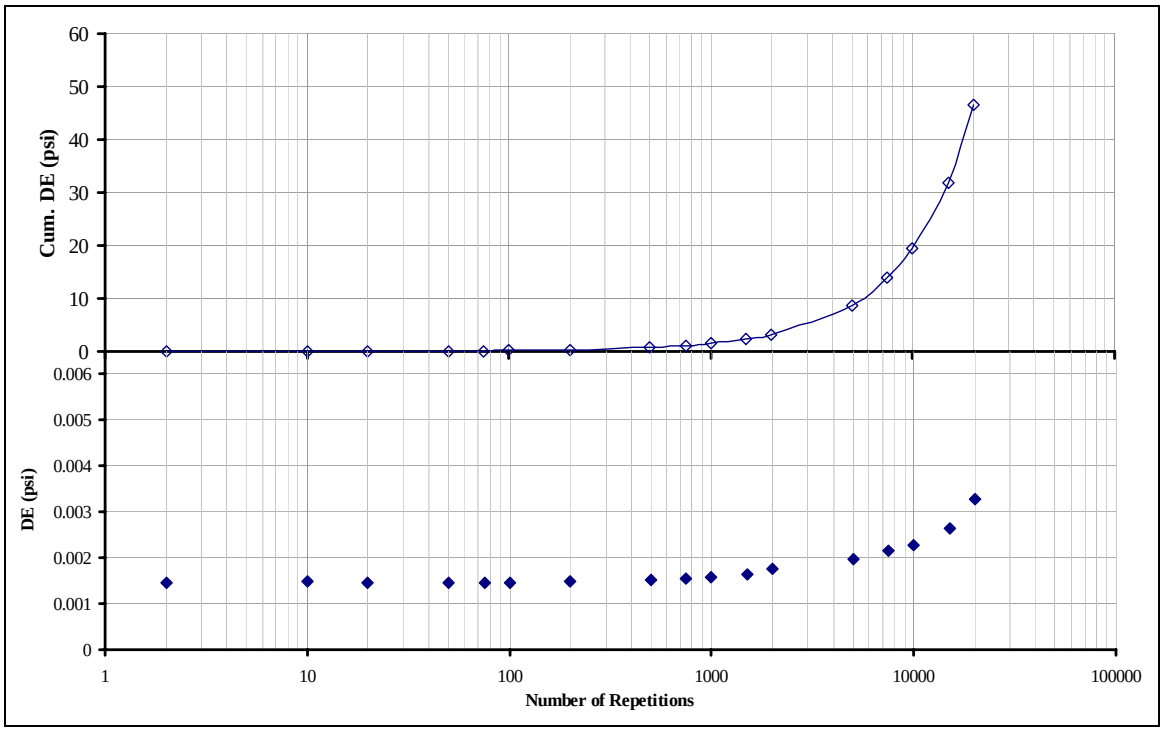


**Figure B.19 Tridem Axle High Stress (Specimen 138)**

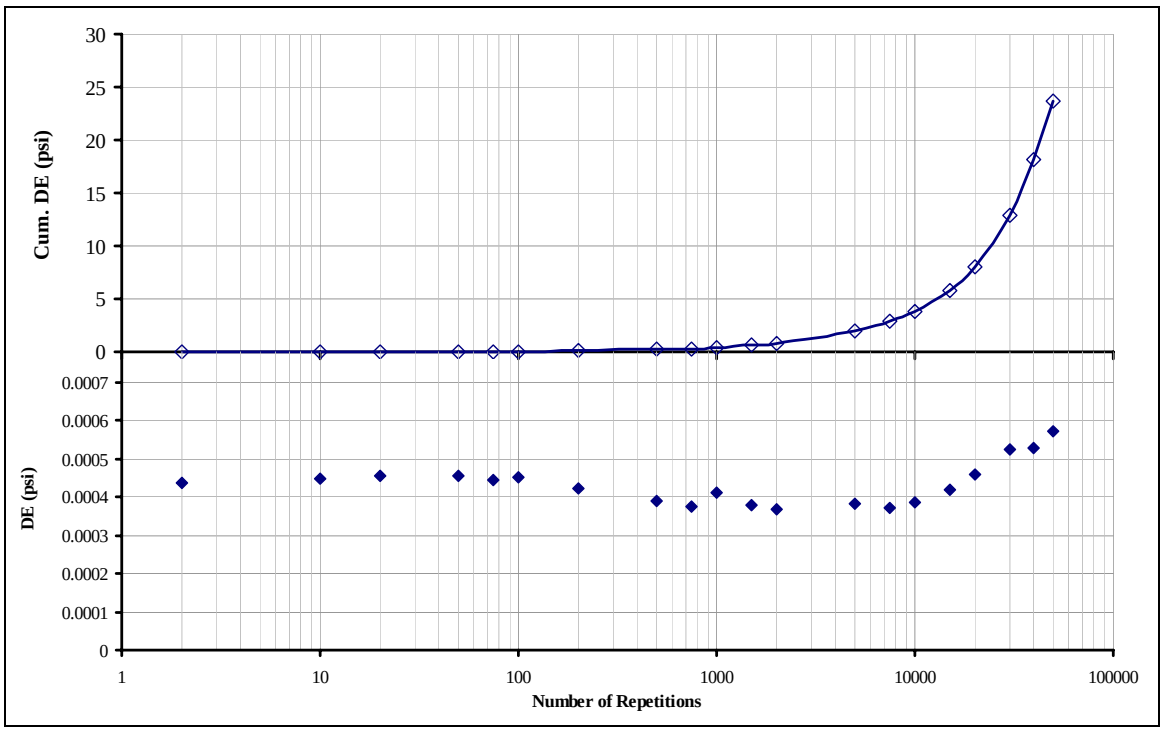


**Figure B.20 4-Axle Medium Stress (Specimen 117)**

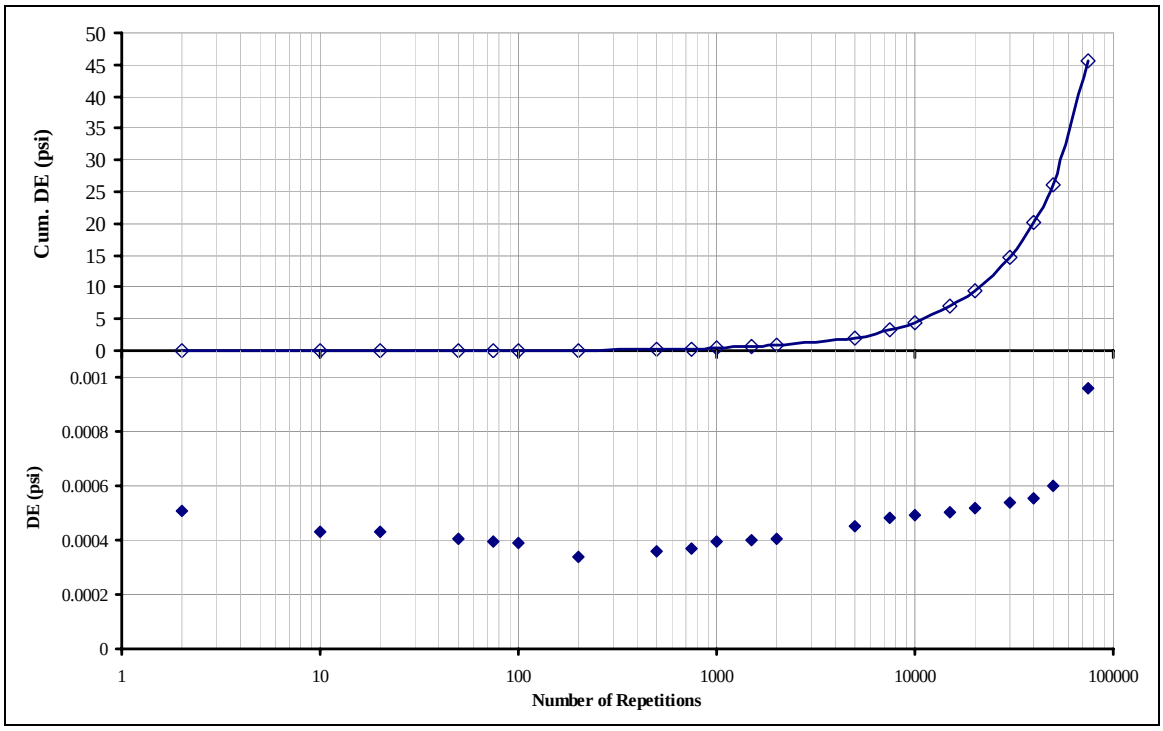


**Figure B.21 4-Axle Medium Stress (Specimen 144)**

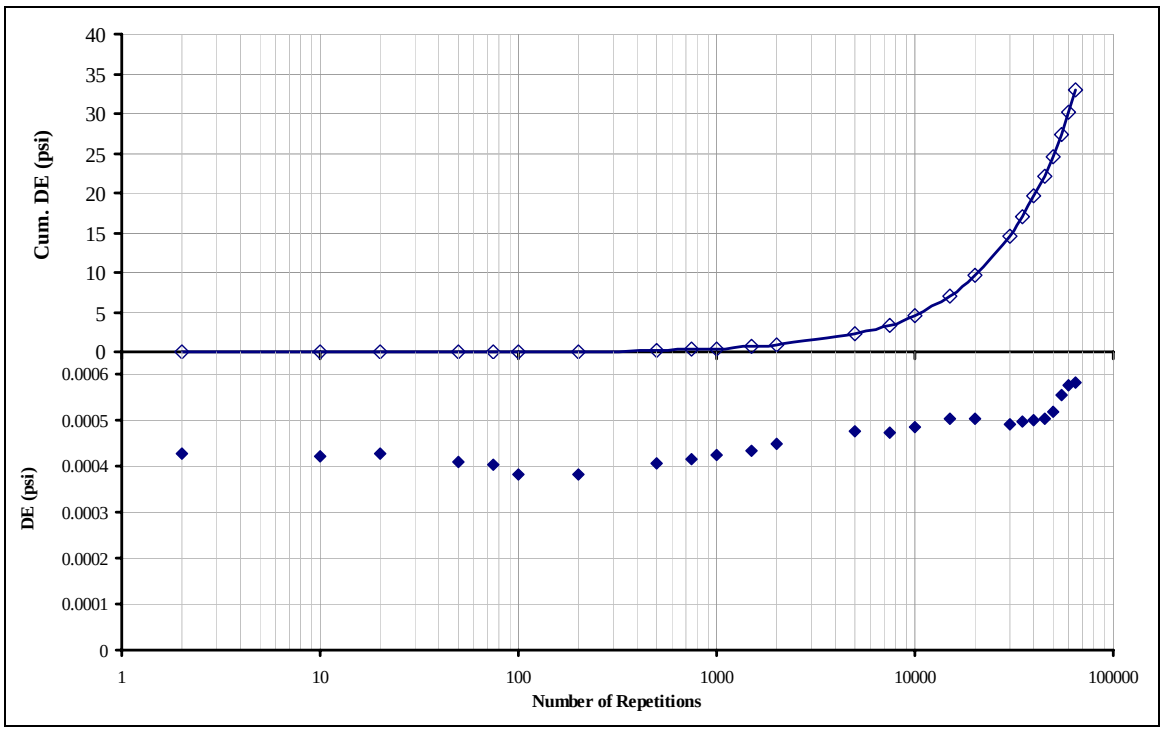


**Figure B.22 4-Axle Medium Stress (Specimen 141)**

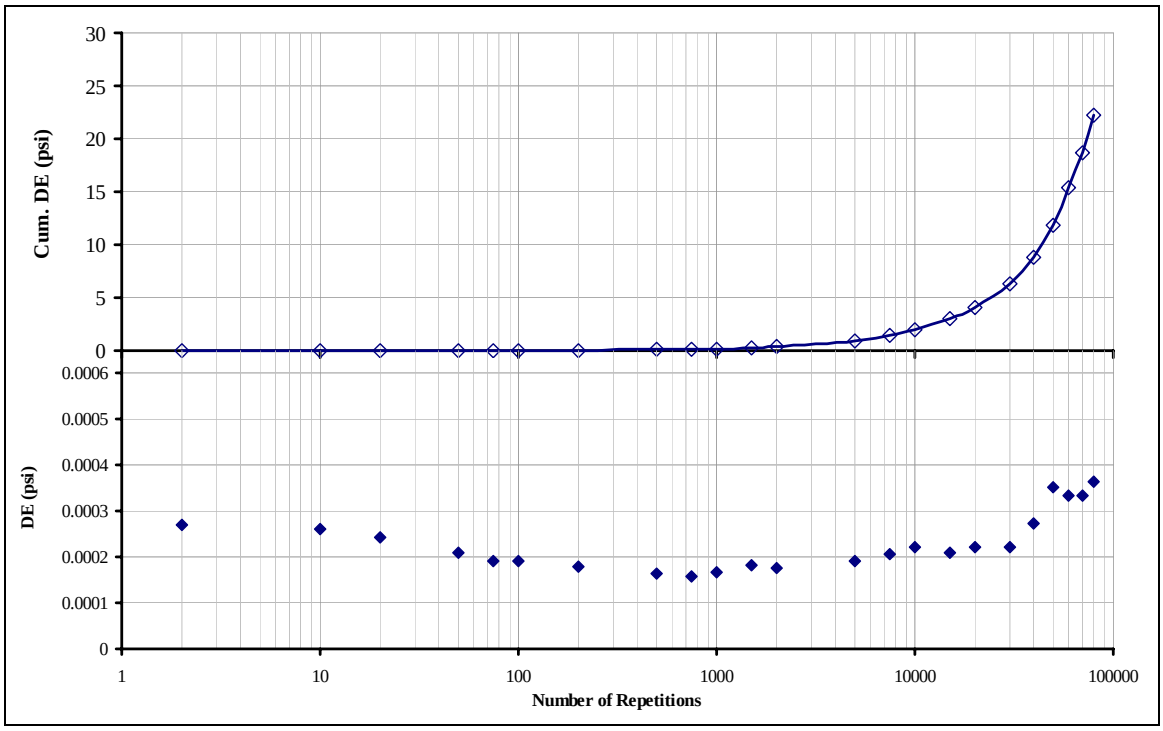


**Figure B.23 8-Axle Low Stress (Specimen 150)**

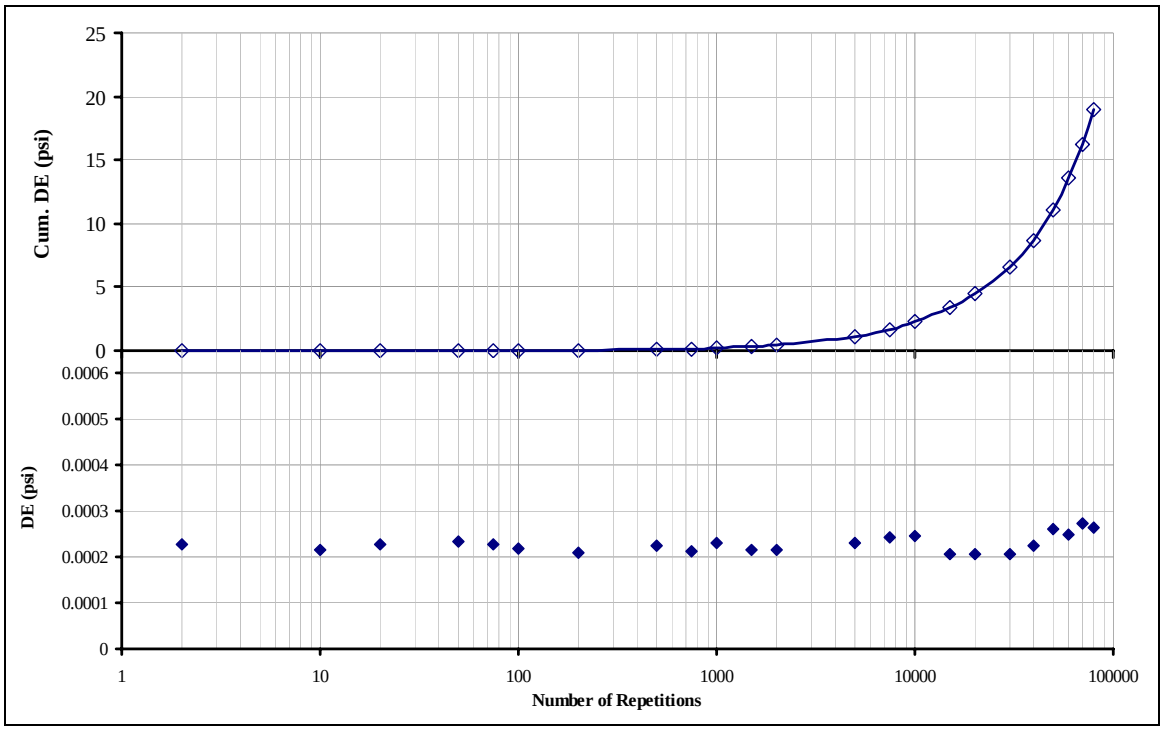


**Figure B.24 8-Axle Low Stress (Specimen 127)**

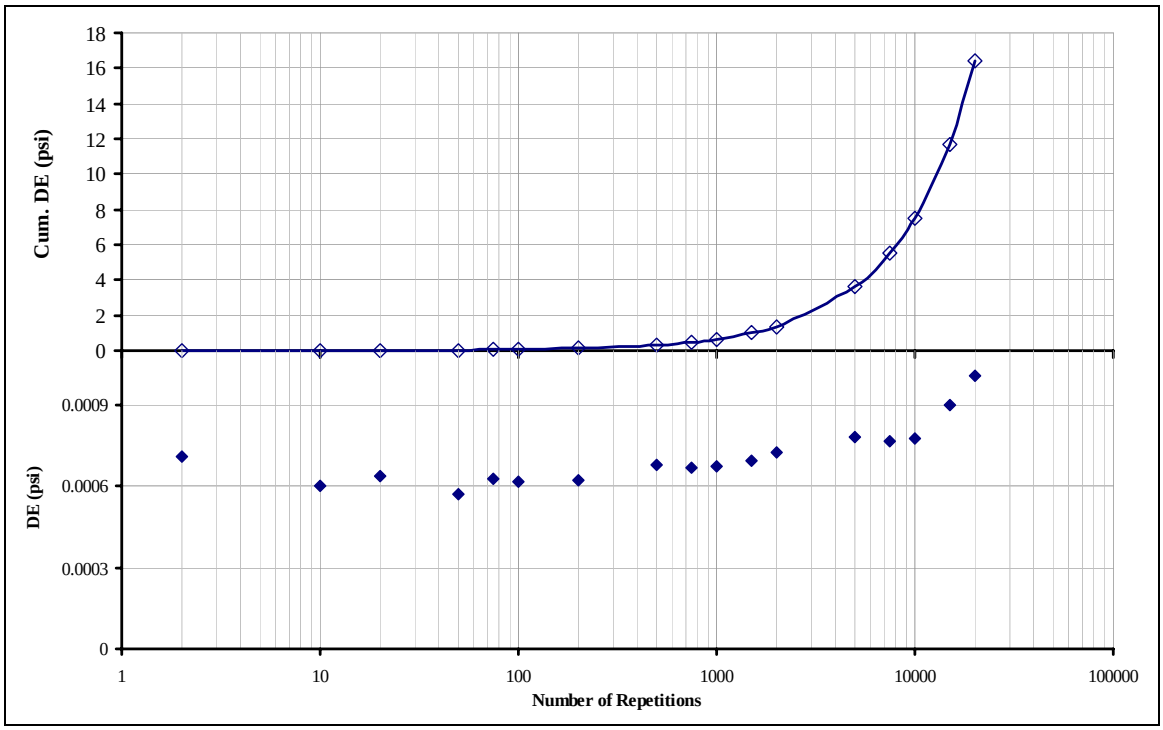


**Figure B.25 8-Axle Medium Stress (Specimen 111)**

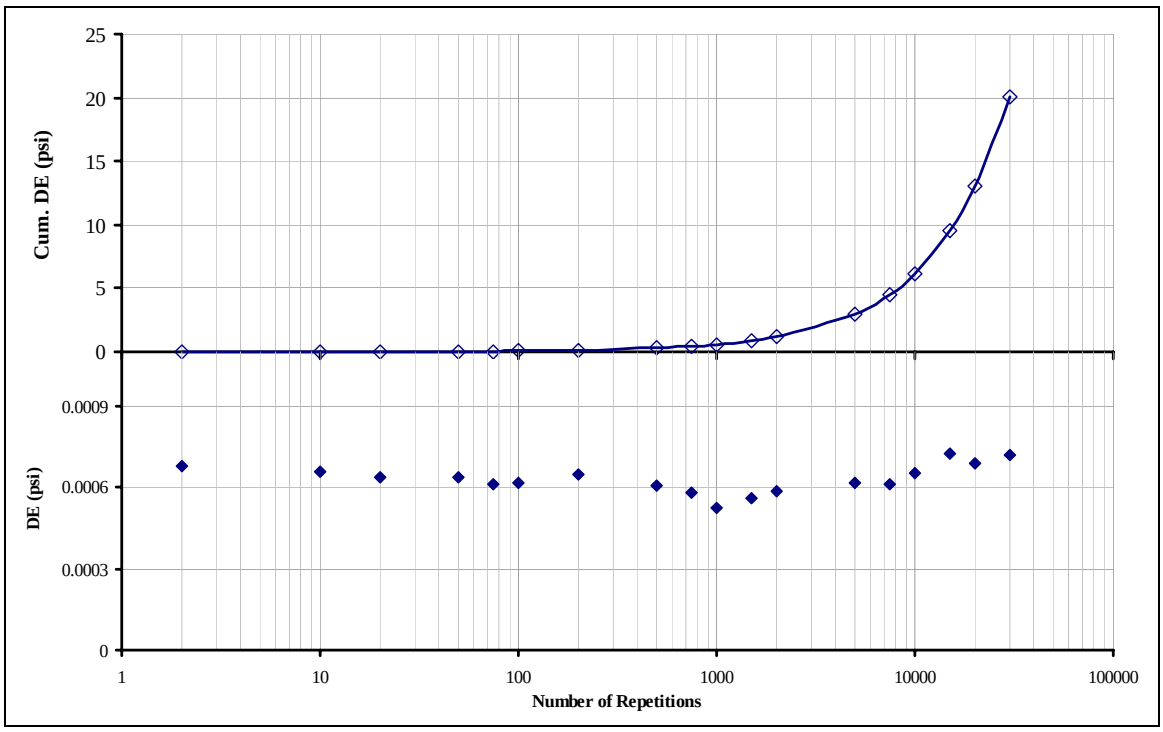


**Figure B.26 8-Axle Medium Stress (Specimen 121)**

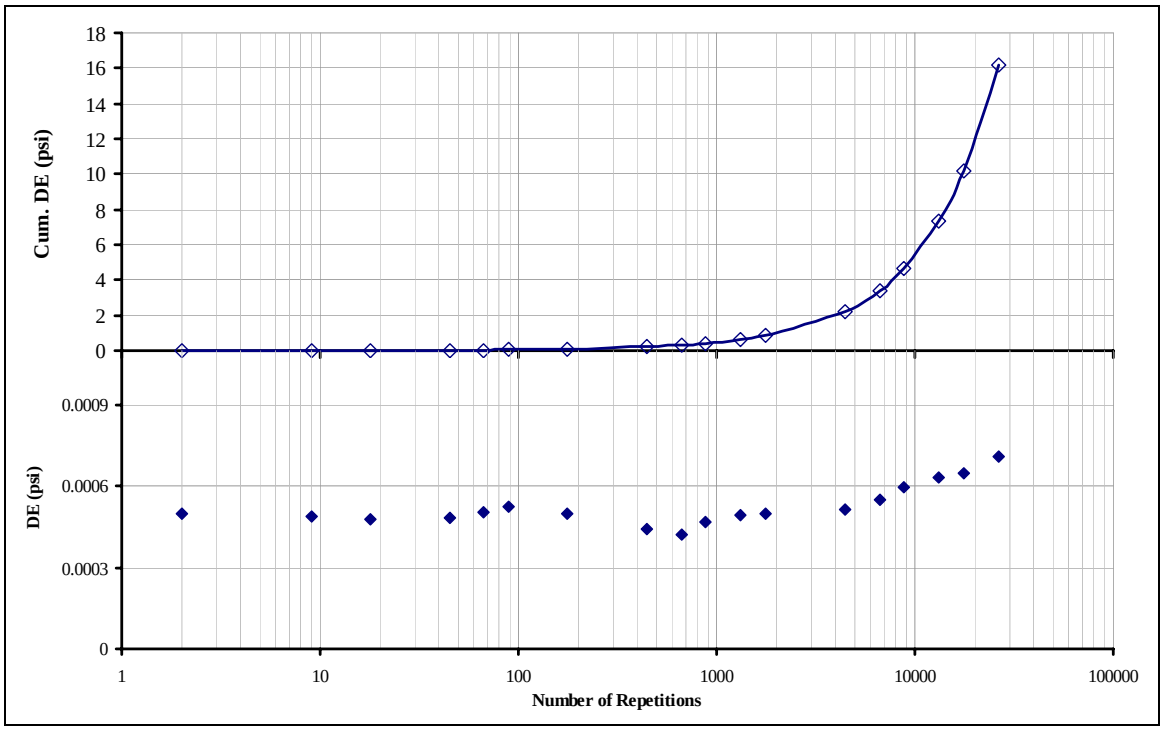


**Figure B.27 8-Axle Medium Stress (Specimen 109)**

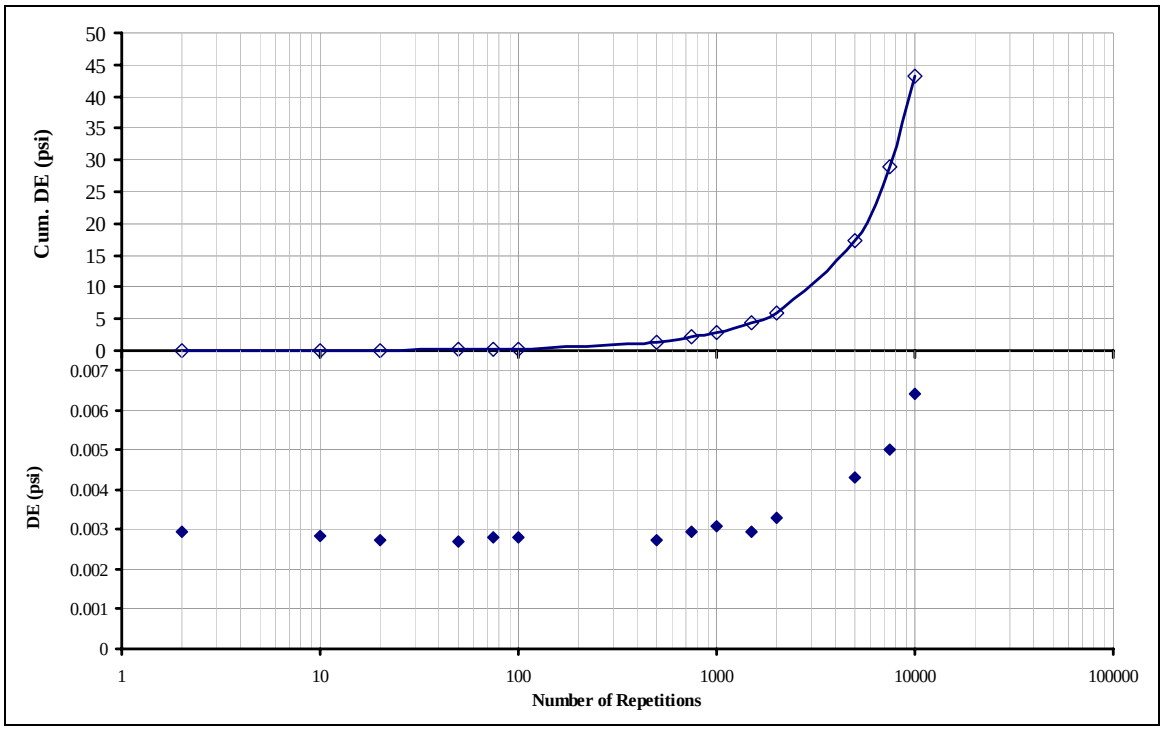


**Figure B.28 8-Axle High Stress (Specimen 106)**

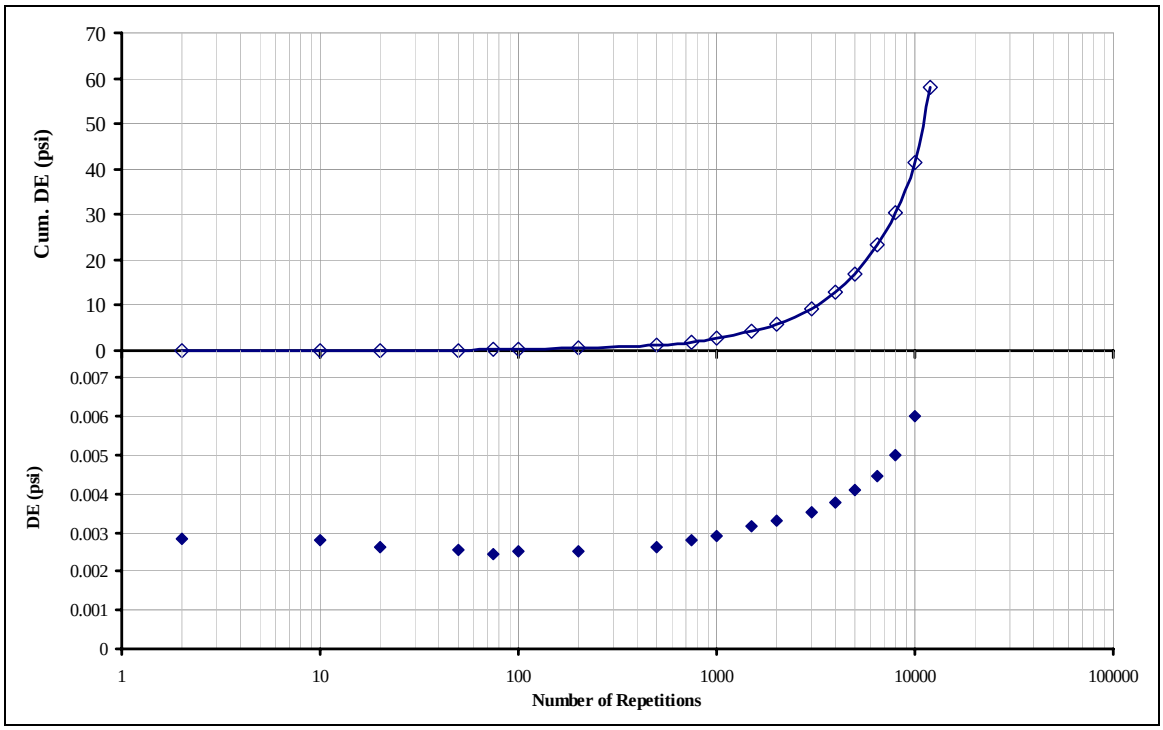


**Figure B.29 8-Axle High Stress (Specimen 118)**

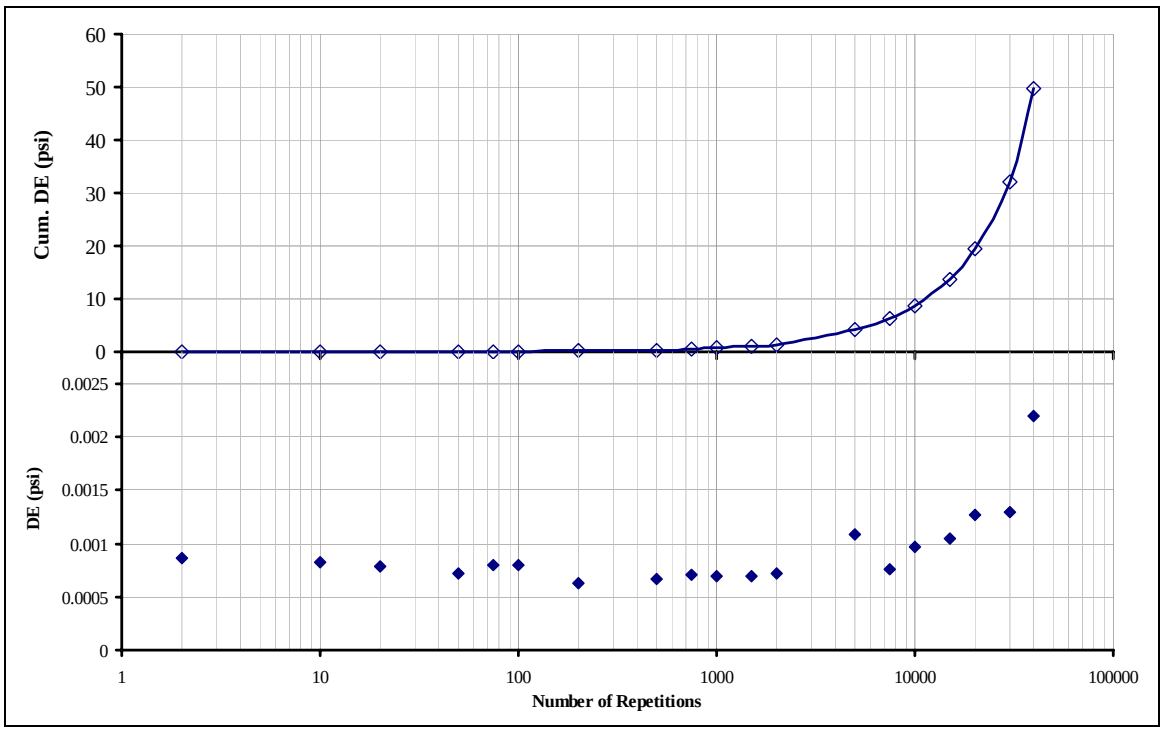


**Figure B.30 8-Axle Medium Stress (75% Interaction) (Specimen 136)**

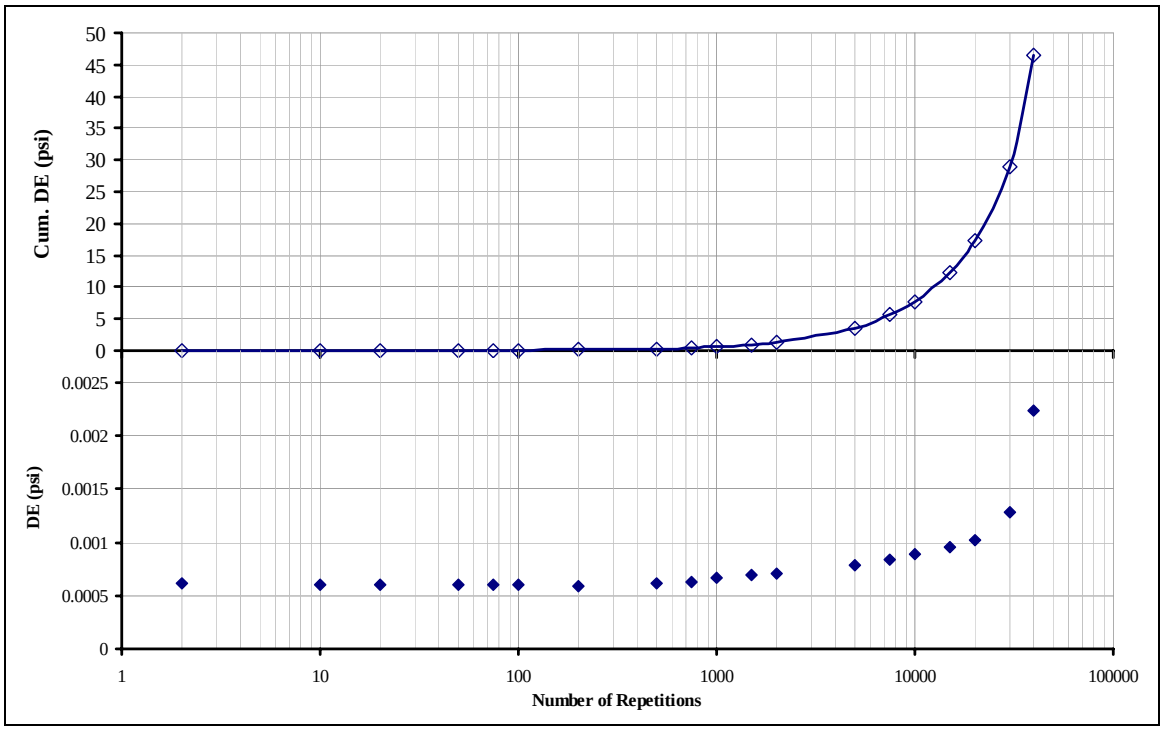


**Figure B.31 8-Axle Medium Stress (75% Interaction) (Specimen 114)**

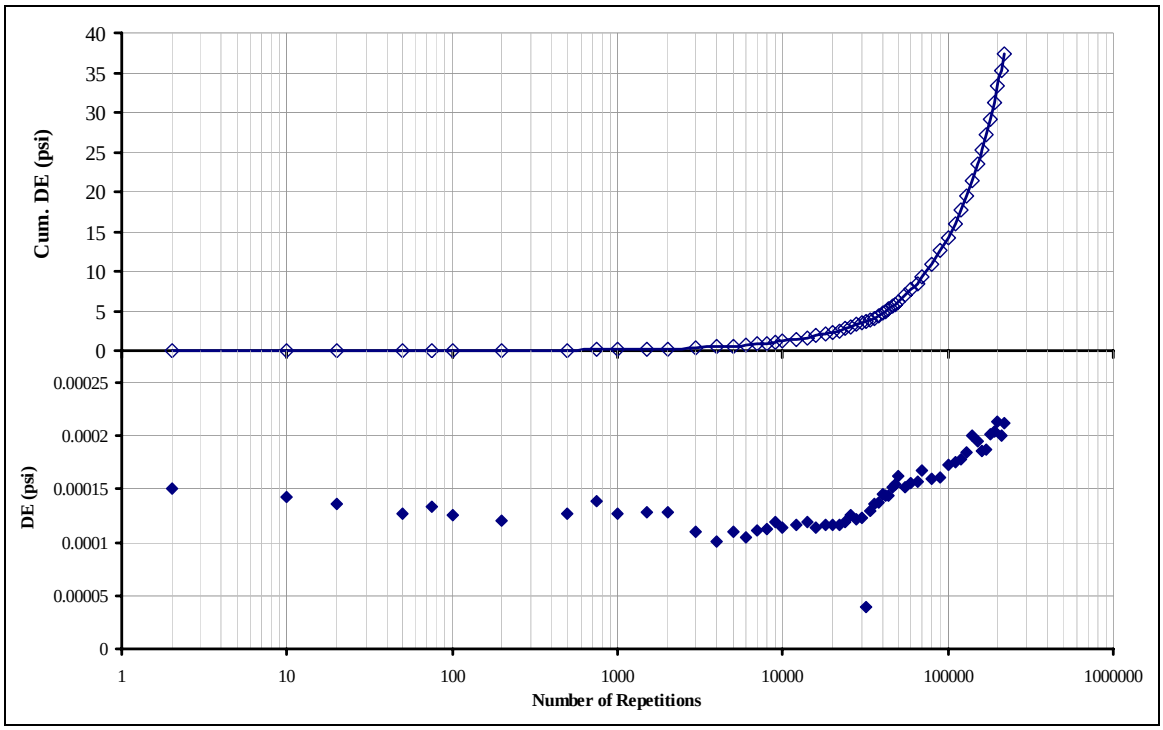


**Figure B.32 Continuous Haversine Pulse Medium Stress (Specimen 110)**

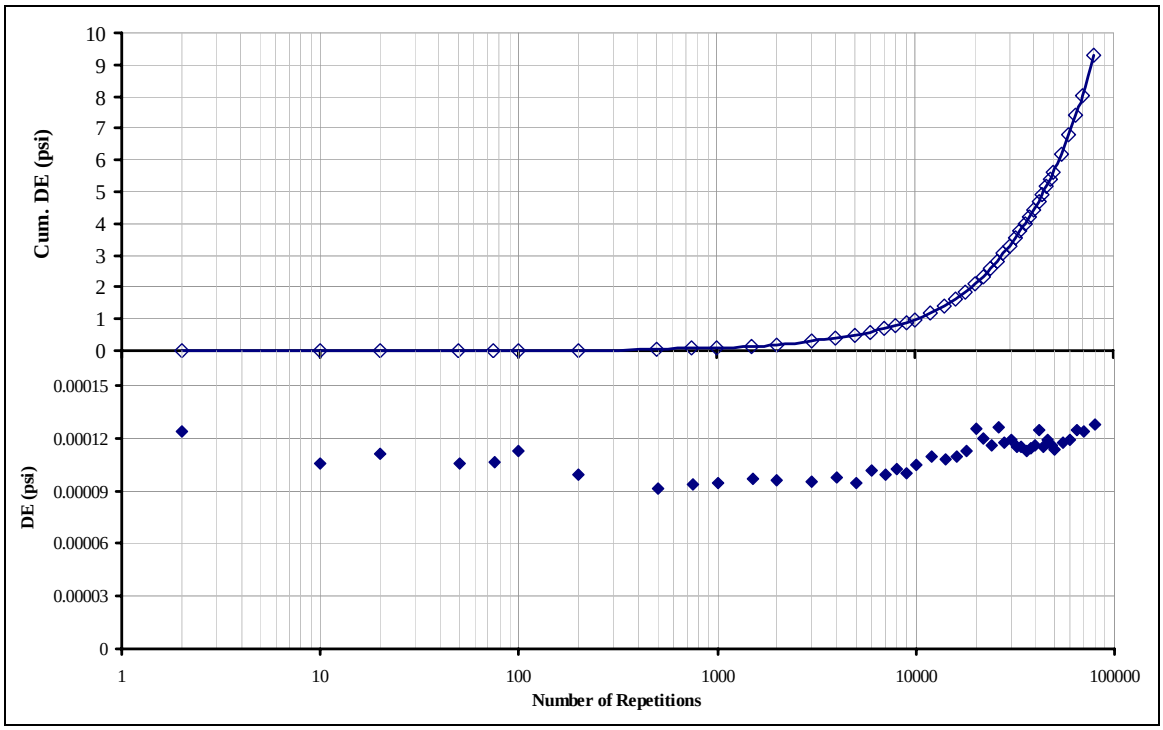


**Figure B.33 Continuous Haversine Pulse Medium Stress (Specimen 152)**

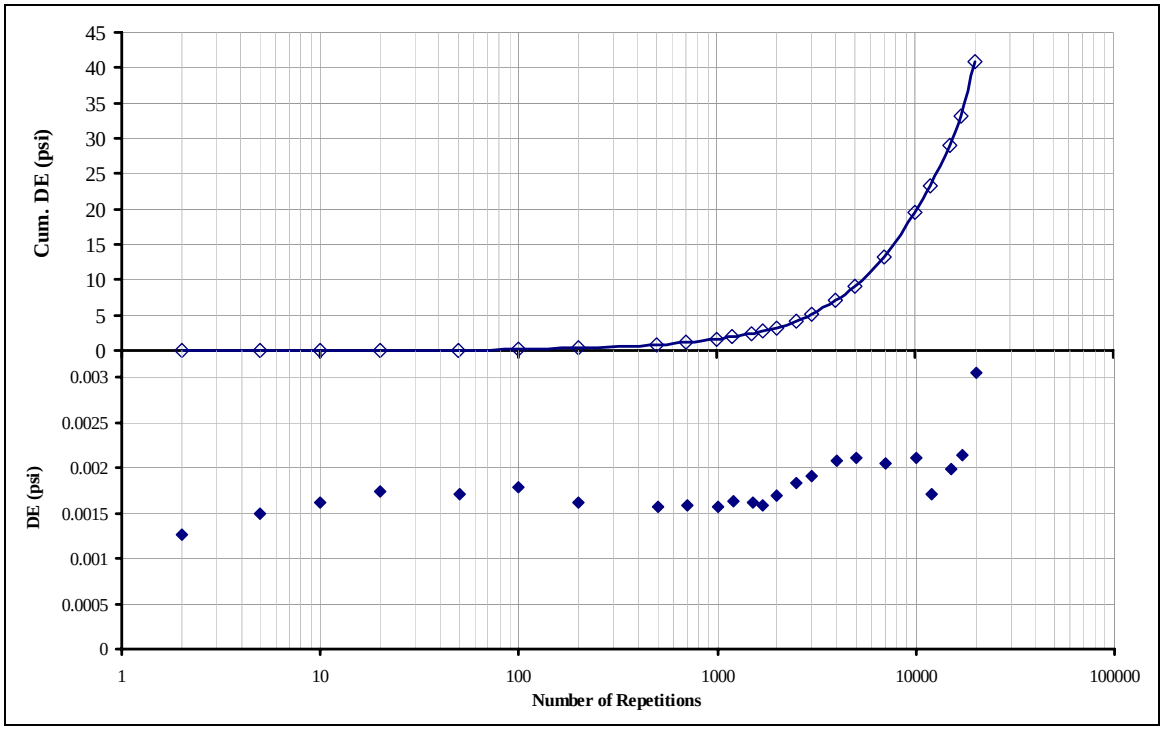


**Figure B.34 Truck 13 (Specimen 131)**

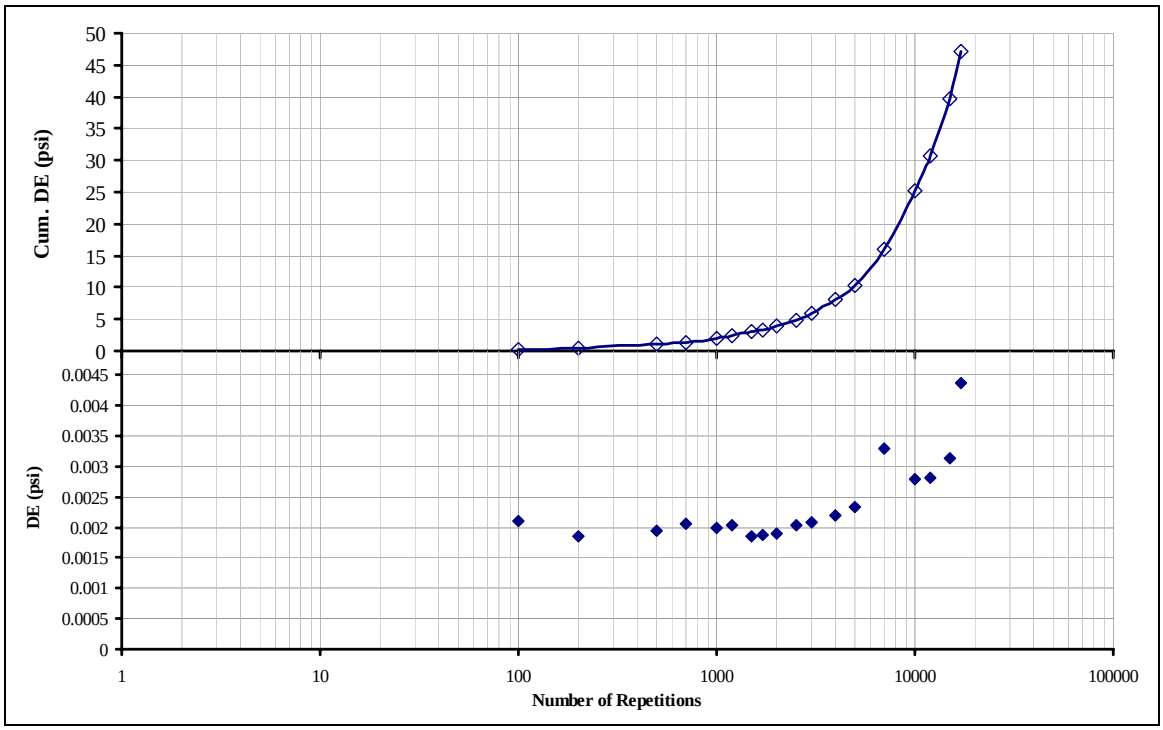


**Figure B.35 Truck 13 (Specimen 120)**

# APPENDIX C - AF and TF Results

**Table C.1 Measured Truck Factors**

| Truck Number | Specimen No. 135 | | | | Specimen No. 125 | | | |
|---|---|---|---|---|---|---|---|---|
| | Nf | Nf*kips | TF | TF/tonnage | Nf | Nf*kips | TF | TF/tonnage |
| Std Axle | 4267 | 76805 | 1.00 | 1.00 | 5388 | 96988 | 1.00 | 1.00 |
| truck 0 | 881 | 64671 | 4.84 | 1.19 | 1197 | 87896 | 4.50 | 1.10 |
| truck 1 | 1207 | 40328 | 3.53 | 1.90 | 1735 | 57946 | 3.11 | 1.67 |
| truck 2 | 1131 | 53587 | 3.77 | 1.43 | 1518 | 71973 | 3.55 | 1.35 |
| truck 3 | 1094 | 59524 | 3.90 | 1.29 | 1438 | 78209 | 3.75 | 1.24 |
| truck 4 | 1053 | 70967 | 4.05 | 1.08 | 1482 | 99900 | 3.64 | 0.97 |
| truck 10 | 635 | 75792 | 6.72 | 1.01 | 801 | 95636 | 6.73 | 1.01 |
| truck 13 | 705 | 106742 | 6.05 | 0.72 | 807 | 122162 | 6.68 | 0.79 |
| truck 14 | 691 | 111595 | 6.17 | 0.69 | 704 | 113659 | 7.65 | 0.85 |
| truck 17 | 878 | 116304 | 4.86 | 0.66 | 923 | 122222 | 5.84 | 0.79 |
| truck 19 | 851 | 117846 | 5.01 | 0.65 | 906 | 125391 | 5.95 | 0.77 |
| truck 20 | 829 | 125584 | 5.14 | 0.61 | 831 | 125869 | 6.48 | 0.77 |

**Table C.2 Effect of Speed on AF**

| Speed | Axle Conf. | Nf | AF |
|---|---|---|---|
| 60 MPH | 1 axle | 7795 | 1.113 |
| | 2 axles | 4216 | 2.058 |
| | 3 axles | 3059 | 2.837 |
| | 4 axles | 2471 | 3.511 |
| | 5 axles | 2130 | 4.075 |
| | 7 axles | 1655 | 5.242 |
| | 8 axles | 1450 | 5.983 |
| 40 MPH | 1 axle | 5960 | 1.122 |
| | 2 axles | 3610 | 1.853 |
| | 3 axles | 2674 | 2.502 |
| | 4 axles | 2159 | 3.099 |
| | 5 axles | 1879 | 3.561 |
| | 7 axles | 1475 | 4.536 |
| | 8 axles | 1359 | 4.922 |
| 27 MPH | 1 axle | 4957 | 1.123 |
| | 2 axles | 2978 | 1.869 |
| | 3 axles | 2304 | 2.415 |
| | 4 axles | 2016 | 2.760 |
| | 5 axles | 1819 | 3.060 |
| | 7 axles | 1187 | 4.688 |
| | 8 axles | 1080 | 5.150 |

**Table C.3 Effect of Thickness (Interaction Level) on AF**

| | | Nf | A F | AF/Tonnage |
|---|---|---|---|---|
| 25% Interaction | 1 axle | 5562 | 1.00 | 1.00 |
| | 2 axles | 3279 | 1.70 | 0.85 |
| | 3 axles | 2547 | 2.18 | 0.73 |
| | 4 axles | 2241 | 2.48 | 0.62 |
| | 5 axles | 2022 | 2.75 | 0.55 |
| | 7 axles | 1322 | 4.21 | 0.60 |
| | 8 axles | 1210 | 4.60 | 0.57 |
| 50% Interaction | 2 axles | 3302 | 1.68 | 0.84 |
| | 3 axles | 2712 | 2.05 | 0.68 |
| | 4 axles | 2426 | 2.29 | 0.57 |
| | 5 axles | 1811 | 3.07 | 0.61 |
| | 7 axles | 1494 | 3.72 | 0.53 |
| | 8 axles | 1436 | 3.87 | 0.48 |
| 75% Interaction | 2 axles | 3493 | 1.59 | 0.80 |
| | 3 axles | 2804 | 1.98 | 0.66 |
| | 4 axles | 2352 | 2.36 | 0.59 |
| | 5 axles | 2035 | 2.73 | 0.55 |
| | 7 axles | 1617 | 3.44 | 0.49 |
| | 8 axles | 1478 | 3.76 | 0.47 |

**Table C.4 Calculated AF from Strain Fatigue Curve Using Peak Method**

| Interaction Level | Axle No | N f | | Axle Factor | | % difference | |
|---|---|---|---|---|---|---|---|
| | | Measured | Calculated | Measured | Calculated | Total | per n |
| 25% | 2 | 2072 | 1649 | 1.59 | 2.00 | 20.4% | 10.2% |
| | 3 | 1800 | 1099 | 1.83 | 3.00 | 38.9% | 13.0% |
| | 4 | 1630 | 824 | 2.02 | 4.00 | 49.4% | 12.4% |
| | 5 | 1410 | 659 | 2.34 | 5.00 | 53.2% | 10.6% |
| | 7 | 816 | 471 | 4.04 | 7.00 | 42.3% | 6.0% |
| | 8 | 761 | 412 | 4.34 | 8.00 | 45.8% | 5.7% |
| 50% | 2 | 1822 | 1649 | 1.81 | 2.00 | 9.5% | 4.8% |
| | 3 | 1535 | 1099 | 2.15 | 3.00 | 28.4% | 9.5% |
| | 4 | 1448 | 824 | 2.28 | 4.00 | 43.1% | 10.8% |
| | 5 | 844 | 659 | 3.91 | 5.00 | 21.8% | 4.4% |
| | 7 | 661 | 471 | 4.99 | 7.00 | 28.8% | 4.1% |
| | 8 | 640 | 412 | 5.16 | 8.00 | 35.6% | 4.4% |
| 75% | 2 | 2032 | 1649 | 1.62 | 2.00 | 18.9% | 9.4% |
| | 3 | 1548 | 1099 | 2.13 | 3.00 | 29.0% | 9.7% |
| | 4 | 1186 | 824 | 2.78 | 4.00 | 30.5% | 7.6% |
| | 5 | 952 | 659 | 3.46 | 5.00 | 30.7% | 6.1% |
| | 7 | 661 | 471 | 4.99 | 7.00 | 28.7% | 4.1% |
| | 8 | 568 | 412 | 5.80 | 8.00 | 27.5% | 3.4% |

**Table C.5 Calculated AF from Strain Fatigue Curve Using Peak-Midway Method**

| Interaction Level | Axle No | N f | | Axle Factor | | % difference | |
|---|---|---|---|---|---|---|---|
| | | Measured | Calculated | Measured | Calculated | Total | per n |
| 25% | 2 | 2072 | 1907 | 1.59 | 1.73 | 8.0% | 4.0% |
| | 3 | 1800 | 1464 | 1.83 | 2.25 | 18.7% | 6.2% |
| | 4 | 1630 | 1188 | 2.02 | 2.78 | 27.1% | 6.8% |
| | 5 | 1410 | 1000 | 2.34 | 3.30 | 29.1% | 5.8% |
| | 7 | 816 | 759 | 4.04 | 4.34 | 7.0% | 1.0% |
| | 8 | 761 | 677 | 4.34 | 4.87 | 10.9% | 1.4% |
| 50% | 2 | 1822 | 2335 | 1.81 | 1.41 | 28.1% | 14.1% |
| | 3 | 1535 | 2037 | 2.15 | 1.62 | 32.7% | 10.9% |
| | 4 | 1448 | 1806 | 2.28 | 1.83 | 24.7% | 6.2% |
| | 5 | 844 | 1623 | 3.91 | 2.03 | 92.3% | 18.5% |
| | 7 | 661 | 1348 | 4.99 | 2.45 | 104.0% | 14.9% |
| | 8 | 640 | 1243 | 5.16 | 2.65 | 94.4% | 11.8% |
| 75% | 2 | 2032 | 2599 | 1.62 | 1.27 | 27.9% | 14.0% |
| | 3 | 1548 | 2476 | 2.13 | 1.33 | 60.0% | 20.0% |
| | 4 | 1186 | 2365 | 2.78 | 1.39 | 99.3% | 24.8% |
| | 5 | 952 | 2263 | 3.46 | 1.46 | 137.7% | 27.5% |
| | 7 | 661 | 2083 | 4.99 | 1.58 | 215.4% | 30.8% |
| | 8 | 568 | 2004 | 5.80 | 1.65 | 252.6% | 31.6% |

**Table C.6 Calculated AF from Strain Fatigue Curve Using Peak Method (After Correction)**

| Interaction Level | Axle No | N f | | Axle Factor | | % difference | |
|---|---|---|---|---|---|---|---|
| | | Measured | Calculated | Measured | Calculated | Total | per n |
| 25% | 2 | 2072 | 2149 | 1.32 | 1.2727806 | 3.7% | 1.8% |
| | 3 | 1800 | 1561 | 1.52 | 1.7521349 | 13.3% | 4.4% |
| | 4 | 1630 | 1248 | 1.68 | 2.1917121 | 23.5% | 5.9% |
| | 5 | 1410 | 1045 | 1.94 | 2.6178783 | 25.9% | 5.2% |
| | 7 | 816 | 780 | 3.35 | 3.5073749 | 4.5% | 0.6% |
| | 8 | 761 | 683 | 3.60 | 4.006492 | 10.3% | 1.3% |
| 50% | 2 | 1822 | 2149 | 1.50 | 1.2727806 | 17.9% | 9.0% |
| | 3 | 1535 | 1561 | 1.78 | 1.7521349 | 1.7% | 0.6% |
| | 4 | 1448 | 1248 | 1.89 | 2.1917121 | 13.8% | 3.5% |
| | 5 | 844 | 1045 | 3.24 | 2.6178783 | 23.8% | 4.8% |
| | 7 | 661 | 780 | 4.14 | 3.5073749 | 17.9% | 2.6% |
| | 8 | 640 | 683 | 4.28 | 4.006492 | 6.7% | 0.8% |
| 75% | 2 | 2032 | 2149 | 1.35 | 1.2727806 | 5.7% | 2.9% |
| | 3 | 1548 | 1561 | 1.77 | 1.7521349 | 0.8% | 0.3% |
| | 4 | 1186 | 1248 | 2.30 | 2.1917121 | 5.2% | 1.3% |
| | 5 | 952 | 1045 | 2.87 | 2.6178783 | 9.7% | 1.9% |
| | 7 | 661 | 780 | 4.14 | 3.5073749 | 18.0% | 2.6% |
| | 8 | 568 | 683 | 4.81 | 4.006492 | 20.1% | 2.5% |

**Table C.7 Calculated AF from Dissipated Energy Fatigue Curve Using Peak Method**

| Interaction Level | Axle No | N f | | Axle Factor | | % difference | |
|---|---|---|---|---|---|---|---|
| | | Measured | Calculated | Measured | Calculated | Total | per n |
| 25% | 2 | 3279 | 2781 | 1.70 | 2 | 15.2% | 7.6% |
| | 3 | 2547 | 1854 | 2.18 | 3 | 27.2% | 9.1% |
| | 4 | 2241 | 1391 | 2.48 | 4 | 38.0% | 9.5% |
| | 5 | 2022 | 1112 | 2.75 | 5 | 45.0% | 9.0% |
| | 7 | 1322 | 795 | 4.21 | 7 | 39.9% | 5.7% |
| | 8 | 1210 | 695 | 4.60 | 8 | 42.5% | 5.3% |
| 50% | 2 | 3302 | 2781 | 1.68 | 2 | 15.8% | 7.9% |
| | 3 | 2712 | 1854 | 2.05 | 3 | 31.6% | 10.5% |
| | 4 | 2426 | 1391 | 2.29 | 4 | 42.7% | 10.7% |
| | 5 | 1811 | 1112 | 3.07 | 5 | 38.6% | 7.7% |
| | 7 | 1494 | 795 | 3.72 | 7 | 46.8% | 6.7% |
| | 8 | 1436 | 695 | 3.87 | 8 | 51.6% | 6.4% |
| 75% | 2 | 3493 | 2781 | 1.59 | 2 | 20.4% | 10.2% |
| | 3 | 2804 | 1854 | 1.98 | 3 | 33.9% | 11.3% |
| | 4 | 2352 | 1391 | 2.36 | 4 | 40.9% | 10.2% |
| | 5 | 2035 | 1112 | 2.73 | 5 | 45.3% | 9.1% |
| | 7 | 1617 | 795 | 3.44 | 7 | 50.9% | 7.3% |
| | 8 | 1478 | 695 | 3.76 | 8 | 53.0% | 6.6% |

**Table C.8 Calculated AF from Dissipated Energy Curve Using Peak-Midway Method**

| Interaction Level | Axle No | N f | | Axle Factor | | % difference | |
|---|---|---|---|---|---|---|---|
| | | Measured | Calculated | Measured | Calculated | Total | per n |
| 25% | 2 | 3279 | 1907 | 1.70 | 2.92 | 41.8% | 20.9% |
| | 3 | 2547 | 1464 | 2.18 | 3.80 | 42.5% | 14.2% |
| | 4 | 2241 | 1188 | 2.48 | 4.68 | 47.0% | 11.7% |
| | 5 | 2022 | 1000 | 2.75 | 5.56 | 50.6% | 10.1% |
| | 7 | 1322 | 759 | 4.21 | 7.33 | 42.6% | 6.1% |
| | 8 | 1210 | 677 | 4.60 | 8.21 | 44.0% | 5.5% |
| 50% | 2 | 3302 | 2335 | 1.68 | 2.38 | 29.3% | 14.7% |
| | 3 | 2712 | 2037 | 2.05 | 2.73 | 24.9% | 8.3% |
| | 4 | 2426 | 1806 | 2.29 | 3.08 | 25.6% | 6.4% |
| | 5 | 1811 | 1623 | 3.07 | 3.43 | 10.4% | 2.1% |
| | 7 | 1494 | 1348 | 3.72 | 4.13 | 9.8% | 1.4% |
| | 8 | 1436 | 1243 | 3.87 | 4.47 | 13.4% | 1.7% |
| 75% | 2 | 3493 | 2599 | 1.59 | 2.14 | 25.6% | 12.8% |
| | 3 | 2804 | 2476 | 1.98 | 2.25 | 11.7% | 3.9% |
| | 4 | 2352 | 2365 | 2.36 | 2.35 | 0.5% | 0.1% |
| | 5 | 2035 | 2263 | 2.73 | 2.46 | 11.2% | 2.2% |
| | 7 | 1617 | 2083 | 3.44 | 2.67 | 28.8% | 4.1% |
| | 8 | 1478 | 2004 | 3.76 | 2.78 | 35.5% | 4.4% |

**Table C.9 Calculated AF from Dissipated Energy Curve Using Peak Method (After Correction)**

| Interaction Level | Axle No | N f | | Axle Factor | | % difference | |
|---|---|---|---|---|---|---|---|
| | | Measured | Calculated | Measured | Calculated | Total | per n |
| 25% | 2 | 3279 | 3543 | 1.70 | 1.5698587 | 8.0% | 4.0% |
| | 3 | 2547 | 2616 | 2.18 | 2.1261517 | 2.7% | 0.9% |
| | 4 | 2241 | 2153 | 2.48 | 2.5839793 | 4.0% | 1.0% |
| | 5 | 2022 | 1875 | 2.75 | 2.9673591 | 7.3% | 1.5% |
| | 7 | 1322 | 1557 | 4.21 | 3.5732517 | 17.8% | 2.5% |
| | 8 | 1210 | 1457 | 4.60 | 3.8167939 | 20.5% | 2.6% |
| 50% | 2 | 3302 | 3543 | 1.68 | 1.5698587 | 7.3% | 3.6% |
| | 3 | 2712 | 2616 | 2.05 | 2.1261517 | 3.5% | 1.2% |
| | 4 | 2426 | 2153 | 2.29 | 2.5839793 | 11.3% | 2.8% |
| | 5 | 1811 | 1875 | 3.07 | 2.9673591 | 3.5% | 0.7% |
| | 7 | 1494 | 1557 | 3.72 | 3.5732517 | 4.2% | 0.6% |
| | 8 | 1436 | 1457 | 3.87 | 3.8167939 | 1.5% | 0.2% |
| 75% | 2 | 3493 | 3543 | 1.59 | 1.5698587 | 1.4% | 0.7% |
| | 3 | 2804 | 2616 | 1.98 | 2.1261517 | 6.7% | 2.2% |
| | 4 | 2352 | 2153 | 2.36 | 2.5839793 | 8.5% | 2.1% |
| | 5 | 2035 | 1875 | 2.73 | 2.9673591 | 7.9% | 1.6% |
| | 7 | 1617 | 1557 | 3.44 | 3.5732517 | 3.7% | 0.5% |
| | 8 | 1478 | 1457 | 3.76 | 3.8167939 | 1.4% | 0.2% |

# APPENDIX D1

## AC Fatigue-based Truck Factors by Class using WIM Data within AASHTO LEF Framework

# Calculation of Truck Factor for Class 5

| Axle load (lb) | EALF | Number of axles | ESAL |
|---|---|---|---|
| Single axle | | | |
| under 3000 | 0.000 | 480085 | 87.536 |
| 3000-3999 | 0.001 | 3212970 | 4077.506 |
| 4000-4999 | 0.003 | 3689060 | 12211.918 |
| 5000-5999 | 0.007 | 3088150 | 22671.987 |
| 6000-6999 | 0.014 | 1664410 | 24127.383 |
| 7000-7999 | 0.026 | 1789680 | 46927.591 |
| 8000-8999 | 0.044 | 1204850 | 53352.778 |
| 9000-9999 | 0.071 | 1243800 | 87991.983 |
| 10000-10999 | 0.108 | 1217440 | 131419.374 |
| 11000-11999 | 0.158 | 752855 | 119290.774 |
| 12000-12999 | 0.225 | 716939 | 161298.177 |
| 13000-13999 | 0.310 | 438587 | 136122.025 |
| 14000-14999 | 0.417 | 434099 | 181221.166 |
| 15000-15999 | 0.549 | 271202 | 148925.760 |
| 16000-16999 | 0.708 | 266017 | 188384.352 |
| 17000-17999 | 0.897 | 166753 | 149628.105 |
| 18000-18999 | 1.119 | 161392 | 180633.793 |
| 19000-19999 | 1.377 | 99249 | 136624.408 |
| 20000-20999 | 1.672 | 90997 | 152152.287 |
| 21000-21999 | 2.008 | 62930 | 126389.761 |
| 22000-22999 | 2.389 | 0 | 0.000 |
| 23000-23999 | 2.816 | 0 | 0.000 |
| 24000-24999 | 3.293 | 0 | 0.000 |
| 25000-25999 | 3.825 | 0 | 0.000 |
| 26000-26999 | 4.415 | 0 | 0.000 |
| 27000-27999 | 5.068 | 0 | 0.000 |
| 28000-28999 | 5.789 | 0 | 0.000 |
| 29000-34999 | 6.176 | 0 | 0.000 |
| 35000-39999 | 6.176 | 0 | 0.000 |
| 40000-50000 | 6.176 | 0 | 0.000 |

ESAL for all trucks weighted : 2063538.665

$$\text{Truck factor} = \frac{\text{18-kip ESALs for all trucks weighted}}{\text{Number of trucks weighted}} = \frac{2.064\text{E+06}}{1.053\text{E+07}} = \boxed{0.196}$$

# Calculation of Truck Factor for Class 6

| Axle load (lb) | EALF | Number of axles | ESAL | Axle load (lb) | EALF | Number of axle | ESAL |
|---|---|---|---|---|---|---|---|
| Single axle | | | | Tandem axle | | | |
| under 3000 | 0.000 | 2847 | 0.519 | under 6000 | 0.00029 | 48965 | 14.19982 |
| 3000-3999 | 0.001 | 9521 | 12.083 | 6000-7999 | 0.00202 | 214535 | 433.0254 |
| 4000-4999 | 0.003 | 13215 | 43.746 | 8000-9999 | 0.00526 | 185744 | 977.9356 |
| 5000-5999 | 0.007 | 20551 | 150.877 | 10000-11999 | 0.01168 | 101730 | 1187.866 |
| 6000-6999 | 0.014 | 26885 | 389.727 | 12000-13999 | 0.02306 | 92258 | 2127.067 |
| 7000-7999 | 0.026 | 70099 | 1838.081 | 14000-15999 | 0.0417 | 85209 | 3553.576 |
| 8000-8999 | 0.044 | 106476 | 4714.936 | 16000-17999 | 0.07043 | 77065 | 5427.609 |
| 9000-9999 | 0.071 | 212628 | 15042.257 | 18000-19999 | 0.11252 | 77577 | 8728.766 |
| 10000-10999 | 0.108 | 314914 | 33994.119 | 20000-21999 | 0.17169 | 95732 | 16436.01 |
| 11000-11999 | 0.158 | 214373 | 33967.658 | 22000-23999 | 0.25201 | 93970 | 23681.66 |
| 12000-12999 | 0.225 | 185032 | 41628.820 | 24000-25999 | 0.35783 | 98041 | 35081.84 |
| 13000-13999 | 0.310 | 109224 | 33899.299 | 26000-27999 | 0.49363 | 94082 | 46441.53 |
| 14000-14999 | 0.417 | 101579 | 42405.684 | 28000-29999 | 0.66397 | 83694 | 55570.18 |
| 15000-15999 | 0.549 | 55406 | 30425.221 | 30000-31999 | 0.87338 | 70361 | 61452.03 |
| 16000-16999 | 0.708 | 46389 | 32851.140 | 32000-33999 | 1.12632 | 53421 | 60169.27 |
| 17000-17999 | 0.897 | 24667 | 22133.794 | 34000-35999 | 1.42714 | 36263 | 51752.41 |
| 18000-18999 | 1.119 | 21560 | 24130.469 | 36000-37999 | 1.7801 | 23820 | 42401.97 |
| 19000-19999 | 1.377 | 12625 | 17379.350 | 38000-39999 | 2.18942 | 15517 | 33973.26 |
| 20000-20999 | 1.672 | 10941 | 18293.990 | 40000-41999 | 2.65937 | 0 | 0 |
| 21000-21999 | 2.008 | 6724 | 13504.604 | 42000-43999 | 3.19434 | 0 | 0 |
| 22000-22999 | 2.389 | 0 | 0.000 | 44000-45999 | 3.79899 | 0 | 0 |
| 23000-23999 | 2.816 | 0 | 0.000 | 46000-47999 | 4.4783 | 0 | 0 |
| 24000-24999 | 3.293 | 0 | 0.000 | 48000-49999 | 5.23775 | 0 | 0 |
| 25000-25999 | 3.825 | 0 | 0.000 | 50000-51999 | 6.08334 | 0 | 0 |
| 26000-26999 | 4.415 | 0 | 0.000 | 52000-53999 | 7.0217 | 0 | 0 |
| 27000-27999 | 5.068 | 0 | 0.000 | 54000-55999 | 8.06014 | 0 | 0 |
| 28000-28999 | 5.789 | 0 | 0.000 | 56000-57999 | 9.20669 | 0 | 0 |
| 29000-34999 | 6.176 | 0 | 0.000 | 58000-69999 | 9.82323 | 0 | 0 |
| 35000-39999 | 6.176 | 0 | 0.000 | 70000-79999 | 9.82323 | 0 | 0 |
| 40000-50000 | 6.176 | 0 | 0.000 | 80000-100000 | 9.82323 | 0 | 0 |

ESAL for all trucks weighted : 816216.574

$$\text{Truck factor} = \frac{\text{18-kip ESALs for all trucks weighted}}{\text{Number of trucks weighted}} = \frac{8.162\text{E+}05}{1.55\text{E+}06} = 0.525$$

# Calculation of Truck Factor for Class 7

| Axle load (lb) | EALF | Number of axles | ESAL | Axle load (lb) | EALF | Number of axles | ESAL |
|---|---|---|---|---|---|---|---|
| Single axle | | | | Tridem axle | | | |
| under 3000 | 0.000 | 1216 | 0.222 | under 9000 | 4E-04 | 1029 | 0.389001 |
| 3000-3999 | 0.001 | 2375 | 3.014 | 9000-11999 | 0.003 | 4002 | 10.53005 |
| 4000-4999 | 0.003 | 2769 | 9.166 | 12000-14999 | 0.007 | 12597 | 86.4571 |
| 5000-5999 | 0.007 | 4564 | 33.507 | 15000-17999 | 0.015 | 22424 | 341.3262 |
| 6000-6999 | 0.014 | 6089 | 88.266 | 18000-20999 | 0.03 | 29618 | 890.166 |
| 7000-7999 | 0.026 | 15660 | 410.624 | 21000-23999 | 0.054 | 27505 | 1495.305 |
| 8000-8999 | 0.044 | 25411 | 1125.242 | 24000-26999 | 0.092 | 21919 | 2012.381 |
| 9000-9999 | 0.071 | 44563 | 3152.586 | 27000-29999 | 0.147 | 21655 | 3176.261 |
| 10000-10999 | 0.108 | 45430 | 4904.046 | 30000-32999 | 0.224 | 20066 | 4490.948 |
| 11000-11999 | 0.158 | 26947 | 4269.784 | 33000-35999 | 0.329 | 17182 | 5644.619 |
| 12000-12999 | 0.225 | 25035 | 5632.418 | 36000-38999 | 0.466 | 17614 | 8216.193 |
| 13000-13999 | 0.310 | 17256 | 5355.657 | 39000-41999 | 0.643 | 15417 | 9920.599 |
| 14000-14999 | 0.417 | 20324 | 8484.560 | 42000-44999 | 0.866 | 13351 | 11555.78 |
| 15000-15999 | 0.549 | 14906 | 8185.365 | 45000-47999 | 1.139 | 9134 | 10399.28 |
| 16000-16999 | 0.708 | 16455 | 11652.881 | 48000-50999 | 1.468 | 5297 | 7777.335 |
| 17000-17999 | 0.897 | 11448 | 10272.334 | 51000-53999 | 1.86 | 0 | 0 |
| 18000-18999 | 1.119 | 11867 | 13281.831 | 54000-56999 | 2.321 | 0 | 0 |
| 19000-19999 | 1.377 | 7506 | 10332.626 | 57000-59999 | 2.854 | 0 | 0 |
| 20000-20999 | 1.672 | 6941 | 11605.756 | 60000-62999 | 3.467 | 0 | 0 |
| 21000-21999 | 2.008 | 4740 | 9519.903 | 63000-65999 | 4.164 | 0 | 0 |
| 22000-22999 | 2.389 | 0 | 0.000 | 66000-68999 | 4.952 | 0 | 0 |
| 23000-23999 | 2.816 | 0 | 0.000 | 69000-71999 | 5.838 | 0 | 0 |
| 24000-24999 | 3.293 | 0 | 0.000 | 72000-74999 | 6.828 | 0 | 0 |
| 25000-25999 | 3.825 | 0 | 0.000 | 75000-77999 | 7.93 | 0 | 0 |
| 26000-26999 | 4.415 | 0 | 0.000 | 78000-80999 | 9.153 | 0 | 0 |
| 27000-27999 | 5.068 | 0 | 0.000 | 81000-83999 | 10.51 | 0 | 0 |
| 28000-28999 | 5.789 | 0 | 0.000 | 84000-86999 | 12 | 0 | 0 |
| 29000-34999 | 6.176 | 0 | 0.000 | 87000-104999 | 12.81 | 0 | 0 |
| 35000-39999 | 6.176 | 0 | 0.000 | 105000-111999 | 12.81 | 0 | 0 |
| 40000-50000 | 6.176 | 0 | 0.000 | 120000-150000 | 12.81 | 0 | 0 |

| Axle load (lb) | EALF | Number of axles | ESAL |
|---|---|---|---|
| Quad axle | | | |
| under 12000 | 0.000 | 391 | 0.179 |
| 12000-15999 | 0.003 | 408 | 1.299 |
| 16000-19999 | 0.008 | 493 | 4.095 |
| 20000-23999 | 0.018 | 1038 | 19.124 |
| 24000-27999 | 0.036 | 1864 | 67.808 |
| 28000-31999 | 0.066 | 3212 | 211.357 |
| 32000-35999 | 0.111 | 5088 | 565.403 |
| 36000-39999 | 0.178 | 7280 | 1292.442 |
| 40000-43999 | 0.271 | 10590 | 2868.765 |
| 44000-47999 | 0.398 | 11789 | 4687.699 |
| 48000-51999 | 0.565 | 11552 | 6522.163 |
| 52000-55999 | 0.779 | 8864 | 6903.822 |
| 56000-59999 | 1.048 | 5165 | 5411.002 |
| 60000-63999 | 1.378 | 2512 | 3461.655 |
| 64000-67999 | 1.777 | 0 | 0.000 |
| 68000-71999 | 2.252 | 0 | 0.000 |
| 72000-75999 | 2.809 | 0 | 0.000 |
| 76000-79999 | 3.455 | 0 | 0.000 |
| 80000-83999 | 4.196 | 0 | 0.000 |
| 84000-87999 | 5.040 | 0 | 0.000 |
| 88000-91999 | 5.994 | 0 | 0.000 |
| 92000-95999 | 7.066 | 0 | 0.000 |
| 96000-99999 | 8.264 | 0 | 0.000 |
| 100000-103999 | 9.598 | 0 | 0.000 |
| 104000-107999 | 11.079 | 0 | 0.000 |
| 108000-111999 | 12.718 | 0 | 0.000 |
| 112000-115999 | 14.527 | 0 | 0.000 |
| 116000-139999 | 15.499 | 0 | 0.000 |
| 140000-159999 | 15.499 | 0 | 0.000 |
| 160000-200000 | 15.499 | 0 | 0.000 |

ESAL for all trucks weighted : 206354.175

$$\text{Truck factor} = \frac{\text{18-kip ESALs for all trucks weighted}}{\text{Number of trucks weighted}} = \frac{2.064\text{E+}05}{309775} = 0.666$$

# Calculation of Truck Factor for Class 8

| Axle load (lb) | EALF | Number of axles | ESAL | Axle load (lb) | EALF | Number of axles | ESAL |
|---|---|---|---|---|---|---|---|
| Single axle | | | | Tandem axle | | | |
| under 3000 | 0.000 | 47700 | 8.697 | under 6000 | 0.0003 | 117362 | 34.03492 |
| 3000-3999 | 0.001 | 216420 | 274.654 | 6000-7999 | 0.002 | 222021 | 448.1354 |
| 4000-4999 | 0.003 | 306637 | 1015.062 | 8000-9999 | 0.0053 | 254319 | 1338.981 |
| 5000-5999 | 0.007 | 312311 | 2292.865 | 10000-11999 | 0.0117 | 207204 | 2419.45 |
| 6000-6999 | 0.014 | 227648 | 3299.998 | 12000-13999 | 0.0231 | 149541 | 3447.764 |
| 7000-7999 | 0.026 | 341950 | 8966.346 | 14000-15999 | 0.0417 | 115820 | 4830.185 |
| 8000-8999 | 0.044 | 372547 | 16497.006 | 16000-17999 | 0.0704 | 91408 | 6437.772 |
| 9000-9999 | 0.071 | 466409 | 32995.862 | 18000-19999 | 0.1125 | 73370 | 8255.405 |
| 10000-10999 | 0.108 | 347090 | 37467.432 | 20000-21999 | 0.1717 | 64690 | 11106.48 |
| 11000-11999 | 0.158 | 185099 | 29329.158 | 22000-23999 | 0.252 | 40702 | 10257.43 |
| 12000-12999 | 0.225 | 191005 | 42972.636 | 24000-25999 | 0.3578 | 26797 | 9588.723 |
| 13000-13999 | 0.310 | 132793 | 41214.291 | 26000-27999 | 0.4936 | 16757 | 8271.728 |
| 14000-14999 | 0.417 | 142793 | 59611.089 | 28000-29999 | 0.664 | 9886 | 6563.992 |
| 15000-15999 | 0.549 | 93963 | 51598.112 | 30000-31999 | 0.8734 | 5987 | 5228.938 |
| 16000-16999 | 0.708 | 95644 | 67731.886 | 32000-33999 | 1.1263 | 3608 | 4063.772 |
| 17000-17999 | 0.897 | 60271 | 54081.399 | 34000-35999 | 1.4271 | 2271 | 3241.037 |
| 18000-18999 | 1.119 | 53720 | 60124.711 | 36000-37999 | 1.7801 | 1299 | 2312.349 |
| 19000-19999 | 1.377 | 29430 | 40512.815 | 38000-39999 | 2.1894 | 761 | 1666.15 |
| 20000-20999 | 1.672 | 24439 | 40863.432 | 40000-41999 | 2.6594 | 0 | 0 |
| 21000-21999 | 2.008 | 15012 | 30150.375 | 42000-43999 | 3.1943 | 0 | 0 |
| 22000-22999 | 2.389 | 0 | 0.000 | 44000-45999 | 3.799 | 0 | 0 |
| 23000-23999 | 2.816 | 0 | 0.000 | 46000-47999 | 4.4783 | 0 | 0 |
| 24000-24999 | 3.293 | 0 | 0.000 | 48000-49999 | 5.2377 | 0 | 0 |
| 25000-25999 | 3.825 | 0 | 0.000 | 50000-51999 | 6.0833 | 0 | 0 |
| 26000-26999 | 4.415 | 0 | 0.000 | 52000-53999 | 7.0217 | 0 | 0 |
| 27000-27999 | 5.068 | 0 | 0.000 | 54000-55999 | 8.0601 | 0 | 0 |
| 28000-28999 | 5.789 | 0 | 0.000 | 56000-57999 | 9.2067 | 0 | 0 |
| 29000-34999 | 6.176 | 0 | 0.000 | 58000-69999 | 9.8232 | 0 | 0 |
| 35000-39999 | 6.176 | 0 | 0.000 | 70000-79999 | 9.8232 | 0 | 0 |
| 40000-50000 | 6.176 | 0 | 0.000 | 80000-100000 | 9.8232 | 0 | 0 |

ESAL for all trucks weighted : 710520.147

$$\text{Truck factor} = \frac{\text{18-kip ESALs for all trucks weighted}}{\text{Number of trucks weighted}} = \frac{7.105\text{E+}05}{1.69\text{E+}06} = 0.420$$

# Calculation of Truck Factor for Class 9

| Axle load (lb) | EALF | Number of axles | ESAL | Axle load (lb) | EALF | Number of axles | ESAL |
|---|---|---|---|---|---|---|---|
| Single axle | | | | Tandem axle | | | |
| under 3000 | 0.000 | 217586 | 39.674 | under 6000 | 0.0003 | 263474 | 76.40732 |
| 3000-3999 | 0.001 | 474182 | 601.773 | 6000-7999 | 0.002 | 851432 | 1718.562 |
| 4000-4999 | 0.003 | 392627 | 1299.716 | 8000-9999 | 0.0053 | 2289300 | 12053.08 |
| 5000-5999 | 0.007 | 435776 | 3199.297 | 10000-11999 | 0.0117 | 3283180 | 38336.57 |
| 6000-6999 | 0.014 | 415293 | 6020.111 | 12000-13999 | 0.0231 | 3237820 | 74650.02 |
| 7000-7999 | 0.026 | 880848 | 23096.908 | 14000-15999 | 0.0417 | 2874240 | 119868 |
| 8000-8999 | 0.044 | 1489430 | 65954.458 | 16000-17999 | 0.0704 | 2601420 | 183215.3 |
| 9000-9999 | 0.071 | 3683550 | 260590.825 | 18000-19999 | 0.1125 | 2387830 | 268672.5 |
| 10000-10999 | 0.108 | 5998950 | 647570.519 | 20000-21999 | 0.1717 | 2503490 | 429818.4 |
| 11000-11999 | 0.158 | 3725460 | 590303.586 | 22000-23999 | 0.252 | 2037270 | 513418.4 |
| 12000-12999 | 0.225 | 2170990 | 488433.089 | 24000-25999 | 0.3578 | 1845260 | 660286.1 |
| 13000-13999 | 0.310 | 633693 | 196676.085 | 26000-27999 | 0.4936 | 1793390 | 885267.9 |
| 14000-14999 | 0.417 | 428790 | 179004.844 | 28000-29999 | 0.664 | 1942570 | 1289805 |
| 15000-15999 | 0.549 | 292044 | 160370.774 | 30000-31999 | 0.8734 | 2107480 | 1840635 |
| 16000-16999 | 0.708 | 365772 | 259027.511 | 32000-33999 | 1.1263 | 1873360 | 2110007 |
| 17000-17999 | 0.897 | 260477 | 233727.010 | 34000-35999 | 1.4271 | 1197970 | 1709672 |
| 18000-18999 | 1.119 | 236156 | 264311.454 | 36000-37999 | 1.7801 | 644266 | 1146858 |
| 19000-19999 | 1.377 | 119596 | 164633.726 | 38000-39999 | 2.1894 | 342570 | 750030.3 |
| 20000-20999 | 1.672 | 86395 | 144457.475 | 40000-41999 | 2.6594 | 0 | 0 |
| 21000-21999 | 2.008 | 47271 | 94939.940 | 42000-43999 | 3.1943 | 0 | 0 |
| 22000-22999 | 2.389 | 0 | 0.000 | 44000-45999 | 3.799 | 0 | 0 |
| 23000-23999 | 2.816 | 0 | 0.000 | 46000-47999 | 4.4783 | 0 | 0 |
| 24000-24999 | 3.293 | 0 | 0.000 | 48000-49999 | 5.2377 | 0 | 0 |
| 25000-25999 | 3.825 | 0 | 0.000 | 50000-51999 | 6.0833 | 0 | 0 |
| 26000-26999 | 4.415 | 0 | 0.000 | 52000-53999 | 7.0217 | 0 | 0 |
| 27000-27999 | 5.068 | 0 | 0.000 | 54000-55999 | 8.0601 | 0 | 0 |
| 28000-28999 | 5.789 | 0 | 0.000 | 56000-57999 | 9.2067 | 0 | 0 |
| 29000-34999 | 6.176 | 0 | 0.000 | 58000-69999 | 9.8232 | 0 | 0 |
| 35000-39999 | 6.176 | 0 | 0.000 | 70000-79999 | 9.8232 | 0 | 0 |
| 40000-50000 | 6.176 | 0 | 0.000 | 80000-100000 | 9.8232 | 0 | 0 |

ESAL for all trucks weighted : 15818647.909

$$\text{Truck factor} = \frac{\text{18-kip ESALs for all trucks weighted}}{\text{Number of trucks weighted}} = \frac{1.582\text{E+07}}{1.81\text{E+07}} = \boxed{0.874}$$

# Calculation of Truck Factor for Class 10

| Axle load (lb) | EALF | Number of axles | ESAL | Axle load (lb) | EALF | Number of axles | ESAL |
|---|---|---|---|---|---|---|---|
| Single axle | | | | Tandem axle | | | |
| under 3000 | 0.000 | 253446 | 46.212 | under 6000 | 0.0003 | 31067 | 9.009413 |
| 3000-3999 | 0.001 | 381335 | 483.943 | 6000-7999 | 0.002 | 66836 | 134.9043 |
| 4000-4999 | 0.003 | 419770 | 1389.567 | 8000-9999 | 0.0053 | 144459 | 760.5716 |
| 5000-5999 | 0.007 | 455130 | 3341.386 | 10000-11999 | 0.0117 | 261587 | 3054.462 |
| 6000-6999 | 0.014 | 311176 | 4510.825 | 12000-13999 | 0.0231 | 287843 | 6636.405 |
| 7000-7999 | 0.026 | 351943 | 9228.374 | 14000-15999 | 0.0417 | 237582 | 9908.176 |
| 8000-8999 | 0.044 | 292155 | 12937.113 | 16000-17999 | 0.0704 | 198224 | 13960.71 |
| 9000-9999 | 0.071 | 472821 | 33449.475 | 18000-19999 | 0.1125 | 175094 | 19701.13 |
| 10000-10999 | 0.108 | 746091 | 80538.517 | 20000-21999 | 0.1717 | 174420 | 29945.77 |
| 11000-11999 | 0.158 | 607189 | 96209.822 | 22000-23999 | 0.252 | 153058 | 38572.6 |
| 12000-12999 | 0.225 | 613503 | 138026.967 | 24000-25999 | 0.3578 | 166578 | 59606.31 |
| 13000-13999 | 0.310 | 371182 | 115201.877 | 26000-27999 | 0.4936 | 192553 | 95049.59 |
| 14000-14999 | 0.417 | 366007 | 152795.135 | 28000-29999 | 0.664 | 216873 | 143996.8 |
| 15000-15999 | 0.549 | 225922 | 124061.053 | 30000-31999 | 0.8734 | 220489 | 192571.1 |
| 16000-16999 | 0.708 | 218932 | 155040.328 | 32000-33999 | 1.1263 | 194198 | 218729.6 |
| 17000-17999 | 0.897 | 134400 | 120597.635 | 34000-35999 | 1.4271 | 146968 | 209744 |
| 18000-18999 | 1.119 | 124175 | 138979.635 | 36000-37999 | 1.7801 | 96892 | 172477.4 |
| 19000-19999 | 1.377 | 68353 | 94093.524 | 38000-39999 | 2.1894 | 58771 | 128674.5 |
| 20000-20999 | 1.672 | 55958 | 93565.037 | 40000-41999 | 2.6594 | 0 | 0 |
| 21000-21999 | 2.008 | 34217 | 68722.048 | 42000-43999 | 3.1943 | 0 | 0 |
| 22000-22999 | 2.389 | 0 | 0.000 | 44000-45999 | 3.799 | 0 | 0 |
| 23000-23999 | 2.816 | 0 | 0.000 | 46000-47999 | 4.4783 | 0 | 0 |
| 24000-24999 | 3.293 | 0 | 0.000 | 48000-49999 | 5.2377 | 0 | 0 |
| 25000-25999 | 3.825 | 0 | 0.000 | 50000-51999 | 6.0833 | 0 | 0 |
| 26000-26999 | 4.415 | 0 | 0.000 | 52000-53999 | 7.0217 | 0 | 0 |
| 27000-27999 | 5.068 | 0 | 0.000 | 54000-55999 | 8.0601 | 0 | 0 |
| 28000-28999 | 5.789 | 0 | 0.000 | 56000-57999 | 9.2067 | 0 | 0 |
| 29000-34999 | 6.176 | 0 | 0.000 | 58000-69999 | 9.8232 | 0 | 0 |
| 35000-39999 | 6.176 | 0 | 0.000 | 70000-79999 | 9.8232 | 0 | 0 |
| 40000-50000 | 6.176 | 0 | 0.000 | 80000-100000 | 9.8232 | 0 | 0 |

| Axle load (lb) | EALF | Number of axles | ESAL | Axle load (lb) | EALF | Number of axles | ESAL |
|---|---|---|---|---|---|---|---|
| 7-axle | | | | 8-axle | | | |
| under 21000 | 0.001 | 8708 | 5.777 | under 24000 | 0.0007 | 30507 | 22.11313 |
| 21000-27999 | 0.005 | 22195 | 102.479 | 24000-31999 | 0.005 | 78497 | 396.0242 |
| 28000-34999 | 0.012 | 17913 | 215.739 | 32000-39999 | 0.0132 | 36058 | 474.5157 |
| 35000-41999 | 0.027 | 9262 | 247.393 | 40000-47999 | 0.0292 | 13208 | 385.4864 |
| 42000-48999 | 0.053 | 5508 | 290.493 | 48000-55999 | 0.0576 | 6664 | 384.0305 |
| 49000-55999 | 0.095 | 5638 | 537.860 | 56000-63999 | 0.1042 | 7991 | 832.9805 |
| 56000-62999 | 0.161 | 7530 | 1213.139 | 64000-71999 | 0.176 | 13736 | 2418.049 |
| 63000-69999 | 0.257 | 10257 | 2640.003 | 72000-79999 | 0.2812 | 22316 | 6276.098 |
| 70000-76999 | 0.393 | 15219 | 5977.086 | 80000-87999 | 0.4291 | 39277 | 16855.09 |
| 77000-83999 | 0.576 | 22345 | 12881.530 | 88000-95999 | 0.6299 | 67015 | 42213.21 |
| 84000-90999 | 0.819 | 27555 | 22554.813 | 96000-103999 | 0.8944 | 99997 | 89436.55 |
| 91000-97999 | 1.129 | 24471 | 27632.230 | 104000-111999 | 1.2338 | 113115 | 139564.1 |
| 98000-104999 | 1.519 | 17000 | 25820.261 | 112000-119999 | 1.6596 | 91930 | 152566.2 |
| 105000-111999 | 1.998 | 10834 | 21644.987 | 120000-127999 | 2.183 | 56756 | 123899.5 |
| 112000-118999 | 2.576 | 0 | 0.000 | 128000-135999 | 2.8152 | 0 | 0 |
| 119000-125999 | 3.265 | 0 | 0.000 | 136000-143999 | 3.5671 | 0 | 0 |
| 126000-132999 | 4.072 | 0 | 0.000 | 144000-151999 | 4.4494 | 0 | 0 |
| 133000-139999 | 5.008 | 0 | 0.000 | 152000-159999 | 5.4725 | 0 | 0 |
| 140000-146999 | 6.083 | 0 | 0.000 | 160000-167999 | 6.6471 | 0 | 0 |
| 147000-153999 | 7.307 | 0 | 0.000 | 168000-175999 | 7.9843 | 0 | 0 |
| 154000-160999 | 8.690 | 0 | 0.000 | 176000-183999 | 9.4956 | 0 | 0 |
| 161000-167999 | 10.244 | 0 | 0.000 | 184000-191999 | 11.194 | 0 | 0 |
| 168000-174999 | 11.981 | 0 | 0.000 | 192000-199999 | 13.092 | 0 | 0 |
| 175000-181999 | 13.916 | 0 | 0.000 | 200000-207999 | 15.205 | 0 | 0 |
| 182000-188999 | 16.062 | 0 | 0.000 | 208000-215999 | 17.551 | 0 | 0 |
| 189000-195999 | 18.438 | 0 | 0.000 | 216000-223999 | 20.146 | 0 | 0 |
| 196000-202999 | 21.060 | 0 | 0.000 | 224000-231999 | 23.012 | 0 | 0 |
| 203000-244999 | 22.471 | 0 | 0.000 | 232000-279999 | 24.553 | 0 | 0 |
| 245000-279999 | 22.471 | 0 | 0.000 | 280000-319999 | 24.553 | 0 | 0 |
| 280000-350000 | 22.471 | 0 | 0.000 | 320000-400000 | 24.553 | 0 | 0 |

ESAL for all trucks weighted : 3484239.303

$$\text{Truck factor} = \frac{\text{18-kip ESALs for all trucks weighted}}{\text{Number of trucks weighted}} = \frac{3.484E+06}{2.43E+06} = 1.437$$

# Calculation of Truck Factor for Class 11

| Axle load (lb) | EALF | Number of axles | ESAL |
|---|---|---|---|
| Single axle under 3000 | 0.000 | 45199 | 8.241 |
| 3000-3999 | 0.001 | 88280 | 112.034 |
| 4000-4999 | 0.003 | 108165 | 358.059 |
| 5000-5999 | 0.007 | 163914 | 1203.392 |
| 6000-6999 | 0.014 | 131316 | 1903.564 |
| 7000-7999 | 0.026 | 173850 | 4558.559 |
| 8000-8999 | 0.044 | 184295 | 8160.892 |
| 9000-9999 | 0.071 | 318663 | 22543.648 |
| 10000-10999 | 0.108 | 314038 | 33899.558 |
| 11000-11999 | 0.158 | 174981 | 27725.948 |
| 12000-12999 | 0.225 | 187849 | 42262.593 |
| 13000-13999 | 0.310 | 140541 | 43618.998 |
| 14000-14999 | 0.417 | 162424 | 67806.345 |
| 15000-15999 | 0.549 | 108747 | 59716.483 |
| 16000-16999 | 0.708 | 103746 | 73469.451 |
| 17000-17999 | 0.897 | 59837 | 53691.969 |
| 18000-18999 | 1.119 | 50726 | 56773.755 |
| 19000-19999 | 1.377 | 26155 | 36004.508 |
| 20000-20999 | 1.672 | 19239 | 32168.729 |
| 21000-21999 | 2.008 | 9745 | 19572.036 |
| 22000-22999 | 2.389 | 0 | 0.000 |
| 23000-23999 | 2.816 | 0 | 0.000 |
| 24000-24999 | 3.293 | 0 | 0.000 |
| 25000-25999 | 3.825 | 0 | 0.000 |
| 26000-26999 | 4.415 | 0 | 0.000 |
| 27000-27999 | 5.068 | 0 | 0.000 |
| 28000-28999 | 5.789 | 0 | 0.000 |
| 29000-34999 | 6.176 | 0 | 0.000 |
| 35000-39999 | 6.176 | 0 | 0.000 |
| 40000-50000 | 6.176 | 0 | 0.000 |

ESAL for all trucks weighted : 585558.763

$$\text{Truck factor} = \frac{\text{18-kip ESALs for all trucks weighted}}{\text{Number of trucks weighted}} = \frac{5.856\text{E+}05}{514342} = \boxed{1.138}$$

# Calculation of Truck Factor for Class 12

| Axle load (lb) | EALF | Number of axles | ESAL | Axle load (lb) | EALF | Number of axles | ESAL |
|---|---|---|---|---|---|---|---|
| Single axle | | | | Tandem axle | | | |
| under 3000 | 0.000 | 10067 | 1.836 | under 6000 | 0.0003 | 17822 | 5.16837 |
| 3000-3999 | 0.001 | 7138 | 9.059 | 6000-7999 | 0.002 | 32409 | 65.41553 |
| 4000-4999 | 0.003 | 12932 | 42.809 | 8000-9999 | 0.0053 | 39129 | 206.0128 |
| 5000-5999 | 0.007 | 29544 | 216.900 | 10000-11999 | 0.0117 | 27951 | 326.3742 |
| 6000-6999 | 0.014 | 26015 | 377.115 | 12000-13999 | 0.0231 | 13549 | 312.3809 |
| 7000-7999 | 0.026 | 39028 | 1023.362 | 14000-15999 | 0.0417 | 7438 | 310.1961 |
| 8000-8999 | 0.044 | 45508 | 2015.171 | 16000-17999 | 0.0704 | 4017 | 282.9132 |
| 9000-9999 | 0.071 | 67223 | 4755.656 | 18000-19999 | 0.1125 | 1730 | 194.6552 |
| 10000-10999 | 0.108 | 64947 | 7010.854 | 20000-21999 | 0.1717 | 708 | 121.5549 |
| 11000-11999 | 0.158 | 38598 | 6115.899 | 22000-23999 | 0.252 | 238 | 59.97908 |
| 12000-12999 | 0.225 | 36550 | 8223.082 | 24000-25999 | 0.3578 | 105 | 37.57196 |
| 13000-13999 | 0.310 | 24510 | 7607.045 | 26000-27999 | 0.4936 | 56 | 27.64318 |
| 14000-14999 | 0.417 | 24950 | 10415.753 | 28000-29999 | 0.664 | 53 | 35.19033 |
| 15000-15999 | 0.549 | 16947 | 9306.144 | 30000-31999 | 0.8734 | 32 | 27.94823 |
| 16000-16999 | 0.708 | 18526 | 13119.494 | 32000-33999 | 1.1263 | 34 | 38.29496 |
| 17000-17999 | 0.897 | 12949 | 11619.187 | 34000-35999 | 1.4271 | 21 | 29.96996 |
| 18000-18999 | 1.119 | 14252 | 15951.180 | 36000-37999 | 1.7801 | 21 | 37.38209 |
| 19000-19999 | 1.377 | 10011 | 13780.965 | 38000-39999 | 2.1894 | 16 | 35.03075 |
| 20000-20999 | 1.672 | 10984 | 18365.888 | 40000-41999 | 2.6594 | 0 | 0 |
| 21000-21999 | 2.008 | 10038 | 20160.503 | 42000-43999 | 3.1943 | 0 | 0 |
| 22000-22999 | 2.389 | 0 | 0.000 | 44000-45999 | 3.799 | 0 | 0 |
| 23000-23999 | 2.816 | 0 | 0.000 | 46000-47999 | 4.4783 | 0 | 0 |
| 24000-24999 | 3.293 | 0 | 0.000 | 48000-49999 | 5.2377 | 0 | 0 |
| 25000-25999 | 3.825 | 0 | 0.000 | 50000-51999 | 6.0833 | 0 | 0 |
| 26000-26999 | 4.415 | 0 | 0.000 | 52000-53999 | 7.0217 | 0 | 0 |
| 27000-27999 | 5.068 | 0 | 0.000 | 54000-55999 | 8.0601 | 0 | 0 |
| 28000-28999 | 5.789 | 0 | 0.000 | 56000-57999 | 9.2067 | 0 | 0 |
| 29000-34999 | 6.176 | 0 | 0.000 | 58000-69999 | 9.8232 | 0 | 0 |
| 35000-39999 | 6.176 | 0 | 0.000 | 70000-79999 | 9.8232 | 0 | 0 |
| 40000-50000 | 6.176 | 0 | 0.000 | 80000-100000 | 9.8232 | 0 | 0 |

ESAL for all trucks weighted : 152271.583

$$\text{Truck factor} = \frac{\text{18-kip ESALs for all trucks weighted}}{\text{Number of trucks weighted}} = \frac{1.523\text{E+}05}{135230} = 1.126$$

# Calculation of Truck Factor for Class 13

| Axle load (lb) Single axle | EALF | Number of axles | ESAL | Axle load (lb) Tandem axle | EALF | Number of axles | ESAL | Axle load (lb) Tridem axle | EALF | Number of axles | ESAL |
|---|---|---|---|---|---|---|---|---|---|---|---|
| under 3000 | 0.000 | 37912 | 6.913 | under 6000 | 3E-04 | 110640 | 32.08554 | under 9000 | 0.000378 | 13424 | 5.07478 |
| 3000-3999 | 0.001 | 50635 | 64.260 | 6000-7999 | 0.002 | 175169 | 353.5676 | 9000-11999 | 0.002631 | 18709 | 49.22705 |
| 4000-4999 | 0.003 | 50241 | 166.313 | 8000-9999 | 0.005 | 187700 | 988.2339 | 12000-14999 | 0.006863 | 8146 | 55.90851 |
| 5000-5999 | 0.007 | 57596 | 422.847 | 10000-11999 | 0.012 | 168902 | 1972.211 | 15000-17999 | 0.015221 | 3992 | 60.7641 |
| 6000-6999 | 0.014 | 42627 | 617.923 | 12000-13999 | 0.023 | 145258 | 3349.016 | 18000-20999 | 0.030055 | 2624 | 78.86406 |
| 7000-7999 | 0.026 | 54693 | 1434.117 | 14000-15999 | 0.042 | 117638 | 4906.003 | 21000-23999 | 0.054365 | 2248 | 122.2122 |
| 8000-8999 | 0.044 | 58670 | 2598.006 | 16000-17999 | 0.07 | 100302 | 7064.167 | 24000-26999 | 0.09181 | 2276 | 208.9593 |
| 9000-9999 | 0.071 | 129457 | 9158.368 | 18000-19999 | 0.113 | 106080 | 11935.85 | 27000-29999 | 0.146676 | 3684 | 540.353 |
| 10000-10999 | 0.108 | 264804 | 28584.880 | 20000-21999 | 0.172 | 155153 | 26637.86 | 30000-32999 | 0.223809 | 6454 | 1444.462 |
| 11000-11999 | 0.158 | 238781 | 37835.135 | 22000-23999 | 0.252 | 190807 | 48085.83 | 33000-35999 | 0.328519 | 10130 | 3327.901 |
| 12000-12999 | 0.225 | 244839 | 55084.302 | 24000-25999 | 0.358 | 229448 | 82102.97 | 36000-38999 | 0.466458 | 16456 | 7676.034 |
| 13000-13999 | 0.310 | 132753 | 41201.876 | 26000-27999 | 0.494 | 230076 | 113572 | 39000-41999 | 0.643484 | 18422 | 11854.27 |
| 14000-14999 | 0.417 | 108003 | 45087.479 | 28000-29999 | 0.664 | 198100 | 131532.2 | 42000-44999 | 0.865537 | 18147 | 15706.9 |
| 15000-15999 | 0.549 | 55565 | 30512.533 | 30000-31999 | 0.873 | 156011 | 136257.2 | 45000-47999 | 1.138524 | 14142 | 16101.01 |
| 16000-16999 | 0.708 | 49355 | 34951.562 | 32000-33999 | 1.126 | 112550 | 126767.6 | 48000-50999 | 1.468253 | 8858 | 13005.78 |
| 17000-17999 | 0.897 | 29025 | 26044.244 | 34000-35999 | 1.427 | 77717 | 110913.1 | 51000-53999 | 1.860394 | 0 | 0 |
| 18000-18999 | 1.119 | 26415 | 29564.301 | 36000-37999 | 1.78 | 50780 | 90393.46 | 54000-56999 | 2.320504 | 0 | 0 |
| 19000-19999 | 1.377 | 14836 | 20422.974 | 38000-39999 | 2.189 | 32271 | 70654.84 | 57000-59999 | 2.854089 | 0 | 0 |
| 20000-20999 | 1.672 | 12490 | 20884.008 | 40000-41999 | 2.659 | 0 | 0 | 60000-62999 | 3.466704 | 0 | 0 |
| 21000-21999 | 2.008 | 8105 | 16278.230 | 42000-43999 | 3.194 | 0 | 0 | 63000-65999 | 4.164085 | 0 | 0 |
| 22000-22999 | 2.389 | 0 | 0.000 | 44000-45999 | 3.799 | 0 | 0 | 66000-68999 | 4.952286 | 0 | 0 |
| 23000-23999 | 2.816 | 0 | 0.000 | 46000-47999 | 4.478 | 0 | 0 | 69000-71999 | 5.83783 | 0 | 0 |
| 24000-24999 | 3.293 | 0 | 0.000 | 48000-49999 | 5.238 | 0 | 0 | 72000-74999 | 6.827832 | 0 | 0 |
| 25000-25999 | 3.825 | 0 | 0.000 | 50000-51999 | 6.083 | 0 | 0 | 75000-77999 | 7.930124 | 0 | 0 |
| 26000-26999 | 4.415 | 0 | 0.000 | 52000-53999 | 7.022 | 0 | 0 | 78000-80999 | 9.153351 | 0 | 0 |
| 27000-27999 | 5.068 | 0 | 0.000 | 54000-55999 | 8.06 | 0 | 0 | 81000-83999 | 10.50704 | 0 | 0 |
| 28000-28999 | 5.789 | 0 | 0.000 | 56000-57999 | 9.207 | 0 | 0 | 84000-86999 | 12.00167 | 0 | 0 |
| 29000-34999 | 6.176 | 0 | 0.000 | 58000-69999 | 9.823 | 0 | 0 | 87000-104999 | 12.80537 | 0 | 0 |
| 35000-39999 | 6.176 | 0 | 0.000 | 70000-79999 | 9.823 | 0 | 0 | 105000-11199 | 12.80537 | 0 | 0 |
| 40000-50000 | 6.176 | 0 | 0.000 | 80000-100000 | 9.823 | 0 | 0 | 120000-15000 | 12.80537 | 0 | 0 |

| Axle load (lb) quad axle | EALF | Number of axles | ESAL | Axle load (lb) 5-axle | EALF | Number of axles | ESAL |
|---|---|---|---|---|---|---|---|
| under 12000 | 0.000 | 3538 | 1.619 | under 15000 | 5E-04 | 583 | 0.309346 |
| 12000-15999 | 0.003 | 9028 | 28.752 | 15000-19999 | 0.004 | 489 | 1.805939 |
| 16000-19999 | 0.008 | 33481 | 278.134 | 20000-24999 | 0.01 | 330 | 3.178985 |
| 20000-23999 | 0.018 | 42015 | 774.075 | 25000-29999 | 0.021 | 286 | 6.110315 |
| 24000-27999 | 0.036 | 26040 | 947.279 | 30000-34999 | 0.042 | 342 | 14.42721 |
| 28000-31999 | 0.066 | 17060 | 1122.585 | 35000-39999 | 0.076 | 479 | 36.55062 |
| 32000-35999 | 0.111 | 13599 | 1511.187 | 40000-44999 | 0.129 | 835 | 107.6012 |
| 36000-39999 | 0.178 | 15151 | 2689.807 | 45000-49999 | 0.206 | 1287 | 264.9583 |
| 40000-43999 | 0.271 | 23421 | 6344.603 | 50000-54999 | 0.314 | 2168 | 681.0476 |
| 44000-47999 | 0.398 | 35393 | 14073.435 | 55000-59999 | 0.461 | 3633 | 1675.202 |
| 48000-51999 | 0.565 | 54083 | 30534.812 | 60000-64999 | 0.655 | 5839 | 3822.893 |
| 52000-55999 | 0.779 | 79669 | 62051.063 | 65000-69999 | 0.903 | 6749 | 6095.628 |
| 56000-59999 | 1.048 | 101051 | 105863.919 | 70000-74999 | 1.215 | 5540 | 6730.329 |
| 60000-63999 | 1.378 | 97171 | 133906.243 | 75000-79999 | 1.598 | 3611 | 5770.465 |
| 64000-67999 | 1.777 | 0 | 0.000 | 80000-84999 | 2.061 | 0 | 0 |
| 68000-71999 | 2.252 | 0 | 0.000 | 85000-89999 | 2.611 | 0 | 0 |
| 72000-75999 | 2.809 | 0 | 0.000 | 90000-94999 | 3.257 | 0 | 0 |
| 76000-79999 | 3.455 | 0 | 0.000 | 95000-99999 | 4.006 | 0 | 0 |
| 80000-83999 | 4.196 | 0 | 0.000 | 100000-104999 | 4.866 | 0 | 0 |
| 84000-87999 | 5.040 | 0 | 0.000 | 105000-109999 | 5.845 | 0 | 0 |
| 88000-91999 | 5.994 | 0 | 0.000 | 110000-114999 | 6.951 | 0 | 0 |
| 92000-95999 | 7.066 | 0 | 0.000 | 115000-119999 | 8.194 | 0 | 0 |
| 96000-99999 | 8.264 | 0 | 0.000 | 120000-124999 | 9.583 | 0 | 0 |
| 100000-103999 | 9.598 | 0 | 0.000 | 125000-129999 | 11.13 | 0 | 0 |
| 104000-107999 | 11.079 | 0 | 0.000 | 130000-134999 | 12.85 | 0 | 0 |
| 108000-111999 | 12.718 | 0 | 0.000 | 135000-139999 | 14.75 | 0 | 0 |
| 112000-115999 | 14.527 | 0 | 0.000 | 140000-144999 | 16.85 | 0 | 0 |
| 116000-139999 | 15.499 | 0 | 0.000 | 145000-174999 | 17.97 | 0 | 0 |
| 140000-159999 | 15.499 | 0 | 0.000 | 175000-199999 | 17.97 | 0 | 0 |
| 160000-200000 | 15.499 | 0 | 0.000 | 200000-250000 | 17.97 | 0 | 0 |

ESAL for all trucks weighted : 1824014.166

Truck factor = $\frac{\text{18-kip ESALs for all trucks weighted}}{\text{Number of trucks weighted}}$ = $\frac{1.824E+06}{1.08E+06}$ = **1.696**

# APPENDIX D2

# AC Rutting-based Truck Factors by Class using WIM Data within AASHTO LEF Framework

# Calculation of Truck Factor for Class 5

| Axle load (lb) | EALF | Number of axles | ESAL |
|---|---|---|---|
| Single axle | | | |
| under 3000 | 0.000 | 480085 | 87.746 |
| 3000-3999 | 0.001 | 3212970 | 4087.253 |
| 4000-4999 | 0.003 | 3689060 | 12241.110 |
| 5000-5999 | 0.007 | 3088150 | 22726.183 |
| 6000-6999 | 0.015 | 1664410 | 24185.058 |
| 7000-7999 | 0.026 | 1789680 | 47039.769 |
| 8000-8999 | 0.044 | 1204850 | 53480.315 |
| 9000-9999 | 0.071 | 1243800 | 88202.322 |
| 10000-10999 | 0.108 | 1217440 | 131733.524 |
| 11000-11999 | 0.159 | 752855 | 119575.931 |
| 12000-12999 | 0.226 | 716939 | 161683.751 |
| 13000-13999 | 0.311 | 438587 | 136447.416 |
| 14000-14999 | 0.418 | 434099 | 181654.364 |
| 15000-15999 | 0.550 | 271202 | 149281.758 |
| 16000-16999 | 0.710 | 266017 | 188834.673 |
| 17000-17999 | 0.899 | 166753 | 149985.782 |
| 18000-18999 | 1.122 | 161392 | 181065.587 |
| 19000-19999 | 1.380 | 99249 | 136951.000 |
| 20000-20999 | 1.676 | 90997 | 152515.997 |
| 21000-21999 | 2.013 | 62930 | 126691.888 |
| 22000-22999 | 2.394 | 0 | 0.000 |
| 23000-23999 | 2.822 | 0 | 0.000 |
| 24000-24999 | 3.301 | 0 | 0.000 |
| 25000-25999 | 3.834 | 0 | 0.000 |
| 26000-26999 | 4.425 | 0 | 0.000 |
| 27000-27999 | 5.080 | 0 | 0.000 |
| 28000-28999 | 5.802 | 0 | 0.000 |
| 29000-34999 | 6.191 | 0 | 0.000 |
| 35000-39999 | 6.191 | 0 | 0.000 |
| 40000-50000 | 6.191 | 0 | 0.000 |

ESAL for all trucks weighted : 2068471.427

$$\text{Truck factor} = \frac{\text{18-kip ESALs for all trucks weighted}}{\text{Number of trucks weighted}} = \frac{2.068E+06}{1.053E+07} = \boxed{0.197}$$

# Calculation of Truck Factor for Class 6

| Axle load (lb) | EALF | Number of axles | ESAL | Axle load (lb) | EALF | Number of axles | ESAL |
|---|---|---|---|---|---|---|---|
| Single axle | | | | Tandem axle | | | |
| under 3000 | 0.000 | 2847 | 0.520 | under 6000 | 0.0004 | 48965 | 17.28071 |
| 3000-3999 | 0.001 | 9521 | 12.112 | 6000-7999 | 0.0025 | 214535 | 526.9773 |
| 4000-4999 | 0.003 | 13215 | 43.850 | 8000-9999 | 0.0064 | 185744 | 1190.115 |
| 5000-5999 | 0.007 | 20551 | 151.238 | 10000-11999 | 0.0142 | 101730 | 1445.593 |
| 6000-6999 | 0.015 | 26885 | 390.658 | 12000-13999 | 0.0281 | 92258 | 2588.569 |
| 7000-7999 | 0.026 | 70099 | 1842.475 | 14000-15999 | 0.0508 | 85209 | 4324.583 |
| 8000-8999 | 0.044 | 106476 | 4726.207 | 16000-17999 | 0.0857 | 77065 | 6605.217 |
| 9000-9999 | 0.071 | 212628 | 15078.215 | 18000-19999 | 0.1369 | 77577 | 10622.61 |
| 10000-10999 | 0.108 | 314914 | 34075.380 | 20000-21999 | 0.2089 | 95732 | 20002.06 |
| 11000-11999 | 0.159 | 214373 | 34048.855 | 22000-23999 | 0.3067 | 93970 | 28819.78 |
| 12000-12999 | 0.226 | 185032 | 41728.331 | 24000-25999 | 0.4355 | 98041 | 42693.41 |
| 13000-13999 | 0.311 | 109224 | 33980.334 | 26000-27999 | 0.6007 | 94082 | 56517.77 |
| 14000-14999 | 0.418 | 101579 | 42507.052 | 28000-29999 | 0.808 | 83694 | 67627.03 |
| 15000-15999 | 0.550 | 55406 | 30497.950 | 30000-31999 | 1.0629 | 70361 | 74785.05 |
| 16000-16999 | 0.710 | 46389 | 32929.669 | 32000-33999 | 1.3707 | 53421 | 73223.97 |
| 17000-17999 | 0.899 | 24667 | 22186.703 | 34000-35999 | 1.7368 | 36263 | 62980.93 |
| 18000-18999 | 1.122 | 21560 | 24188.151 | 36000-37999 | 2.1663 | 23820 | 51601.77 |
| 19000-19999 | 1.380 | 12625 | 17420.895 | 38000-39999 | 2.6645 | 15517 | 41344.31 |
| 20000-20999 | 1.676 | 10941 | 18337.720 | 40000-41999 | 3.2364 | 0 | 0 |
| 21000-21999 | 2.013 | 6724 | 13536.886 | 42000-43999 | 3.8874 | 0 | 0 |
| 22000-22999 | 2.394 | 0 | 0.000 | 44000-45999 | 4.6232 | 0 | 0 |
| 23000-23999 | 2.822 | 0 | 0.000 | 46000-47999 | 5.4499 | 0 | 0 |
| 24000-24999 | 3.301 | 0 | 0.000 | 48000-49999 | 6.3742 | 0 | 0 |
| 25000-25999 | 3.834 | 0 | 0.000 | 50000-51999 | 7.4032 | 0 | 0 |
| 26000-26999 | 4.425 | 0 | 0.000 | 52000-53999 | 8.5452 | 0 | 0 |
| 27000-27999 | 5.080 | 0 | 0.000 | 54000-55999 | 9.8089 | 0 | 0 |
| 28000-28999 | 5.802 | 0 | 0.000 | 56000-57999 | 11.204 | 0 | 0 |
| 29000-34999 | 6.191 | 0 | 0.000 | 58000-69999 | 11.955 | 0 | 0 |
| 35000-39999 | 6.191 | 0 | 0.000 | 70000-79999 | 11.955 | 0 | 0 |
| 40000-50000 | 6.191 | 0 | 0.000 | 80000-100000 | 11.955 | 0 | 0 |

ESAL for all trucks weighted : 914600.232

$$\text{Truck factor} = \frac{\text{18-kip ESALs for all trucks weighted}}{\text{Number of trucks weighted}} = \frac{9.146\text{E+}05}{1.55\text{E+}06} = 0.589$$

# Calculation of Truck Factor for Class 7

| Axle load (lb) | EALF | Number of axles | ESAL | Axle load (lb) | EALF | Number of axles | ESAL |
|---|---|---|---|---|---|---|---|
| Single axle | | | | Tridem axle | | | |
| under 3000 | 0.000 | 1216 | 0.222 | under 9000 | 5E-04 | 1029 | 0.52828 |
| 3000-3999 | 0.001 | 2375 | 3.021 | 9000-11999 | 0.004 | 4002 | 14.30025 |
| 4000-4999 | 0.003 | 2769 | 9.188 | 12000-14999 | 0.009 | 12597 | 117.4124 |
| 5000-5999 | 0.007 | 4564 | 33.587 | 15000-17999 | 0.021 | 22424 | 463.5354 |
| 6000-6999 | 0.015 | 6089 | 88.477 | 18000-20999 | 0.041 | 29618 | 1208.883 |
| 7000-7999 | 0.026 | 15660 | 411.606 | 21000-23999 | 0.074 | 27505 | 2030.688 |
| 8000-8999 | 0.044 | 25411 | 1127.932 | 24000-26999 | 0.125 | 21919 | 2732.898 |
| 9000-9999 | 0.071 | 44563 | 3160.122 | 27000-29999 | 0.199 | 21655 | 4313.495 |
| 10000-10999 | 0.108 | 45430 | 4915.769 | 30000-32999 | 0.304 | 20066 | 6098.896 |
| 11000-11999 | 0.159 | 26947 | 4279.991 | 33000-35999 | 0.446 | 17182 | 7665.63 |
| 12000-12999 | 0.226 | 25035 | 5645.882 | 36000-38999 | 0.633 | 17614 | 11157.94 |
| 13000-13999 | 0.311 | 17256 | 5368.460 | 39000-41999 | 0.874 | 15417 | 13472.59 |
| 14000-14999 | 0.418 | 20324 | 8504.842 | 42000-44999 | 1.175 | 13351 | 15693.24 |
| 15000-15999 | 0.550 | 14906 | 8204.932 | 45000-47999 | 1.546 | 9134 | 14122.66 |
| 16000-16999 | 0.710 | 16455 | 11680.737 | 48000-50999 | 1.994 | 5297 | 10561.95 |
| 17000-17999 | 0.899 | 11448 | 10296.890 | 51000-53999 | 2.526 | 0 | 0 |
| 18000-18999 | 1.122 | 11867 | 13313.580 | 54000-56999 | 3.151 | 0 | 0 |
| 19000-19999 | 1.380 | 7506 | 10357.326 | 57000-59999 | 3.876 | 0 | 0 |
| 20000-20999 | 1.676 | 6941 | 11633.499 | 60000-62999 | 4.708 | 0 | 0 |
| 21000-21999 | 2.013 | 4740 | 9542.659 | 63000-65999 | 5.655 | 0 | 0 |
| 22000-22999 | 2.394 | 0 | 0.000 | 66000-68999 | 6.725 | 0 | 0 |
| 23000-23999 | 2.822 | 0 | 0.000 | 69000-71999 | 7.928 | 0 | 0 |
| 24000-24999 | 3.301 | 0 | 0.000 | 72000-74999 | 9.272 | 0 | 0 |
| 25000-25999 | 3.834 | 0 | 0.000 | 75000-77999 | 10.77 | 0 | 0 |
| 26000-26999 | 4.425 | 0 | 0.000 | 78000-80999 | 12.43 | 0 | 0 |
| 27000-27999 | 5.080 | 0 | 0.000 | 81000-83999 | 14.27 | 0 | 0 |
| 28000-28999 | 5.802 | 0 | 0.000 | 84000-86999 | 16.3 | 0 | 0 |
| 29000-34999 | 6.191 | 0 | 0.000 | 87000-104999 | 17.39 | 0 | 0 |
| 35000-39999 | 6.191 | 0 | 0.000 | 105000-111999 | 17.39 | 0 | 0 |
| 40000-50000 | 6.191 | 0 | 0.000 | 120000-150000 | 17.39 | 0 | 0 |

| Axle load (lb) | EALF | Number of axles | ESAL |
|---|---|---|---|
| Quad axle | | | |
| under 12000 | 0.001 | 391 | 0.268 |
| 12000-15999 | 0.005 | 408 | 1.946 |
| 16000-19999 | 0.012 | 493 | 6.135 |
| 20000-23999 | 0.028 | 1038 | 28.647 |
| 24000-27999 | 0.054 | 1864 | 101.575 |
| 28000-31999 | 0.099 | 3212 | 316.606 |
| 32000-35999 | 0.166 | 5088 | 846.957 |
| 36000-39999 | 0.266 | 7280 | 1936.038 |
| 40000-43999 | 0.406 | 10590 | 4297.321 |
| 44000-47999 | 0.596 | 11789 | 7022.028 |
| 48000-51999 | 0.846 | 11552 | 9769.998 |
| 52000-55999 | 1.167 | 8864 | 10341.712 |
| 56000-59999 | 1.569 | 5165 | 8105.513 |
| 60000-63999 | 2.064 | 2512 | 5185.452 |
| 64000-67999 | 2.662 | 0 | 0.000 |
| 68000-71999 | 3.373 | 0 | 0.000 |
| 72000-75999 | 4.207 | 0 | 0.000 |
| 76000-79999 | 5.175 | 0 | 0.000 |
| 80000-83999 | 6.286 | 0 | 0.000 |
| 84000-87999 | 7.550 | 0 | 0.000 |
| 88000-91999 | 8.979 | 0 | 0.000 |
| 92000-95999 | 10.585 | 0 | 0.000 |
| 96000-99999 | 12.380 | 0 | 0.000 |
| 100000-103999 | 14.378 | 0 | 0.000 |
| 104000-107999 | 16.596 | 0 | 0.000 |
| 108000-111999 | 19.050 | 0 | 0.000 |
| 112000-115999 | 21.760 | 0 | 0.000 |
| 116000-139999 | 23.218 | 0 | 0.000 |
| 140000-159999 | 23.218 | 0 | 0.000 |
| 160000-200000 | 23.218 | 0 | 0.000 |

ESAL for all trucks weighted : 246193.557

$$\text{Truck factor} = \frac{\text{18-kip ESALs for all trucks weighted}}{\text{Number of trucks weighted}} = \frac{2.462\text{E+}05}{309775} = 0.795$$

# Calculation of Truck Factor for Class 8

| Axle load (lb) | EALF | Number of axles | ESAL | Axle load (lb) | EALF | Number of axles | ESAL |
|---|---|---|---|---|---|---|---|
| Single axle | | | | Tandem axle | | | |
| under 3000 | 0.000 | 47700 | 8.718 | under 6000 | 0.0004 | 117362 | 41.41934 |
| 3000-3999 | 0.001 | 216420 | 275.310 | 6000-7999 | 0.0025 | 222021 | 545.3657 |
| 4000-4999 | 0.003 | 306637 | 1017.489 | 8000-9999 | 0.0064 | 254319 | 1629.494 |
| 5000-5999 | 0.007 | 312311 | 2298.346 | 10000-11999 | 0.0142 | 207204 | 2944.389 |
| 6000-6999 | 0.015 | 227648 | 3307.887 | 12000-13999 | 0.0281 | 149541 | 4195.812 |
| 7000-7999 | 0.026 | 341950 | 8987.779 | 14000-15999 | 0.0508 | 115820 | 5878.172 |
| 8000-8999 | 0.044 | 372547 | 16536.441 | 16000-17999 | 0.0857 | 91408 | 7834.551 |
| 9000-9999 | 0.071 | 466409 | 33074.736 | 18000-19999 | 0.1369 | 73370 | 10046.55 |
| 10000-10999 | 0.108 | 347090 | 37556.996 | 20000-21999 | 0.2089 | 64690 | 13516.21 |
| 11000-11999 | 0.159 | 185099 | 29399.267 | 22000-23999 | 0.3067 | 40702 | 12482.95 |
| 12000-12999 | 0.226 | 191005 | 43075.359 | 24000-25999 | 0.4355 | 26797 | 11669.15 |
| 13000-13999 | 0.311 | 132793 | 41312.811 | 26000-27999 | 0.6007 | 16757 | 10066.41 |
| 14000-14999 | 0.418 | 142793 | 59753.585 | 28000-29999 | 0.808 | 9886 | 7988.157 |
| 15000-15999 | 0.550 | 93963 | 51721.454 | 30000-31999 | 1.0629 | 5987 | 6363.441 |
| 16000-16999 | 0.710 | 95644 | 67893.794 | 32000-33999 | 1.3707 | 3608 | 4945.473 |
| 17000-17999 | 0.899 | 60271 | 54210.677 | 34000-35999 | 1.7368 | 2271 | 3944.232 |
| 18000-18999 | 1.122 | 53720 | 60268.436 | 36000-37999 | 2.1663 | 1299 | 2814.051 |
| 19000-19999 | 1.380 | 29430 | 40609.658 | 38000-39999 | 2.6645 | 761 | 2027.648 |
| 20000-20999 | 1.676 | 24439 | 40961.114 | 40000-41999 | 3.2364 | 0 | 0 |
| 21000-21999 | 2.013 | 15012 | 30222.448 | 42000-43999 | 3.8874 | 0 | 0 |
| 22000-22999 | 2.394 | 0 | 0.000 | 44000-45999 | 4.6232 | 0 | 0 |
| 23000-23999 | 2.822 | 0 | 0.000 | 46000-47999 | 5.4499 | 0 | 0 |
| 24000-24999 | 3.301 | 0 | 0.000 | 48000-49999 | 6.3742 | 0 | 0 |
| 25000-25999 | 3.834 | 0 | 0.000 | 50000-51999 | 7.4032 | 0 | 0 |
| 26000-26999 | 4.425 | 0 | 0.000 | 52000-53999 | 8.5452 | 0 | 0 |
| 27000-27999 | 5.080 | 0 | 0.000 | 54000-55999 | 9.8089 | 0 | 0 |
| 28000-28999 | 5.802 | 0 | 0.000 | 56000-57999 | 11.204 | 0 | 0 |
| 29000-34999 | 6.191 | 0 | 0.000 | 58000-69999 | 11.955 | 0 | 0 |
| 35000-39999 | 6.191 | 0 | 0.000 | 70000-79999 | 11.955 | 0 | 0 |
| 40000-50000 | 6.191 | 0 | 0.000 | 80000-100000 | 11.955 | 0 | 0 |

ESAL for all trucks weighted : 731425.777

$$\text{Truck factor} = \frac{\text{18-kip ESALs for all trucks weighted}}{\text{Number of trucks weighted}} = \frac{7.314\text{E+}05}{1.69\text{E+}06} = 0.433$$

# Calculation of Truck Factor for Class 9

| Axle load (lb) | EALF | Number of axles | ESAL | Axle load (lb) | EALF | Number of axles | ESAL |
|---|---|---|---|---|---|---|---|
| Single axle | | | | Tandem axle | | | |
| under 3000 | 0.000 | 217586 | 39.768 | under 6000 | 0.0004 | 263474 | 92.98512 |
| 3000-3999 | 0.001 | 474182 | 603.212 | 6000-7999 | 0.0025 | 851432 | 2091.432 |
| 4000-4999 | 0.003 | 392627 | 1302.822 | 8000-9999 | 0.0064 | 2289300 | 14668.2 |
| 5000-5999 | 0.007 | 435776 | 3206.944 | 10000-11999 | 0.0142 | 3283180 | 46654.31 |
| 6000-6999 | 0.015 | 415293 | 6034.502 | 12000-13999 | 0.0281 | 3237820 | 90846.55 |
| 7000-7999 | 0.026 | 880848 | 23152.120 | 14000-15999 | 0.0508 | 2874240 | 145875.3 |
| 8000-8999 | 0.044 | 1489430 | 66112.118 | 16000-17999 | 0.0857 | 2601420 | 222966.9 |
| 9000-9999 | 0.071 | 3683550 | 261213.752 | 18000-19999 | 0.1369 | 2387830 | 326965.4 |
| 10000-10999 | 0.108 | 5998950 | 649118.497 | 20000-21999 | 0.2089 | 2503490 | 523074.5 |
| 11000-11999 | 0.159 | 3725460 | 591714.670 | 22000-23999 | 0.3067 | 2037270 | 624812.8 |
| 12000-12999 | 0.226 | 2170990 | 489600.658 | 24000-25999 | 0.4355 | 1845260 | 803545.9 |
| 13000-13999 | 0.311 | 633693 | 197146.227 | 26000-27999 | 0.6007 | 1793390 | 1077341 |
| 14000-14999 | 0.418 | 428790 | 179432.744 | 28000-29999 | 0.808 | 1942570 | 1569649 |
| 15000-15999 | 0.550 | 292044 | 160754.131 | 30000-31999 | 1.0629 | 2107480 | 2239991 |
| 16000-16999 | 0.710 | 365772 | 259646.700 | 32000-33999 | 1.3707 | 1873360 | 2567808 |
| 17000-17999 | 0.899 | 260477 | 234285.720 | 34000-35999 | 1.7368 | 1197970 | 2080613 |
| 18000-18999 | 1.122 | 236156 | 264943.274 | 36000-37999 | 2.1663 | 644266 | 1395687 |
| 19000-19999 | 1.380 | 119596 | 165027.273 | 38000-39999 | 2.6645 | 342570 | 912761.5 |
| 20000-20999 | 1.676 | 86395 | 144802.791 | 40000-41999 | 3.2364 | 0 | 0 |
| 21000-21999 | 2.013 | 47271 | 95166.888 | 42000-43999 | 3.8874 | 0 | 0 |
| 22000-22999 | 2.394 | 0 | 0.000 | 44000-45999 | 4.6232 | 0 | 0 |
| 23000-23999 | 2.822 | 0 | 0.000 | 46000-47999 | 5.4499 | 0 | 0 |
| 24000-24999 | 3.301 | 0 | 0.000 | 48000-49999 | 6.3742 | 0 | 0 |
| 25000-25999 | 3.834 | 0 | 0.000 | 50000-51999 | 7.4032 | 0 | 0 |
| 26000-26999 | 4.425 | 0 | 0.000 | 52000-53999 | 8.5452 | 0 | 0 |
| 27000-27999 | 5.080 | 0 | 0.000 | 54000-55999 | 9.8089 | 0 | 0 |
| 28000-28999 | 5.802 | 0 | 0.000 | 56000-57999 | 11.204 | 0 | 0 |
| 29000-34999 | 6.191 | 0 | 0.000 | 58000-69999 | 11.955 | 0 | 0 |
| 35000-39999 | 6.191 | 0 | 0.000 | 70000-79999 | 11.955 | 0 | 0 |
| 40000-50000 | 6.191 | 0 | 0.000 | 80000-100000 | 11.955 | 0 | 0 |

ESAL for all trucks weighted : 18438749.796

$$\text{Truck factor} = \frac{\text{18-kip ESALs for all trucks weighted}}{\text{Number of trucks weighted}} = \frac{1.844\text{E+}07}{1.81\text{E+}07} = 1.019$$

# Calculation of Truck Factor for Class 10

| Axle load (lb) | EALF | Number of axles | ESAL | Axle load (lb) | EALF | Number of axles | ESAL |
|---|---|---|---|---|---|---|---|
| Single axle | | | | Tandem axle | | | |
| under 3000 | 0.000 | 253446 | 46.323 | under 6000 | 0.0004 | 31067 | 10.96415 |
| 3000-3999 | 0.001 | 381335 | 485.100 | 6000-7999 | 0.0025 | 66836 | 164.1739 |
| 4000-4999 | 0.003 | 419770 | 1392.889 | 8000-9999 | 0.0064 | 144459 | 925.5899 |
| 5000-5999 | 0.007 | 455130 | 3349.373 | 10000-11999 | 0.0142 | 261587 | 3717.177 |
| 6000-6999 | 0.015 | 311176 | 4521.608 | 12000-13999 | 0.0281 | 287843 | 8076.281 |
| 7000-7999 | 0.026 | 351943 | 9250.434 | 14000-15999 | 0.0508 | 237582 | 12057.92 |
| 8000-8999 | 0.044 | 292155 | 12968.039 | 16000-17999 | 0.0857 | 198224 | 16989.72 |
| 9000-9999 | 0.071 | 472821 | 33529.434 | 18000-19999 | 0.1369 | 175094 | 23975.61 |
| 10000-10999 | 0.108 | 746091 | 80731.039 | 20000-21999 | 0.2089 | 174420 | 36442.99 |
| 11000-11999 | 0.159 | 607189 | 96439.806 | 22000-23999 | 0.3067 | 153058 | 46941.55 |
| 12000-12999 | 0.226 | 613503 | 138356.912 | 24000-25999 | 0.4355 | 166578 | 72538.86 |
| 13000-13999 | 0.311 | 371182 | 115477.259 | 26000-27999 | 0.6007 | 192553 | 115672.1 |
| 14000-14999 | 0.418 | 366007 | 153160.383 | 28000-29999 | 0.808 | 216873 | 175239.3 |
| 15000-15999 | 0.550 | 225922 | 124357.613 | 30000-31999 | 1.0629 | 220489 | 234352.6 |
| 16000-16999 | 0.710 | 218932 | 155410.943 | 32000-33999 | 1.3707 | 194198 | 266186.5 |
| 17000-17999 | 0.899 | 134400 | 120885.916 | 34000-35999 | 1.7368 | 146968 | 255251.4 |
| 18000-18999 | 1.122 | 124175 | 139311.857 | 36000-37999 | 2.1663 | 96892 | 209899.2 |
| 19000-19999 | 1.380 | 68353 | 94318.449 | 38000-39999 | 2.6645 | 58771 | 156592.5 |
| 20000-20999 | 1.676 | 55958 | 93788.698 | 40000-41999 | 3.2364 | 0 | 0 |
| 21000-21999 | 2.013 | 34217 | 68886.323 | 42000-43999 | 3.8874 | 0 | 0 |
| 22000-22999 | 2.394 | 0 | 0.000 | 44000-45999 | 4.6232 | 0 | 0 |
| 23000-23999 | 2.822 | 0 | 0.000 | 46000-47999 | 5.4499 | 0 | 0 |
| 24000-24999 | 3.301 | 0 | 0.000 | 48000-49999 | 6.3742 | 0 | 0 |
| 25000-25999 | 3.834 | 0 | 0.000 | 50000-51999 | 7.4032 | 0 | 0 |
| 26000-26999 | 4.425 | 0 | 0.000 | 52000-53999 | 8.5452 | 0 | 0 |
| 27000-27999 | 5.080 | 0 | 0.000 | 54000-55999 | 9.8089 | 0 | 0 |
| 28000-28999 | 5.802 | 0 | 0.000 | 56000-57999 | 11.204 | 0 | 0 |
| 29000-34999 | 6.191 | 0 | 0.000 | 58000-69999 | 11.955 | 0 | 0 |
| 35000-39999 | 6.191 | 0 | 0.000 | 70000-79999 | 11.955 | 0 | 0 |
| 40000-50000 | 6.191 | 0 | 0.000 | 80000-100000 | 11.955 | 0 | 0 |

| Axle load (lb) | EALF | Number of axles | ESAL | Axle load (lb) | EALF | Number of axles | ESAL |
|---|---|---|---|---|---|---|---|
| 7-axle | | | | 8-axle | | | |
| under 21000 | 0.001 | 8708 | 9.885 | under 24000 | 0.0013 | 30507 | 39.06051 |
| 21000-27999 | 0.008 | 22195 | 175.361 | 24000-31999 | 0.0089 | 78497 | 699.5352 |
| 28000-34999 | 0.021 | 17913 | 369.169 | 32000-39999 | 0.0232 | 36058 | 838.1821 |
| 35000-41999 | 0.046 | 9262 | 423.336 | 40000-47999 | 0.0516 | 13208 | 680.9212 |
| 42000-48999 | 0.090 | 5508 | 497.087 | 48000-55999 | 0.1018 | 6664 | 678.3495 |
| 49000-55999 | 0.163 | 5638 | 920.379 | 56000-63999 | 0.1841 | 7991 | 1471.372 |
| 56000-62999 | 0.276 | 7530 | 2075.907 | 64000-71999 | 0.311 | 13736 | 4271.23 |
| 63000-69999 | 0.440 | 10257 | 4517.537 | 72000-79999 | 0.4968 | 22316 | 11086.07 |
| 70000-76999 | 0.672 | 15219 | 10227.908 | 80000-87999 | 0.758 | 39277 | 29772.73 |
| 77000-83999 | 0.986 | 22345 | 22042.697 | 88000-95999 | 1.1127 | 67015 | 74565.19 |
| 84000-90999 | 1.401 | 27555 | 38595.486 | 96000-103999 | 1.5798 | 99997 | 157980.3 |
| 91000-97999 | 1.932 | 24471 | 47283.891 | 104000-111999 | 2.1794 | 113115 | 246525.3 |
| 98000-104999 | 2.599 | 17000 | 44183.275 | 112000-119999 | 2.9315 | 91930 | 269492.1 |
| 105000-111999 | 3.419 | 10834 | 37038.605 | 120000-127999 | 3.8561 | 56756 | 218855.4 |
| 112000-118999 | 4.409 | 0 | 0.000 | 128000-135999 | 4.9728 | 0 | 0 |
| 119000-125999 | 5.586 | 0 | 0.000 | 136000-143999 | 6.301 | 0 | 0 |
| 126000-132999 | 6.968 | 0 | 0.000 | 144000-151999 | 7.8593 | 0 | 0 |
| 133000-139999 | 8.570 | 0 | 0.000 | 152000-159999 | 9.6665 | 0 | 0 |
| 140000-146999 | 10.410 | 0 | 0.000 | 160000-167999 | 11.741 | 0 | 0 |
| 147000-153999 | 12.504 | 0 | 0.000 | 168000-175999 | 14.103 | 0 | 0 |
| 154000-160999 | 14.871 | 0 | 0.000 | 176000-183999 | 16.773 | 0 | 0 |
| 161000-167999 | 17.530 | 0 | 0.000 | 184000-191999 | 19.772 | 0 | 0 |
| 168000-174999 | 20.502 | 0 | 0.000 | 192000-199999 | 23.125 | 0 | 0 |
| 175000-181999 | 23.812 | 0 | 0.000 | 200000-207999 | 26.859 | 0 | 0 |
| 182000-188999 | 27.485 | 0 | 0.000 | 208000-215999 | 31.002 | 0 | 0 |
| 189000-195999 | 31.550 | 0 | 0.000 | 216000-223999 | 35.586 | 0 | 0 |
| 196000-202999 | 36.038 | 0 | 0.000 | 224000-231999 | 40.649 | 0 | 0 |
| 203000-244999 | 38.452 | 0 | 0.000 | 232000-279999 | 43.371 | 0 | 0 |
| 245000-279999 | 38.452 | 0 | 0.000 | 280000-319999 | 43.371 | 0 | 0 |
| 280000-350000 | 38.452 | 0 | 0.000 | 320000-400000 | 43.371 | 0 | 0 |

ESAL for all trucks weighted : 4307019.025

$$\text{Truck factor} = \frac{\text{18-kip ESALs for all trucks weighted}}{\text{Number of trucks weighted}} = \frac{4.307E+06}{2.43E+06} = 1.776$$

# Calculation of Truck Factor for Class 11

| Axle load (lb) | EALF | Number of axles | ESAL |
|---|---|---|---|
| Single axle under 3000 | 0.000 | 45199 | 8.261 |
| 3000-3999 | 0.001 | 88280 | 112.302 |
| 4000-4999 | 0.003 | 108165 | 358.915 |
| 5000-5999 | 0.007 | 163914 | 1206.269 |
| 6000-6999 | 0.015 | 131316 | 1908.115 |
| 7000-7999 | 0.026 | 173850 | 4569.456 |
| 8000-8999 | 0.044 | 184295 | 8180.400 |
| 9000-9999 | 0.071 | 318663 | 22597.537 |
| 10000-10999 | 0.108 | 314038 | 33980.592 |
| 11000-11999 | 0.159 | 174981 | 27792.226 |
| 12000-12999 | 0.226 | 187849 | 42363.619 |
| 13000-13999 | 0.311 | 140541 | 43723.267 |
| 14000-14999 | 0.418 | 162424 | 67968.432 |
| 15000-15999 | 0.550 | 108747 | 59859.232 |
| 16000-16999 | 0.710 | 103746 | 73645.075 |
| 17000-17999 | 0.899 | 59837 | 53820.317 |
| 18000-18999 | 1.122 | 50726 | 56909.469 |
| 19000-19999 | 1.380 | 26155 | 36090.574 |
| 20000-20999 | 1.676 | 19239 | 32245.626 |
| 21000-21999 | 2.013 | 9745 | 19618.822 |
| 22000-22999 | 2.394 | 0 | 0.000 |
| 23000-23999 | 2.822 | 0 | 0.000 |
| 24000-24999 | 3.301 | 0 | 0.000 |
| 25000-25999 | 3.834 | 0 | 0.000 |
| 26000-26999 | 4.425 | 0 | 0.000 |
| 27000-27999 | 5.080 | 0 | 0.000 |
| 28000-28999 | 5.802 | 0 | 0.000 |
| 29000-34999 | 6.191 | 0 | 0.000 |
| 35000-39999 | 6.191 | 0 | 0.000 |
| 40000-50000 | 6.191 | 0 | 0.000 |

ESAL for all trucks weighted : 586958.505

$$\text{Truck factor} = \frac{\text{18-kip ESALs for all trucks weighted}}{\text{Number of trucks weighted}} = \frac{5.870\text{E+05}}{514342} = \boxed{1.141}$$

# Calculation of Truck Factor for Class 12

| Axle load (lb) | EALF | Number of axles | ESAL | Axle load (lb) | EALF | Number of axles | ESAL |
|---|---|---|---|---|---|---|---|
| Single axle | | | | Tandem axle | | | |
| under 3000 | 0.000 | 10067 | 1.840 | under 6000 | 4E-04 | 17822 | 6.289732 |
| 3000-3999 | 0.001 | 7138 | 9.080 | 6000-7999 | 0.002 | 32409 | 79.60849 |
| 4000-4999 | 0.003 | 12932 | 42.911 | 8000-9999 | 0.006 | 39129 | 250.7106 |
| 5000-5999 | 0.007 | 29544 | 217.419 | 10000-11999 | 0.014 | 27951 | 397.1864 |
| 6000-6999 | 0.015 | 26015 | 378.016 | 12000-13999 | 0.028 | 13549 | 380.157 |
| 7000-7999 | 0.026 | 39028 | 1025.808 | 14000-15999 | 0.051 | 7438 | 377.4982 |
| 8000-8999 | 0.044 | 45508 | 2019.988 | 16000-17999 | 0.086 | 4017 | 344.2958 |
| 9000-9999 | 0.071 | 67223 | 4767.024 | 18000-19999 | 0.137 | 1730 | 236.8888 |
| 10000-10999 | 0.108 | 64947 | 7027.613 | 20000-21999 | 0.209 | 708 | 147.9282 |
| 11000-11999 | 0.159 | 38598 | 6130.519 | 22000-23999 | 0.307 | 238 | 72.99251 |
| 12000-12999 | 0.226 | 36550 | 8242.739 | 24000-25999 | 0.435 | 105 | 45.72381 |
| 13000-13999 | 0.311 | 24510 | 7625.229 | 26000-27999 | 0.601 | 56 | 33.64082 |
| 14000-14999 | 0.418 | 24950 | 10440.652 | 28000-29999 | 0.808 | 53 | 42.82544 |
| 15000-15999 | 0.550 | 16947 | 9328.390 | 30000-31999 | 1.063 | 32 | 34.01205 |
| 16000-16999 | 0.710 | 18526 | 13150.856 | 32000-33999 | 1.371 | 34 | 46.60368 |
| 17000-17999 | 0.899 | 12949 | 11646.962 | 34000-35999 | 1.737 | 21 | 36.47243 |
| 18000-18999 | 1.122 | 14252 | 15989.310 | 36000-37999 | 2.166 | 21 | 45.49274 |
| 19000-19999 | 1.380 | 10011 | 13813.907 | 38000-39999 | 2.664 | 16 | 42.63124 |
| 20000-20999 | 1.676 | 10984 | 18409.791 | 40000-41999 | 3.236 | 0 | 0 |
| 21000-21999 | 2.013 | 10038 | 20208.695 | 42000-43999 | 3.887 | 0 | 0 |
| 22000-22999 | 2.394 | 0 | 0.000 | 44000-45999 | 4.623 | 0 | 0 |
| 23000-23999 | 2.822 | 0 | 0.000 | 46000-47999 | 5.45 | 0 | 0 |
| 24000-24999 | 3.301 | 0 | 0.000 | 48000-49999 | 6.374 | 0 | 0 |
| 25000-25999 | 3.834 | 0 | 0.000 | 50000-51999 | 7.403 | 0 | 0 |
| 26000-26999 | 4.425 | 0 | 0.000 | 52000-53999 | 8.545 | 0 | 0 |
| 27000-27999 | 5.080 | 0 | 0.000 | 54000-55999 | 9.809 | 0 | 0 |
| 28000-28999 | 5.802 | 0 | 0.000 | 56000-57999 | 11.2 | 0 | 0 |
| 29000-34999 | 6.191 | 0 | 0.000 | 58000-69999 | 11.95 | 0 | 0 |
| 35000-39999 | 6.191 | 0 | 0.000 | 70000-79999 | 11.95 | 0 | 0 |
| 40000-50000 | 6.191 | 0 | 0.000 | 80000-100000 | 11.95 | 0 | 0 |

ESAL for all trucks weighted : 153097.706

$$\text{Truck factor} = \frac{\text{18-kip ESALs for all trucks weighted}}{\text{Number of trucks weighted}} = \frac{1.531\text{E+}05}{135230} = \boxed{1.132}$$

# Calculation of Truck Factor for Class 13

| Axle load (lb) Single axle | EALF | Number of axles | ESAL | Axle load (lb) Tandem axle | EALF | Number of axles | ESAL | Axle load (lb) Tridem axle | EALF | Number of axles | ESAL |
|---|---|---|---|---|---|---|---|---|---|---|---|
| under 3000 | 0.000 | 37912 | 6.929 | under 6000 | 4E-04 | 110640 | 39.04702 | under 9000 | 0.0005 | 13424 | 6.891764 |
| 3000-3999 | 0.001 | 50635 | 64.413 | 6000-7999 | 0.002 | 175169 | 430.2798 | 9000-11999 | 0.0036 | 18709 | 66.85241 |
| 4000-4999 | 0.003 | 50241 | 166.711 | 8000-9999 | 0.006 | 187700 | 1202.647 | 12000-14999 | 0.0093 | 8146 | 75.92611 |
| 5000-5999 | 0.007 | 57596 | 423.858 | 10000-11999 | 0.014 | 168902 | 2400.114 | 15000-17999 | 0.0207 | 3992 | 82.52021 |
| 6000-6999 | 0.015 | 42627 | 619.401 | 12000-13999 | 0.028 | 145258 | 4075.64 | 18000-20999 | 0.0408 | 2624 | 107.1007 |
| 7000-7999 | 0.026 | 54693 | 1437.545 | 14000-15999 | 0.051 | 117638 | 5970.44 | 21000-23999 | 0.0738 | 2248 | 165.9693 |
| 8000-8999 | 0.044 | 58670 | 2604.216 | 16000-17999 | 0.086 | 100302 | 8596.853 | 24000-26999 | 0.1247 | 2276 | 283.7755 |
| 9000-9999 | 0.071 | 129457 | 9180.261 | 18000-19999 | 0.137 | 106080 | 14525.53 | 27000-29999 | 0.1992 | 3684 | 733.8221 |
| 10000-10999 | 0.108 | 264804 | 28653.210 | 20000-21999 | 0.209 | 155153 | 32417.38 | 30000-32999 | 0.3039 | 6454 | 1961.64 |
| 11000-11999 | 0.159 | 238781 | 37925.577 | 22000-23999 | 0.307 | 190807 | 58518.83 | 33000-35999 | 0.4461 | 10130 | 4519.429 |
| 12000-12999 | 0.226 | 244839 | 55215.978 | 24000-25999 | 0.435 | 229448 | 99916.54 | 36000-38999 | 0.6335 | 16456 | 10424.38 |
| 13000-13999 | 0.311 | 132753 | 41300.366 | 26000-27999 | 0.601 | 230076 | 138213.3 | 39000-41999 | 0.8739 | 18422 | 16098.6 |
| 14000-14999 | 0.418 | 108003 | 45195.258 | 28000-29999 | 0.808 | 198100 | 160070.2 | 42000-44999 | 1.1754 | 18147 | 21330.63 |
| 15000-15999 | 0.550 | 55565 | 30585.471 | 30000-31999 | 1.063 | 156011 | 165820.4 | 45000-47999 | 1.5462 | 14142 | 21865.85 |
| 16000-16999 | 0.710 | 49355 | 35035.112 | 32000-33999 | 1.371 | 112550 | 154271.9 | 48000-50999 | 1.9939 | 8858 | 17662.4 |
| 17000-17999 | 0.899 | 29025 | 26106.501 | 34000-35999 | 1.737 | 77717 | 134977.5 | 51000-53999 | 2.5265 | 0 | 0 |
| 18000-18999 | 1.122 | 26415 | 29634.973 | 36000-37999 | 2.166 | 50780 | 110005.8 | 54000-56999 | 3.1513 | 0 | 0 |
| 19000-19999 | 1.380 | 14836 | 20471.794 | 38000-39999 | 2.664 | 32271 | 85984.55 | 57000-59999 | 3.876 | 0 | 0 |
| 20000-20999 | 1.676 | 12490 | 20933.930 | 40000-41999 | 3.236 | 0 | 0 | 60000-62999 | 4.7079 | 0 | 0 |
| 21000-21999 | 2.013 | 8105 | 16317.142 | 42000-43999 | 3.887 | 0 | 0 | 63000-65999 | 5.655 | 0 | 0 |
| 22000-22999 | 2.394 | 0 | 0.000 | 44000-45999 | 4.623 | 0 | 0 | 66000-68999 | 6.7254 | 0 | 0 |
| 23000-23999 | 2.822 | 0 | 0.000 | 46000-47999 | 5.45 | 0 | 0 | 69000-71999 | 7.928 | 0 | 0 |
| 24000-24999 | 3.301 | 0 | 0.000 | 48000-49999 | 6.374 | 0 | 0 | 72000-74999 | 9.2725 | 0 | 0 |
| 25000-25999 | 3.834 | 0 | 0.000 | 50000-51999 | 7.403 | 0 | 0 | 75000-77999 | 10.769 | 0 | 0 |
| 26000-26999 | 4.425 | 0 | 0.000 | 52000-53999 | 8.545 | 0 | 0 | 78000-80999 | 12.431 | 0 | 0 |
| 27000-27999 | 5.080 | 0 | 0.000 | 54000-55999 | 9.809 | 0 | 0 | 81000-83999 | 14.269 | 0 | 0 |
| 28000-28999 | 5.802 | 0 | 0.000 | 56000-57999 | 11.2 | 0 | 0 | 84000-86999 | 16.299 | 0 | 0 |
| 29000-34999 | 6.191 | 0 | 0.000 | 58000-69999 | 11.95 | 0 | 0 | 87000-104999 | 17.39 | 0 | 0 |
| 35000-39999 | 6.191 | 0 | 0.000 | 70000-79999 | 11.95 | 0 | 0 | 105000-111999 | 17.39 | 0 | 0 |
| 40000-50000 | 6.191 | 0 | 0.000 | 80000-100000 | 11.95 | 0 | 0 | 120000-150000 | 17.39 | 0 | 0 |

| Axle load (lb) quad axle | EALF | Number of axles | ESAL | Axle load (lb) 5-axle | EALF | Number of axles | ESAL |
|---|---|---|---|---|---|---|---|
| under 12000 | 0.001 | 3538 | 2.425 | under 15000 | 8E-04 | 583 | 0.488644 |
| 12000-15999 | 0.005 | 9028 | 43.069 | 15000-19999 | 0.006 | 489 | 2.852668 |
| 16000-19999 | 0.012 | 33481 | 416.636 | 20000-24999 | 0.015 | 330 | 5.021535 |
| 20000-23999 | 0.028 | 42015 | 1159.540 | 25000-29999 | 0.034 | 286 | 9.651874 |
| 24000-27999 | 0.054 | 26040 | 1418.995 | 30000-34999 | 0.067 | 342 | 22.78927 |
| 28000-31999 | 0.099 | 17060 | 1681.597 | 35000-39999 | 0.121 | 479 | 57.73548 |
| 32000-35999 | 0.166 | 13599 | 2263.712 | 40000-44999 | 0.204 | 835 | 169.9671 |
| 36000-39999 | 0.266 | 15151 | 4029.247 | 45000-49999 | 0.325 | 1287 | 418.529 |
| 40000-43999 | 0.406 | 23421 | 9504.019 | 50000-54999 | 0.496 | 2168 | 1075.785 |
| 44000-47999 | 0.596 | 35393 | 21081.570 | 55000-59999 | 0.728 | 3633 | 2646.155 |
| 48000-51999 | 0.846 | 54083 | 45740.202 | 60000-64999 | 1.034 | 5839 | 6038.654 |
| 52000-55999 | 1.167 | 79669 | 92950.571 | 65000-69999 | 1.427 | 6749 | 9628.674 |
| 56000-59999 | 1.569 | 101051 | 158580.871 | 70000-74999 | 1.919 | 5540 | 10631.25 |
| 60000-63999 | 2.064 | 97171 | 200587.404 | 75000-79999 | 2.524 | 3611 | 9115.046 |
| 64000-67999 | 2.662 | 0 | 0.000 | 80000-84999 | 3.255 | 0 | 0 |
| 68000-71999 | 3.373 | 0 | 0.000 | 85000-89999 | 4.125 | 0 | 0 |
| 72000-75999 | 4.207 | 0 | 0.000 | 90000-94999 | 5.145 | 0 | 0 |
| 76000-79999 | 5.175 | 0 | 0.000 | 95000-99999 | 6.328 | 0 | 0 |
| 80000-83999 | 6.286 | 0 | 0.000 | 100000-104999 | 7.686 | 0 | 0 |
| 84000-87999 | 7.550 | 0 | 0.000 | 105000-109999 | 9.232 | 0 | 0 |
| 88000-91999 | 8.979 | 0 | 0.000 | 110000-114999 | 10.98 | 0 | 0 |
| 92000-95999 | 10.585 | 0 | 0.000 | 115000-119999 | 12.94 | 0 | 0 |
| 96000-99999 | 12.380 | 0 | 0.000 | 120000-124999 | 15.14 | 0 | 0 |
| 100000-103999 | 14.378 | 0 | 0.000 | 125000-129999 | 17.58 | 0 | 0 |
| 104000-107999 | 16.596 | 0 | 0.000 | 130000-134999 | 20.29 | 0 | 0 |
| 108000-111999 | 19.050 | 0 | 0.000 | 135000-139999 | 23.3 | 0 | 0 |
| 112000-115999 | 21.760 | 0 | 0.000 | 140000-144999 | 26.61 | 0 | 0 |
| 116000-139999 | 23.218 | 0 | 0.000 | 145000-174999 | 28.39 | 0 | 0 |
| 140000-159999 | 23.218 | 0 | 0.000 | 175000-199999 | 28.39 | 0 | 0 |
| 160000-200000 | 23.218 | 0 | 0.000 | 200000-250000 | 28.39 | 0 | 0 |

ESAL for all trucks weighted : 2253983.791

Truck factor = $\frac{\text{18-kip ESALs for all trucks weighted}}{\text{Number of trucks weighted}}$ = $\frac{2.254E+06}{1.08E+06}$ = **2.096**